ACOUSTIC METAMATERIALS COMPRISED OF DEAD-END PORES AND BLACK HOLE EFFECT FOR LOW FREQUENCY SOUND ABSORPTION IN LINEAR AND NONLINEAR REGIMES

Daniel Craig Brooke

A PhD thesis submitted to the University of Salford in accordance with the requirements for award of the degree of Doctor of Philosophy in the Faculty of Computing, Science and Engineering at the Acoustics Research Centre.

Supervisors – Dr. Olga Umnova * Prof. Philippe Leclaire

August 2021

Abstract

The aim of this work is to design and test acoustic metamaterial absorbers particularly for mitigation of low frequency sound of high intensity. The absorbers designed are formed of a series of plates with a central perforation, separated by air cavities. Two types of structures are investigated: the first has a central perforation with a constant radius (pancake structure), while in the second the pore radius gradually decreases along the thickness of the absorber (profile structures). In the structures of the first type, the wave speed reduction is abrupt, while in the second a gradual impedance matching with air is achieved. The structures developed are tested in a range of various experimental set-ups. This includes performing measurements in a conventional impedance tube (linear regime), in a specially modified impedance tube that allows pressures (RMS) up to 250 Pa using sine wave excitation (weakly nonlinear regime for continuous sound) and in a shock tube (nonlinear regime for pulsed sound of amplitude of up to 100 kPa). The models developed allow the predictions of the metamaterial structure performance at low and high sound pressure levels. In order to test the models, the absorbers of various dimensions are built, tested and the results of the measurements are compared with the model predictions. The analytical model for the pancake absorber is used to derive simple formulae for the frequency and the peak value of the absorption coefficient at the lowest frequency resonance in the linear regime, depending on the geometrical parameters. This model is complemented by a Transfer Matrix Model (TMM) and Finite Element Model (FEM) for both pancake and profile structures. The latter accounts for the influence of the structural resonances and tortuosity effect of the plates on the absorber performance.

To investigate the nonlinear regime, flow resistivity measurements are performed on the samples to directly measure Forchheimer's nonlinearity parameter. Flow resistivity measurements at low flow rates show that the periodic set of cavities does not modify resistivity significantly when compared to a simple perforated cylinder with same thickness. As flow rate increases, the flow resistivity grows linearly according to Forchheimer's law and has a significant dependence on the absorber thickness. A nonlinear numerical model is developed accounting for the growth of flow resistivity with particle velocity amplitude in the central perforation and compared with the measurements at high amplitudes of the continuous incident sound. It is confirmed by measurements, that the peak absorption coefficient values for both types of absorbers decrease as the sound amplitude grows (irrespective of dimensions of pore radius and value of open surface area ratio). Where the peak values of absorption coefficient for the pancake absorbers are shown to be significantly reduced compared to the profile structures as amplitude strength grows to nonlinear regime. The resonance frequencies, however, remain close to their measured values independent of amplitude strength and is advantageous for both structures. Measurements in a shock tube are performed in both rigid backing and transmission set-ups, in time domain. Fast Fourier Transform (FFT) is later performed to investigate the signals. It is demonstrated that the profile absorber design is advantageous for the absorption of high amplitude pulsed sound.

Dedication and Acknowledgements

To begin, I would like to express my sincere gratitude to my supervisors, Dr Olga Umnova and Prof Philippe Leclaire for the support given to me throughout the 4 years of the PhD. Your expertise and guidance over the duration of the project has enabled me to continuously learn, grow and improve my knowledge in the field of acoustic metamaterials and rigid porous materials. Your support has been very much appreciated, especially in the domain of modelling and experimental techniques, which have been mastered over the course of the PhD. Your generosity, friendship and professionalism will always be remembered, and I have been greatly privileged to have you as my supervisors. I would also like to express my gratitude to Dr Thomas Dupont for who has provided me with some valuable experimental methods and introduction to FEM modelling. Special thanks also go to Dr Andy Elliott for his advice on experimental techniques involving the shock tube. It has been an honour to work with you all and without your guidance this PhD would not have been possible. Time spent at the University of Salford was very enjoyable and I will forever be eternally grateful to my main supervisor, Dr Olga Umnova. Your expertise and friendship will never be forgotten, and I had the pleasure to learn from you, especially attributing to modelling skills.

To my friends at the University of Salford, I have enjoyed our time spent together, including the trips travelling to conferences, both in the UK and France. I am also forever grateful to Prof Philippe Leclaire for the support and guidance shown to me for my period of time spent in Nevers, France. Your valuable experimental skills and friendship will always be remembered. The support and guidance of both supervisors has enabled me to complete the PhD project and submit this thesis. Thank you for our time spent together and for your friendship. I am also thankful to my friends in Nevers, for your generosity and friendship given to me for my time spent in France. I had some memorable times and wish you all well in the future. To my supervisors and work colleagues, it has been a pleasure and I hope that we may work together again in the near future on exciting new projects. Finally, a special acknowledgement is made to DSTL, for whom this PhD would not have materialised. With the support and funding of the sponsor and especially Prof John Smith – TP, I have been fortunate to be granted the opportunity to travel and present at various conferences, both national and international. Last but certainly not least, I am forever grateful for the unconditional support of my loving family.

To my son Logan Ivan

Contents

List of Figures

List of Tables

List of Symbols

ω – angular sound frequency

P – pressure of sound wave

v – particle velocity of sound wave

c – sound speed in air

ρ_0 – density of air

η – viscosity of air

$C_0 = \frac{1}{\rho_0 c^2}$ - compressibility of air

$k = \frac{\omega}{c}$ – wavenumber of air

N_{pr} – Prandtl number

γ – adiabatic constant

Re – Reynolds number

R – outer radius of the absorber

r_0 – radius of central perforation

d_p – plate thickness

d_c – width of lateral cavity (distance between the plates)

L – absorber thickness

$\rho(\omega), C(\omega)$ – effective density and effective compressibility of air inside the perforation with the lateral cavities

$\rho_p(\omega), C_p(\omega)$ – effective density and effective compressibility of air inside the main perforation without lateral cavities

$\rho_c(\omega), C_c(\omega)$ – effective density and effective compressibility of air inside the lateral cavities

$k_c = \omega\sqrt{C_c(\omega)\rho_c(\omega)}$ – wavenumber of air in the lateral cavity

$q = \omega\sqrt{\rho(\omega)C(\omega)}$ - wavenumber of air inside the absorber

$\phi_p = \left(\frac{r_0}{R}\right)^2$ - surface porosity of the absorber

$\phi_w = \frac{d_c}{d_c + d_p}$ – porosity of the main perforation wall

ξ – Forchheimer's nonlinearity parameter

V_f – flow velocity in the flow resistivity rig tube

$U = \frac{V_f}{\phi_p}$ – flow velocity in the main perforation

$\sigma_{p,c}, \sigma$ – static flow resistivity of the main perforation, cavity, and the whole sample, respectively

$\Lambda_{\mathrm{p,c}}$ - characteristic viscous length for the main perforation and cavity, respectively

$\alpha_{\infty\, p,c}$ - high frequency tortuosity for the main perforation and cavity, respectively

$\kappa'_{p,c}$ - thermal permeability for the main perforation and cavity, respectively

$\Lambda'_{p,c}$- thermal characteristic length for the main perforation and cavity, respectively

f_r – frequency of the first absorber resonance

α_r – peak value of the absorption coefficient at resonance

p_i – incident pressure amplitude

M – Mach number

r_l – normalized specific acoustic resistance

x_l – normalized specific acoustic reactance

r_{nl} – normalized specific acoustic resistance

x_{nl} – normalized specific acoustic reactance

Z_{nl} – nonlinear acoustic impedance

Z_R – normalized radiation impedance

s – entropy

E – Youngs modulus

ν_{poi} – Poisson ratio

κ – heat conductivity

$\boldsymbol{V}$ – vector of components u, v, w

ψ – velocity potential

x_s – shock formation distance

ε – medium nonlinearity

δ – dissipation in medium

i , j – imaginary unit of complex number

1. Introduction

Sound waves are encountered each day and in most cases provide only a small deviation around atmospheric pressure. This regime is known as linear acoustics. However, if the amplitude of a sound wave is large enough so that pressure disturbance is relatively high (but still much smaller than atmospheric pressure) then the assumptions of nonlinear acoustics break. High amplitude sound resulting from e.g. factory noise or explosions is harmful and should be mitigated. Sound pressure levels considered in this work range between 60 dB and 194 dB. Nonlinear effects (from response of the structured absorbers) begins at approximately 120 dB, therefore, noise mitigating structures must be designed specifically to account for high pressure amplitudes. It is shown later that implemented designs combined from [1-3] can be effective for a better control of noise reducing methods compared to conventional materials. The behaviour of nonlinear acoustic waves differs depending on medium properties, dispersion (sound speed dependence on frequency) and sound energy dissipation and, of course, the type of the dominating nonlinearity. Examples of high intensity sounds include those from tornados, jet engines and explosives.

Nonlinear acoustics, also known as acoustics of weak shock waves, could be considered relating from dynamics of compressible flow in fluids and thermodynamics. Wave speed of high amplitude waves in fluids grows with their amplitude. The Mach number is a dimensionless quantity that describes the ratio between the local speed, such as particle velocity in the wave, and the sound speed [4]. Even at relatively low Mach numbers in gases and liquids for nonlinear acoustics and continuum mechanics [5-6] an originally sinusoidal wave is transformed into a saw-tooth profile due to their peaks travelling faster than troughs. The shock front is formed some distance away from the source. The well-known Burgers equation becomes an appropriate solution of the propagating wave in this case. The wave profile will rapidly become linear where smoothing from dissipative and dispersion factors dominate during the nonlinear distorsion of the acoustic wave. An example of a typical shock formation is shown by Figure 1.1. which illustrates a high intensity wave forming a propagating sawtooth profile. Due to attenuation of the propagating shock wave from dispersion effects the amplitude decreases and becomes linear.

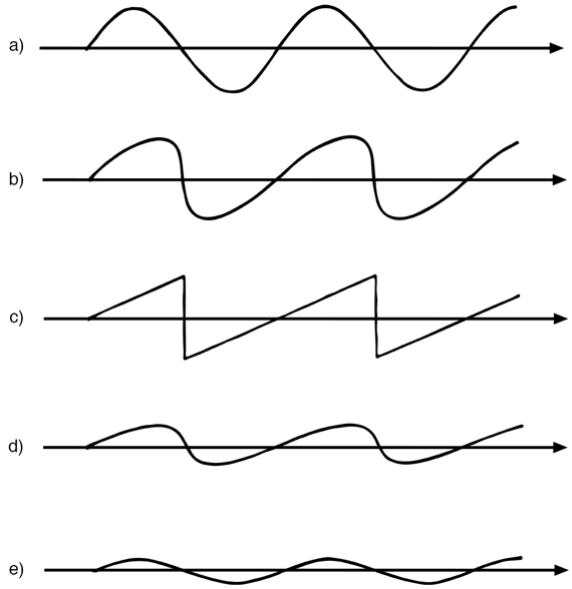

Figure 1.1. Stages of an intense sound wave propagating some distance away from a source. (a) A pressure signal close to an intense source. (b) The signal becomes distorted after small time propagating away from the source. (c) The shock wave becomes fully developed and takes a sawtooth wave profile propagating away from the source. (d) Dissipation of the aging shock wave after loss of the higher-frequency components. (e) The amplitude of the shock wave is reduced after attenuation of the former propagating shock [136].

An extensive literature review of simple and more complex structures is presented in Chapter 3, however, in this Chapter, the reader is introduced to some background knowledge consisting of simple perforations, micro-perforated sheets and design of the structures investigated within this work. Investigation of conventional materials under high amplitude acoustic excitation has been studied first for simple designs. Single orifices and the resultant acoustic phenomena have been of interest for many decades. For example, in 1935 work Sivian [17] studied acoustic flow with singular orifices to determine the acoustic reactance, and resistance parts of impedance. Later, Westervelt [18] investigated orifice interactions with finite amplitude acoustic waves, and around the same time, Ingard and Labate [19] investigated the acoustic circulation effects and nonlinear impedance of orifices. Slightly later still, in 1958 Lippert [20] measured sound transmission through orifices in ducts with application to resonators. Micro-perforated panel absorbers (MPPAs) where many perforations exist at the sample surface are later studied, for example in [22], [24], [32 – 33], [35] and [75] nonlinear effects at orifices have been investigated. The MPPAs are commonly good candidates for noise attenuation at high sound pressure levels. A cavitation after a perforated sheet is investigated for low and high sound pressure levels, for instance, see work by Maa [37], who introduces a model relating Mach number and the wave interaction with the fluid at the orifices.

The model is later modified by Parks [36] who uses sound pressure level instead of Mach number to investigate linear and nonlinear acoustic phenomena due to vibrating fluid interaction with orifices. Other rigid porous materials have been explored including nonlinear effects at high sound pressure levels, for example see work by Umnova et al [39 – 40]. Furthermore, other type of materials that have been investigated as interacting with high amplitude sound are granular media, where Forchheimer's nonlinearity and transient effects have been investigated by Turo and Umnova [41]. Metamaterials first appeared at the turn of the millennium resulting from Sir John Pendry's work in electromagnetism [137]. Pendry was influenced by the work of Victor Veselago who in 1968 investigated the thermodynamics of

isotropic substances with negative permeability and permittivity. [138]. Possibilities of acoustic metamaterials was realised soon after and since has led to the investigation of perfect absorbers, acoustic cloaking, acoustic flat lens, and double negative materials constituting of negative mass and bulk density [107]. Hence, these metamaterial structures are more advanced than the conventional materials and have been leading the way for control of acoustic waves [7]. The interaction of such meta-structures can manipulate and therefore alter natural characteristics of the waves. Metamaterial bulk properties arise from its material features and in some circumstances, the associated macroscopic parameters (effective density and bulk modulus in acoustic metamaterials) can attain negative values (analogous to electric permittivity and permeability used in electromagnetics where the parameters can also become modified). The effective density and bulk modulus of structures investigated within this thesis is shown later (see Chapter 6) accounting for their properties used for predicting the peak absorption and first resonance frequency of the absorbers. From being artificial structures, the metamaterials are specifically designed with particular applications in mind, and this depends on which wave is to be manipulated and for what purpose. Applications can include acoustic total absorption, negative refraction, and others [8]. The principal objective of this research is to develop an effective absorber based on metamaterial design for shock wave or continuous high amplitude wave absorption. Shock waves are high amplitude signals hence material and (possibly) air nonlinearity is essential to this task. The absorbers have to be effective for high amplitude sound and they also have to be structurally robust, withstand high temperatures and mechanical load but be relatively thin and light for application. The idea investigated in this work is based on combining both acoustic black hole effect (ABH) and dead-end pore design (DEP) to achieve an effective absorber for high intensity sound. The former (ABH) benefits in being able to accomplish broadband absorption in frequency domain. Moreover, in the latter (DEP) design utilises its lateral dimensions for acoustic wave absorption and slows down wave speed. These metamaterials are frequency selective and rely on resonance phenomena for impedance matching with air to achieve maximum absorption of incident sound. These two conceptual approaches are investigated throughout the thesis. In structures with DEP, see references [1],[3],[44],[45], fluid propagates along a waveguide axis and encounters lateral dead-end pores from structured material which could be 3D printed or achieved otherwise. The DEP are suggested first by Leclaire et al [1] involving dead-end channels, and later investigated by Dupont et al [3] where the dead-ends are circumferential in the material design. Low frequency first resonance peaks are achieved in the linear regime by propagation of acoustic waves.

In ABH design [2] the dead-ends are combined with a varying radius of the main pore along the sample length, and utilises gradual impedance matching with air. Work by Mironov and Pislyakov [2] show that acoustic wave amplitudes in retarding structures consisting of periodically arranged rings, decreases to zero with only a small amount of dissipative material required at its far end. This is achieved due to the existence of the structural cavities between consecutive rings that have constant outer radius, while gradually decreasing the radius of the main channel. To be effective, the thickness of the structure needs to be comparable to sound wavelength. It should be noted that in the original study by [2] viscous and thermal losses inside the cavities including central perforation were not considered. Furthermore, they focus on very low sound levels only. However, in this thesis, the losses have been accounted for and is shown to be essential in calculating the absorber performance. The metamaterials are

investigated at both low and high sound pressure levels (Chapters 4 – 7) and moreover, dimensions of the structures are much smaller, compared to that of [2]. DEP and ABH (pancake and profile) structures are shown by Figures 1.2 – 1.3 which illustrate the internal configurations of the designs. Figure 1.2 a. shows DEP configuration from [1]. Volume of the dead-ends is later maximised by using a series of distributed cavities in a periodic arrangement, shown in Figure 1.2 b [3]. It is demonstrated in Figure 1.3 a retarding structure encompassing acoustic black hole effect and takes advantage of impedance matching capabilities. The design is first introduced by [2] shown by Figure 1.3 a, and built later by [103], see Figure 1.3 b.

(a) (b)

Figure 1.2. Dead-end pore design utilising sample lateral dimensions (a), and dead-end pore volume maximised (b).

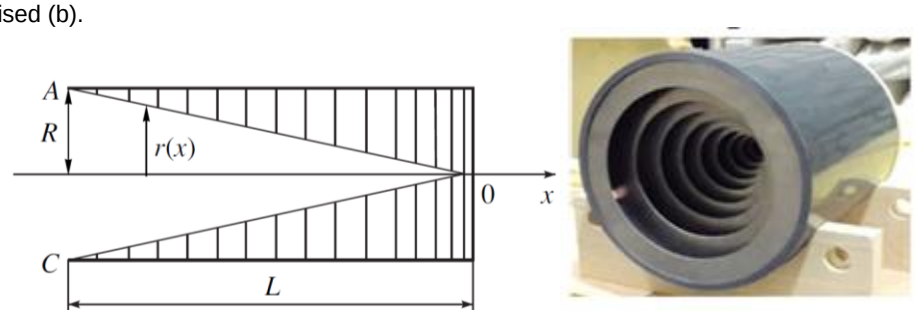

(a) (b)

Figure 1.3. Acoustic black hole design shown as retarding structures. Central pore decreases to zero (a) and a tapered absorber which is built using its design (b) [2], [103].

Acoustic metamaterial structures shown by Figures 1.2 – 1.3 are just few examples of a wide range of various structures that exist. For instance, flexural waves in tapered plates have been investigated by many authors for the damping of resonant flexural vibrations, see references [92-97] which for example use the concept of ABH in the form of truncated and profile quadratic wedges. The ABH design for tapered wedges was first suggested by Krylov [9] to deal with the absorption of flexural waves in plates. They consist in gradually decreasing the thickness of the plate towards its edges thus creating a wave speed profile. Theoretically, the wave speed is decreased to zero meaning full absorption. In practice, small number of absorbers is attached to the plate edge to absorb the residual waves. Since ABH effect for airborne sound was first given by [2], other profile duct terminations have also been investigated and can be seen in [104]. ABH design has been explored as an omnidirectional absorber, consisting of metamaterial matching layer and a porous core [10]. More details of all the structures, both simple, conventional and the metamaterial designs can be seen in Chapter 3 which presents a literature review.

1.1. Project Motivation

Sponsorship of the PhD reasearch project that lead to this thesis has been provided by the Defence Science and Technology Laboratory DSTL, and is part of the Anglo – French PhD scheme, 2016 – 2020.

Due to high amplitude waves resulting from blast explosion, there is a need for effective sound absorbing materials with consideration of environmental characteristics involving temperature variations, flow and motion. Absorbers for nonlinear high amplitude acoustic waves are in high demand especially in areas such as aerospace and engineering, including defence and military purposes. The magnitude of the sound intensities considered throughout the thesis would naturally be discovered from the form of blast or shock waves. Large sound amplitudes could also result from machinery or large turbines, where high sound pressure levels may exist. Extensive research efforts have been applied with emphasis of controlling a particular sound waves path in order to minimise any of its reflected energy. Conventional materials which may contain structures with simple perforations, foams or fibres are disadvantaged and could require to being developed bulky in order to absorb energy effectively arising from high sound pressure waves. The rigidity is also of importance within the design, since the absorbers must be capable to withstand large pressure amplitudes. Acoustic metamaterials have an advantage over a general, or conventional absorber since they are tailor-made to this specific application. They are commonly built involving a periodic arrangement of the cells that are contained in the structure. The control of a sound waves path or moreover, its disturbance to an absorber can be tuned to output the desired performance.

1.2. Aims and Objectives

The project aims at developing acoustic metamaterial structures that are able to be effective for low frequency sound absorption in linear and nonlinear regimes. The absorbers are to be built with consideration of high sound impact, temperature variations, and must be robust. A key focus of the structures is to achieve broadband absorption and/or large peak values of absorption coefficient. Metamaterial structures investigated throughout the project are optimised so that the first resonance frequency of the absorbers is the lowest possible for lengths $L = 30\ \mathrm{mm} - 60\ \mathrm{mm}$ for pancakes and $L = 60\ \mathrm{mm} - 100\ \mathrm{mm}$ for profiles. A key focus of the reasearch is that both linear and nonlinear acoustic waves are to be absorbed effectively in the low frequency range – less than 1600 Hz. The metamaterial absorbers are to be designed and tested for its performance in both linear and nonlinear regimes; where the former benefits from impedance tube use, and the latter obtained due to a specially modified impedance tube based at ISAT – Nevers, France. Shock tube measurements are performed for the testing of extreme pressure amplitudes, against the developed designs in the advanced acoustics labortaory based at Salford, UK.

1.3. Challenges and Statement of the Problem

There are many challenges which must be overcome in order to achieve the aim of developing a structure which is able to withstand the mechanical load of high intensity acoustic waves. Some of the requirements of the absorber design are shown in Table 1.1. Viscous and thermal losses are also required to be tuned for since it is these losses that contribute to the absorbers achieving low frequency sound absorption. Viscous losses are mainly associated with the main pore channel of the structures, while the cavities by the separation of plates contribute mainly to the thermal losses. A series of distributed cavities are built in the pancake and profile designs with several thicknesses. Various cavity depths are investigated and accounted for in computing the performance of the structures and compared with experimental data. Introduction to some of the challenges are presented below. A short description is given to satisfy the requirements of the problem. Several experimental procedures have been performed to measure the performance of the absorbers structures. These are the following;

- Impedance tube, continuous sound, low sound pressure levels.
- Modified Impedance tube, continuous sound, high sound pressure levels.
- Flow resistivity measurements at low and high flow rates.
- Accelerometer measurements of structural vibrations.
- Shock tube measurements, pulsed sound, high sound pressure levels.

Determining absorption coefficient values.

The acoustic properties of the structures are measured to obtain the performance of the absorbers using a standard impedance tube at frequencies between $f = 50\ \mathrm{Hz}$ and $f = 1600\ \mathrm{Hz}$. Sound source is white noise excitation and radius of the tube is $R = 50\ \mathrm{mm}$. Two microphone and three microphone methods have been used to obtain the surface impedance of the DEP and ABH designs (pancakes and profiles). Data obtained at low sound pressure levels enables the absorption coefficient to be determined as well as the resonance frequencies. Peak absorption values are selected from the data obtained, beginning with the first resonance frequency of the absorbers, and later investigated in a specially modified impedance tube (with increased sound levels, around 142 dB). Pancake and profile measurements have been performed at the frequency of the absorption coefficient peaks. Sine wave excitation measurements are performed at high sound pressure levels (HSPL) since there is no guarantee that each frequency component has the same amplitude if white noise excitation is used. This method of using sine wave excitation allows better control over the amplitude of the incident wave by investigating individual frequencies of interest. Linear and nonlinear measurements performed in the specially modified impedance tube are presented in Chapter 4.

Measuring flow resistivity of the structures and Forchheimer's nonlinearity.

Flow resistivity measurements have been performed to obtain the static flow resistivity values on several absorbers, including solid cylinders with same thickness. The samples were built having the same value of the central perforated radius. The latter was measured to investigate the effect of lateral cavities on the flow resistivity values, for comparison of samples with and without cavities. Static flow resistivity of the samples is measured for as low flow velocity as is allowed by the setup. The flow rate is later increased drastically in order to obtain values of the Forchheimer's nonlinearity, describing the increase

of flow resistivity with flow rate. Values of the Forchheimer's nonlinearity parameter are required to validate the experimental data for those performed at high sound pressure levels. These values are used by a developed model to predict the absorption coefficient for several absorbers.

Determining the performance of pancake and profile structures at extremely large pressures.

The investigation of nonlinear acoustics is possible due to shock tube use where shock waves of various amplitudes up to 100 KPa are created and later analysed. Structures consisting of simple and more complex geometry are measured in rigid backing and transmission set ups. A thorough investigation of the structures which involve conventional samples including the developed designs have been measured in time domain. Modifications of the absorber material design throughout the length of the project has enabled improvements of sample efficiency and effectivity from previous prototypes.

The challenges encountered in the design and modelling include the following.

Viscous and thermal losses must be accounted for predicting the absorber performance.

Several computation techniques are used to model the performance of the structures and account for viscous and thermal losses within the structure of the incident wave. Theoretical results are necessary to predict optimum performance of the absorbers and the first resonance frequency.

Main perforation of the profile absorber is required to be adapted from the pancake absorber.

Profile structures are more complex than the pancakes. For instance, profiles include a varying central pore radius and differs from the pancake absorber design, which utilises a central pore with constant radius. The decision about the variations of the perforation radius across the sample length is selected based on the modelling results.

Further challenges and the requirements to the designs are summarised in Table 1.1.

Requirements for the absorbers	**Achieved result regarding the absorber requirements**
Sample length is required to be short.	The structures are developed being only a few centimeters thick.
Samples have to be robust and withstand high impact.	The Pancake and Profile absorbers are built first as prototypes with 3D printer technology and later built with metallic material.
Temperature variations of samples to be considered.	Final structures are built with metallic plates and rings. This means that the absorber designs could be used in high temperature environments.
Ease of assembly/disassembly	3D printer technology is used and employs quick manufacture. Additional metallic design enables the absorbers to be quickly and easily configured.
Low frequency sound absorption.	Structures have been developed to account for low frequency sound absorption whilst maintaining a short sample length.
Designs must be capable of achieving peak values of sound absorption at low	Pancake absorbers are able to attain sound absorption with large peak values at several resonance frequencies and

frequencies including broadband sound absorption.	broadband sound absorption is achieved for the profiled designs.
Absorbers must consider both linear and nonlinear regimes.	The structures are measured for both low and high sound pressure levels ranging 60 dB – 194 dB. Retarded profiles are proven to be more resistant to performance deterioration at high amplitudes.
Viscous and thermal losses to be accounted for within the structures in both linear and nonlinear regimes.	Computational methods have been performed to predict the performance of the absorbers accounting for viscous and thermal losses. Comparisons are later made between the theoretical and experimental data.

Table 1.1. Requirements of the absorber design and its solutions.

2. Thesis Structure and Methodology

To fully investigate the metamaterial designs it is therefore proposed to carry out multiple measurements for each structure testing the absorbers in different sound environments (two impedance tubes and a shock tube, various sound amplitudes, frequencies, and pulse durations) for determination of their performance. Pancake and profile absorbers are modelled using computational and analytical methods. The thesis begins with a foundation comprising simple structured materials and progressively introduces the investigation of further material designs. Section 2.1 gives a general description of the outline for each Chapter and an overview of what is presented. In section 2.2 modelling techniques are given which have been performed to investigate the absorber performance computationally. Section 2.3 presents the experimental methods used through the project duration to determine the absorber performance physically.

2.1. Thesis Chapter Overview

The outline of content is presented here with a short description of each chapter.

- **Chapter 1.** Introduction. Main scope of the research is presented and project motivation for design of acoustic metamaterial structures considered in this thesis. Overview of the project including aims and objectives and main scope of the absorber configurations is given. Challenges of work to overcome and statements of the problem are presented.
- **Chapter 2.** Thesis Structure and Methodology. Provides the proposed outline and structure content which makes up the thesis. Experimental methods are introduced for determining the performance of the metamaterial designs. Thesis aims and objectives are also presented in order to give the reader clarity of the work investigated and the challenges involved.
- **Chapter 3.** Literature Review. A literature review is presented from existing works which investigate sound absorbing qualities and behavior of rigid porous media and single perforations in thin plates. The reader will be able to identify various porous materials which have been studied previously by many authors. A background of works is presented dating around a century and leads to the current time. Models are presented which allow determination of rigid porous materials properties including conventional and metamaterial designs.
- **Chapter 4.** Experiments for Continuous Sound. Impedance tube measurements with continuous sound are described in both linear and nonlinear regimes for the metamaterial structures (both pancake absorbers and profile structures). The data obtained from direct measurements are presented and comparisons are given of the results, for sample performance.
- **Chapter 5.** Flow Resistivity Measurements. Experiments are described to obtain the values for the flow resistivity of the structures, notably the metamaterial pancake absorbers, for both low and high flow rates. This is necessary in order to use the values to determine the absorber performance at high sound pressure levels, where the Forchheimer’s nonlinearity parameter is used to validate the measured impedance tube data with a developed model.

- **Chapter 6.** Frequency Domain Models and Comparisons. Model comparisons with the measured data is given which involves the results from analytical, TMM and FEM approaches. A developed model is presented which accounts for absorber effective properties and allows validation of the measured data for high sound pressure levels. Frequency domain is investigated for the metamaterial structures and absorption coefficient compared for both designs, with varying microstructure parameters.
- **Chapter 7.** Shock Tube Measurements. The metamaterial structures are tested in the shock tube in time domain. This is when the pressure amplitude is largest and the wave interaction with a metamaterial is highly nonlinear. Various amplitudes are investigated ranging between 10000 Pa and 100000 Pa (approximately 194 dB). Incident and reflected shocks are measured prior to, and after the samples. The results are presented with a combination of time domain and frequency domain analysis, where the latter is obtained after performing FFT on the signal data.
- **Chapter 8.** Conclusion and Future work**.** The main body content of the work in this thesis is summarized with the findings of the research and moreover, future work is considered for progression of the studies.

2.2. Modelling Techniques

To predict the performance of the metamaterial structures contained in this work, various models are investigated which ultimately enable the comparison of the measured results with their predictions.

Transfer Matrix Method. A TMM used allows for the determination of the absorption coefficient for the structured designs. Both pancake and profile absorbers are investigated using a TMM approach and is later compared with the experimental data, obtained by performing measurements in a specially modified impedance tube. Comparisons are made in linear regime.

Effective Properties. A model is developed which accounts for the metamaterial effective density and its effective compressibility. The model also predicts the first resonance frequency of the absorbers and enables peak values of the absorption coefficient to be compared with the measured impedance tube data. This allows for the determination of low frequency sound absorption for the metamaterial structures. The effective properties model begins with linear regime approximation and is later extended accounting for nonlinear regime of the absorbers, i.e. including Forchheimer's nonlinearity. The data computed by the model is later validated with both low and high sound pressure level measurements, obtained in a specially modified impedance tube.

COMSOL Multiphysics. FEM modelling is performed which considers the metamaterial geometry being induced with acoustic and vibrational interactions. Acoustic performance of the absorbers is investigated with addidtion of fluid and mechanical disturbance of the material frame. Evaluation of the sound absorption properties of the structures is possible due to the design of a virtual built impedance tube. The FEM data is later compared with experimental data obtained by impedance tube use. Comparisons are made in linear regime.

Fast Fourier Transform. FFT is performed on time domain signals of the measured data obtained from shock tube measurements. Absorption coefficient is determined for the metamaterial structures targeted with high amplitude shock waves. Energy absorption coefficient is also calculated using the spectral density of the data and pulse spectra obtained.

2.3. Experimental Methods

The experimental methods used in this thesis are based upon a combination of several techniques involving continuous and impulsive sound sources (which include white noise and pure tone excitation including shock waves). Flow resistivity measurements are also performed which is necessary for investigating absorber nonlinear capabilities. A brief introduction is given below for each of the experimental set-ups.

Low Sound Pressure Level (LSPL) Impedance Tube Measurements**.** Linear regime impedance tube measurements are performed in order to investigate a samples performance when targeted with sound pressure levels between 60 dB and 100 dB. This is also the starting point of determining the sound absorbing qualities of all the samples investigated and is essential for future works where measurements are performed with a much higher sound pressure level i.e. HSPL experiments. Sound source used is white noise excitation. The measurements are performed in frequency domain.

High Sound Pressure Level (HSPL) Impedance Tube Measurements**.** The sound source is significantly increased from LSPL and investigates the metamaterial designs (pancake absorbers and profile structures) at high sound pressure levels with white noise excitation (100 dB – 120 dB) and under sine wave excitation. The sound source for the latter is able to achieve sound pressure levels at approximately 150 dB. When the sound pressure level reaches around 120 dB and above, the weakly nonlinear regime becomes apparent. The HSPL impedance tube measurements allow the convergence between linear and slightly nonlinear regimes to be explored. The measurements are performed in frequency domain.

Flow Resistivity Measurements. Several measurements are performed for the metamaterial pancake and profile structures (including conventional samples for reference) where a fluid flow rate is targeted at the samples. Air leakage is prevented by using sealing tape and vaseline, including securely fixing the sample and tubes by a bolt fixing mechanism. The Measurements are performed altering the flow velocity in order to obtain values of flow resistivity and Forchheimer's parameter. Flow resistivity measurements allow the determination of sample permeability and its sound absorption capabilities.

Accelerometer Measurements. To investigate mechanical disturbance applied to the material frame of the structures the absorbers have been tested by using an accelerometer, attached to the sample surface.

Shock Tube Measurements. Metamaterial pancake and profile structures are explored when induced with extremely high sound pressure levels, where pulsed excitation with sound pressure levels around 194 dB are achieved. The sound source differs from the applied continuous sound of the impedance tube to where sound source becomes impulsive, for the shock tube. The pulses of various amplitudes

and durations are generated by rupturing membranes of different tensile strength. The measurements are performed in the time domain. Further details of performing the measurements mentioned above are presented later in each of the respective Chapters 4-7 (for each of the metamaterial structures and their various configurations.

Experimental methods are illustrated in in Figure 2.1 showing impedance tube and microphone positions (a), shock tube set-ups and sample position (b) and flow resistivity rig indicating sample location and direction of fluid flow.

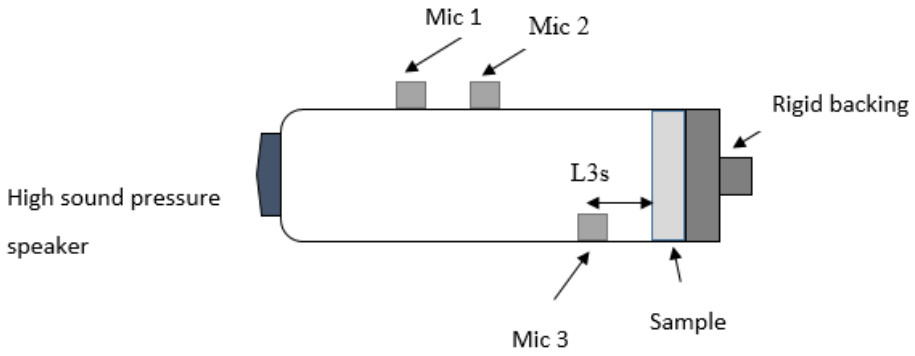

(a)

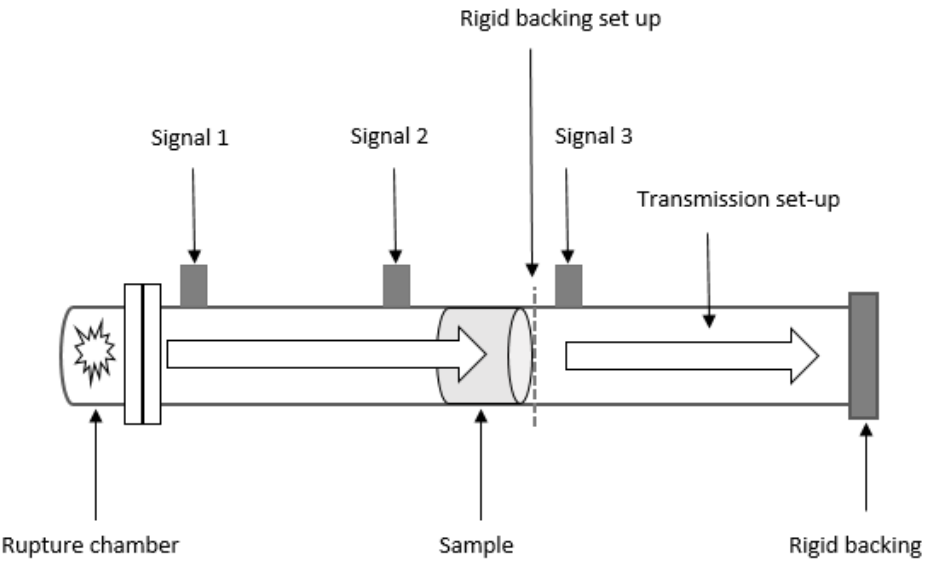

(b)

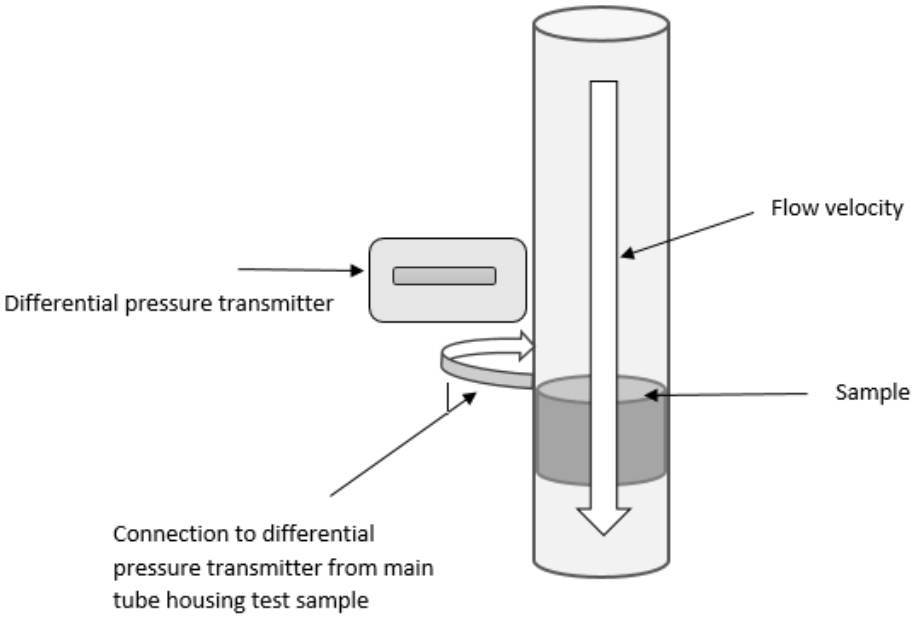

(c)

Figure 2.1. Illustration of the various method used to investigate the performance of the developed samples. Impedance tube set-up is shown in (a), shock tube with sample position and set-ups (b) and flow resistivity rig indicating sample position and region of flow (c).

3. Literature Review

Main scope of Chapter 3 is to introduce the reader to the principles of acoustic wave propagation and a literature review containing porous media and the metamaterial designs considered in the scope of the thesis. The starting point naturally is linear acoustics which considers propagation of sound waves consisting of low amplitudes and hence small deviations of pressure, density, and temperature from their equilibrium values. This is followed by considering air nonlinearity and Burger equation for weak shock waves which considers an acoustic wave undergoing sudden changes in pressure, density, and temperature thus an increase in thermal energy and increased wave speed. Shock waves have been created and then their interactions with the samples analysed and discussed in Chapter 7. The leading nonlinearity in porous samples, i.e. Forchheimer's nonlinearity leading to the growth of flow resistivity with flow velocity, is then discussed in this review. The laboratory measurements of flow resistivity at high flow are presented in Chapter 5. The interaction of an acoustic wave with a thin plate containing a single orifice is then brought to the reader's attention. This is followed by investigating a plate with a combination of many pores distributed over its surface area known as a micro perforated plate absorber (MPPA). The idea of maximising the volume porosity of a structure by introducing very flat thin distributed cavities, by arranging thin plates progressively, leads to the introduction of an artificial material (metamaterial) which allows control of the reflected and transmitted waves. This concept is one of two approaches to the development an effective metamaterial sound absorber developed in this thesis. The metamaterial structure is known as a 'pancake absorber' studied in [3, 45] and is based on the earlier introduced concept of "dead end pores" (DEP) [1]. It is shown to be an effective design for attaining low frequency sound absorption of linear acoustic waves and was first designed and tested by Leclaire et al [1,3]. The pancake structure is built and tested, and the main results are presented in Chapter 6. A design which utilises DEP (as in the pancake design) is combined with another approach which uses "acoustic black hole effect" (ABH). ABH design is a sound retarding structure that enables broadband absorption and was first described by Mironov & Pislyakov [3]. The ABH effect, allowing gradual impedance matching, is achieved by modifying the internal configuration so that the central pore radii of the plates vary along the structure length. The ABH design is discussed in more detail in Chapters 6 and 7 for measurements performed in both the linear and nonlinear regimes. Note: to keep originality of author's work imaginary units i and j are presented in the literature review thus, keeping time convention adopted by the authors. However, in the models developed as part of this project (see Chapter 6, Model Comparisons) time convention $e^{-i\omega t}$ is assumed.

3.1. Linear and Nonlinear Acoustic Waves in Air. Burger Equation and Air Nonlinearity

For any sound to propagate, a disturbance within a medium must first take place. The speed of the disturbance (wave speed) is a characteristic of the medium itself and is mechanical in nature. This disturbance creates a combination of compressions and rarefactions and is the result of density changes which give rise to the nature of a propagating sound wave in a medium such as air. Any wave propagation whether it is sound or light carry energy along the spatial direction of travel and, for the

sound wave in air these compressions and rarefactions result in a longitudinal wave, whereas displacement of air particles is aligned with the direction of wave propagation. The total energy associated with that of the travelling wave is made up of both the potential and kinetic energies and dissipates when a wave is transmitted, reflected, and absorbed. Wave attenuation will occur for any sound wave due to the transfer of a fluid's viscous and thermal energies from the interaction of various velocity layers and because of interaction of another medium. As an acoustic wave propagates its strength will decay in space and time. In three dimensions the so called "geometrical spreading" which results from an inverse square law for spherical sound sources relating the intensity of the wave with the distance travelled, also leads to the decrease of the wave amplitude. The greater the distance a wave travels from its sound source the weaker its intensity at the wave front. However, only plane (i.e. 1D waves) will be considered here, so the spreading effect is not present. Acoustic structures may limit the acoustic wave by making it travel in one direction only such, as that of a waveguide. It is assumed that the wave under consideration travelled in a waveguide with cross section linear dimension being much smaller than its wavelength. Under these assumptions, the wave may be considered as plane. Discussion of the following equations are presented from the text by D.Raichel [50]. For an ideal gas, the wave speed is related to the thermodynamic state of the fluid which is shown by equation of state.

$$p = p(\rho, T) \qquad (1)$$
$$s = s(\rho, T)$$

where p, ρ, s, T is pressure, density, entropy, and temperature, respectively. Because sound velocity depends upon a medium's elastic properties the speed of sound is much more rapid in a medium where the atoms or molecules are closer together and more compact thus the sound speed is much less in gasses than that of solids. For a solid, the speed of sound is defined by its physical properties – modulus of elasticity and the material density and is for a rod shape solid:

$$c = \sqrt{\frac{E}{\rho}} \qquad (2)$$

where E is Young's modulus, and ρ is material density. In the fluid, the sound speed is given as

$$c = \sqrt{\left(\frac{\partial p}{\partial \rho}\right)_s} = \sqrt{\frac{\gamma p_0}{\rho_0}} = \sqrt{\gamma R T} \qquad (3)$$

where γ is the thermodynamic ratio of specific heats $\frac{c_p}{c_v}$ (adiabatic constant), ρ_0 is equilibrium gas density and p_0 the equilibrium gas pressure, R is specific gas constant. We assume adiabatic equation of state $1 + \frac{p}{p_0} = \left(1 + \frac{\rho}{\rho_0}\right)^{\gamma}$ and linearise it. The particle velocity $\boldsymbol{V}$ is the velocity at which the molecules in the fluid are set in motion moving back and forth about their equilibrium states. It is related with the variations of pressure p by the Navier – Stokes equation

$$\rho\left(\frac{d\boldsymbol{V}}{dt} + \boldsymbol{V}.\nabla\,\boldsymbol{V}\right) = -\nabla \mathrm{p} + \eta\nabla^2\boldsymbol{V} + \left(\zeta + \frac{1}{3}\eta\right)\nabla(\nabla.\boldsymbol{V}) \qquad (4)$$

The variations of the entropy s obey the equation of heat transfer:

$$\left(\frac{ds}{dt} + \boldsymbol{V}.\nabla\, s\right) = \frac{\eta}{2}\left(\frac{\partial v_k}{\partial x_k} + \frac{\partial v_k}{\partial x_i} - \frac{2}{3}\delta i_k \frac{\partial v_l}{\partial x_l}\right)^2 + \zeta(\nabla.\mathbf{V})^2 + \kappa\nabla^2 T \qquad (5)$$

Symbols η and ζ denote shear and bulk viscosity coefficients, κ is heat conductivity coefficient. Navier-Stokes equation (4) and equation of entropy conservation (5) should be complemented by the continuity equation,

$$\frac{\partial \rho}{dt} + \rho_0 \nabla . V = 0 \tag{6}$$

to form the full system of equations of motion. The continuity equation or mass conservation where the net flow into a volume is equal to any gain or loss of fluid inside and shown for a compressible flow. If the fluid, however, is stated incompressible which therefore density is equal to being constant (meaning then time/space function not considered) then equation (6) is simplified accounting velocity components in the directions x, y and z and so becomes,

$$\nabla . V = \frac{\partial u}{\partial x} + \frac{\partial v}{\partial y} + \frac{\partial w}{\partial z} = 0 \tag{7}$$

where u, v, w are components of vector $\boldsymbol{V}$. An equation of state is necessary which relates variables of a gas for temperature, pressure, and density.

$$p = c^2 \rho \, , \qquad c^2 = \left(\frac{\partial P}{\partial \rho}\right) \tag{8}$$

The linear regime is defined as the range of pressure, density, temperature, and particle velocity variations where equations of motion and equations of state can be linearized with a good accuracy. For the velocity potential ψ so that $V = \nabla \psi$, in the linear regime, these equations can be transformed into a single wave equation,

$$\frac{\partial^2 \psi}{\partial t^2} - c_0^2 \nabla^2 \psi = 0 \tag{9}$$

If the variations of pressure, density, temperature, and particle velocity are such that the linearized equations of motion and equation of state are no longer accurate, the quadratic and higher order terms have to be considered. Nonlinear acoustics owes its originality to Euler whose equations of momentum and continuity relate gas pressure, density, and velocity for finite amplitude waves [12]. However, it would be over a century later before significant progress was made to describe shock waves more accurately. Nonlinear effects may differ depending on medium properties, amplitude range, wave dispersion and dissipation. Nonlinear acoustics known as physics of weak shock waves could be considered resulting from fluid dynamics, compressible flows, and thermodynamics. At first the study of finite amplitude waves was slow in progress because the thermodynamics notably considering energy dissipation was not quite understood. The velocity of the high amplitude wave c_{nl} is no longer constant but depends on the values of acoustic disturbances. This follows from, for instance, expansion of the equation of state for pressure (1), retaining quadratic terms in ρ. Indeed, starting from adiabatic equation of state $1 + \frac{p}{p_0} = \left(1 + \frac{\rho}{\rho_0}\right)^{\gamma} \approx 1 + \gamma \frac{\rho}{\rho_0} + \frac{\gamma(\gamma-1)}{2} \left(\frac{\rho}{\rho_0}\right)^2$ we have,

$$c_{nl} = \sqrt{\left(\frac{\partial p}{\partial \rho}\right)_s} = \sqrt{\gamma \frac{p_0}{\rho_0} \left(1 + (\gamma - 1) \frac{\rho}{\rho_0}\right)} \approx c \left(1 + \frac{\gamma - 1}{2} \left(\frac{\rho}{\rho_0}\right)\right). \tag{10}$$

It is clear from this equation, that the speeds of the different points of the wave profile are not the same. The compression phase of the profile ($\rho > 0$) moves faster than the rarefaction part ($\rho < 0$). This

phenomenon is known to be due to an irreversible process and the velocity is characterised by a Mach number, defined as the ratio of particle velocity to sound speed [13]. In fluids where a high amplitude initially, sinusoidal wave propagates [14], it is undergoing a change in pressure, temperature, and density, i.e. is transformed into a saw-tooth profile [15]. This, however, happens when the wave travels a significant distance. The so-called shock formation distance is defined as $x_s = \frac{2c^2}{(\gamma+1)\omega v_0}$, where ω is the angular frequency of the sound wave [16]. For a one-dimensional case, the well-known Burger's equation becomes an appropriate means to describe the propagating wave. The formation of a triangular pulse (a visual representation is given in Figure 1.1) is created by a shock front undergoing sudden steepening. The wave profile will rapidly become linear where smoothing from dissipative and dispersion factors dominates during the nonlinear decay of the acoustic wave. The propagation of a one-dimensional wave $\boldsymbol{V} = (u, 0, 0)$ in the fluid with quadratic nonlinearity is described by [16] and leads to the following Burger's equation,

$$\frac{\partial u}{\partial x} - \alpha u \frac{\partial u}{\partial y} = \delta \frac{\partial^2 u}{\partial y^2} \tag{11}$$

where a nonlinear parameter $\varepsilon = \frac{\gamma+1}{2}$ gives nonlinearity of the medium, $\alpha = \frac{\varepsilon}{c_0^2}$ and dissipation in the medium is described by parameter δ, which in the case of viscous losses domination is given as $\delta = \frac{\eta}{2\rho_0 c^3}$. This equation plays a role similar to a wave equation for low amplitude waves. Burger's equation can be further generalised including effects of dispersion [16]. This however is not essential for the waves propagating in simple fluids such as air, where wavenumber k is a linear function of wave speed: $k = \frac{\omega}{c}$. We focus on nonlinear wave propagation in structures, assuming that nonlinearities in air can be neglected. This is ensured by always checking that the distances between the sample surface and the microphones (in shock tube) as well as between the source and the microphones (for high amplitude measurements in the impedance tube) are shorter than shock formation distance. Similar assumption has been made in [43].

3.2. Single Orifices in Thin Plates and MPPAs in Linear and Nonlinear Regimes

Absorption of low and higher levels of sound by using porous absorbers which will be described in 3.3.1. To begin with discussing porous materials, it is necessary to introduce an acoustic wave interaction with only a single pore in a solid plate. The research in this thesis directly focuses on rigid porous materials and so fibrous and foamed porous materials are not concerned. There are many applications of absorber types and notably one of the most promising is a micro perforated panel absorber (MPPA). For applications that require an absorber to be rigid, the scope of multiple orifices becomes of interest. The panel absorber design consists of the arrangement of an array of holes or perforations over a solid surface area and being backed by a cavity. The construction parameters needed to understand the absorptive properties of a rigid porous panel absorber arise from the arrangement of perforated holes separated by a distance and its pore dimensions. Another important parameter is the open to closed surface area ratio. This allows for absorbing a range of pressure waves. Long before micro perforated

plates (containing many perforations) were investigated, simple constructions of a single orifice in rigid plates have been studied, references include for example, works by [17-25]. Over the past few decades, thorough measurements have established the characteristic behaviours for a range of low, medium, and high-sound pressure levels. The interaction of acoustic waves with an orifice has been studied intensively to determine the acoustic nonlinearity and orifice impedance. An illustration of a single pore with incident, reflected and transmitted waves is shown in Figure 3.1.

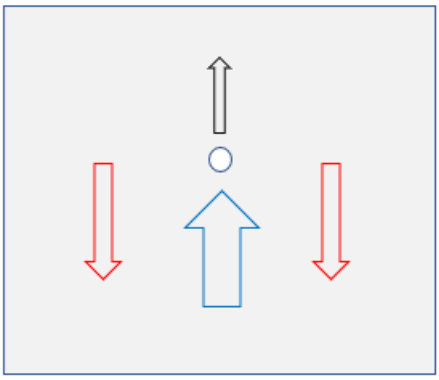

Figure 3.1 A single plate design of small thickness containing a single orifice. Blue indicates incident wave, red reflected and black transmitted.

In 1935 Sivian, see ref [17], investigated impedance of small orifices in steel plates containing circular and rectangular singular arrangements and noted that reactance is independent of particle velocity (hence linear), and explained the nonlinear resistance of very small orifices from kinetic energy loss. In reference [18] in 1947, the acoustic properties of orifices have been investigated using Bernoulli's law. Three years later in 1950 Ingard and Labate [19] had shown that jet formation is seen to exit the holes from circular apertures when being targeted with high amplitude waves, resulting in vortices. The measurement of sound transmission through an orifice in a duct was performed by Lippert in 1958, see ref [20]. Orifices in square ducts and brass plates were tested with low sound pressure levels in order to ensure linearity regime valid for evaluating reflected and transmission loss at low intensities. Ingard and Ising [21] measured oscillatory flow velocity amplitudes for both high and low sound pressure levels. Especially when flow velocity is sufficiently high, [21] considered the case where the oscillatory amplitude of flow is of the same order of magnitude as the steady flow. Uno Ingard see ref [23] later (1970) compares his experimental results from his previous paper in 1968 [21] on nonlinear sound transmission through an orifice to theory, expressing the fact that transmission becomes distorted resulting in change of frequency spectrum from the incident pressure. Other works consisting of acoustic impedance variations by jet flow under medium and high sound pressure levels are carried out by Melling, Hersh, Walker, Sharkawy and Bechert with focus on plates containing orifices, see refs [24-27].

Jet formation in ducts containing a nozzle is later investigated by Cummings in his paper where high amplitude sound transmission through duct terminations [28] is studied. The theory with and without the presence of mean flow has been developed. It is indicated that previous work from [29] and [30-31] agree with the theory considering jet formation and energy attenuation. It is seen that orifice impedance is nonlinear at high amplitudes and states that reflection coefficient significantly reduces because of nonlinearity caused by turbulence. Over the next several years many more papers were published by

Cummings who would describe nonlinear phenomena associated with jet formation by orifices, perforated plates, see refs [32-34] and tube silencers [35]. The nonlinear effects of finite wave interaction with orifices and perforated plates are of interest in applications, where exceptionally high noise levels are to be reduced. An example of this could be the testing of aircraft and vehicle design amongst others, where exceptionally loud noise is created and needs to be attenuated [58-62]. The acoustic energy of a propagating wave is partially converted to vortical energy when a vortex is formed, and results from the interaction of the wave at the origin of an orifice. The vortical energy is transmitted through the orifice and the reflected energy is generated at the solid boundary of the plate. Mostly, the reflected energy is directed back toward the incident path of the wave whereas some of the reflected energy will pass through the orifice because of a pressure difference on either side of the solid boundary [51-55].

One approach of experimental investigation of acoustic waves interaction with orifices is by using a visualization method. Salikuddin and Brown [51] in 1989 investigate the nonlinear effects of finite wave propagation with orifices and perforated plates. They used a camera to photograph an acoustic pulse propagating in a duct and interacting with an orifice at the exit point. At the location of the orifice, a vortex is generated (depending on the orifice dimension and geometry) and observed as a smoke ring. This is known as the visualization method pictured by a camera by means of an electrically heated element which is coated with oil. The interaction of the acoustic wave upon contact of the orifice creates smoke to form, and this smoke produced in the form of a vortex where its speed can be monitored by a camera as it propagates in time. They Investigated the behavior of the reflection coefficient of various sound pressure levels (for low and high sound intensities 100 dB – 147 dB) and showed that the reflection coefficient of the incident sound wave sufficiently minimalizes with increasing sound intensity by nonlinear effects due to the overlapping of reflected waves from the duct termination region.

An analytical model by Cummings and Eversman [28] produced in earlier work in 1983, is used to compare and describe the reflection coefficient from plates containing orifices in ducts and having different open to closed surface area ratios. This was led from work prior in 1980 [57] which see Cummings and Eversman investigate the acoustic energy loss from ducts to the far field at low frequencies, for low and high sound pressure levels. They show that the amplitude of the reflected wave from the boundary for low frequency is seen to depend on the open to closed surface area ratio and varies with sound strength of the incident pulse. Furthermore, it is the nonlinearity of the reflected wave that causes the reflection coefficient amplitude to decrease with increasing sound intensity and observed from measurements when the open to closed surface area ratio is largest. There is a comparable difference between low and high intensity pulses directed toward a termination containing an orifice inside a tube and initiated by a spark. The behavior of the reflected pulses depends upon the acoustic intensity and seen that in one particular case that there is a combination of pulses that come together to form a single pulse (for high intensity pulses) and another case (for low intensity pulses) when various reflections are independent on amplitude strength and propagate with distinct time intervals for each reflection. It is therefore apparent that an acoustic wave in a gas encounters two separate regions (regardless of wave intensity) when directed at a solid plate containing an orifice or a combination of orifices (as for perforated plates). On one hand there is a solid boundary which is the plate itself, and on the other, is an open surface area containing air. An acoustic wave will therefore interact with both regions (solid and gas) upon contact of an orifice/s in a solid plate and result in amplitude difference and

time delay of reflected waves depending on any modification of the wave itself (which is dependent upon the initial wave intensity).

For low sound intensity pulses both the gas and solid regions influences the reflected wave. The interaction of the solid part of the plate causes the reflected wave to propagate slightly before the reflected part of any open area of a plate containing an orifice. This is observed in measurements made by M.Salikuddin and W.H.Brown [51]. However, for the high intensity pulses, there is a significant difference such that the reflected wave is a combination of both solid and gas regions of the plate resulting from the air-nonlinearity and causes the reflections to overlap, thus the reduction in reflection coefficient amplitude. For high sound intensity measurements, the different orifice diameters ranged between 0.125 and 2 mm and reflection coefficient amplitude were plotted for various values of orifice diameter. The model from Cummings and Eversman [28] used to predict the behavior of radiation impedance is compared with the testing of orifices for different intensity strengths. The comparisons are seen to show good agreement for linear sound interaction of orifices and perforated plates where the model is assuming reactance is linear and nonlinear propagation is considered for the resistivity thus modified and computed, to account for high sound intensities.

Cummings and Eversman in 1983 [28] measured the net energy loss by examining the behaviour of sound waves interacting with nozzles and orifices to explain what was observed in Lockheed aerospace measurements. Prior to this, earlier work by Bechert [27] in 1979 measured sound absorption by vortices shedding and works by Howe [30,53] in 1979 – 1980 respectively investigated the effect of edges of orifices and how the energy losses are related by the transforming of partial acoustic energy to vortical energy thus further dissipating into thermal energy. Works by [30, 52,53] consider mean and non-mean flow and note that energy attenuation is the result when the incident wave has large enough amplitude for creation of nonlinear effects. Cummings and Eversman [28] considered both low and high sound levels and describe how the influence of mean flow from nozzle or an orifice creates a jet-like flow for high amplitudes by means of shear layers concerning the nonlinear impedance of the orifice. They describe theoretically from introducing a model using Fourier transformed transient signals. In the paper these graphs are plotted for various perforated plates and nozzles as a function of sound power for a variety of open to closed surface area ratios, including single orifices for duct terminations at high amplitudes to 160 dB. In each plot the sound power transfer function is calculated showing good agreement between comparison of the theoretical and experimental values. In the absence of mean flow and assuming low frequency approximation, they show how the power reflection coefficient differs for a changed value of open to closed surface area ratios and furthermore, state that either a phase or antiphase of the incident and reflected waves exist dependent on orifice dimensions and incident pressure amplitude.

Salikuddin [54] later in 1990 uses an identical approach using the spectral contents from the incident, reflected, and transmitted pulses from similar findings and is accompanied in conjunction as a companion paper to M.Salikuddin and W.H.Brown [51]. These in and out of phase reflected pulses are contribution to the increase of the reflected amplitude and an optimum level of maximum cancellations is found. They explain how the low frequency cancellation alters and is dependent upon the value of in phase reflection propagating along the incident wave path in a conical nozzle being identical in magnitude to the open-end reflection at the nozzle exit. Similar findings are comparable for the case of

single orifices and that of multiple orifices such as perforated plates. M.Salikuddin and W.H.Brown [51] and Salikuddin [54] set out to determine the effect of in and out of phase reflections on initially different size nozzles. They find that the internal reflections are also apparent inside the nozzle due to the contraction ratio by the geometrical difference and angle change along the nozzle shoulder. This is further led to the examining behavior of reflections of single orifices and perforated plates. An FFT signal analyzer is used to compute the complex transfer function in order to gain the complex spectral power reflection coefficient of the termination by Fourier transform. The normalized radiation resistance $\frac{R}{\rho c}$ and reactance $\frac{\chi}{\rho c}$ is determined from finding the magnitudes of the ratio of reflected and incident pressures.

$$\frac{R}{\rho c} = \frac{1 - |\vartheta|^2}{(1 + |\vartheta|^2 - 2|\vartheta| cos\emptyset)} \tag{12}$$

$$\frac{\chi}{\rho c} = \frac{2|\vartheta|^2 sin\emptyset}{(1 + |\vartheta|^2 - 2|\vartheta| cos\emptyset)} \tag{13}$$

where ϑ is the complex reflection coefficient,

$$\vartheta = \frac{P_r}{P_i} e^{i\emptyset} \tag{14}$$

and the normalized radiation impedance Z_R is,

$$Z_R = \frac{\left(1 + |\vartheta| e^{i\emptyset}\right)}{(1 - |\vartheta| e^{i\emptyset})} \tag{15}$$

Plane wave propagation is assumed throughout experimentation so that the incident and reflected powers can be calculated and justified which gives good agreement by measurements by the transmitted power in order to determine the power absorption. Salikuddin [54] expressed the amplitude of the reflection coefficient as the power reflection coefficient so that the power absorption is the power loss and stated in dB.

$$\vartheta = 10\log_{10}\left(\frac{P_r^2}{P_i^2}\right) \tag{16}$$

Later in (1998) Work by Maa [37] investigated microperforated panel absorbers. He set out to determine the effective parameters necessary in order to obtain maximum acoustic absorption of various perforated plates. It was shown that the value of the perforation constant is essential to designing an absorber where there is unwanted fibrous material. This work is built further from his earlier work on the theory and design of microperforated panels for sound absorbing materials [63]. The investigation was based on submillimetre perforations which focuses on wide band sound absorption from the acoustic resistance due to the small radius pores in panels. The approach to fully describe the characteristics needed to build an MPPA uses the frequency dependant acoustic resistance resonance frequency and perforate constant for an absorber characteristic length. An improvement from earlier theories of MPPA's led to developing an approximate formula for all values of the perforation constant (which is proportional to the ratio of the perforation radius to the viscous boundary layer inside the absorber perforations). Maa [37] adopted the specific acoustic impedance of a short tube from works [64-65] and to account for end

corrections more precisely by considering the wave motion in the tubes or pores by [66-67]. This approach allows a more precise calculation for the acoustic impedance for a constant value of the perforate constant between 1 and 10. The work discussed here by Maa is adopted further by Park, see ref [36] which uses the theory by Maa for micro-perforated panels consumed with low and high sound pressure levels for different cavity thicknesses terminated with a solid plate.

Other models have been developed for describing nonlinearity at an orifice, see ref [68] by Jing and Sun in 2001. They describe that it is the rate of vortex shedding at the orifice edge responsible for the nonlinear behaviour along with the speed of the vortex at close distance to the orifice location. In their model they considered that at a small distance close to the outflow point beyond the orifice is a so-called slug. This slug was realised by earlier works of Saffman [69] who indicated that the slug force acts as the body that drives the vortices forward by means of a pushing motion. Jing and Sun [68] validate the proposed model by conducting measurements in an impedance tube by applying a sinusoidal sound pressure and computing the orifice flow in time domain. The jet flow formation through the orifice is accounted for by using values obtained from Rouse and Abul-Fetouh [70] who investigated irrotational flow through an orifice. This is compared to their own measurements by using a hot wire fixed in several locations including the orifice centre in the region close beyond the orifice plate. A semi-analytical model from previous work by Jing and Sun [71] in year 2000 is used to compute the velocity around the orifice, and the associated volume flux. It is reported in [71] that a good agreement is found when compared with impedance tube measurements using a single microphone method. This approach first proposed by Chu [72] is adopted to enable the determination of the impedance to be known. The set up requires the microphone to be placed in two fixed locations of the tube in front of the orifice plate so that independently measured values of the phase and amplitudes can be determined. In their impedance tube measurements, another microphone is also used which considers the pressure at the front surface of the orifice plate itself. The tube set-up consists of an anechoic wedge terminated by a rigid backing boundary, from where a cavity exists directly after the foamed wedge. The behaviour of orifices in series has also been of great interest when the control of fluid flow is required for engineering applications such as the operation of machines, hydraulics systems, noise vibration control and industrial piping systems where corrosion may occur [73]. The behaviour of fluid flow for two orifices in series was investigated by [74] who use computational fluid dynamics to numerically solve for the pressure differences obtained in a piping system.

It is seen that when a fluid flow encounters two orifices separated by a distance of at least one pipe size diameter, it produces a higher recovery rate for the pressure as opposed to a lower recovery rate for pressure at when the last orifice is separated by two pipe diameters. The vena contracta and discharge coefficient is accounted for when computing the jet-like flow. This is necessary for a more valid behaviour and nonlinearity resulting from the maximum fluid velocity of the orifice at tapered outflow point. The design and construction of perforated (millimetre) and micro-perforated (submillimetre) plates as is also another good approach which allows for effective sound absorption in both low and higher sound levels (70 – 130 dB). The pore size and perforation rate or porosity of a perforated panel governs how acoustic effects interact with the plates front surface, and consequently immediately afterwards due to acoustic interaction influencing viscosity and inertial effects. Attalla and Sgard [75] in 2007 showed how these effects can be contributed to modelling different arrangements of perforated plates (backed by a cavity

and with additional porous layers) for case of an equivalent fluid technique accounting for dynamic tortuosity by the Johnson-Allard approach [76]. The effective fluid model can compute very well the phenomena for a range of porous materials and uses a coupling technique. Attalla and Sgard use this approach but also account for the effective tortuosity relating to the effective density of the fluid in their papers [75]. The results are obtained and compared to experimental data showing good agreement with the Johnson-Allard model using Johnson's complex dynamic tortuosity.

Other approaches of using an equivalent fluid model (Johnson-Champoux-Allard) is to determine sound absorption properties of perforated plates using flow resistivity measurements accounting for high noise levels using Forchheimer's nonlinearity, see ref [77]. A modified impedance tube allowing high sound levels (up to 135 dB) to be achieved is used to compare and validate using an equivalent fluid approach using a transfer matrix model (TMM) for coupling of the system (perforated plate and porous material) including a cavity. To account for nonlinear effects the Forchheimer's law (used for porous materials to describe nonlinear behaviour) is used given by airflow resistivity values where a linear relationship consisting of a line of best fit as a function of inlet Reynolds number is plotted and gives good agreement of results obtained. Park [36] has shown that in the case of both low and high incident pressure levels an MPPA can be effective either by choosing an optimum surface open area perforation ratio or simply by addition of a cavity dependent upon application dimension limitations. Such MPPA absorbers can be found especially useful in exhaust/aircraft systems. Park [36] investigated MPPAs for use of space launch vehicles and for application within rocket launcher fairings. Because the MPPA is a structure that is non-porous (unless added within a design) then it is extremely compatible for high sound pressure levels where porous materials are not required or restricted due to the rising of dust particles. Minute holes in a plate can be arranged in a number of different lattices depending on application. It is the surface open area perforation ratio and hole diameter size that determines how effective the MPPA is for a given range of amplitudes or frequency. The model proposed by Maa [37] considering a perforated panel absorber, rigidly backed, and containing a cavity is later adopted upon by Park [36]. Where Maa had previously investigated the effects of impedance from micro perforated panel absorbers with relations to Mach number, Park accounts for the mass reactance and relative acoustic resistance in a new approach where he uses sound pressure levels instead of interaction velocities of the inner apertures. Different sound pressure levels have been investigated within the model. The linear acoustic impedance model for an MPPA has its limitations and works if only pressure level is much less than 100 dB. The normalized specific acoustic resistance and reactance r_1 and x_1 respectfully at low sound pressure level is,

$$r_l = \frac{32\eta t}{\rho_0 c_0 d^2}\left(\sqrt{1+\frac{k_p^2}{32}}+\frac{\sqrt{2}}{32}k_p\frac{d}{t}\right) \tag{17}$$

$$x_l = \frac{\omega}{c_0}\frac{t}{\phi}\left(1+\frac{1}{\sqrt{9+\frac{k_p^2}{2}}}+0.85\frac{d}{t}\right)-\cot\left(\frac{\omega D}{c_0}\right) \tag{18}$$

where ω is angular frequency, ratio between hole diameter d and viscous boundary layer thickness is $k_p = 0.5d\sqrt{\frac{\rho_0\omega}{\eta}}$, cavity depth is D, perforation ratio is ϕ, thickness of MPPA is t. For high sound pressure levels for micro perforated absorbers this becomes,

$$x_{nl} = \frac{\omega}{c_0}\frac{t}{\phi}\left(1 + \frac{1}{\sqrt{9 + \frac{k_p^2}{2}}} + 0.85\frac{d}{t}\left(1 + \frac{u_0\sqrt{2}}{\phi c_0}\right)^{-1}\right) - \cot\left(\frac{\omega D}{c_0}\right) \tag{19}$$

where the RMS particle velocity is u_0,

$$r_{nl} = r_l + 1.59\left(\frac{d}{t}\right)^{0.06}\phi^{-0.845}\left[\phi\left(\sqrt{0.25 + \frac{2p_i\sqrt{2}}{\rho_0 c_0^2\phi^2}} - 0.5\right) - 0.5\right] \tag{20}$$

Where p_i is RMS incident pressure. The velocity in the hole is expressed by equation (21),

$$\frac{u_0}{c_0} = \frac{1}{\sqrt{2}}\frac{\phi}{1-\phi^2}\left(\sqrt{0.25 + \frac{2\sqrt{2}p_i 1-\phi^2}{\rho_0 c_0^2\ \phi^2}} - 0.5\right) \tag{21}$$

Combining equations (19) and (20) for high sound pressure levels the normalized specific acoustic impedance is,

$$Z_{nl} = r_{nl} + jx_{nl} \tag{22}$$

Absorption and reflection coefficients for a range of amplitudes for perforated plates can then be input into the code for any given range of open area perforations for a desired MPPA absorber to work and theoretically test for a frequency range. The absorption coefficients for various sound pressures is demonstrated later for low and high sound pressure levels, including membranes used in the shock tube with rigid backing set up comprised of a cavity comprising 100 mm. An MPPA with high perforation ratios and hole diameters >1.0 mm is seen to be more effective for high sound pressure levels for the low frequency range. And work by Tayong, Dupont and Leclaire [38] showed that variations in holes interaction effect and Foks function under medium and high sound pressure levels alters sound absorption dependant at different strengths of acoustic wave interactions.

3.3. Rigid Porous Materials

3.3.1. Porous Materials in Linear and Nonlinear Regimes Including Forchheimer's Nonlinearity

Porous materials make generally good sound absorbers and can be either rigid, foamed, cellular or fibrous. In naturally occurring materials these can be seen as sand, soils and rocks contained of cracks and pores and organic material such as wood, bones, and marine sponge, for example see Figure 3.2 [105].

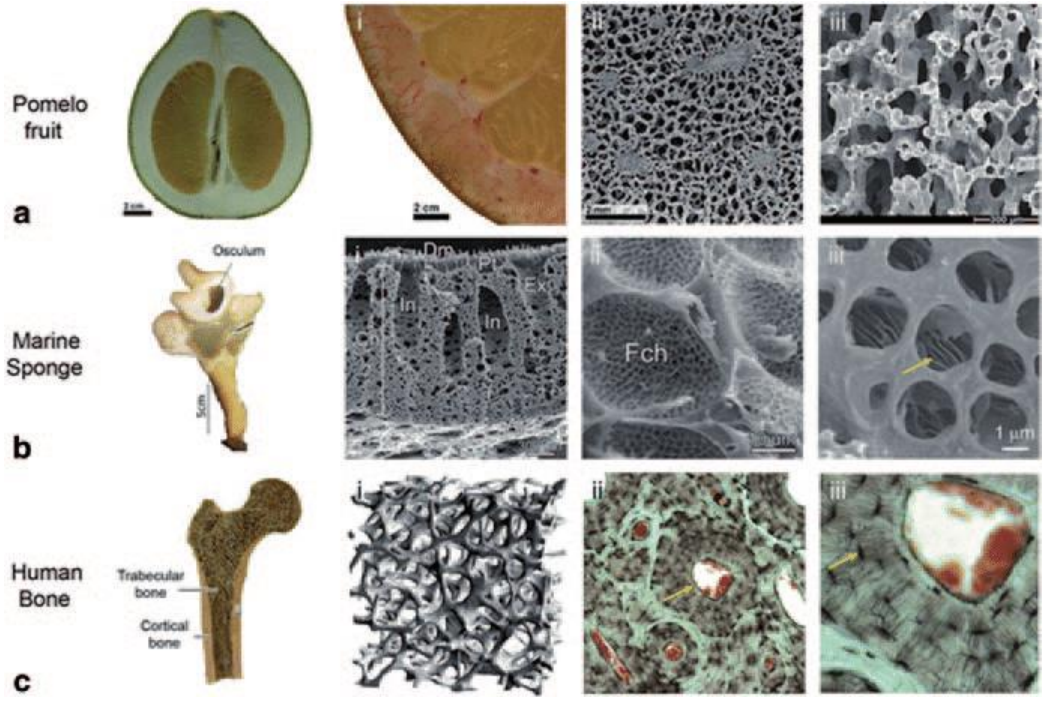

Figure 3.2. Naturally occurring porous materials found (a) above land (Pomelo fruit), in the ocean as marine sponge (b) and in human bones (c) [105].

Sound propagation in rigid frame porous materials is governed by the effective density and the effective bulk modulus of the fluid in the pore space [79]. To gain an insight into the behaviour and the mechanism for sound absorption of the fluid in the pores, the density and bulk modulus which are both complex quantities are used in modelling techniques. To describe the physical behaviour, measurement procedures can be performed by flow resistivity testing of a porous sample, its tortuosity and other parameters required by the model. The effective density and bulk modulus are both frequency dependent thus sound absorption at given frequencies is achieved and depends on a porous material's thickness and its physical properties. The wavenumber and characteristic impedance for rigid frame porous materials including sound propagation in the volume pore space allow the quantities of reflection and absorption to be determined. A model representing an effective fluid approach for porous media and considering an incompressible Newtonian fluid was introduced in [80] where the wavelength of sound is regarded much larger than the individual pores contained in a rigid framed porous structure.

They considered a harmonic pressure drop and show that the dynamic permeability or dynamic tortuosity are analytical functions of frequency for air saturated porous material. The physically correct low and high frequency limits are explored and seen to be dependent on pore radius dimensions and its connection to the surrounding pore network. Only viscous effects are considered in the constructed model. No temperature variations are considered which allows the pressure-density effects to be eliminated from any thermal effects. An average fluid velocity is used for describing the macroscopic behavior of fluid that encounters an area filled with pores which for any frequency linearly related to the pressure gradient. It is seen that the low frequency properties are dependent upon the value of permeability k and high frequency properties are dependent on the value of tortuosity. The viscous effects are known to be dominant for low frequency content for porous media from drag sustained to the fluid from interaction by the solid walls. Inertial effects become the dominating factor for high frequency

content. The equation of motion which includes viscous and inertial effects onto the relative motion of fluid and presented in equations 4.1a and 4.1b of [80].

$$\phi\rho_f \frac{\partial^2 U}{\partial t^2} = \hat{\rho}_{12}(\omega)\left[\frac{\partial^2 U}{\partial t^2} - \frac{\partial^2 u}{\partial t^2}\right] + (spatial\ derivitive\ terms), \tag{23}$$

where ρ_f is fluid density and ϕ is porosity of a porous solid. The average displacement of the fluid and solid is u and U respectively, $\hat{\rho}_{12}(\omega)$ is,

$$\hat{\rho}_{12}(\omega) = -[\hat{\alpha}(\omega) - 1]\phi\rho_f \tag{24}$$

Assuming there is no movement from the solid the frequency dependent tortuosity $\hat{\alpha}$ appears in the momentum conservation equation as follows,

$$\hat{\alpha}(\omega)\rho_f \frac{\partial v}{\partial t} = -\nabla P \tag{25}$$

The frequency dependent permeability $\hat{k}(\omega)$ and tortuosity $\hat{\alpha}(\omega)$ is shown to be related as the following,

$$\hat{\alpha}(\omega)\frac{i\eta\phi}{\hat{k}(\omega)\omega\rho_f} \tag{26}$$

and since the fluid velocity and material porosity is related to the pressure gradient, the frequency dependent permeability is defined as,

$$\phi v = -\frac{\hat{k}(\omega)}{\eta}\nabla P \tag{27}$$

where η is the viscosity and P the pressure. A thorough detailed derivation of dispersion relations and analogy to electrodynamics accounting for frequency dependant permeability and tortuosity is given in [80] along with the energy flux density and rate of energy dissipation per unit volume for a material slab with thickness including lateral area. The final expressions used for $\hat{k}(\omega)$ and $\hat{\alpha}(\omega)$ in the model are,

$$\hat{k}(\omega) = \frac{k_0}{\left(1 - \frac{4i\alpha_\infty^2 k_0^2 \rho_f \omega}{\eta\Lambda^2\phi^2}\right)^{\frac{1}{2}} - \frac{i\alpha_\infty^2 k_0 \rho_f \omega}{\eta\phi}} \tag{28}$$

$$\hat{\alpha}(\omega) = \alpha_\infty + \frac{i\eta\phi}{\omega k_0 \rho_f}\left(1 - \frac{4i\alpha_\infty^2 k_0^2 \rho_f \omega}{\eta\Lambda^2\phi^2}\right)^{\frac{1}{2}} \tag{29}$$

where $2/\Lambda$ is given as the ratio of area and volume of pore walls and solid interface with field U_p

$$\frac{2}{\Lambda} = \frac{\int \left|U_p(r_w)\right|^2 dA}{\int \left|U_p(r)\right|^2 dV} \tag{30}$$

The quantity Λ is called characteristic viscous length. Measured permeability allows the effective tube radius as regarded in [80] to be derived and circular geometry is considered treating the space occupied pore. From using equation (28) a plot of the dynamic permeability is presented in Figure 3.3 a. and 3.3 b showing comparability between model predictions and simulations (measured directly for absolute value in 3.3 a, and phase permeability using an exponential probability distribution of tube radii in 3.3 b).

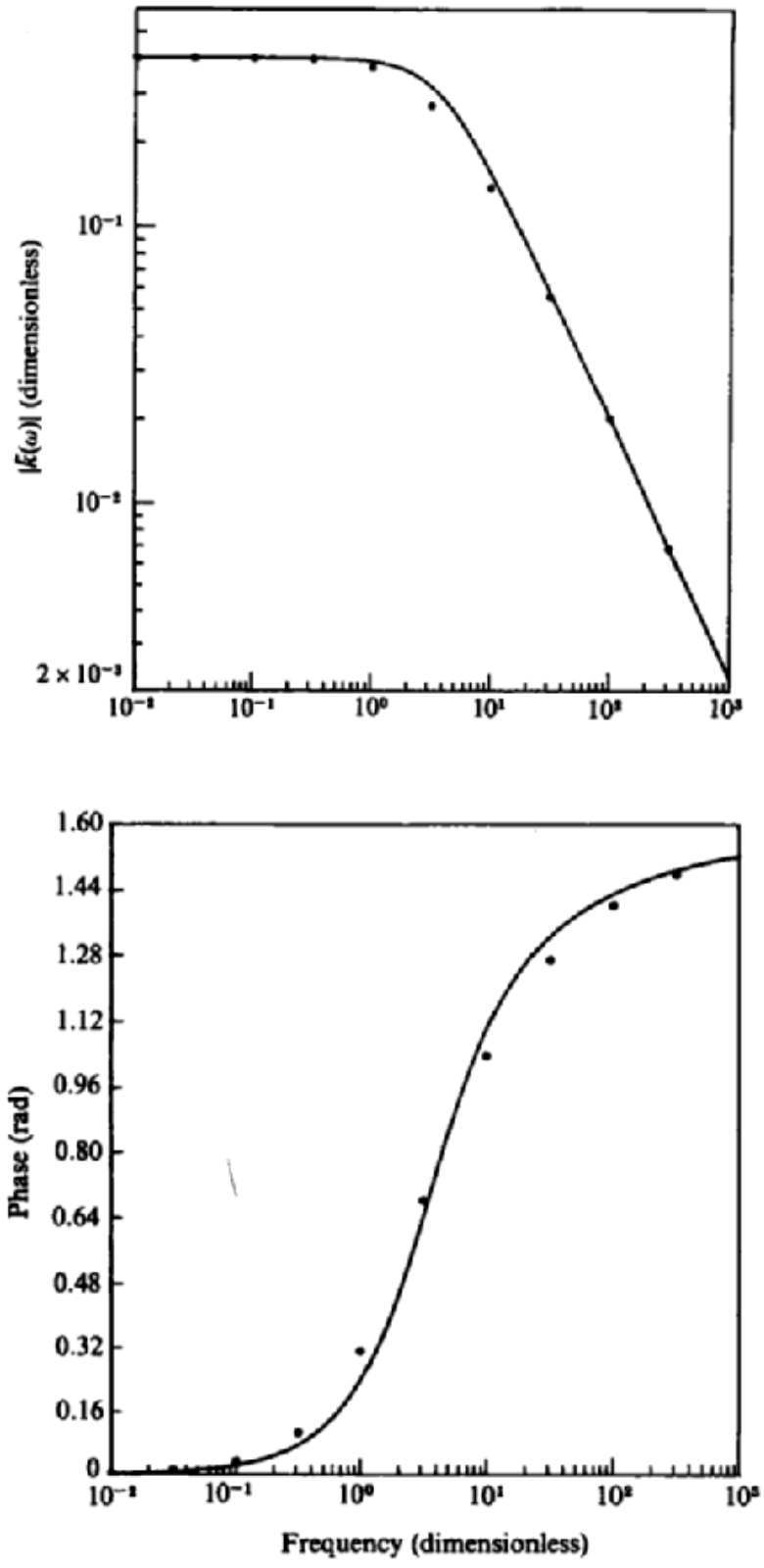

Figure 3.3. (a) A Plot of dynamic permeability as absolute value, and b) its phase. Data given by the solid line and points are predicted model and direct simulation respectively from [80].

The exact high frequency behaviour is predicted for the dynamic tortuosity over a large frequency range by means of using characteristic length Λ, see ref [80]. Later in 1991 Champoux and Allard [83] extend the work by Johnson et al [80] to account for the complex effective density of a rigid porous material, assuming the fluid being incompressible on the microscopic scale. To model the fluid in the pores

properly, the dynamic tortuosity is used to obtain the exact high frequency asymptotic behaviour of bulk modulus. In the high frequency range, the pore size is considered to be much larger than the viscous boundary layer thickness. The characteristic length Λ from [80] can be given as,

$$\Lambda = 2\frac{\int|v(r)|^2 dV}{\int|v(r_w)|^2 dA}. \tag{31}$$

Note that notation U_p from [80] is replaced by v which is particle fluid velocity in the pores. The numerator and denominator show that Volume V over Surface area A is weighted by the ratio of v. The viscous skin depth δ_v can be found in the time dependant asymptotic high frequency limit of dynamic tortuosity,

$$\lim\ \hat{\alpha}(\omega) = \alpha_\infty[1 + (1-i)\delta_v/\Lambda] \tag{32}$$

$$\delta_v = \left(\frac{2\eta}{\rho_0\omega}\right)^{\frac{1}{2}} \tag{33}$$

where ρ_0 is equilibrium fluid density, fluid viscosity η and angular frequency ω, $\sqrt{-1} = i$. The model proposed by Champoux and Allard requires a new characteristic length Λ' in order to predict a high frequency limit of the fluid dynamic bulk modulus $K(\omega)$ (for case of a porous medium containing pores that are nonuniform). The new characteristic length Λ' differs from the characteristic length Λ (as given from work by Johnson and co-authors) [80] due to dimension differences. The characteristic length given in (34 a) is equal to twice the volume to pore surface ratio for typical pores which are uniform.

$$\Lambda' = 2\textstyle\int_V dV / \int_A dA \tag{34}$$

As opposed to [80] where the characteristic length Λ is a ratio of weighted velocities on the microscopic scale, the new characteristic length Λ' given by [83] is the ratio of unweighted velocities (equation 34). Champoux and Allard consider the thermal effects at high frequencies for the saturated fluid and associate Λ' with temperature variations in and outside the pore regions resulting in an excess of temperature related to the dynamic bulk modulus of the saturated fluid. The dynamic tortuosity and dynamic bulk modulus represented with its real and imaginary parts are given by Figures 3.4 a, b and Figures 3.5 a, b from ref [83]. The high frequency limit $(\omega \to \infty)$ of the dynamic bulk modulus relating to the equilibrium pressure P_0 and temperature T_0 for the fluid regarding thermal effects becomes,

$$K(\omega) = \gamma P_0\left[\gamma - (\gamma-1)\left(1 - (1-i)\frac{\delta_v}{N_{Pr}^{1/2}\Lambda'}\right)\right]^{-1} \tag{35}$$

involving the specific heat ratio $\frac{C_p}{C_v} = \gamma$ and the Prandtl number N_{Pr}. The equation for the dynamic bulk modulus $K(\omega)$ for a porous material of uniform pores and for high frequencies relating to effective density is

$$K(\omega) = \gamma P_0\left(\gamma - \frac{\gamma-1}{1 - \left(i\sigma\phi/\rho_0\alpha_\infty N_{pr}\omega\right)(1 + 4i\alpha_\infty^2\eta\rho_0 N_{pr}\omega/\sigma'^2\Lambda^2\phi^2)^{1/2}}\right)^{-1} \tag{36}$$

where N_{pr} is the Prandtl number, P_0 is the fluid equilibrium pressure and the specific heat ratio for fluid is γ. For consideration of a porous material where pores are nonuniform equation (36) is modified for the characteristic length Λ to be replaced by Λ'. This results in equation (34) being replaced by equation

(37) in order to determine the high frequency limit for the fluid dynamic bulk modulus and its relationship with effective density. Considering the low to middle frequencies, it is required that quantity σ to be replaced by σ'.

$$\Lambda = c\left(\frac{8\alpha_\infty \eta}{\sigma\phi}\right)^{\frac{1}{2}} \tag{37}$$

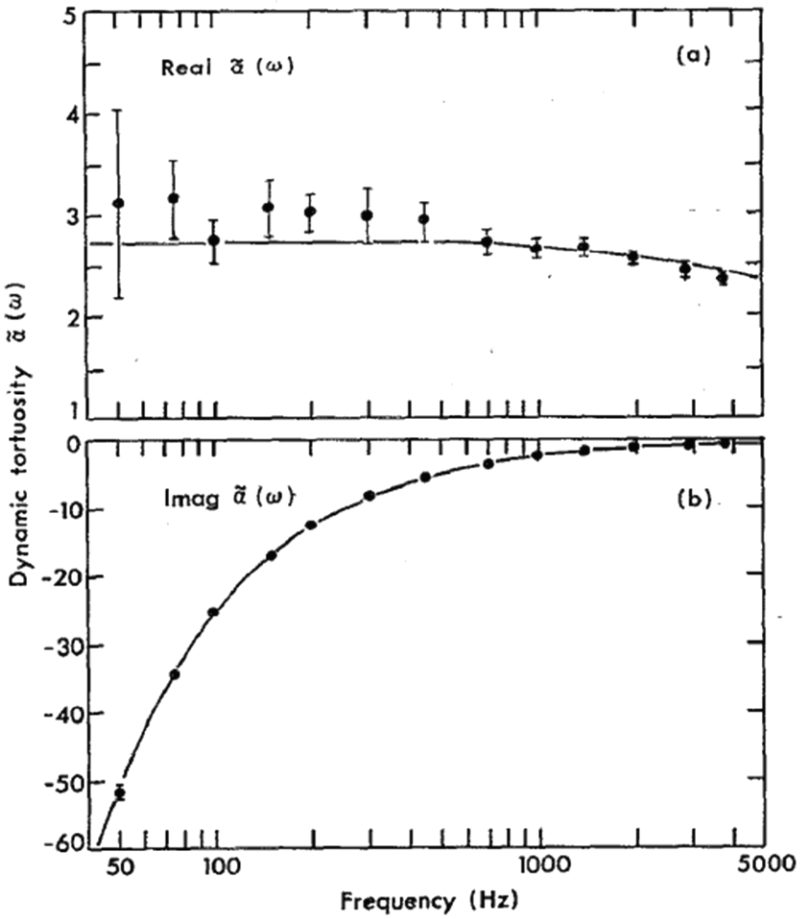

Figure 3.4. (a) Dynamic tortuosity of air plotted for a porous ceramic strcture for its real parts and (b) Imaginary parts. Experimental data is points and model prediction is solid line [83].

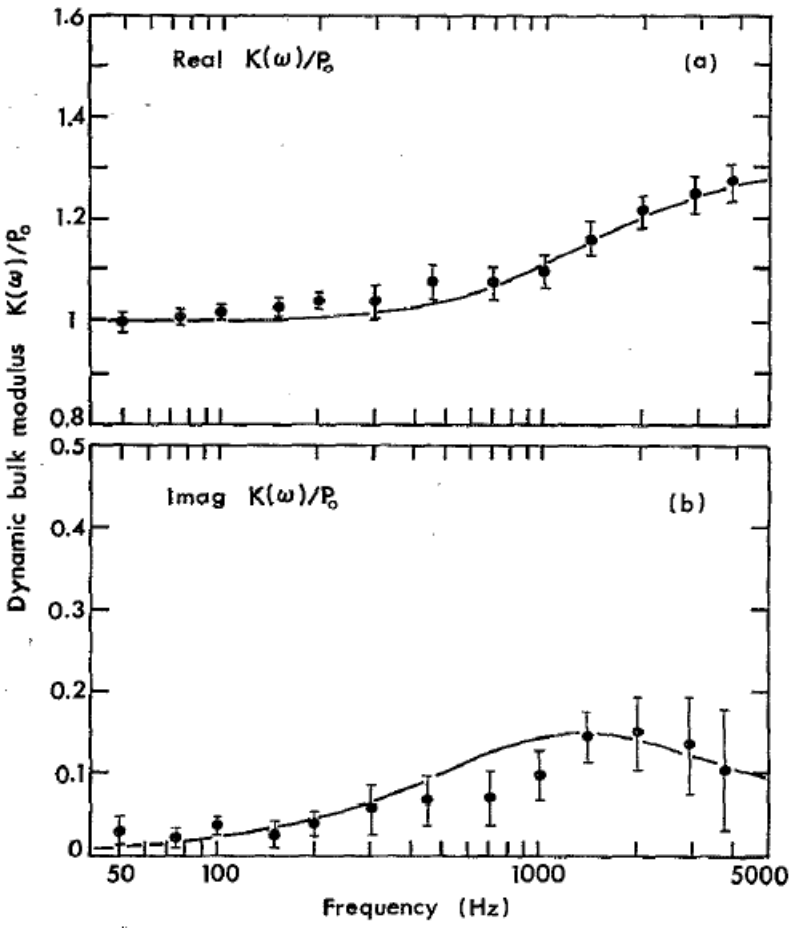

Figure 3.5. (a) Dynamic bulk modulus of air plotted for a porous ceramic strcture for its real parts and (b) Imaginary Dynamic bulk modulus is normalized by P_0. Experimental data (points) and model prediction (solid line) [83].

Champoux and Allard showed that their model described well the thermal effects associated at medium and high frequencies. For high frequencies, the asymptotic behavior of dynamic tortuosity and dynamic bulk modulus is compared against experimental measurements and shown to be valid with the proposed model from introducing the new characteristic length Λ' and accounting for static flow resistivity σ. Further investigation of porous media, accounting for thermal effects at low frequencies is later approached by Lafarge et al [106] extending the works of Johnson et al [80] and Champoux, Allard [83]. Lafarge et al introduces a new parameter, the static thermal permeability k_0' in addition to characteristic thermal length Λ', in order to describe the thermal effects that characterise the thermal exchanges between a saturated fluid, and frame of porous media, at low frequency. The modelling of the dynamic air compressibility for glass wool and foam is compared with experimental data and is shown in Figure 3.6. A normalized dynamic compressibility $\beta(\omega)$ (inverse of bulk modulus) is firstly presented which relates the adiabatic bulk modulus of air K_a and macroscopic parameters acoustic pressure $\langle p \rangle$ and density $\langle \rho \rangle$ (where the brackets denote an average of the fluid phase intrinsically) and lastly, density at rest ρ_0.

$$\frac{\beta(\omega)}{\mathrm{K}_a}\langle \rho \rangle = \frac{1}{\rho_0}\rho_0 \tag{38}$$

The approach using a thermal analogue of the dynamic viscous permeability is used to account for temperature variations of air. This way the low frequency content of both the dynamic viscous and

thermal permeability is obtained. Flow resistivity and viscosity of air both related to the viscous static permeability also provide low frequency information for the viscous effects. After considering Darcy law and wavelength being much greater than the pore size, a dimensionless shape factor M, and dimensionless frequency $\widehat{\omega}$ is used which yields $k(\omega)$ as the following,

$$k(\omega) = k_0/[(1 - \left(\frac{M}{2}\right) i\widehat{\omega})^{\frac{1}{2}} - i\,\omega] \tag{39}$$

where $M = 8\alpha_\infty k_0/\phi$, and $\widehat{\omega} = (\omega/v)(k_0\alpha_\infty/\phi)$. Furthermore, the equation of state and thermal conduction is used in order to describe the thermal effects of the dynamic compressibility $\beta(\omega)$ of the equivalent fluid, where a detailed description is given in [106] thus the obtained equation is,

$$\beta(\omega) = y - (y-1)\left[1 + \frac{1}{-i\widehat{\omega}}\left(1 - \frac{M'}{2} - i\widehat{\omega}'\right)^{\frac{1}{2}}\right]^{-1} \tag{40}$$

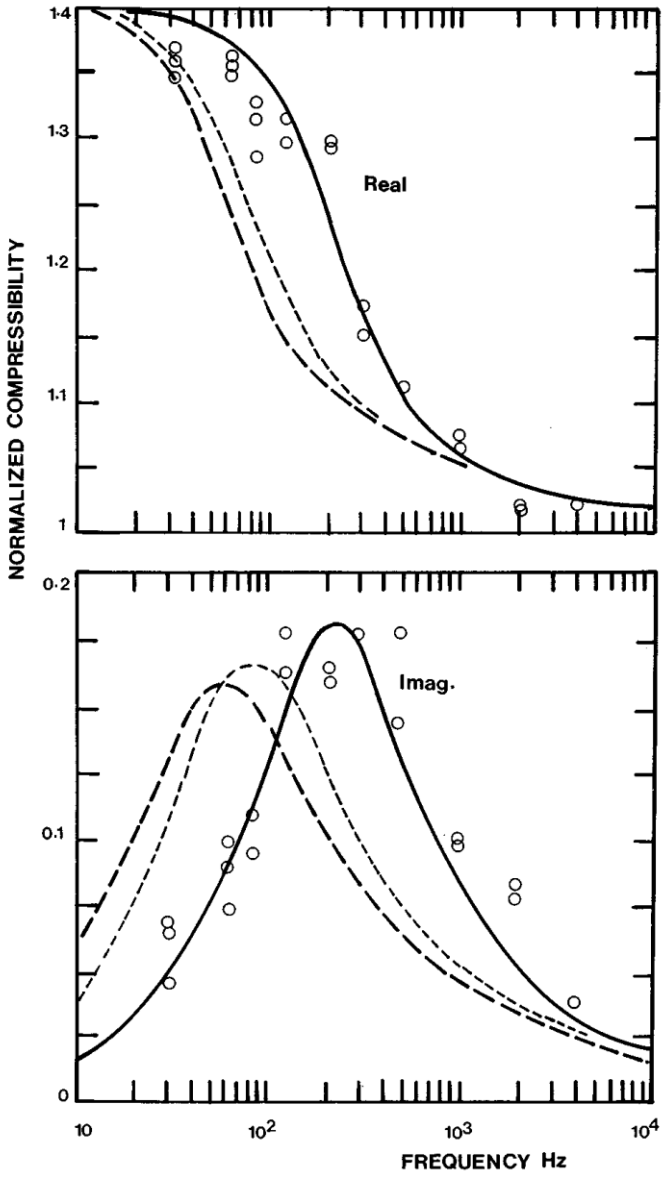

Figure 3.6. Normalized compressibility plotted for porous experimental data showing points, and model predictions showing lines (solid and thickest most dashed line for Lafarge et al) and thinnest most dash line with prediction by Attenborough's model. [106].

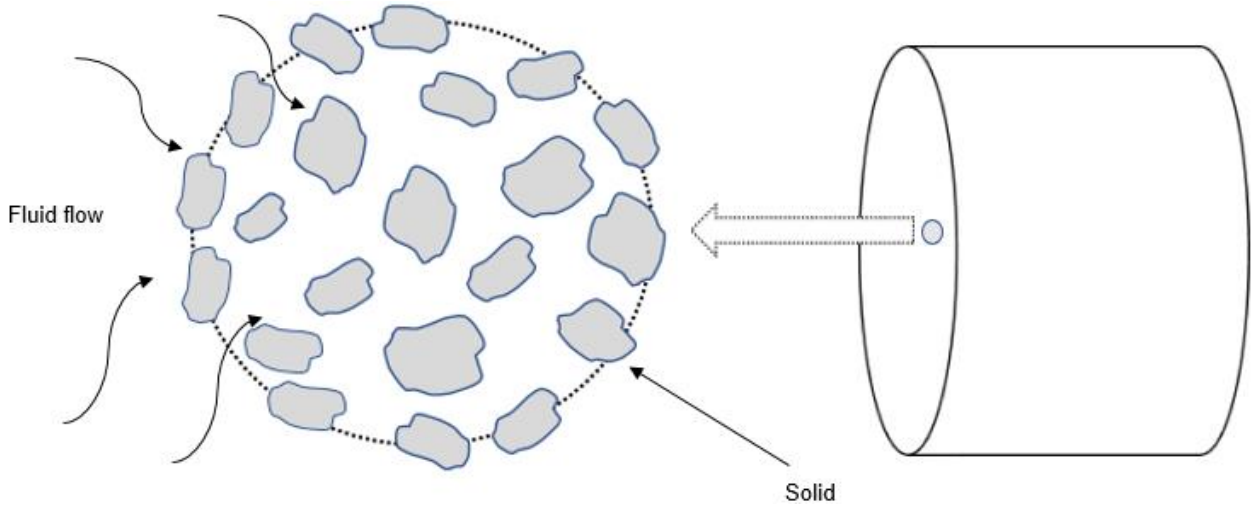

Figure 3.7. A representative elementary volume of fluid (rev) regarded larger than a single pore volume. A similar schematic is presented by [85].

Figure 3.7 shows a representative elementary volume of fluid (rev) illustrating flow region with a porous material. The air inside the pores of rigid porous materials can be considered as a dissipative fluid since the motion of the wave is confined to the pores and the amplitude of the wave becomes attenuated because of viscous and thermal effects. This results from the wave at the solid boundary of the porous structure where viscosity causes a loss of acoustic energy. Thermal effects will also contribute to energy loss and wave attenuation which occur from temperature fluctuations due to pressure differences in the medium. Other phenomenon can exist depending on the initial amplitude of the incident wave similar to single or multiple orifices as previously discussed in the form of turbulence. The interacting sound energy of rigid porous media is therefore dissipated, and some transformed to thermal energy as heat [84]. The characteristics of a permeable porous medium arise from its total porosity and pore size dimensions. Darcy's law known by works of Henry Darcy (1865) describes the behaviour of fluid flow through a porous medium determined by experiments investigating water flow through sand.

$$q = -\frac{k}{\mu}\nabla P \tag{41}$$

where instantaneous flow rate q, is a measure of Pressure drop ∇P across a porous material of thickness, with material permeability k and fluid viscosity μ. When a porous sample is saturated with fluid the pressure gradient across the sample is relation of fluid flow and pressure drop for when flow is deemed laminar, and low values of Reynolds number [85]. When Reynolds numbers become sufficiently high enough as to exhibit the behaviour of nonlinear effects, then the need for an additional correction term to Darcy's equation is required. This extra term is called Forchheimer's nonlinearity. The additional Forchheimer's term is used to account for the physical behaviour of the fluid interacting with porous media by the presence of turbulent features due to high flow rates. This can be seen from the dependence of flow resistivity on flow velocity and commonly known as Forchheimer's nonlinearity.

$$\sigma(V_f) = \frac{\Delta P}{V_f L} = \sigma_0(1 + \xi V_f) \tag{42}$$

The effects of fluid flow through randomly packed columns have been investigated by Ergun and Orning [117] in 1949 who studied increasing gas flows and monitored the fluid behaviour. It was known that at high enough velocity rates turbulence occurs. They develop an equation which relates pressure drops

relating to fluid flow in fixed beds. Zorumski and Parrott [22] in 1971 investigated rigid porous materials by measuring material resistance, impedance, and absorption coefficient. They showed that flow resistivity grows with flow rate and consequently absorption coefficient changes with the amplitude of incident sound. A porous absorbers performance depends on the amplitude of the incident sound. For large amplitudes, an important factor when designing an absorber is how effective it is when resistivity growth with particle velocity (and, consequently, pressure) is considered and needs to be accounted for due to Forchheimer's nonlinearity. Different methods have been used to describe the nonlinear effects of high flow rates with porous media such as a thorough detail given by Whittaker, see reference [86]. A volume averaging approach is considered to derive the Forchheimer's correction which begins with the Navier Stokes equation. In 1987 the nonlinear effects of porous materials are investigated by Kuntz and Blackstock [87] by which they observe the nonlinearity associated with the resistivity of two types of different porous structures. The two types of structures tested was batted Kevlar and BAF foam. An 'extra attenuation and saturation' term is used to determine the rate of nonlinear attenuation of intense sinusoidal waves with the air saturated, bulk porous samples. The porosity of the samples differed including the resistivities of the materials. The latter is in the case of when material is either a foam or fibre. This variation in structure therefore affects the overall sample tortuosity which consequently can impact material resistivity.

Relative nonlinearity is measured for both the Kevlar and foam with the latter reported to have a higher nonlinearity. This is thought to be due to the porous matrix of the sample where blockages of some pores are thought to exist. Kuntz and Blackstock start by assuming a square law dependence for the high flow rates considered (100 – 172 dB) to determine the decay from the nonlinearity associated with the resistivity of the porous samples. This approach stems firstly from noting that the decay of sawtooth waves in an ordinary fluid follows an exponential decay law $Pe^{-\alpha x}$ for small signals. The small signal dissipation and nonlinear effects is product of the total rate of the decay. The relation of the pressure amplitude P_1 (which represents the fundamental component of the wave), distance x and small signal attenuation coefficient α is given by,

$$\frac{dP_1}{dx} = -\alpha P_1 \tag{43}$$

Two decay rates are considered, firstly, the decay associated with nonlinear flow resistance assuming power law dependence,

$$\frac{dP_1}{dx} = -\frac{P_1^2}{\Upsilon} \tag{44}$$

and small signal exponential decay law which together yields the total decay rate due to nonlinear effects [87], [108].

$$\frac{dP_1}{dx} = -\alpha P_1 - \frac{P_1^2}{\Upsilon} \tag{45}$$

The coefficient Υ (to be determined) is presented as an equivalent factor which is considered for porous materials by the difference in the role of nonlinearity relative to ordinary attenuation. This is regarded as a type of Gol'dberg number, g = $P_{10}/\alpha\Upsilon$. A saturation amplitude P_{1s} is determined to describe the dependence of the Gol'dberg number, in other words, of which decay law governs the nonlinear behaviour decay rate.

$$P_1 = \frac{\alpha \Upsilon e^{-\alpha x}}{1 - e^{-\alpha x}} \tag{46}$$

$$P_1 = \frac{P_{10} e^{-\alpha x}}{1 + (P_{10}/\alpha\Upsilon)(1 - e^{\alpha x})} \tag{47}$$

Equation (47) represents the boundary condition solution $P_1 = P_{10}$ at $x = 0$ which is used to plot the results obtaining the saturation curves and determining α and Υ (see Figure 3.8). The curves show the values of the physical data from a received sound pressure level at a fixed point plotted as a function of source level. The dependence of the points indicates the values of α and Υ by fitting equation (47) to either the lower or higher parts. The former provides a value of the small signal coefficient, and for the latter the acoustic nonlinearity parameter.

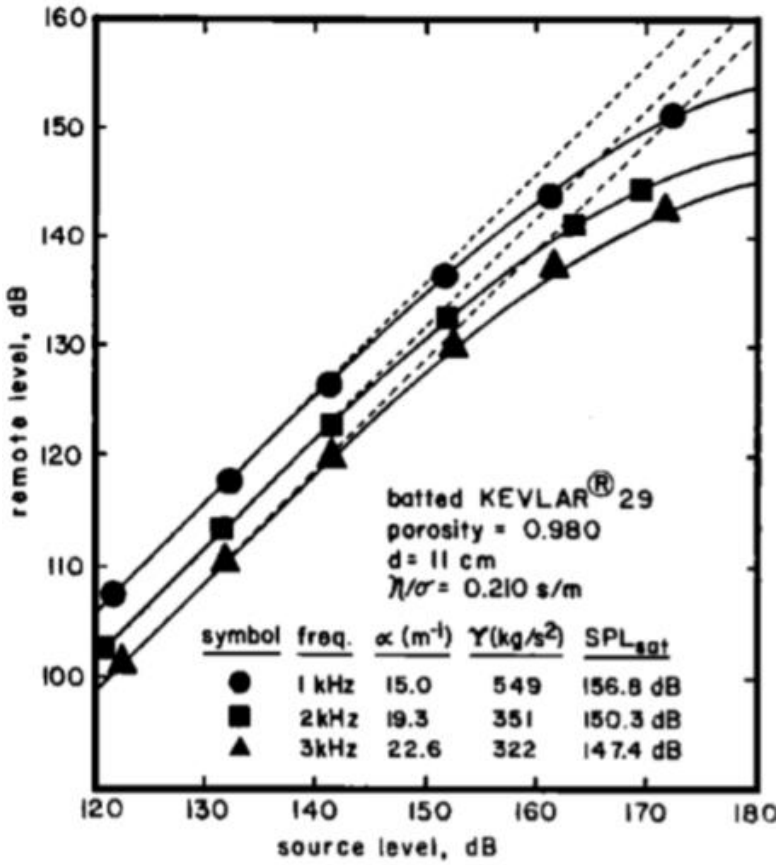

Figure 3.8. Remote level as a function of the source level. Battered Kevlar at 1, 2 and 3 kHz with saturation curves plotted, given as Figure 4 in [87]. values of α and Υ by fitting equation (47) to either the lower or higher parts.

The dc flow resistivity σ, is measured in steady flow tests which, for porous materials is related to the velocity through a porous medium given by Darcy law for a sample with length L. The static flow resistivity is represented by measured coefficient σ_0, which for low flow rates $\sigma_0 \approx \sigma$, where $\sigma = \Delta P / vL$. This enables the pressure drop to be determined for the porous samples for linear flow. Flow resistivity measurements with increased velocity flow rates are further required to attain the coefficients of the relative nonlinearity of the material ξ/σ. Note that the chosen representation used in [87] equation (11) is a type of Forchheimer correction to illustrate the velocity dependence of the velocity at high flow rates,

$\sigma V_f = \sigma + \xi v$. The author makes it clear however, that no regard of solving the nonlinear equations of motion is used, and that the sign of v influences the resistivity. This is the case for when v is negative which results in a decrease of resistance. V_f are increased chosen flow rates, for measurements of flow resistivity. This is the inlet flow directly before a porous sample surface. Nelson [108] is referred to by [87], for modifying σV_f by replacing v with $|v|$ or, v sign (v). This concept is later chosen in other works, see references [4], [41], and [110]. Steady state flow resistivity measurements are plotted and seen in Figure 3.9 and Figure 3.10 for the Kevlar and BAF samples of different porosities. Samples are reported by averaging nearly a length of around 8 cm, and flow velocities were measured to be 0.0007 – 1.6 m/s. The value R_m included in the static flow measurements indicates a threshold of when laminar flow is altered, and the onset of turbulence begins, $R_m > 1$ [111]. This is a type of Reynolds number which is modified,

$$R_m = v/\eta S \tag{48}$$

where $\eta =$ kinematic viscosity and $S =$ ratio of surface area of the frame to the volume of the sample, given as equation (10) in [87].

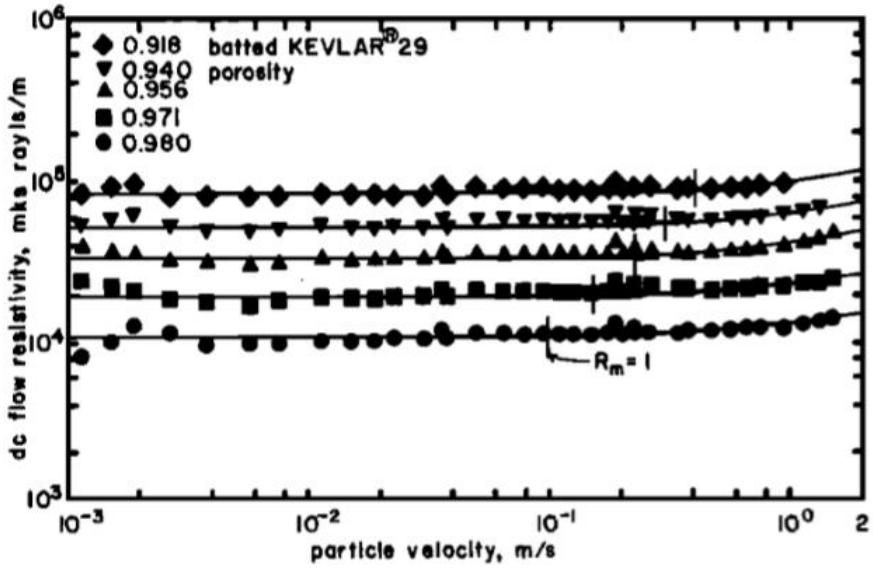

Figure 3.9. Flow resistivity measurements for different porosities. Material tested is Kevlar.

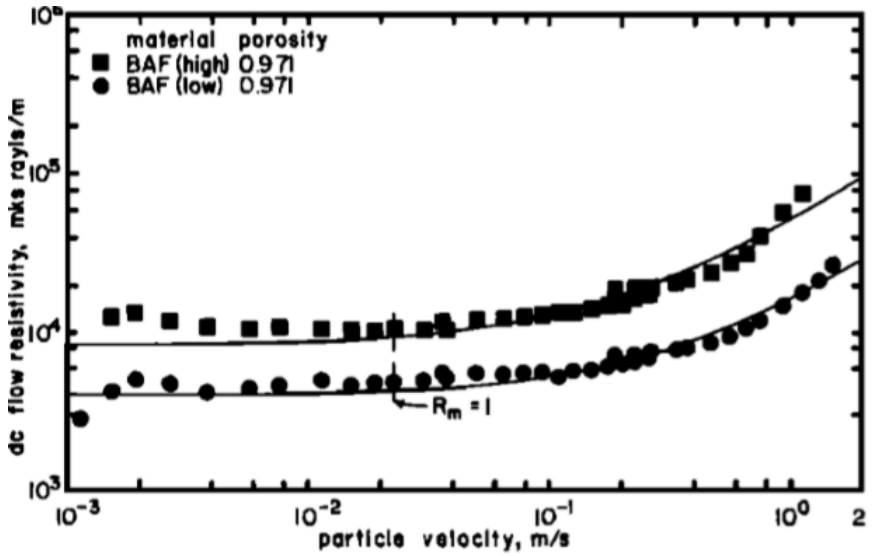

Figure 3.10. Flow resistivity measurements for different porosities. Material tested is BAF.

The porosities of the samples were correlated to the flow resistivity data. In each case the sample weight and volume were used to do so. For Kevlar, the porosities ranged from 0.919 – 0.980, and 0.970 – 0.972 for BAF. Pulsed sinusoids were used in the testing of a square waveguide to measure the propagation characteristics. The waveguide consisted of microphones inserted within the inner frame of the system. Microphones positioned at several distances were notably given, beginning at 2 cm, and ranging to 20 cm. Frequencies tested were 1,2 and 3 kHz with amplitudes generated to a maximum of 173 dB for nonlinear regime. The data gained from the flow resistivity tests are used to predict the saturation curves by the performed measurements of sinusoidal pulses as a function of particle velocity and flow resistivity. An empirical formula given for Υ, determined by the fitting to the data from the measurements performed leads to,

$$\Upsilon = \left(9446/\sqrt{f}\right)(\xi/\sigma)^{0.4} \tag{49}$$

where the coefficient Υ is deemed constant in the efforts of Kuntz and Blackstock in order to solve the extra attenuation, associated with the total decay rate by equation (45). The dependence of Υ is however, shown to result an inconsistency for the attenuation on source level. It is reported by [87] that this is due to the nonlinear flow resistance, and assumption that Υ is held constant. Another factor is that coupling effects may have occurred between motions of both the frame and fluid. Results are given in Figure 3.11 and Figure 3.12 for Kevlar, showing attenuation decreasing over a distance measured to be 25 cm. The fundamental and higher harmonics are presented for 1 kHz, see Figure 3.11 and for 2 kHz and 3 kHz, see Figure 3.12. The porosity is 0.980 and relative nonlinearity has been averaged at a value of 0.210. The solution representing the boundary condition equation (47) is used to compare with the linear attenuation for small signals.

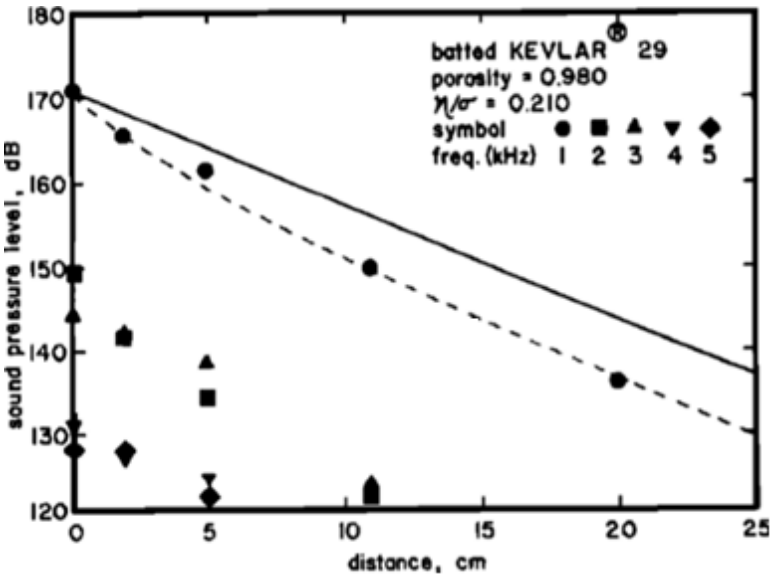

Figure 3.11. Sound pressure level versus distance for Kevlar. Frequency tested = 1 kHz. Small signal sinusoid (solid line), circles (fundamental) and corresponding markers (numbered), are propagation of the harmonic components.

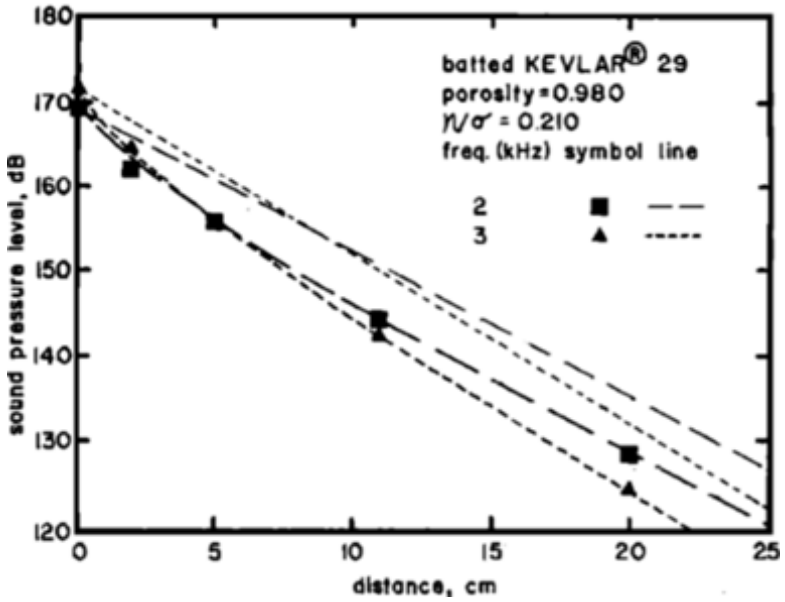

Figure 3.12. Sound pressure level versus distance for Kevlar. Frequency tested = 2 kHz and 3 kHz. Small signal sinusoid (straight lines), markers indicate wave propagation for 2 kHz (squares) and 3 kHz (triangle).

Kuntz and Blackstock [87] show that by performing flow resistivity measurements above a steady state where turbulence is reached, the governing nonlinear phenomena can be evaluated by the flow resistivity growth on incident pressure for a porous material. The relative attenuation decay, accelerated by nonlinear effects from a porous medium, is compared with small signal attenuation. Sinusoidal pulse measurements were performed for both low and high intensities from a sound source in a square waveguide. It was further shown that data obtained from the flow resistivity tests, allow a nonlinear parameter to be known. At high intensities nonlinear wave phenomena and its decay, can be described usually by wave distortion by a 'hydrodynamic nonlinearity' arising harmonic generation and shock formation. However, porous materials are shown to be responsible for the nonlinear effects of the wave by static flow resistivity dependence on flow velocity.

Other works that studied turbulence due to large Reynolds numbers is given by Kolmogorov [119], who investigated the local structure of turbulence in incompressible viscous fluids. In 1991, work by Nield [120] presents a study on the limitations of modelling fluid flow in saturated porous mediums using a Forchheimer's type equation. They evaluate an interface region between a porous medium and a fluid layer. Porous materials have been studied by Umnova et al in 2001 [4], where it was shown that the dispersion and attenuation of sound waves can be described by a cell model. The developed cell model accounts for a relationship between the complex density and complex compressibility for rigid porous media and requires knowledge of flow resistivity. Two existing models were considered 1. Happel, Strout [112],[113] and 2. Kuwabara, Strout [109], [113] which use specific boundary conditions (for the stress and fluid velocity components) for spherical particle surfaces. [4] Introduce a new concept on the existing models to describe a new boundary condition for media with high volume fractions of spherical particles. A complete cell model was developed by modifying the previous existing models to describe the acoustical properties of granular media. In the new model developed, there are less parameters required, and good agreement was found when compared to other models [114].

In 2003, Umnova et al [39] investigated Forchheimer's correction to Darcy's law. It was shown for various materials possessing different properties, the reflection coefficient can increase or decrease as the amplitude of incident sound grows. The model predicted reflection coefficient and impedance at high sound pressure levels up to 500 Pa. Umnova et al [40] further investigated in 2004, rigid multilayer materials accounting for Forchheimer's nonlinearity due to high sound excitations of 1 KPa. A nonlinear model was proposed to predict the phenomena between consecutive layers and associated acoustic properties. Furthermore, it was shown that by altering one of the layer thicknesses, the resulting absorption can change. Flow resistivity and Forchheimer's parameters were measured and compared for lead shot and gravel layers. It is emphasised that sound attenuation increases if the thickness of top layer is chosen correctly. Reflection coefficient was investigated as a function of top layer thickness for a range of different frequencies along with various incident pressure levels. In 2006 Lucas et al [115] evaluate the increase of Reynolds numbers of fluid flow through a crenelated channel or porous medium. They focus on flow and non-flow periodicity including how they are related to a quadratic deviation of Darcy's law. A weak and strong inertia regime is investigated, the former for when Reynolds numbers are low $(Re{\sim}1)$, and the latter for high Reynolds numbers $(Re{\sim}200)$. It is reported how nonlinear effects can be reduced by the inertia forces by the straightening of streamlines.

Tayong et al [78] in 2010 propose a model based on high Reynolds numbers and low Mach numbers of flow velocity in the Forchheimer regime for micro-perforated panels (MPPA's). The perforations within the MPPA's are subject to high intensity sound pressures up to 160 dB in a modified impedance tube using a three-microphone method. Reference is given to Maa's [37] linear model for MPPA's in a cylindrical duct, and from Auregan and Pachebat [116] who study the nonlinear regime for rigid framed porous materials at high sound pressures. [78] perform measurements of MPPA's which are backed by an air cavity of various depths. They validate a new refined model which accounts for the variations of the absorption peak dependence on Mach number. Impedance tube data is used to observe the phenomena leading up to, and beyond a critical Mach number which is seen to be a function of a linear regime limit of the perforated plate. Turo and Umnova [41] in 2013, developed a model for transient effects and Forchheimer's nonlinearity so an improved model could provide predictions for lower

amplitude short pulse durations for different materials. Frequency domain models are not sufficient for describing the nonlinearity phenomena as they do not account for the interactions between the spectral components due to nonlinearity. In [41] a model for the complex tortuosity function was suggested, that is easily transformable in time domain in the following,

$$\alpha(\omega) = \alpha_\infty + \frac{\sigma_0 \phi}{-i\omega\rho_0} + \frac{2\alpha_\infty}{\Lambda}\sqrt{\frac{\eta}{-i\omega\rho_0}} \tag{50}$$

This scaling function is different from [80], however, it still describes the physically correct low and high frequency limits in time domain, it leads to the following expression for the viscous drag force acting for a porous material and unit volume of air,

$$F(t) = \rho_0(\alpha_\infty - 1)\frac{dv}{dt} + \sigma\phi v + \frac{2\alpha_\infty}{\Lambda}\sqrt{\frac{\eta}{\pi\rho_0}}\int_{-\infty}^{t}\frac{dv}{dt}\frac{dt}{\sqrt{t-\tau}} \tag{51}$$

This is like an expression relating a friction force on sphere of radius R with velocity v in an incompressible fluid,

$$f(t) = \frac{2}{3}\pi\rho_0 R^3\frac{dv}{dt} + 6\pi\eta R v + 6\rho_0 R^2\sqrt{\frac{\eta\pi}{\rho_0}}\int_{-\infty}^{t}\frac{dv}{dt}\frac{dt}{\sqrt{t-\tau}} \tag{52}$$

The second and third terms are Stokes and transient forces, respectively. The transient term considers the particle velocity history until the present time. If considering a long pulse duration for time domain, then the end term can be eliminated by the viscous boundary layer being negligible at early stages. For the short pulse duration and high frequency content $\omega \gg \omega_c$ transient effect is implied and negligible if $\omega \ll \omega_c$ where the medium has a critical angular frequency ω_c;

$$\omega_c = \frac{\sigma_0^2\phi^2\Lambda^2}{4\eta\rho_0\alpha_\infty^2} \tag{53}$$

Because the condition $\omega \gg \omega_c$ is proposed, thermal effects are included for complex compressibility for region of high frequency limit,

$$C(\omega) = 1 + \frac{2(\gamma-1)}{\Lambda}\sqrt{\frac{\eta}{-i\omega N_{pr}\rho_0}} \tag{54}$$

Fourier transform is applied to linear equations for frequency domain, and previous complex functions of both compressibility and tortuosity are used. Forchheimer's correction to Darcy's law is assumed then, giving the following equations of motion,

$$\alpha_\infty\rho_0\frac{dv}{dt} + \frac{2\alpha_\infty\rho_0}{\Lambda}\sqrt{\frac{\eta}{\pi\rho_0}}\int_{-\infty}^{t}\frac{dv}{dt'}\frac{dt'}{\sqrt{t-t'}} + \sigma_0\phi(1+\xi[v])v = -\phi\frac{dp}{dx} \tag{55}$$

$$\frac{\partial p}{\partial t} + \frac{2(\gamma-1)}{\Lambda'}\int_{-\infty}^{t}\frac{\partial p}{\partial t'}\frac{dt'}{\sqrt{t-t'}} = \frac{\rho_0 c^2}{\phi}\frac{\partial v}{\partial x} \tag{56}$$

which are solved numerically. Umnova and Turo [41] validate a proposed model by reflection coefficient data compared to model results at excitations with low amplitude and with no nonlinearity considered. Measurements from shock tube where high amplitudes are created are shown to be in good agreement with the model which accounts for Forchheimer's nonlinearity and transient effects.

In 2016 Achilleos et al [121] investigate high amplitude waves with a Helmholtz resonator side-loaded to a cylindrical waveguide. The wavelength is assumed much larger than that of the neck dimensions,

so pressure distribution is considered uniform in the cavity region. The conversion of partial acoustical energy into turbulent energy at the edges of the resonator neck leads to increase sound absorption. One of the configurations tested was that of single-sided incidence resonator. They present a model to study wave propagation with the Helmholtz resonator accounting for visco-thermal losses. The maximum sound absorption is seen to reach its peak value (0.5) at when the resonator is critically coupled. For experimental measurements, an impedance tube is used to calculate the acoustic response of the Helmholtz resonator. The termination end of the impedance tube is fitted with an anechoic stop end. A four-microphone method enables the absorption, reflectance, and transmittance to be known. The measurements are in apparent agreement with a nonlinear impedance model for the resonator.

Recently, Laly et al [122] in 2018 investigated micro-perforated panels and its behaviour at high sound levels ranging up to 150 dB. A model was proposed in order to characterise the perforated panel using its impedance and moreover, using essential flow resistivity data. The equivalent fluid approach and its equivalent parameters is used (Johnson-Allard). It is seen that a large pore (which is less effective for sound absorption in linear regime) in comparison to smaller pores, can be important for high pressure levels. Note, the phrase 'large pore' in [122] is subjective since maximum pore diameter in their work was 1.5 mm (which can be deemed small in some cases). The configurations of the perforated panels include either a cavity or porous screen, or resistive layer. The model developed by Laly et al is to account more accurately the acoustic behaviour of an MPPA when backed by a porous material immediately at the rear of the plate. A series of perforated plates are also considered, this enables a double layer of porous material in-between two MPPA's to be investigated followed by a rigid backing. In the nonlinear impedance model, they propose a new approach of describing the phenomenon of the perforated plate and its equivalent tortuosity by applying a correction term. This approach leads to a modification of the plate tortuosity and flow resistivity. This is because the tortuosity is a function of the correction length itself. This applies to the case of when high sound pressures are regarded in nonlinear regime. The impedance model begins with adopting equivalent fluid approach by works [124] in linear regime, the normalized acoustic impedance Z_l of the perforated plate [75]

$$Z_l = j\frac{\omega h}{\rho_0 c_0 \phi}\rho_e \tag{57}$$

and the dynamic tortuosity for the low and high frequency limits are,

$$\lim_{\omega\to 0}\alpha(\omega) = \alpha_\infty + \frac{\sigma_0\phi}{-i\omega\rho_0} + \frac{2\alpha_\infty^2\eta}{\sigma_0\phi\Lambda^2} \tag{58}$$

$$\lim_{\omega\to \infty}\alpha(\omega) = \alpha_\infty 1 + \frac{1-j}{\Lambda} + \sqrt{\frac{2\eta}{\omega\rho_0}} \tag{59}$$

in the case of high frequency limit of tortuosity, the effective density $\rho_e(\omega)$ becomes,

$$\rho_e(\omega) = \alpha_\infty\rho_0(1+)\frac{(1-j)}{\Lambda}\sqrt{\frac{2\eta}{\omega\rho_0}} \tag{60}$$

thus, the new normalized acoustic impedance for linear regime, for the low and high frequency limits, is presented by equation (15) and (17) from [122] and given as,

$$Z_l = j\frac{\omega h}{c_0\phi}\alpha_\infty\left(1+\frac{2\eta\alpha_\infty}{\phi\Lambda\sigma^2}\right)+\frac{\sigma h}{\rho_0 c_0} \tag{61}$$

$$Z_l = j\frac{\omega h}{c_0\phi}\alpha_\infty\left(1+\sqrt{\frac{2\eta}{\omega\rho_0\Lambda^2}}\right)+\rho_e\frac{h\alpha_\infty}{\rho_0 c_0\phi\Lambda}\sqrt{2\eta\rho_{0\omega}} \tag{62}$$

where equations (61) and (62) are for the low and high frequency limits, respectively. They are both modified forms of equation (57) with acknowledging that the effective density is linked to the air density by the dynamic tortuosity. The expressions for (61) and (62) are valid for low sound pressures only, as given by [122] since the correction term accounted for remains unchanged. This is because the end correction is not affected, which is for the case of linear regime. The flow resistivity is to be a main factor for describing the nonlinear behaviour of the perforated plates for nonlinear regime, and accounting for a correction term for the tortuosity. The jet formation and turbulence exhibit a conversion of energy (as previously discussed) and at which, at the vicinity near the orifice, the air mass is modified. The nonlinear resistance of an orifice has been well known for decades, seen in many works as early as [19], [21], [24], [55], and in some cases a discharge coefficient C_D is accounted for. A constant between the values 0.6 - 0.8 is usually assumed for the discharge coefficient (a value to denote the jet-like stream exiting the orifice). An expression is needed which accounts for the flow resistivity and nonlinear resistance of the plate containing orifices. Using works by [24], [67] which includes the discharge coefficient, the flow resistivity used by Laly et al [122] becomes,

$$\sigma(V_f) = \frac{8\eta}{\phi r^2}+\beta\frac{\rho_0(1-\phi^2)}{\pi h\phi C_D^2}v \tag{63}$$

where $\sigma(V_f)$ represents high flow resistivity rates, v is orifice particle velocity, and β is a constant set to 1.6. Normalized acoustic impedance can be calculated using an iteration process for the high sound pressure levels for the perforated panel absorber. Effective density used in characterising the normalized impedance of the MPP is related to the dynamic tortuosity. At high pressures where nonlinear effects arise from the distorted wave, the modified correction length ς_{nl} is made to the dynamic tortuosity as,

$$\alpha_{\infty nl} = \left(1+\frac{2\varsigma_{nl}}{h}\right) \tag{64}$$

In which ς_{nl} is expressed as equation (22) in [122] as the following,

$$\varsigma_{nl} = \frac{\Psi}{(1+v/(\phi c_0))}0.48\sqrt{\pi r^2}\left[\sum_{n=0}^{8}a_n\left(\sqrt{\phi}\right)^n\right] \tag{65}$$

Ψ is given as a set value which is constant given to be 4/3. Laly et al present the parameters of a_n which can be seen given in [122] supplementary to equation (22). At high sound pressure levels, the normalized acoustic impedance of the perforated plate is,

$$Z_{MPP} = j\frac{\omega h}{\rho_0 c\phi}\rho_e \tag{66}$$

where the effective density is given as,

$$\rho_e(\omega) = \rho_0\,\alpha_{\infty nl}\left(1 + \frac{\sigma(V_f)\phi}{j\omega\rho_0\alpha_{\infty nl}}\alpha_\infty\sqrt{1 + \frac{4j\omega\rho_0\eta\alpha_{\infty nl}^2}{\phi^2\Lambda^2\sigma(V_f)^2}}\right)_e \tag{67}$$

Using equations (64 – 67) enables to determine the normalized impedance of the MPPA at high sound levels for when a porous material or screen is not considered, and therefore not positioned directly behind the plate. Further information is needed in order to obtain the characteristics of the MPPA when in contact with a porous layer. A modification of the equivalent tortuosity is required to account for viscous and inertial effects of the porous media. Laly et al [122] use the approach of [75] and work by [124] to use a new correction term to account for the equivalent tortuosity as follows,

$$\alpha_{\infty nl} = 1 + \frac{\varsigma_{nl}}{h}\left(1 + Re(\alpha_p)\right) \tag{68}$$

and in the case of a double layer of porous media positioned in-between two MPPA's, the equivalent tortuosity is expressed by equation (69),

$$\alpha_{\infty nl} = 1 + \frac{\varsigma_{nl}}{h}\left(Re(\alpha_{p1}) + Re(\alpha_{p2})\right) \tag{69}$$

where α_{p1} and α_{p2} are the dynamic tortuosity of the porous materials. A high sound pressure level impedance tube is used to obtain the surface impedance of the samples tested and compute the absorption coefficient. Measurements performed consisted of a two-microphone method with an inner tube diameter of 29 mm. This allows a cut-off frequency in the range of approximately 6900 Hz. A transfer matrix method is used to get the acoustic properties of the porous material. For the porous media, the TMM is as follows,

$$M_p = \begin{bmatrix} \cos(k_p L_p) & j\dfrac{\omega\rho_p}{k_p}\sin(k_p L_p) \\ j\dfrac{k_p}{\omega\rho_p}\sin(k_p L_p) & \cos(k_p L_p) \end{bmatrix} \tag{70}$$

where M_p can be for any porous layer and, $k_p, L_p,$ and ρ_p is the wavenumber, thickness, and density of the porous material. The absorber transfer matrix of the perforated plate and porous media is given as, $T = N_1 M_{p1} N_2 M_{p2}$ where N_i is given by,

$$N_i = \begin{bmatrix} 1 & Z_{MPP} \\ 0 & 1 \end{bmatrix} \tag{71}$$

By using flow resistivity, given by equation (63), an iterative process is used [126] to determine and characterise the response of the perforated plate for the high sound levels. The rms velocity in the orifice is estimated as $\overline{V_a} = P_{ref}10^{P_{SPL}/20}/\rho_0 c_0|Z|$ where $P_{ref} = 20\ \mu$Pa and P_{SPL} is sound pressure level. The normalized impedance of the plate is $|Z|$. New values of $\overline{V_a}$ are obtained until there is a convergence of the impedance using equation (66). Laly et al show that their theoretical model when compared to experimental data provides a good agreement, see Figure 3.13 for flow resistivity data and Figures 3.14 – 3.15 for absorption coefficient data. The reflected pressure coefficient R_f is calculated by the iteration procedure which is used to determine the incident pressure $P_i = P_{ref}10^{P_L/20}/|1 + R_f|$.

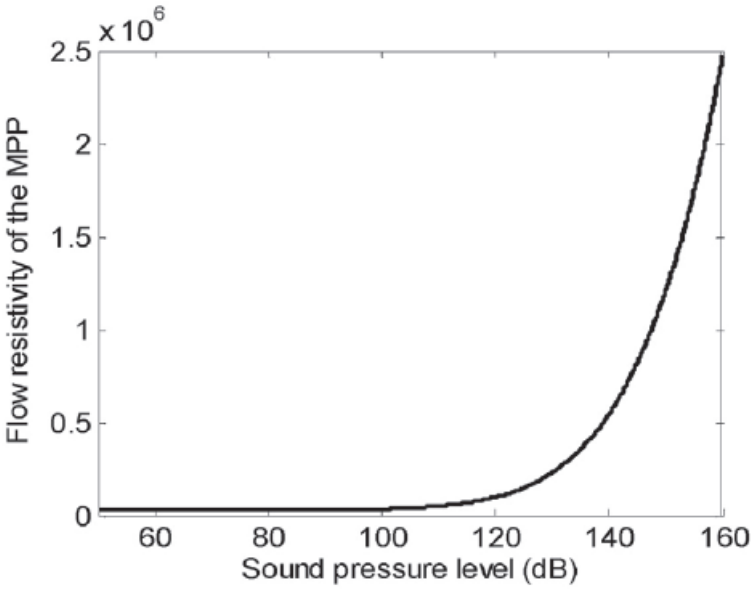

Figure 3.13. Flow resistivity for MPPA, 1.2 mm thickness and hole diameter 0.8 mm [122].

The flow resistivity seen in Figure 3.13 remains a constant value below the range of 110 dB and then reaches a critical value. This results in an abrupt increase of flow resistivity growth as sound pressure levels become larger. The dimension of the pore radius is effective for when the fluid interaction is at low pressure and Reynolds number is lower. Moreover, at higher pressures the flow resistivity grows due to the nonlinear response of the MPPA, and consequently at higher Reynolds number. Percentage ratio of the open area is 1.8 %. In Figure 3.14 absorption coefficient is plotted for 90 dB and 120 dB for experimental data and compared to the model developed by [122]. Perforated plate thickness 1 mm, hole diameter is 1.43 mm and percentage open area is 13.6 %. A porous layer is in contact directly behind the plate with its thickness, 42 mm. For Figure 3.15 a, it can be seen that the influence of accounting for the corrected tortuosity leads to a more accurate prediction by the model. The measurement data at 130 dB is compared to other models by Park [36] and Maa [125] showing a discrepancy in the predicted data. It can be seen that the model proposed by Laly et al [122] appears to justify the use of modifying the tortuosity for perforated plates backed by a porous layer or resistive screen. The dimensions given for MPPA of Figure 3.14 also apply to Figure 3.15 a. Figure 3.15 b shows a sound pressure level at 150 dB for the measurement data versus the model given by equation (66) and case for a double layer of porous media between two perforated plates. Dimensions for MPPA-1 and MPPA-2 for Figure 3.15 b, given in [122] are as follows. For the former, plate thickness is 1 mm, hole diameter 1.43 mm, and perforation ratio consisted of 13.6 %. The dimensions for the latter are plate thickness 0.8 mm, hole diameter is 1.5 mm and perforation ratio 5.3 %. The porous layers backed behind MPPA-1 and MPPA-2 are 20 mm each.

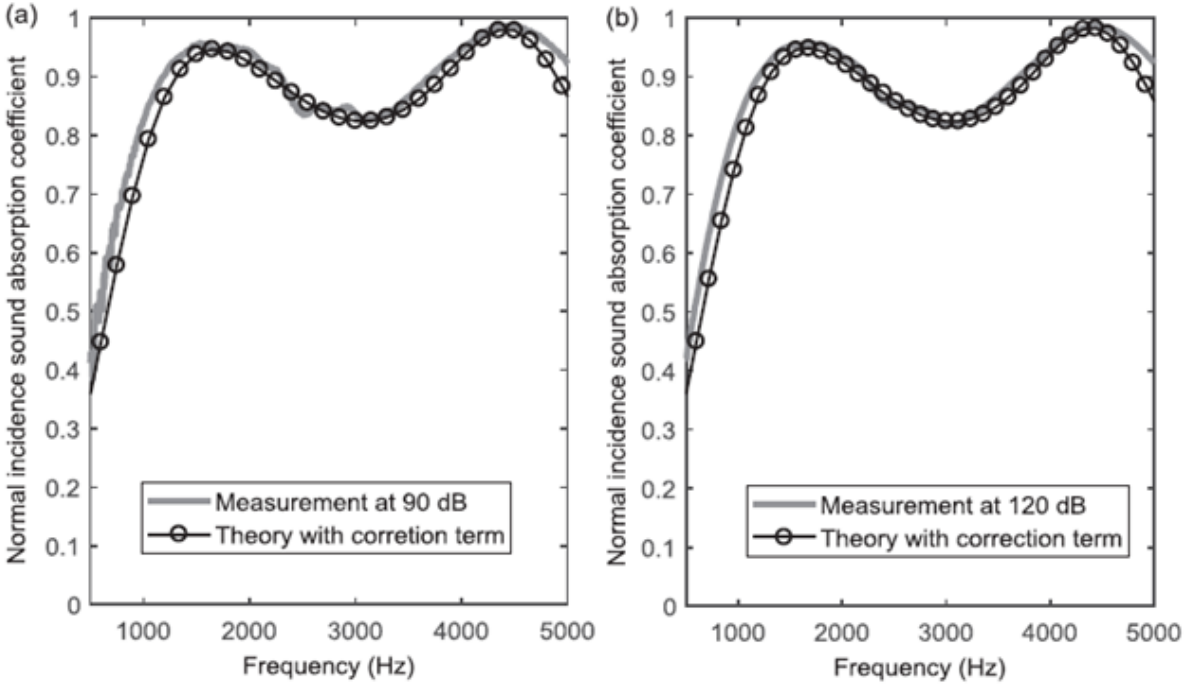

Figure 3.14. Absorption coefficient is plotted for an MPPA with a porous material backing for (a) 90 dB and (b) 120 dB. Peak absorption is observed at 1500 Hz and 4500 Hz [122].

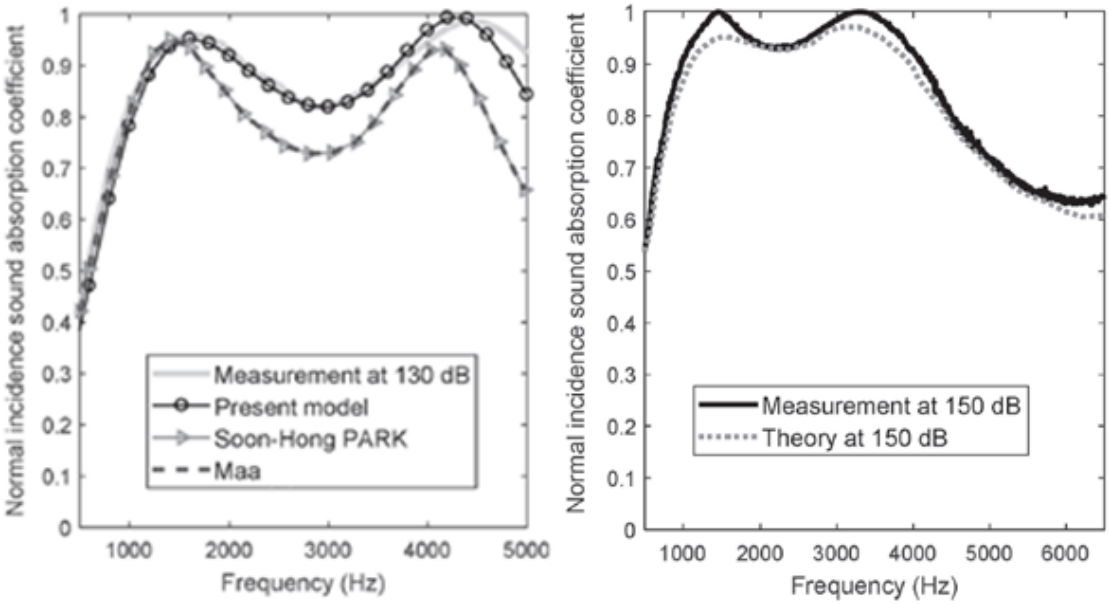

Figure 3.15. Absorption coefficient is plotted for an MPPA with a porous material backing [122].

More recently, in 2020 Kawell et al [123] also studied nonlinear effects due to high fluid flow. They investigated nonlinearity of area contractions namely in the form of expansion chambers and ducts. A high velocity in a chamber is directed towards a contraction and an impedance model is developed to account for nonlinear effects that exist in combustion systems.

3.3.2. Metamaterial Absorbers (Including Pancakes). Comparisons Between Conventional Absorbers vs Metamaterial Absorbers

Acoustic metamaterials range from porous material, graded index materials or perforated plate design amongst others and have been investigated since the turn of the millennium [107]. Convential absorbers are limited for sound attenuation as they rely on structure thickness rather than internal configuration. Metamaterials have been leading the way for control of both acoustic, and electromagnetic waves [7]. The interaction with such materials can manipulate and alter natural characteristics of the waves. Metamaterial properties arise from the configured material properties and in some circumstances the associated macroscopic parameters (such as effective density and bulk modulus in acoustic metamaterials) are able to attain negative values. There are various approaches for application of metamaterials, and this depends on which wave is to be manipulated and for what purpose. The applications include acoustic cloaking, total absorption, negative refraction, and others [8]. In 2015 the investigation of a design [1] containing open and closed pores forms the basis of a new acoustic metamaterial absorber. In works by Leclaire et al [1] a porous structure design containing dead-end pores and having a low perforation rate is built and tested. A model is developed for the wave propagation of the structure. The design uses a combination of a straight pore and benefiting from laterally spaced dead-end pores (DEP) which surround the propagation axis along the structure thickness. The work in which this thesis is based on, utilizes the concept of dead-end pore design within the development of a low frequency metamaterial absorber. Leclaire et al shows that by introducing periodicity into the sound absorber design enables interesting acoustical properties of the sound absorption of the incident wave. The absorber showing the combination of both the main pore, which can be considered as a Biot pore, and series of dead-ends can be seen in Figure 3.16.

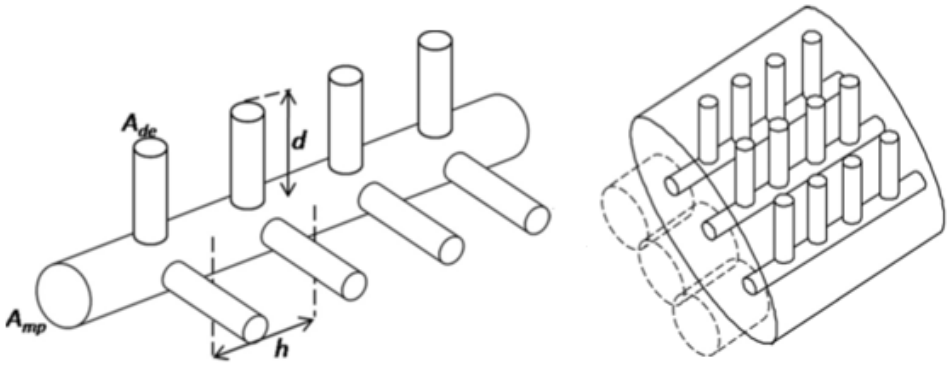

Figure 3.16. The dead-ends cross sectional area A_{de} are located at nodes along main pore cross sectional area A_{mp} (left). The period h of a unit cell, and dead-end length d are illustrated (Right). Each pore is associated an air channel for the modelling of the structure [1].

Microstructure design is shown to be effective for low frequency sound absorption at just only a few centimetres in thickness. The absorber benefits from use of its lateral dimensions which enables the thickness to be reduced. It is demonstrated by the proposed model of [1] that visco-thermal effects exist in the main pore and dead-ends. The model which uses TMM approach uses a low frequency limit to derive the properties of the porous structure and is adopted to account for the absence of fluid flow in the dead-ends. Dead-end pores prevent fluid flow and therefore classical models based on Biot theory

for flow in porous materials does not fully describe or predict the flow phenomenon that is encountered for both open and closed pores in a structure. A transfer matrix method (TMM) developed assumes the wavelength of the sound in the (open) main pore is larger than the distance between that of the (closed) dead-end pores. The geometrical parameters of the dead-ends can be altered, by changing the DEP length and thickness thus enabling sound absorption at desired frequencies. The periodicity is shown to be a great factor of the structure's design. Frequency stop-bands become present because of the periodicity of the DEP arranged at intervals located at nodes. The DEPs separated by equal distance regarded as individual unit cells, create low frequency resonances arising from the open-closed cavities. Periodicity of the absorber introduces the notion of Bloch waves thus a dispersion relation is used since the assumption of waves inside the pores are plane, hence Bloch wave number q is used and period h in the following,

$$\cos(qh) = \cos\left(k_{mp}h\right) + iX\sin\left(\ddot{k}_{mp}h\right) \tag{72}$$

where q is wavenumber in the absorber effective fluid and k_{mp} is wavenumber in the main pore.

$$X = -\frac{N}{2}\frac{A_{de}}{A_{mp}}\frac{1}{Zs_{de}} \tag{73}$$

where Zs_{de} is the surface impedance at the entrance of the dead-end. Consider a single dead-end pore, the normalized surface impedance yields,

$$Zs_{de}i = \frac{Z_{de}}{Z_{mp}}cotan(k_{de}d) \tag{74}$$

wavenumber in the dead-end is k_{de} thus X becomes,

$$X = -\mathrm{i}\frac{N}{2}\frac{A_{de}}{A_{mp}}\frac{Z_{mp}}{Z_{de}}tan(k_{de}d) \tag{75}$$

To determine the case for N non-identical dead-end pores per period h, a new expression for X is presented and assuming a time dependence $\exp(-i\omega t)$, equation (73) is generalized to obtain an expression of matrix $\mathbf{T_c}$, for Bloch waves propagating at some distance either side of period h.

$$X = -\frac{1}{2}\frac{Z_{mp}}{A_{mp}}\sum_{k=1}^{N}\frac{A_{de}^{(k)}}{Z_{de}^{(k)}}tan\left(k_{de}^{(k)}d_{de}^{(k)}\right) \tag{76}$$

$$\mathbf{T_c} = \begin{pmatrix} (1+X)y + & X \\ -X & \dfrac{(1+X)}{y} \end{pmatrix} \tag{77}$$

where $y = \exp i\, k_{mp}h$. Equation (77) relating Bloch waves per period h combines for an (n) set of periods to account for the forward and backward Bloch waves for periodic structure with thickness so that,

$$\mathbf{M} = (\boldsymbol{T_c})^{\boldsymbol{n}} = \begin{pmatrix} M_{11} & M_{12} \\ M_{21} & M_{22} \end{pmatrix} \tag{78}$$

Considering a main pore consisting of n periods, the pressure reflection r_n and pressure transmission t_n is given as,

$$\begin{pmatrix} t_n \\ 0 \end{pmatrix}\mathbf{M} = \begin{matrix} (1) \\ r_n \end{matrix} \tag{79}$$

where $r_n = -M_{21}/M_{22}$ and $t_n = -1/M_{22}$. Equation (79) refers to one-unit cell and its pressure reflection and pressure transmission coefficients, assuming that flow is prohibited outside the dead-end pores.

Integer value of 1 is set equal to the determinant of **M.** For case of a rigidly backed wall after the dead-end, then the power reflection coefficient becomes,

$$r_n' = \frac{M_{11-}M_{21}}{M_{21-}M_{22}} \tag{80}$$

The amplitudes of forward and backward waves associated with the main pore element can be described by using cross sectional area of A, of the straight pore channel having surface perforation ϕ. For the material in rigid backing the reflection coefficient of the structure containing the dead-ends R_n' is given by the product of M and **T**.

$$R_n' = \frac{M'_{11-}M'_{21}}{M'_{22-}M'_{12}} \tag{81}$$

where $\mathrm{M}' = \mathrm{M} \times \mathbf{T}$ and $\mathrm{M} = \mathbf{T^{-1}} \times \mathrm{M}'$

$$\mathbf{T} = \begin{pmatrix} \dfrac{1+\phi'}{2\phi} & -\dfrac{1-\phi'}{2\phi} \\ -\dfrac{1-\phi'}{2\phi'} & \dfrac{1+\phi'}{2\phi'} \end{pmatrix} \tag{82}$$

Absorption coefficient α is calculated as,

$$\alpha = 1 - |R_n'|^2 \tag{83}$$

The low frequency limit is investigated assuming the wavelength of sound is larger than the distance between the dead-ends. The behaviour of sound propagation in the pore is described after forward and backward wave propagation across the unit cell length is treated. Setting boundary conditions for pressure and particle velocity at the entry and exit point of the unit cell (containing one dead-end) enables expressions for effective density ρ_e and effective compressibility C_e to be found. A full detailed description can be seen in [1] for a low frequency approximation considered for the pore filled with effective fluid for a periodic arrangement.

$$\rho_e = \rho_{mp} \tag{84}$$

Effective density in the main pore is shown to not be influenced from the presence of the dead-ends. However, the effective compressibility does become modified due to the dead-ends which results from thermal exchanges between the DEP and main pore. The effective compressibility of pore with dead-ends is,

$$C_e = C_{mp} + C_{de}\frac{NA_{de}}{A_{mp}}\frac{d}{h}\left(\frac{\tan(k_{de}d)}{k_{de}d}\right) \tag{85}$$

The characteristic acoustic and material impedances, z and z_m respectively are given by equations (86) and (87).

$$z = \sqrt{\frac{\rho_e}{C_e}} = \sqrt{\frac{\rho_{mp}}{C_{mp} + C_{de}\dfrac{NA_{de}}{A_{de}}\dfrac{d}{h}}}\left(\frac{\tan(k_{de}d)}{k_{de}d}\right) \tag{86}$$

$$z_m = \frac{z}{\phi} = \frac{1}{\phi}\sqrt{\frac{\rho_{mp}}{C_{mp} + C_{de}\dfrac{NA_{de}}{A_{mp}}\dfrac{d}{h}}}\left(\frac{\tan(k_{de}d)}{k_{de}d}\right) \tag{87}$$

Wave number q of the effective fluid is equal to,

$$q = \omega\sqrt{\rho_e C_e} = \omega\sqrt{\rho_{mp}\left(C_{mp} + C_{de}\frac{NA_{de}}{A_{mp}}\frac{d}{h}\left(\frac{\tan(k_{de}d)}{k_{de}d}\right)\right)} \quad (88)$$

Sound speed is drastically reduced due to the presence of the dead-end pores which contribute to energy attenuation of the acoustic wave. This results in the predicted decrease of sound at low resonance frequencies and increased absorptive peaks. The increase in absorption coefficient is significantly below the frequency predicted value arising from resonance phenomena of the dead-ends, shown in Figure 3.17.

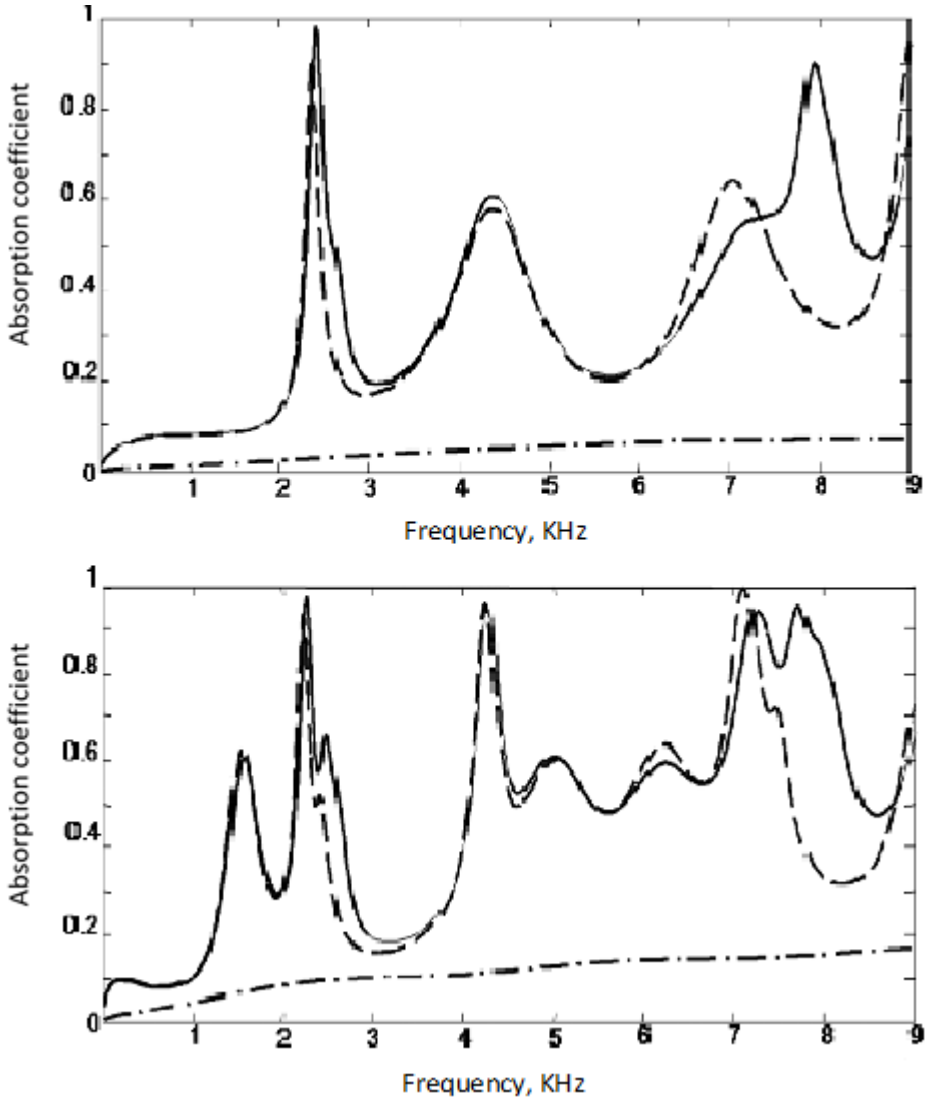

Figure 3.17. Absorption coefficient vs frequency for structure comprised of dead-end pore. Sample main pore thickness of graph a) L=2 cm, and for graph b) main pore L=5 cm. TMM represented by dash line and solid line by including low frequency limit of the dead-ends. The case for a main pore in the absence of dead-ends is represented by the dash-dot line [1].

Other works by Leclaire et al [44-45] sees the development of a microstructure containing dead-ends which are created artificially by use of 3D printing. The structure consisted of dead-ends located at the surface of the sample with partial perforations ending in the bulk of the structure. The previous works by Leclaire aforementioned, leads to maximising the volume of dead-ends in other designs. In recent work (2018) by Dupont et al, [3], a 3D printed microstructure was considered that contains a periodic

arrangement of thin plates with central perforation separated by cavities, see Figure 3.18, the so-called “pancake absorber”. The pancake absorber is one of the realizations of the microstructure design suggested earlier in work by Leclaire et al [44] where the additional laterally arranged pores are coupled with the main perforation. Low value of sound speed through the perforation achieved in these structures [3] leads to the existence of the absorption peaks at low frequencies. In [3], a transfer matrix model (TMM) is used to predict the frequency dependence of the absorption coefficient of the absorber, which gives a good agreement with the measurements. The pancake absorbers are proven to be effective for low frequency sound absorption at only a few centimetres in thickness.

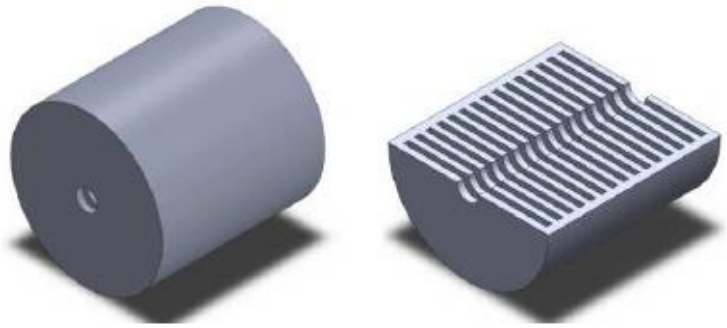

Figure 3.18. A 3D microstructure comprised with dead end pores. Structured internal geometry of the “pancake” absorber [3].

Pancake absorber developed in [3] allowed the dead-ends to be kept thin, made possible from precision of 3D engineering modelling devices. The advantage of using 3D printer capabilities has an overall effect on cost and the overall thickness of the microstructure. The building of the individual dead-ends was achieved on the order of one millimetre which makes the pancake design effective in many ways. This is because the acoustic properties of porous media saturated with air are dependable on the sample thickness as well as structure [76]. Sound absorption at low frequencies is challenging because conventional acoustic absorbers must be relatively thick for them to be effective. The introduction of cavities behind MPPAs or Helmholtz resonators have been of interest especially for absorption at medium and higher frequencies. There is, however, still a requirement for effective low frequency absorption by means of a relatively thin size absorber compared to conventional acoustic treatments. In ref [1] the dead-ends are shown to influence the effective compressibility due to thermal exchanges interacting with the main pore but not change the effective density. Low frequency sound absorption is also made possible due to the result of stop bands present from the quarter wavelength resonators. The pancake absorber increases the absorptive phenomenon associated with the dead-ends by each dead-end cell using the structure circumference as opposed to a neck or tube. In using the structure circumference, this approach of using each dead-end maximizes the volume obtained within the design across the sample thickness, as seen in Figure 3.18. The wave speed in the central pore of periodic structures is known to slow down due to ‘wave slowing materials’ [88] thus, increasing sound absorption. The TMM is extended further in [3] to account for dead-ends with a geometrical difference as seen in [1].

To begin, the effective parameters as of [1] are proposed but with the approach of using a coherent potential approximation [89]. Since the effective density is unchanged, equation (84) remains valid. The effective compressibility of equation (85) reduces to equation (89).

$$C_e = C_{mp} + C_{de}\frac{NA_{de}}{A_{mp}}\frac{d}{h} = C_{mp} + C_{de}\frac{V_{de}}{V_{mp}}. \tag{89}$$

Where V_{de} and V_{mp} are the dead-end and main pore volumes per period h. Cross-section areas for the dead-end and main pore are $A_{de} = 2\pi r_{mp}h_{de}$ and $A_{mp} = \pi r_{mp}^2$ respectively. Sound speed is drastically decreased by the dead-ends which act like quarter wavelength resonators. The effective sound speed (combination of both the main pore and dead-ends) is considered for an array of dead-ends periodically distributed along the thickness of the sample L. The first resonance frequency f_{res1}, of a quarter wavelength structure for the main pore is,

$$f_{res1} = \frac{c_{mp}}{4L} \tag{90}$$

where effective sound speed in the main pore is c_{mp}. Low frequency approximation of the sound speed given by the real parts of effective density and compressibility associating the wavenumber in the dead-ends is,

$$c_e = \frac{1}{Re\left(\sqrt{\rho_e C_e}\right)} \xrightarrow[Re(k_{de}d)\ll 1]{} \frac{1}{Re\left(\sqrt{\rho_e\left(c_{mp} + c_{de}\frac{V_{de}}{V_{mp}}\right)}\right)} \tag{91}$$

Considering now the contribution of the dead-ends and the effective sound speed of the structure, the first resonance frequency f^*_{res1} for series of cavities and main pore is,

$$f^*_{res1} = \frac{c_{mp}}{4L}\frac{1}{Re\left(\sqrt{\rho_e\left(c_{mp} + c_{de}\frac{V_{de}}{V_{mp}}\right)}\right)} \tag{92}$$

Since it is seen from equation (92) that by increasing the effective compressibility will reduce the first resonance frequency. The thermal exchanges between the dead-ends and main pore can be increased by extending the volume ratio V_{de}/V_{mp} within the material. Dupont et al [3] consider introducing a lumped parameter approach with the transfer matrix method. A single cell of the pancake structure (named pancake due to the combination of many parallel cells) is considered since the structure is periodic. A single cell is defined as being two half main pores separated between a dead-end and a common pore (volume between dead-ends) which can be seen in Figure 3.19. The common pore is surrounded by a virtual wall that is not considered rigid. It is a volume between the centres of the propagation axis occupying the spatial domain to the entrance of two dead-ends or pancake cavities. The common pore (for thickness $d_{de}/2$) given as a transfer matrix where thermo-viscous effects are neglected since no rigidity is present is,

$$\mathbf{T}_{\boldsymbol{com}}^{(h_{de/2})} = \begin{pmatrix} cos(k_0 h_{de}/2) & jZ_0 sin(k_0 h_{de}/2) \\ \frac{j}{Z_0} sin(k_0 h_{de}/2) & cos(k_0 h_{de}/2) \end{pmatrix} \tag{93}$$

where k_0 and Z_0 are wave number and characteristic impedance of air.

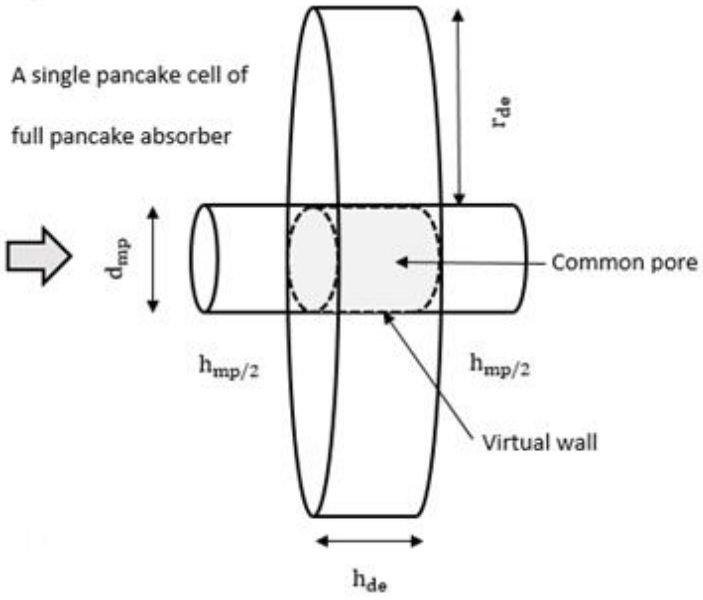

(a)

A single cell is is shown for the pancake absorber above illustrating the main and common pores along with the virtual wall. The combination of a series of cells over the sample length can be seen below.

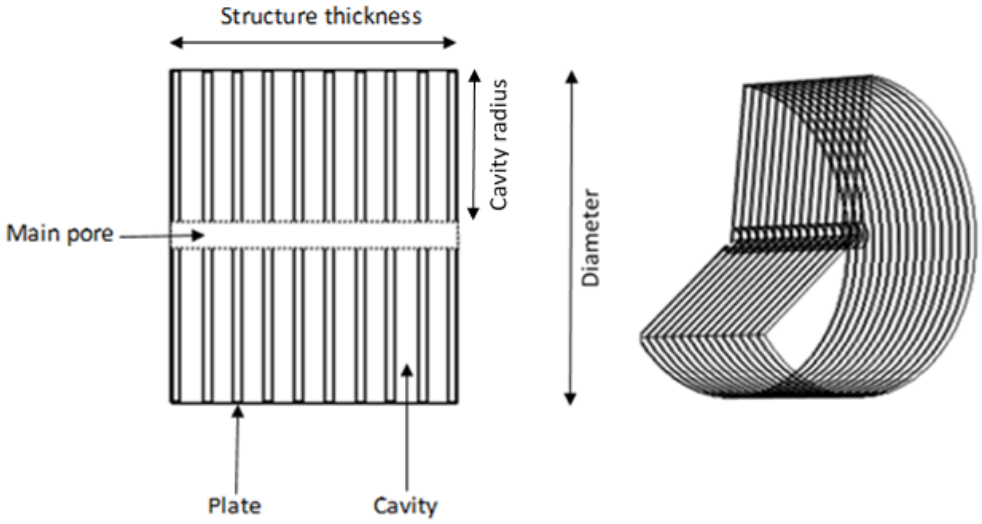

(b)

Figure 3.19. (a) Single pancake cell, and (b), an array of pancake cells

The transfer matrix for a periodic cell of the pancake structure consisting of two half main pores (thickness $h_{mp}/2$) is,

$$\mathbf{T}_{\boldsymbol{mp}}^{(h_{\mathrm{mp}/2})} = \begin{pmatrix} cos(k_{mp}h_{mp}/2) & jZ_{mp}sin(k_{mp}h_{mp}/2) \\ \frac{j}{Z_{mp}}sin(k_{mp}h_{mp}/2) & cos(k_{mp}h_{mp}/2) \end{pmatrix} \tag{94}$$

where k_{mp} and Z_{mp} are effective fluid parameters from [83]. Surface impedance of a pancake cavity is considered by [3], identical to a Helmholtz resonator. An expression from Dickey and Selamet [90] is

used and modified for use of effective properties. The pancakes consist of open-open cavities separated by a virtual pore, however in the expression from [90] the open-closed configuration can be used by treating each cavity point. Wave number and the impedance of the dead-ends are then calculated using JCA model and Bessel functions applied to obtain surface impedance of the cavity using a slit geometry and side branch. The final transfer matrix T_{samp} for a number N cells in the period structure is obtained using the three matrices, 1. From single pore plate (contraction matrix), 2. Cavity and main pore (cell matrix) and 3. Final pore (end matrix).

$$T_{samp} = T_{\phi} T_{end} T_{\phi} (T_{cell})^{N} T_{end} T_{\phi}^{-1} \tag{95}$$

where T_{ϕ}, T_{cell} and T_{end} are the following,

$$T_{\phi} = \begin{pmatrix} 1 & 0 \\ 0 & MA_{mp}/A_{sample} \end{pmatrix} \tag{96}$$

where M is number of main pores of the material and A_{sample} is the cross-sectional area.

$$T_{cell} = T_{\boldsymbol{mp}}^{h_{mp/2}} T_{\boldsymbol{com}}^{h_{de/2}} T_{de} T_{\boldsymbol{com}}^{h_{de/2}} T_{\boldsymbol{mp}}^{h_{mp/2}} \tag{97}$$

$$T_{end} = \begin{pmatrix} cos(k_{mp} h_{end}) & jZ_{mp} sin(k_{mp} h_{end}) \\ \frac{j}{Z_{mp}} sin(k_{mp} h_{end}) & cos(k_{mp} h_{end}) \end{pmatrix}. \tag{98}$$

Where h_{end} is end correction length and T_{end} given by (98) is transfer matrix for the pore end effect. Equations for the sound absorption coefficient and transmission loss for the pancake absorber is given in [3] and correction length used from [124], given by equation (9.18). Moreover, data obtained by measurements performed in impedance tube for linear regime is compared with TMM approach and FEM. The effective parameter values from JCA model are also included. Two external diameters (29 mm and 44.4 mm) of the ‘metamaterial’ pancake absorber are tested in separate impedance tubes for each absorber diameter. Results can be seen in Figure 3.20 showing good agreement between the models. Models compared with experimental data are from TMM approach discussed, and COMSOL Multiphysics software. The material properties computed in COMSOL Multiphysics is of the product Acrylonitrile Butadiene Styrene (ABS) which is result of a 3D printed fabrication process.

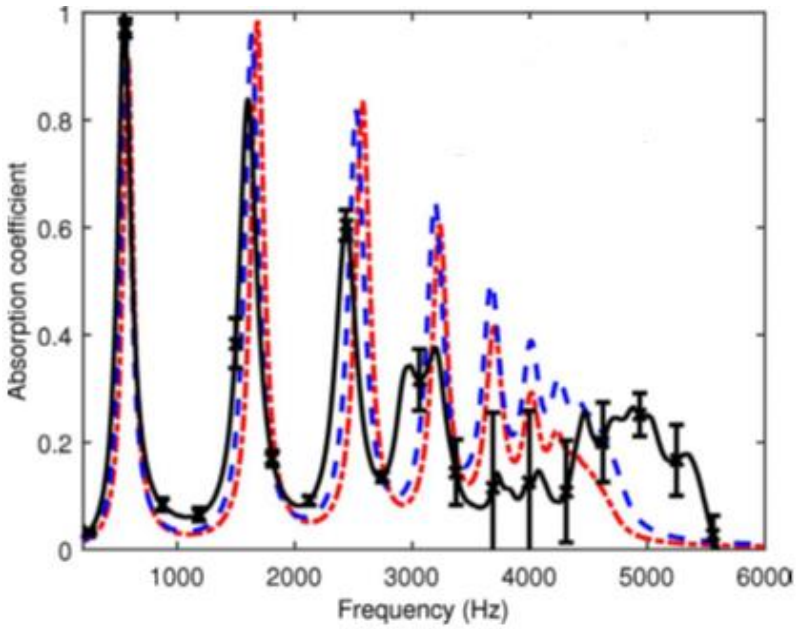

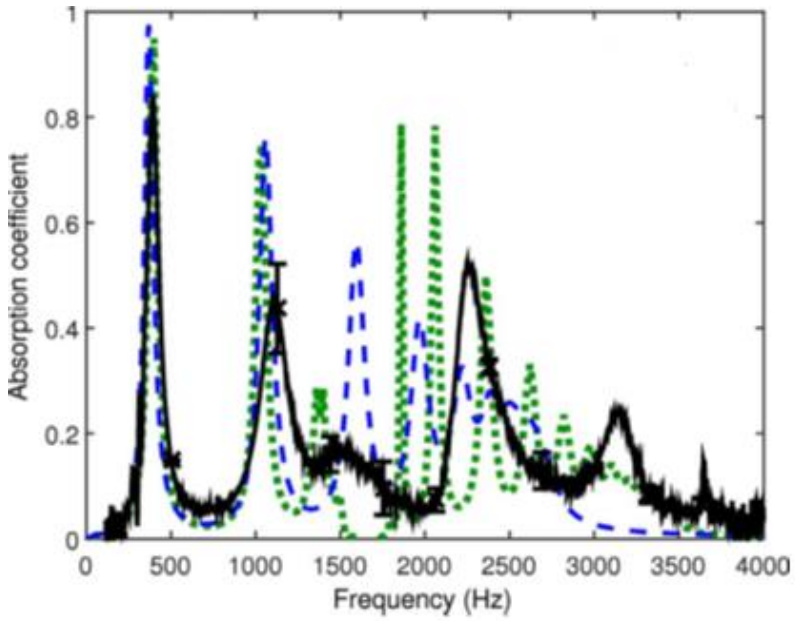

Figure 3.20. Pancake with external diameter 29 mm (top). Data markers, black (solid) experimental, red (dash-dot) FE rigid frame, and blue (dash) TMM. Pancake with external diameter 44.4 mm (below). Data markers, black (solid) experimental, green (dash-dot) FE vibro-acoustic, and blue (dash) TMM [3].

Absorption coefficient shown in Figure 3.20 is seen to show a discrepancy at some frequencies. This is explained by Dupont et al [3] for both pancake absorbers of different external diameter. For 29 mm external diameter the largest discrepancy is given at 3500 Hz – 4700 Hz and again above 5700 Hz. Similarly, for pancake absorber with external diameter of 44.4 mm, the largest discrepancy is given at 1500 Hz – 2000 Hz and above 2500 Hz. The explanation for this is bandgap phenomena from the material and acoustic resonance. Elasticity of the ABS sample is accounted for in the COMSOL Multiphysics model for Youngs modulus and Poisson's ratio. The computed results from FEM thus give better matching between the theoretical and experimental data. Plane wave propagation is assumed in the analytical model and wavelength considered much larger than the period thickness of cells. An extensive study of pancake absorbers built using 3D printer technology is investigated by [3]. A periodic structure consisting of an array of cavities is shown for effective low frequency sound absorption. For the same thickness (for case of a solid cylinder) the first resonance peak is much higher in frequency. This allows the pancake absorber thickness to therefore be effectively reduced for around factor 5 and 7 for external diameters of 29 mm and 44.4 mm, respectively.

3.4. Profiled and Graded Absorbers (Including Black Holes)

The principal objective of this research is to develop an effective absorber for shock waves and explosions. Shock waves are high amplitude signals hence material and air nonlinearity are essential to the understanding of shock formations. The absorbers have to be effective for high amplitude sound and they have to be structurally robust, withstand high temperatures and mechanical load but be thin and light for application. Unlike conventional materials that depend on material thickness and cavities for sound absorption, the idea is to combine both (ABH) and (DEP), with the former having benefits in being frequency broadband, and the latter by utilising its lateral dimensions for acoustic wave absorption. Many metamaterials are frequency selective and rely on resonance phenomena for

impedance matching of the airborne sound. Impedance matching allows the incident sound wave to be effectively absorbed therefore minimizing reflections. This is achieved by reducing the reflected waves from the solid boundaries of a structure. The black hole effect is one approach of using impedance matching and reducing wave propagation. The impedance matching of waves to a structure allows for reduction of reflection coefficient. Structures built utilising the black hole effect of having different designs are shown to be effective for wave absorption.

Black hole effects had first been suggested in 1988 by Mironov [91] by introducing tapered edges of plates and bars which eliminate any reflections. The thickness of these structures smoothly decreases to the point where any flexural waves slow down along the plate or bars length and eventually stops. A power law is used to describe the phenomena accounting for the spatial coordinate of plate thickness at its edges being zero. A flexural wave is seen to never reach the plate edge because the time taken would have to be infinite. Other works using the same concept is presented by Krylov [92 – 94] in 2002 and 2004 who investigated the absorption of flexural waves and vibrations. Krylov utilises the black hole effect for flexural waves as effective vibration dampers gradually decreasing the thickness of the plate towards its edges therefore creating a wave speed profile. Theoretically the wave speed is decreased to zero meaning full absorption. In practice, small number of absorbers are attached to the plate edge to absorb the residual waves. [94] Introduces the idea of additional thin damping layers on the surface of quadratic shaped elastic wedges. This method helps to reduce the reflection coefficient by the decomposition layers. In 2007 Krylov et al [95] apply the method of attaching absorbing layers in strips to steel wedges at one of its sides. Measurements are performed with plates of constant thickness and compared to quadratic shapes. The resonant peaks of the wedges with and without the additional absorbing layers are then compared experimentally. It is shown that using relatively thin films for improved absorption supresses the vibration peaks for the reduced reflection coefficient of flexural waves therefore increasing damping.

Different geometries have also been explored in 2011 using the black hole effect as seen by O'Boy and Krylov [96]. In this approach flexural waves are investigated by the method of using circular plates with tapered central holes. The holes have either a constrained or an absorbing layer shown by results of a numerical approach to suppress resonant peaks up to 17 dB. In 2014 Zhao et al [97] investigate the black hole effect of tapered wedges of thin plates for broadband energy harvesting. The designs of wedges are evaluated numerically by finite element methods for steady state and transient excited conditions having surface mounted piezo transducers. In 2015 Denis et al [98] show that the reflection coefficients of acoustic black hole effect in wedges decrease with increased frequency. The investigation of using beam extremities of flexural waves with acoustic black hole terminations shows that oscillations occur from the reflection coefficient. The use of different models is compared to one another with respect to experimental results obtained. A power law thickness profile is used for the spatial component of a wedge, as suggested by [91] for the black hole terminations. The idea has been extended to different types of waves including airborne sound [2], [10]. It is shown that acoustic black hole structures can vary depending on its application, amplitude strength and frequency spectrum of interest for desired absorption. Another example of black hole design is utilising the material external structure. Omnidirectional absorbers have been studied by [102] with up to 80 percent energy absorption achieved above 1 kHz. An omnidirectional absorber has been built using graded index matching layers as given

in recent work by Elliott et al [10]. This design arrangement is comprised of an impedance matching layer and a cylindrical porous absorbing core, see Figure 3.21. It has been shown that the structure provides effective omnidirectional absorption of incident waves. In the structure matching layer, there are rods with varying radius and concentration used to provide a gradual impedance matching between the air and porous absorbing core. It is demonstrated that a structure containing a hollow absorbing core follows to be nearly as effective to one possessing a full core with a graded index of 6 layers of rods.

Figure 3.21. Omnidirectional acoustic black hole with impedance matching layer [10].

The full structure is built and tested in an anechoic chamber and compared to a semi-analytical scattering model for comparison. The omnidirectional absorber is then validated, and its losses accounted for within the structure. The device is an analogue of omnidirectional absorbers used for electromagnetic fields which can be seen in works by Narimanov and Kildishev [99]. The black hole structure designed by [10] is investigated with aim to absorb low frequency sound by combining both porous material with metamaterials. The thermal and viscous boundary layers have been accounted for and shown to be of great importance for absorption at low frequencies. A hollow core and the use of mineral wool is compared to a full porous core, where an approximate matching method is used. To obtain the porous properties of the absorber, an effective fluid model is used [80] to obtain the values for the effective density and bulk modulus. Experimental methods are performed using an impedance tube to obtain the wavenumber and characteristic impedance of mineral wool.

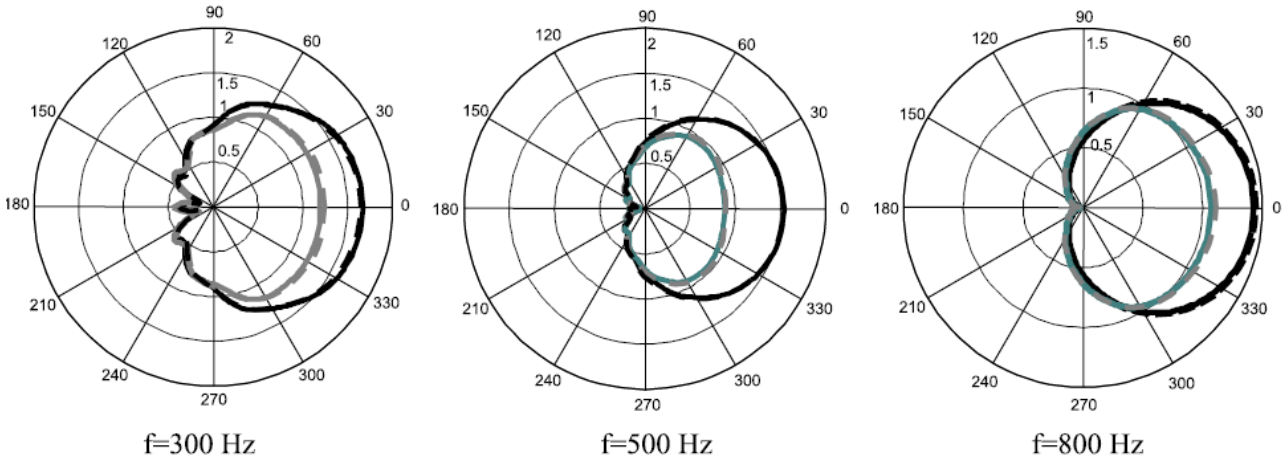

Figure 3.22. Comparison for angular distribution of normalized rms pressure for surface of an omnidirectional absorber and hollow porous cylinder given by grey lines and black lines respectiveley [10].

In Figure 3.22 the comparison for the two cylindrical structures is shown by [10] accounting for the angular distribution of normalized rms pressure on the surface. The models developed for case of a semi-analytical and 2D Finite element method are represented by dashed and solid lines, respectively. The losses are presented also [10] for angular distribution of normalized rms pressure on the surface at 300 Hz and 1000 Hz. The viscous and thermal losses are seen largest for lowest frequencies due to the increased boundary layer skin depths, shown in Figure 3.23.

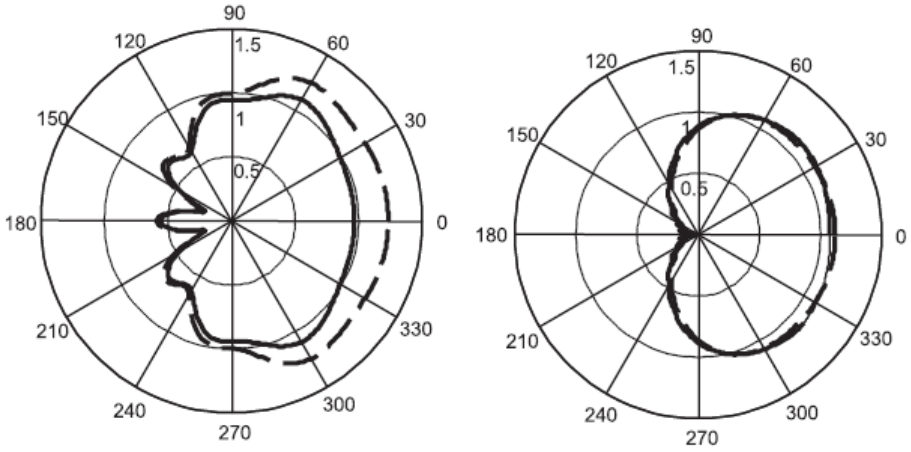

Figure 3.23. Comparison for angular distribution of normalized rms pressure at 300 Hz (left) and 1000 Hz (right) for surface of an omnidirectional absorber with porous a core. Losses and no losses are solid and dashed lines respectiveley [10].

Mironov and Pislyakov [2] in 2001 proposed the idea of an acoustic wave propagating in a waveguide being completely absorbed. The concept to this is due to no reflections existing within the cross section along the tube axis. The sound velocity ultimately decreasing to zero, gradually along the thickness of the waveguide by the elastic-type wall admittance. The dimension of the walls is to be reduced smoothly and directed inwards with the increasing tube thickness. The sound propagation velocity depends on the admittance of the tube walls and is represented by a varying inner radius cross section. This concept of modifying a wave's amplitude and velocity in such a way is known as an acoustic black hole retarding structure. A schematic diagram can be seen in Figure 3.24 from Mironov and Pislyakov [2] where the

radius $r_{(x)}$ decreases to zero at the end of a tube having thickness L. The radius R at the sample surface $x = 0$ is shown between A and C which are the outer-most entry points for the incoming wave.

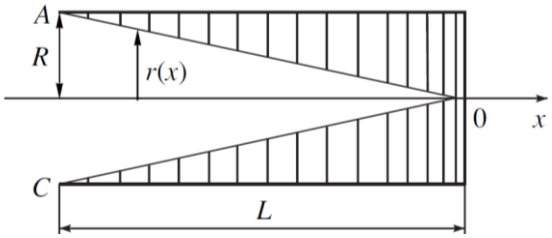

Figure 3.24. An acoustic black hole retarding structure comprised of rings with varying size. The inner radius of the waveguide shown to be decreasing to zero. The proposed design is given by [2].

The sound propagation described by the one-dimensional wave equation to account for the varying wall admittance is replaced to sound waves in horns. The reason for this is because the cross-sectional area being constant is no longer valid. The generalized Webster equation used to describe the propagation of sound in a tube with varying cross-section is obtained,

$$\frac{1}{c^2}\frac{\partial^2 p}{\partial t^2} + \frac{2Y\rho_0}{r}\frac{\partial p}{\partial t} = \frac{\partial^2 p}{\partial x^2} + \frac{\partial p}{\partial x}(\ln S)_x{}' \tag{99}$$

$$p'' + p(lnS)' + p\left(k_0^2 + \frac{2Y\rho}{r}(i\omega)\right) = 0 \tag{100}$$

where ρ_0, p, r, and S are the medium density, pressure, waveguide radius and cross-sectional area, respectively. $k_0 = \omega/c$, and prime represents the derivate with respect to x. The cylindrical tube is rigid with solid walls thus the admittance Y is varied with structure thickness by solid tapered rings which affect the compressibility hence,

$$Y = (-i\omega)\frac{1}{\rho_0 c^2}\frac{R^2 - r^2}{2r} \tag{101}$$

Firstly, the area of the cross section in conjunction with (100) and (101) is used to account for the small change in radius, equations as given by [2]. The notion that $p(x)\sim\exp(ikx)$ further yields the wavenumber $k = k(x)$ after substituting into equation (80) thus,

$$p'' + 2p'(lnr)' + k_0^2\frac{R^2}{r^2}p = 0 \tag{102}$$

and $k(x)$ becomes,

$$k(x) = \sqrt{k_0^2\frac{R^2}{r^2} - ((lnr)')^2} = \frac{1}{r}\sqrt{k_0^2R^2 - (r')^2} \tag{103}$$

A power law function with respect to x for the changing radius $r(x) = \varepsilon x^n$ enables equation (103) to be transformed for the case of when $k(x)^{-1}$ and for small variations so that $|k| \gg 1/x$ is valid.

$$k(x) = \frac{1}{\varepsilon x^n}\sqrt{k_0^2R^2 - \varepsilon^2 n^2 x^{2(n-1)}} \tag{104}$$

From equation (104) the WKB approximation with its applicability gives,

$$\frac{1}{\varepsilon x^{n-1}}\sqrt{k_0^2R^2 - \varepsilon^2 n^2 x^{2(n-1)}} \gg 1 \tag{105}$$

where ε is the ratio of the radius at the entry of the waveguide across the length of tube to the edge of the last ring. For a propagating wave in the positive x direction the wavenumber is reduced for $n = 1$. If the decrease of tube radius is smooth and small enough with increasing thickness then $k(x)$ becomes,

$$k(x) = \frac{1}{-x}\sqrt{k_0^2 L^2 - 1} \tag{106}$$

To describe the behaviour of the incident pressure wave, a form of power law functions is seen to give exact particular solutions so that,

$$p(x) = A_\alpha \left(\frac{x}{L}\right)^\alpha. \tag{107}$$

Solutions for α are given as quadratic equations, α_{12}

$$\alpha_{12} = -\frac{1}{2} \pm \sqrt{\frac{1}{4} - (k_0 L)^2} \tag{108}$$

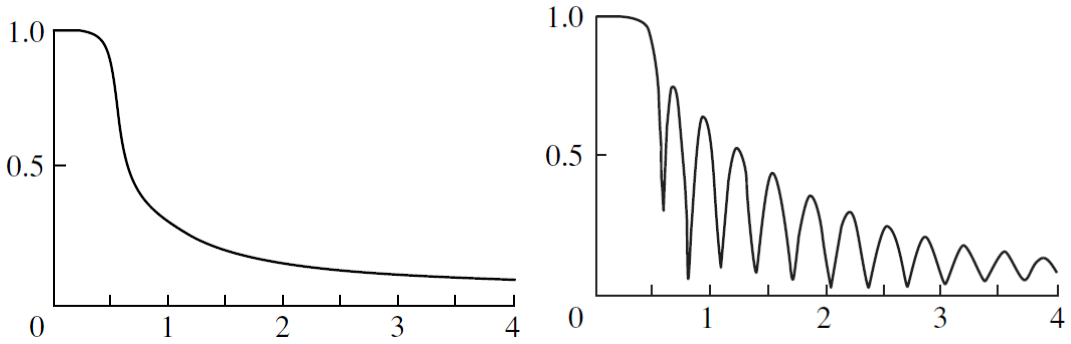

(a) (b)

Figure 3.25. Acoustic black hole reflection coefficient for non-reflecting (a), cross-section waveguide. Reflections become apparent if the termination (b), is abrupt in the waveguide from any discontinuities [2].

In Figure 3.25 the reflection coefficient is shown for case of reflected and non-reflected waves for an acoustic black hole waveguide. The frequency is representation of $k_0 L$ as presented in [2]. The sound velocity is decreased gradually and vanishes completely for a pressure wave existing in the positive direction only with zero reflections in the cross-section (Figure 3.25 a). Resonance phenomena impacts the behaviour of the reflection coefficient from the existence of two waves propagating in opposite directions as seen in Figure 3.25 b. Reflected waves will occur if the end point of the waveguide is presented with sharp abruptness. In the case of a rigid plate at the termination (instead of the waveguide decreasing to zero smoothly) the acoustic admittance of the black hole retarding structure Y_{BH} becomes,

$$Y_{BH} = \frac{1}{\rho_0 c}\frac{e^{-ikl} - Ve^{ikL}}{e^{-ikl} + Ve^{ikL}} = \frac{1}{i\rho_0 \omega L}\frac{\alpha_1 + W\alpha_2}{1 + W} \tag{109}$$

where $W = A_2/A_1$ are the amplitudes of the incident and reflected waves e^{-ikL} and Ve^{+ikL} with $A_1 + A_2 = e^{-ikL} + Ve^{+ikL}$. Where the reflection coefficient is determined by any discontinuities within the structure. If reflections do occur in the waveguide, then V is given by,

$$V = \frac{1 + W + \frac{c}{i\omega L}(\alpha_1 + W\alpha_2)}{1 + W - \frac{c}{i\omega L}(\alpha_1 + W\alpha_2)} e^{-2ikL} \tag{110}$$

For case of a varying waveguide being smoothed such that no discontinuity produces any reflections then V becomes,

$$V = \frac{1+\frac{\alpha_1 c}{i\omega L}}{1-\frac{\alpha_1 c}{i\omega L}} e^{-2ikL} \tag{111}$$

It is seen by [2] that specialist structures can achieve full sound absorption if velocity is decreased fully over some segment length. The acoustic admittance of the black hole structure eliminates reflections by means of a smooth varying radius. The absorber is always terminated with small increments of decreasing values of its inner radius. In reality however, the presence of reflected waves is unavoidable for application purposes. Absorbers are mostly to be built keeping sample thickness to a minimum. The retarding black hole design shown in works by Mironov and Pislyakov [2] does not consider losses. Other authors also investigated the retarding structure by building and performing measurements [100, 103]. Slightly over a decade later, since Mironov and Pislyakov [2], the linear profile design has been extended by Oriol et al [104] using a Transfer Matrix Method (TMM) to model the structure with losses. This is accounted for by using an empirical Delany and Bazley model suitable for fibrous materials. The linear profile is reviewed by [104] with the addition of using TMM approach to analyse the parameters of the profile. This is achieved by control of the number of rings and cavities including their thicknesses. The waveguide is investigated for both linear and quadratic profiles [104] but no further discussion on linear profiles is necessary.

A generalization of Webster's equation used for describing a plane wave propagating in the varying cross-sectional waveguide is used as shown from [2]. The wall admittance is determined from linearized continuity and momentum conservation equations hence, time harmonic dependence of acoustic pressure for frequency domain is given by equation (100). For a quadratic profile from equation (107) it is extended to represent its quadratic geometry distinguishing it from linear case which is the power-law solution. Once the governing equation for the quadratic black hole is established, then the general solution is determined from using the real constants applied given in the power law solution. The group velocity and wavenumber for a wave packet entering the quadratic black hole is obtained and time taken to travel to the end point of the duct deemed infinite. [104] determine the transfer matrices describing the overall structure in terms of cell comprised of a ring plus a cavity. A lumped element approach is used for determining the influence of the cavity and the entrance and exit point for a given ring. The true nature of energy attenuation is not presented in [104] since viscous-thermal losses are not accounted for. The TMM approach does, however, give a general method of providing a tool to quickly establish the realization of parameter dependence of the structure.

More recently in 2020, work by Mironov and Pislyakov [127] developed new structures which involve the concept of using acoustic black hole effect. One sample is a combination of metal discs, and another sample contains mass layers of a material in a cylindrical tube. For the former, (SBH-1), a structure is designed and later built using a number of aluminium alloy discs. The discs are solid and do not contain any orifices. The sample is constructed by means of steel rods, fixed along the longitudinal axis which keep the plates positioned in place separated by a fixed distance. The structure is referred to as a sonic black hole (SBH). The testing of the SBH was performed in an impedance tube having diameter 10 cm. The structure forms a waveguide once inserted within the tube and measured acoustically using

standard two microphone method to obtain the reflection coefficient. The SBH-1 sample can be seen in Figure 3.26.

Figure 3.26. Acoustic black hole effect, design SBH-1 of solid discs secured by four steel rods. The left image shows design without any filling, whilst right image contains foam filling between discs. Images presented as from [127].

The SBH is studied with aim of deriving exact analytical solutions. In the case of SBH-1, the diameters of the discs are arranged such that the radii follow a parabolic law. The sound wave is to be reduced from the envelope created due to the plate arrangement, or waveguide geometry. The velocity of the propagating wave within the profile c_0, over sample length L is,

$$c(x) = c_0 \frac{x}{L} \tag{112}$$

and its solution is given by equation (107) which is a form of power law solutions, re-introduced with $p(x) = A_\alpha \left(\frac{x}{L}\right)^\alpha$. The wavenumber at the sample surface (for SBH-1) is,

$$k_0 = \frac{\omega}{c_0(1 - i\varepsilon)} \tag{113}$$

Where ε is coefficient of loss induced by absorption material, ω is frequency, and sound propagation velocity in the medium is given by c_0. Absorbing materials used in experiments consisted of foam, cotton wool, and padding polyester. Its exponents α for SBH-1 is given by equation (108). The corresponding reflection coefficient V becomes,

$$V = \frac{1 + W - \frac{c}{i\omega L}(\alpha_1 + W\alpha_2)}{1 + W + \frac{c}{i\omega L}(\alpha_1 + W\alpha_2)} e^{-2ik_0 L} \tag{114}$$

Equation (114) is similar to equation (110) with the difference in change of sign terms in the numerator and denominator since the propagating wave profile is changed starting at the entrance of the absorber. The acoustic black hole absorber SBH-1 as presented in works by [127], is however bulky in terms of its dimensions. The structure is reported to being nearly half a metre in length at 0.47 m. Furthermore, the theoretical data vs the experimental data as seen in Figure 3.27, shows a comparison of the sample true length (experimental) plotted with theoretical length having a difference of 36 %.

$$\mathrm{W} = \frac{\alpha_1}{\alpha_2}\left(\frac{l}{L}\right)^{\alpha_1 - \alpha_2} \tag{115}$$

where $W = A_2/A_1$ are amplitudes of the incident and reflected waves e^{-ikL} and Ve^{+ikL} with $A_1 + A_2 = e^{-ikL} + Ve^{+ikL}$.

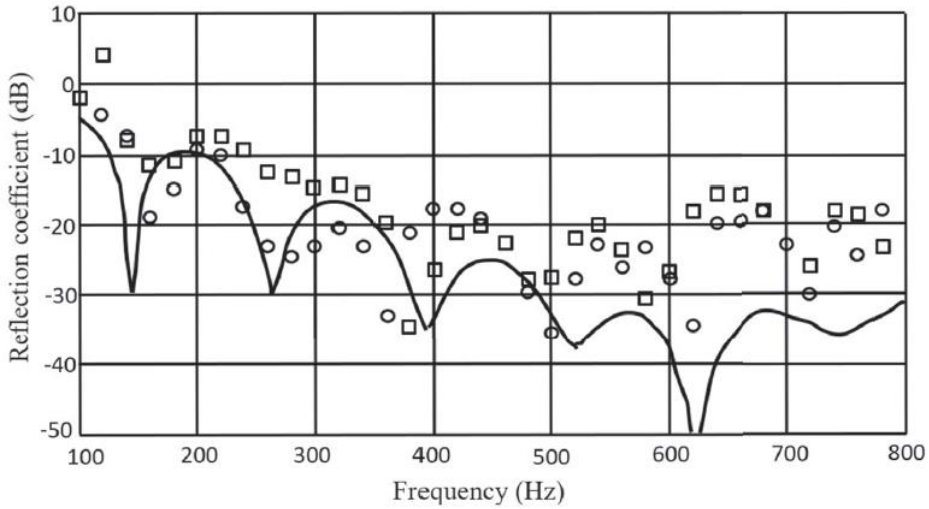

Figure 3.27. Reflection coefficient vs frequency for SBH-1 shown in dB [127]. Theoretical curve (solid line) is plotted using equations (114) and (115). Markers indicate experimental data.

3.5. Conclusion

An extensive literature review has been conducted to demonstrate the works of several authors and begins with introducing the reader to wave propagation in rigid porous media. The interaction of acoustic waves with single orifices containing thin plates is first presented and is later followed by the investigation of multiple perforations which exist over a surface area, known as a micro perforated panel absorber. Reactance and resistance is shown to be an essential method of describing the impedance and acoustic interaction with the solid structures containing the perforations. These conventional structures are discussed for both low and high sound pressure levels and describe the behaviour of the material response for linear and nonlinear regimes. It is well known that Forchheimer's parameter is the dominating nonlinearity associated with rigid porous materials, and a discussion is given for the Forchheimer's nonlinearity leading to the growth of flow resistivity with flow velocity.

This is essential for the investigation of the designs used within this thesis, where the Forchheimer's nonlinearity parameter has been measured and later used to predict the performance of the metamaterial absorbers with a developed model. After a discussion of the perforated rigid materials, an introduction and detailed review is given for the metamaterial pancake and profiled structures. This follows the same idea of the perforated structures previously given i.e. materials containing single or multiple orifices and describing the fluid interaction, particle velocity, and absorbing capabilities with the inclusion of describing how the metamaterial absorbers are advantageous over the conventional structures. The pancake absorber and its design is introduced and follows from using a dead-end pore approach, first realised from previous works which encompassed a difference of the geometry and dead-end pore volume. Lastly, first design and concept of the profiled absorber is discussed which uses the notion of acoustic black hole effect, which is one of the design approaches used within this thesis. It is later shown in the consecutive Chapters that these metamaterial structures are effective for low

frequency sound absorption for linear regime including nonlinear regime when the designs are combined together. The sound absorbing capabilities for both the pancake and profiled structures is demonstrated in the next Chapter, where the metamaterial structures have been tested for their effective properties at both low and high sound pressure levels.

Note: In previous works from other authors where a background is given for the profiled absorbers the viscous and thermal losses in the cavities and central perforation have not been accounted for. The work of this thesis does account for these losses including investigating the structures at high sound pressure levels using an impedance tube. Moreover, the profiled absorbers are investigated using different configurations (linear and exponential and comparing their performance in terms of their absorption and reflection coefficients) which has not been carried out in previous works by other authors. Additionally, the profiled structures have been tested at extremely large sound pressure levels by conducting measurements in a shock tube and analysing the performance of the absorbers against shock waves against different amplitude strengths. Both the pancake and profiled structures designed in this work consist of 3D printed and metallic structures.

4. Experiments of Continuous Sound

Chapter 4 presents the experiments of continuous sound and the experimental methodologies used. The chapter begins with a description of the samples tested followed by the dimensions for each of the absorbers, given by section 4.1. The Methodology of the measurements performed is then shown in section 4.2 illustrating the impedance tube tests for both low and high sound pressure levels. In section 4.3 the results obtained from low sound pressure levels are given for pancake absorbers with $R = 25$ mm. Subsection 4.3.1 presents the pancake absorbers with different configurations and when the plate radius $R = 50$ mm, including accelerometer measurements. Results for profile absorbers which have been 3D printed are given by subsection 4.3.2. The metallic profiled absorbers are presented in 4.3.3. In section 4.4 the results from impedance tube measurements performed at high sound pressure levels is discussed. It is divided into subsections 4.4.1 and 4.4.2 which provides the data for both the pancake and profiled absorbers, respectively. In 4.4.3 a comparison for the structures with identical sample lengths is given. A conclusion for the absorbers is provided in Section 4.5.

4.1 Description of the Samples Tested

Metamaterial structures tested are similar to “pancake absorbers” described in [1],[3] where the principles of their operation are based on dead-end pore effect. The absorber is built with periodically arranged metallic plates containing a central perforation. Other type of absorbers considered here are structured in a similar way but with the radius of the central pore decreasing from the front to back of the sample. This design uses the concept from what is known as the “acoustic black hole effect” [2] and will be referred as profiled absorbers. Absorption coefficient data for the different approaches of both pancake and profiled structures are compared to identify the advantages and disadvantages of each design. An introduction to the absorbers is given in Chapter 1 (pancake and profiled metamaterials) and in Chapter 3 a literature review is presented on such structures. Chapter 4 provides the data obtained from the performed acoustic measurements, where pancake and profiled designs have been built and tested at various amplitudes using an impedance tube with several internal configurations.

4.1.1. Pancake Absorbers and their Dimensions

For the pancake absorber the main perforation for all metallic plates is kept constant. This arrangement of the structure ensures periodicity of the absorber if each volume ratio of dead-ends and main pore remains equal for each of the pancake cells. The geometry of pancake absorbers is characterised by the following parameters: Plate thickness d_p, separation distance between the plates d_c, external radius of the structure R and the central perforation radius $r_{0.}$ This is illustrated in Figure 4.1. The dimensions which have been selected to use for the absorbers are those that enable the building of the structures to be kept reasonable thin whilst maintaining being rigid. The radius of the external plates is developed to maximize the volume of the dead-ends. The absorbers have also been built to match the dimensions of the testing equipment used. The orifices in the sample configurations have been selected after investigating acoustic interaction for a range of different pore radii. Therefore, the material parameters

used for determining the effective properties and performance of the absorbers are those that enable the largest values of the peak absorption at the lowest possible resonance frequency.

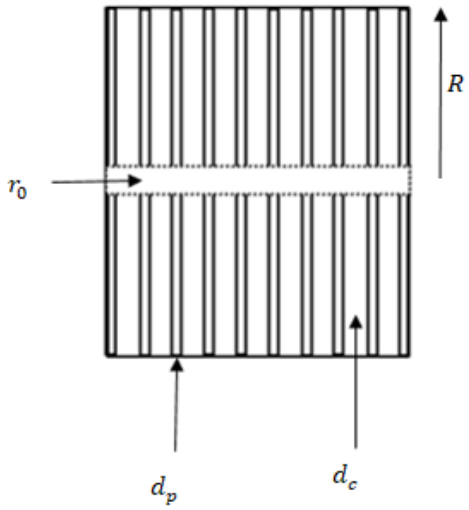

Figure 4.1. Geometry of the pancake absorber containing a simple perforation at its centre.

Smallest and largest external radii of all samples tested is $R = 25$ mm and $R = 50$ mm, respectively. The sample length varied by changing the number of plates in each design. The cylindrical structures are constructed of aluminium alloy for both plates and spacers. Thickness of the rings was $1\ \mathrm{mm}$ and its outer radius $R = 50$ mm. Cavitiy thickness could be varied depending on the number of spacers used (since different ring thinknesses were manufactured to allow variability upon the building of the structures). This approach enabled flexibility of the building for both the pancake, and profile absorbers. For the pancake absorbers with outer radius $R = 50$ mm, experiments have been performed on the samples composed of plates with thickness $d_p = 1$ mm and spacings between them which make up the cavities $d_c = 1\ \mathrm{mm},\ 2\ \mathrm{mm}, 4\ \mathrm{mm}, 5$ mm, and 6 mm. Larger plate sizes include thickness $d_p = 3$ mm with rings $d_c = 3$ mm. Radius of the central perforation for pancakes was $r_0 = 4$ mm and $r_0 = 5$ mm.

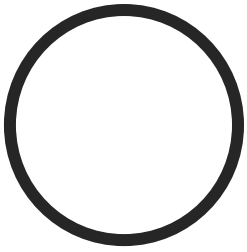

Figure 4.2. A simple cylindrical ring, 1 mm in thickness, that acts as a spacer to create the cavity thickness. The cavity thickness d_c is equal to an integer number of ring thicknesses.

Surface porosity, defined as $\left(\frac{r_0}{R}\right)^2$ was $\phi_p = 6.4 \times 10^{-3}$ when $r_0 = 4$ mm. Thickness of the samples was not always exactly equal to the multiple of the unit cell, $d_p + d_c$, due to the discrete nature of the material structure and imperfections of the plates and the spacers (Figure 4.2). The minimum ring, or spacer thickness manufactured was 1 mm and the maximum was manufactured at 3 mm. This approach was desirable in the building process of the absorbers (after comparing computational predictions to enable maximum absorption at the lowest possible frequency). Porosity of the main pore walls for the pancake structure due to the presence of the cavities was defined as the fraction of the main perforation wall

occupied by the cavities, $\frac{d_c}{d_c+d_p}$, and varied between $\phi_w = 0.5$ for $d_c = 1$ mm and $\phi_w = 0.87$ for $d_c = 6$ mm. In addition to the samples constructed of 1 mm plates, we performed impedance tube measurements on the samples constructed with 3 mm plates. A sample holder is manufactured in the laboratory at ISAT, University of Burgundy, Nevers, France for the testing of pancake structures with $R = 25$ mm. This is since the inner wall of the impedance tube has a diameter as aforementioned of $R = 50$ mm. Pore radius of the metallic pancake of this smaller radius are $r_0 = 5$ mm per plate.

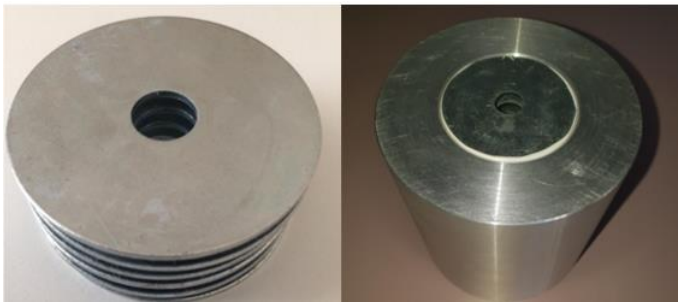

Figure 4.3. Metallic plates (first tested) separated and stacking for pancake absorber where each plate has $R = 25$ mm (left). Stacked plates are inserted into sample holder where $R = 50$ mm (right).

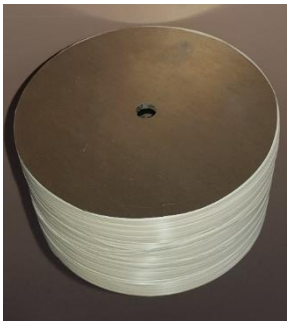

Figure 4.4. Pancake absorber after completion of building consisting larger plates than the design shown in Figure 4.3. Overall external radius of the absorber remains the same. Configuration of the plates and cavities is varied for a set number of structure thicknesses. Isolation and PTFE tape surrounds the sample to prevent any air leakage. Plate has $R = 50$ mm and pores with $r_0 = 4$ mm.

Figure 4.5. Pancake absorber sealed before insertion (left) into HSPL impedance tube based at ISAT, Nevers, France. Amplitude strength up to 160 dB is possible using a modified system. Plate has $R = 50$ mm and pores $r_0 = 4$ mm.

4.1.2. Profiled Absorbers and their Dimensions

Profiled absorbers considered in this work are considerably thinner than those proposed in [2] for absorption of sound in a retarding waveguide. The profiled absorbers have a main perforation that varies along its length. Two types of profiled absorbers have been tested – composed of metallic plates separated by the cavities and also profiles that are 3D printed. The difference of the pore radii for each

metallic plate breaks the full periodicity of the structure while the outer radius R of the cavity remains for each cell. The cell is represented by one plate and one cavity. Two different plate diameters have been used in the building process of the profile structures. 3D printed and metallic profile structures are composed of 50 mm plate diameters which contain a single central pore. Furthermore, profile absorbers of both linear and exponential configurations have been built and tested with plate diameter being 100 mm. For the 100 mm diameter plates the minimum size front central pore used was 30 mm diameter. The largest front pore diameter used was 50 mm. For the 30 mm diameter pore, the sample consisted of a cavity thickness throughout the sample held constant at 3 mm after each plate. The profile samples with 100 mm plates and 50 mm front central pore are built containing 2 mm and 3 mm cavities.

Ring no. per plate	$2R$ (mm)	Linear / Exponential Orifice $2r_0$ (mm)	3D Printed / Metallic d_p (mm)	$2R = 50$ mm/100 mm d_c (mm)
1	50 /100	50 / 50	2 / 1	2 / 1
2	50 /100	48 /48	2 / 1	2 / 1
3	50 /100	46 / 45	2 / 1	2 / 1
4	50 /100	44 / 41	2 / 1	2 / 1
5	50 /100	42 / 38	2 / 1	2 / 1
6	50 /100	40 / 35	2 / 1	2 / 1
7	50 /100	38 / 32	2 / 1	2 / 1
8	50 /100	36 / 29	2 / 1	2 / 1
9	50 /100	34 / 26	2 / 1	2 / 1
10	50 /100	32 / 24	2 / 1	2 / 1
11	50 /100	30 / 22	2 / 1	2 / 1
12	50 /100	28 / 19	2 / 1	2 / 1
13	50 /100	26 / 16	2 / 1	2 / 1
14	50 /100	24 / 14	2 / 1	2 / 1
15	50 /100	22 / 12	2 / 1	2 / 1
16	50 /100	20 / 10	2 / 1	2 / 1
17	50 /100	18 / 9	2 / 1	2 / 1
18	50 /100	16 / 8	2 / 1	2 / 1
19	50 /100	14 / 7	2 / 1	2 / 1
20	50 /100	12 / 6	2 / 1	2 / 1
21	50 /100	10 / 5	2 / 1	2 / 1
22	50 /100	8 / 4	2 / 1	2 / 1
23	50 /100	6 / 3	2 / 1	2 / 1
24	50 /100	4 / 2	2 / 1	2 / 1
25	50 /100	2 / 1	2 / 1	2 / 1

Table 4.1. Dimensions for linear and exponential profiles for 3D printed and metallic samples. External plate diameters and different configurations for the profiles are given including cavity depths. All dimensions are given in millimetres.

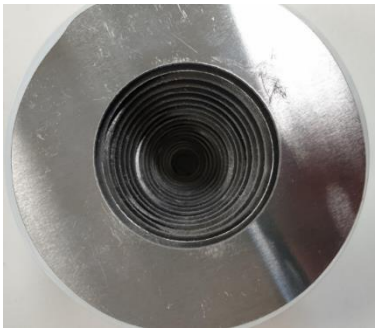

Figure 4.6. Profile absorber comprised with cylindrical rings with $R = 50$ mm.

Dimensions of linear and exponential profiles are given in Table 1. The front view of the metal profiled absorber is shown in Figure 4.6. Exact absorber thickness depends on the fixing process of the sample and its configuration. In all cases the plates and cavity rings must be clamped together to form the discrete sections of the full sample configuration. This part of the building process was done to each

configuration before the sample external diameter is sealed and checked for no leakages. These discrete sections are shown in Figure 4.7. Each sample is sealed with isolation tape and PTFE tape with additional use of Vaseline to enable the sample to be airtight. This prevents any leakages between the external surface of the absorber and the inner surface of the impedance tube, shock tube or flow resistivity system.

Figure 4.7. Metallic plates for profile absorber building are comprised together in discrete sections with increasing pore diameter.

3D printed samples were designed using Multiphysics software COMSOL, and later printed using 3D printer technology based in the laboratory at University of Salford. The samples are profiled structures, the first being a linear profile, and secondly, an exponential profile. Many profiled absorbers have been tested in both impedance and shock tubes; the latter experiments are described in Chapter 7. The linear profile absorber has inner radius r, which decreases linearly along sample length L, where $r\ (L) = 0$ at the far end of the sample according to equation $r(x) = R\left(1 - \frac{x}{L}\right)$. For the exponential profile absorber, it is developed where $r(x) = R\left(2 - e^{x \ln 2/L}\right)$, where x is distance from the surface of the absorber and R is plate radius. The dependence of the pore radius on the distance from the sample surface x is shown in Figure 4.8.

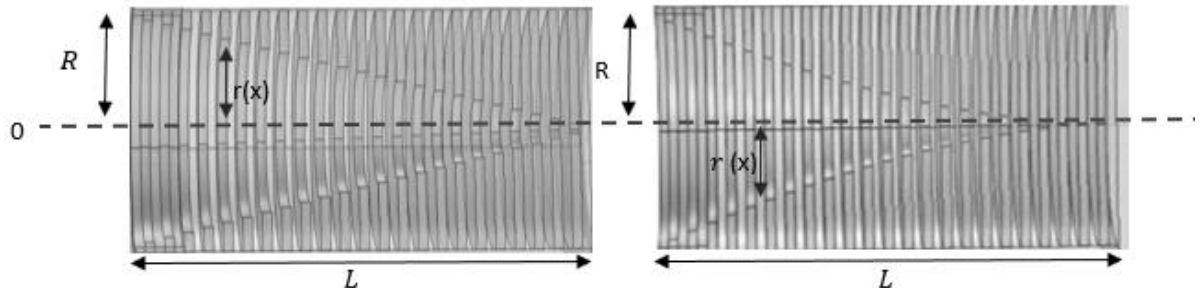

Figure 4.8. Linear profile (left) and exponential profile (right) with structure length L, and decreasing pore radii $r(x)$ from plate radius R to zero.

The 3D printed linear and exponential profiles are tested in linear and weakly nonlinear regime using HSPL impedance tube with white noise excitation. Diameters of both structures are $2R = 50$ mm and sample thicknesses were the identical at $L = 100$ mm. The front pore begins at 50 mm and decreases to zero, with rigid termination and $r(x)$ given as above. Ring thicknesses were $d_p = 2$ mm and cavity thickness also $d_c = 2$ mm. 3D printed absorbers comprised of two parts, clamped together during the measurements. They are shown in Figure 4.9.

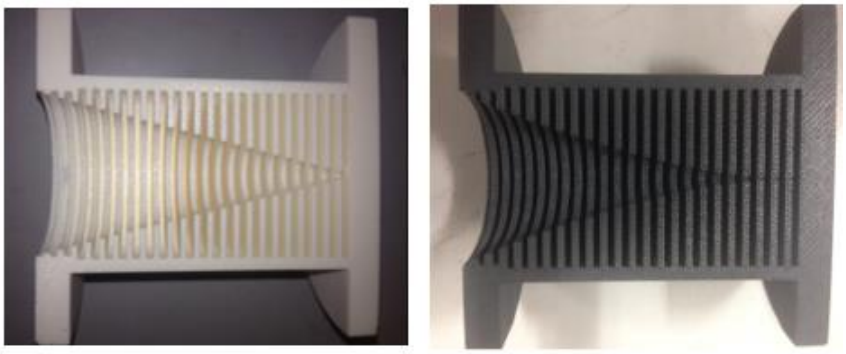

Figure 4.9. 3D printed linear profile (left) and exponential profile (right). The front and end terminations included the external shell of the structure having $R = 50$ mm. This was to allow the fitting of each sample within the impedance and shock tubes.

4.2. Methodology: Impedance Tube Measurements at Low and High Sound Pressure Levels

Experiments with continuous sound are performed using impedance tubes. Signals consisted white noise and sine waves. The former was used for both low and high amplitudes, while the latter was used to investigate the dependence of the absorption coefficient on incident pressure amplitude. Measurements for all absorbers were performed in a Mecanum impedance tube using a two-microphone and three-microphone method. The former set-up was used for conducting measurements to obtain surface impedance data and absorption coefficients for the absorbers. The latter set-up allowed to obtain data for the absorber properties. With the two-microphone method all measurements were performed according to BS EN ISO 10534-2:2001. All samples for the two-microphone method were rigidly backed and each microphone was mounted to the tube at fixed locations (see Figures 4.10 – 4.12).

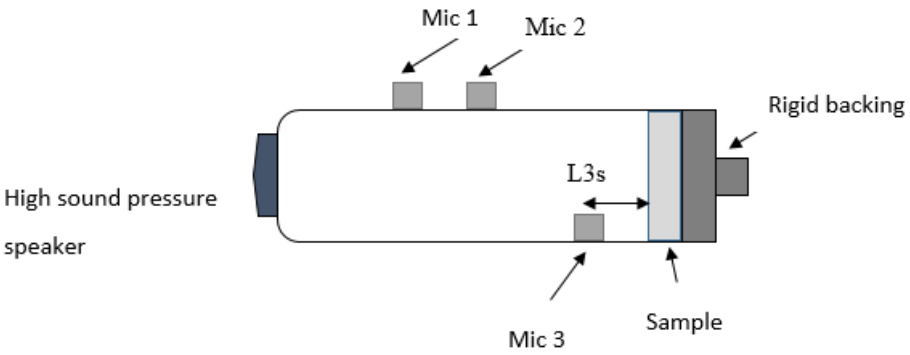

Figure 4.10. High sound pressure level impedance tube with standard 2-microphone set-up including reference microphone at sample surface.

Figure 4.11. High sound pressure level impedance tube reference microphone.

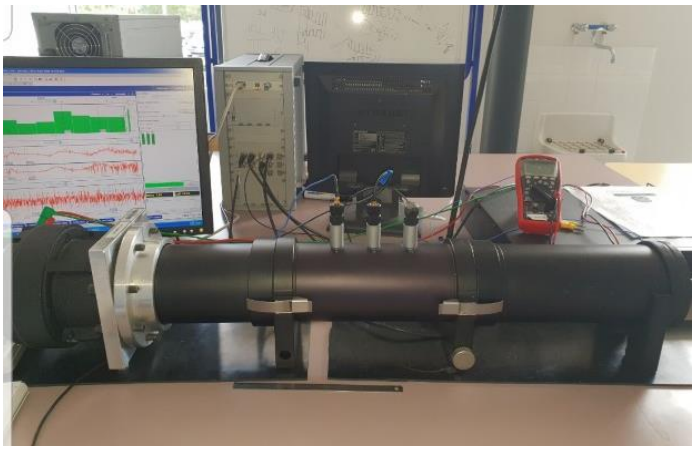

Figure 4.12. High sound pressure level impedance tube with standard 2-microphone set-up.

Pancake and profile absorbers were measured using a Mecanum impedance tube with an inner diameter 100 mm. The tube is modified for high sound pressure level testing. Working range of the apparatus was $35\ \mathrm{Hz} - 1800\ \mathrm{Hz}$ and the frequency resolution was 1 Hz. The impedance tube was cylindrical, and its wall thickness was sufficient enough to eliminate any vibrational effects as required by standard BS EN ISO 10534-2:2001. The testing equipment of the high sound pressure level (HSPL) tube is a specially modified impedance tube which is based at ISAT - University of Burgundy, Nevers, France. A sound source is fixed at one end of the tube which houses a membrane. A compression chamber is isolated within a closed chamber to help eliminate any structure-borne excitation of the impedance tube. Sound wave is plane and directed towards the sample which is located at a fixed position at some distance at half tube length. A microphone calibration process is performed to obtain the satisfactory requirements of sensitivity according to the impedance tube standard BS EN ISO 10534-2:2001. This procedure is completed for all microphones regardless of which set up is used. Measurements are performed firstly with anechoic termination in order to obtain the correct transfer functions used in the calibration process. All microphone sensitivities are recorded and saved once the microphone calibration has been completed. A phase calibration of the microphones is then conducted which allows correcting for the measured transfer function data. This is achieved by performing a measurement with each microphone (1 and 2) located in the normal working position so that the transfer function H_{12}^{I} is obtained. It is then required to inter-change the microphones once the measurement has been completed and obtain the new transfer function H_{12}^{II}. The transfer function representing both normal and interchanged positions of the microphones can be given as,

$$H_{12} = (H_{12}^{I} \cdot H_{12}^{II}) \quad (1)$$

From determining the calibration factor, it is possible to correct for any amplitude and phase mismatches between the two positioned microphones. The transfer function is complex,

$$H_c = \left(\frac{H_{12}^I}{H_{12}^{II}}\right) = |H_{12}|e^{j\theta} \tag{2}$$

After performing a measurement in the impedance tube the acoustic transfer function is computed. It is related to the complex pressures of the microphone and their arrangements. In terms of its real and imaginary components the transfer function is expressed as (3),

$$H_{12} = \left(\frac{S_{12}}{S_{11}}\right) = |H_{12}|e^{i\theta} = H_r + iH_i \tag{3}$$

where H_r and H_i are the real and imaginary parts of transfer function H_{12}. The complex sound pressure at microphone positions 1 and 2 is given by S_{12} and for the complex sound pressure for microphone position 1 only is S_{11}. Figure 4.13 indicates the positioning of the microphones for the measured transfer function. This process is for determining the phase calibration factor prior to performing any measurements.

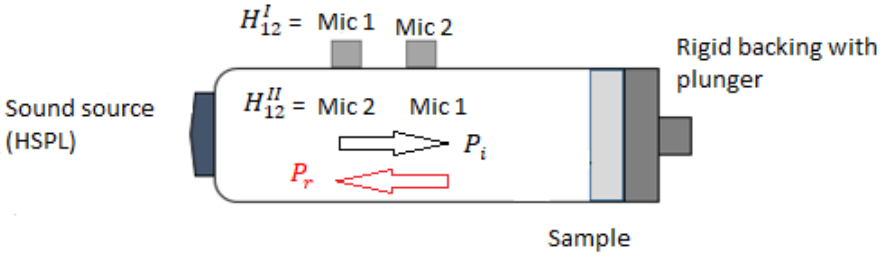

$$H_{12} = (H_{12}^I \cdot H_{12}^{II})$$

Where H_{12}^I is microphone normal positions and H_{12}^{II} are microphone positions interchanged.

Figure 4.13. Determining calibration factor using microphone normal and interchangeable positions.

The reflection coefficient which is the ratio of pressures of the reflected and incident waves (both complex) is

$$r = \frac{P_r}{P_i} = |r|e^{i\theta_r} \tag{4}$$

where $|r|$ is the amplitude of the reflected wave relative to the incident wave, and θ_r is the phase angle. The reflection can be expressed in terms of the transfer function H_{12}

$$H_{12} = \frac{P_2}{P_1} = \frac{P_i e^{ik_0x_2} + P_r e^{-ik_0x_2}}{P_i e^{ik_0x_1} + P_r e^{-ik_0x_1}} = \frac{e^{ik_0x_2} + re^{-ik_0x_2}}{e^{ik_0x_1} + re^{-ik_0x_1}} \tag{5}$$

which is the total sound field for the transfer function for microphone positions 1 (x_1) and 2 (x_2) with ratio P_2/P_1. The reflection coefficient factor presented as a ratio of the transfer functions itself, is given

in equation (6). It is obtained after computing the transfer functions H_i and H_r using the pressures of the incident and reflected waves and becomes

$$\mathbf{r}_{fact} = \frac{H_{12} - H_i}{H_r - H_{12}} = e^{2jk_0x_1} \tag{6}$$

where $H_i = P_2i/P_1r$ and $H_r = P_2r/P_1i$. Specific acoustic impedance of an acoustic wave Z can be represented as the ratio of the acoustic pressure to that of the particle velocity.

$$Z = \frac{p}{u} \tag{7}$$

Surface acoustic impedance Z_s is defined as the ratio of pressure and velocity at the surface of the sample. Using equation (4) surface impedance can be given in terms of reflection coefficient r,

$$Z_s = Z_0 \frac{(1+r)}{(1-r)} \tag{8}$$

where $Z_0 = \rho_0 c$ is characteristic impedance of air. And the absorption coeffcient α can be determined,

$$\alpha = 1 - |r|^2 \tag{9}$$

Absorption coefficient equals to the fraction of incident energy absorbed within the sample for rigid backing. The pancake and profile absorbers are investigated in the nonlinear regime using white noise and sine wave excitation. Continuous sound with SPL ranging between 80 – 125 decibels is possible for the white noise excitation, and higher SPL are achieved using sine wave excitation. Measurements are first performed using white noise to gain values of structure resonance frequencies followed by performing high sound levels with sine waves around the resonances. Maximum sound level reached for pure tones is 160 decibels approximately. The selected values of frequencies consisted of using sine waves, obtained from LSPL white noise data corresponding to the peak frequencies at first resonance of the absorption coefficient. Further values are also selected close to the absorptive peaks and furthermore, for chosen successive peaks across the frequency spectrum. Sine wave excitation is then performed for each of the frequencies which begins firstly, at low amplitude, and increasing approximately 10 dB per additional measurement. This process is repeated for each frequency of interest until a maximum amplitude strength is reached. The maximum amplitude achieved varies with the frequency of the signal. For the high sound pressure levels, the membrane of the sound source is monitored taking due care to not damage it. The voltage and pressure (Pascals) values recorded are shown for a number of measurements and seen presented in the corresponding tables throughout Chapter 4 for determining incident sound pressure.

For white noise excitation absorption coefficient is measured as a function of frequency for different SPL levels of the noise. The minimum and maximum frequency data obtained for peak values of absorption coefficient from the measurements conducted in the HSPL impedance tube is approximately 129 Hz and 1600 Hz. For sine wave measurements, as the frequency is fixed (single value), the variations of the absorption coefficient with incident pressure amplitude P_i was investigated. The incident sound pressure level of each measurement in the impedance tube is achieved using a reference microphone (microphone 3) positioned near a sample surface, see Figure 4.11. Microphone 3 records the pressure of the superimposed wave (incident plus reflected) near the sample surface. The true account of the incident pressure is obtained by calculating for reflection coefficient using known pressure values at

each given measurement, and surface impedance obtained as a result of this measurement. Comparisons of incident sound pressure measured with this microphone in the presence of anechoic termination is made with the structures. To determine the incident pressure, values of voltage and pressures are recorded and consequently compared for different configurations of the pancake and profile absorbers with different thicknesses. All measurements performed determining incident pressure is carried out with rigid backing termination of the impedance tube, and when the sample is closed at the far end. For each measurement (independent of sample used) the pressure value at microphone 3 is recorded. The total pressure is a combination of both incident and reflected waves,

$$P = P_i(1 + re^{-2ik_0L_{3s}}) \tag{10}$$

where $L_{3s} = 5$ mm is the distance from microphone 3 to the surface of the sample. Surface impedance data for frequency tested allows reflection coefficient to be determined from surface impedance of the sample Z_s and characteristic impedance of air Z_0, Rearranging equation (8)

$$r = \frac{Z_s - Z_0}{Z_s + Z_0} \tag{11}$$

Then, rearranging equation (10) P_i is obtained as a function of reflection coefficient (which in turn can be found from measured values of characteristic impedance according to (11)):

$$|P_i| = \frac{|P|}{|1 + r\, e^{-2ik_0L_{3s}}|} \tag{12}$$

where $|P|$ is pressure amplitude in Pascals measured by microphone 3. The values of the absorption coefficients obtained by sine wave measurement are plotted as a function of incident pressure amplitude $|P_i|$ for each frequency tested. In addition to the absorption coefficient and impedance measurements described above, accelerometer tests have been performed in a conventional (low sound pressure level) standard Bruel and Kjaer impedance tube with inner radius $R = 50$ mm, using a two-microphone method. The aim of these measurements was to see whether possible vibrations of the plates could interfere with the peak absorption data. The performed tests are shown for same configuration of a pancake absorber (same values of d_c and L) but differing in plate thickness d_p. An accelerometer (Bruel and Kjaer 4507B00433565) is fixed to the surface of the front plate by a strong bond of super glue, as shown in Figure 4.14. It is positioned carefully such that no obstruction is made to the pore of the plate. Any mechanical disturbance of the plate and structure is precisely measured by the conversion of mechanical energy to electrical energy. To measure the disturbance from each measurement performed, it is required that the mass of the accelerometer be much smaller than the mass of the plate. The mass of the accelerometer and that of each plate was 5 g and 20 g, respectively. Therefore, it is assumed that the disturbance to the structure due to presence of the accelerometer was not significant.

Figure 4.14. Accelerometer measurements performed using Bruel & Kjaer 4507B00433565 and a Bruel & Kjaer impedance tube with standard 2-microphone set-up.

4.3. Results of Measurements at Low Sound Pressure Levels

Measurements performed in the impedance tube with low sound pressures and white noise excitation only, are described here in sections 4.3.1 and 4.3.2. Firstly, the testing of a pancake absorber built with plate radius $R = 25$ mm (see Figures 4.15 – 4.16) is given with its comparison of peak absorptive values for two different thicknesses (30 mm and 40 mm). This is followed by pancake absorbers built with a larger plate radius (where $R = 50$ mm) of various configurations (see Figures 4.17 – 4.23) including data obtained by the accelerometer measurements (Figures 4.24 – 4.25). The profile absorbers are then investigated showing the results for when the profiles have a main pore $r_0 = 25$ mm and 3D printed (Figures 4.26 – 4.27), and metallic profile structures with $r_0 = 25$ mm, see Figures 4.28 – 4.37.

4.3.1. Pancake Absorber Including Accelerometer tests

Two typical results of absorption coefficient dependence on frequency are shown in Figures 4.15 – 4.16. They demonstrate that the frequency of the peak strongly depends on the thickness of the sample. The pancake absorber shown in these Figures (4.15 – 4.16) are built with plate thickness $d_p = 2$ mm and $d_c = 4$ mm. Pore radius is $r_0 = 5$ mm and sample lengths are 30 mm and 40 mm. The sample has an external radius $R = 50$ mm. Peak absorption value is maximum (0.98) at $f = 710$ Hz, shown in Figure 4.15 for sample with $L = 30$ mm. Increasing the sample thickness by 10 mm shifts the peak resonance frequency lower to frequency $f = 523$ Hz, shown in Figure 4.16. Furthermore, a second peak also occurs and has a maximum absorption coefficient value of 0.53.

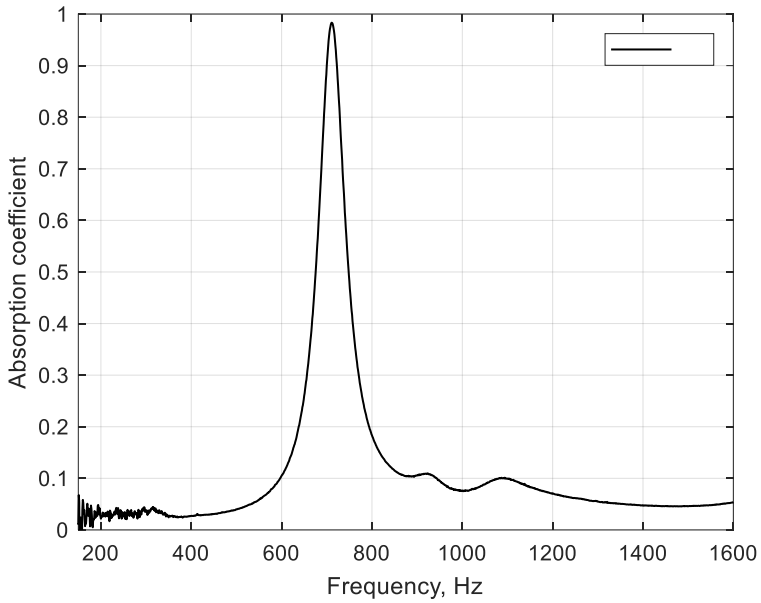

Figure 4.15. Absorption coefficient as a function of frequency for pancake configuration $d_p = 2$ mm and $d_c = 4$ mm. Pore radius is $r_0 = 5$ mm, $L = 30$ mm, and $R = 50$ mm.

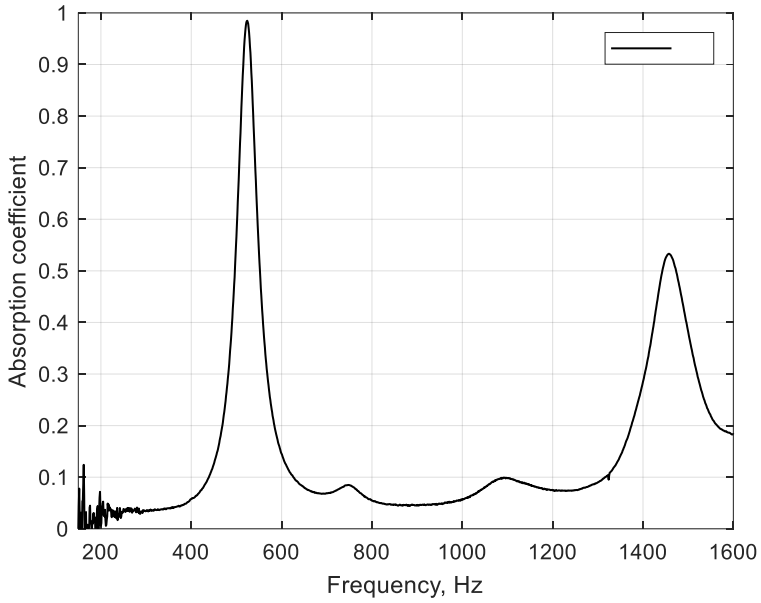

Figure 4.16 Absorption coefficient as a function of frequency for pancake configuration $d_p = 2$ mm and $d_c = 4$ mm. Pore radius is $r_0 = 5$ mm, $L = 40$ mm, and $R = 50$ mm.

In Figures 4.17 – 4.22, plates are $d_p = 1$ mm and pore radius is $r_0 = 4$ mm, for all pancake absorbers. Number of the dead-end is given by N_{de}. Measurements are performed with white noise excitation in a Mecanum impedance tube, based at ISAT, Nevers, France. Figures 4.17 – 4.19 show absorption coefficient dependence on frequency for absorbers with thickness close to $L = 30$ mm but different values d_c. Increasing cavity thickness affects the dependence of the absorption coefficient on frequency and thus absorber performance. For pancake absorber comprised with $d_c = 1$ mm (Figure 4.17), the first resonance frequency is at $f = 262$ Hz and has an absorptive peak value of 0.84 with sample $L =$ 31 mm. Other absorptive peaks are found at frequencies 572 Hz, 769 Hz and 1015 Hz. The normalized absorption coefficient values at these frequencies are 0.32, 0.48 and 0.26, respectively. After around $f = 1200$ Hz the absorption coefficient reduces to 0.13 towards the end of the frequency spectrum.

In Figure 4.18 the data shows the case for pancake absorber with cavity thickness d_c being 3 mm and sample $L = 32$ mm. The first resonance frequency is at $f = 229$ Hz and found to be lower than sample with $d_c = 1$ mm. The absorptive peak is higher with a value 0.99. Second absorptive peak is at $f = 530$ Hz with a value 0.71, and the third and fourth absorptive peaks are found at 765 Hz and 1027 Hz. Absorption coefficient values for these frequencies are 0.77 and 0.45, respectively. At 1195 Hz the absorption coefficient is 0.3 and reduces to 0.1 towards 1600 Hz. Figure 4.19 shows the results from when cavity thickness is doubled from $d_c = 3$ mm (Figure 4.18) to $d_c = 6$ mm, and sample length is 35 mm. First resonance frequency at 223 Hz is seen to be reduced further still when compared to $d_c = 1$ mm and $d_c = 3$ mm. Second absorptive peak is at 558 Hz with a value of 0.85, and third absorptive peak is at 775 Hz and its value is 0.83. Absorption coefficient is 0.59 at $f = 1044$ Hz and 0.4 at $f = 1200$ Hz. This then reduces to 0.15 towards $f = 1600$ Hz. It can be determined from the data shown in Figures 4.17 – 4.19 that by increasing the cavity thickness reduces the first resonance frequency. The corresponding normalized absorptive peaks are shown to have higher values when d_c is increased. However, as d_c is increased, the absorptive peaks after the first resonance frequency are shifted slightly higher in frequency. The absorption coefficient values are shown to be the same (0.99) for when $d_c = 3$ mm and $d_c = 6$ mm. This is for when the first resonance frequency has a difference of only 6 Hz. When $d_c = 3$ mm, first resonance frequency is $f = 229$ Hz and when $d_c = 6$ mm, first resonance frequency $f = 223$ Hz.

Figure 4.20 shows absorptive peaks vary between 0.4 and 0.5 in the frequency range up to around $f = 900$ Hz. And in Figure 4.21 it can be observed that the absorptive peaks vary between 0.71 ($f = 432$ Hz) to 0.28 ($f = 760$ Hz) in the frequency range up to around $f = 800$ Hz. The next absorptive peak (0.63) is then measured at $f = 1428$ Hz. In Figure 4.22 the absorptive peaks are seen to vary between 0.65 and 0.85 up until $f = 920$ Hz and then 0.48 and 0.38 between $f = 1049$ Hz to $f = 1147$ Hz. This means that larger values of absorptive peaks, including some additional peaks, are present for when cavity dimensions are built larger in the pancake samples. When d_c is increased from $d_c = 1$ mm to $d_c = 6$ mm, the absorbers become more effective in the middle to higher frequency region of the spectrum, $f = 600$ Hz $- 1200$ HZ. The effect of changing cavity thickness for larger samples (60 mm) is illustrated in Figures 4.20 – 4.22. They show the absorption coefficient dependence on frequency for absorbers with lengths close to $L = 60$ mm with different values of cavity thickness d_c. First resonance frequency is measured $f = 144$ Hz for a sample containing a 1 mm cavity thickness and comprised of 1 mm plates, see Figure 4.20. The peak absorption is lowest for when cavity thickness is 1 mm. This is true for the first resonance frequency (peak absorptive value 0.89) and corresponding peaks when compared to other samples (Figures 4.21 – 4.22) which have increased cavity thicknesses $d_c = 3$ mm and $d_c = 6$ mm. In Figure 4.21 it can be observed that when pancake absorber is built with 3 mm cavities, the first resonance frequency is seen at $f = 150$ Hz, when compared to pancake with 1 mm cavities where first resonance frequency is at $f = 144$ Hz. The peak absorption value however becomes larger, at 0.96 for sample with 3 mm cavities. Figure 4.22 shows that by doubling the cavity thickness (now built with 6 mm cavities), the first resonance frequency is reduced and found to be $f = 135$ Hz The peak absorptive value is slightly increased and reaches a maximum value of 1.0. Cavity thickness is seen to affect the corresponding frequencies of the absorptive peaks after the first resonance frequency for the samples as shown by Figures 4.20 – 4.23.

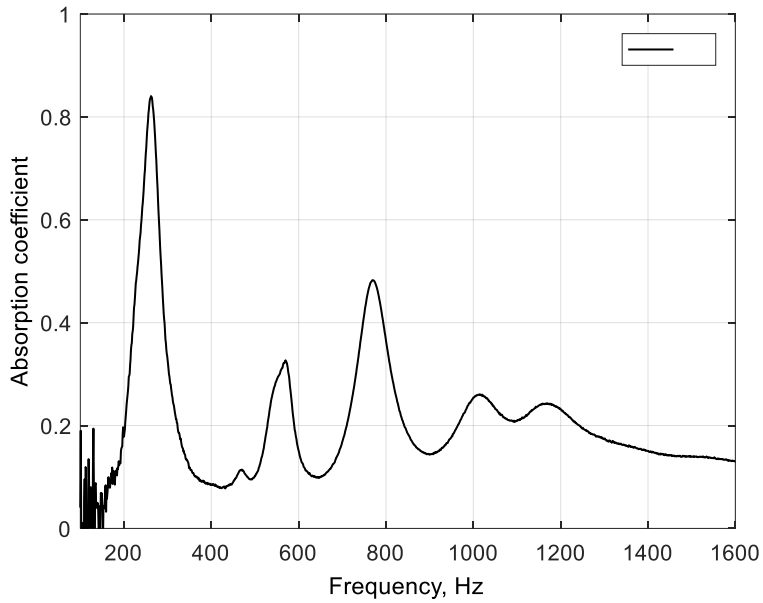

Figure 4.17. Absorption coefficient as a function of frequency for configuration d_p = 1 mm and d_c = 1 mm. Pore radius is r_0 = 4 mm, L = 31 mm, N_{de} = 16, and R = 50 mm.

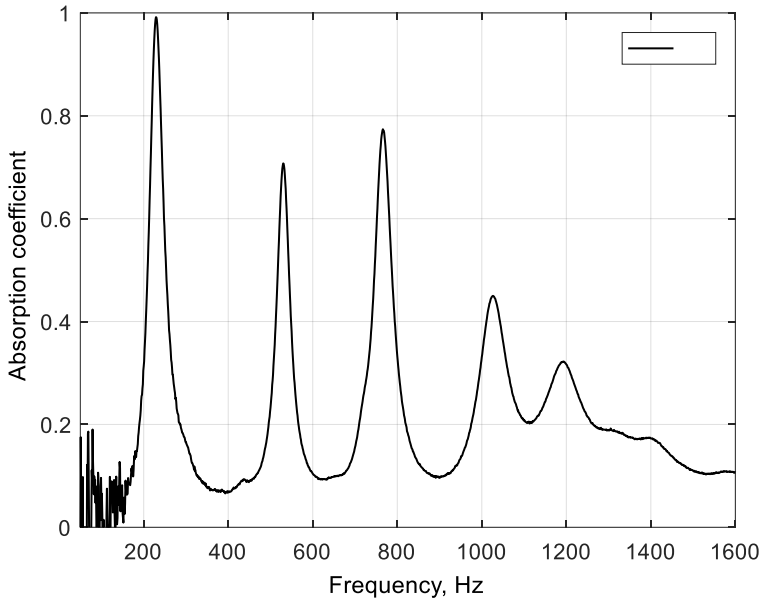

Figure 4.18. Absorption coefficient as a function of frequency for configuration d_p = 1 mm and d_c = 3 mm. Pore radius is r_0 = 4 mm, L = 32 mm, N_{de} = 8, and R = 50 mm.

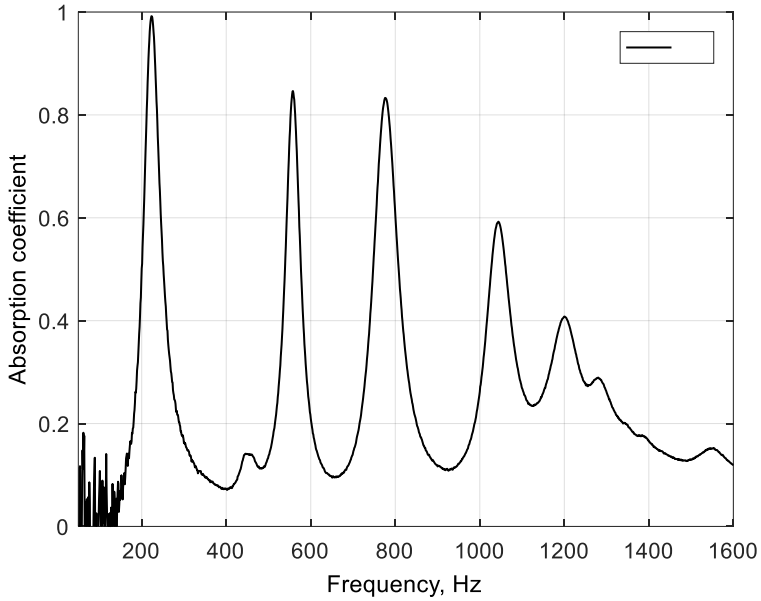

Figure 4.19. Absorption coefficient as a function of frequency for configuration d_p = 1 mm and d_c = 6 mm. Pore radius is r_0 = 4 mm, L = 35 mm, N_{de} = 5, and R = 50 mm.

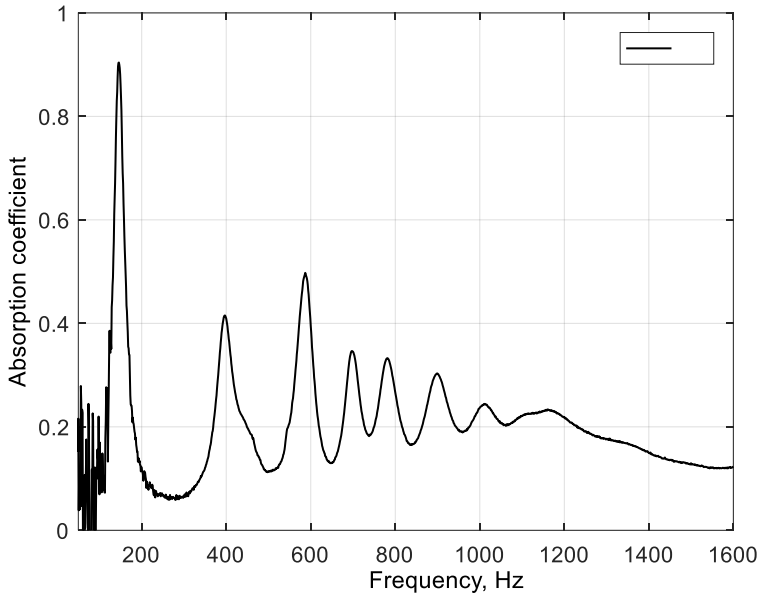

Figure 4.20. Absorption coefficient as a function of frequency for configuration d_p = 1 mm and d_c = 1 mm. Pore radius is r_0 = 4 mm, L = 62 mm, N_{de} = 30, and R = 50 mm.

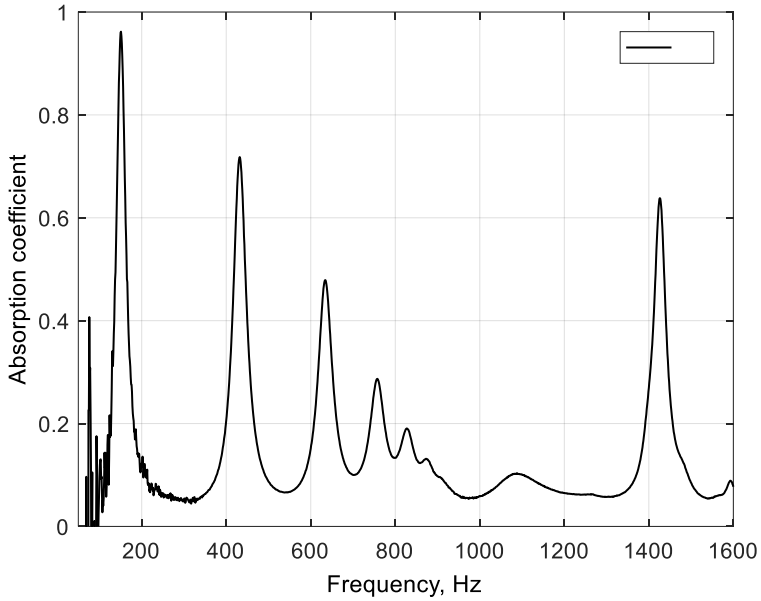

Figure 4.21. Absorption coefficient as a function of frequency for configuration d_p = 1 mm and d_c = 3 mm. Pore radius is r_0 = 4 mm, L = 61 mm, N_{de} = 15, and R = 50 mm.

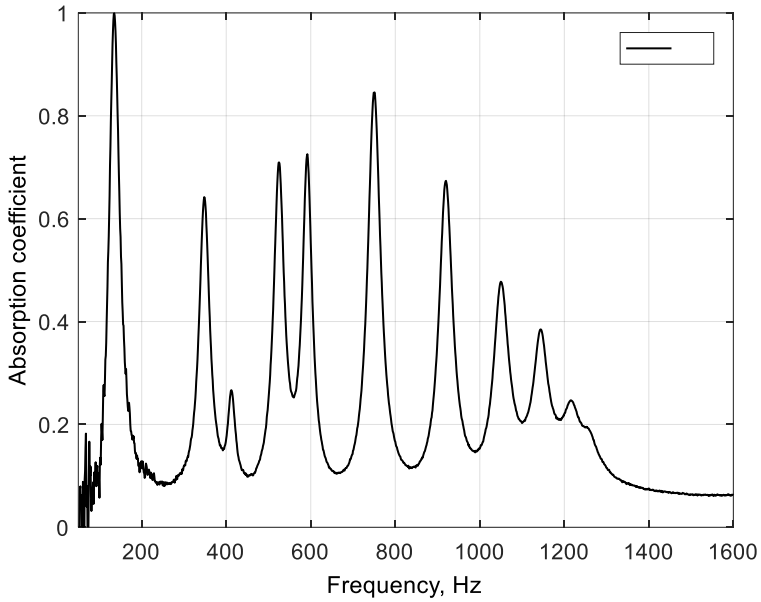

Figure 4.22. Absorption coefficient as a function of frequency for configuration d_p = 1 mm and d_c = 6 mm. Pore radius is r_0 = 4 mm, L = 63 mm, N_{de} = 9, and R = 50 mm.

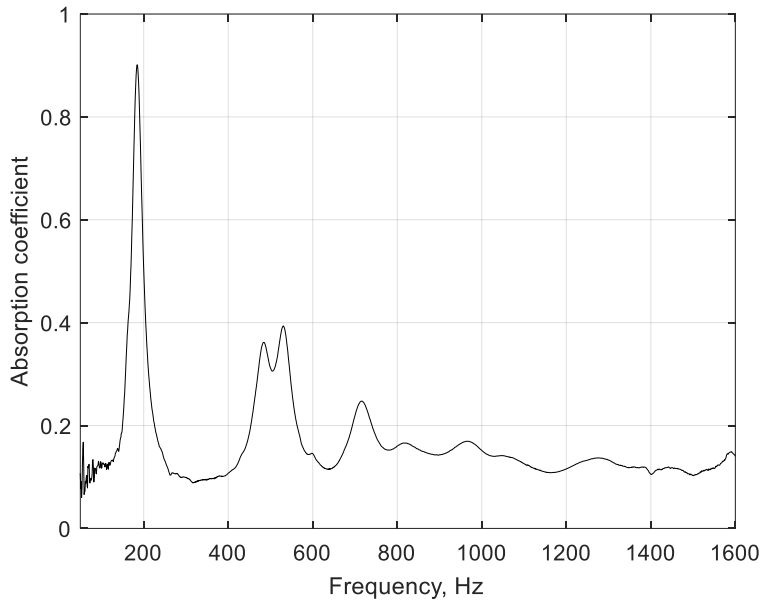

Figure 4.23. Absorption coefficient as a function of frequency for configuration $d_p = 3$ mm and $d_c = 1$ mm. Pore radius is $r_0 = 4$ mm, $L = 62$ mm, and $R = 50$ mm.

To illustrate the effect of different plate thicknesses of the samples, measurements have been performed for two different pancake absorbers with the same thickness. For instance, Figure 4.20 and Figure 4.23 show absorption coefficient dependence as a function of frequency for two different plate thicknesses (1 mm and 3 mm, respectively). Pore diameter and cavity thickness remains the same and sample lengths are approximately $L = 62$ mm. For the pancake absorber comprised with $d_p = 3$ mm, see Figure 4.23, the first resonance peak is seen to be observed at $f = 185\ \mathrm{Hz}$ with a normalized absorptive peak value of 0.9. Furthermore, the second peak is reduced with its absorptive peak value 0.39 and observed at $f = 530\ \mathrm{Hz}$. A third peak is found to be at $f = 715\ \mathrm{Hz}$ with a normalized absorptive peak value of 0.25. The pancake absorber built with 1 mm plate thicknesses has double the number of peaks within the frequency spectrum measured $f = 50\ \mathrm{Hz} - 1600\ \mathrm{Hz}$). Comparison of the first resonance frequency for the 1 mm plate sample, see Figure 4.20, is observed to be much lower at $f = 144\ \mathrm{Hz}$. It has an absorptive peak value of 0.89, and the second and third peaks are found at frequencies $f = 396\ \mathrm{Hz}$ and $f = 574\ \mathrm{Hz}$ with absorptive peak values 0.42 and 0.54, respectively. The results from the above-mentioned Figures 4.20 and 4.23, show that the plate thickness indeed affects the performance of the absorber. The thicker the plate within the sample leads to the first resonance frequency (and corresponding peaks) being shifted to higher frequencies. Absorptive peaks also have larger normalized absorption values for when the pancake sample contains $L = 62$ mm and $d_p = 1$ mm. Furthermore, there are an additional number of absorptive peaks present for the pancake absorber built with $d_p = 1$ mm. Accelerometer measurements for samples with thickness around $L = 62$ mm are shown by Figures 4.24 a, b.

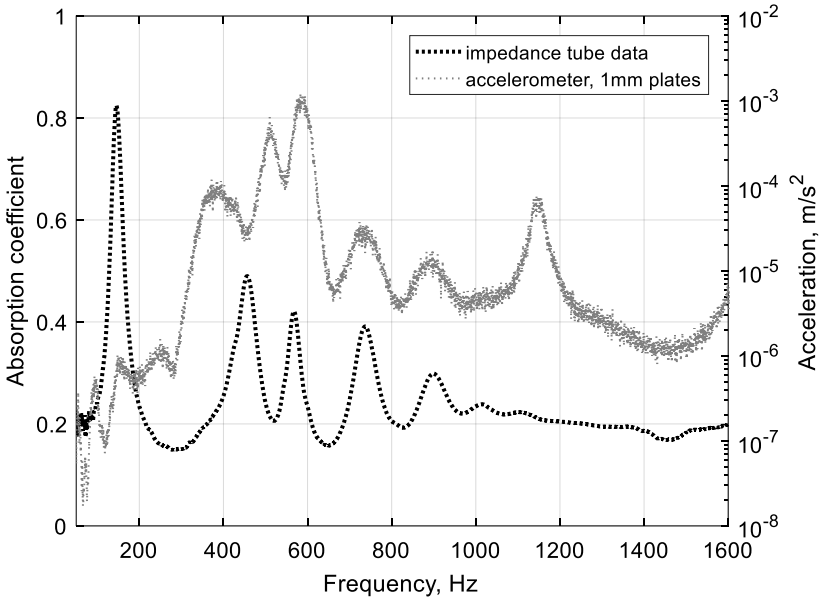

(a)

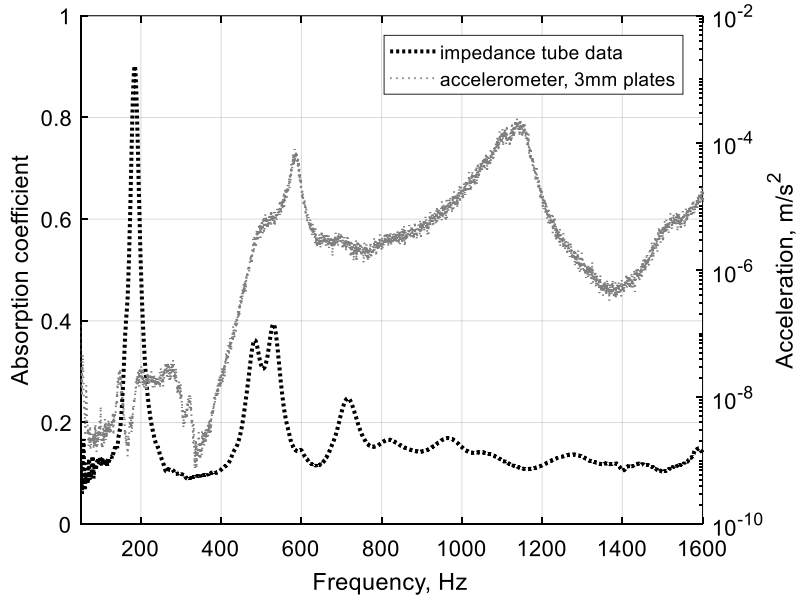

(b)

Figure 4.24. (a) Absorption coefficient and acceleration data with dependence on frequency for pancake absorber comprised $r_0 = 4$ mm, $d_p = 1$ mm, $d_c = 1$ mm, $L = 62$ mm and $R = 50$ mm. In (b) configuration is $r_0 = 4$ mm, $d_p = 3$ mm, $d_c = 1$ mm, $L = 62$ mm and $R = 50$ mm.

Measurements performed using an accelerometer are plotted to account for the phenomena from the disturbance of the metallic frame structure, see Figures 4.24 a, b. Absorption coefficient is also plotted as a function of frequency, given in Figure 4.24 a, for sample with 1 mm plate thickness, and in Figure 4.24 b, for sample with 3 mm plate thickness. The accelerometer data clearly indicates that structural resonance is dependent on the thickness of the plates that make-up the sample. The mechanical disturbance of the frame is included to show the effects of the phenomena caused by the mechanical resonance in addition to acoustic resonance. It is shown later in Chapter 6 (showing model and experimental comparisons), where a model is developed accounting for absorber performance with mechanical resonance contribution. Figure 4.24 a - shows that the accelerometer data follows the trend

of the data obtained by acoustic interaction from use of the impedance tube at frequencies around $f = 300\ \text{Hz} - 900\ \text{Hz}$. And in Figure 4.24 b - it is seen that the accelerometer data follows the trend of acoustic interaction at frequencies around $f = 300\ \text{Hz} - 600\ \text{Hz}$.. The accelerometer data for both Figures (4.24 a, b) presents mechanical resonance in the higher frequency range for the rest of the frequency spectrum $f = 900\ \text{Hz} - 1600\ \text{Hz}$.. This phenomenon provides a more detailed account of the absorber and validates that mechanical disturbance of the frame must be included with acoustic resonance. It is observed in Figures 4.24 a, b, that the first resonance does not appear to be affected by the mechanical disturbance of the plate, at low frequencies below $f = 350\ \text{Hz}$. This is seen to be the contrary for the higher order resonances for the case when $d_p = 1$ mm (Figure 4.24 a) and for $d_p = 3$ mm (Figure 4.24 b).

4.3.2. 3D Printed Profile Absorbers

Linear and exponential profile absorbers have been constructed using 3D printer technology and measured acoustically using an impedance tube with standard two-microphone set-up, (see Figures 4.25 a, b). The samples have configurations with front pore $r_0 = 25$ mm, $d_p = 2$ mm, $d_c = 2$ mm, $L = 100$ mm and $R = 25$ mm. The opening pore for both linear and exponential profile absorbers begin with $r_0 = 25$ mm. Sound excitation used is white noise ranging from 90 dB – 120 dB. Figure 4.25 a - shows absorption coefficient data by a 3D printed linear profile. The first absorptive peak begins at approximately $f = 300\ \text{Hz}$ and progressively increases to a maximum peak value of 0.79 at $f = 560\ \text{Hz}$. At $f = 770\ \text{Hz}$ the absorption coefficient reduces after the first absorptive peak to a value 0.39 and then increases to a second absorptive peak with a value of 0.82. After the second peak the absorption coefficient reduces again to 0.56, at $f = 1305\ \text{Hz}$, before a third peak. A third absorptive peak is observed at $f = 1505\ \text{Hz}$ with an absorptive value of 0.67.

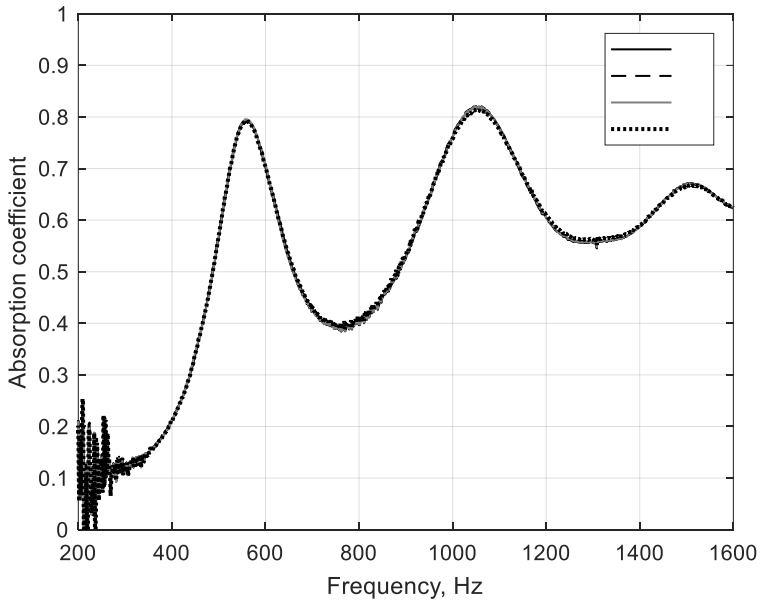

(a)

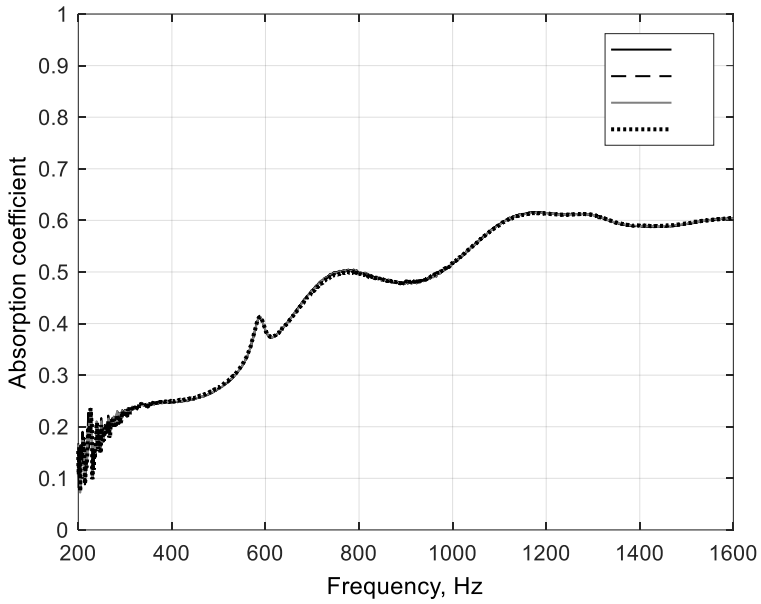

(b)

Figure 4.25. Absorption coefficient as a function of frequency. Linear 3D printed profile is shown in (a) and the exponential profile 3D printed is presented by data given in (b). Front pore is $r_0 = 25$ mm, $d_p = 2$ mm, $d_c = 2$ mm, $L = 100$ mm and $R = 25$ mm. Amplitudes 90 dB (solid black), 100 dB (dash), 110 dB (solid grey), 120 dB (dot).

Figure 4.25 b - shows the absorption coefficient data obtained by a 3D printed exponential profile. It is presented showing a clear difference in absorption phenomena with comparability to the linear profile given by Figure 4.25 a. In the exponential profile case, the absorption coefficient progressively increases in a more continuous manner with increasing frequency. In contrast to Figure 4.25 a, It is shown in Figure 4.25 b, that prominent absorptive peaks occur, which are not observed for the exponential profile, Figure 4.25 b. A key difference between the linear profile (4.25 a) and exponential profile (4.25 b) is observed around $f = 400\ \text{Hz} - 700\ \text{Hz}$ and $f = 900\ \text{Hz} - 1200\ \text{Hz}$. The linear profile proves to be much more effective at these frequencies. In both the linear and exponential profiles, it is also observed that increasing the amplitudes has very little effect on peak absorption for the amplitudes tested against the absorbers (between 90 – 120 dB SPL). This is one of the advantages posed by the profile absorbers, (See Figures 4.25 a, b) yet this is seen to be on the contrary for conventional porous absorbers. The exponential profile absorber is seen to be slightly more effective than the linear profile at lower frequencies ($f = 300\ \text{Hz} - 400\ \text{Hz}$) and middle frequencies ($f = 700\ \text{Hz} - 850\ \text{Hz}$). The minimum absorptive peak values are in the frequency range between $f = 100\ \text{Hz} - 650\ \text{Hz}$.

4.3.3. Metallic Profile Absorbers

Profile absorbers containing a linear decreasing central perforation have been built and tested with the front pore of the samples being $r_0 = 15\ \text{mm}$ and $r_0 = 25\ \text{mm}$. For the former, the d_c is constant at $d_c = 3\ \text{mm}$ after each plate, and the latter is built with $d_c = 2\ \text{mm}$ and rebuilt with $d_c = 3\ \text{mm}$. In all cases the orifices in the plates decrease 2 mm per plate for the samples, where the external plate radius is $R = 50\ \text{mm}$. Figures 4.26 – 4.27, show absorption coefficient versus frequency measured for a linear profile absorber with a pore opening radius $r_0 = 15\ \text{mm}$, $d_p = 1$ mm, and $d_c = 3$ mm. The amplitude SPL gradually increases in 10 dB intervals ranging from 60 dB – 100 dB. Sample length is $L = 60\ \text{mm}$.

Figures 4.28 – 4.29 show absorption coefficient versus frequency measured for a linear profile sample with a pore opening radius $r_0 = 25\ \mathrm{mm}$, $d_p = 1$ mm, and $d_c = 2$ mm. The amplitude SPL gradually increases in 10 dB intervals ranging from 70 dB – 100 dB. Sample $L = 80\ \mathrm{mm}$. Absorption coefficient dependence on frequency is presented by Figures 4.30 – 4.31 showing data obtained for a linear profile sample with a pore opening radius $r_0 = 25\ \mathrm{mm}$, $d_p = 1$ mm and $d_c = 3$ mm. Sample length is $L = 80\ \mathrm{mm}$. These measurements are all performed using white noise excitation. The amplitude SPL is higher for this configuration gradually increasing in 10 dB intervals ranging from 70 dB – 120 dB. Absorption coefficient dependence on frequency for the linear profile with $r_0 = 15\ \mathrm{mm}$ is shown (Figure 4.26) to be comprised of two absorptive peaks which are forked at a low frequency, 260 Hz, and absorption coefficient value of 0.53. Between the amplitudes of when sound pressure level is low (60 dB – 80 dB), the first peak maxima are at $f = 229\ \mathrm{Hz}$ with absorption coefficient value of 0.82. The second peak maxima are at $f = 295\ \mathrm{Hz}$ and has the absorption coefficient value of 0.90. When the incident amplitude is increased further (see Figure 4.27) these two absorptive peaks are modified. A single peak is obtained at $f = 276\ \mathrm{Hz}$ having an absorption coefficient value of 0.84 and eliminating the peak separation previously observed at $f = 260\ \mathrm{Hz}$. The absorptive peaks with maximum values are observed at 668 Hz, 883 Hz and 1060 Hz with absorption coefficient data showing to be 1.0, 1.0, and 0.98, respectively. After $f = 1060\ \mathrm{Hz}$ other absorptive peaks are seen to range for the remainder of the frequency spectrum ranging from 0.8 to 0.58.

The number of plates and cavities are then extended which increases the total sample length to $L = 80\ \mathrm{mm}$ (see Figure 4.28). In this arrangement the front pore radius $r_0 = 25\ \mathrm{mm}$ and d_c is changed to $d_c = 2\ \mathrm{mm}$. The sample contains a linear inner profile and decreases 2 mm for each pore, per plate thereafter until rigid backing is reached. The first resonance frequency of the absorber is $f = 308\ \mathrm{Hz}$ and has an absorption coefficient value of 0.97 when induced by SPL 70 dB and 80 dB with white noise excitation. The absorber is then measured for amplitudes 90 dB and 100 dB (given by Figure 4.29) which is seen to reduce the absorption coefficient values slightly to 0.93 and 0.90, respectively. Peak values of the absorption coefficient are then shown (see Figure 4.29) to increase between frequencies $f = 350\ \mathrm{Hz}$ and $f = 628\ \mathrm{Hz}$. This is for when amplitude strength is at 100 dB compared to lower sound pressure levels (60 dB – 90 dB). Absorption coefficient values for the rest of the frequency spectrum after $f = 628\ \mathrm{Hz}$, in Figures 4.28 – 4.29, are seen to remain unchanged for all the measurements consisting of white noise excitations. Profile thicknesses differ $L = 20\ \mathrm{mm}$ for the sample with $r_0 = 15\ \mathrm{mm}$ (4.26 – 4.27) and sample with $r_0 = 25\ \mathrm{mm}$ (4.28 – 4.29). Plates are of same thickness where $d_p = 1$ mm, but cavity thickness differs by $d_c = 1$ mm. The central pores as aforementioned reduce 2 mm per plate for (4.26 – 4.27) and (4.28 – 4.29). Linear profile sample with $r_0 = 25\ \mathrm{mm}$ is seen to be more effective at frequencies $f = 1100\ \mathrm{Hz} - 1600\ \mathrm{Hz}$ shown by Figures 4.28 – 4.29. The linear profile sample with $r_0 = 15\ \mathrm{mm}$ is seen to be more effective at slightly lower frequency at $f = 229\ \mathrm{Hz}$ which differs 79 Hz to that from linear profile with $r_0 = 25\ \mathrm{mm}$. The maximum absorptive peak values arise from the linear profile absorber which has $d_c = 2$ mm and $r_0 = 25\ \mathrm{mm}$ when compared to linear profile absorber with $d_c = 3$ mm and $r_0 = 15\ \mathrm{mm}$.

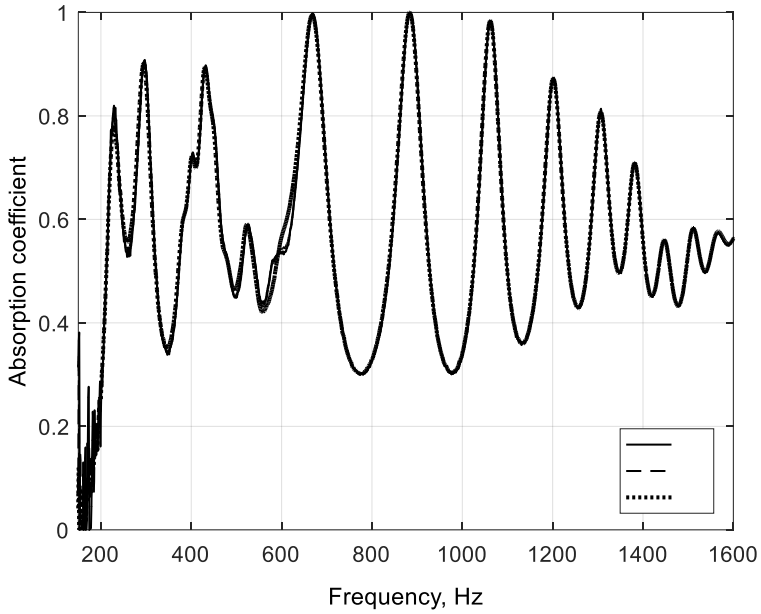

Figure 4.26. Absorption coefficient as a function of frequency for linear profile. Front pore is $r_0 = 15$ mm, $d_p = 1$ mm, $d_c = 3$ mm, $L = 60$ mm and $R = 50$ mm. Each plate thereafter has a 2 mm pore decrease. Amplitudes 60 dB (solid line), 70 dB (dash), 80 dB (dot).

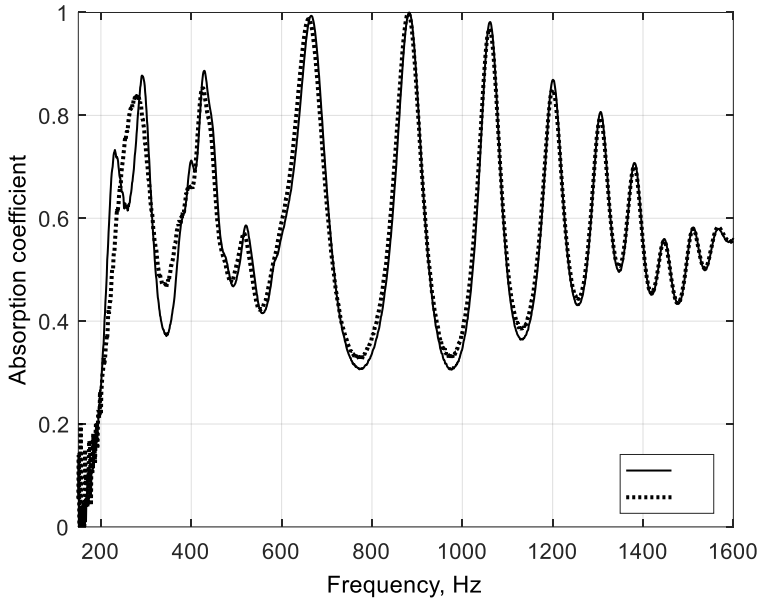

Figure 4.27. Absorption coefficient as a function of frequency for linear profile. Front pore is $r_0 = 15$ mm, $d_p = 1$ mm, $d_c = 3$ mm, $L = 60$ mm and $R = 50$ mm. Each plate thereafter has a 2 mm pore decrease. Amplitudes 90 dB (solid line), 100 dB (dot).

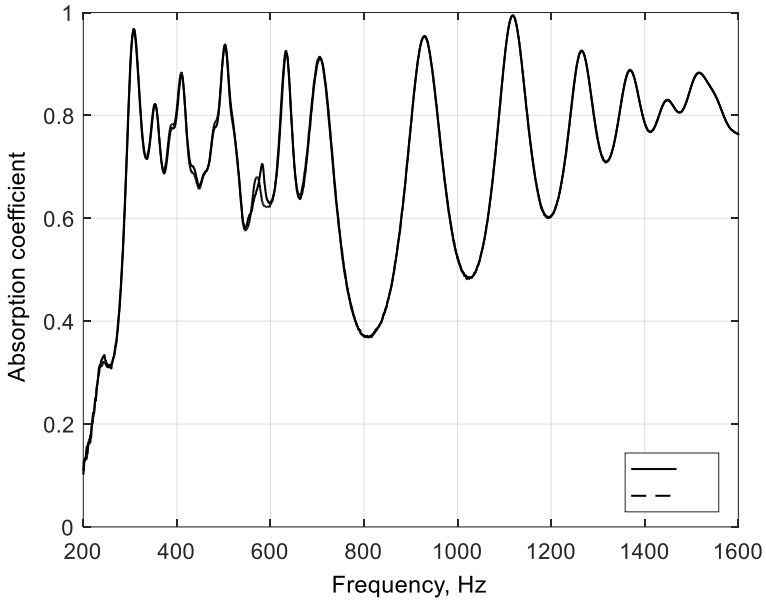

Figure 4.28. Absorption coefficient as a function of frequency for linear profile. Front pore is $r_0 = 25$ mm, $d_p = 1$ mm, $d_c = 2$ mm, $L = 80$ mm and $R = 50$ mm. Each plate thereafter has a 2 mm pore decrease. Amplitudes 70 dB (solid line), 80 dB (dash).

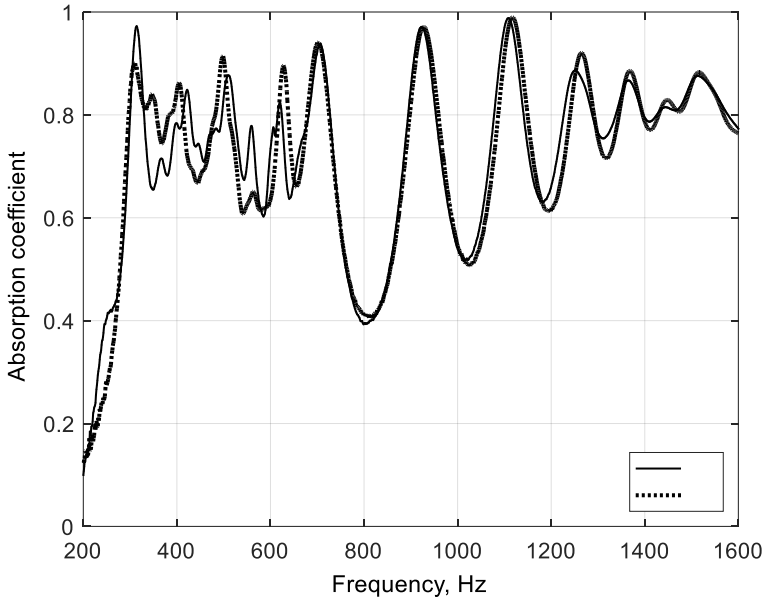

Figure 4.29. Absorption coefficient as a function of frequency for linear profile. Front pore is $r_0 = 25$ mm, $d_p = 1$ mm, $d_c = 2$ mm, $L = 80$ mm and $R = 50$ mm. Each plate thereafter has a 2 mm pore decrease. Amplitudes 90 dB (solid line), 100 dB (dot).

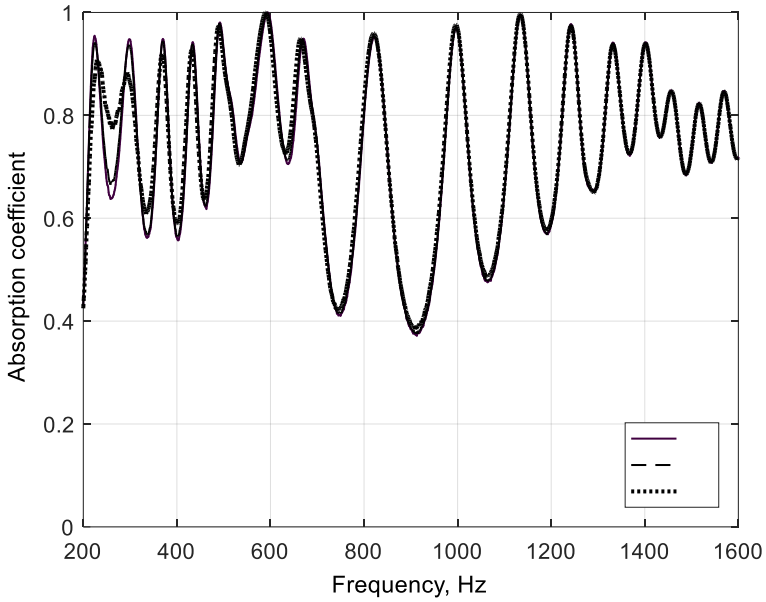

Figure 4.30. Absorption coefficient as a function of frequency for linear profile. Front pore is $r_0 = 25$ mm, $d_p = 1$ mm, $d_c = 3$ mm, $L = 100$ mm and $R = 50$ mm. Each plate thereafter has a 2 mm pore decrease. Amplitudes 70 dB (solid line), 80 dB (dash), 90 dB (dot).

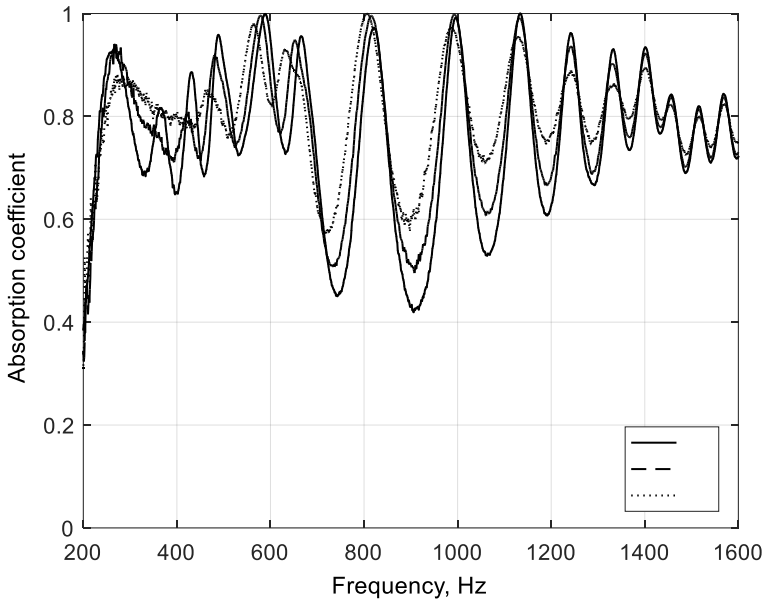

Figure 4.31. Absorption coefficient as a function of frequency for linear profile. Front pore is $r_0 = 25$ mm, $d_p = 1$ mm, $d_c = 3$ mm, $L = 100$ mm and $R = 50$ mm. Each plate thereafter has a 2 mm pore decrease. Amplitudes 100 dB (solid line), 110 dB (dash), 120 dB (dot).

Figures 4.30 – 4.31 show absorption coefficient dependence with frequency when linear profile sample is disassembled. A new configuration is built so that d_c is now made to be $d_c = 3$ mm instead of $d_c = 2$ mm, with plate thickness and pore sizes remaining the same. The dimensions of the pores reduce in diameter 2 mm per plate and results in an increase of total sample thickness, thus absorber thickness now becomes $L = 100$ mm. A linear profile containing $d_c = 3$ mm and front pore with $r_0 = 25$ mm is shown to be more effective still, when amplitude strength grows to 120 dB (see Figures 4.30 – 4.31). First resonance peak at 100 dB is at $f = 264$ Hz and has an absorption coefficient value of 0.93 (Figure 4.30). When increasing the amplitude to 120 dB (considered threshold of linear regime) the first resonance peak increases to $f = 284$ Hz (Figure 4.31). The absorption coefficient reduces for the first

resonance frequency at 120 dB and becomes 0.87. However, all other values of the absorption coefficient are seen to be larger such that the absorber becomes more effective until the amplitude strength reaches a critical value. Consequently, the absorptive peak values slightly reduce over the frequency spectrum. When sound amplitude is below the linear threshold limit (lower than about 120 dB) the first resonance frequency is at $f = 224$ Hz when excited with white noise excitation at 90 dB. This results in an absorption coefficient value of 0.95. Several absorptive peak values are shown to reach 1.0 and remainder absorptive peak values are close to 0.95 up until $f = 1458$ Hz. The lowest absorptive peak values reduce only to 0.85 and 0.82 for the remaining frequencies.

Profile thicknesses differ by $L = 40$ mm for the sample with $r_0 = 15$ mm (Figures 4.26 – 4.27) and sample with its opening pore $r_0 = 25$ mm (Figures 4.30 – 4.31). Plates thickness is $d_p = 1$ mm and cavity thickness remains the same value so $d_c = 3$ mm. The cental pores reduce 2 mm per plate for Figures 4.26 – 4.27 and Figures 4.30 – 4.31. The linear profile with $r_0 = 25$ mm is seen to be considerably much more effective at frequencies across the frequency spectrum. These frequencies are found to be most apparent at $f = 220$ Hz $- 635$ Hz and $f = 1090$ Hz $- 1600$ Hz, see Figures 4.30 – 4.31. The linear profile with opening pore $r_0 = 25$ mm and $d_c = 3$ mm is seen to be more effective across the frequency spectrum when comparing all linear profile configurations, see Figures 4.26 – 4.31. The first resonance frequency is also lowest for when the sample contains $r_0 = 25$ mm and when $d_c = 3$ mm. Maximum absorptive peak values are also largest when compared to linear profile absorbers $d_c = 3$ mm and $r_0 = 15$ mm, and the linear profile absorber $d_c = 3$ mm and $r_0 = 25$ mm. Figures 4.32 – 4.33, show absorption coefficient versus frequency for an exponential profile absorber with a main open pore $r_0 = 25$ mm, $d_p = 1$ mm and $d_c = 2$ mm. The measurements are performed using white noise excitation. The amplitude SPL gradually increases in 10 dB intervals ranging from 70 dB – 100 dB. Sample length $L = 80$ mm.

Absorption coefficient dependence on frequency is presented by Figures 4.34 – 4.35 showing data obtained for an exponential profile with also a pore opening radius $r_0 = 25$ mm and when $d_p = 1$ mm. The absorber is re-built so that instead of $d_c = 2$ mm, it now becomes $d_c = 3$ mm and results in a sample length $L = 100$ mm. These measurements are also performed using white noise excitation. The amplitude SPL is higher for this configuration gradually increasing in 10 dB intervals ranging from 70 dB – 120 dB. Absorption coefficient measured for the first resonance frequency for both when $d_c = 2$ mm and $d_c = 3$ mm is close to 0.55 (see Figures 4.32 – 4.35). The value of absorption coefficient progressively increases to 0.8 at $f = 150$ Hz towards $f = 600$ Hz, for the sample with $d_c = 2$ mm (Figures 4.32 – 4.33) and increases further to a value 0.9 for exponential profile with 3 mm cavities (Figures 4.34 – 4.35). Another trend is seen between $f = 1200$ Hz and $f = 1600$ Hz by the absorption coefficient values ranging between 0.8 and reaching 0.9 at the end of the frequency of interest. Absorption coefficient becomes 0.9 and increases to 1.0 In the frequency range where the maximum peak values occur. The different thicknesses used for the exponential profile absorbers differ by $L = 20$ mm for $d_c = 2$ mm and $d_c = 3$ mm. Absorption coefficient is shown to be larger for the low and higher frequencies for when $d_c = 3$ mm, compared to when $d_c = 2$ mm. This can be observed within the frequency range $f = 150$ Hz $- 600$ Hz given by Figures 4.32 – 4.33, compared to Figures 4.34 – 4.35. A common trend of peak convergence is observed for all of the profile absorbers (both linear and exponential) and is shown to lie in the frequency range $f = 50$ Hz $- 400$ Hz. For the low sound amplitude

when sound pressure level (SPL), is lower than around 95 dB (in SPL tested this is 60 dB – 95 dB), the first resonance peaks of all samples remain constant. When the SPL is raised above 95 dB the first resonance absorptive peak minima and maxima, are modified and peak maxima begins to merge with other peaks maxima in the frequency spectrum up to $f = 400\ \mathrm{Hz}$. This consequently raises the absorptive peak minima values more so within frequency $f = 50\ \mathrm{Hz} - 400\ \mathrm{Hz}$. This phenomenon is also extended throughout the frequency spectrum up to the maximum frequency of interest $f = 1600\ \mathrm{Hz}$, as amplitude grows. The results for the metallic structures for both pancake and profile absorbers with $R =$ 50 mm, are shown for these samples for both linear, and nonlinear regimes including accelerometer measurements. The effect of the linear and exponential profile absorbers show that broadband absorption is possible for reasonably low and middle range ampltudes (70 dB – 120 dB). This is presented from the results shown by Figures 4.25 a, b, for 3D printed absorbers, and Figures 4.26 – 4.35 for metallic absorbers. Metallic profile structures are shown to be more effective than the 3D printed structures, especially at low frequencies, shown for white noise excitation up to 120 dB. This is even for when the linear and exponential 3D printed profile absorbers have additional thickness $L =$ 40 mm compared to a linear profile with $r_0 =$ 15 mm. Again, this is also the case for when linear and exponential 3D printed profile absorbers have additional $L =$ 20 mm compared to profile metallic structures with $d_c =$ 2 mm (for both the linear and exponential profiles). Another comparison between the linear profile and the exponential profile is that the linear profile is more effective at lower frequencies and generally most of the frequency spectrum. However, it is observed that the exponential profile absorbers are slightly more effective at $f = 140\ \mathrm{Hz} - 1600\ \mathrm{Hz}$.

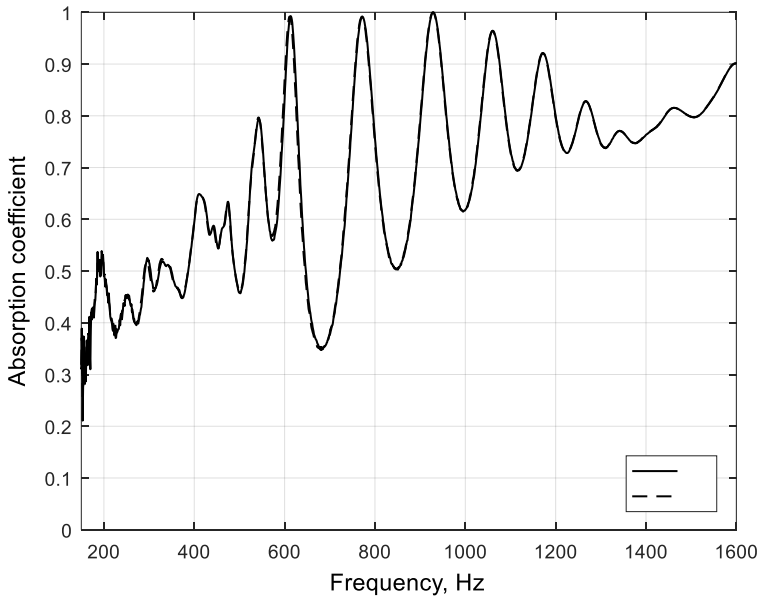

Figure 4.32. Absorption coefficient as a function of frequency for exponential profile. Front pore is $r_0 =$ 25 mm, $d_p =$ 1 mm, $d_c =$ 2 mm, $L =$ 80 mm, $R =$ 50 mm. Amplitudes 70 dB (solid line), 80 dB (dash).

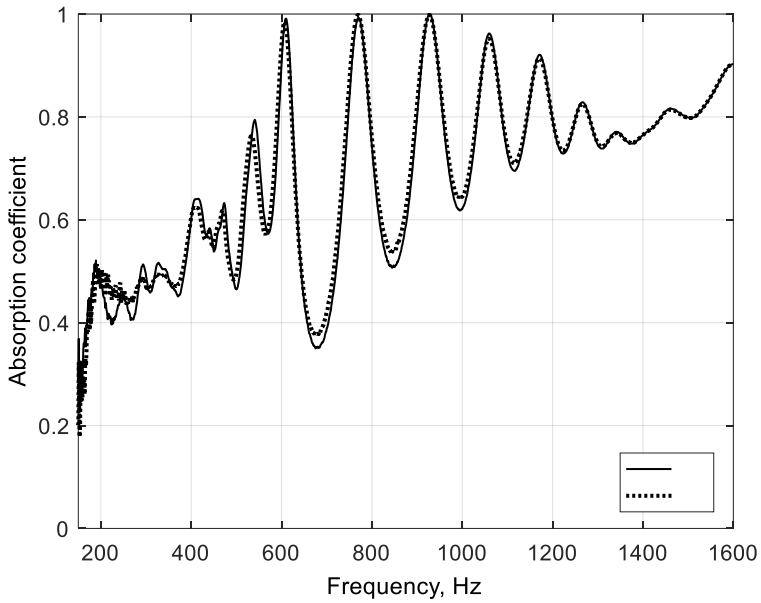

Figure 4.33. Absorption coefficient as a function of frequency for exponential profile. Front pore is $r_0 = 25$ mm, $d_p = 1$ mm, $d_c = 2$ mm, $L = 80$ mm, $R = 50$ mm. Amplitudes 90 dB (solid line), 100 dB (dot).

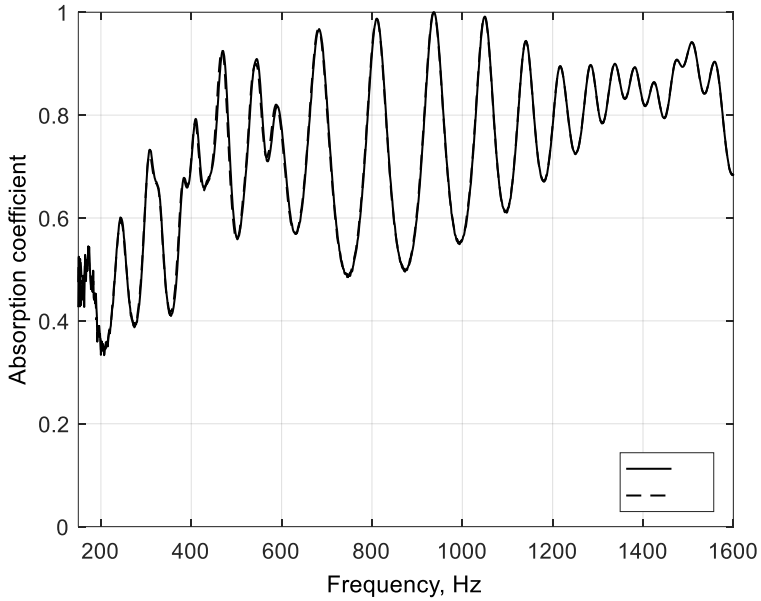

Figure 4.34. Absorption coefficient as a function of frequency for exponential profile. Front pore is $r_0 = 25$ mm, $d_p = 1$ mm, $d_c = 3$ mm, $L = 100$ mm, $R = 50$ mm. Amplitudes 70 dB (solid line), 80 dB (dash).

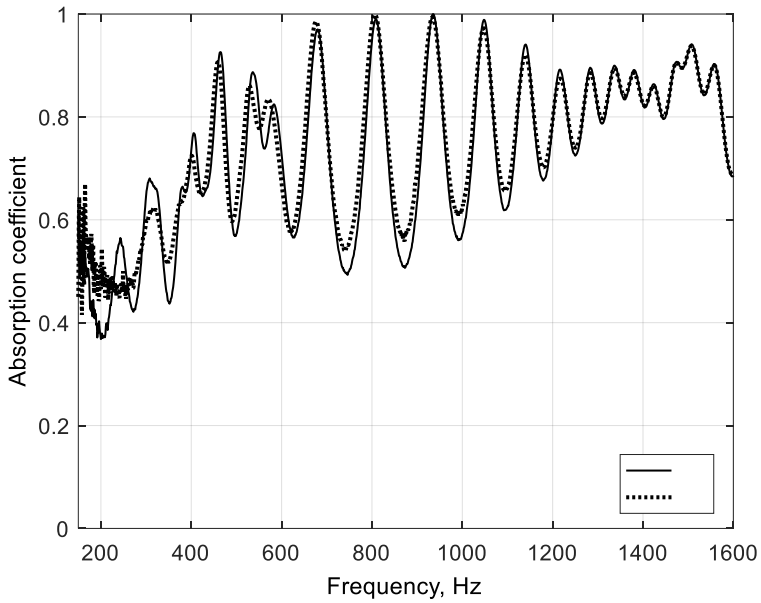

Figure 4.35. Absorption coefficient as a function of frequency for exponential profile. Front pore is $r_0 = 25$ mm, $d_p = 1$ mm, $d_c = 3$ mm, $L = 100$ mm, $R = 50$ mm. Amplitudes 90 dB (solid line), 100 dB (dot).

All the metallic samples discussed thus far are investigated further against much larger amplitudes (for pancake and profiled absorbers built with $R = 50$ mm, $d_c = 2$ mm, $d_c = 3$ mm and $d_p = 1$ mm). The measurements are performed using an impedance tube with sine wave excitation. This method is advantageous since amplitude strengths are now enabled to be obtained stronger by the membrane used as part of the sound source. The membrane is fixed to its limitations and the accuracy of the equipment used. This also eliminates any unwanted frequencies to be measured. The focus of the project is sample effectiveness at low frequencies and even though the working range of the impedance tube was $f = 50\ \text{Hz} - 1600\ \text{Hz}$ the desirable frequencies of interest are the first few hundred Hertz. Therefore, the samples are developed to be effective at the lowest possible frequencies and considering both low and highest possible amplitudes attainable. Linear and exponential profile absorbers with varying central pores are shown to be proficiently effective for broadband absorption at $f = 100\ \text{Hz} - 1600\ \text{Hz}$.

4.4. Results of Impedance Tube Measurements at High Sound Pressure Levels Using Pure Tones

Pancake and profile absorbers at high sound pressure levels are investigated with the aim of testing their performance at low frequencies. Dependence of the absorption coefficient on incident pressure amplitude is calculated from the data obtained by direct measurements in a HSPL impedance tube.

4.4.1. Pancake Absorbers – HSPL

Sine wave excitation is performed for pancake absorbers comprised of various configurations. Different strengths of incident pressure amplitude are targeted at the pancakes to investigate the dependence of absorption on incident pressure. The incident pressure is calculated and presented in the Tables below

(Tables 2 – 7), calculated as RMS pressure and peak pressure. Frequencies investigated are selected by data from low sound pressure levels, firstly obtained by white noise excitation. Several frequencies for each pancake absorber for approximate sample lengths, $L = 30$ mm – 60 mm are shown (absorption coefficient vs incident pressure plots, including the Tables). Five frequencies for each configuration (structure cavity thickness variations) are shown in both the plots (data points) and Tables (values). Number of the dead-end contained in each pancake is given by N_{de}. Absorption coefficient values are directly taken from the data by each single measurement. The data is given for each of the frequencies selected. Samples with $L = 30$ mm is presented first (Figures 4.36 – 4.41), followed by the larger samples, (Figures 4.42 – 4.47). In each case, the smallest cavity configuration is given, i.e. when $d_c = 1$ mm, $d_c = 3$ mm, followed by $d_c = 6$ mm. External plate radius for the pancake absorbers is $R = 50$ mm, pore radii $r_0 = 4$ mm and plate thickness $d_p = 1$ mm. Measurements performed in a HSPL impedance tube using pure tones excitation is shown by sections 4.4.1 (pancake absorbers) and 4.4.2 (profile absorbers). Different pancake configurations are presented in the following order. Figures 4.36 – 4.37 show for when $d_p = 1$ mm, $d_c = 1$ mm, and $L = 31$ mm. Cavity thickness is then increased (shown by Figures 4.38 – 4.39) so that $d_c = 3$ mm, $d_p = 1$ mm, and sample thickness becomes $L = 32$ mm. Figures 4.40 – 4.41 show pancake when $d_p = 1$ mm, $d_c = 6$ mm, and $L = 35$ mm. The pancake absorbers are then disassembled and later built with larger sample sizes. The following figures show when samples are made closely to $L = 60$ mm. Figures 4.42 – 4.43 show pancake when $d_p = 1$ mm, $d_c = 1$ mm, and sample length $L = 62$ mm. When $d_c = 3$ mm and $d_p = 1$ mm the pancake absorber has sample length $L = 60$ mm and shown by the data in Figures 4.44 – 4.45. Cavity thickness is then doubled so that $d_c = 6$ mm and $d_p = 1$ mm, sample length $L = 63$ mm, shown by Figures 4.46 – 4.47.

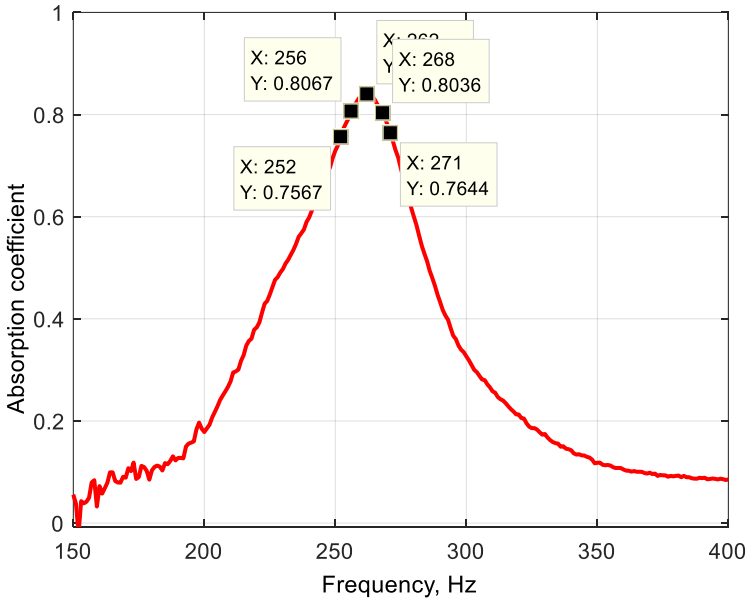

Figure 4.36. Absorption coefficient as a function of frequency. Pancake configuration is $r_0 = 4$ mm, $d_p = 1$ mm, $d_c = 1$ mm, $R = 50$ mm, $N_{de} = 16$, and $L = 31$ mm.

The absorption curve (see Figure 4.36) is the first resonance frequency for Pancake configuration which has pore radius $r_0 = 4$ mm, $d_p = 1$ mm and $d_c = 1$ mm. Sample has $L = 31$ mm. Sound excitation is white noise, and the selected frequencies are later tested with pure tones in a HSPL impedance tube, see Figure 4.37. The selected frequencies are those presented in Table 4.2.

Frequency (Hz)	252	252	252	252	252	252	252
Abs Coefficient	0.77	0.77	0.78	0.76	0.69	0.57	0.45
RMS Pressure, Pa	0.53	1.74	5.85	16.11	49.70	140.11	319.65
Peak Pressure, Pa	0.75	2.46	8.27	22.78	70.29	198.14	452.05

Frequency (Hz)	256	256	256	256	256	256	256
Abs Coefficient	0.80	0.79	0.77	0.73	0.67	0.54	0.42
RMS Pressure, Pa	0.52	1.65	5.47	15.42	48.66	138.32	430.37
Peak Pressure, Pa	0.74	2.33	7.74	21.81	68.82	195.61	608.64

Frequency (Hz)	262	262	262	262	262	262	262
Abs Coefficient	0.79	0.80	0.79	0.75	0.68	0.56	0.41
RMS Pressure, Pa	0.50	1.61	5.41	15.16	47.84	137.91	454.50
Peak Pressure, Pa	0.71	2.28	7.65	21.44	67.66	195.03	642.76

Frequency (Hz)	268	268	268	268	268	268	268
Abs Coefficient	0.78	0.78	0.78	0.73	0.66	0.54	0.42
RMS Pressure, Pa	0.49	1.56	5.18	14.58	46.63	135.95	430.77
Peak Pressure, Pa	0.69	2.21	7.33	20.62	65.94	192.26	609.20

Frequency (Hz)	271	271	271	271	271	271	271
Abs Coefficient	0.77	0.76	0.76	0.71	0.65	0.53	0.43
RMS Pressure, Pa	0.48	1.51	5.05	14.28	45.96	135.14	431.98
Peak Pressure, Pa	0.68	2.13	7.14	20.19	65.00	191.12	610.91

Table 4.2. Pancake absorber values of absorption coefficient dependence on incident pressure amplitude. Configuration is $r_0 = 4$ mm, $d_p = 1$ mm, $d_c = 1$ mm, $R = 50$ mm and $L = 31$ mm.

Figures 4.37 shows absorption coefficient dependence on incident pressure measured in Pascals. Sample is pancake absorber with a constant pore opening diameter throughout the length of the structure. Pore radius $r_0 = 4$ mm, $d_p = 1$ mm and $d_c = 1$ mm. Measurements are performed using sine wave excitation. The amplitude SPL gradually increases in approximately 10 dB intervals. Sample length is approximately $L = 31$ mm and external plate radius $R = 50$ mm. Table 4.2 shows the measured values of absorption coefficient data obtained from direct measurements performed in a HSPL impedance tube. The RMS pressure and peak pressures are calculated (see section 4.2) with the latter indicating the incident pressure amplitude, as seen in Figure 4.37. It can be determined by the data presented by Table 4.2 that the pancake absorber was slightly more effective at lower incident sound pressure amplitudes at frequency 262 Hz. It is demonstrated that it was slightly more effective at 252 Hz for increased incident sound pressures levels.

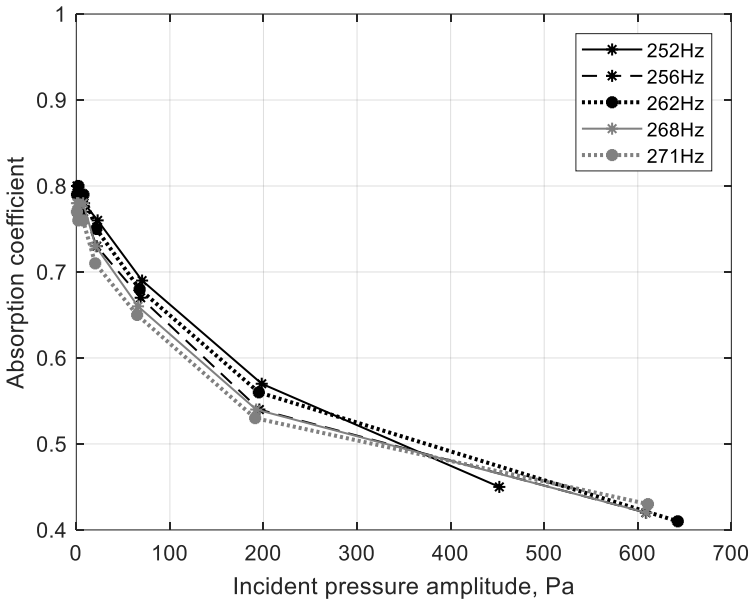

Figure 4.37. Absorption coefficient as a function of incident amplitude. Pancake configuration is $r_0 = 4$ mm, $d_p = 1$ mm, $d_c = 1$ mm, $R = 50$ mm, $N_{de} = 16$, and $L = 31$ mm.

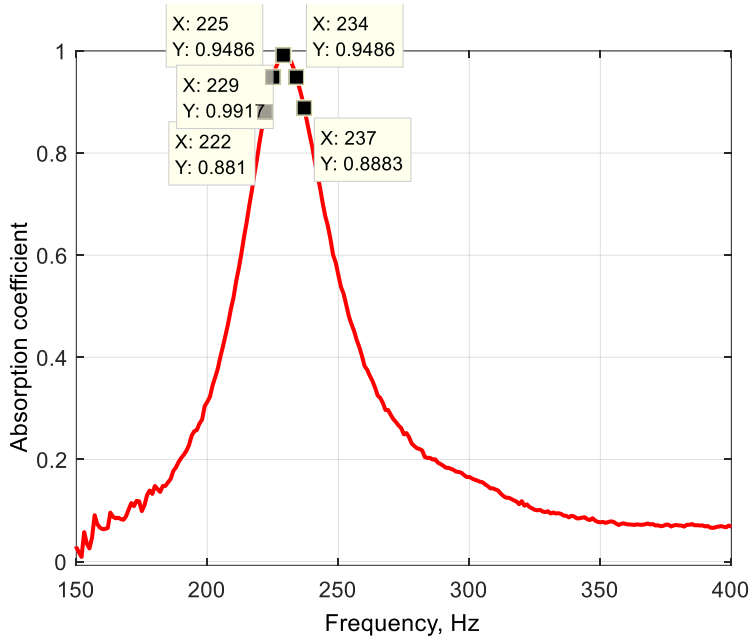

Figure 4.38. Absorption coefficient as a function of frequency. Pancake configuration is $r_0 = 4$ mm, $d_p = 1$ mm, $d_c = 3$ mm, $R = 50$ mm, $N_{de} = 8$, and $L = 32$ mm.

The absorption curve shown in Figure 4.38 is the first resonance frequency for Pancake configuration which has pore radius $r_0 = 4$ mm, $d_p = 1$ mm and $d_c = 3$ mm. Sample length is $L = 32$ mm. Sound excitation is white noise, and the selected frequencies are later tested with pure tones in a HSPL impedance tube, see Figure 4.39. The selected frequencies are those presented in Table 4.3.

Frequency (Hz)	222	222	222	222	222	222	222
Abs Coefficient	0.88	0.88	0.85	0.73	0.64	0.48	0.45
RMS Pressure, Pa	0.73	2.11	6.29	15.77	45.93	129.98	213.15
Peak Pressure, Pa	1.03	2.98	8.89	22.30	64.95	183.82	301.44

Frequency (Hz)	225	225	225	225	225	225	225
Abs Coefficient	0.95	0.94	0.90	0.77	0.65	0.48	0.47
RMS Pressure, Pa	0.69	2.10	6.24	15.96	45.74	130.09	180.96

Peak Pressure, Pa	0.98	2.97	8.82	22.57	64.69	183.97	255.92

Frequency (Hz)	229	229	229	229	229	229	229
Abs Coefficient	0.99	0.98	0.92	0.79	0.63	0.48	0.45
RMS Pressure, Pa	0.64	1.97	6.00	15.73	44.96	129.44	159.66
Peak Pressure, Pa	0.90	2.79	8.48	22.25	63.58	183.06	225.79

Frequency (Hz)	234	234	234	234	234	234	234
Abs Coefficient	0.93	0.92	0.88	0.79	0.61	0.48	0.47
RMS Pressure, Pa	0.56	1.66	5.40	15.28	44.68	129.34	160.38
Peak Pressure, Pa	0.79	2.35	7.64	21.61	63.19	182.91	226.81

Frequency (Hz)	237	237	237	237	237	237	237
Abs Coefficient	0.87	0.86	0.84	0.79	0.60	0.48	0.47
RMS Pressure, Pa	0.52	1.55	5.16	15.02	44.50	129.40	160.18
Peak Pressure, Pa	0.74	2.19	7.30	21.24	62.93	183.00	226.53

Table 4.3. Pancake absorber values of absorption coefficient dependence on incident amplitude. Configuration is $r_0 = 4$ mm, $d_p = 1$ mm, $d_c = 3$ mm, $R = 50$ mm and $L = 32$ mm.

Figure 4.39, shows absorption coefficient dependence on incident pressure measured in Pascals. Sample is pancake absorber with a constant pore opening diameter throughout the length of the structure. Pore radius is $r_0 = 4$ mm, $d_p = 1$ mm and $d_c = 3$ mm. The measurements are performed using sine wave excitation. The amplitude SPL gradually increases in approximately 10 dB intervals. Sample length is $L = 32$ mm and external plate radius $R = 50$ mm. Table 4.3 shows the measured values of absorption coefficient data obtained from direct measurements performed in a HSPL impedance tube. The RMS pressure and peak pressures are calculated (see section 4.2) with the latter indicating the incident pressure amplitude, as seen in Figure 4.39. It can be determined by the data presented by Table 4.3 that the pancake absorber was slightly more effective at lower incident sound pressure amplitudes at frequency 229 Hz. It is demonstrated that it was slightly more effective at 222 Hz for increased incident sound pressures levels.

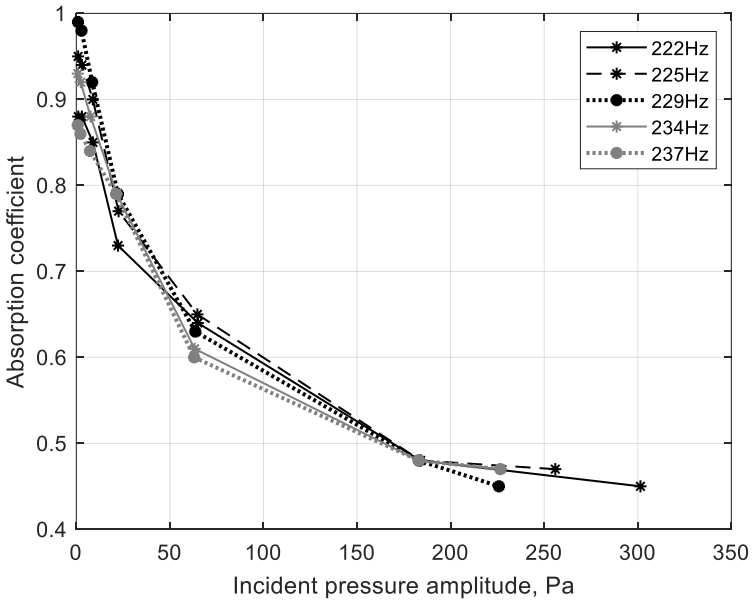

Figure 4.39. Absorption coefficient as a function of incident amplitude. Pancake configuration is $r_0 = 4$ mm, $d_p = 1$ mm, $d_c = 3$ mm, $R = 50$ mm, $N_{de} = 8$, and $L = 32$ mm.

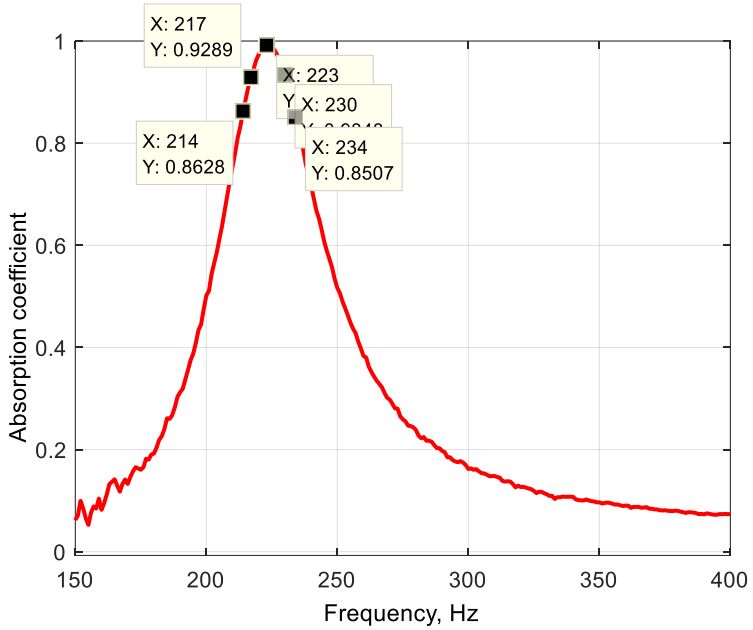

Figure 4.40. Absorption coefficient as a function of frequency. Pancake configuration is $r_0 = 4$ mm, $d_p = 1$ mm, $d_c = 6$ mm, $R = 50$ mm, $N_{de} = 5$, and $L = 35$ mm.

Figure 4.40 indicates the selected frequencies. Absorption curve is the first resonance frequency for Pancake configuration which has pore radius $r_0 = 4$ mm, $d_p = 1$ mm and $d_c = 6$ mm. Sample has length $L = 35$ mm. Sound excitation is white noise, and the selected frequencies are later tested with pure tones in a HSPL impedance tube, see Figure 4.41. The selected frequencies are those presented in Table 4.4.

Frequency (Hz)	214	214	214	214	214	214	214
Abs Coefficient	0.87	0.87	0.86	0.74	0.58	0.47	0.43
RMS Pressure, Pa	0.75	2.15	6.60	16.42	45.60	80.38	100.14
Peak Pressure, Pa	1.06	3.04	9.33	23.22	64.49	113.67	141.62

Frequency (Hz)	217	217	217	217	217	217	217
Abs Coefficient	0.93	0.93	0.91	0.79	0.61	0.55	0.42
RMS Pressure, Pa	0.76	2.30	6.61	15.97	38.88	52.97	110.20
Peak Pressure, Pa	1.07	3.25	9.35	22.58	54.98	74.91	155.85

Frequency (Hz)	223	223	223	223	223	223	223
Abs Coefficient	1.00	0.99	0.95	0.82	0.66	0.55	0.52
RMS Pressure, Pa	0.67	2.17	6.21	15.86	28.41	52.73	64.89
Peak Pressure, Pa	0.95	3.07	8.78	22.43	40.18	74.57	91.77

Frequency (Hz)	230	230	230	230	230	230	230
Abs Coefficient	0.93	0.93	0.91	0.82	0.67	0.56	0.52
RMS Pressure, Pa	0.55	1.68	5.36	14.96	28.13	52.40	64.72
Peak Pressure, Pa	0.78	2.38	7.58	21.16	39.78	74.10	91.53

Frequency (Hz)	234	234	234	234	234	234	234
Abs Coefficient	0.84	0.85	0.85	0.80	0.67	0.55	0.52
RMS Pressure, Pa	0.50	1.44	4.98	14.46	27.82	51.96	64.61
Peak Pressure, Pa	0.71	2.04	7.04	20.45	39.34	73.48	91.37

Table 4.4. Pancake absorber values of absorption coefficient dependence on incident amplitude. Configuration is $r_0 = 4$ mm, $d_p = 1$ mm, $d_c = 6$ mm, $R = 50$ mm and $L = 35$ mm.

Figure 4.41, shows absorption coefficient dependence on incident pressure measured in Pascals. Sample is pancake absorber with a constant pore opening diameter throughout the length of the structure. Pore radius $r_0 = 4$ mm, $d_p = 1$ mm and $d_c = 6$ mm. The measurements are performed using

sine wave excitation. The amplitude SPL gradually increases in approximately 10 dB intervals. Sample thickness is around 35 mm and external plate radius $R = 50$ mm Table 4.4 shows the measured values of absorption coefficient data obtained from direct measurements performed in a HSPL impedance tube. The RMS pressure and peak pressures are calculated (see section 4.2) with the latter being indicating the incident pressure amplitude, as seen in Figure 4.41. It can be determined by the data presented by Table 4.4 that the pancake absorber was slightly more effective at lower incident sound pressure amplitudes at frequency 223 Hz. It is demonstrated that it was slightly more effective at 214 Hz and 230 Hz, for increased incident sound pressures levels.

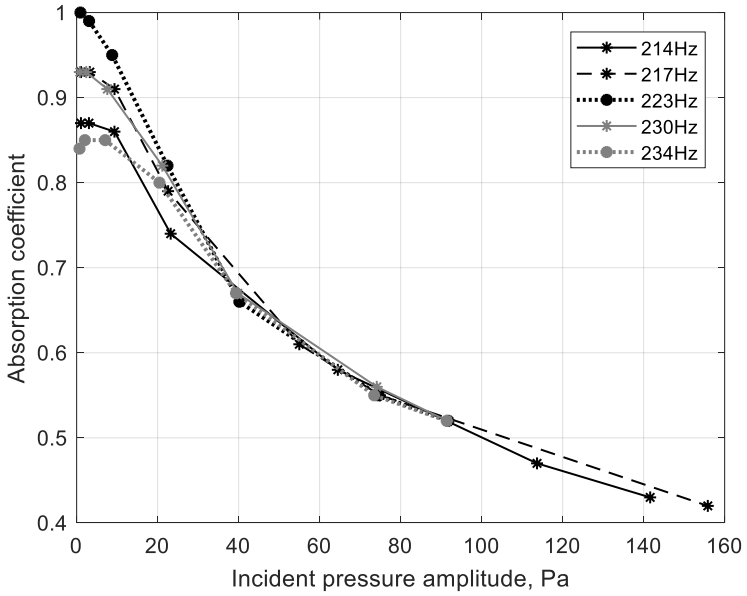

Figure 4.41. Absorption coefficient as a function of incident amplitude. Pancake configuration is $r_0 = 4$ mm, $d_p = 1$ mm, $d_c = 6$ mm, $R = 50$ mm, $N_{de} = 5$, and $L = 35$ mm.

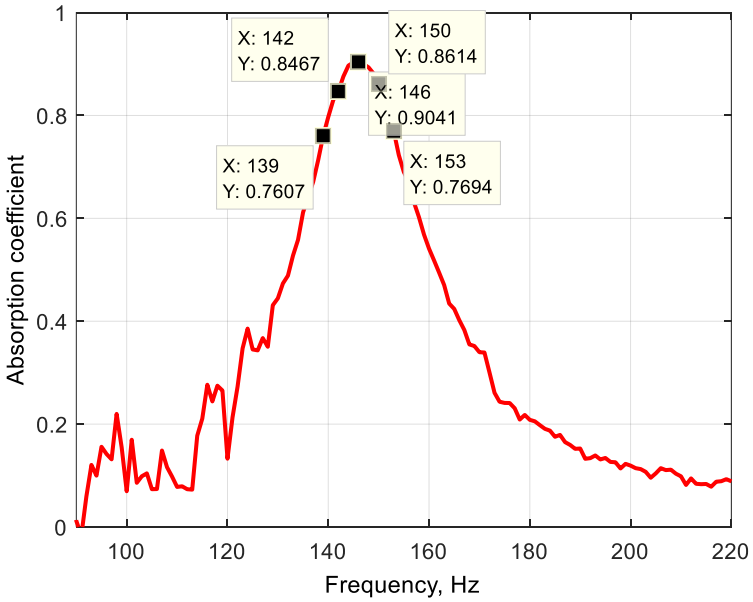

Figure 4.42. Absorption coefficient as a function of frequency. Pancake configuration is $r_0 = 4$ mm, $d_p = 1$ mm, $d_c = 1$ mm, $R = 50$ mm, $N_{de} = 30$, and $L = 62$ mm.

Figure 4.42 indicates the selected frequencies. The absorption curve is the first resonance frequency for Pancake configuration has pore radius $r_0 = 4$ mm, $d_p = 1$ mm and $d_c = 1$ mm. Sample length $L =$

62 mm. Sound excitation is white noise, and the selected frequencies are later tested with pure tones in a HSPL impedance tube, see Figure 4.43. The selected frequencies are those presented in Table 4.5.

Frequency (Hz)	139	139	139	139	139	139
Abs Coefficient	0.76	0.75	0.75	0.73	0.69	0.65
RMS Pressure, Pa	0.51	1.60	5.79	14.58	40.35	59.86
Peak Pressure, Pa	0.72	2.26	8.19	20.62	57.06	84.65

Frequency (Hz)	142	142	142	142	142	142
Abs Coefficient	0.85	0.85	0.82	0.78	0.71	0.67
RMS Pressure, Pa	0.53	1.67	6.14	14.87	45.90	60.33
Peak Pressure, Pa	0.75	2.36	8.68	21.03	64.91	85.32

Frequency (Hz)	146	146	146	146	146	146
Abs Coefficient	0.90	0.90	0.85	0.80	0.72	0.68
RMS Pressure, Pa	0.53	1.66	6.01	14.59	45.20	59.65
Peak Pressure, Pa	0.75	2.35	8.50	20.63	63.92	84.36

Frequency (Hz)	150	150	150	150	150	150
Abs Coefficient	0.86	0.86	0.80	0.77	0.69	0.66
RMS Pressure, Pa	0.49	1.54	6.45	14.03	44.06	58.65
Peak Pressure, Pa	0.69	2.18	9.12	19.84	62.31	82.94

Frequency (Hz)	153	153	153	153	153	153
Abs Coefficient	0.77	0.77	0.73	0.71	0.66	0.63
RMS Pressure, Pa	0.45	1.44	6.12	13.43	42.98	57.54
Peak Pressure, Pa	0.64	2.04	8.65	18.99	60.78	81.37

Table 4.5. Pancake absorber values of absorption coefficient dependence on incident amplitude. Configuration is $r_0 = 4$ mm, $d_p = 1$ mm, $d_c = 1$ mm, $R = 50$ mm and $L = 62$ mm.

Figure 4.43, shows absorption coefficient dependence on incident pressure measured in Pascals. Sample is pancake absorber with a constant pore opening diameter throughout the length of the structure. Pore radius $r_0 = 4$ mm, $d_p = 1$ mm and $d_c = 1$ mm. The measurements are performed using sine wave excitation. The amplitude SPL gradually increases in approximately 10 dB intervals. Sample length $L = 62$ mm and external plate radius $R = 50$ mm. Table 4.5 shows the measured values of absorption coefficient data obtained from direct measurements performed in a HSPL impedance tube. The RMS pressure and peak pressures are calculated (see section 4.2) with the latter indicating the incident pressure amplitude, as seen by Figure 4.43. It can be determined from the data presented by Table 4.5 that the pancake absorber was most effective at incident sound pressure amplitudes at frequency 146 Hz.

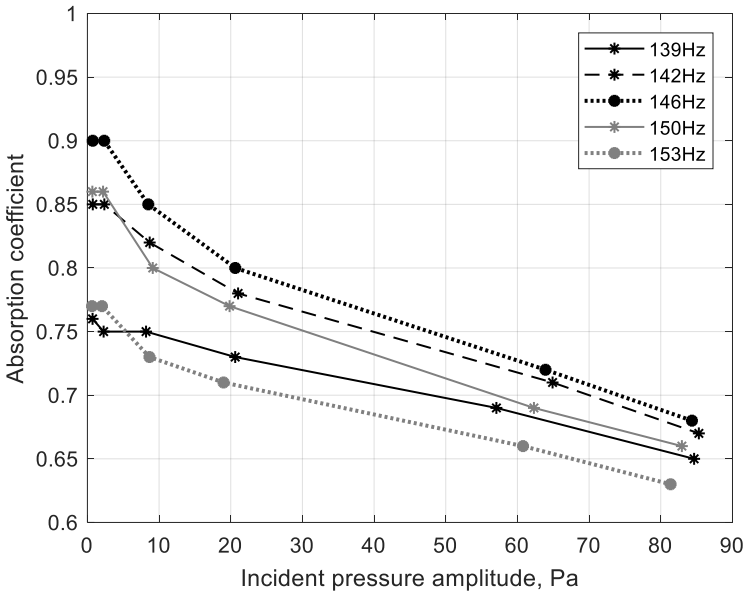

Figure 4.43. Absorption coefficient as a function of incident amplitude. Pancake configuration is $r_0 = 4$ mm, $d_p = 1$ mm, $d_c = 1$ mm, $R = 50$ mm, $N_{de} = 30$, and $L = 62$ mm.

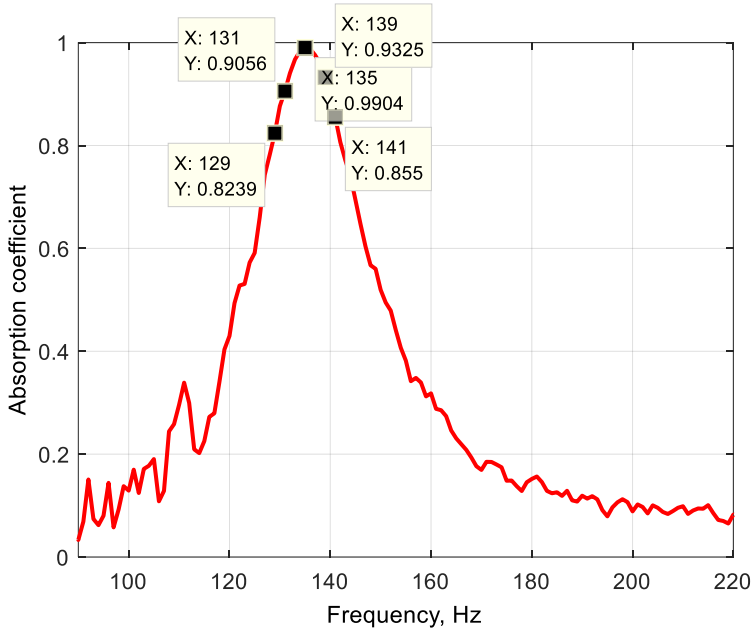

Figure 4.44. Absorption coefficient as a function of frequency. Pancake configuration is $r_0 = 4$ mm, $d_p = 1$ mm, $d_c = 3$ mm, $R = 50$ mm, $N_{de} = 15$, and $L = 62$ mm.

The absorption curve shown in Figure 4.44 is the first resonance frequency for Pancake configuration which has pore radius $r_0 = 4$ mm, $d_p = 1$ mm and $d_c = 3$ mm. Sample length $L = 60$ mm. Sound excitation is white noise, and the selected frequencies are later tested with pure tones in a HSPL impedance tube, see Figure 4.45. The selected frequencies are those presented in Table 4.6.

Frequency (Hz)	130	130	130	130	130	130
Abs Coefficient	0.87	0.87	0.82	0.77	0.74	0.70
RMS Pressure, Pa	0.57	1.71	4.91	13.94	30.96	47.48
Peak Pressure, Pa	0.81	2.42	6.94	19.71	43.78	67.15

Frequency (Hz)	132	132	132	132	132	132
Abs Coefficient	0.94	0.93	0.87	0.79	0.73	0.69
RMS Pressure, Pa	0.61	1.88	5.18	14.60	31.30	48.74
Peak Pressure, Pa	0.86	2.66	7.33	20.65	44.26	68.93

Frequency (Hz)	135	135	135	135	135	135
Abs Coefficient	0.99	0.97	0.91	0.78	0.70	0.66
RMS Pressure, Pa	0.63	1.89	5.15	14.41	30.81	48.23
Peak Pressure, Pa	0.89	2.62	7.28	20.38	43.57	68.21

Frequency (Hz)	139	139	139	139	139	139
Abs Coefficient	0.92	0.92	0.89	0.76	0.64	0.61
RMS Pressure, Pa	0.55	1.74	5.02	13.68	29.79	45.81
Peak Pressure, Pa	0.78	2.46	8.00	19.35	42.13	64.78

Frequency (Hz)	141	141	141	141	141	141
Abs Coefficient	0.86	0.86	0.86	0.74	0.63	0.59
RMS Pressure, Pa	0.51	1.89	5.07	13.78	29.41	45.87
Peak Pressure, Pa	0.72	2.67	7.17	19.49	41.59	64.87

Table 4.6. Pancake absorber values of absorption coefficient dependence on incident amplitude. Configuration is $r_0 = 4$ mm, $d_p = 1$ mm, $d_c = 3$ mm, $R = 50$ mm and $L = 62$ mm.

Figure 4.45 shows absorption coefficient dependence on incident pressure measured in Pascals. Sample is pancake absorber with a constant pore opening diameter throughout the length of the structure. Pore radius $r_0 = 4$ mm, $d_p = 1$ mm and $d_c = 3$ mm. The measurements are performed using sine wave excitation. The amplitude SPL gradually increases in approximately 10 dB intervals. Sample length is approximately $L = 60$ mm and external plate radius $R = 50$ mm. Table 4.6 shows the measured values of absorption coefficient data obtained from direct measurements performed in a HSPL impedance tube. The RMS pressure and peak pressures are calculated (see section 4.2) with the latter being indicating the incident pressure amplitude, as seen in Figure 4.45. It can be determined by the data presented by Table 4.6 that the pancake absorber was slightly more effective at lower incident sound pressure amplitudes at frequency 146 Hz. It is demonstrated that it was slightly more effective at 130 Hz and 132 Hz, for increased incident sound pressures levels.

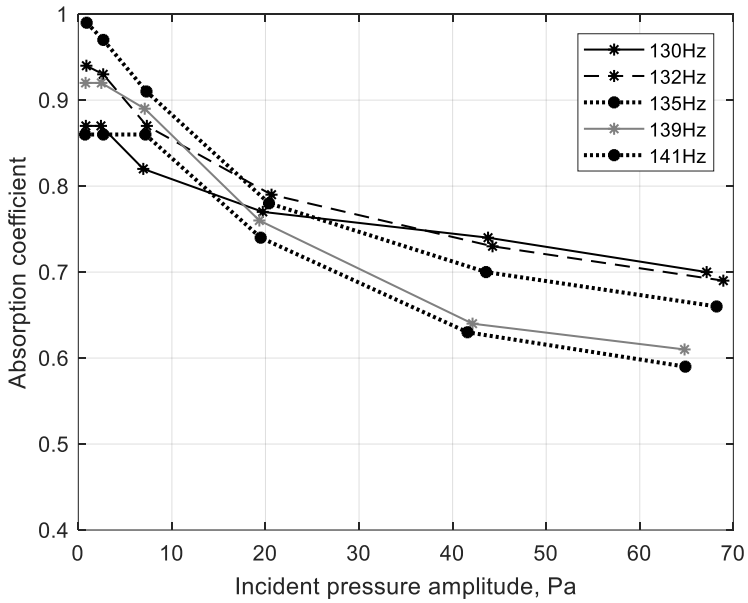

Figure 4.45. Absorption coefficient as a function of incident amplitude. Pancake configuration is $r_0 = 4$ mm, $d_p = 1$ mm, $d_c = 3$ mm, $R = 50$ mm, $N_{de} = 15$, and $L = 62$ mm.

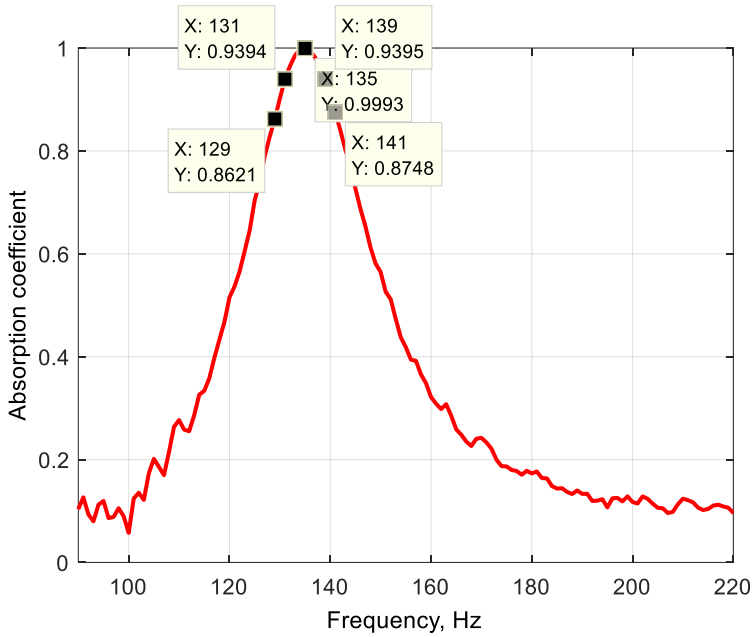

Figure 4.46. Absorption coefficient as a function of frequency. Pancake configuration is $r_0 = 4$ mm, $d_p = 1$ mm, $d_c = 6$ mm, $R = 50$ mm, $N_{de} = 9$, and $L = 63$ mm.

Absorption curve shown in Figure 4.46 is the first resonance frequency for Pancake configuration which has pore radius $r_0 = 4$ mm, $d_p = 1$ mm and $d_c = 6$ mm. Sample length $L = 63$ mm. Sound excitation is white noise, and the selected frequencies are later tested with pure tones in a HSPL impedance tube, see Figure 4.47. The selected frequencies are those presented in Table 4.7.

Frequency (Hz)	129	129	129	129	129
Abs Coefficient	0.87	0.87	0.84	0.68	0.55
RMS Pressure, Pa	0.64	1.91	6.46	14.10	40.69
Peak Pressure, Pa	0.90	2.70	9.14	19.94	57.54

Frequency (Hz)	131	131	131	131	131
Abs Coefficient	0.94	0.93	0.88	0.70	0.54
RMS Pressure, Pa	0.67	1.95	6.55	14.00	41.59
Peak Pressure, Pa	0.95	2.76	9.26	19.80	58.82

Frequency (Hz)	135	135	135	135	135
Abs Coefficient	1.00	0.98	0.92	0.74	0.55
RMS Pressure, Pa	0.64	1.93	5.84	14.46	41.94
Peak Pressure, Pa	0.90	2.73	8.26	20.45	59.31

Frequency (Hz)	139	139	139	139	139
Abs Coefficient	0.94	0.94	0.91	0.75	0.55
RMS Pressure, Pa	0.53	1.67	5.54	14.35	41.61
Peak Pressure, Pa	0.75	2.36	7.83	20.29	58.84

Frequency (Hz)	141	141	141	141	141
Abs Coefficient	0.87	0.88	0.88	0.75	0.55
RMS Pressure, Pa	0.51	1.60	5.35	14.15	41.56
Peak Pressure, Pa	0.72	2.26	7.57	20.01	58.77

Table 4.7. Pancake absorber values of absorption coefficient dependence on incident amplitude. Configuration is $r_0 = 4$ mm, $d_p = 1$ mm, $d_c = 6$ mm, $R = 50$ mm and $L = 63$ mm.

Figure 4.47 shows absorption coefficient dependence on incident pressure measured in Pascals. Sample is pancake absorber with a constant pore opening diameter throughout the length of the structure. Pore radius $r_0 = 4$ mm, $d_p = 1$ mm and $d_c = 6$ mm. The measurements are performed using sine wave excitation. The amplitude SPL gradually increases in approximately 10 dB intervals. Sample

length $L = 63$ mm and external plate radius $R = 50$ mm. Table 4.7 shows the measured values of absorption coefficient data obtained from direct measurements performed in a HSPL impedance tube. The RMS pressure and peak pressures are calculated (see section 4.2) with the latter being indicating the incident pressure amplitude, as seen in Figure 4.47. It can be determined by the data presented by Table 4.7 that the pancake absorber was slightly more effective at lower incident sound pressure amplitudes at frequency 135 Hz. It is demonstrated that it was slightly more effective at 135 Hz and 139 Hz, for increased incident sound pressures levels.

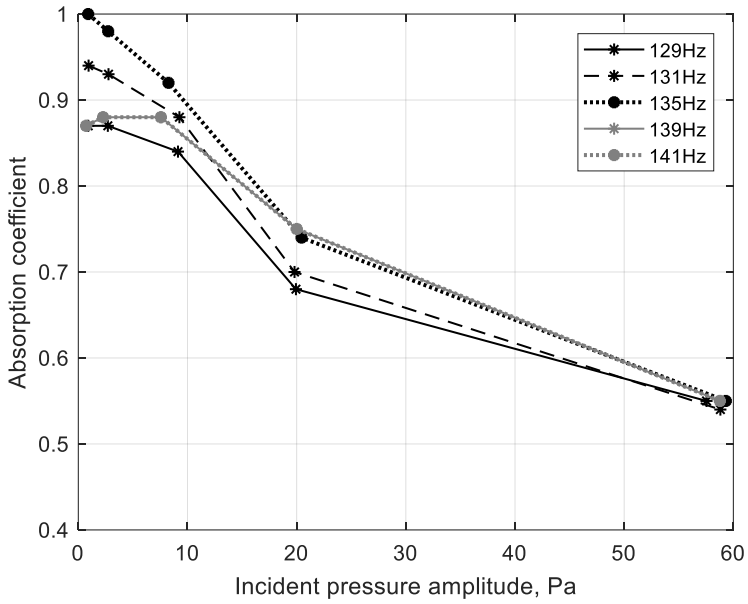

Figure 4.47. Absorption coefficient as a function of incident amplitude. Pancake configuration is $r_0 = 4$ mm, $d_p = 1$ mm, $d_c = 6$ mm, $R = 50$ mm, $N_{de} = 9$, and $L = 63$ mm.

It is shown that the performance of the pancake absorbers (Figures 4.36 – 4.47) is affected by the strength of the incident amplitude. At sufficiently low sound levels or when sound pressure is considered small enough to be regarded in the linear regime, the pancake absorber performance is steady or unaffected. When the incident sound pressure level is increased above 110 dB, it affects the absorber performance, and peak absorption coefficient values are reduced independent of the frequencies tested. This can also be observed in the absorption coefficient dependence on incident pressure amplitude (shown by Figures 4.36 – 4.47) for the different configured pancake absorbers. A reduction in the absorptive peaks is observed to be quite abrupt as incident sound pressure level grows. The performance of the pancake absorber depends on not just the capabilities of the inner structure, but also on the outer structure. For instance, when sound pressure amplitude is considered low (linear regime) the energy of the incident wave is more easily transferred beyond the boundary of the front plate with pore radius r_0. Peak absorption coefficient values are therefore affected when sound pressure amplitude is high (nonlinear regime). This is because at the boundary of the first plate, the main pore opening with radius r_0 is not sufficiently large enough to allow the same net flow of energy to pass the air/solid interface. Consequently, the performance of the absorber is affected at higher amplitudes, such as the case when nonlinear phenomenon occurs. If the incident wave is considered strong enough then larger reflections will also occur at the solid plate boundary of the first plate. This is directly related to the flow resistivity of plates which contain pores with radius r_0. First resonance of the pancake absorbers is

therefore not severely affected as amplitude strength grows. This can be assumed since the inner structure of the absorbers remains constant, unchanged and are rigid. Put simply, the same resonant frequencies of the acoustic waves remain the same or vary only slightly for both linear and weakly nonlinear regime but result in a variation of the absorptive peaks at those frequencies. This is due to the variation in magnitude of the waves allowed to enter the inner structure of the sample itself and results in the absorption at the same (or close to) frequencies, and independent of amplitude strength. It is also one of the realizations for the optimization of the absorber for future works.

4.4.2. Metallic Profile Absorbers – HSPL

Sine wave excitation is performed for both linear and exponential profile absorbers comprised of various configurations. Different strengths of incident pressure are targeted at the profiles to investigate the dependence of absorption with incident pressure. The incident pressure is obtained and presented in the Tables below (see Tables 4.8 – 4.12) shown calculated as RMS pressure and peak pressure. Frequencies investigated are selected by low sound pressure levels, firstly obtained by white noise excitation. Several frequencies for each of the profile structures have approximate sample lengths $L =$ 60 mm, $L = 80$ mm and $L = 100$ mm, shown by Figures 4.48 – 4.57. Absorption coefficient vs incident pressure plots are included, and data shown in the Tables below. Five frequencies for each of the configurations (linear and exponential profiles with cavity thickness variations) are shown in both the plots (data points), and Tables (values). The absorption coefficient values are directly taken from the data by each single measurement. The data is given for each of the frequencies selected. Samples with $L = 60$ mm is presented first, followed by samples with $L = 80$ mm and $L = 100$ mm.

Figures 4.48 – 4.53 show the linear profile followed by Figures 4.54 – 4.57 which show the exponential profile. In the former (Figures 4.48 – 4.53) the data is presented firstly when main pore opening $r_0 = 15$ mm, $d_p = 1$ mm, $d_c = 3$mm and sample length is $L = 60$ mm (given by Figures 4.48 – 4.49). It is then shown afterwards a profile with an increased main pore radius (see Figures 4.50 – 4.51) so that the main pore opening becomes $r_0 = 25$ mm, $d_p = 1$ mm, $d_c = 2$ mm and sample length is $L = 80$ mm. The last linear profile configuration is when $d_c = 3$ mm instead of $d_c = 2$ mm, furthermore, main pore opening remains the same so $r_0 = 25$ mm, $d_p = 1$ mm, and sample length becomes $L = 100$ mm. Exponential profile absorbers are built and later presented in Figures 4.54 – 4.57. It is shown first when, $d_p = 1$ mm, $d_c = 2$ mm and sample length $L = 80$ mm (Figures 4.54 – 4.55). This is followed by an exponential profile when $d_p = 1$ mm, $d_c = 3$ mm and $L = 100$ mm. The main pore opening remains the same size, where $r_0 = 25$ mm for both cases, for when the exponential profile consists $d_c = 2$ mm and $d_c = 3$ mm.

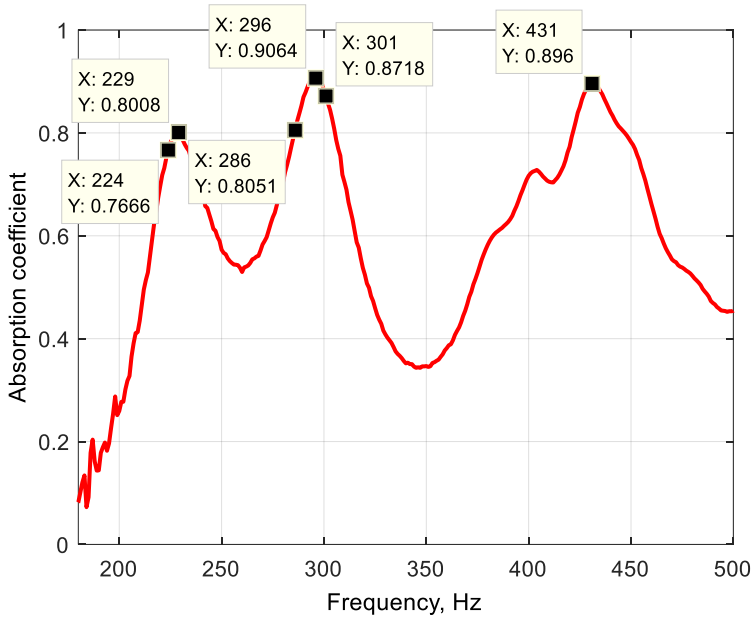

Figure 4.48. Absorption coefficient as a function of frequency for linear profile. Front pore is $r_0 = 15$ mm, $d_p = 1$ mm, $d_c = 3$ mm, $L = 60$ mm and $R = 50$ mm.

Figure 4.48 shows absorption coefficient dependence on frequency and furthermore, indicates the selected frequencies. The absorption curve is the resonance frequency for a profile absorber with linear configuration which has a front pore radius $r_0 = 15$ mm, $d_p = 1$ mm and $d_c = 3$ mm. Sample length $L = 60$ mm. Sound excitation is white noise, and the selected frequencies are later tested with pure tones in a HSPL impedance tube, see Figure 4.49. The selected frequencies are shown in Table 4.8.

Frequency (Hz)	224	224	224	224	224	224	224	224
Abs Coefficient	0.77	0.77	0.71	0.60	0.47	0.40	0.39	0.36
RMS Pressure, Pa	0.07	0.15	0.61	1.82	4.61	14.81	36.98	112.02
Peak Pressure, Pa	0.10	0.21	0.86	2.57	6.52	20.94	52.30	158.42

Frequency (Hz)	229	229	229	229	229	229	229	229
Abs Coefficient	0.80	0.79	0.76	0.68	0.53	0.44	0.42	0.40
RMS Pressure, Pa	0.07	0.15	0.56	1.70	4.83	15.76	40.23	111.83
Peak Pressure, Pa	0.10	0.21	0.79	2.40	6.83	22.29	56.89	158.15

Frequency (Hz)	282	282	282	282	282	282	282	282
Abs Coefficient	0.77	0.76	0.81	0.80	0.84	0.81	0.70	0.65
RMS Pressure, Pa	0.05	0.15	0.64	1.61	4.98	16.96	61.18	130.54
Peak Pressure, Pa	0.07	0.21	0.90	2.28	7.04	23.98	86.52	184.61

Frequency (Hz)	296	296	296	296	296	296	296	296
Abs Coefficient	0.90	0.88	0.87	0.81	0.73	0.79	0.72	0.69
RMS Pressure, Pa	0.06	0.20	0.66	1.40	4.38	18.80	49.86	128.39
Peak Pressure, Pa	0.08	0.28	0.93	1.98	6.19	26.59	70.51	181.57

Frequency (Hz)	301	301	301	301	301	301	301	301
Abs Coefficient	0.85	0.82	0.78	0.75	0.69	0.78	0.72	0.69
RMS Pressure, Pa	0.06	0.16	0.63	1.45	5.30	16.91	45.86	131.88
Peak Pressure, Pa	0.08	0.23	0.89	2.05	7.49	23.91	64.86	186.51

Frequency (Hz)	431	431	431	431	431	431	431	431
Abs Coefficient	0.90	0.90	0.89	0.87	0.85	0.79	0.71	0.67
RMS Pressure, Pa	0.09	1.15	0.61	1.76	4.27	14.95	50.27	128.96
Peak Pressure, Pa	0.13	1.63	0.86	2.49	6.04	21.14	71.09	182.38

Table 4.8. Linear profile values of absorption coefficient dependence on incident amplitude. Configuration is $r_0 = 15$ mm, $d_p = 1$ mm, $d_c = 3$ mm, $L = 60$ mm and $R = 50$ mm.

Figure 4.49, shows absorption coefficient dependence on incident pressure measured in Pascals. Sample is profile absorber with linear configuration and front pore radius $r_0 = 15$ mm. The diameter of the central pore decreases 2 mm per plate. Each plate consists $d_p = 1$ mm and backed by $d_c = 3$ mm. Measurements are performed using sine wave excitation. The amplitude SPL gradually increases in approximately 5 dB – 10 dB intervals. Sample length $L = 60$ mm and the external plate radius is $R = 50$ mm. Table 4.8 shows the measured values of absorption coefficient data obtained from direct measurements performed in a HSPL impedance tube. The RMS and peak pressures are calculated (see section 4.2) with the latter indicating the incident pressure amplitude, as seen in Figure 4.49. It can be determined by the data presented by Table 4.8 that the profile was more effective at lower incident sound pressure amplitudes at frequencies 229 Hz, 296 Hz, and 431 Hz. It is demonstrated that it was more effective at 282 Hz, 296 Hz, 301 Hz and 431 Hz for increased incident sound pressure levels, which can be observed by Figure 4.49.

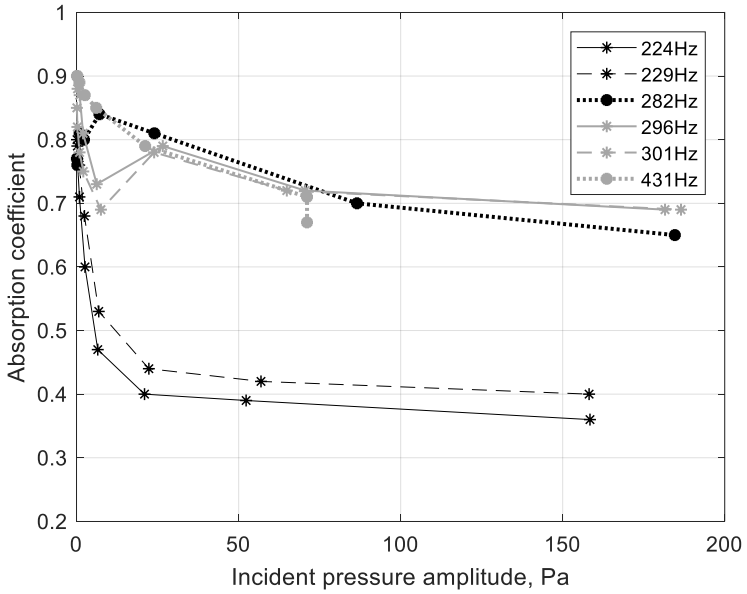

Figure 4.49. Absorption coefficient as a function of incident amplitude for linear profile. Front pore is $r_0 = 15$ mm, $d_p = 1$ mm, $d_c = 3$ mm, $L = 60$ mm and $R = 50$ mm.

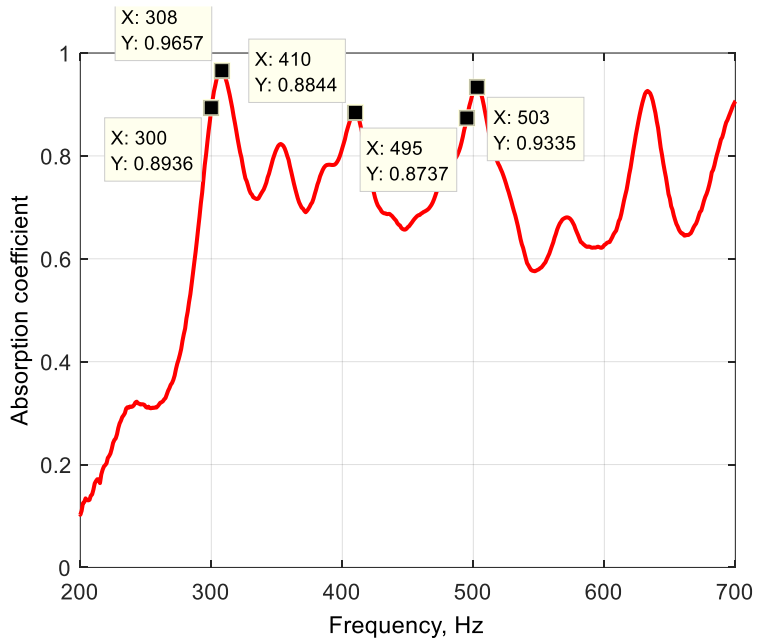

Figure 4.50. Absorption coefficient as a function of frequency for linear profile. Front pore is $r_0 = 25$ mm, $d_p = 1$ mm, $d_c = 2$ mm, $L = 80$ mm and $R = 50$ mm.

Absorption curve shown in Figure 4.50 shows absorption coefficient and selected frequencies for linear profile configuration which has front pore radius $r_0 = 25$ mm, $d_p = 1$ mm and $d_c = 2$ mm. Sample length $L = 80$ mm. Sound excitation is white noise, and the selected frequencies are later tested with pure tones in a HSPL impedance tube, see Figure 4.51. The selected frequencies are those presented in Table 4.9.

Frequency (Hz)	300	300	300	300	300	300	300	300
Abs Coefficient	0.88	0.89	0.88	0.87	0.79	0.69	0.63	0.55
RMS Pressure, Pa	0.08	0.24	0.76	2.23	6.20	18.35	50.89	138.88
Peak Pressure, Pa	0.11	0.34	1.07	3.15	8.77	25.95	71.97	196.41

Frequency (Hz)	308	308	308	308	308	308	308	308
Abs Coefficient	0.97	0.97	0.96	0.94	0.86	0.75	0.68	0.60
RMS Pressure, Pa	0.07	0.29	0.69	2.27	6.40	19.95	55.10	146.92
Peak Pressure, Pa	0.10	0.41	0.98	3.21	9.05	28.21	77.92	207.78

Frequency (Hz)	410	410	410	410	410	410	410	410
Abs Coefficient	0.88	0.88	0.88	0.87	0.84	0.82	0.83	0.84
RMS Pressure, Pa	0.07	0.20	0.57	1.94	5.72	15.79	55.88	155.65
Peak Pressure, Pa	0.10	0.28	0.81	2.74	8.09	22.33	79.03	220.12

Frequency (Hz)	495	495	495	495	495	495	495	495
Abs Coefficient	0.90	0.91	0.92	0.93	0.93	0.89	0.82	0.77
RMS Pressure, Pa	0.08	0.25	0.68	1.91	6.24	17.09	53.19	154.48
Peak Pressure, Pa	0.11	0.35	0.96	2.70	8.82	24.17	75.22	218.47

Frequency (Hz)	503	503	503	503	503	503	503	503
Abs Coefficient	0.94	0.94	0.94	0.93	0.89	0.83	0.80	0.77
RMS Pressure, Pa	0.09	0.26	0.66	2.04	6.39	16.79	53.03	155.67
Peak Pressure, Pa	0.13	0.37	0.93	2.88	9.04	23.74	75.00	220.15

Table 4.9. Linear profile values of absorption coefficient dependence on incident amplitude. Configuration is $r_0 = 25$ mm, $d_p = 1$ mm, $d_c = 2$ mm, $L = 80$ mm and $R = 50$ mm.

Figure 4.51, shows absorption coefficient dependence on incident pressure measured in Pascals. Sample is profile absorber with linear configuration with a main front pore opening diameter of 50 mm. The diameter of the central pore decreases 2 mm per plate. Each plate consists $d_p = 1$ mm and $d_c =$

2 mm. Measurements are performed using sine wave excitation. The amplitude SPL gradually increases in approximately 5 dB – 10 dB intervals. Sample length $L = 80$ mm and external plate radius is $R = 50$ mm. Table 4.9 shows the measured values of absorption coefficient data obtained from direct measurements performed in a HSPL impedance tube. The RMS pressure and peak pressures are calculated (see section 4.2) with the latter indicating the incident pressure amplitude, as seen in Figure 4.51. It can be determined by the data presented by Table 4.9 that the profile absorber was slightly more effective at lower incident sound pressure amplitudes at frequencies 308 Hz, 410 Hz, and 503 Hz. It is demonstrated that it was more effective at 410 Hz, 495 Hz and 503 Hz, for increased incident sound pressures levels, which can be observed by Figure 4.51.

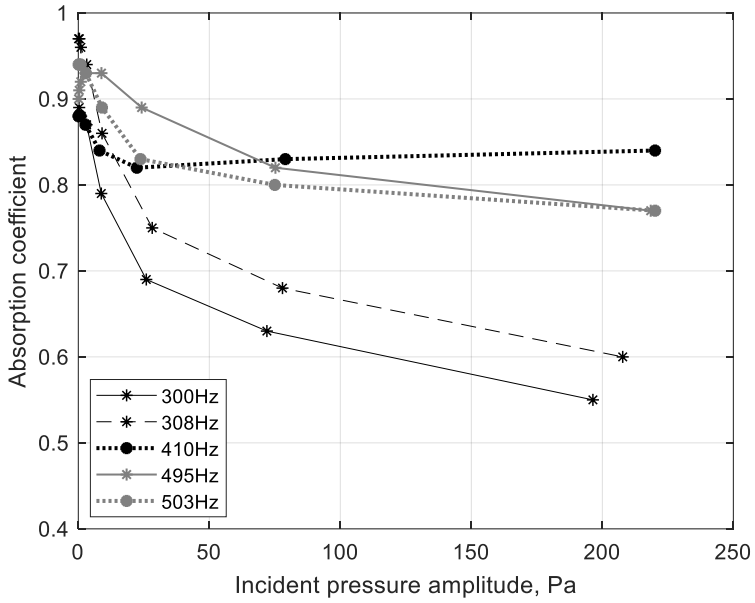

Figure 4.51. Absorption coefficient as a function of incident amplitude for linear profile. Front pore is $r_0 = 25$ mm, $d_p = 1$ mm, $d_c = 2$ mm, $L = 80$ mm and $R = 50$ mm.

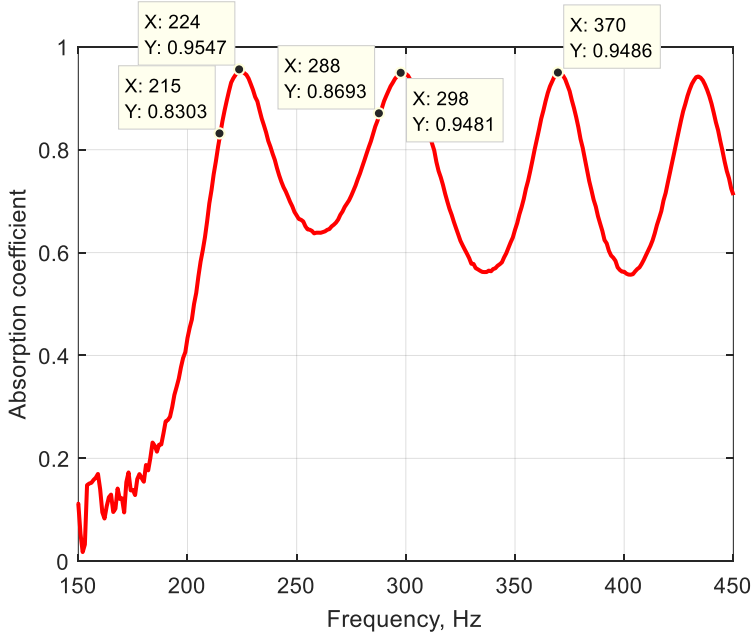

Figure 4.52. Absorption coefficient as a function of frequency for linear profile. Front pore is $r_0 = 25$ mm, $d_p = 1$ mm, $d_c = 3$ mm, $L = 100$ mm and $R = 50$ mm.

Figure 4.52 shows absorption coefficient dependence on frequency and indicates the selected frequencies. The absorption curve is the resonance frequency for a profile absorber with linear configuration which has front pore radius $r_0 = 25$ mm, $d_p = 1$ mm and $d_c = 3$ mm. Sample length $L =$ 100 mm. Sound excitation is white noise, and the selected frequencies are later tested with pure tones in a HSPL impedance tube, see Figure 4.53. The selected frequencies are those presented in Table 4.10.

Frequency (Hz)	215	215	215	215	215	215	215	215
Abs Coefficient	0.81	0.80	0.77	0.66	0.59	0.55	0.53	0.53
RMS Pressure, Pa	0.06	0.22	0.63	2.05	5.64	15.25	47.36	132.19
Peak Pressure, Pa	0.08	0.31	0.89	2.90	7.98	21.57	66.98	186.94

Frequency (Hz)	224	224	224	224	224	224	224	224
Abs Coefficient	0.94	0.94	0.90	0.80	0.69	0.61	0.60	0.58
RMS Pressure, Pa	0.06	0.21	0.67	2.11	5.88	17.85	51.68	139.39
Peak Pressure, Pa	0.08	0.30	0.95	2.98	8.32	25.24	73.09	197.13

Frequency (Hz)	288	288	288	288	288	288	288	288
Abs Coefficient	0.80	0.81	0.84	0.88	0.94	0.89	0.84	0.80
RMS Pressure, Pa	0.07	0.22	0.72	2.18	6.58	21.74	63.13	198.37
Peak Pressure, Pa	0.09	0.31	1.02	3.08	9.30	30.74	89.28	280.54

Frequency (Hz)	298	298	298	298	298	298	298	298
Abs Coefficient	0.89	0.90	0.91	0.93	0.96	0.93	0.88	0.85
RMS Pressure, Pa	0.08	0.26	0.71	2.07	6.40	23.29	70.27	200.72
Peak Pressure, Pa	0.11	0.37	1.00	2.93	9.05	32.94	99.38	283.86

Frequency (Hz)	370	370	370	370	370	370	370	370
Abs Coefficient	0.96	0.97	0.97	0.96	0.90	0.84	0.91	0.89
RMS Pressure, Pa	0.07	0.18	0.62	2.05	5.84	16.58	54.32	189.00
Peak Pressure, Pa	0.10	0.25	0.88	2.90	8.26	23.45	76.82	267.29

Table 4.10. Linear profile values of absorption coefficient dependence on incident amplitude. Configuration is $r_0 =$ 25 mm, $d_p = 1$ mm, $d_c = 3$ mm, $L = 100$ mm and $R = 50$ mm.

Figure 4.53, shows absorption coefficient dependence on incident pressure measured in Pascals. Sample is profile absorber with linear configuration with a front pore opening radius $r_0 = 25$ mm. The diameter of the central pore decreases 2 mm per plate. Each plate consists $d_p = 1$ mm and $d_c = 3$ mm. The measurements are performed using sine wave excitation. The amplitude SPL gradually increases in approximately 5 dB – 10 dB intervals. Sample length $L = 100$ mm and external plate radius is $R = 50$ mm. Table 4.10 shows the measured values of absorption coefficient data obtained from direct measurements performed in a HSPL impedance tube. The RMS pressure and peak pressures are calculated (see section 4.2) with the latter indicating the incident pressure amplitude, as seen in Figure 4.53. It can be determined by the data presented by Table 4.10 that the profile absorber was slightly more effective at lower incident sound pressure amplitudes at frequencies 224 Hz, 298 Hz, and 370 Hz. It is demonstrated that it was more effective at 288 Hz, 298 Hz and 370 Hz, for increased sound pressures levels, see Figure 4.53.

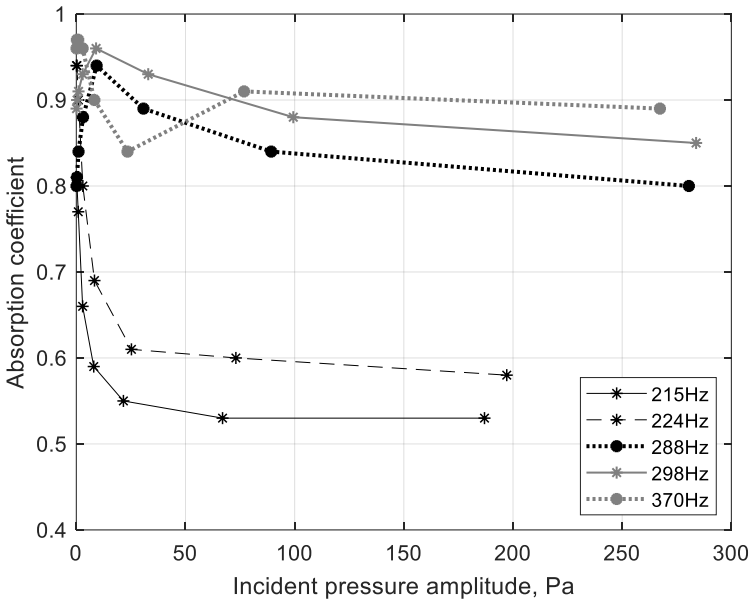

Figure 4.53. Absorption coefficient as a function of incident amplitude for linear profile. Front pore is $r_0 = 25$ mm, $d_p = 1$ mm, $d_c = 3$ mm, $L = 100$ mm and $R = 50$ mm.

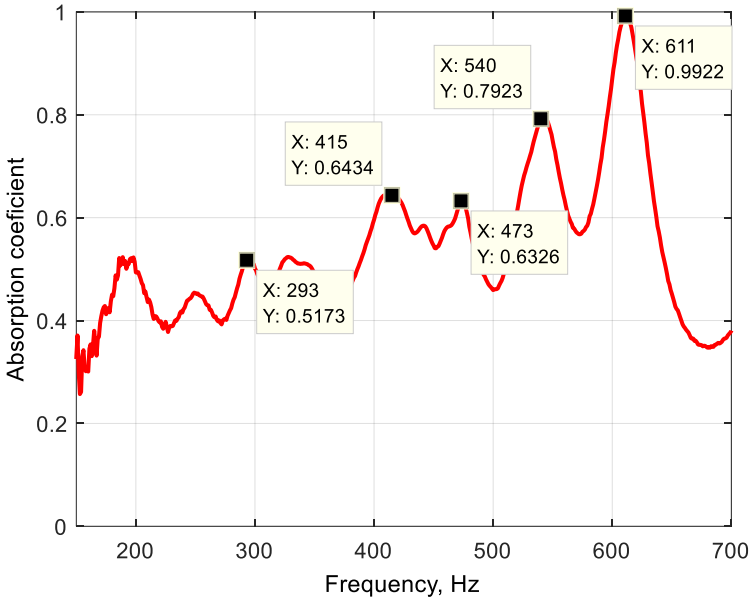

Figure 4.54. Absorption coefficient as a function of frequency for exponential profile. Front pore is $r_0 = 25$ mm, $d_p = 1$ mm, $d_c = 2$ mm, $L = 80$ mm and $R = 50$ mm.

Figure 4.54 shows the selected frequencies of the absorption curve for profile with exponential configuration. Front pore radius $r_0 = 25$ mm, $d_p = 1$ mm and $d_c = 2$ mm, sample length $L = 80$ mm. Sound excitation is white noise, and the selected frequencies are later tested with pure tones in a HSPL impedance tube, see Figure 4.55. The selected frequencies are those presented in Table 4.11.

Frequency (Hz)	293	293	293	293	293	293	293	293
Abs Coefficient	0.49	0.49	0.49	0.49	0.48	0.50	0.50	0.49
RMS Pressure, Pa	0.06	0.16	0.46	1.45	5.46	13.82	42.41	114.88
Peak Pressure, Pa	0.08	0.23	0.65	2.05	7.72	19.54	59.98	162.46

Frequency (Hz)	415	415	415	415	415	415	415	*
Abs Coefficient	0.59	0.59	0.59	0.59	0.59	0.59	0.58	*
RMS Pressure, Pa	0.06	0.16	0.64	1.71	4.89	16.02	128.32	*
Peak Pressure, Pa	0.08	0.23	0.90	2.42	6.92	22.66	181.47	*

Frequency (Hz)	473	473	473	473	473	473	473	473
Abs Coefficient	0.55	0.55	0.56	0.56	0.57	0.57	0.56	0.58
RMS Pressure, Pa	0.07	0.21	0.52	1.76	5.78	16.31	51.40	122.47
Peak Pressure, Pa	0.10	0.30	0.74	2.49	8.17	23.07	72.69	173.20

Frequency (Hz)	540	540	540	540	540	540	540	540
Abs Coefficient	0.81	0.81	0.81	0.77	0.73	0.65	0.57	0.65
RMS Pressure, Pa	0.09	0.20	0.53	1.79	6.20	17.67	48.87	143.40
Peak Pressure, Pa	0.13	0.28	0.75	2.53	8.77	24.99	69.11	202.80

Frequency (Hz)	611	611	611	611	611	611	611	611
Abs Coefficient	0.99	0.99	0.99	0.98	0.96	0.92	0.84	0.75
RMS Pressure, Pa	0.09	0.24	0.58	2.11	5.91	16.37	51.91	145.61
Peak Pressure, Pa	0.13	0.34	0.82	2.98	8.36	23.15	73.41	205.92

Table 4.11. Exponential profile values of absorption coefficient dependence on incident amplitude. Configuration is $r_0 = 25$ mm, $d_p = 1$ mm, $d_c = 2$ mm, $L = 80$ mm and $R = 50$ mm.

Figure 4.55, shows absorption coefficient dependence on incident pressure measured in Pascals. Sample is profile absorber with exponential configuration with a front pore opening radius $r_0 = 25$ mm. Dimensions of each central pore can be seen in Table 4.1. Each plate consists $d_p = 1$ mm and $d_c = 2$ mm. The measurements are performed using sine wave excitation. The amplitude SPL gradually increases in approximately 5 dB – 10 dB intervals. Sample length $L = 80$ mm and external plate radius is $R = 50$ mm. Table 4.11 shows the measured values of absorption coefficient data obtained from direct measurements performed in a HSPL impedance tube. The RMS pressure and peak pressures are calculated (see section 4.2) with the latter indicating the incident pressure amplitude, as seen in Figure 4.55. It can be determined by the data presented by Table 4.11 that the profile absorber was slightly more effective at lower incident sound pressure amplitudes at frequencies 293 Hz, 415 Hz, 540 Hz, and 611 Hz. It is demonstrated that it was more effective at 540 Hz, and 611 Hz, for increased incident sound pressures levels and seen by Figure 4.55.

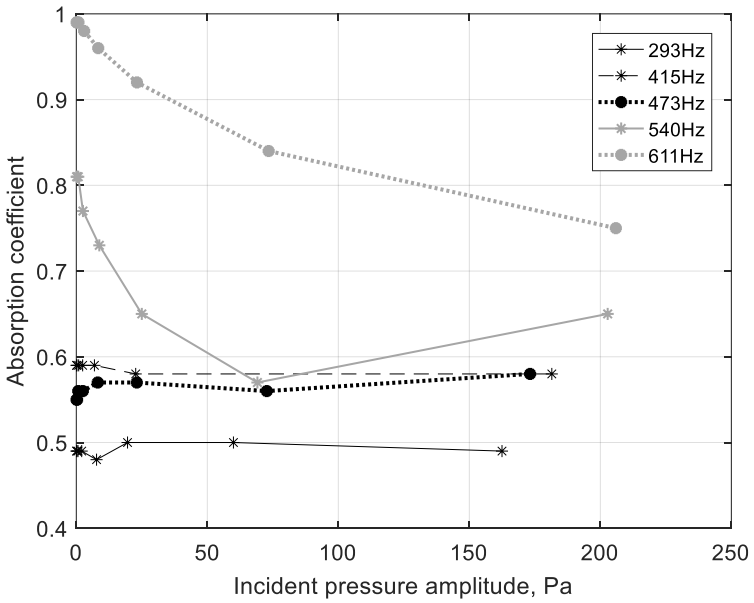

Figure 4.55. Absorption coefficient as a function of incident amplitude for exponential profile. Front pore is $r_0 = 25$ mm, $d_p = 1$ mm, $d_c = 2$ mm, $L = 80$ mm and $R = 50$ mm.

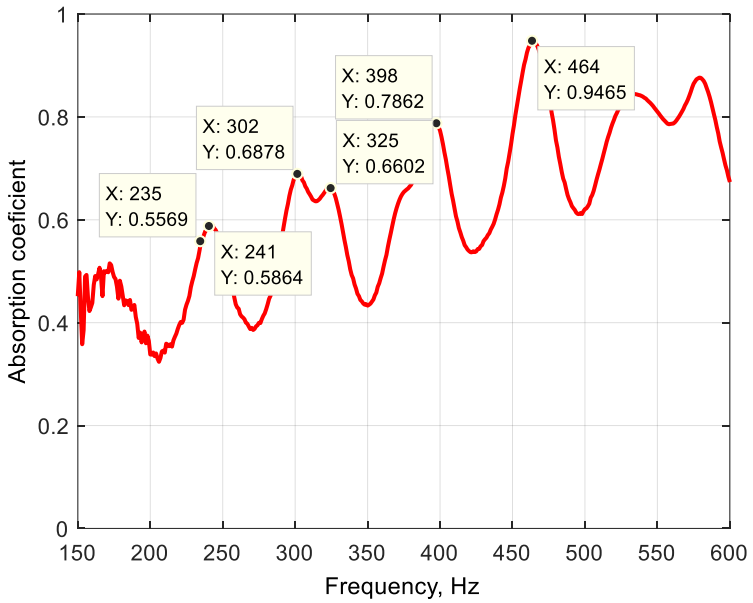

Figure 4.56. Absorption coefficient as a function of frequency for exponential profile. Front pore is $r_0 = 25$ mm, $d_p = 1$ mm, $d_c = 3$ mm, $L = 100$ mm and $R = 50$ mm.

Figure 4.56 shows selected frequencies for the profile with exponential configuration where front pore radius is $r_0 = 25$ mm, $d_p = 1$ mm and $d_c = 3$ mm. Sample length $L = 100$ mm. Sound excitation is white noise, and the selected frequencies are later tested with pure tones in a HSPL impedance tube, see Figure 4.57. Frequencies are those presented in Table 4.12.

Frequency (Hz)	235	235	235	235	235	235	235	235
Abs Coefficient	0.55	0.54	0.52	0.46	0.40	0.50	0.52	0.50
RMS Pressure, Pa	0.07	0.16	0.49	1.33	4.00	13.51	41.79	104.85
Peak Pressure, Pa	0.10	0.23	0.69	1.88	5.66	19.11	59.10	148.28

Frequency (Hz)	241	241	241	241	241	241	241	241
Abs Coefficient	0.58	0.58	0.54	0.48	0.41	0.50	0.52	0.50
RMS Pressure, Pa	0.07	0.14	0.54	1.29	4.46	14.33	38.64	107.85
Peak Pressure, Pa	0.10	0.20	0.76	1.82	6.31	20.27	51.82	152.52

Frequency (Hz)	302	302	302	302	302	302	302	302
Abs Coefficient	0.69	0.68	0.66	0.62	0.58	0.53	0.59	0.57
RMS Pressure, Pa	0.07	0.22	0.50	1.64	4.69	14.24	41.56	141.77
Peak Pressure, Pa	0.10	0.31	0.71	2.32	6.63	20.14	58.77	200.49

Frequency (Hz)	325	325	325	325	325	325	325	325
Abs Coefficient	0.66	0.66	0.66	0.63	0.60	0.57	0.60	0.59
RMS Pressure, Pa	0.08	0.15	0.57	1.61	4.44	15.11	53.65	182.53
Peak Pressure, Pa	0.11	0.21	0.81	2.28	6.28	21.37	75.87	253.14

Frequency (Hz)	398	398	398	398	398	398	398	398
Abs Coefficient	0.79	0.77	0.77	0.72	0.67	0.63	0.65	0.71
RMS Pressure, Pa	0.07	0.18	0.51	1.75	5.30	19.56	52.82	137.69
Peak Pressure, Pa	0.10	0.25	0.72	2.47	7.49	27.66	74.70	194.72

Table 4.12. Exponential profile values of absorption coefficient dependence on incident amplitude. Configuration is $r_0 = 25$ mm, $d_p = 1$ mm, $d_c = 3$ mm, $L = 100$ mm and $R = 50$ mm.

Figure 4.57, shows absorption coefficient dependence on incident pressure measured in Pascals. Sample is profile absorber with exponential configuration with a front pore opening radius $r_0 = 25$ mm. Dimensions of each central pore can be seen in Table 4.1. Each plate consists $d_p = 1$ mm and $d_c = 3$ mm. The measurements are performed using sine wave excitation. The amplitude SPL gradually

increases in approximately 5 dB – 10 dB intervals. Sample length $L = 100$ mm and external plate radius is $R = 50$ mm. Table 4.12 shows the measured values of absorption coefficient data obtained from direct measurements performed in a HSPL impedance tube. The RMS pressure and peak pressures are calculated (see section 4.2) with the latter indicating the incident pressure amplitude, as seen in Figure 4.57. It can be determined by the data presented by Table 4.12 that the profile absorber was slightly more effective at lower incident sound pressure amplitudes at frequencies 241 Hz, 302 Hz, and 398 Hz. The absorber is also effective at higher frequencies as seen by Figure 4.56, and cab be seen at 464 Hz for low amplitudes, an absorption coefficient value 0.94 with white noise excitation. It is demonstrated that it was more effective at 325 Hz, and 398 Hz, for increased incident sound pressures levels observed by Figure 4.57.

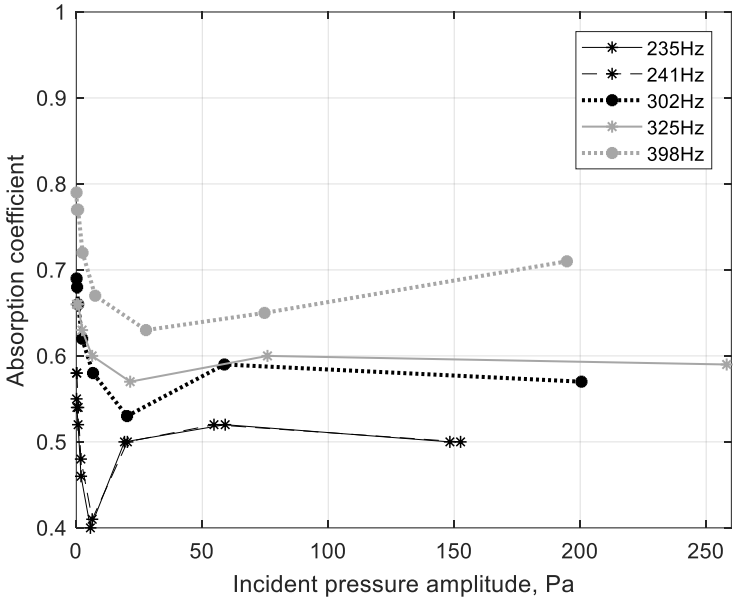

Figure 4.57. Absorption coefficient as a function of incident amplitude for exponential profile. Front pore is $r_0 = 25$ mm, $d_p = 1$ mm, $d_c = 3$ mm, $L = 100$ mm and $R = 50$ mm.

It is shown that the performance of the profile absorbers (Figures 4.49 – 4.57) are not as affected by the strength of the incident amplitude compared to pancake absorbers. At sufficiently low sound levels or when sound pressure is considered small enough to be in the linear regime, the profile absorber performance is steady or unaffected. When the incident sound pressure level grows above 120 dB, the peak absorption coefficient values are reduced similarly like pancake structures. However, in some cases the peak absorption for the profiles is also increased as pressure grows. This can also be observed (see Figures 4.49 – 4.57) by data showing absorption coefficient dependence on incident pressure amplitude. A reduction of the absorptive peaks is seen (4.49 – 4.57) to be not quite as abrupt when compared to the pancake absorbers (Figures 4.36 – 4.47) for when incident sound pressure levels are also increased. Similarly to pancake absorbers, the performance of the profile absorber depends on not just the capabilities of the inner structure, but also on the outer structure. When sound pressure amplitude is considered low (linear regime) the energy of the incident wave is more easily transferred beyond the boundary of the front plate with pore radius r_0.

The absorptive peak values are affected when sound pressure amplitude becomes large (nonlinear regime). However, a comparison of the absorptive properties of the profile and pancake absorbers at

HSPL are dependable on the structure boundary parameter of the first plate which contains the front central pore. For the profile absorbers the main pore opening is much greater than r_0 of the pancake absorbers. Consequently, the performance of the profile absorber (observed in Figures 4.49 – 4.57) is more efficient than that of the pancake structures at high amplitudes. This is also the case when nonlinear phenomena occurs since a larger content of energy is able to pass through the spatial region of the plate. Any reflections that occur are much less at the solid plate boundary where $x = 0$ for the profiles (where $x = 0$ is beginning of sample length with sample thicknesss L). Another similarity to pancake absorbers is that the first resonance of the profile absorber is not severely affected as the amplitude strength grows since the inner structure of the absorber remains constant, unchanged and rigid. The metamaterial structures investigated here in this thesis therefore have a variation in the magnitude of the absorptive peaks at high SPL but not the resonant frequencies. It is later validated and presented in Chapter 6 the influence of nonlinearity and its effect on the first resonant frequency as pressure amplitude grows. This is one of the attributes of the dead-end pores configured within the pancake and profile structures and seen to be independent of central pore radius r_0. The dead-end pore effect is illustrated in other works for low frequency sound absorption, see [1],[3],[44],[45] and most recently [139]. Moreover, the ABH effect and impedance matching from different configured structures can be seen in works by [2], [10]. A literture review is presented in Chapter 3 which provides a background of rigid porous media including the aforementioned design approaches of DEP and ABH.

4.4.3. Absorber Comparisons for Same Thickness

Incident sound pressure amplitudes measured in the HSPL impedance tube are shown to be much higher for the profile structures than for the pancake absorbers, (see sections 4.4.1 – 4.4.2). Careful attention was applied to the disturbance of the membrane due to a previous repair and service of the sound source system. This resulted in SPL being performed at lower pressures for pancakes than both of the linear and exponential profiles. The pancake and profiled absorbers have been investigated at low and high sound pressure levels with focus on low frequency sound absorption. Typical frequencies investigated for the pancake absorbers were in the range 130 Hz – 300 Hz. In all cases, the full frequency spectrum ($f = 50\ \mathrm{Hz} - 1600\ \mathrm{Hz}$) is shown (see sections 4.3 and 4.4) for white noise excitation for both the pancake and profiles. The pancake absorber, however, shows to be most effective for low frequency sound absorption (linear regime) at frequencies, observed as low as $f = 130\ \mathrm{Hz} - 150\ \mathrm{Hz}$, (see Figures 4.44 – 4.45 when the pancake absorber has $d_p = 1$ mm, $d_c = 3$ mm) and Figures 4.46 – 4.47, (for pancake with $d_p = 1$ mm and $d_c = 6$ mm). The pancake absorbers at HSPL in contrast, to both the linear and exponential profile structures, are shown to be least effective for broadband absorption, see Figures 4.42, 4.45 and 4.47. This is because the absorption coefficient is seen to significantly reduce as incident pressure grows. The reduction of absorption coefficient as a function of incident amplitude, can be observed in Figures 4.45 and 4.47 to reduce to as much as 40 % – 45 % respectively, as the incident amplitude is increased from 1 Pa – 60 Pa. This is due to the pancake absorber being more nonlinear than the profile structures and containing a much lesser value for the surface wall porosity. Hence, as pressure amplitude grows, the performance of the panacke is much more significantly affected, compared to the profiled structures.

Figure 4.58 shows absorption coefficient dependence on frequency and its comparison for different d_c with similar absorber lengths. Data shown is obtained by white noise excitation for a pancake absorber with $d_c = 1$ mm, $d_c = 3$ mm and $d_c = 6$ mm. All plates have thickness $d_p = 1$ mm, and all pores are constant at $r_0 = 4$ mm. External plate radius $R = 50$ mm is for all the pancake absorber configurations. The first resonance peak for $d_c = 1$ mm is at $f = 262$ Hz and $\alpha = 0.84$. Absorption coefficient is greater for the first resonance peaks when $d_c = 3$ mm and $d_c = 6$ mm. For $d_c = 3$ mm the first resonance peak is found at $f = 229$ Hz and $\alpha = 0.99$. For $d_c = 6$ mm the first resonance peak is at $f = 223$ Hz and $\alpha = 0.99$. It can be seen by Figure 4.58 that as d_c increases from 1 mm – 6 mm the absorptive peak values also increase after the first resonance peak. An advantage of when $d_c = 6$ mm is that sample weight becomes less when compared to $d_c = 1$ mm and $d_c = 3$ mm. Furthermore, internal volume of fluid in the sample is greater for $d_c = 6$ mm than when the sample has $d_c = 1$ mm or $d_c = 3$ mm. The pancake absorber with $d_p = 1$ mm and $d_c = 1$ mm provides the least effective performance. It also requires the most material to develop the structure and consequently, has a greater sample weight in contrast to when $d_p = 1$ mm and $d_c = 6$ mm.

Figure 4.59 shows absorption coefficient dependence on frequency and its comparison for different d_c with similar lengths close to $L = 60$ mm. Data shown is obtained by white noise excitation for pancake absorber with $d_c = 1$ mm, $d_c = 3$ mm and $d_c = 6$ mm. All plates contain $d_p = 1$ mm, and all pores are $r_0 = 4$ mm. The first resonance peak for $d_c = 1$ mm is $f = 146$ Hz and $\alpha = 0.90$. Absorption coefficient is greater for the first resonance peaks when $d_c = 3$ mm and $d_c = 6$ mm. For $d_c = 3$ mm and $d_c = 6$ mm the first resonance peaks are both at $f = 135$ Hz and have absorptive peak values $\alpha = 0.99$ and $\alpha = 1.0$ respectively. It can be seen from Figure 4.59 that as d_c increases from 1 mm – 6 mm the absorptive peak values also increase after the first resonance peak. An advantage of when $d_c = 6$ mm is that sample weight becomes less when compared to $d_c = 1$ mm and $d_c = 3$ mm. When the absorber is built with less material ($d_c = 6$ mm) for similar sample length close to $L = 60$ mm (compared to $d_c = 1$ mm or $d_c = 3$ mm) the internal fluid volume is greater. Pancake absorber with $d_p = 1$ mm and $d_c = 1$ mm is least effective for absorber performance since α is lower than when $d_c = 3$mm and $d_c = 6$ mm. As aforementioned (see also Figure 4.58), the sample which consists $d_c = 1$ mm requires additional material for the structure development compared to other samples which contain lesser plates. Furthermore, it has a greater sample weight in contrast with $d_p = 1$ mm and $d_c = 6$ mm.

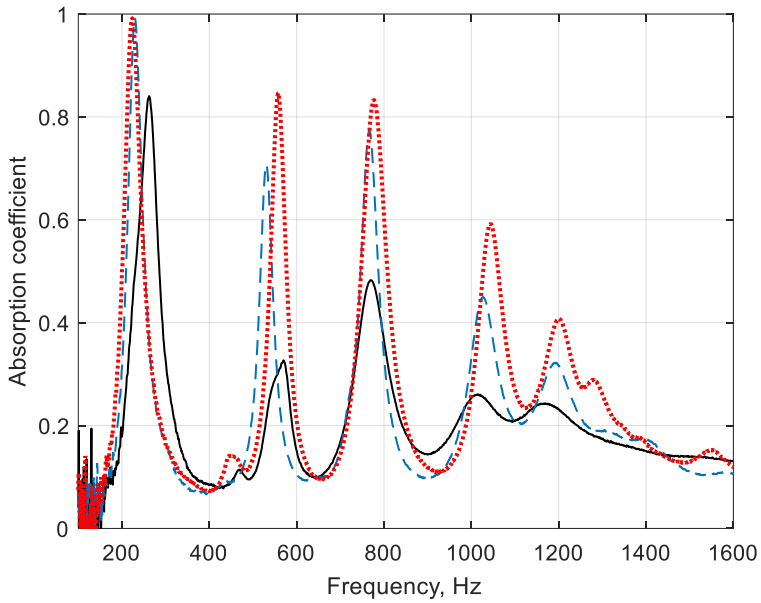

Figure 4.58. Absorption coefficient as a function of frequency. Pancake absorbers of various configurations, $r_0 = 4$ mm, and $R = 50$ mm. Sample lengths are close to $L = 30$ mm and $d_p = 1$ mm. $d_c = 1$ mm, $N_{de} = 16$, (black solid), $d_c = 3$ mm, $N_{de} = 8$, (blue dash), and $d_c = 6$ mm, $N_{de} = 5$, (red dot).

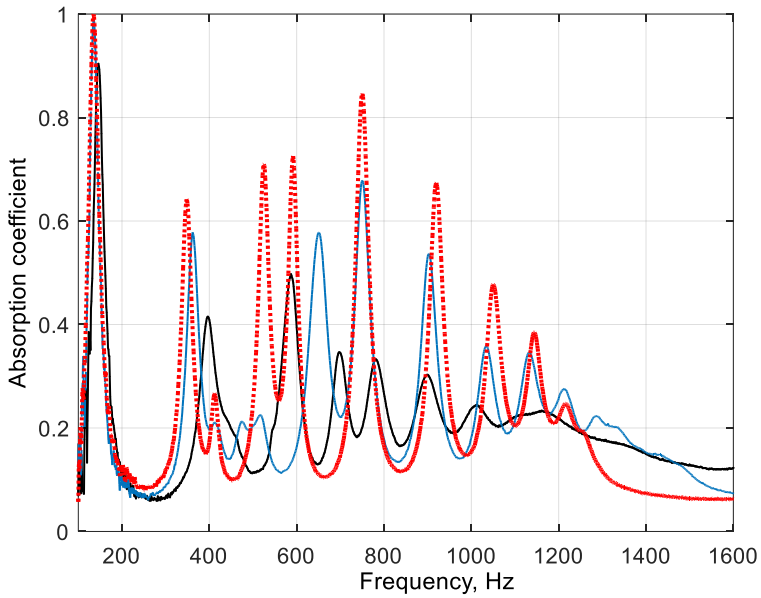

Figure 4.59. Absorption coefficient as a function of frequency for pancake absorbers with various configurations, $r_0 = 4$ mm, and $R = 50$ mm. Sample lengths are close to $L = 60$ mm, $d_p = 1$ mm, $d_c = 1$ mm, $N_{de} = 30$, (black solid), $d_c = 3$ mm, $N_{de} = 15$, (blue dash), and $d_c = 6$ mm, $N_{de} = 9$, (red dot).

The results of the profile structures are, however, more varied than the pancake absorber. This is because the linear and exponential profiles are both broadband and values of α exist across the full frequency spectrum. Absorption values for both linear and exponential profiles do not alter as significantly when compared to the pancake absorbers. It is demonstrated in Tables 4.2 – 4.12, see sections 4.4.1 and 4.4.2, (which shows absorption coefficient dependence with amplitude growth) that as the peak pressure grows then α values decrease and, in some circumstances, they increase due to nonlinear phenomena. Linear profile configurations are observed to be effective for its absorptive qualities when targeted with white noise excitation. This is previously illustrated by Figures 4.52 – 4.53, and seen also by Figure 4.62, where broadband absorption is achieved at frequencies $f = 50$ Hz –

1600 Hz. Moreover, this is when the surface and consecutive central orifices in the neighbouring plates is largest and configured in series. These larger dimensions of the linear profile ($d_p = 1$ mm, $d_c = 3$ mm, and $L = 100$ mm) enabled the performance of the profile to be most effective. The profiled structures investigated thus far, are compared for identical sample lengths. Figure 4.60 shows a comparison for the absorption coefficient dependence on frequency when tested with white noise excitation in linear regime, for a pancake absorber and linear profile structure. Sample lengths for both the absorbers is $L = 60$ mm. Their configurations both contain $d_p = 1$ mm and $d_c = 3$ mm. The structure parameter variations between the pancake and profile is the central perforation radius and Inner pore trajectory. Figures 4.61 – 4.62 show a comparison for the absorption coefficient dependence on frequency when tested with white noise excitation in linear regime for the linear and exponential designs. Figure 4.61 shows the data for same sample thicknesses (where $L = 80$ mm) for both the linear and exponential profiles which are configured $d_p = 1$ mm and $d_c = 2$ mm. And Figure – 4.62 shows data for when the samples are built with $L = 100$ mm (linear and exponential profiles configured with $d_p = 1$ mm and $d_c = 3$ mm).

First and consecutive resonance peaks for both the linear and exponential absorbers are shown in Figure 4.61 with comparison of sample absorption coefficient for same sample thicknesses. For the exponential and linear profiles the first resonance peak values are $\alpha = 0.52$ and $\alpha = 0.11$, respectively, at $f = 189$ Hz. However, α is seen being the same value at $f = 290$ Hz, where $\alpha = 0.50$. Absorption coefficient for the linear profile (with $d_c = 2$ mm) after 290 Hz increases dramatically and surpasses the exponential profile. At $f = 308$ Hz the peak absorptive value for the linear profile is much greater compared to the exponential profile. For the former, $\alpha = 0.97$ compared to exponential profile where $\alpha = 0.47$. Both the linear and exponential absorbers prove to be effective for broadband absorption when built with $d_c = 2$ mm, $d_p = 1$ mm, and main pore $r_0 = 25$ mm. Figure 4.62 shows absorption coefficient dependence on frequency for the linear and exponential absorbers. The samples are reassembeled with additional $L = 20$ mm (compared to profiles of Figure 4.61). Sample length becomes $L = 100$ mm and built with $d_p = 1$ mm and $d_c = 3$ mm. Absorption coefficient for both the linear and exponential profiles at $f = 130$ Hz shows being $\alpha = 0.12$ and $\alpha = 0.56$, respectively. At $f = 196$ Hz the values are $\alpha = 0.38$ for both the linear and exponential profile absorbers. A significant variation of α is observed at $f = 223$ Hz between the profiles, shown by Figure 4.62 similarly to that seen in Figure 4.61 at $f = 308$ Hz. For instance, both profile configurations show a significant difference of α, where $\alpha = 0.56$ and $\alpha = 0.95$ for the exponential and linear structures, respectively (see Figure 4.62). Peak values of α for the linear profile is therefore much larger than the exponential profile at low frequencies beginning $f = 223$ Hz.

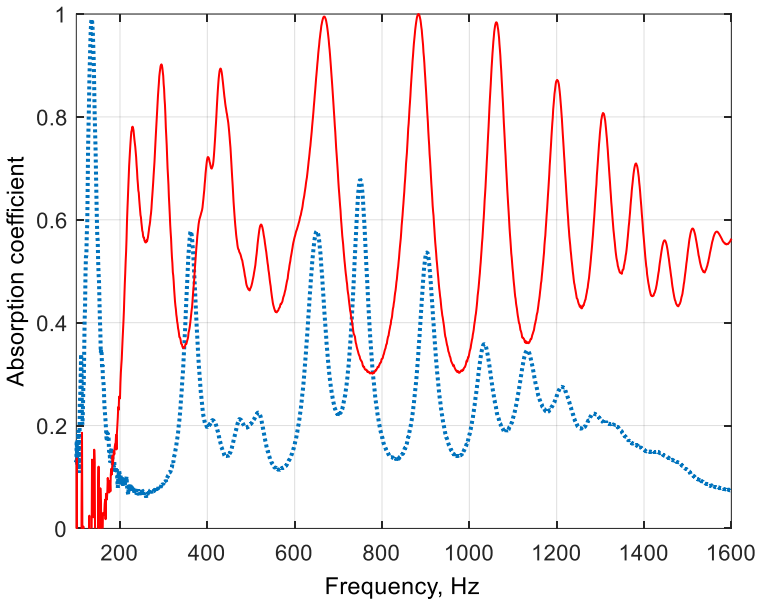

Figure 4.60. Absorption coefficient as a function of frequency. Pancake absorber (blue) vs linear profile (red). Configurations $d_c = 3$ mm, $d_p = 1$ mm, $L = 60$ mm, $N_{de} = 15$, and $R = 50$ mm.

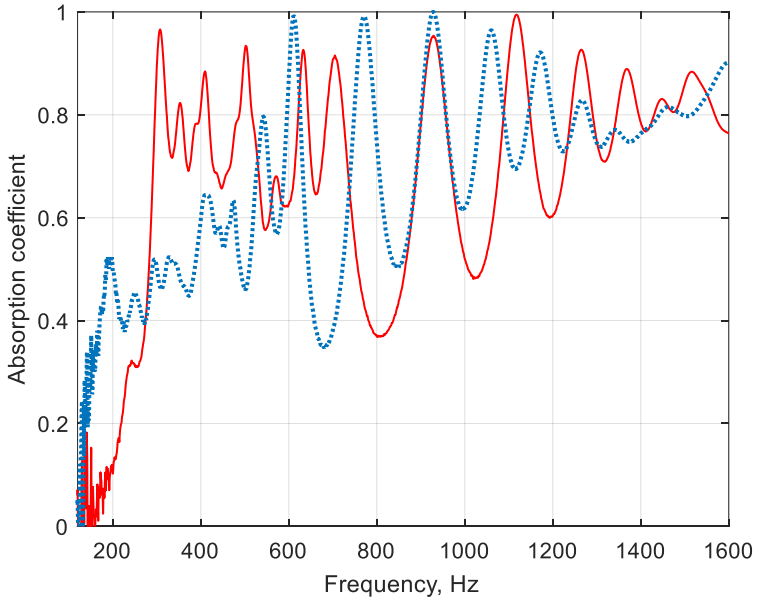

Figure 4.61. Absorption coefficient as a function of frequency. Linear profile (red line) and exponential profile (blue dot), $d_c = 2$ mm, $d_p = 1$ mm, $L = 80$ mm, $N_{de} = 25$, and $R = 50$ mm.

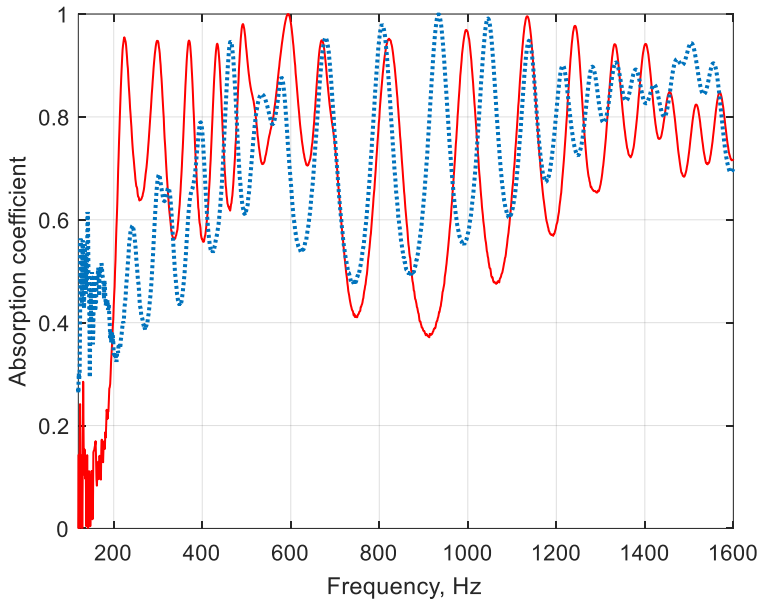

Figure 4.62. Absorption coefficient as a function of frequency. Linear profile (red line) and exponential profile (blue dot), $d_c = 3$ mm, $d_p = 1$ mm, $L = 100$ mm, $N_{de} = 25$, and $R = 50$ mm.

Profile absorbers measured at HSPL with sine wave excitation are discussed in terms of the variations of the normalized absorption coefficients, and presented in the following order. The main opening surface perforation of the absorbers is reprented by r_0. A Linear profile is discussed with $r_0 = 15$ mm, $d_p = 1$ mm, and $d_c = 3$ mm (Figure 4.49) followe by a linear profile absorber, $r_0 = 25$ mm, $d_p = 1$ mm, and $d_c = 2$ mm (Figure 4.51). The last of the linear profile absorber is when $r_0 = 25$ mm, $d_p = 1$ mm, and $d_c = 3$ mm (Figure 4.53). Exponential profiles are then discussed thereafter, firstly with $r_0 = 25$ mm, $d_p = 1$ mm, and $d_c = 2$ mm (Figure 4.55) and again when the cavity depty is increased, so $r_0 = 25$ mm $d_p = 1$ mm, and $d_c = 3$ mm, see Figure 4.57. Linear profile data given by Figure 4.49 shows at $f = 224$ Hz the value of α reduces to nearly as much as 48 % as incident amplitude grows from 1 Pa – 20 Pa. A similar magnitude in the reduction of α is found at $f = 229$ Hz with a reduced absorptive value of 45 % (1 Pa – 22 Pa). This is not seen at the other frequencies investigated in Figure 4.49 (282 Hz – 301 Hz), where α reduces only around 5 % – 12 % as incident amplitude grows from 1 Pa – 25 Pa. When incident pressure is increased from 25 Pa – 200 Pa, the absorption coefficient does not reduce as abruptly when compared to 1 Pa – 25 Pa. At $f = 224$ Hz and $f = 229$ Hz absorption coefficient α reduces up to 10 % for pressure amplitude growth 25 Pa – 160 Pa. Then α reduces 19.7 % and 12.7 % at $f = 282$ Hz and $f = 296$ Hz respectively, from 25 Pa – 185 Pa. Furthermore, at $f = 301$ Hz and $f = 431$ Hz the absorption coefficient is reduced by 11.5 % and 15.2 % respectively, for incident pressure growth (25 Pa – 185 Pa).

Profile absorber (linear) given by Figure 4.51 (for when $r_0 = 25$ mm, $d_p = 1$ mm, and $d_c = 2$ mm) shows that at low frequencies ($f = 300$ Hz and $f = 308$ Hz) α reduces to nearly as much as 22 % as the incident amplitude grows from 1 Pa – 50 Pa. It then reduces 20 % at $f = 300$ Hz and $f = 308$ Hz when the pressure is increased towards 220 Pa. Furthermore, at higher frequencies investigated ($f = 410$ Hz – 495 Hz), absorption coefficient reduces only around 6.8 % and 1.1 % respectively, from 1 Pa – 25 Pa. When incident pressure is increased (25 Pa – 220 Pa) then α increases 2.4 % at $f = 410$ Hz and decreases 13.5 % at $f = 495$ Hz. Absorption coefficient is reduced 11.7 % between 1 Pa – 25 Pa for

frequency $f = 503$ Hz. A further 7.2% of α occurs at $f = 503$ Hz when incident sound pressure amplitude is increased from 25 Pa – 220 Pa. When cavity depth is increased, see Figure 4.53 (for linear profile with $r_0 = 25$ mm, $d_p = 1$ mm, and $d_c = 3$ mm), α reduces 34.5 % and 36.1 % for $f = 215$ Hz and $f = 224$ Hz respectively (from 1 Pa – 25 Pa).

The absorption coefficient only reduces around 3.3 % when incident pressure amplitude grows from 25 Pa – 200 Pa. At $f = 288$ Hz the absorption coefficient is seen to increase 5 % (from 1 Pa – 10 Pa) and then α decreases 4.8 % from 30 Pa – 280 Pa. At $f = 298$ Hz the absorption coefficient is seen to increase 4.5% from 1 Pa – 10 Pa and then decrease 5.4 % from 10 Pa – 30 Pa. A further reduction of 3.4 % occurs at $f = 298$ Hz from 30 Pa – 285 Pa. This completes the linear profile configurations tested with $d_c = 2$ mm and $d_c = 3$ mm, with opening main pores $r_0 = 15$ mm, and $r_0 = 25$ mm. Variation of the absorption coefficient reduction with growth of incident pressure amplitude indicates that the largest reduction of α is found in the pressure region 1 Pa – 50 Pa (see Figures 4.49, 4.51, and 4.53). When the incident pressure is increased much stronger from 30 Pa – 250 Pa, the reduction of α is much less significant and only in the region 2 % – 10 %. It is also established that largest reductions of α for the linear profile configurations appear to be in the frequency range between $f = 200$ Hz – 300 Hz.

For the exponential profile with $d_p = 1$ mm and $d_c = 2$ mm (see Figure 4.55) absorption coefficient only reduced 1.7 % for $f = 293$ Hz – 415 Hz, from 1 Pa – 200 Pa. At $f = 473$ Hz the values of α increased by 3.6 %, from 1 Pa – 175 Pa. It is at higher frequencies ($f = 540$ Hz – 611 Hz) that see a significant reduction in the absorbtion coefficient. And at $f = 540$ Hz there is a 19.7 % reduction from 1 Pa – 25 Pa. Furthermore, α is reduced 12.3 % when the incident pressure amplitude grows from 25 Pa – 70 Pa. The highest frequency investigated shown in Figure 4.55 for pure tones was $f = 611$ Hz. It appears the absorption coefficient reduces around 7.1 % from 1 Pa – 25 Pa, at this frequency. When incident pressure amplitude is increased from 25 Pa – 75 Pa, α is reduced 8.7 %. The incident pressure amplitude is increased further, from 75 Pa – 205 Pa, and results in a 10.7 % reduction for the absorption coefficient.

The exponential profile structure is rebuilt with $d_p = 1$ mm and $d_c = 3$ mm (HSPL data is shown by Figure 4.57). A total of 10 % reduction of α is seen at $f = 235$ Hz is when the incident pressure amplitude grows 1 Pa – 20 Pa. The value of the absorption coefficient remains unchanged as the incident pressure increases from 20 Pa – 150 Pa. At $f = 241$ Hz, α reduces around 13.8 % from 1 Pa – 20 Pa, and also remains unchanged as incident pressure grows, from 20 Pa – 150 Pa. The slightly higher frequencies investigated and presented in Figure 4.57 are those at $f = 302$ Hz, $f = 325$ Hz, and $f = 398$ Hz. A much larger reduction of α occurs at these higher frequencies as incident pressure amplitude grows from 1 Pa – 30 Pa. At frequency 302 Hz, the absorption coefficient encounters a 23 % reduction from 1 Pa – 20 Pa. The absorption coefficient value then increases 7.5 % as the incident pressure grows from 20 Pa – 200 Pa. A similar reduction and increase of α occurs at $f = 325$ Hz. There is a 14 % reduction of the absorption coefficient from 1 Pa – 20 Pa followed by an increase of 3.5 % for α which occurs as the pressure amplitude grows from 20 Pa – 250 Pa. There is a large reduction of the absorption coefficient occurring $f = 398$ Hz. As the pressure amplitude grows from 1 Pa – 30 Pa α is reduced 20 %. However, there is also the largest absorption coefficient increase of 12.7 % which occurs at $f = 398$ Hz. This increase of α occurs when the incident pressure amplitude grows from 30 Pa – 200 Pa. For the

exponential profile absorbers α is mostly affected in the frequency range $f = 500\ \text{Hz} - 600\ \text{Hz}$, for when $d_c = 2$ mm as the incident pressure amplitude grows. The aborption coefficient for the exponential profile with $d_c = 3$ mm is found to be reduced mostly at frequencies $f = 300\ \text{Hz} - 400\ \text{Hz}$ for increasing pressure amplitude. The largest reduction of α is found to be in the pressure region between 1 Pa – 50 Pa, (see Figures 4.55, 4.57). When the incident pressure is increased much stronger from 30 Pa – 250 Pa, reduction of the absorption coefficient is much less significant.

4.5. Conclusion

Pancake and profiled absorbers have been measured with low and high sound pressure levels using an impedance tube. The pancake absorbers show that they perform in a tonal manner whereas profiled structures provide broadband absorption. This is the case for the various amplitude strengths investigated and shown in sections 4.3 – 4.4. It is also demonstrated that mechanical resonance exists and affects the performance of the pancake and profiled absorbers such that absorption coefficient values are altered, including the first resonance frequency of the absorbers. The vibrations impact the peak absorption curve and as sound amplitude strength increases nonlinearity of frame vibration arises. Both acoustic and mechanical resonance must therefore be considered within the design of the absorbers to determine maximum sound absorption and for optimisation of these metamaterial structures. Large values of absorption coefficient at low frequency is achieved for the pancakes. Profiled structures are able to attain broadband absorption and results in additional absorptive peaks across the frequency spectrum. The linear profile performed best when compared to the exponential profile (where comparisons between profiled absorbers are presented in section 4.4.3. including the pancake versus a linear profile structure). The comparisons are given for when the structures have same values of d_p, d_c, L and R showing absorption coefficient as a function of frequency.

5. Flow Resistivity Measurements

Chapter 5 aims at presenting the flow resistivity data (used in conjunction with a developed model provided in Chapter 6 showing model comparisons) for describing the nonlinear aspects and sound absorbing capabilities of the absorbers. Its layout is presented in the following: Section 5.1 gives a general background and a description of the various types of samples with their dimensions and configurations for each of the structures. Subsection 5.1.1 presents the flow resistivity of solid cylinders containing a simple perforation at low flow rates. These measurements have been performed in order to compare the flow resistivity of pancake absorbers with those of the solid cylinders possessing a single perforation. In subsection 5.1.2 the flow resistivity data of the pancake absorbers are given, and in subsection 5.1.3 the profile absorber is measured for its values of flow resistivity, again at low flow rates. The incoming fluid velocity is then increased such that high flow rates are achieved. Section 5.2 discusses flow resistivity with increased flow rates and introduces the Forchheimer's nonlinearity parameter. And section 5.3 shows comparisons of the flow resistivity dependence on sample length for all samples investigated (solid cylinder with simple pore, pancake absorbers and the profile structure) including a discussion for the main findings. The pancake and profile absorbers tested have variation in the cavity thickness, where $d_c = 1 \text{ mm} \rightarrow 6 \text{ mm}$. A conclusion is given in section 5.4 for the absorbers.

5.1. Methodology and Low Flow Rates

Flow resistivity measurements have been performed at the acoustic research laboratory based at the University of Salford, UK. It is demonstrated extensively in previous works, see Chapter 3 (Literature review), that the flow resistivity can be used to characterize rigid porous media. The pancake and profile absorbers presented in this chapter are identical structures tested previously (see Chapter 4, experiments for continuous sound) built with same dimensions where the external plate radius $R = 50 \text{ mm}$. Static flow resistivity measurements have been discussed previously, see Chapter 3, section 3.3.1 (porous materials in linear and nonlinear regimes including Forchheimer's nonlinearity) which gives an extensive literature review and detailed account of flow resistivity in rigid and porous media. The static flow resistivity is represented by a measured coefficient σ_0, which for low flow rates is,

$$\sigma(V_f) = \frac{\Delta P}{V_f L} \tag{1}$$

where ΔP is the pressure difference over sample of length L for flow velocity V_f (measured within the tube). The dc flow resistivity σ, is commonly measured in steady flow tests for porous materials, at low flow rates and moreover, the determination of the pressure drop can be obtained for a sample with length L. Note, that this is for when the flow is linear. The equation given by (1) is modified for when high flow rates occur, where a nonlinear parameter needs to be accounted for (see section 5.2, Flow resistivity – high flow rates, equation (2)). In this work the flow resistivity of the structures (notably pancake absorbers) have been measured for both low and high flow rates. The performance of acoustic absorbers is seen to be directly related to the structure flow resistivity (see Chapter 3, Literature review) for determining the permeability of air saturated porous materials. This is because the ability of sound waves to enter a material relies on the permeability contrast of the structure, or porous medium to the

surrounding fluid. If the airflow resistivity is deemed high enough then permeability will become low thus, the sound absorption properties of a structure will consequently be reduced preventing the sound waves from entering it. Sound wave interaction can therefore be restricted depending on whether a porous material, or absorber is easily permeable or not.

Low flow rates are firstly investigated for all the samples tested obtaining values in the laminar regime (inside the rig tube). The flow resistivity rig is described elsewhere by Turo in [43]. The rig has now been updated to install a new testing tube (which houses a sample) with an inner tube radius $R = 50\ \mathrm{mm}$ to fit the samples. The data obtained from the flow resistivity measurements is limited to the working range of the flow rig system. Sensitivity of the pressure transmitters used in the flow rig system are out of scope for the lowest velocities needed to determine the static airflow resistivity of the samples. Lowest flow rate achieved by the flow rig was approximately 10 $\mathrm{mm/s}$ however, according to BS EN29053 [133], a value of 0.5 mm/s flow rate is recommended for determining the static flow resistivity σ_0. An interpolation process is used to fit a linear relationship of the static airflow resistivity to its static value by the data obtained at low velocities, see equation 1. Measured flow resistivity values of the absorbers are validated and compared to their associated theoretical static airflow resistivity values. The theoretical value for the straight cylindrical pore with $r_0 = 4\ \mathrm{mm}$ gives a static flow resistivity value approximately $\sigma_0 = 1405\ \mathrm{Pa\,s/m^2}$ (which is obtained using the surface porosity, where $\phi_p = a^2/R^2$). Pore radius and plate radius are given by a and R respectively. The static flow resistivity is determined therefore accounting for the dynamic viscosity of air η and results in the following expression, $\sigma_0 = 8\eta/(a^2\emptyset)$. Surface porosity of the sample is approximately $\phi_p = 6.41 \times 10^{-3}$.

The operation of the flow rig in order to perform a measurement is achieved by the following process. A lever is used mechanically in order to control the incoming flow pressure to the flow rig. The lever is displaced from its neutral position and allows the airflow to travel through the flow pipe system from a pressurized network. The flow is then directed towards a region where exists various sensitive mounted pressure flow meters which are connected. Afterwards, the Incoming pressure flows towards the sample parallel at some fixed distance above the sample surface. Several differential pressure transmitters are used to record the pressure for the required flow rates for each measurement. Many data points are required to obtain a good account of the pressure drop over the sample thickness. A new flow rate (represented by each data point) is required for each measurement of the flow resistivity obtained. Pancake structures composed of different configurations ($d_p = 1\ \mathrm{mm}$ and $d_c = 1\ \mathrm{mm} \rightarrow 6\ \mathrm{mm}$) are measured for both low and high flow velocities. The samples are reassembled depending on the cavity depth d_c, and a resulting sample of each configuration is tested. Solid cylinders containing only a simple central perforation are tested as well and compared with the pancake structures (both with same pore radius r_0). This approach allows the behaviour of the sample containing cavities (pancake absorber) be compared to the solid cylinder, where d_c does not exist (or equal to zero).

Solid cylinders are presented first showing flow resistivity values at low flow rates for sample lengths $L = 30\ \mathrm{mm}$, $L = 60\ \mathrm{mm}$, and $L = 90\ \mathrm{mm}$. Each solid sample has a central pore diameter of 8 mm which is kept constant in order to compare with the pancakes. The pancake absorbers are presented in terms of the configuration thicknesses. Sample thickness of the pancake absorbers are approximately $L = 30\ \mathrm{mm}$ and $L = 60\ \mathrm{mm}$ where $d_c = 1\ \mathrm{mm}$, $d_c = 3\ \mathrm{mm}$, $d_c = 5\ \mathrm{mm}$ and $d_c = 6\ \mathrm{mm}$. Plate thickness $d_p =$

$1\ \mathrm{mm}$ for the pancake absorbers. All plates d_c have an outer radius where $R = 50\ \mathrm{mm}$. Each pancake configuration is wrapped and sealed using PTFE, and insulation tape before mounting into the sample tube holder of the flow rig, see Figure 5.1. Several bolts and clamps are used to fix the sample holder to the main tube of the rig system. Measurements can be performed once the sample is secured tightly in place, and all power leads are connected accordingly for working use. An inspection of the flow resistivity rig is then carried out by increasing the flow velocity to check for any leaks around the sample holder, and flow pipes. The flow resistivity rig set-up can be seen in Figure 5.2 showing a sample inserted into the sample holder, fixed to the rig and ready for testing. A differential pressure transmitter is used for recording low pressure values of flow resistivity and has a working range of 1 Pa – 100 Pa. After low flow rates of the sample have been performed a change of differential pressure transmitter must be used. The working range of the differential pressure transmitter for the high flow rates is 100 Pa – 2 KPa.

Figure 5.1. Flow rig sample holder and sample segments (left), pancake structure inserted into the sample holder which is then sealed, bolted, and clamped to the flow rig system.

Figure 5.2. Flow resistivity rig set up. Sample is inserted into a sample holder which is then sealed, bolted, and clamped.

5.1.1. Solid Cylinder with Simple Pore – Low Flow Rates

Solid cylindrical structures which comprise a central pore have been built in the workshop at ISAT, Nevers, France. Measurements of the flow resistivity are later performed at Salford laboratory, UK. The solid structures containing only a central pore (no presence of cavities) were built in order to compare

against the metamaterial structures which do contain cavities. A comparison of the flow resistivity is later determined from the structures tested (with and without the presence of d_c). The data from flow resistivity comparisons is given in section 5.3. An interpolation process is used to fit a linear relationship of the static airflow resistivity to its static value by data obtained at low velocities (due to experimental limitation of the flow rig system and sensors) results in a continuous decrease of the slopes given by the flow resistivity plots. The measured data is later validated against the theoretical values.

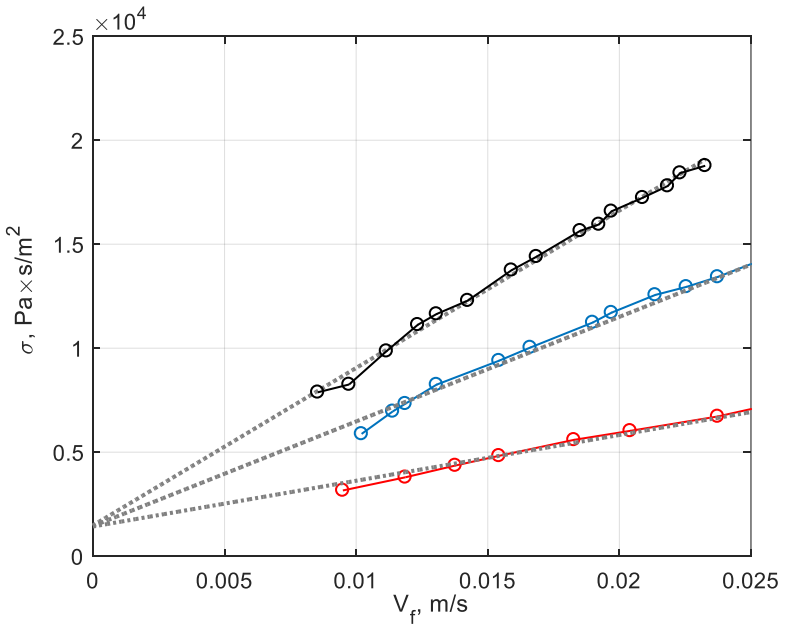

Figure 5.3. Flow resistivity measurements for solid cylinders with simple central perforation. At low flow rates sample lengths are $L = 30$ mm (black), $L = 60$ mm (blue) and $L = 90$ mm (red).

Figure 5.3 shows flow resistivity data of solid cylinders containing a central perforation. A single perforation was the same as the pancake absorbers so that $r_0 = 4\ \mathrm{mm}$ and since no cavities are present with the structure then $d_c = 0$. All samples had outer radius $R = 50\ \mathrm{mm}$ so they could remain sealed tightly to the tube mount walls. Flow resistivity dependence on structure thickness (solid cylinders containing a simple perforation) is measured for samples with length $L = 30$ mm, $L = 60$ mm, and $L = 90$ mm. It can be observed in Figure 5.3 that flow resistivity becomes a lesser value with increasing sample length. The flow resistivity values measured for three solid sample thicknesses are also given in Table 1. For the sample with $L = 30$ mm the static flow resistivity measured 1481 $\mathrm{Pa\,s/m^2}$. When sample length $L = 60$ mm static flow resistivity becomes 1449 $\mathrm{Pa\,s/m^2}$. And for $L = 90$ mm the static flow resistivity was 1425 $\mathrm{Pa\,s/m^2}$. The theoretical value for a simple perforated cylinder is given by equation (1). The solid samples containing a simple pore are measured. This results in the values being a close approximation to the theoretical value of the static flow resistivity for a pore with radius $r_0 = 4\ \mathrm{mm}$, which is 1405 $\mathrm{Pa\,s/m^2}$. The error between the theoretical and experimental values for σ_0 (for the solid cylinders with simple pores) was 5.4 %, 3.2 % and 1.48 % for $L = 30$ mm, $L = 60$ mm, and $L = 90$ mm, respectively.

5.1.2. Pancake Absorber – Low Flow Rates

Results of flow resistivity measurements and low flow rates ranging between 0.19 $\mathrm{m/s}$ and 0.025 $\mathrm{m/s}$ (for pancake absorbers with sample length close to 30 mm) is shown by Figure 5.4. This is when the configuration is built with $r_0 = 4$ mm, $d_p = 1$ mm, $d_c = 1$ mm and $R = 50$ mm. The flow resistivity value obtained from the measurements performed in the flow rig at low flow rates is 1482.5 $\mathrm{Pa\,s/m^2}$. Sample length is $L = 31$ mm. For pancake with $L = 30$ mm and $r_0 = 4$ mm, $d_p = 1$ mm, $d_c = 3$ mm and $R = 50$ mm, the flow resistivity value measured was slightly lower at 1471.2 $\mathrm{Pa\,s/m^2}$. When sample length was $L = 30$ mm and $d_c = 5$ mm the static flow resistivity value obtained was higher than other samples around $L = 30$ mm. The flow resistivity value was measured at 1505.9 $\mathrm{Pa\,s/m^2}$. Pancake absorber with $d_c = 6$ mm and $L = 35$ mm had the static flow resistivity being 1414.5 $\mathrm{Pa\,s/m^2}$. These measured values are close approximation to the theoretical value of the static flow resistivity for a pore with radius $r_0 = 4$ mm, which is 1405 $\mathrm{Pa\,s/m^2}$. The error between the theoretical and experimental values for σ_0 for the pancake absorbers was 5.51 %, 4.71 %, 7.18 % and 1 % for the pancakes with $d_c = 1$ mm, $d_c = 3$ mm, $d_c = 5$ mm and $d_c = 6$ mm, respectively.

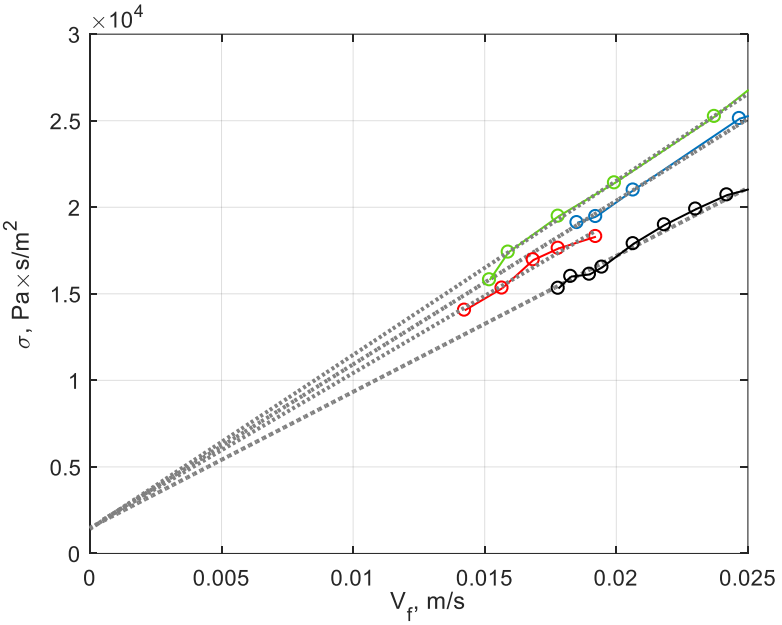

Figure 5.4. Flow resistivity measurement for pancake absorber, low flow rates. Sample consists of $r_0 = 4$ mm, $d_p = 1$ mm, and $R = 50$ mm. Black-$d_c = 1$ mm, blue-$d_c = 3$ mm, red-$d_c = 5$ mm, and green-$d_c = 6$ mm. Sample lengths are close to $L = 30$ mm.

It was shown in section 5.1.1 that solid cylinders containing a simple pore only (where $d_c = 0$) that a cylinder with $L = 30$ mm has been investigated at low flow rates (Figure 5.3). The static flow resistivity is measured 1481 $\mathrm{Pa\,s/m^2}$ for the proposed sample with a central perforation the same as the pancake absorbers with $r_0 = 4$ mm. The values of static flow resistivity at low flow rates does not deviate significantly for the pancakes when compared to the solid cylinder with a simple perforation. To illustrate the effect of the cavities with different values of d_c the pancake absorbers are shown in Figures 5.4 for samples with length close to $L = 30$ mm. The absorbers show that flow resistivity values differ only slightly for when sample lengths are similar, but cavity thickness is changed. For example, when $d_c = 1$ mm and $L = 31$ mm, the static flow resistivity is measured 1482.5 $\mathrm{Pa\,s/m^2}$and becomes only 1414.5

$\mathrm{Pa\,s/m^2}$ for when the pancake absorber is configured with $d_c = 6$ mm, see Figure 5.4. This is when cavity thickness is, at the least and largest, for values of d_c for the absorbers which are close to $L = 30$ mm. When the pancake is built with $d_c = 3$ mm then the static flow resistivity is in the region between when $d_c = 1$ mm and pancake has $d_c = 6$ mm, which is measured 1471.2 $\mathrm{Pa\,s/m^2}$. Lowest value of flow resistivity is attributed to the sample with largest length, approximately $L = 35$ mm and the pancake absorber with $d_c = 6$ mm. The effect of sample length of the structures is discussed in more detail later in the Chapter, see section 5.3, Flow resistivity comparisons. Various samples containing the different lengths are shown in section 5.3 with different values of d_c. Pancake absorber configurations are extended (after the flow resistivity testing of samples with length around $L = 30$ mm) so that the metamaterial pancake absorbers are now investigated with length close to $L = 60$ mm, see Figure 5.5.

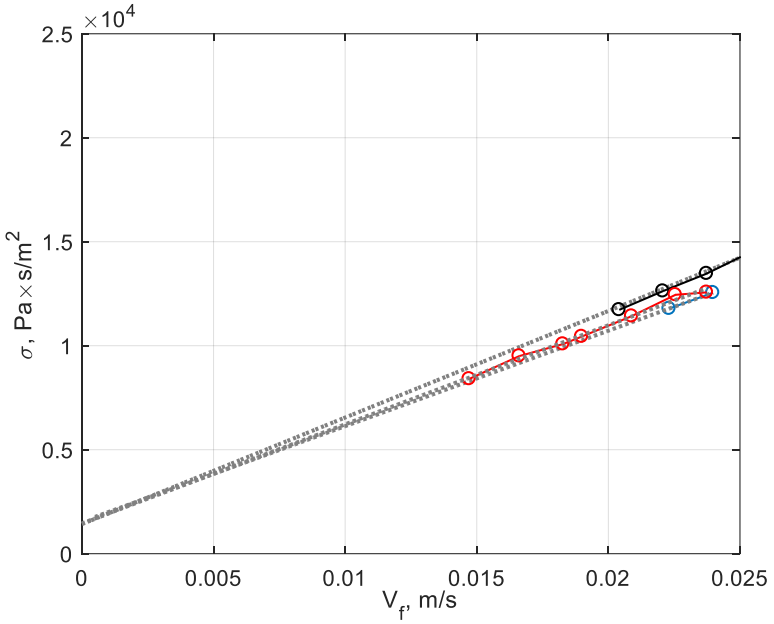

Figure 5.5. Flow resistivity measurement for pancake absorber, low flow rates. Sample consists of $r_0 = 4$ mm, $d_p = 1$ mm, and $R = 50$ mm. Black-$d_c = 1$ mm, blue-$d_c = 3$ mm, red-$d_c = 6$ mm. Approximate length for all absorbers is close to $L = 60$ mm.

Measurements performed at low flow rates for the pancakes (around $L = 60$ mm) have been tested with a flow rate $0.025\mathrm{m/s}$. Figure 5.5 shows the flow resistivity data of the pancake absorbers with $r_0 = 4$ mm, $d_p = 1$ mm, and $R = 50$ mm. Cavity depth for the absorbers ranged between $d_c = 1\,\mathrm{mm} - 6\,\mathrm{mm}$. The flow resistivity value obtained from the measurements performed in the flow rig at low flow rates for $d_c = 1$ mm and $L = 60$ mm was 1422.5 $\mathrm{Pa\,s/m^2}$. When the pancake cavity was $d_c = 3$ mm and sample length $L = 58$ mm the measured static flow resistivity value obtained was slightly higher for $d_c = 3$ mm, compared to when $d_c = 1$ mm and $d_c = 6$ mm. At low flow rates the flow resistivity value was measured 1541.6 $\mathrm{Pa\,s/m^2}$. For the pancake with the largest value of d_c (where $d_c = 6$ mm) the flow resistivity measured 1456.2 $\mathrm{Pa\,s/m^2}$ where sample length $L = 63$ mm. These measured values are close approximation to the theoretical value of the static flow resistivity containing a single perforation with $r_0 = 4$ mm (were $\sigma_0 = 1405\ \mathrm{Pa\,s/m^2}$). The error between the theoretical and experimental values for σ_0 for the pancake absorbers was 1.24 %, 9.72 %, and 3.64 % for the pancakes with $d_c = 1$ mm, $d_c = 3$ mm and $d_c = 6$ mm respectively, for samples with length close to $L = 60$ mm. Flow resistivity measurements performed for pancake structures with sample length nearly double that of the samples

given by Figures 5.4 show that d_c values do not considerably modify the value of σ_0 (for pancakes close to $L = 60$ mm, shown by Figure 5.5). This is also the case for when solid cylinders are tested in the flow resistivity rig at low flow rates (where static flow resistivity values remain similar, and close to σ_0 either for when $d_c = 0$ or when $d_c = 1\text{ mm} \rightarrow 6\text{ mm}$). For instance, a solid cylinder with $r_0 = 4$ mm (see Figure 5.3) gives a value 1449 Pa s/m^2. When a pancake absorber is built with $d_c = 1$ mm and has $L = 60$ mm the static flow resistivity is measured 1422.5 Pa s/m^2. When the pancake structure is configured with largest value of d_c (so $d_c = 6$ mm) then the static flow resistivity becomes 1456.2 Pa s/m^2 and is still close to the value of σ_0, for the solid cylinder containing only a simple pore and when $d_c = 0$. It is determined by the data shown by Figures 5.4 – 5.5 (for pancake structures with sample lengths around $L = 30$ mm and $L = 60$ mm) that flow resistivity values are reduced as the thickness of the sample increases. Values for the flow resistivity and Forchheimer's parameter is shown by Table 1 for all structures and comparisons of the sample thickness (both for all pancake structures and solid cylinders with simple perforations and presented further in section 5.3 describing effects of pressure variations that exist along sample length L, by means of contraction and expansion zones). The error between the theoretical and experimental values for the static flow resistivity σ_0, (associated with all sample measurements obtained in the flow-rig) was within a 10 % margin. It is indicated that the presence of the cavities in the metamaterial structures show a weak influence on the absorbers for σ_0. This is the case for all the values of d_c configurations ($d_c = 1\text{ mm} \rightarrow 6\text{ mm}$).

5.1.3. Profile Absorber – Low Flow Rates

Low flow rate measurements for the profile configurations are performed in the flow rig where the maximum flow rate was measured 0.036 m/s (see Figure 5.6). The profile tested in the flow-rig for the flow resistivity is the absorber with a linear configuration (details of the profile are presented in Chapter 4, see section 4.1.2. for profiled absorber dimensions, including Table 4.1). Absorber dimensions are built as the following, front plate has pore radius $r_0 = 25$ mm, and end plate has pore radius $r_0 = 4$ mm. Plate and cavity thicknesses are $d_p = 1$ mm, $d_c = 1$ mm and $R = 50$ mm. The static flow resistivity value obtained from the measurements performed in the flow rig at low flow rates is $\sigma_0 = 1895.7\ \text{Pa s/m}^2$. Sample length was approximately $L = 42$ mm. The linear profile absorber has also been measured to obtain the flow resistivity data for when the sample length is nearly double the thickness to that of the previous given profile. For instance, sample length was built $L = 85$ mm. The material parameters of both samples were the same excluding only the cavity depth (where d_c is changed from $d_c = 1\text{ mm} \rightarrow 3\text{ mm}$). At low flow rates $\sigma_0 = 1063.6\ \text{Pa s/m}^2$. The theoretical values for the static flow resistivity for the first and last plates for the profile absorber are $\sigma_0 = 5.23\ \text{Pa s/m}^2$ (for when $r_0 = 25$ mm) and $\sigma_0 = 1405\ \text{Pa s/m}^2$ (when $r_0 = 4$ mm). The value of σ_0 varied between the two samples with lengths $L = 42$ mm and $L = 85$ mm. Profile structures tested in the flow-rig differ from the pancake absorbers since σ_0 is dependent on the surface porosity of the sample. For example, the profiles are developed with varying perforations contained in each plate whereas r_0 for the pancake is constant and does not modify the effect of σ_0 significantly for sample with L.

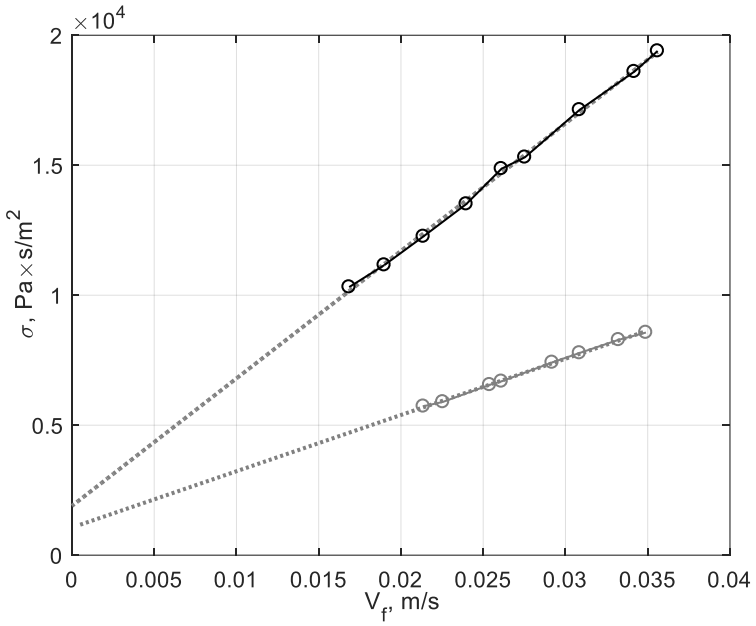

Figure 5.6. Flow resistivity measurements for linear profile absorber, low flow rates. Sample length is $L = 42$ mm (black) and $L = 85$ mm (grey).

5.2. Flow Resistivity – High Flow Rates

In this section the flow resistivity values for high flow rates are determined. This is achieved by the flow velocity being increased much further than flow rates given by section 5.1. An additional term to equation (1) is required (see equation (2)) in order to describe the nonlinear phenomena for measuring the pressure drop along the sample ΔP, at several flow rates V_f. This is determined by accounting for Forchheimer's nonlinear parameter which is in accordance with Forchheimer's law [32] (Forchheimer's nonlinearity is discussed previously, Chapter 3). Metamaterial structures studied in this work have been investigated for high flow rates. This is necessary in order to obtain each configuration with its associated Forchheimer's parameter ξ value. The values for pancake structures are presented in Table 5.1. A straight-line interpolation process is used similarly to that for the low flow rates (performed for the velocity equal to zero to account for each value of flow resistivity and obtain each value of ξ).

$$\sigma(V_f) = \frac{\Delta P}{V_f L} = \sigma_0(1 + \xi V_f) \tag{2}$$

Forchheimer's parameter values presented in Table 5.1 is given for solid cylinders containing a simple perforation only (where $r_0 = 4$ mm). Values of ξ is different for when sample length measures $L = 30$ mm, $L = 60$ mm and $L = 90$ mm and is reduced as sample length increases. This phenomena is also the case for the metamaterial structures tested. For instance, the Forchheimer's parameter obtained by performing high flow rate measurements is seen to differ for the pancake absorbers. The variation of the measured ξ is significantly larger between the samples for when sample length dimensions differ largest i.e. around $L = 30$ mm and $L = 60$ mm, as opposed to samples with lengths similar but with different values of d_c ($L = 30$ mm and $L = 35$ mm). It is also determined that it is the largest pancake samples (with length L) that have the lowest values of ξ, compared to the absorbers with lower sample length. Variation of the Forchheimer's measured parameter is illustrated in section 5.3 showing comparisons for the metamaterial pancakes with L. The value of ξ is different even for same material

configurations, excluding sample length. For example, the measured Forchheimer's parameter is a much higher value for the pancake structure with $L = 30$ mm compared to samples with $L = 60$ mm (for when both samples contain same values of plate thickness, pore radius and cavity depth). This is the case for all the configurations investigated i.e. when $d_c = 1$ mm, $d_c = 3$ mm or $d_c = 6$ mm. The value of the Forchheimer's parameter becomes dependent on the sample length of the structures and therefore ξ is weaker for the larger samples, see section 5.3 showing flow resistivity comparisons. Contribution of sample length ξ is discussed further in section 5.3 where the fluid encounters contraction and expansion zones within the structure. The measured flow resistivity and Forchheimer's data are presented in Table 5.1 for solid cylinders with central perforations including the pancake structures containing different values of L and d_c.

Similarly, like the pancake absorbers, the Forchheimer's parameter is reduced for the profile structures having different sample lengths. The absorbers are built with the same value d_p (including same values of pore radius r_0 distributed along the sample contained in each plate). The reduction of ξ for samples with $L = 42$ mm and $L = 85$ mm is not as drastic (for a difference of $L = 43$ mm between the profiles) as is the value ξ for the pancake absorbers (where difference between the pancakes is around $L = 30$ mm). This is due to the plates for the profiles d_p having much larger values of r_0 for most of its sample length (compared to the pancakes where r_0 of the pores are significantly less). Surface porosity of the profiles is therefore much larger than the surface porosity of the pancakes (since r_0 for the profiles of the front plate has a surface porosity $\phi_p = 2.50 \times 10^{-2}$ compared to $\phi_p = 6.41 \times 10^{-3}$ for the pancakes). The value of the Forchheimer's parameter becomes dependent on the sample length for the structures and therefore ξ is weaker for larger samples, see section 5.3 showing flow resistivity comparisons.

5.3. Flow Resistivity Comparisons

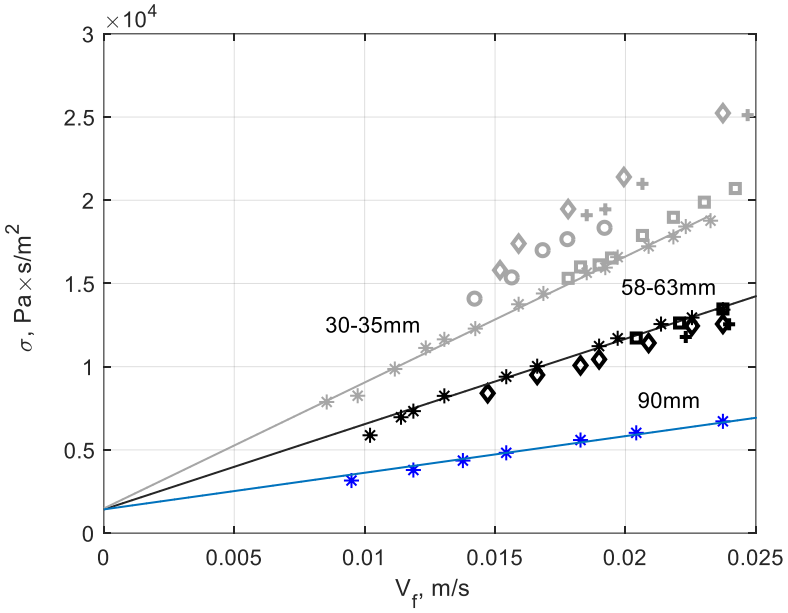

Figure 5.7. Flow resistivity of the absorbers and the solid cylinders with central perforation for low flow rates, for sample lengths $L = 30 - 35$ mm, $L = 58 - 63$ mm and $L = 90$ mm at low flow rates $\mathrm{V_f}$. Stars – solid cylinders with central perforation, squares – $d_c = 1$ mm, crosses – $d_c = 3$ mm, circles – $d_c = 5$ mm, diamonds – $d_c = 6$ mm, lines – linear fit for solid cylinders with orifice.

Flow resistivity values at low flow rates for the pancake absorbers and cylinders is shown by Figure 5.7. The flow rates measured for all the samples lie within the flow range $V_f \leq 0.025$ m/s. Different configured samples are shown by the data which is represented by various markers. Flow resistivity is shown by the markers indicating different values of d_c. The samples of solid cylinders are also included which contain a simple central perforation only and additional straight lines indicate a least squares approximation. Table 5.1 shows all the measured static flow resistivity σ_0 and Forchheimer's parameter ξ for the structures.

L, mm	d_p, mm	d_c, mm	σ_0, Pa s/m^2	ξ, s/m
3.1	1	1	1482.5	529.8
3.0	1	3	1471.2	642.6
3.0	1	5	1505.9	592.1
3.5	1	6	1414.5	710.6
3.0	circular	orifice	1481.0	511.1
6.0	1	1	1422.5	360.2
5.8	1	3	1541.6	297.8
6.3	1	6	1456.2	327.1
6.0	circular	orifice	1449.4	346.9
9.0	circular	orifice	1425.8	154.4

Table 5.1. Measured static flow resistivity σ_0 and Forchheimer's parameter ξ for pancake absorbers and samples of solid cylinders containing a simple perforation.

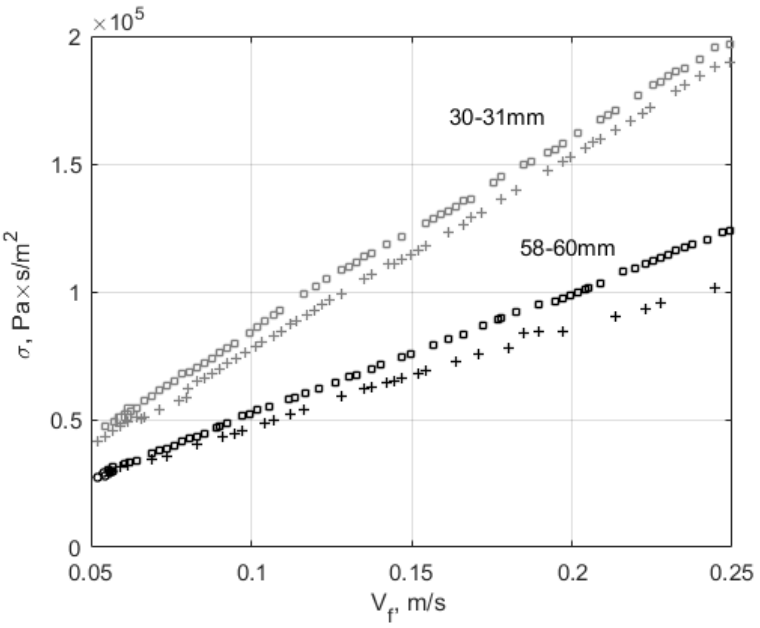

(a)

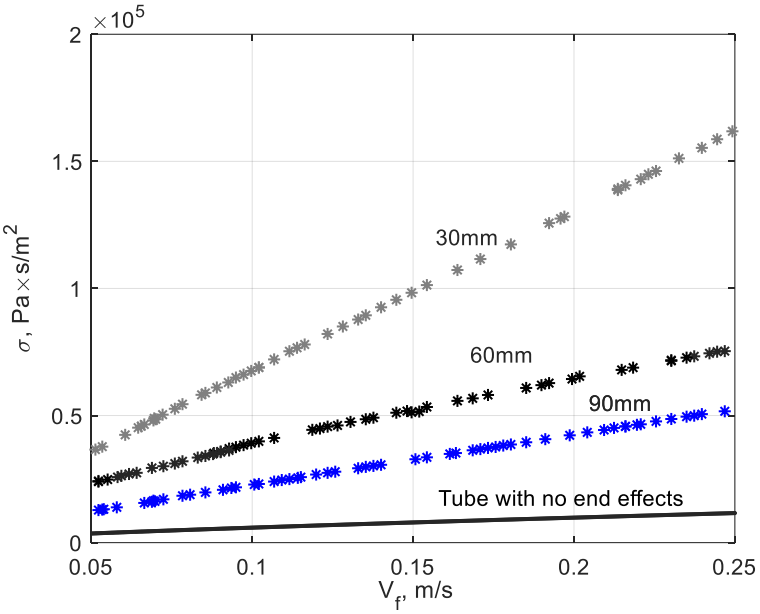

(b)

Figure 5.8. Flow resistivity of the absorbers (a) and solid cylinders with the central perforation (b) for high flow rates. Crosses – $d_c = 3$ mm, squares - $d_c = 1$ mm, stars – solid cylinders with central perforation, line – flow resistivity of the tube.

The flow resistivity values from the measurements performed at various high flow rates is given by Figure 5.8, where $V_f \leq 0.25$ m/s. The pancake absorbers are shown in Figure 5.8 a, for different values of d_c and same values of d_p. Absorber thicknesses range from approximately $L = 30$ mm and $L = 60$ mm showing the variation in flow resistivity as the sample length is increased. Figure 5.8 b shows the flow resistivity data for solid cylinders with a central perforation. The cylinders have lengths ranging $L = 30$ mm and $L = 90$ mm. Various markers given in Figure 5.8 a, indicates different d_c. Dimensions of r_0 and d_p remain the same values irrespective of the markers shown. Same markers given in Figure 5.8 b, represents flow resistivity with the same values of r_0 and R, but different values of length L.

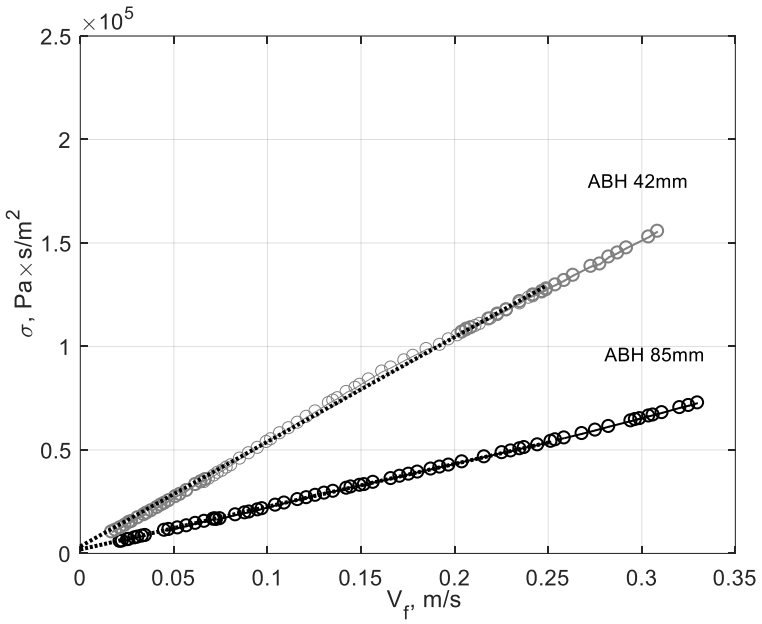

Figure 5.9. Flow resistivity measurements for ABH linear profile absorber, low and high flow rates comparison. Sample lengths are $L = 42$ mm and $L = 85$ mm. Sample consists with the first plate having a pore radius $r_0 = 25$ mm and the exit pore has radius $r_0 = 4$ mm. Plate thickness is $d_p = 1$ mm, $d_c = 3$ mm and sample radius $R = 50$ mm. The central perforation decreases 2 mm per plate until termination at the rear of the sample.

Profile data consisting of two different lengths containing a decreasing linear configuration of the central pore is shown by Figure 5.9. The corresponding measured static flow resistivity σ_0 and Forchheimer's parameter ξ is given by Table 5.2. Samples shown in Figure 5.9 have dimensions of its opening main pore, and end pore the same as those presented in section 5.1 (Figure 5.6).

L, mm	d_p, mm	d_c, mm	σ_0, Pa s/m^2	ξ, s/m
42	1	1	1895.7	258.7
85	1	3	1063.6	203.5

Table 5.2. Measured static flow resistivity σ_0 and Forchheimer's parameter ξ for the linear profile samples.

Flow resistivity has been measured for different samples to investigate its dependence on the sizes of the lateral cavities with different values of d_c. It is determined from the data obtained by the performed measurements in the flow-rig that the presence of the cavities does not significantly modify the flow resistivity in the range of low flow rates. This is shown to be the case when sample thicknesses are the same, or similar to a close approximation for the solid cylinders with simple perforation to that of the pancake absorbers. It is also determined from the data (see Tables 5.1 and 5.2) that as the sample length increases the flow resistivity and Forchheimer's parameter values are reduced. This is the same for both the pancake and profile absorbers, including the solid cylindrical samples containing simple pores (see Figures 5.7 – 5.9. The weak dependence of σ_0 on the presence of the cavities confirms a high permeability contrast for the pancake and profiles. It is seen in Chapter 6 (model comparisons) that the metamaterial structures investigated uses the approach of regarding the absorbers as being a double porosity material. The main pore is treated separately to that of the dead-ends. And since the presence of the cavities shows not to greatly modify the flow resistivity then $d_c = 0$ and $d_c = 1$ mm $-$ 6 mm has no effect on the effective density.

Results presented In Tables 5.1 – 5.2 for all samples show that the structure with the lowest value of σ_0 was the pancake absorber with $d_c = 6$ mm, $d_p = 1$ mm, $r_0 = 4$ mm, and $L = 35$ mm. When pancake

absorbers were built with larger sample lengths the sample with the lowest static flow resistivity value was when the configuration is built with $d_c = 1\ \text{mm}, d_p = 1\ \text{mm}, r_0 = 4\ \text{mm}$ and $L = 60\ \text{mm}$. Forchheimer parameter has its lowest value for the solid cylinder with simple perforation with $L = 90\ \text{mm}$ when comparing the sample data presented in Tables 5.1 – 5.2. A comparison between the pancake and profile structures shows that the Forchheimer's value is lowest for the linear profile sample (see Figure 5.9) with $d_c = 3\ \text{mm}, d_p = 1\ \text{mm}$, main pore $r_0 = 25\ \text{mm}$, end pore $r_0 = 4\ \text{mm}$ and $L = 85\ \text{mm}$. Values of static flow resistivity σ_0 for all measured pancake samples were close within a 10% error margin to that of the theoretical value of 1405 Pa s/m^2 (for when $r_0 = 4\ \text{mm}$). However, σ_0 is much more complex for the profile structures since each plate d_p separated by d_c contains a new value of r_0. The static flow resistivity value was much different for when the linear profile had sample length $L = 42\ \text{mm}$ and $L = 85\ \text{mm}$. The static flow resistivity measured (see Table 5.2 and Figure 5.9) was $\sigma_0 = 1895.7\ \text{Pa s/m}^2$ and $\sigma_0 = 1063.6\ \text{Pa s/m}^2$ for the smaller and larger profiles, respectively. However, the large comparison of σ_0 at low flow rates for the profile structures is seen to be the contrary at high flow rates. When V_f increases to $V_f \leq 0.32\ \text{m/s}$ then the Forchheimer's parameter value $\xi = 258.7\ \text{s/m}$ for $L = 42\ \text{mm}$ and $\xi = 203.5\ \text{s/m}$ for the sample with $L = 85\ \text{mm}$ which only differs by $55.2\ \text{s/m}$ (over the difference in L and d_c which differ by $42\ \text{mm}$ and $2\ \text{mm}$, respectively). The flow resistivity and Forchheimer's parameter values seen in other works, see [41], show that sample thickness had no influence on the materials investigated such as lead shot and gravel. The Forchheimer's value was reported being $\xi = 3.70\ \text{s/m}$ and $\xi = 4.06\ \text{s/m}$ which around two orders of magnitude is lower than values of ξ obtained from the metamaterial structures investigated here, within this work presented in the thesis.

This difference is due to the high flow velocity $U = \frac{V_f}{\phi_p}$ in the sample main pore with radius r_0 thus pancake absorbers have low surface porosity $\phi_p = 6.4 \times 10^{-3}$ and is smaller than the surface porosity from materials investigated by [41]. Forchheimer's parameter values are larger for thinner samples. For samples with $L = 30\ \text{mm} - 35\ \text{mm}$, the values of ξ are between $\xi = 511.1\ \text{s/m}$ and $\xi = 710.6\ \text{s/m}$. For those with sample length where $L = 58\ \text{mm} - 63\ \text{mm}$, the Forchheimer's parameter ranges around $\xi = 297.8\ \text{s/m}$ and $\xi = 360.2\ \text{s/m}$. And finally, for the sample with $L = 90\ \text{mm}$, ξ is measured $\xi = 154.4\ \text{s/m}$. The accuracy of the flow resistivity measurements at high flow rates reduces with increasing flow velocity due to fluctuations in the fluid when performing the measurements (shown by Figures 5.7 – 5.9). This is for when flow rate is increased towards $V_f = 0.03\ \text{m/s}$. The error from the measurements performed in the flow-rig at the University of Salford for obtaining the Forchheimer's parameter values was 10 %. Consequently, the error is approximately doubled when V_f increases from low to high flow rates, i. e. $V_f \leq 0.03\ \text{m/s} \rightarrow V_f \leq 0.3\ \text{m/s}$. The effect of sample length on the Forchheimer's parameter could be identified by an emperical formulation of the sudden contraction zone from some area with cross sectional A, for the fluid between two different cross-sectional areas (see Figure 1, in Astarita and Greco [134]. Following [134], the pressure drop ΔP can be shown to be related due to extra losses which account from different cross sectional areas, where $\Delta P = p_{ent} - P_0$. Pressure at the entrance p_{ent} and P_0 are pressure values some distance upstream and downstream of the sample, where the end effects are negligible. Thus, the change in pressure can be seen to be a combination of pressure losses throughout the sample length, where fluid interacting in the contraction and expansion zones takes place. The pressure drop due to this phenomena can be expressed as $\Delta P = (p_{ent} - p_a) + (p_a - p_b) +$

$(p_b - P_0)$, where p_a and p_b are pressure at the positions a and b inside the pore, where the flow is fully developed. Tube aperture is reduced dramatically such that a sharp decrease is present (beginning at the orifice entrance and exit of the pore). This results in the Δp_1 and Δp_2 which consist of a reversible pressure decrease and increase attributable to Bernoulli effects due to a change in the velocity, where $\Delta p_1 = p_{ent} - p_a$ and $\Delta p_2 = p_b - P_0$. The net effect of these pressure drops can then be assumed zero if $\phi_p \ll 1$ eliminating contraction and expansion losses. Other work which can be seen by Oliveira and Pinho, see [135], investigate pressure drops of sudden expansions. Flow characteristics are studied from these expansion processes that a fluid encounters which are described in [135] by its recirculation length. Since there is a cross sectional area difference the fluid experiences an acceleration and deceleration stage creating recirculation zones which results in irreversible pressure drops. When Reynolds number is considered large enough such that a laminar flow is transformed to a high velocity profile where extra losses occur, the pressure drops are considered to be proportional to V_f^2. See also Figure 4 in [134] and Figure 9 a, in [135]. For the metamaterial structures considered in this thesis the effect of the pressure drop at high Reynolds numbers can be described as the combined attribution of extra losses occuring due to the sudden contraction and expansion zones so that $(p_{ent} - p_a) + (p_b - P_0) = AV_f^2$ (where A is some coefficient). The contributions of the end effects to the measured flow resistivity value could be approximated as,

$$\sigma(V_f) = \frac{\Delta P}{V_f L} \approx \frac{AV_f}{L} + \sigma_{tube}(V_f) \tag{3}$$

where $\sigma_{tube}(V_f) = \frac{(p_a - p_b)}{V_f L}$ is the flow resistivity value in case of infinite tube and no end effects and $\frac{AV_f}{L}$ is the contribution of the extra losses occurring in the regions of sudden contraction and sudden expansion. Comparisons between (2) and (3) allow us to conclude that the excess pressure drops in the flow through sudden contraction and expansion contributes to the gradient of $\sigma(V_f)$, i.e. Forchheimer's parameter. Moreover, the appearance of the sample thickness L in the denominator of the first term in (2) explains the stronger influence of the end effects on the Forchheimer's parameter value of shorter samples. In the case of shorter samples (where approximate sample lengths close to $L = 30\ \mathrm{mm}$ are tested in the flow-rig) the losses due to the contraction and expansion zones would be much less than the larger samples tested ($L = 60\ \mathrm{mm}$). Therefore, the total energy loss occurring from mechanical losses within the structures is less. Consequently, the fluid velocity at the exit pore of the shorter samples is greater compared to the larger samples. This can be observed in Figure 5.8 which shows flows resistivity dependence on flow rate for $0.05\ \mathrm{m/s} \leq V_f \leq 0.25\ \mathrm{m/s}$ where higher $\sigma(V_f)$ gradients for shorter samples are shown. Typical pore Reynolds number achieved by samples in Table 5.1 range $4000 \leq Re \leq 20718$ which is for samples 1, 2, 4, and 5. Reynolds number higher than $Re = 3000$ is well known to be in the range where fluid turbulence occurs, see also Chapter 3, Literature review section 3.3.1, where porous materials in linear and nonlinear regimes including Forchheimer's nonlinearity is discussed. In works by Landau and Lifshitz [136], p.177 the high Reynolds number and resulting turbulent flow regime corresponds from air within the pore which again confirms the effect of flow resistivity dependence for sample thickness. Smaller sample lengths given by samples 1 and 4, in Table 5.1 show larger flow resistivity values than samples 2 and 5 (given also in Table 5.1). In Figure 5.8 an additional plot can be observed for the case of the flow resistivity considering a single pore only

with r_0. From [136] equations (43.4) – (43.5) in implicit form are combined for expressing the dependence of $\sigma_{tube}(V_f)$, and results in the following,

$$\sigma_{tube}(V_f) = \frac{\rho_0 V_f}{4 r_0 \phi_p^2}\left(0.44 \ln\left(\frac{16 r_0^3 \rho_0 V_f}{\eta^2}\sigma_{tube}(V_f)\right) - 0.85\right)^{-2} \tag{4}$$

Equation (4) accounts only for the losses considering a simple pore, and neglecting any losses previously discussed by the effects of contraction and expansion within the structures. This allows for the comparison of the straight cylinderical structures with simple pore only, which has been investigated and shown in section 5.1.1 and section 5.2 (including Figure 5.8 for samples with lengths $L = 30$ mm, $L = 60$ mm and $L = 90$ mm). However, since the samples tested comprised of metamaterial design given by the series of dead-ends, or addition of d_c within the samples, their associated flow resistivity values differ compared to equation (4) due to the influence of end effects. This can be observed in Figure 5.8 where the predicted data showing a tube neglecting any end effects is given, presented by the black solid line and predicted by equation (4). Consequently, flow resistivity of the samples tested with contribution of end effects differ (for different sample thicknesses) and is dependent on the total energy loss associated within the arrangment of contraction, and expansion regions contained within the samples consisting of d_c. Thus, comparing Figure 5.8 a and Figure 5.8 b, shows that for high flow rates, the flow resistivity of the absorbers is significantly larger than that of the cylinders with central perforation. Similarly, this is also the case for the profile absorbers as seen in Figure 5.9 however, the effects of the contraction and expansion zones is not as drastic for the profiles as it is for the pancake absorbers. This is because the contraction and expansion regions are dependent on the value of r_0, built within the design of the structures. For instance, the front and corresponding pores for the pancake absorber consists of $r_0 = 4$ mm, whereas for the profile absorber, the front pore is built with $r_0 = 25$ mm. Moreover, the corresponding orifices have values of $r_0 \gg 4$ mm. This results in the Forchheimer's parameter values of the linear profile structure being measured less when compared to the pancake absorber.

The presence of cavities d_c within the structures (given by Figure 5.8 a) shows that the influence of d_c is weak. At high flow (turbulent regime) the effect of d_c results in a relatively little difference between the data for the samples when $d_c = 1$ mm and $d_c = 3$ mm. However, in the laminar flow regime (see Figure 5.7) the data obtained from the flow resistivity measurements indicates that the flow resistivity is slightly higher as d_c increases from $d_c = 1$ mm to $d_c = 6$ mm. This is seen to be the contrary for sample configurations shown by Figure 5.8 a, for when flow rate is increased towards $V_f \leq 0.25$ m/s in contrast to Figure 5.7 for the effects of d_c when flow rate is $V_f \leq 0.025$ m/s. Markers indicate which value of d_c is measured for the flow resistivity within various sample thicknesses, see Figures 5.7 – 5.9. Contribution of end effects is stronger for shorter samples than for the samples with larger thicknesses L, this is expected as seen from equation (3). Hence, the Forchheimer's parameter value is therefore reduced as sample L, increases for configurations with same r_0 (see Tables 5.1 – 5.2, and Figures 5.8 a, b, and Figure 5.9). It is observed that the presence of the cavities within the pancake structures does not significantly modify the flow resistivity values of the samples. The results of the flow resistivity measurements present a clear indication that it is the sample length L, and pore dimensions r_0, which are the main contributions that affect the sample flow resistivity, and consequently the value of ξ at high flow rates.

5.4. Conclusion

Flow resistivity measurements have been performed for simple perforated, pancake, and profiled structures at low and high flow rates. A straight-line interpolation process has been used for when flow rate is low to obtain the static values of airflow resistivity which is validated against the theoretical values for the samples. Simple perforated structures (solid cylinders containing a single orifice and absent any cavities) is compared against the pancake absorbers to investigate if the lateral cavities affect the flow resistivity of the samples. The cavities show not to significantly affect the values of the measured flow resistivity at low flow rates. When flow rate is deemed laminar (low profile velocity and low Reynolds number) the resistivity values of the structures is therefore invariant, but this is seen to be the contrary for when the flow rate is increased for high flow rates. It is demonstrated that the measured flow resistivity is a function of the sample thickness and becomes significantly reduced as the structure length increases. This means that structures built with shorter sample lengths ($L = 30\ \mathrm{mm}$) are much more highly nonlinear than when the samples are built larger ($L = 60\ \mathrm{mm} - 90\ \mathrm{mm}$). Changes in pressure can be seen to be a combination of pressure losses throughout the sample length, where fluid interacting in contraction and expansion zones takes place. Thus, these losses occurring at the entry, exit, and the internal configuration d_p and d_c results in additional energy losses for the larger samples, due to the extra zones of contraction and expansion regions, compared to the shorter structures. A straight-line interpolation process is used similarly at high flow rates when the flow velocity is increased, and the turbulent regime reached. This process is performed to account for each value of the flow resistivity and to obtain each value of ξ. The dominating nonlinearity for rigid porous media can be described by a Forchheimer's parameter ξ (achieved by measuring the pressure drop along the sample ΔP, at several flow rates with high velocity V_f). Various thicknesses of simple perforated, pancake and profiled absorbers have been built, including different configurations of the cavity thickness, and investigated at several high flow rates in order to obtain the values of ξ. The flow resistivity data including the values of the Forchheimer's nonlinearity parameter is later used in a developed model to predict the performance of the absorbers (accounting for the absorber effective properties to validate the structures at both low and high sound pressure levels, see Chapter 6 which compares the measured and predicted data).

6. Frequency Domain Models and Comparisons

The obtained measured data from the physical testing of the metamaterial structures is given in Chapter 6 with regards to the frequency domain models used for comparison of the absorber performance. Contents of this chapter are as follows: section 6.1 introduces the metamaterial pancake absorbers with scope of using the TMM method. Subsection 6.1.1 presents the TMM model in linear regime and is compared against the measured impedance tube data. Pancake absorbers with lengths close to $L = 30$ mm and $L = 60$ mm consist of three different configurations for each approximate length. A sample containing a single pore is also modelled for reference when comparing the influence of the cavities upon each absorber performance. This is shown in several Figures throughout 6.1.1 where absorption coefficient is plotted as a function of frequency. In subsection 6.1.2 profile absorbers are investigated and the results obtained by the TMM model are compared with the measured impedance tube data. Section 6.2 introduces a new model by considering the absorber effective properties in linear regime, with focus on the metamaterial pancake samples for different sample lengths. In subsection 6.2.1 the first resonance of the absorbers is presented which allows for the determination of the sample performance at low frequencies. And subsection 6.2.2 shows the effect of the mechanical disturbance to the material membrane (plates and rings) of the samples for two different plate thicknesses, and is shown by accelerometer measurements which have been performed in an impedance tube. Section 6.3 generalises the effective properties model to nonlinear regime (pancake absorbers). Subsection 6.3.1 presents a validation of the model which is given by using the measured impedance tube data, obtained from high sound pressure level measurements in a specially modified impedance tube. Lastly, section 6.4. introduces COMSOL, and in 6.4.1 the metamaterial pancake structures are modelled by COMSOL Multiphysics software. The FEM is used to predict the performance of the absorber properties. Subsection 6.4.2 shows a profile computed for its broadband absorptive qualities and compared against the data obtained by the impedance tube. In section 6.4.3 comparisons are given between the various model approaches used and plotted against the physical measured data for both the pancake and profile structures. A conclusion is given in section 6.5.

6.1. Linear Regime – TMM

Chapter 6 aims at presenting the frequency domain models for both the pancake absorber and for the profile structures. The former is presented first where the radius of the main pore r_0 is kept constant throughout the thickness of the structure. A TMM model is used first to predict the performance of the pancake absorber (TMM approach by Dupont et al [3] is introduced previously, see Chapter 3, Literature review). The new TMM model in this work is slightly different and gives similar results to that of [3] in the linear regime. This is presented in this part (section 6.1). A model is later (section 6.2) introduced accounting for the pancake absorber's effective properties, which is new and developed together with the main supervisor. The effective properties model starts with determining the absorber effective properties firstly in linear regime, followed by effective properties in nonlinear regime (where the flow reistivity data obtained directly from the flow resistivity rig measurements based at University of Salford is used in the modelling process, see Chapter 5, flow resistivity measurements). This is shown thoughout

section 6.3. This is necessary since the numerical model is required to use a Forchheimer's nonlinearity parameter when the nonlinearity phenomena are observed in rigid porous materials. The model uses the nonlinear parameter with an iteration procedure, it is later compared to the data obtained by measurements performed directly in a specially modified impedance tube, for high sound pressure levels. Further details of the impedance tube testing in both linear and nonlinear regimes is presented in Chapter 4, Impedance tube measurements of continuous sound. The maximum SPL of the incident sound pressure amplitude achieved by the impedance tube was approximately 160 dB.

6.1.1. Pancake Absorber - TMM

TMM approach is the same for both the pancake absorber and the profile structures. It considers a single cell of the absorber built with a total number of N cells. Time dependence $e^{-i\omega t}$ is used here and throughout Chapter 6. Elementary cell C_j consists of the segment of the main pore with a lateral cavity, the thickness of this is d_c and the segment is constricted by a plate with thickness d_p, see Figure 6.1. Radius of the central pore in C_j is r_j and the cells are counted from the front surface. The radius of the central pore next to C_j, i.e. C_{j+1}, is r_{j+1}.

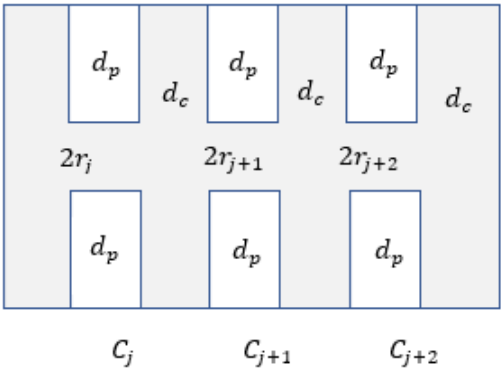

Figure 6.1. Elementary cells C_j, C_{j+1} and C_{j+2} are illustrated along with d_p, d_c and pore radii associated with each cell with r_j, r_{j+1} and r_{j+2}.

The matrix A_j describing sound propagation through cell C_j is the product of three matrices:

$$A_j = A_{1_j} \times A_{2_j} \times A_{con} \tag{1}$$

where A_1 describes the properties of the part with the lateral cavity, A_2 – the part constricted by the plate and A_{con} is constriction matrix, so that $A_{con} = \begin{pmatrix} 1 & 0 \\ 0 & \left(\frac{r_{j+1}}{r_j}\right)^2 \end{pmatrix}$.

For A_{1_j}, wavenumbers k_c , k_p and characteristic impedances Z_c, Z_p of air in the slit and in the cylindrical pore are calculated first. Then effective surface admittance of slit is calculated as,

$$\Gamma_j = \frac{i\,\rho_0 c}{Z_c} \frac{\left(J_1(k_c r_j) - \frac{J_1(k_c R)}{H_1(k_c R)} H_1(k_c r_j)\right)}{\left(J_0(k_c r_j) - \frac{J_1(k_c R)}{H_1(k_c R)} H_0(k_c r_j)\right)}. \tag{2}$$

where J and H correspond to Bessel and Hankel functions of the first kind, respectively. Cavity radius is R. Then, wavenumber in the main pore between the cavities is calculated as,

$$k_{1_j} = k_p \sqrt{1 + \frac{2i\Gamma_j}{C_p k r_j}} \tag{3}$$

and characteristic impedance of air in this segment of the pore is calculated as

$$z_{1_j} = \frac{Z_p}{\sqrt{1 + \frac{2i\Gamma_j}{C_p k r_j}}} \tag{4}$$

Here C_p is effective compressibility of air in the main pore. This follows from equations (5), (6) of [139] assuming porosity of the pore wall $\phi_w = 1$. This gives expression for A_{1_j}

$$A_{1_j} = \begin{pmatrix} \cos(k_{1_j} d_c) & -iz_{1_j} \sin(k_{1_j} d_c) \\ -\frac{i}{z_{1_j}} \sin(k_{1_j} d_c) & \cos(k_{1_j} d_c) \end{pmatrix} \tag{5}$$

For the part of the pore between the rings, the matrix is written as

$$A_{2_j} = \begin{pmatrix} \cos(k_p d_p) & -iZ_p \sin(k_p d_p) \\ -\frac{i}{Z_p} \sin(k_p d_p) & \cos(k_p d_p) \end{pmatrix} \tag{6}$$

The product of the matrices for all cells is then calculated numerically accounting (profiles) or not (pancakes) for the variation of pore radius along the sample thickness:

$$A = A_{ent} \times \prod_{j=1}^{N} A_j \tag{7}$$

where $A_{ent} = \begin{pmatrix} 1 & 0 \\ 0 & \left(\frac{r_1}{R}\right)^2 \end{pmatrix}$ accounts for constriction at the entrance to the main pore, i.e. from tube radius R to the radius of the pore in the first cell r_1. If the open-ended sample is considered, A is multiplied by an expansion matrix, accounting for transition from r_N back to R. Data for the pancake structures having various configurations and different sample lengths are shown in Figures 6.2 – 6.4 for absorbers with lengths close to $L = 30$ mm, and Figures 6.5 – 6.7 around $L = 60$ mm. Figure 6.2 shows absorption coefficient comparison between the absorber measured impedance tube data and the TMM model. Dimensions are $r_0 = 4$ mm $d_p = 1$ mm, $d_c = 1$ mm and $L = 31$ mm. Total number of the dead-ends contained within the absorber configurations is given by N_{de}.

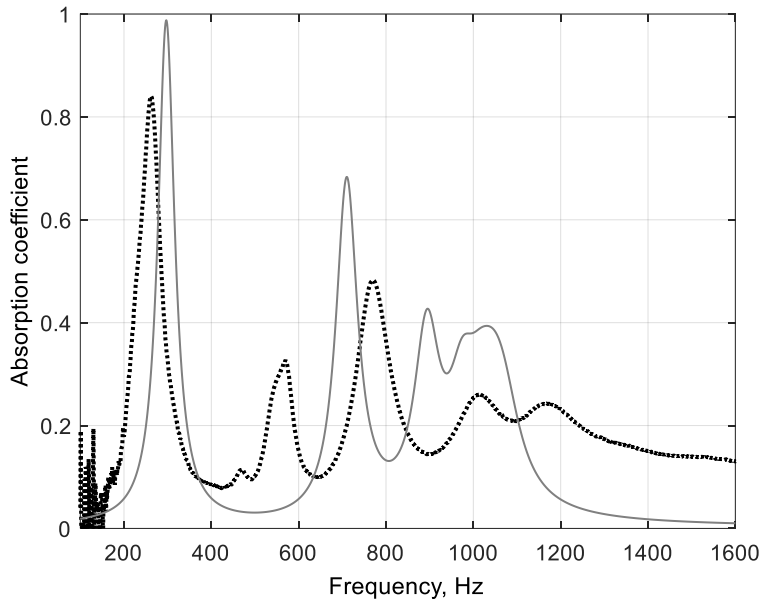

Figure 6.2. Absorption coefficient as a function of frequency showing comparison of TMM prediction vs experimental. Pancake absorber with $r_0 = 4$ mm, $d_p = 1$ mm, $d_c = 1$ mm, $R = 50$ mm, $N_{de} = 16$, and $L = 31$ mm. Data given by impedance tube measurement, represented by black dot, and TMM, solid line.

The first resonance frequency of the pancake absorber (see Figure 6.2) is $f_r = 262\ \mathrm{Hz}$ and has an absorption coefficient value of 0.84 when induced by a sound pressure level of 80 dB, sound source is white noise excitation. The next three absorptive peaks are found at the following frequencies, $f = 570\ \mathrm{Hz}$, $f = 770\ \mathrm{Hz}$, and $f = 1014\ \mathrm{Hz}$. Absorption coefficient values at these frequencies are $\alpha = 0.33$, $\alpha = 0.68$, and $\alpha = 0.26$, respectively. These absorptive values are from data obtained by the impedance tube measurements. Predicted data by the TMM model gives a first resonance peak $f_r = 297\ \mathrm{Hz}$ with an absorption coefficient value $\alpha = 0.99$. Second and third absorptive peaks predicted by the TMM model are at frequencies $f = 710\ \mathrm{Hz}$, and $f = 896\ \mathrm{Hz}$ with $\alpha = 0.68$ and $\alpha = 0.43$ respectively. A further peak is found at $f = 1014\ \mathrm{Hz}$, where absorption coefficient has the value $\alpha = 0.39$.

The measured and predicted absorption coefficient data α for the pancake absorber at peak resonance frequencies f, are presented in Table 6.1. The value of the first resonance peak is seen to differ by $f = 35\ \mathrm{Hz}$ between the measured impedance tube data and the TMM prediction. The difference, partially, is attributed to mounting conditions. Also, TMM model does not account for the end correction, which effectively adds $0.85\, r_0$ to the thickness of the absorber. This correlates with the fact that TMM model predicts higher frequency of the first peak than the measured one. Furthermore, the remainder absorptive peaks differ between the measured and TMM model predictions for α across the frequency spectrum. Performance of the pancake absorber with $d_c = 1\ \mathrm{mm}$ is least effective for low frequency sound absorption compared to when $d_c = 3\ \mathrm{mm}$ and $d_c = 6\ \mathrm{mm}$.

Impedance tube, f (Hz)	**Impedance tube (α)**	**TMM data, f f (Hz)**	**TMM data (α)**
262	0.84	297	0.99
570	0.33	710	0.68
770	0.68	896	0.43
1014	0.26	1014	0.39

Table 6.1. Measured and predicted values of peak absorption coefficient α and frequency f for pancake absorber obtained from impedance tube use and predictions from the TMM model. Pancake absorber $r_0 = 4$ mm, $d_p = 1$ mm, $d_c = 1$ mm and $L = 31$ mm.

Absorption coefficient as a function of frequency is shown by Figure 6.3 for when cavity thickness is extended to $d_c = 3$ mm. Sample thickness is $L = 32$ mm and radius of the external plates and rings remain invarient to pancake absorber from Figure 6.2, i.e. $R = 50\ \text{mm}$ and $d_p = 1$ mm. The measured impedance tube data is given first, which is then followed by the absorption coefficient values predicted by the TMM model. First resonance frequency for pancake sample shown in Figure 6.3 is measured with $f_r = 229\ \text{Hz}$ and absorption coefficient has the value $\alpha = 0.99$. Resonance frequency of the second and third peaks is measured $f = 530\ \text{Hz}$ and $f = 765\ \text{Hz}$ where values $\alpha = 0.71$ and $\alpha = 0.77$, respectively. Fourth and fifth absorptive peaks are at $f = 1027\ \text{Hz}$ and $f = 1195\ \text{Hz}$ and $\alpha = 0.45$ and $\alpha = 0.32$ for the fourth and fifth peak absorption values, respectively. Predicted first resonance frequency computed by the TMM model is $f_r = 232\ \text{Hz}$ with a peak value $\alpha = 0.90$. The second and third absorptive peaks are at frequencies $f = 604\ \text{Hz}$ and $f = 816\ \text{Hz}$ with absorption coefficient values $\alpha = 1.00$ and $\alpha = 0.89$ respectively. The fourth and fifth absorptive peaks are at frequencies $f = 928\ \text{Hz}$ and $f = 988\ \text{Hz}$ with absorption coefficient values $\alpha = 0.73$ and $\alpha = 0.62$ respectively.

A comparison of the peak absorption coefficient data in relation to Figure 6.3 is presented in Table 6.2. For pancake absorbers measured with approximate sample lengths close to $L = 30\ \text{mm}$, the first resonance frequency f_r is matched with better agreement between the experimental and theoretical data. For instance, f_r differs only $f = 3\ \text{Hz}$ from the predicted data by the TMM model when compared to the measured impedance tube data. Increasing cavity thicknesses within the pancake structure (where $d_c = 3\ \text{mm}$) allows for improved matching of other absorptive peaks, compared to the data presented by Figure 6.2 and Table 6.1 and when $d_c = 1\ \text{mm}$. Compared to the absorber (when $d_c = 1\ \text{mm}$), the structure with increased cavity depth ($d_c = 3\ \text{mm}$), results in the first resonance frequency f_r reduced by $f = 33\ \text{Hz}$ and the second resonance peak similarly is reduced further, by $f = 40\ \text{Hz}$, compared to $d_c = 1\ \text{mm}$. Measured and predicted values obtained from impedance tube and TMM model for the pancake absorber with $r_0 = 8\ \text{mm}$, $d_c = 3\ \text{mm}$ and $L = 32\ \text{mm}$ are presented in Table 6.2 showing peak values of α at resonance frequency f.

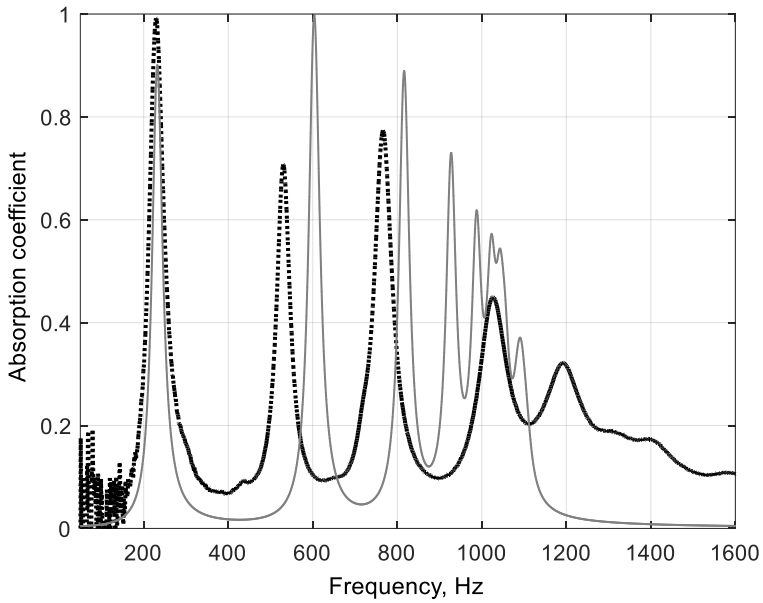

Figure 6.3. Absorption coefficient as a function of frequency showing comparison of TMM prediction vs experimental. Pancake absorber with $r_0 = 4$ mm, $d_p = 1$ mm, $d_c = 3$ mm, $R = 50$ mm, $N_{de} = 8$, and $L = 32$ mm. Data given by impedance tube measurement, represented by black dot, and TMM, solid line.

Impedance tube, f (Hz)	**Impedance tube (α)**	**TMM data, f f (Hz)**	**TMM data (α)**
229	0.99	232	0.90
530	0.71	604	1.00
765	0.77	816	0.89
1027	0.45	928	0.73
1195	0.32	988	0.62

Table 6.2. Measured and predicted values of peak absorption coefficient α and frequency f for pancake absorber obtained from impedance tube use and prediction from the TMM model. Pancake absorber with $r_0 = 4$ mm, $d_p = 1$ mm, $d_c = 3$ mm, $R = 50$ mm, and $L = 32$ mm.

The absorption coefficient data for the absorber with cavity depth increased further to $d_c = 6$ mm is shown by Figure 6.4. Sample length is $L = 35$ mm and is only slightly larger than previous pancake absorbers of Figures 6.2 – 6.3, where sample has additional $L = 4$ mm from Figure 6.2 and additional $L = 3$ mm from that of Figure 6.3. Dimensions of external plates and rings with radius R, including perforation r_0 is the same as pancake samples of Figures 6.2 – 6.3. Measured impedance tube data is as follows; first resonance frequency of the pancake absorber is $f_r = 223$ Hz and has an absorption coefficient value $\alpha = 0.99$ when induced by SPL around 80 dB, sound source is white noise excitation. Other absorptive peaks are found at the following frequencies, $f = 558$ Hz, $f = 775$ Hz, 1044 Hz, and $f = 1200$ Hz. The absorption coefficient values at these frequencies are respectively $\alpha = 0.85$, $\alpha = 0.83$, $\alpha = 0.59$, and $\alpha = 0.41$. Predicted data by the TMM model gives the first resonance peak $f_r = 200$ Hz and absorption coefficient value $\alpha = 0.99$. The second and third absorptive peaks predicted by the TMM model are at frequencies $f = 539$ Hz and $f = 757$ Hz where absorption coefficient values are $\alpha = 0.99$ and $\alpha = 0.99$, respectively. Further peaks are predicted being at $f = 882$ Hz, $f = 951$ Hz, and $f = 1052$ Hz. The associated frequency absorption coefficient data is $\alpha = 0.94, \alpha = 0.88$ and $\alpha = 0.56$. Measured and predicted values of α for the pancake absorber at peak resonance frequency f, are presented also in Table 6.3. The value of the first resonance peak is seen to differ by only $f = 23$ Hz between the measured impedance tube data and the computed TMM prediction. However, for this

sample the predicted frequency of the first peak is lower than the measured one. We attribute this partially to the fact that the absorber with larger cavities is less stable and prone to variations in thickness during the mounting process. Moreover, the influence of the end correction is smaller for this sample as it is a smaller proportion to its thickness. Absorption coefficient is of larger value for the measured data where $\alpha = 0.99$ (from direct measurement in the impedance tube) and $\alpha = 0.86$ by the prediction from the TMM.

Pancake absorber built with $d_c = 6\ \mathrm{mm}$ has a better agreement between the data by the TMM model and the experimental data (for the first three absorptive peaks) than any other pancake sample measured with lengths close to $L = 30\ \mathrm{mm}$. Second and third absorptive peaks only differ by $f = 19\ \mathrm{Hz}$ and $f = 18\ \mathrm{Hz}$ for the former and latter respectively, see Table 6.3. The absorption coefficient values are also largest when the configuration contains $d_c = 6\ \mathrm{mm}$. The TMM model, however, predicts two additional absorptive peaks which is not produced from the measured impedance tube data and is between $f = 800\ \mathrm{Hz}$ – 1000 Hz. Absorption coefficient is largest for the first resonance frequency f_r only, for the measured data compared to the TMM. However, this is seen to be the contrary for values of α at other resonance frequencies after f_r, where α is predicted with larger values by the TMM compared to the measured impedance tube data. Values of α and resonance frequency f can be seen by Figure 6.4 and Table 6.3.

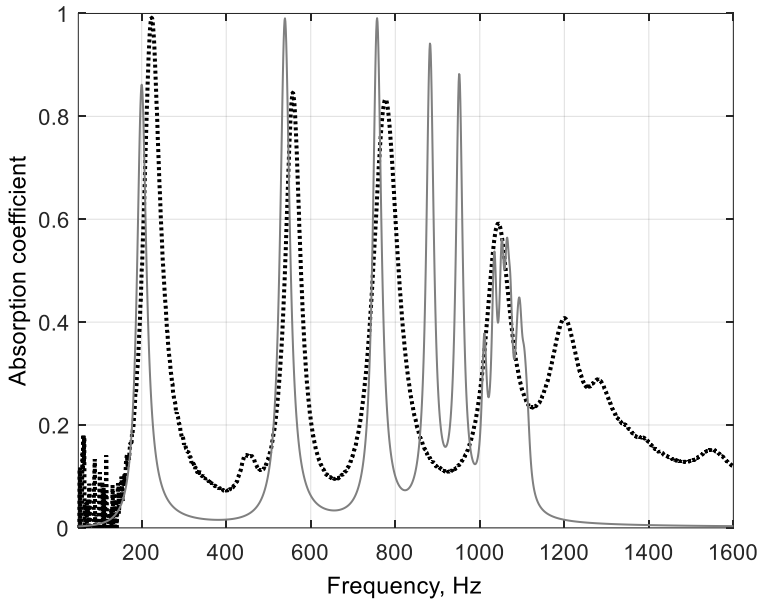

Figure 6.4. Absorption coefficient as a function of frequency showing comparison of TMM prediction vs experimental. Pancake absorber with $r_0 = 4$ mm, $d_p = 1$ mm, $d_c = 6$ mm, $R = 50$ mm, $N_{de} = 5$, and $L = 35$ mm. Data given by impedance tube measurement, represented by black dot, and TMM, solid line.

Impedance tube, f (Hz)	**Impedance tube (α)**	**TMM data, f f (Hz)**	**TMM data (α)**
223	0.99	200	0.86
558	0.85	539	0.99
775	0.83	757	0.99
1044	0.59	882	0.94
1200	0.41	951	0.88

Table 6.3. Measured and predicted values of peak absorption coefficient α and frequency f for pancake absorber obtained from impedance tube use and prediction from the TMM model. Pancake absorber with $r_0 = 4$ mm, $d_p = 1$ mm, $d_c = 6$ mm, $R = 50$ mm, and $L = 35$ mm.

It should be noted, that for all samples considered, both measurements and TMM show a decrease in α for frequencies higher than $f = 1200$ Hz. This happens despite the fact that the thicknesses of the elementary cell for three samples are different. The wavelength in air at $f = 1200$ Hz is 29 cm. The quarter wavelength resonance of the cavity slits of length 48 mm is achieved at the frequency $f = 1700$ Hz (if the same wave speed in the slit as in free air is assumed). Thus, low sound absorption coefficient at higher frequencies is manifestation of the bandgap due to this quarter wavelength resonance. Of course, the bandgap is not complete due to losses in the system.

This completes the pancake structures with various values of d_c and having approximate sample thicknesses close to $L = 30$ mm. Larger pancake absorber lengths have been measured for their performance and shown by Figures 6.5 – 6.7. The sample thicknesses range between $L = 60$ mm and $L = 63$ mm. Absorption coefficient as a function of frequency is given by Figure 6.5 for the pancake absorber with configuration $r_0 = 4$ mm, $R = 50$ mm, $d_p = 1$ mm, $d_c = 1$ mm and $L = 62$ mm. The measured impedance tube data of the first resonance frequency is measured $f_r = 144$ Hz and absorption coefficient has the value $\alpha = 0.89$. Resonance frequency for the second and third peaks is $f = 396$ Hz and $f = 574$ Hz where $\alpha = 0.42$ and $\alpha = 0.54$, respectively. Fourth and fifth absorptive peaks are at $f = 769$ Hz and $f = 895$ Hz and $\alpha = 0.36$ and $\alpha = 0.30$ for the fourth and fifth peak absorption values, respectively. The predicted first resonance frequency computed by the TMM model is $f_r = 151$ Hz with a peak value $\alpha = 0.90$. Second and third absorptive peaks are at frequencies $f = 430$ Hz , and $f = 637$ Hz with absorption coefficient values $\alpha = 0.72$ and $\alpha = 0.53$ respectively. The fourth and fifth absorptive peaks are at $f = 774$ Hz and $f = 867$ Hz with absorption coefficient $\alpha = 0.39$ and $\alpha = 0.34$. A comparison of the peak absorption coefficient data referring to the data presented by Figure 6.5 is presented also in Table 6.4. Only the first five absorptive peak values have been described, where other values of α at the resonance frequency can be observed in Table 6.4. This is the case also for Table 6.5 and Table 6.6 from other pancake samples which contain all absorption coefficient data for peak values at resonance frequency f.

Figure 6.5 shows first resonance frequency f_r is matched with a better agreement between the experimental and theoretical data as opposed to other pancakes with approximate lengths close to $L = 30$ mm. Resonance frequency for the first peak f_r differs only $f = 7$ Hz from the predicted data by the TMM model when compared to the measured impedance tube data. The second and third resonance frequencies differ $f = 34$ Hz and $f = 63$ Hz respectively, between the measured and predicted data. Absorption coefficient for the first resonance frequency differs only slightly where $\alpha = 0.89$ for the measured data and $\alpha = 0.90$ by the TMM data. Absorption coefficient is almost always predicted with a larger value of α compared to the measured data, see Table 6.4 for comparison of absorptive peak and resonance frequency data. Only exception when a lower value of α for the TMM exists is for the third resonance frequency, where $\alpha = 0.54$ and $\alpha = 0.53$ for the measured and predicted values, respectively.

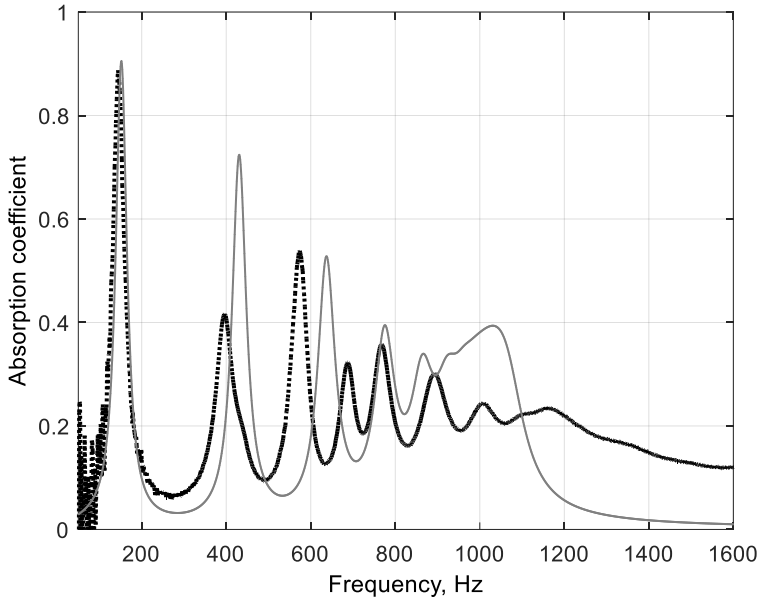

Figure 6.5 Absorption coefficient as a function of frequency showing comparison of TMM prediction vs experimental. Pancake absorber with $r_0 = 4$ mm, $d_p = 1$ mm, $d_c = 1$ mm, $R = 50$ mm, $N_{de} = 30$, and $L = 62$ mm. Data given by impedance tube measurement, represented by black dot, and TMM, solid line.

Impedance tube, f (Hz)	**Impedance tube (α)**	**TMM data, f f (Hz)**	**TMM data (α)**
144	0.89	151	0.90
396	0.42	430	0.72
574	0.54	637	0.53
769	0.36	774	0.39
895	0.30	867	0.34
1005	0.24	1016	0.39

Table 6.4. Measured and predicted values of peak absorption coefficient α and frequency f for pancake absorber obtained from impedance tube use and prediction from the TMM model. Pancake absorber with $r_0 = 4$ mm, $d_p = 1$ mm, $d_c = 1$ mm, $R = 50$ mm, and $L = 62$ mm.

It can be seen from Figure 6.5 that the drastic reduction of α is predicted and observed in approximately the same frequency range, despite the sample length being doubled. This confirms the previous statement that this reduction is the result of the quarter wavelength resonance of the cavities. Figure 6.6 shows absorption coefficient as a function of frequency when d_c is extended. The pancake absorber is comprised with cavities $d_c = 3$ mm and sample thickness around $L = 60$ mm. Radius of the external plates and rings is $R = 50$ mm and plate thickness $d_p = 1$ mm. The measured impedance tube data is presented followed by the absorption coefficient values predicted by the TMM model. First resonance frequency for the pancake given by Figure 6.6 is measured $f_r = 135$ Hz and absorption coefficient has the value $\alpha = 0.99$. Resonance frequency of the second and third peaks is $f = 364$ Hz and $f = 647$ Hz where $\alpha = 0.56$ and $\alpha = 0.57$, respectively. Fourth and fifth absorptive peaks are at $f = 750$ Hz and $f = 902$ Hz and $\alpha = 0.68$ and $\alpha = 0.54$, for the fourth and fifth peak absorption values, respectively. The first resonance frequency predicted by the TMM model is $f_r = 126$ Hz with a peak value $\alpha = 0.98$. The second and third absorptive peaks are at frequencies $f = 363$ Hz and $f = 556$ Hz, with absorption coefficient values $\alpha = 0.99$ and $\alpha = 0.91$ respectively. The fourth and fifth absorptive peaks are at frequencies $f = 701$ Hz and $f = 804$ Hz with absorption coefficient values $\alpha = 0.81$ and $\alpha = 0.70$ respectively. Comparison of the peak absorption coefficient data in relation to Figure 6.6 is presented in

Table 6.5. The predicted data by the TMM model matches reasonably well for the first two resonance frequencies when compared to the measured data, see Figure 6.6

Absorption coefficient is predicted of larger value for the second resonance frequency compared to the data obtained from the pancake impedance tube measurement. However, absorptive peak value for f_r is in good agreement, where $\alpha = 0.99$ and $\alpha = 0.98$, for the measured and TMM data. Second resonance frequency differs only by $f = 1\,\text{Hz}$. Absorption coefficient values of the measured and predicted data shows a disagreement between the two at the second resonance frequency, see Figure 6.6 which shows the measured data with $\alpha = 0.56$, and the TMM data as $\alpha = 0.99$. A bandgap appears to create a discrepancy after the second resonance frequency and is shown to occur in the frequency region between $f = 400\,\text{Hz}$ and $f = 530\,\text{Hz}$. The band gap exists due to mechanical resonance of the sample frame and consequently creates a disagreement at other resonance frequencies afterward the second resonance frequency between the experimental and predicted data, see Figure 6.6. Measured and predicted values obtained from the impedance tube and TMM model for the absorber with $r_0 = 8\,\text{mm}$, $d_c = 3\,\text{mm}$ and $L = 60\,\text{mm}$ are presented in Table 6.5 showing peak values of α at resonance frequency f.

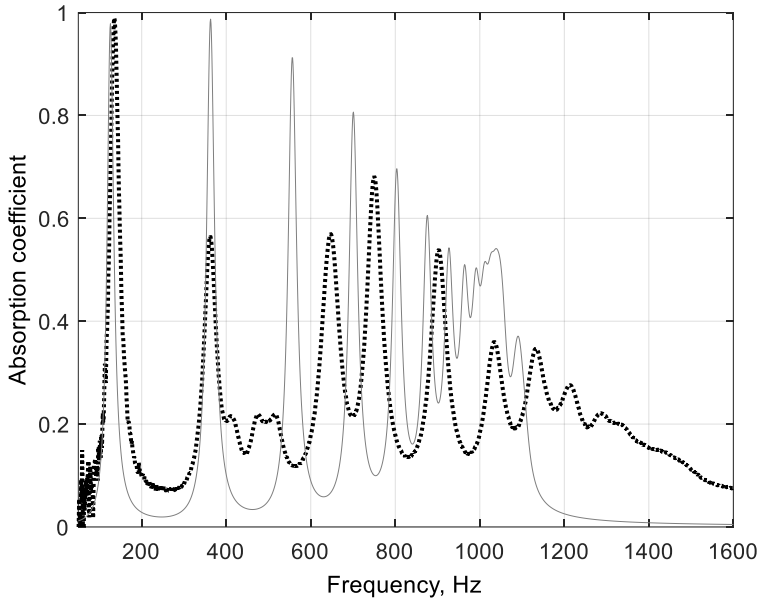

Figure 6.6 Absorption coefficient as a function of frequency showing comparison of TMM prediction vs Experimental. Pancake absorber with $r_0 = 4$ mm, $d_p = 1$ mm, $d_c = 3$ mm, $R = 50$ mm, $N_{de} = 15$, and $L = 60$ mm. Data given by impedance tube measurement, represented by black dot, and TMM, solid line.

Impedance tube, f (Hz)	**Impedance tube (α)**	**TMM data, f f (Hz)**	**TMM data (α)**
135	0.99	126	0.98
364	0.56	363	0.99
647	0.57	556	0.91
750	0.68	701	0.81
902	0.54	804	0.70
1034	0.36	875	0.60
1134	0.35	927	0.54

Table 6.5. Measured and predicted values of peak absorption coefficient α and frequency f for pancake absorber obtained from impedance tube use and prediction from the TMM model. Pancake absorber with $r_0 = 4$ mm, $d_p = 1$ mm, $d_c = 3$ mm, $R = 50$ mm, and $L = 60$ mm.

Pancake absorber data with $r_0 = 4$ mm, $R = 50$ mm, $d_p = 1$ mm, $d_c = 6$ mm and $L = 63$ mm is shown by Figure 6.7. First resonance frequency is $f_r = 135$ Hz and $\alpha = 1.0$ when induced by a sound pressure level of 80 dB, sound source is white noise excitation. The next four successive absorptive peaks are found at the following frequencies, $f = 348$ Hz, $f = 412$ Hz, $f = 524$ Hz, and $f = 592$ Hz. The absorption coefficient values at these frequencies are $\alpha = 0.64$, $\alpha = 0.27$, $\alpha = 0.71$, and $\alpha = 0.72$, respectively. Predicted data by the TMM model gives a first resonance peak to be at $f_r = 112$ Hz with an absorption coefficient value $\alpha = 0.95$. The second and third absorptive peaks predicted by the TMM model are $f = 327$ Hz and $f = 510$ Hz, with absorption coefficient values $\alpha = 1.00$ and $\alpha = 0.97$, respectively. Further absorptive peaks are found to be at $f = 653$ Hz and $f = 760$ Hz with absorption coefficient $\alpha = 0.92$ and $\alpha = 0.86$. The measured and predicted absorption coefficient data α for the pancake absorber at peak resonance frequency f, are presented in Table 6.6 with additional absorptive peak data at other resonance frequencies. Similarly, like the pancake of Figure 6.6 the first resonance frequency from the impedance tube data for pancake of Figure 6.7 is measured $f_r = 135$ Hz, moreover, $\alpha = 1.00$. The TMM predicted f_r to be lower at $f_r = 112$ Hz, meaning that a discrepancy $f = 23$ Hz occurs between the impedance tube data and predicted TMM data. The TMM predicts consistently a reduction of the first resonance peak frequency, as the cavity depth d_c increases from $d_c = 1$ mm $\rightarrow 6$ mm. However, this consistency is not observed in experiment. The absorption coefficient is measured with a slightly larger value for the experimental data when compared to the predicted data (where $\alpha = 1.00$ and $\alpha = 0.95$ respectively, for the former and latter).

Absorptive peak value at the second resonance frequency differs from the predicted TMM value due to a disturbance occurring from mechanical resonance of the plates (see also the accelerometer measurements given in Chapter 4, sections 4.3.1 and 6.2.2 of this Chapter). The number of absorptive peaks at their associated resonance frequency is increased further, for when the pancake structure is close to $L = 60$ mm with $d_c = 6$ mm, compared to when $d_c = 1$ mm and $d_c = 3$ mm. Measured and predicted values obtained from the impedance tube and TMM model for the pancake absorber with $r_0 = 8$ mm, $d_c = 6$ mm and $L = 63$ mm are presented in Table 6.6 showing the peak values of α at resonance frequency f. Largest peak values of α for pancake structures built with sample lengths to $L = 60$ mm exist for when $d_c = 6$ mm, compared to Figure 6.5 where $d_c = 1$ mm and Figure 6.6 where $d_c = 3$ mm.

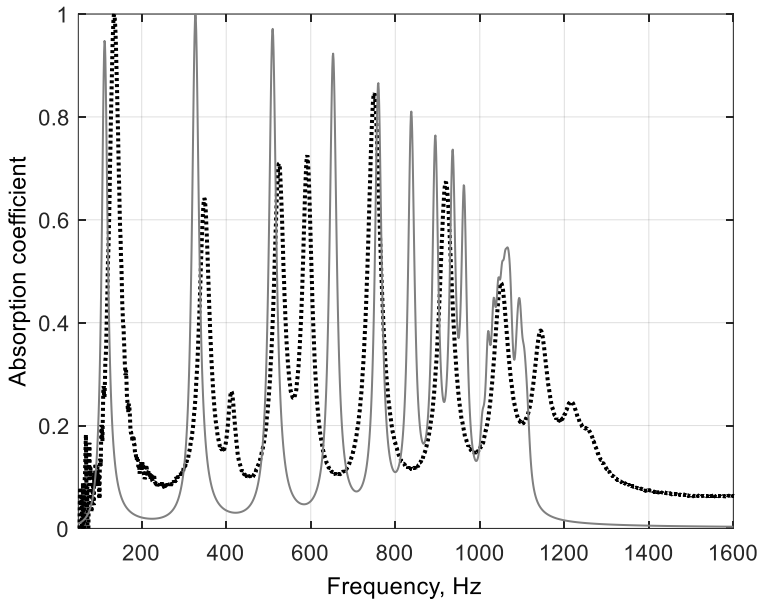

Figure 6.7. Absorption coefficient as a function of frequency showing comparison of TMM prediction vs experimental. Pancake absorber with $r_0 = 4$ mm, $d_p = 1$ mm, $d_c = 6$ mm, $R = 50$ mm, $N_{de} = 9$, and $L = 63$ mm. Data given by impedance tube measurement, represented by black dot, and TMM, solid line.

Impedance tube, f (Hz)	**Impedance tube (α)**	**TMM data, f f (Hz)**	**TMM data (α)**
135	1.00	112	0.95
348	0.64	327	1.00
412	0.27	510	0.97
524	0.71	653	0.92
592	0.72	760	0.86
750	0.84	838	0.81
919	0.67	895	0.76
1050	0.48	936	0.74
1143	0.38	962	0.67
1215	0.25	1063	0.54

Table 6.6. Measured and predicted values of peak absorption coefficient α and frequency f for pancake absorber obtained from impedance tube use and prediction from the TMM model. Pancake absorber with $r_0 = 4$ mm, $d_p = 1$ mm, $d_c = 6$ mm, $R = 50$ mm, and $L = 63$ mm.

Comparisons of pancake absorbers consisting of same configurations but when sample length is approximately doubled is discussed. For instance, Figure 6.5 uses the same pancake configuration to that of the pancake configuration associated with Figure 6.2, with exception of the structure thickness. The geometrical parameters are identical such as the main perforation, radius of the plates and plate thickness including the cavity depths. Sample length referring to Figure 6.5 is nearly doubled to that of the pancake length given by Figure 6.2 (where $L = 31$ mm and $L = 62$ mm). This results in f_r being reduced to $f_r = 144$ Hz (which is $f = 118$ Hz reduction in f for the pancake with $d_c = 1$ mm and $L = 62$ mm, compared to when $d_c = 1$ and $L = 31$ mm). Measured absorption coefficient values at f_r and at other frequencies becomes slightly larger, thus, performance of the pancake absorber is improved with $d_c = 1$ mm and $L = 62$ mm, compared to the pancake with $d_c = 1$ mm and $L = 31$ mm. The pancake data given by Figures 6.3 and 6.6 are for when the samples have approximate length $L = 32$ mm and $L = 60$ mm respectively, configured with $d_c = 3$ mm. Other geometrical parameters remain the same such as r_0, R and d_p. When sample length is nearly doubled then f_r from the measured data is reduced to lower frequency $f_r = 135$ Hz (reduction of $f = 94$ Hz for sample with $L = 60$ mm from that of pancake

with $L = 32$ mm). The peak absorption coefficient value remains the same at f_r and $\alpha = 0.99$. Second and third resonance frequencies are reduced from the measured data by $f = 166$ Hz and $f = 118$ Hz respectively. Additional absorptive peaks exist for the pancakes with $L = 60$ mm. The data showing values of α and f for pancake absorbers with $d_c = 3$ mm is shown by Table 6.2 and Table 6.4. Pancakes given by Figure 6.4 and Figure 6.7 are configured with cavity with $d_c = 6$ mm and $L = 35$ mm and $L = 63$ mm, respectively. In this case, it results in f_r being reduced to $f_r = 135$ Hz (which equates to a reduction in frequency $f = 88$ Hz for the pancake with $d_c = 6$ mm and $L = 60$ mm, compared to when the pancake has $d_c = 3$ mm and $L = 31$ mm). The measured absorption coefficient value at f_r for sample with $L = 31$ mm is $\alpha = 0.99$, and the absorption coefficient is $\alpha = 1.00$ for when $L = 60$ mm. Pancake absorber with a configuration $d_c = 6$ mm also has same value of f_r to when its built with $d_c = 3$ mm, and close to $L = 60$ mm. Moreover, other resonance frequencies after the first resonance frequency are also reduced for the pancake absorber with $d_c = 6$ mm and $L = 60$ mm as opposed to when $d_c = 3$ mm and sample length close to $L = 60$ mm.

This means that keeping the same value of cavity depth d_c and increasing the sample length to nearly double has no, or little effect on the value of α at the first resonance frequency f_r. However, doubling the sample length from $L = 30$ mm to $L = 60$ mm does reduce the first peak frequency f_r. Furthermore, the doubling of $d_c = 3$ mm to $d_c = 6$ mm for the same approximate sample lengths close to $L = 60$ mm, does not modify the value of α for the first resonance frequency. All other resonance frequencies are however, reduced to lower frequency and results in additional total number of the resonance frequency being increased. Figures 6.8 – 6.10 shows α as a function of frequency for when the samples have different sample length (around $L = 30$ mm and $L = 60$ mm) but have the same values of d_c. It is clear from Figures 6.8 – 6.10 that the frequency range where α is dramatically reduced does not depend on d_c or L. Pancake absorbers with sample lengths that are similar but having various d_c is shown by Figure 6.11 for length close to $L = 30$ mm and Figure 6.12 at nearly $L = 60$ mm. The first resonance frequency for the pancake with $d_c = 1$ mm is $f_r = 262$ Hz and $\alpha = 0.84$. First resonance frequency is reduced slightly lower to $f_r = 229$ Hz and α increases to $\alpha = 0.99$ for $d_c = 3$ mm. Furthermore, when the pancake structure is built with $d_c = 6$ mm then f_r is reduced slightly further still to $f_r = 223$ Hz. Absorption coefficient value α remains the same value to when $d_c = 3$ mm, so that $\alpha = 0.99$ for the pancake built with $d_c = 6$ mm.

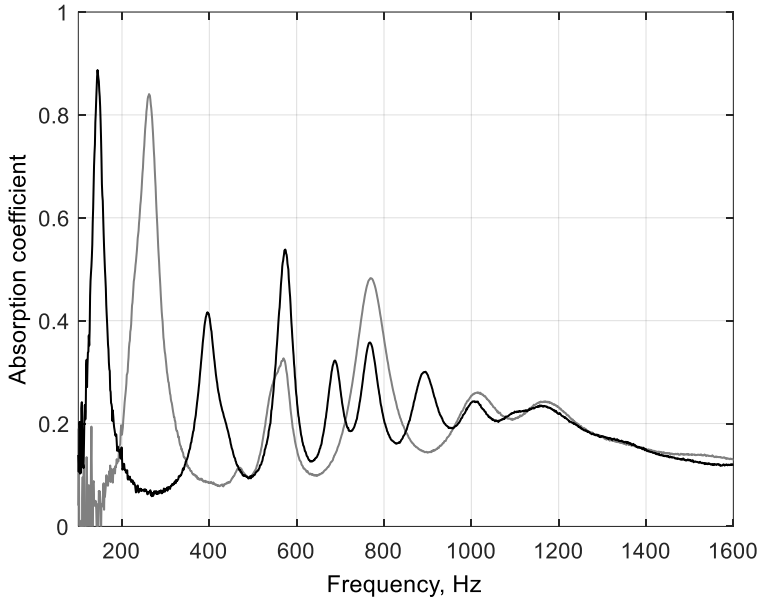

Figure 6.8. Absorption coefficient as a function of frequency for pancake absorbers with sample thicknesses close to $L = 30$ mm and $L = 60$ mm. Pancakes have $d_c = 1$ mm. Pancake with $L = 30$ mm, grey data and pancake with $L = 60$ mm, black data. $R = 50$ mm.

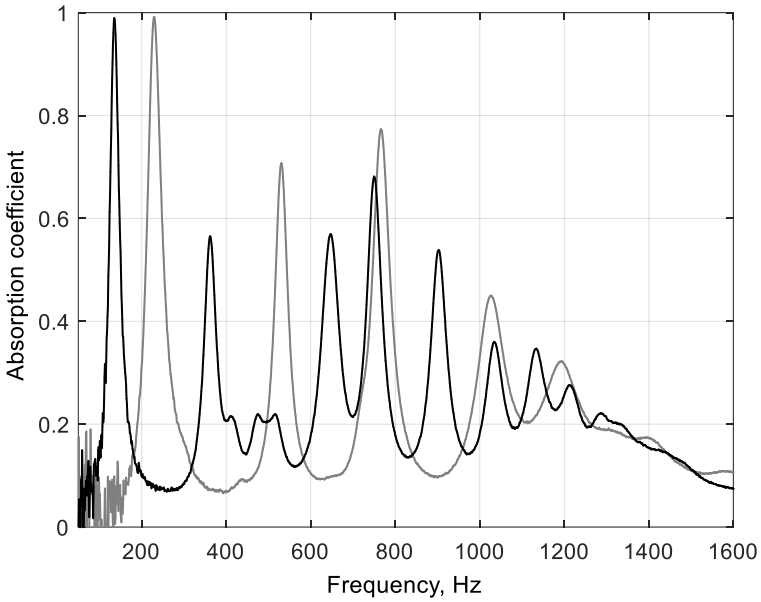

Figure 6.9. Absorption coefficient as a function of frequency for pancake absorbers with sample thicknesses close to $L = 30$ mm and $L = 60$ mm. Pancakes have $d_c = 3$ mm. Pancake with $L = 30$ mm, grey data, and pancake with $L = 60$ mm, black data. $R = 50$ mm.

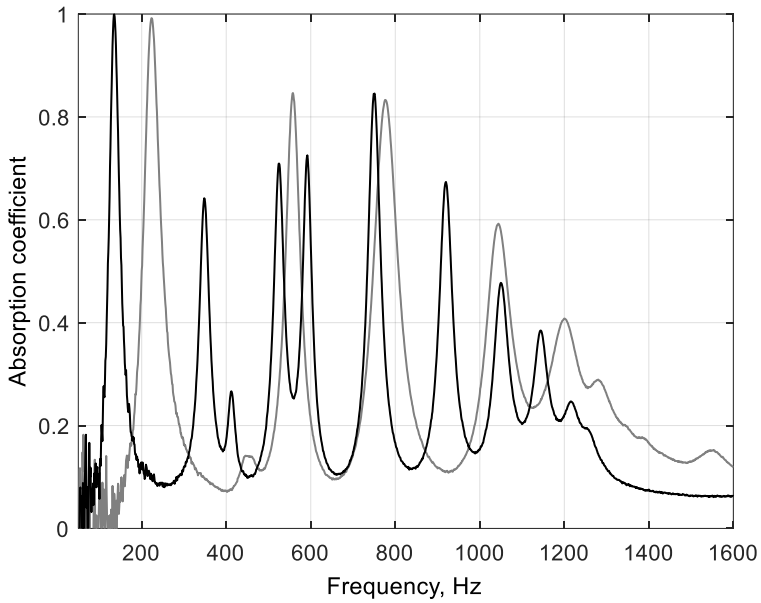

Figure 6.10. Absorption coefficient as a function of frequency for pancake absorbers with sample thicknesses close to $L = 30$ mm and $L = 60$ mm. Pancakes have $d_c = 6$ mm. Pancake with $L = 30$ mm, grey data, and pancake with $L = 60$ mm, black data. $R = 50$ mm.

As the cavity thickness is increased from $d_c = 1$ mm to $d_c = 6$ mm the first resonance frequency is reduced but α is the same value when $d_c = 3$ mm and $d_c = 6$ mm. Increasing d_c in the samples with L close to $L = 30$ mm also increases the value of α at other resonance frequencies for the pancake absorbers, and a maximum value of α is reached for when $d_c = 6$ mm. Absorption coefficient data at the corresponding resonance frequency can be seen for the pancake samples for sample lengths close to $L = 30$ mm, by the data shown in Tables 6.1 – 6.3. Similarly, like Figure 6.11 showing performance of the pancake absorbers with various d_c, Figure 6.12 shows also an identical trend of the absorption coefficient data for when $d_c = 1$ mm, $d_c = 3$ mm and $d_c = 6$ mm. The first resonance frequency for the pancake with $d_c = 1$ mm and $L = 62$ mm is $f_r = 144$ Hz with $\alpha = 0.84$. For the pancake built $d_c = 3$ mm the measured $f_r = 135$ Hz and therefore reduced $f = 9$ Hz compared to $d_c = 1$ mm. Furthermore, α increases to $\alpha = 0.99$ for when $d_c = 3$ mm from when $d_c = 1$ mm. First resonance frequency remains unchanged when cavity thickness is increased to $d_c = 6$ mm from when $d_c = 3$ mm. Absorption coefficient $\alpha = 1.00$ at f_r and α is largest at other frequencies for when $d_c = 6$ mm.

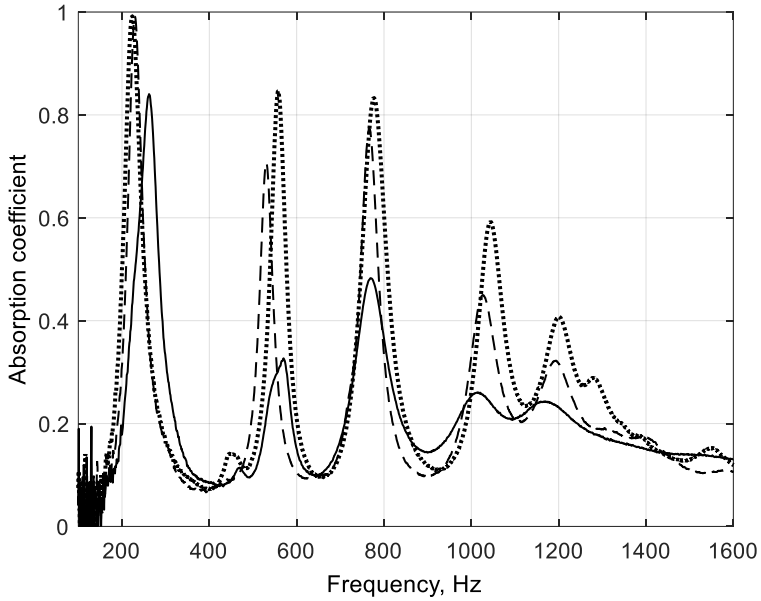

Figure 6.11. Absorption coefficient as a function of frequency for sample thicknesses close to $L = 30$ mm having various values of cavity depths. Pancake with $d_c = 1$ mm, solid line, pancake with $d_c = 3$ mm, dash line, and Pancake with $d_c = 6$ mm, dot. $R = 50$ mm.

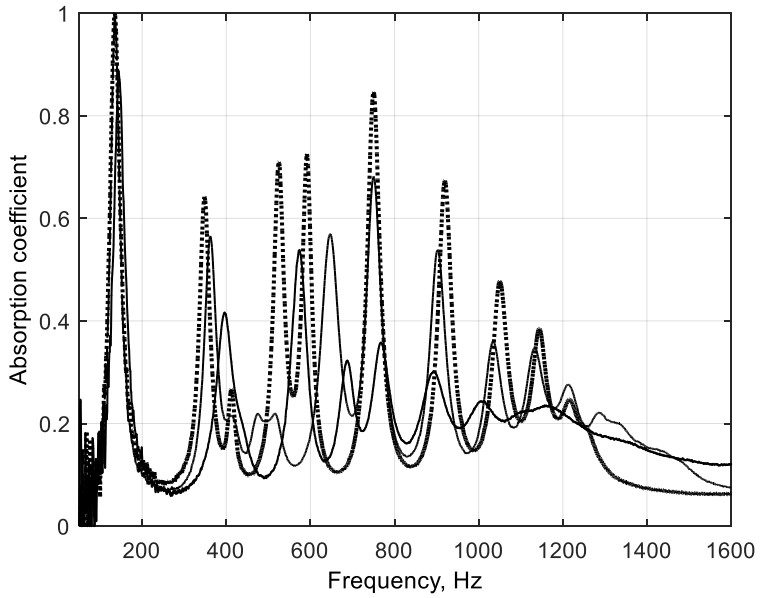

Figure 6.12. Absorption coefficient as a function of frequency for pancake absorbers with sample thicknesses close to $L = 60$ mm consisting of various values of cavity depths. Pancake with $d_c = 1$ mm, solid line, pancake with $d_c = 3$ mm, dash line, and Pancake with $d_c = 6$ mm, dot. $R = 50$ mm.

6.1.2. Profile Absorbers (Black Hole Effect) – TMM

Profile absorbers for both linear and exponential configurations are compared against the TMM predictions, given by Figures 6.13 – 6.17. The linear profile absorber data is presented in Figures 6.13 – 6.15 followed by the exponential profiles, see Figures 6.16 – 6.17. All the measured data obtained by impedance tube experiments are for when the profiles are rigidly backed and a standard two-microphone method is used. Linear and exponential samples are built with metallic plates (dimensions of the absorbers can be seen in Chapter 4, see Table 4.1). Measured impedance tube data and the

computational predictions are presented for linear regime only, where the measured data is given for amplitudes ranging 70 dB and 80 dB. The first five measured absorptive peaks, of impedance tube data and that predicted by the TMM, are given for each of the profile absorbers. Absorptive peaks associated for the profiles for the remainder of the frequency spectrum after the fifth absorptive peak, for linear and exponential profiles can be seen by the data presented in Tables 6.7 – 6.11, where the linear profile data is given by Tables 6.7 – 6.9 and the exponential profile absorption coefficient data is presented in Tables 6.9 – 6.11. Data in Figure 6.13 shows absorption coefficient as a function of frequency for the linear profile (for the measured and TMM data) and for when main pore opening is $2r = 30$ mm, $d_p = 1$ mm, $d_c = 3$ mm and $L = 60$ mm. The measured impedance tube data is given first, which is then followed by the α values predicted by the TMM model. In this case, the first resonace frequency is measured $f_r = 230\ \mathrm{Hz}$ and absorption coefficient has the value $\alpha = 0.80$. The second and third frequency data is measured $f = 294\ \mathrm{Hz}$ and $f = 430\ \mathrm{Hz}$ with $\alpha = 0.90$ and $\alpha = 0.90$, respectively. Fourth and fifth absorptive peaks are $f = 525\ \mathrm{Hz}$ and $f = 668\ \mathrm{Hz}$ with $\alpha = 0.59$ and $\alpha = 1.0$, for the peak absorption values, respectively. The predicted first resonance frequency computed by the TMM model is $f_r = 230\ \mathrm{Hz}$ which contains a peak value $\alpha = 0.99$. The second and third absorptive peaks are found at $f = 401\ \mathrm{Hz}$ and $f = 590\ \mathrm{Hz}$ with absorption coefficient being $\alpha = 0.99$ and $\alpha = 0.98$, respectively. Fourth and fifth absorptive peaks are at frequencies $f = 710\ \mathrm{Hz}$ and $f = 772\ \mathrm{Hz}$ and $\alpha = 0.67$ and $\alpha = 1.0$. There is a good agreement of f_r from the measurement obtained by the impedance tube and the TMM data. First resonance frequency is measured $f_r = 230\ \mathrm{Hz}$ for both the experimental and the theoretical data. Absorption coefficient is of lesser value for the measured profile, compared to that predicted by the TMM (where $\alpha = 0.80$ is from experimental and $\alpha = 0.99$ by the TMM).

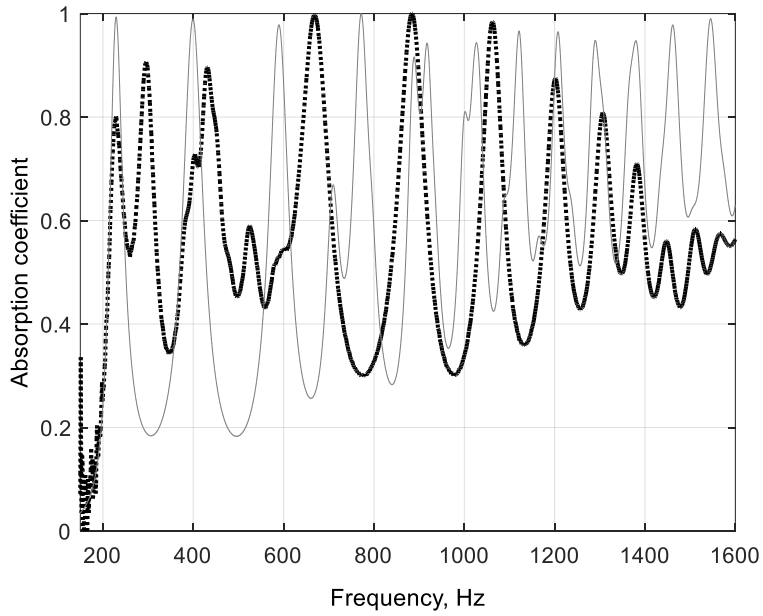

Figure 6.13. Absorption coefficient as a function of frequency showing comparison of TMM prediction vs experimental. Sample is linear profile with opening main pore radius $r_0 = 15$ mm, $d_p = 1$ mm, $d_c = 3$ mm, $R = 50$ mm and $L = 60$ mm. Data given by impedance tube measurement, represented by black dot, and TMM, solid line.

Absorption coefficient values are seen to have a largest discrepancy at higher frequencies between the measured and TMM data. For instance, at around $f = 1100\ \mathrm{Hz} \rightarrow f = 1600\ \mathrm{Hz}$ the absorptive peak values increasingly differ from the predicted TMM data and the measured data. A reduction of the absorption coefficient at higher frequencies can be seen in Figure 6.13. At $f = 1062\ \mathrm{Hz}$, $\alpha = 0.98$ and

reduces to $\alpha = 0.56$ at frequency $f = 1600$ Hz. In comparison, the TMM model predicts from around $f = 1100$ Hz → $f = 1600$ Hz that absorption coefficient does not reduce below a value of $\alpha = 0.94$. The predicted value of α at $f = 1600$ Hz is $\alpha = 0.99$. In contrast, the measured impedance tube data is of larger values than that predicted for α at the middle frequencies, where $f = 850$ Hz → $f = 1100$ Hz. The measured and predicted values obtained from the impedance tube and TMM model for the linear profile with $r_0 = 15$ mm, $d_c = 3$ mm and $L = 60$ mm are presented in Table 6.7 showing α at resonance frequency f. The profile performance has been discussed previously for values of α at several measured resonance frequencies, see also Chapter 4, metallic profiles section 4.3.3.

Impedance tube, f (Hz)	**Impedance tube (α)**	**TMM data, f f (Hz)**	**TMM data (α)**
230	0.80	230	0.99
294	0.90	401	0.99
430	0.90	590	0.98
525	0.59	710	0.67
668	1.00	772	1.00
884	1.00	889	0.92
1062	0.98	918	0.94
1200	0.88	1027	0.94
1308	0.81	1120	0.96
1382	0.71	1209	0.96
1448	0.56	1290	0.95
1512	0.58	1380	0.95
1567	0.57	1462	0.98
1600	0.56	1545	0.99

Table 6.7. Measured and predicted values obtained from impedance tube and TMM model for linear profile for peak absorption coefficient α at frequency f. Sample is linear profile with main pore radius $r_0 = 15$ mm, $d_p = 1$ mm, $d_c = 3$ mm, and $L = 60$ mm.

Figure 6.14 shows absorption coefficient versus frequency measured for a linear profile sample with a larger pore opening diameter, compared to the pancake of Figure 6.13. The number of plates and cavities are extended which increases the total sample length to $L = 80$ mm. In this arrangement the first plate has radius $r_0 = 25$ mm and the cavity thickness is changed from $d_c = 3$ mm to $d_c = 2$ mm. The single orifices contained in each plate with $d_p = 1$ mm, decrease 2 mm per plate until rigid backing is reached. First resonance frequency of the absorber is $f_r = 308$ Hz and has an absorption coefficient value $\alpha = 0.97$. The next four absorptive peaks are found at the following frequencies, $f = 421$ Hz, $f = 509$ Hz, $f = 620$ Hz, and $f = 706$ Hz. The absorption coefficient values at these frequencies are $\alpha = 0.85$, $\alpha = 0.88$, $\alpha = 0.82$ and $\alpha = 0.94$, respectively. Comparison of the experimental data to that of the TMM model given by Figure 6.14 shows the TMM data for the first five resonance peaks, where the first resonance peak is at $f_r = 301$ Hz and $\alpha = 0.99$. Second and third absorptive peaks are at frequencies $f = 488$ Hz and $f = 679$ Hz where $\alpha = 0.93$ and $\alpha = 0.94$, respectively. The fourth and fifth absorptive peaks are at $f = 842$ Hz and $f = 963$ Hz, with absorption coefficient values $\alpha = 0.99$ and $\alpha = 0.99$. Other absorptive peaks exist across the remainder of the frequency spectrum, and absorption coefficient data for the absorber can be seen further, as given by values of α and f in Table 6.8. The absorptive peak data given by Figure 6.14 shows that a slightly better agreement between the measured and TMM data is obtained when compared to the data from Figure 6.13.

The linear profile absorber has been investigated increasing the front pore radius from $r_0 = 15$ mm to $r_0 = 25$ mm, and increasing the sample length from $L = 60$ mm to $L = 80$ mm. Cavity thickness is less for profile sample of Figure 6.14 compared to the profile of Figure 6.13. The absorptive peak of the first

resonance frequency differs by $f = 12$ Hz between the measured and TMM data. Values of α are close for the measured and TMM at f_r, where $\alpha = 0.97$ for the former and $\alpha = 0.99$ for the latter. Peak absorption coefficient data is of larger values for the measured profile, compared to that predicted by the TMM in the frequency region around $f = 350$ Hz towards $f = 650$ Hz. Exception to this is α at only the second resonance frequency where $\alpha = 0.93$ for the TMM and is nearly $\alpha = 0.80$ for the measured data. In the frequency spectrum from $f = 800$ Hz towards $f = 1600$ Hz the TMM predicts slightly larger values of absorption coefficient, see Figure 6.14 and data presented by Table 6.8. After $f = 800$ Hz there are a lesser number of resonance frequencies that exist for the measured impedance tube data compared to the prediction of the TMM, and moreover, the resonance absorptive peaks are shifted to slightly higher frequency for the measured data. This can be seen mostly in Figure 6.14 for frequency ranging from $f = 800$ Hz towards $f = 1300$ Hz. Discussion of the profile absorber has been presented also in Chapter 4, see metallic profile absorbers section 4.3.3 (measured values of impedance tube data only is discussed for α at several measured resonance frequencies. Measured and predicted values obtained from impedance tube and TMM model for linear profile with $r_0 = 25$ mm, $d_c = 2$ mm and $L = 80$ mm are presented in Table 6.8 showing α at resonance frequency f.

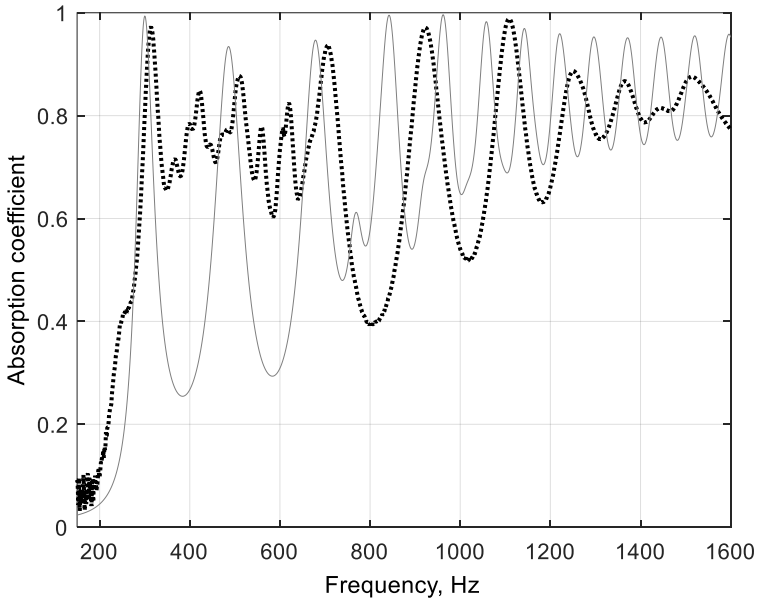

Figure 6.14. Absorption coefficient as a function of frequency showing comparison of TMM prediction vs experimental. Sample is linear profile with opening main pore radius $r_0 = 25$ mm, $d_p = 1$ mm, $d_c = 2$ mm, $R = 50$ mm, and $L = 80$ mm. Impedance tube data, black dot, and TMM, solid line.

Impedance tube, f (Hz)	**Impedance tube (α)**	**TMM data, f f (Hz)**	**TMM data (α)**
313	0.97	301	0.99
421	0.85	488	0.93
509	0.88	679	0.94
620	0.82	842	0.99
706	0.94	963	0.99
921	0.97	1059	0.94
1111	0.99	1145	0.95
1250	0.89	1218	0.95
1364	0.87	1296	0.95
1504	0.87	1371	0.95
1600	0.77	1445	0.95

1687	0.80	1519	0.95
1727	0.90	1596	0.95

Table 6.8. Measured and predicted values obtained from impedance tube and TMM model for linear profile for peak absorption coefficient α at frequency f. Sample is linear profile with main pore radius $r_0 = 25$ mm, $d_p = 1$ mm, $d_c = 2$ mm, $R = 50$ mm, and $L = 80$ mm.

Absorption coefficient dependence as a function of frequency is presented by Figure 6.15 showing data obtained for when a linear profile sample has additional length $L = 20\ \text{mm}$. Pore opening radius remains $r_0 =$ 25 mm, $d_p = 1$ mm and $d_c = 3$ mm. Sample length is built $L = 100\ \text{mm}$. Measurements are performed using white noise excitation. The first resonance frequency of the measured impedance tube data for the absorber is $f_r = 224\ \text{Hz}$ and the absorption coefficient is $\alpha = 0.94$. The second and third frequency data is measured $f = 300\ \text{Hz}$ and $f = 370\ \text{Hz}$ with absorption coefficient values $\alpha = 0.93$ and $\alpha = 0.94$, respectively. Fourth and fifth absorptive peaks are at $f = 433\ \text{Hz}$ and $f = 490\ \text{Hz}$ and $\alpha = 0.94$ and $\alpha = 0.98$, respectively. The predicted first resonance frequency computed by the TMM model is $f_r = 222\ \text{Hz}$ with a peak value $\alpha = 0.98$. Second and third absorptive peaks are at frequencies $f = 369\ \text{Hz}$, and $f = 543\ \text{Hz}$ with absorption coefficient values $\alpha = 0.91$ and $\alpha = 0.86$, respectively. The fourth and fifth absorptive peaks are at frequencies $f = 691\ \text{Hz}$ and $f = 730\ \text{Hz}$, where $\alpha = 1.0$ and $\alpha = 0.99$. Figure 6.15 shows a relatively good agreement of the first resonance frequency from the measurement obtained by the impedance tube data and that from the TMM. First resonance frequency is measured $f_r = 224\ \text{Hz}$ for the experimental data and $f_r = 222\ \text{Hz}$ for the theoretical data.

Absorption coefficient is of lesser value for the measured profile, compared to that predicted by the TMM (where $\alpha = 0.94$ for experimental and $\alpha = 0.98$ for the TMM). Lowest resonance frequency is determined for the linear configuration with $d_c = 3\ \text{mm}$ and $L = 100\ \text{mm}$ compared to when $d_c = 2\ \text{mm}$ and $L = 80\ \text{mm}$, which is profile configurations of Figure 6.15 and 6.14 respectively. Increasing the values of d_c and L whilst keeping same values of R and r_0 gives a reduction of $f_r = 89\ \text{Hz}$, for the linear profile structure of Figure 6.15. The linear profile absorbers are discussed elsewhere, see also Chapter 4, metallic profile absorbers section 4.3.3 for comparisons of measured data. The TMM predicted values observed in Figure 6.15 show that at $f = 369\ \text{Hz}$ the peak absorption is $\alpha = 0.91$ whereas at $f = 370\ \text{Hz}$ absorption coefficient is $\alpha = 0.94$, for the measured impedance tube data. The measured data also has an absorptive peak between f_r and $f = 370\ \text{Hz}$ which is seen to be the contrary for the case of the TMM. For instance, the measured data given by Figure 6.15 shows an absorptive peak also at $f = 300\ \text{Hz}$ where $\alpha = 0.93$. Absorption coefficient values for the measured data is of larger value compared to the TMM data for α, at frequency approximately ranging between $f = 250\ \text{Hz} \rightarrow f = 700\ \text{Hz}$. Values of α across the frequency spectrum are in better agreement for peak values of α with the TMM model, compared to other profile structures presented by Figures 6.13 – 6.14. The measured and predicted values obtained from the impedance tube and TMM model for the linear profile with $r_0 = 25\ \text{mm}$, $d_c = 3\ \text{mm}$ and $L = 100\ \text{mm}$ are given in Table 6.9 showing α at resonance frequency f.

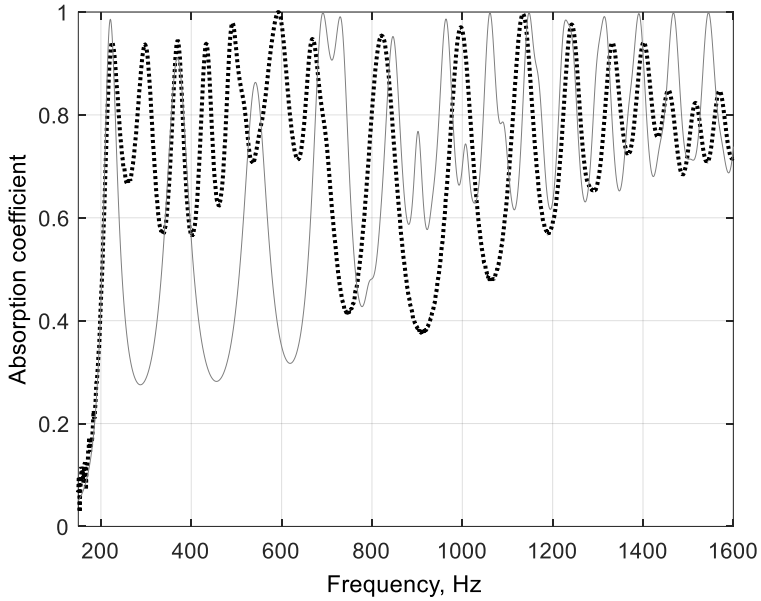

Figure 6.15. Absorption coefficient as a function of frequency showing comparison of TMM prediction vs experimental. Sample is linear profile with opening main pore radius $r_0 = 25$ mm, $d_p = 1$ mm, $d_c = 3$ mm, $R = 50$ mm and $L = 100$ mm. Impedance tube data, black dot, and TMM, solid line.

Impedance tube, f (Hz)	**Impedance tube (α)**	**TMM data, f f (Hz)**	**TMM data (α)**
224	0.94	222	0.98
300	0.93	369	0.91
370	0.94	543	0.86
433	0.94	691	1.00
490	0.98	730	0.99
592	1.00	847	0.95
668	0.95	902	0.77
820	0.95	962	0.98
995	0.97	1061	1.00
1134	1.00	1148	1.00
1240	0.97	1232	0.98
1331	0.94	1314	0.99
1400	0.94	1391	1.00
1456	0.85	1467	1.00
1514	0.82	1545	1.00
1569	0.85	1624	1.00

Table 6.9. Measured and predicted values obtained from impedance tube and TMM model for linear profile for peak absorption coefficient α at frequency f. Sample is linear profile with main pore radius $r_0 = 25$ mm, $d_p = 1$ mm, $d_c = 3$ mm, $R = 50$ mm, and $L = 100$ mm.

Measurements have been performed in the impedance tube with exponential profile absorbers and a comparison is shown against the TMM, for its performance of absorptive capabilities. Figure 6.16 shows absorption coefficient as a function of frequency with comparison of the predicted TMM and the data obtained by impedance tube measurements. The absorber is an exponential profile structure where the opening main pore radius is $r_0 = 25$ mm, $d_p = 1$ mm, $d_c = 2$ mm and $L = 80$ mm. The impedance tube data shows that the measured first resonance frequency $f_r = 195$ Hz and absorption coefficient has the value $\alpha = 0.52$. Second and third resonance frequencies are measured at $f = 250$ Hz and $f = 295$ Hz, with values $\alpha = 0.45$ and $\alpha = 0.52$, respectively. Fourth and fifth absorptive peaks are at $f = 331$ Hz and $f = 410$ Hz where $\alpha = 0.52$ and $\alpha = 0.64$, respectively. The predicted first resonance frequency computed by the TMM model is $f_r = 276$ Hz with a peak value $\alpha = 0.67$. Second and third absorptive peaks are at frequencies $f = 427$ Hz and $f = 568$ Hz and the absorption coefficient values are $\alpha = 0.86$

and $\alpha = 0.90$. The fourth and fifth absorptive peaks are at $f = 690$ Hz and $f = 787$ Hz with values of $\alpha = 0.98$ and $\alpha = 0.96$, respectively. Exponential profile absorber with $d_c = 2$ mm and $L = 80$ mm shown in Figure 6.16 has f_r at lower frequency than any of the linear profiles, given prior by Figures 6.13 – 6.15. This means that the exponential profile absorbers are able to obtain larger values of α for the measured first resonance frequency f_r at slightly lower frequency with a difference $f = 35$ Hz, for identical sample length, see profile data given by Figure 6.14.

First resonance frequency predicted by the TMM, and shown in Figure 6.16 is seen to differ from the measured f_r by a difference $f = 81$ Hz. Broadband absorption is attainable for the exponential absorbers similar to the linear profiles. The TMM data shown by Figure 6.16 has closest match to the measured data at the middle frequencies. For instance, at $f = 787$ Hz absorption coefficient $\alpha = 0.96$ for the predicted TMM data, whilst the measured data at $f = 770$ Hz shows that $\alpha = 0.99$. Impedance tube data at slightly higher frequencies, where $f = 928$ Hz, $f = 1057$ Hz, and $f = 1170$ Hz, the absorption coefficient values are $\alpha = 1.00$, $\alpha = 0.96$ and $\alpha = 0.92$, respectively. In contrast the TMM however, predicts peaks at $f = 936$ Hz, $f = 1052$ Hz, and $f = 1173$ Hz and absorption coefficient is $\alpha = 0.92$, $\alpha = 0.89$ and $\alpha = 0.95$, respectively. There is a larger disagreement between the TMM and the measured data for f_r and α values at lower frequency $f = 195$ Hz → $f = 600$ Hz, and at higher frequency $f = 1300$ Hz → $f = 1600$ Hz. Nevertheless, the general trend in the dependence of the sound absorption coefficient on frequency is correctly captured by TMM (see Figure 6.16). Measured and predicted values obtained from the impedance tube and TMM model for the exponential profile with a first plate containing $r_0 = 25$ mm, $d_p = 1$ mm and $L = 80$ mm is presented by Table 6.10 showing peak values of α at resonance frequency f.

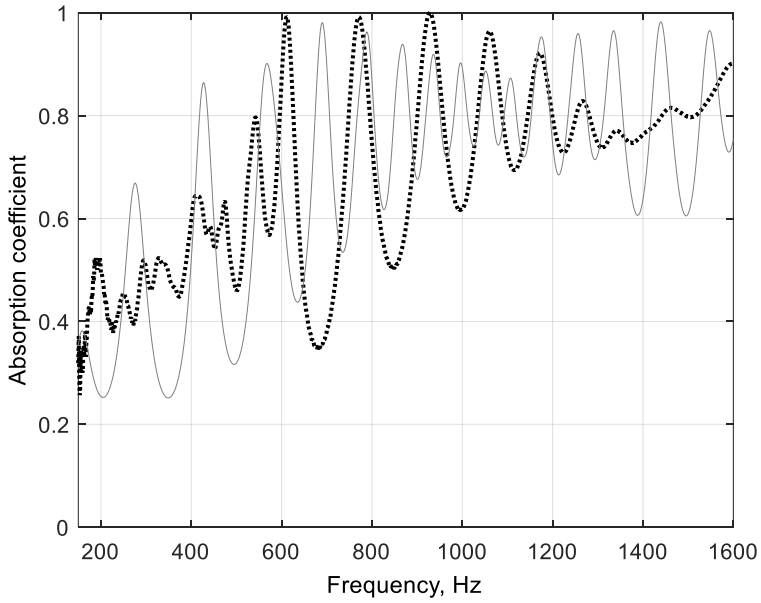

Figure 6.16. Absorption coefficient as a function of frequency showing comparison of TMM prediction vs experimental. Sample is exponential profile with opening main pore radius $r_0 = 25$ mm, $d_p = 1$ mm, $d_c = 2$ mm, $R = 50$ mm and $L = 80$ mm. Impedance tube data, black dot, and TMM, solid line.

Impedance tube, f (Hz)	**Impedance tube (α)**	**TMM data, f f (Hz)**	**TMM data (α)**
195	0.52	276	0.67
250	0.45	427	0.86

295	0.52	568	0.90
331	0.52	690	0.98
410	0.64	787	0.96
476	0.63	865	0.93
542	0.80	936	0.92
610	0.99	995	0.90
770	0.99	1052	0.89
928	1.00	1106	0.87
1057	0.96	1173	0.95
1170	0.92	1257	0.96
1265	0.83	1336	0.96
1339	0.77	1439	0.98
1445	0.81	1545	0.96
1600	0.90	1600	0.75

Table 6.10. Measured and predicted values obtained from impedance tube and TMM model for linear profile for peak absorption coefficient α at frequency f. Sample is exponential profile with opening main pore radius $r_0 = 25$ mm, $d_p = 1$ mm, $d_c = 2$ mm, and $L = 80$ mm.

Figure 6.17 shows absorption coefficient as a function of frequency for an exponential profile sample with additional plates and cavities. The absorber is reassembled so that the sample length becomes $L = 100$ mm. This sample has an opening main pore where its radius is $r_0 = 25$ mm, $d_p = 1$ mm and cavity thickness is altered from $d_c = 2$ mm (from previous sample) to $d_c = 3$ mm. The first resonance frequency measured for the profile is $f_r = 131$ Hz and $\alpha = 0.54$. Sound source is white noise excitation, and the sound pressure level is 80 dB. The next four measured absorptive peaks have larger values of α with increasing frequency. This is found at the following, when $f = 172$ Hz, $f = 243$ Hz, $f = 307$ Hz, and $f = 408$ Hz. The respective absorption coefficient values obtained at the given frequencies are $\alpha = 0.53$, $\alpha = 0.59$, $\alpha = 0.72$ and $\alpha = 0.78$. A comparison between the experimental to that of the predicted data by the TMM model (given by Figure 6.17) shows the first resonance peak being at $f_r = 200$ Hz and has a peak value $\alpha = 0.64$. Second and third absorptive peaks are at frequencies $f = 321$ Hz and $f = 442$ Hz with absorption coefficient values $\alpha = 0.86$ and $\alpha = 0.94$, respectively.

The fourth and fifth absorptive peaks are at $f = 565$ Hz and $f = 664$ Hz, and $\alpha = 1.00$ (for both fourth and fifth peaks). The measured and predicted values obtained from the impedance tube and TMM model for the exponential profile absorber with first plate containing $r_0 = 25$ mm, $d_c = 3$ mm and $L = 100$ mm are presented in Table 6.11, showing peak values of α at resonance frequency f. The measured first resonance frequency for the exponential profile of Figure 6.17 is at $f_r = 131$ Hz and is comparable to pancake absorbers given by Figures 6.3 – 6.4, in terms of the value f_r. This is because the pancake data by Figure 6.3 has $f_r = 135$ Hz and also $f_r = 135$ Hz for the pancake given by Figure 6.4. Absorption coefficient, however, is much of a lesser value for the exponential profile seen by Figure 6.17 compared to the previous pancake absorbers. Where $\alpha = 0.54$ for the exponential profile (Figure 6.17) and $\alpha = 0.99$ and $\alpha = 1.00$ for pancake absorber with $d_c = 3$ mm and $d_c = 6$ mm, given by Figure 6.3 and Figure 6.4 respectively. First resonance frequency predicted by the TMM, and shown in Figure 6.17 differs from the measured first resonance frequency f_r by $f = 69$ Hz. Additional absorptive peaks exist for the exponential profile which contain $d_c = 3$ mm and $L = 100$ mm shown by Figure 6.17, compared to the exponential profile with $d_c = 2$ mm and $L = 80$ mm. The profile performance has been discussed previously for values of α at several measured resonance frequencies including comparisons with other profile absorbers, see also Chapter 4, section 4.3.3. The TMM data given by Figure 6.17 shows a discrepency with the measured impedance tube data for the measured resonance frequency content across the spectrum. However, absorption coefficient values for the measured data are similar to that

of the TMM data except at $f = 300$ Hz, and again at higher frequencies $f = 1200$ Hz → $f = 1400$ Hz. The general trend in absorption coefficient dependence on frequency is also captured by the TMM. The model has been used to predict the peak absorption and resonance frequency of both the pancake and profiled absorbers. Structures tested are composed of different lengths and configurations and their performance from the measured impedance tube data is validated against the predicted data computed by the TMM. It is demonstrated that the model provides a reasonably good match when compared to the measured data.

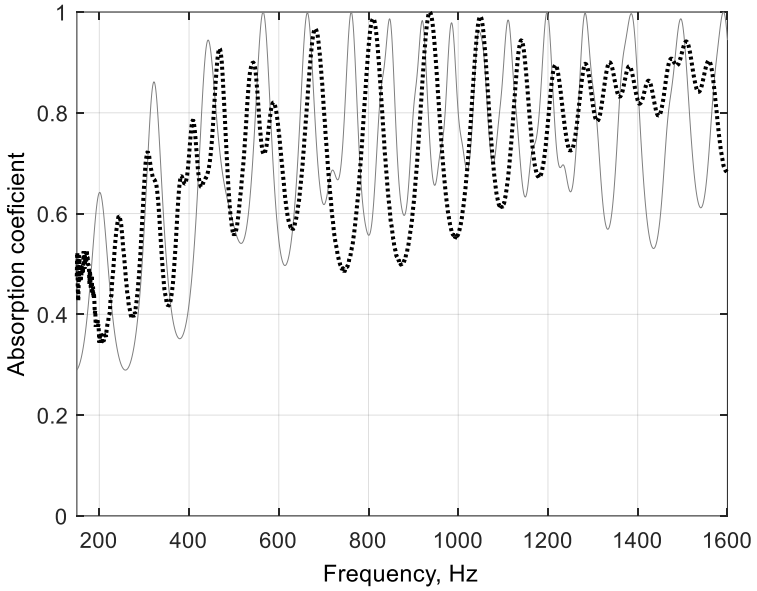

Figure 6.17. Absorption coefficient as a function of frequency showing comparison of TMM prediction vs experimental. Sample is exponential profile with opening main pore radius $r_0 = 25$ mm, $d_p = 1$ mm, $d_c = 3$ mm, $R = 50$ mm, and $L = 100$ mm. Impedance tube data, black dot, and TMM, solid line.

Impedance tube, f (Hz)	**Impedance tube (α)**	**TMM data, f f (Hz)**	**TMM data (α)**
131	0.54	200	0.64
172	0.53	321	0.86
243	0.59	442	0.94
307	0.72	565	1.00
408	0.78	664	1.00
468	0.93	761	1.00
542	0.90	847	0.99
587	0.82	920	0.98
682	0.97	985	0.98
810	0.99	1049	0.96
936	1.00	1111	0.98
1048	0.99	1198	1.00
1139	0.94	1283	1.00
1215	0.89	1385	1.00
1284	0.90	1495	0.99
1337	0.90	1591	1.00
1380	0.89	1595	0.99
1425	0.86	1600	1.00
1475	0.91	1632	0.69
1506	0.94	1645	0.75
1559	0.90	1677	0.99

Table 6.11. Measured and predicted values obtained from impedance tube and TMM model for linear profile for peak absorption coefficient α at frequency f. Sample is exponential profile with opening main pore radius $r_0 = 25$ mm, $d_p = 1$ mm, $d_c = 3$ mm, $R = 50$ mm, and $L = 100$ mm.

6.2. Pancake Absorber – Effective Properties in Linear Regime

Section 6.2. aims at introducing a new model developed together with the main supervisor which accounts for the absorber effective properties. The effective density of the structure $\rho_{p,c}\,(\omega)$ and the effective compressibility $C_{p,c}\,(\omega)$ is obtained and used in conjunction with the parameters of the JCAL model to predict the first resonance frequency, and peak values of the absorption coefficient (details are given in section 6.2.1. for obtaining $f_{r,}$ and in section 6.2.2. the mechanical disturbance of the absorber is shown for vibrational effects). Concept of using dead-end pore approach is first introduced by Leclaire et al [1] who investigated porous materials with periodically distributed dead-end pores. In this thesis the idea remains similar, although the geometry has changed. The effective properties model for linear and nonlinear regimes focussing on the new material geometry has recently been presented in [139]. A change in geometry maximizes the volume occupied by the dead-end pores and takes advantage of utilizing the absorber lateral dimensions.

Here, we will explain the sample geometry, for completeness. The metamaterial pancake is composed of equally spaced identical rigid plates, which are distributed in a periodic arrangement along sample thickness L, with sample radius R. Each plate "p" in the periodic structure has equal thickness d_p. The annular cavities "c" which are located separately between each plate have thickness d_c. At the outer boundary the cavities are rigidly backed at R. A central perforation exists for each plate d_p which has a pore radius r_0, located at the front surface plate which is in series until the last plate (last plate rigidly backed). The pancake absorber can also be set-up in transmission mode so that r_0 is constant from first to last plate. The geometry is first introduced in Chapter 4, see Figure 4.1. It is presented here also for structure clarity, see Figure 6.18. Low frequency approximation is considered meaning that wavelength of sound travelling through the main perforation is much larger than the period of the structure, $Re(k_{mp}h) \ll 1$. Here subscript mp stands for "main perforation", k_{mp} is wavenumber of air in the main perforation without cavities present and $h = d_p + d_c$ is the period of the structure. Expressions for the characteristic impedance Z and wavenumber q of air in the pore with the dead-ends present are given by equations (28) and (32) by Leclaire et al [1].

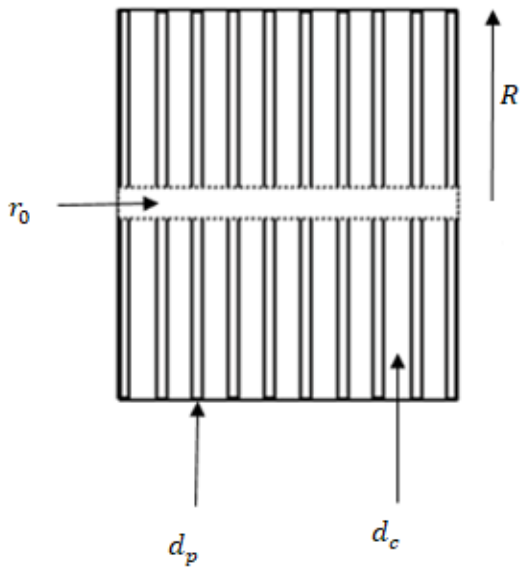

Figure 6.18. Geometry of the pancake absorber containing a simple perforation at its centre.

Characteristic impedance Z and wavenumber q of air in the pore with the dead-ends are shown by equations (8)-(9).

$$Z = \frac{Z_{mp}}{\sqrt{1 + \frac{2X}{ik_{mp}h}}} \tag{8}$$

$$q = k_{mp}\sqrt{1 + \frac{2X}{ik_{mp}h}} \tag{9}$$

where time convention is $e^{-i\omega t}$. Parameter X is defined by Equation (2) in [1]

$$X = -\frac{NA_{de}}{2\,A_{mp}}\frac{1}{Z_{s\,de}} \tag{10}$$

where N is the number of dead-end pores per period, A_{mp} is the cross-sectional area of the main pore and A_{de} is the cross-section area of the dead-end pore opening into the main pore. For the former, $A_{mp} \rightarrow \pi r_0^2$ due to the surface area of the main perforation in plate d_p. In the case of the latter, surface area of the cavity opening into the main perforation per period, is equal to $2\pi r_0 d_c$ so that $NA_{de} \rightarrow 2\pi r_0 d_c$. Surface “s” impedance of the single dead-end pore is $Z_{s\,de}$ which is normalised to the characteristic impedance of air in the main pore, Z_{mp}. The surface admittance of the cavity is normalised by the characteristic admittance of air $\frac{1}{\rho_0 c}$, $G(\omega) = \frac{\rho_0 c}{Z_{s\,de}\,Z_{mp}}$ thus (10) is expressed thereafter by equation (11),

$$X = -\frac{1}{\rho_0 c}\frac{d_c}{r_0}\,G(\omega)\,Z_{mp}. \tag{11}$$

$$\rho(\omega) = \frac{qZ}{\omega} = \rho_p, \tag{12}$$

$$C(\omega) = \frac{q}{\omega Z} = C_p + iC_0\frac{2}{kr_0}\,G_w(\omega). \tag{13}$$

Expressions for the effective density $\rho(\omega)$ and effective compressibility $C(\omega)$ of air within the perforation with the side cavities can be derived from (8), (9) and (11). For the cylindrical geometry of the absorber, subscript p and subscript c are used for the change of geometry which refer to the main pore and cavity,

(mp and c). These subscripts replace mp and de and are shown in equations (12) and (13), where $k = \frac{\omega}{c}$ is wavenumber of air, $C_0 = \frac{1}{\rho_0 c^2}$ is compressibility of air, the admittance of the main perforation wall is $G_w(\omega) = G(\omega), \phi_w = \frac{\rho_0 c}{Z_{s\,c}\ Z_p}\phi_w$ and $\phi_w = \frac{d_c}{h}$ can be treated as porosity of the main perforation wall. The lateral cavities associated within the absorber are treated separately to that of the main pore of the perforated plate and as such, the pancake is regarded to be a double porosity material. The concept of describing a material with its double porosity nature can be seen in other works, as first given by Olny and Boutin in [140]. The pancake absorber treated as a double porosity material results in having a high permeability contrast. In this case the normalised effective density is equal to that of the meso-domain and the porosity of the central pore is defined as the ratio of the main pore surface area to that of the absorber with plate diameter $2R$. Here meso-domain and micro-domains are regarded as the central perforation and lateral cavities, respectively. Pressure "p" and particle velocity "v" in the cavity are given by equations (14) and (15) respectively,

$$p = A\left(J_0(k_c r) - \frac{J_1(k_c R)}{H_1(k_c R)} H_0(k_c r)\right) \tag{14}$$

$$v = \frac{iAk_c}{\omega\rho_c}\left(J_1(k_c r) - \frac{J_1(k_c R)}{H_1(k_c R)} H_1(k_c r)\right) \tag{15}$$

which have been obtained using a Bessel function J_1 and Hankel function H_1 of the first kind. The associated boundary condition is $p'(R) = 0$ since the cavity is rigidly backed at $r = R$. As shown in [139] Euler's equation relates the pressure and particle velocity $v = -ip'/\omega\rho_c(\omega)$ for the radial components of the structure. Surface admittance of the perforation wall $G_w(\omega)$ refers to the plate only and applicable from centre of main pore distance by polar coordinate r. The Helmholtz equation is used $p'' + (1/r)p'' + k_c^2 p = 0$, to describe the relationship for pressure "p" inside the cavity. Derivatives shown are with respect to r and cavity thickness d_c is the spatial region occupied between plates d_p that are assumed rigid. The effective wavenumber which occupies the spatial region of cavitation with thickness d_c is $k_c(\omega)$. Normalised surface admittance of the wall of the main perforation is calculated as $G_w = \rho_0 c \phi_w \frac{v(r_0)}{p(r_0)}$

$$G_w = \frac{i\,\phi_w \rho_0 c}{Z_c} \frac{\left(J_1(k_c r_0) - \frac{J_1(k_c R)}{H_1(k_c R)} H_1(k_c r_0)\right)}{\left(J_0(k_c r_0) - \frac{J_1(k_c R)}{H_1(k_c R)} H_0(k_c r_0)\right)} \tag{16}$$

where $Z_c(\omega) = \sqrt{\frac{\rho_c(\omega)}{C_c(\omega)}}$ is characteristic impedance of air in the cavity. The surface impedance Z_s of the pancake structure and absorption coefficient α is shown in equation (17) and equation (18) respectively,

$$Z_s = i\frac{Z}{\phi_p}\ \mathrm{cotan}(qL), \tag{17}$$

$$\alpha = 1 - \left|\frac{Z_s - \rho_0 c}{Z_s + \rho_0 c}\right|^2, \tag{18}$$

which is obtained by using equations (12), (13) and (16) from expressions for the effective density, effective compressibility, and normalised surface admittance of the wall of the main perforation. Front surface porosity ϕ_p used in equation (17) is,

$$\phi_p = \left(\frac{r_0}{R}\right)^2 \tag{19}$$

$$Z = \sqrt{\frac{\rho(\omega)}{C(\omega)}} \quad , \quad q(\omega) = \omega\sqrt{\rho(\omega)C(\omega)} \tag{20}$$

The above expressions are valid when the sample is rigidly backed and the pancake having thickness L. These analytical approximations are later used to to predict the peak value of the absorption coefficient on the structure comprised with cylinderical geometry. This is obtained by using the also predicted lowest resonance frequency by the model.

Parameter	Perforation (subscript *p*)	Cavity (subscript *c*)
$\sigma_{p,c}$	$8\eta/r_0^2$	$12\eta/d_c^2$
$\alpha_{\infty\, p,c}$	1	1
$\Lambda_{p,c}$	r_0	d_c
$\Lambda'_{p,c}$	r_0	d_c
$\kappa'_{p,c}$	$r_0^2/8$	$d_c^2/12$
$\omega_{b\, p,c} = \omega'_{b\, p,c}$	$16\eta/\rho_0\, r_0^2$	$36\eta/\rho_0\, d_c^2$

Table 6.12. Parameters of JCAL model for the perforation and the cavities [106].

Parameters of the model are shown in Table 6.12 for the central perforation of radius r_0, and cavities with thickness d_c. The parameters of the model are those required by Johnson-Champoux-Allard-Lafarge equivalent fluid model (JCAL model) [80], [83], [106]. Parameters are as follows; static air flow resistivity σ, characteristic viscous length Λ, high frequency tortuosity α_∞, thermal permeability κ' and thermal characteristic length Λ'. The effective density of the pancake structure $\rho_{p,c}\,(\omega)$ and effective compressibility $C_{p,c}\,(\omega)$ which include that of both the central pore 'p' and cavity 'c' are calculated using expressions presented in Table 6.12 and given by equations (21)-(22).

$$\rho_{p,c}(\omega) = \rho_0\, \alpha_{\infty\, p,c}\left(1 + \frac{\sigma_{p,c}}{-i\omega\alpha_{\infty\, p,c}\rho_0}\sqrt{1 + \frac{-i\omega}{\omega_{b\, p,c}}}\right) \tag{21}$$

where C_p is dependent on the geometrical aspect of the cylindrical cavities.

$$C_{p,c}(\omega) = C_0\left(\gamma - \frac{\gamma - 1}{1 + \frac{\eta}{-i\omega'\rho_0\kappa'_{p,c}}\sqrt{1 + \frac{-i\omega'}{\omega'_{b\, p,c}}}}\right) \tag{22}$$

where $\omega' = \omega N_{pr}$, N_{pr} is Prandtl number, $\omega_{b\, p,c} = \frac{\sigma_{p,c}^2 \Lambda_{p,c}^{\prime\, 2}}{4\, \alpha_{\infty\, p,c}^2\, \rho_0 \eta}$ and $\omega'_{b\, p,c} = \frac{\Lambda'^{\,2}_{p,c}\eta}{4\, \kappa'^2_{pc}\rho_0}$ are characteristic viscous and thermal frequencies of the main pore (p) and lateral cavities (c). The model is valid when the microstructure periodicity is much smaller than the sound wavelength as it propagates through the sample after interaction with the front plate and pore radius r_0. The series of distributed lateral cavities does not modify the effective density of the structure.

$$\rho_p = \frac{Z_p k_p}{\omega} \tag{23}$$

This is seen to be the contrary of the effective compressibility between the central perforation and fluid within the absorber configuration with cavities d_c,

$$C_p = \frac{k_p}{\omega Z_p} \tag{24}$$

where C_p is dependent on the geometrical aspect of the cylindrical cavities.

6.2.1. Prediction of First Resonance Frequency f_r and Absorption Coefficient α_r

To model the absorber performance, it is necessary to use effective density and effective compressibility in order to predict the dependence of the position of the lowest resonance frequency, and the peak value of the absorption coefficient on the geometry of the design structure. The estimation of the first resonance frequency uses assumptions that allow the approximated first resonance f_r to be obtained. This is such that wavelength of the sound in the distributed cavities with thickness d_c of the structure is much larger than the plates radii used in the design thus, $|k_c(2\pi f_r)|\ R \ll 1$. Also, the viscous and thermal characteristic frequencies of the main central pore in each plate and cavity is much lower than the resonance frequency f_r. Surface porosity of the sample ϕ_p is smaller than the porosity of the central perforation wall ϕ_w so that $\phi_p \ll \phi_w$. The JCAL expressions given by Table 6.12 are used (and considered assumptions) to show that sound propagation in the pancake internal configuration is expressed being in the inertial regime,

$$f_r \gg \frac{1}{2\pi}\frac{36\eta}{d_c^2\rho_0} \text{ and } f_r \gg \frac{1}{2\pi}\frac{16\eta}{\rho_0 r_0^2}. \tag{25}$$

To obtain a simple expression for the effective compressibility $C(\omega)$ of the fluid in the structure a Taylor series for small arguments is used of Bessel functions and their combinations. These account for the linear terms in ε, of [28]. So that $k_c R = O(\varepsilon)$ and $k_c r_0 = O(\varepsilon)$. This leads to the following expansions,

$$J_0(k_c r_0) \approx 1 \tag{26}$$

$$J_1(k_c r_0) \approx \frac{k_c r_0}{2} = O(\varepsilon)$$

$$\frac{J_1(k_c R)}{H_1(k_c R)} H_0(k_c r_0) \approx -(k_c R)^2 \log k_c r_0 = O(\varepsilon)$$

$$\frac{J_1(k_c r_0)}{H_1(k_c R)} H_1(k_c R) \approx \frac{k_c R}{2}\frac{R}{r_0} = O(\varepsilon) \tag{27}$$

The pancake structure with effective compressibility $C(\omega)$ is given by equation (28) as weighted terms involving both the cavities and the main pore of the sample,

$$C(\omega) \approx C_p + \frac{(1-\phi_p)\phi_w}{\phi_p} C_c, \tag{28}$$

Since the inertial regime at resonance is considered by both the main pore and cavities then effective compressibility of air as such ($C_{p,c}$) is approximated as equation (29) obtained using also the JCAL model parameters. Furthermore, a final approximation of the effective compressibility, see equation (30) is given due to a low porosity approximation for ϕ_p meaning that porosity is much lower than that of the wall porosity $\phi_p \ll \phi_w$ thus,

$$C_{p,c}(\omega) \approx C_0\left(1+(\gamma-1)\frac{2}{x_{p,c}}\sqrt{\frac{\eta}{-i\omega N_{pr}\rho_0}}\right), \tag{29}$$

$$C(\omega) \approx C_0\left(1+\frac{\phi_w}{\phi_p}+\frac{(\gamma-1)}{\sqrt{N_{pr}}}\frac{2}{r_0}\sqrt{\frac{\eta}{-i\omega\rho_0}}\left(1+\frac{r_0}{d_c}\frac{\phi_w}{\phi_p}\right)\right), \tag{30}$$

where $x_p = r_0$ and $x_c = d_c$. Moreover, the effective compressibility $C(\omega)$ is given further as equation (31) since for the developed pancake structures $\frac{\phi_w}{\phi_p} \gg 1$. Where that in the absence of the cavities ($\phi_w = 0$) described by the first terms in the brackets.

$$C(\omega) \approx C_0\frac{\phi_w}{\phi_p}\left(1+\frac{(\gamma-1)}{\sqrt{N_{pr}}}\frac{2}{r_0}\sqrt{\frac{\eta}{-i\omega\rho_0}}\frac{r_0}{d_c}\right), \tag{31}$$

In the inertial regime defined by Equation (17), effective density (5) is approximated as

$$\rho(\omega) \approx \rho_0\left(1+\frac{2}{r_0}\sqrt{\frac{\eta}{-i\omega\rho_0}}\right). \tag{32}$$

Wavenumber and characteristic impedance of the fluid in the pancake absorber is obtained using the effective properties equations given by the effective compressibility (31) and effective density (32).

$$q(\omega) \approx k\sqrt{\frac{\phi_w}{\phi_p}}\left(1+\frac{1}{r_0}\sqrt{\frac{\eta}{-i\omega\rho_0}}\left(1+\frac{\gamma-1}{\sqrt{N_{pr}}}\frac{r_0}{d_c}\right)\right). \tag{33 a}$$

$$Z(\omega) \approx \rho_0 c\sqrt{\frac{\phi_p}{\phi_w}}\left(1+\frac{1}{r_0}\sqrt{\frac{\eta}{-i\omega\rho_0}}\left(1-\frac{\gamma-1}{\sqrt{N_{pr}}}\frac{r_0}{d_c}\right)\right). \tag{33 b}$$

where wavenumber $q(\omega) = \omega\sqrt{\rho(\omega)C(\omega)}$ and characteristic impedance $Z = \sqrt{\rho(\omega)/C(\omega)}$. The resonance frequency f_r is estimated as the following,

$$f_r \approx f_0\sqrt{\frac{\phi_p}{\phi_w}}\left(1-\frac{1}{4}\sqrt{\frac{f_{b\,p}}{2f_0}\sqrt{\frac{\phi_w}{\phi_p}}}\left(1+\frac{\gamma-1}{\sqrt{N_{pr}}}\frac{r_0}{d_c}\right)\right). \tag{34}$$

Which has been estimated using a quadratic equation for the square root of the resonance frequency for a rigid backed quarter wavelength resonance $f_0 = \frac{c}{4L}$ with thickness L. Full approximation and its positive solution leading to f_r can be seen in [139]. The normalised surface impedance can be estimated using equation given by (33 b) and absorption coefficient at resonance α_r, see equation (36).

$$Z_s \approx \frac{\rho_0 c}{\sqrt{\phi_w\phi_p}}\left(1+\frac{1}{r_0}\sqrt{\frac{\eta}{-i\omega\rho_0}}\left(1-\frac{\gamma-1}{\sqrt{N_{pr}}}\frac{r_0}{d_c}\right)\right)\frac{1-e^{-n}}{1+e^{-n}}, \tag{35}$$

where $n \approx \pi\left(1-\frac{f_r}{f_0}\sqrt{\frac{\phi_w}{\phi_p}}\right)$ the normalised surface impedance is estimated noting that resonance frequency $qL = \frac{\pi}{2}\left(i+1-\frac{f_r}{f_0}\sqrt{\frac{\phi_w}{\phi_p}}\right)$. It is then convenient to substitute n into the expression used applying Taylor series given by (18) which then leads to the absorption coefficient at resonance, given by expression used in (36).

$$\alpha_r \approx \frac{4\sqrt{\phi_w\phi_p}(1-e^{-2n})}{\left(\left(\sqrt{\phi_w\phi_p}+1\right)-e^{-n}\left(1-\sqrt{\phi_w\phi_p}\right)\right)^2}. \quad (36)$$

Predictions of f_r and α_r are used to investigate the performance of the pancake structure, including samples with different d_c and L. The effective properties model is compared against the data obtained directly from measurements, where the absorber measurements are all performed in a Mecanum impedance tube using a two-microphone method. All the pancake (and profile) samples tested with a two-microphone method were all rigidly backed, and each microphone was mounted to the tube at fixed locations. The working range of the apparatus was $50\ \mathrm{Hz} - 1800\ \mathrm{Hz}$ and the frequency resolution was $1\ \mathrm{Hz}$ The impedance tube was cylindrical, and its wall thickness was sufficient to eliminate any vibrational effects as required by standard BS EN ISO 10534-2:2001. A white noise continuous sound source is used in linear regime and compared against the model predictions for f_r and α_r.

Porosity of the main pore walls for the pancake structure due to the presence of the cavities was defined as the fraction of the main perforation wall occupied by the cavities, $\frac{d_c}{d_c+d_p}$, and varied between $\phi_w = 0.5$ for $d_c = 1$ mm and $\phi_w = 0.87$ for $d_c = 6$ mm. Figure 6.19 shows absorption coefficient dependency with frequency predicted by the model for various pore diameters. Sample thickness is $L = 49$ mm. Plate and cavity parameters used in the model is $d_p = 1$ mm and $d_c = 3$ mm. The model prediction of the first resonance frequency is for when the pancake absorber has $r_0 = 2.5$ mm, $r_0 = 3.0$ mm and $r_0 = 3.5$ mm. Also included is the prediction for a single pore only, for the case of when $d_c = 0$ for comparison.

Figure 6.20 shows absorption coefficient as a function of frequency predicted by the model for various pore diameters with $L = 49$ mm. Plate and cavity parameters used in the model are $d_p = 1$ mm and $d_c = 3$ mm. Model predictions for α is when the pancake absorber has an increase of its pore radius, from that of the pore radius dimensions shown by Figure 6.19. Altering the pore radius by as little as 0.5 mm creates a shift in frequency and changes the peak absorption coefficient. Pore radius $r_0 = 4.0$ mm, $r_0 = 4.5$ mm and $r_0 = 5.0$ mm. A single pore only ($d_c = 0$) is included to show a comparison between the pancake absorber. Absorptive peak at f_r (simple pore case) is found at $f = 1740$ Hz. A comparison for single pores and different values of r_0 is presented later is section 6.4 (for the performance of solid cylinders and simple orifices showing the effectiveness of the metamaterial pancake absorbers for same sample length).

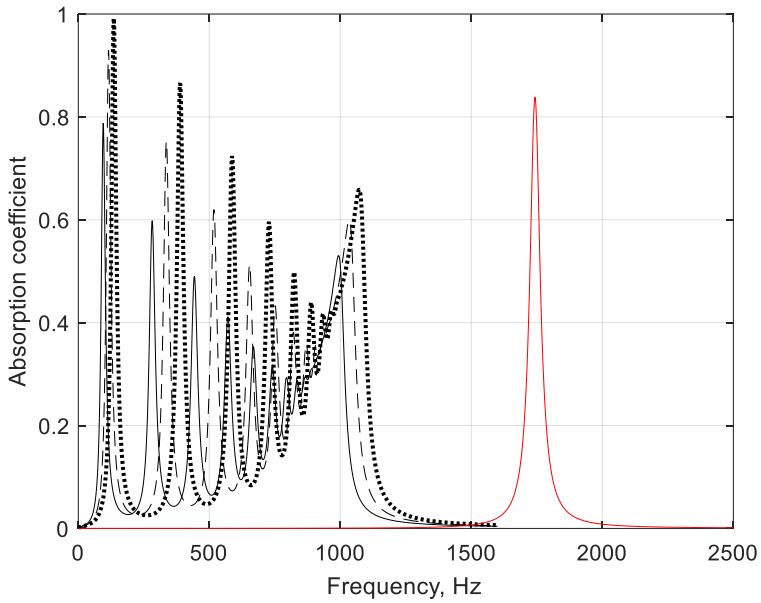

Figure 6.19. Effective properties model showing the effect of pore diameter for the predicted peak absorption coefficient. Cavity thickness $d_c = 3$ mm, $R = 50$ mm and $L = 49$ mm. Single pore radius comparison, $r_0 = 2.5$ mm (black solid line), $r_0 = 3$ mm (dash) and $r_0 = 3.5$ mm (dot). Solid cylinder with pore $r_0 = 4$ mm (red solid line).

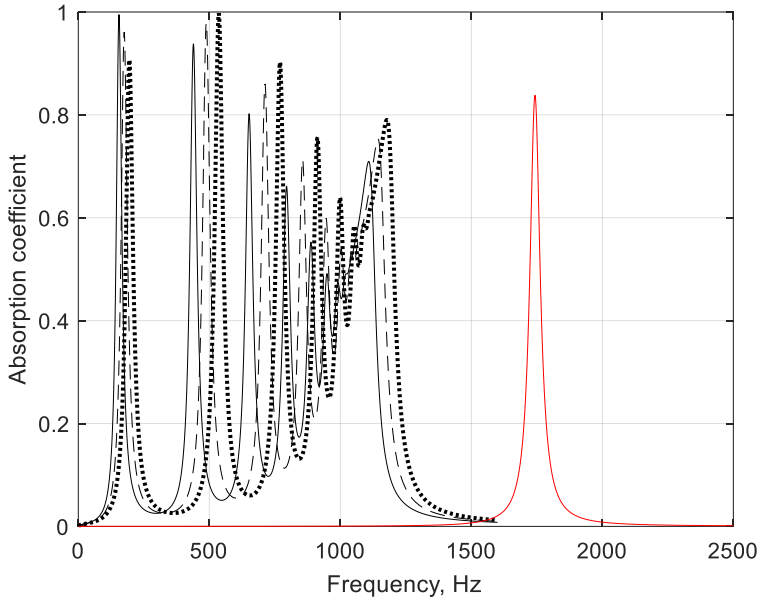

Figure 6.20. Effective properties model showing the effect of pore diameter for the predicted peak absorption coefficient. Cavity thickness $d_c = 3$ mm, $R = 50$ mm and $L = 49$ mm. Single pore radius comparison, $r_0 = 4$ mm (black solid line), $r_0 = 4.5$ mm (dash) and $r_0 = 5$ mm (dot). Solid cylinder with pore $r_0 = 4$ mm (red solid line).

In Figure 6.21 data is presented showing absorption coefficient as a function of frequency as predicted by the model for a larger sample thickness L. A pore radius $r_0 = 4$ mm is selected since this dimension of r_0 is considered to result in the optimum performance of the structure for low frequency sound absorption. Pancake configuration is as follows and starts with smallest value of d_c that is used in the pancake designs. Pore radius $r_0 = 4$ mm , $d_p = 1$ mm, $d_c = 1$ mm and $L = 60$ mm. It can be seen that the influence of cavities d_c reduces f_r by nearly 10 times even for a small value of d_c, when compared to a solid cylinder with single pore ($d_c = 0$). The model prediction of the first resonance frequency is later validated using white noise excitation used in the impedance tube. Figure 6.22 shows the first resonance frequency as a function of the spacing between the rings d_c. Pancake dimensions are $r_0 = 4$ mm, $d_p = 1$ mm, $d_c = 1$ mm and sample length $L = 60$ mm. Figure 6.23 shows the variation in α as a function of the spacing between the rings d_c. The predictions of the first resonance frequency f_r and absorption coefficient variations with d_c and L allow the design to be selected carefully for the overall optimum performance for the structure. Figure 6.24 presents the data showing α dependency with frequency as predicted by the model. Pore radius $r_0 = 4$ mm remains, due to optimum performance of the structure being achieved for low frequency sound absorption. Pancake configuration is $r_0 = 4$ mm, $d_p = 1$ mm, and d_c is increased so that $d_c = 3$ mm. Sample thickness is $L = 60$ mm. The increase of d_c results in the improved peak absorption coefficient values (as opposed to $d_c = 1$ mm). This also introduces further additional absorptive peaks, seen at higher frequencies. The peak absorptive value remains the same since L remains of same value (from the data shown by Figure 6.21 for when $d_c = 1$ mm). Number of the dead-end is given by N_{de}.

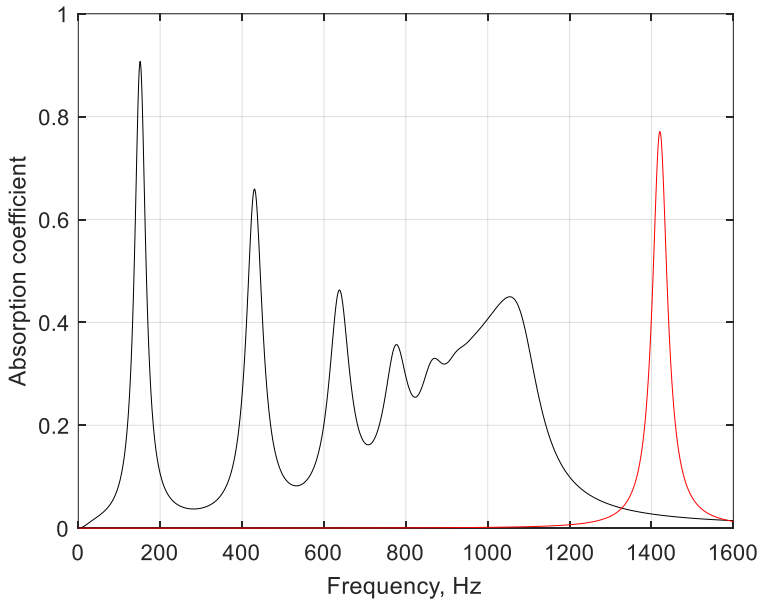

Figure 6.21. Absorption coefficient as a function of frequency for pancake absorber with $r_0 = 4$ mm, $L = 60$ mm, $d_p = 1$ mm, $R = 50$ mm, $N_{de} = 30$, and $d_c = 1$ mm. Effective properties model showing pancake absorber (black), solid structure with simple pore (red).

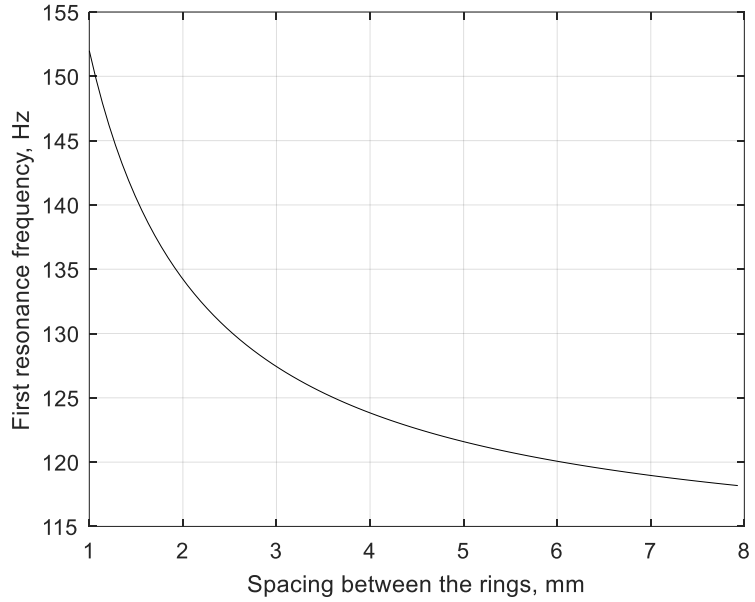

Figure 6.22. First resonance frequency as a function of spacing between rings for pancake absorber with $r_0 = 4$ mm, $L = 60$ mm, $d_p = 1$ mm, $R = 50$ mm, $N_{de} = 30$, and $d_c = 1$ mm. Data shown is that predicted by effective properties model.

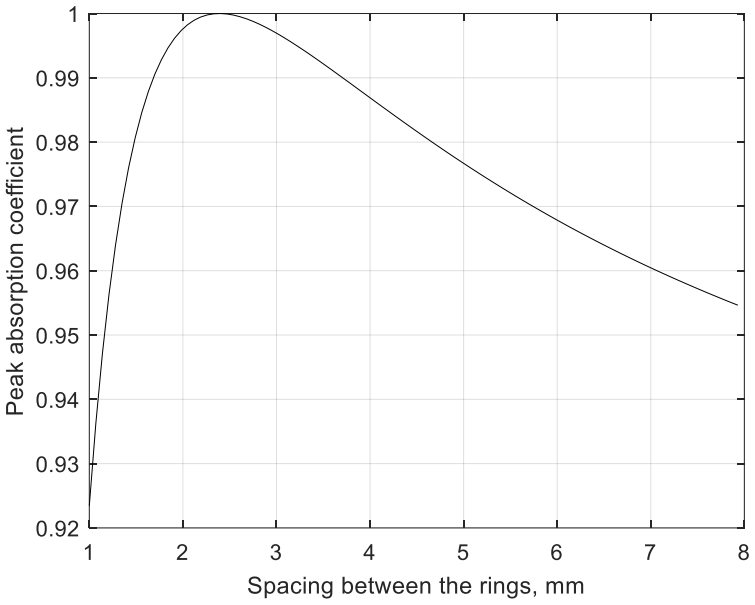

Figure 6.23. Peak absorption coefficient as a function of spacing between rings for pancake absorber with $r_0 = 4$ mm, $L = 60$ mm, $d_p = 1$ mm, $R = 50$ mm, $N_{de} = 30$, and $d_c = 1$ mm. Data shown is that predicted by effective properties model.

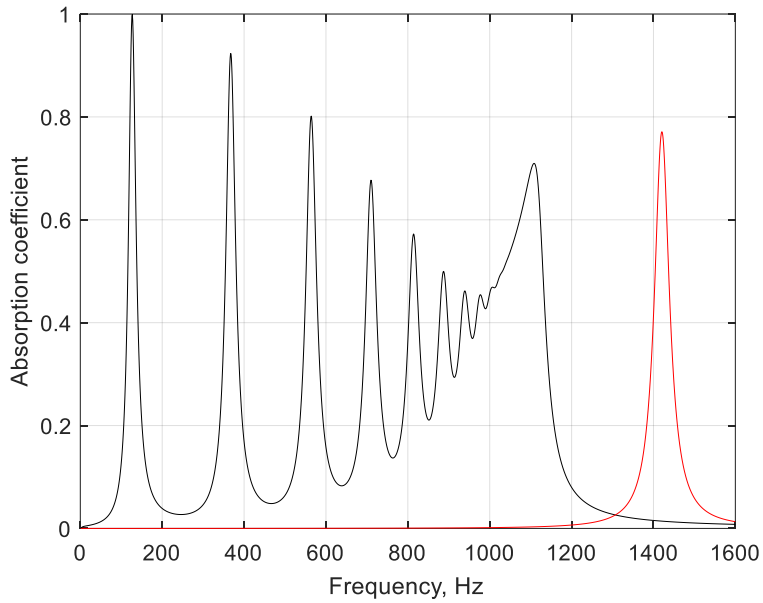

Figure 6.24. Absorption coefficient as a function of frequency for pancake absorber with $r_0 = 4$ mm, $L = 60$ mm, $d_p = 1$ mm, $R = 50$ mm, $N_{de} = 15$, and $d_c = 3$ mm. Effective properties model data showing pancake absorber (black), solid structure with simple pore (red).

First resonance frequency as a function of the spacing between the rings d_c is presented by Figure 6.25. Structure parameters are $r_0 = 4$ mm, plate thickness $d_p = 1$ mm, cavity thickness $d_c = 3$ mm, and sample length $L = 60$ mm. And in Figure 6.26 the model prediction is shown for the absorption coefficient as a function of the spacing between the rings d_c for same values of L, including r_0, and d_p. To validate the model in linear regime the data for various pancake configurations is compared against the experimental data, see Figures 6.27 – 6.32.

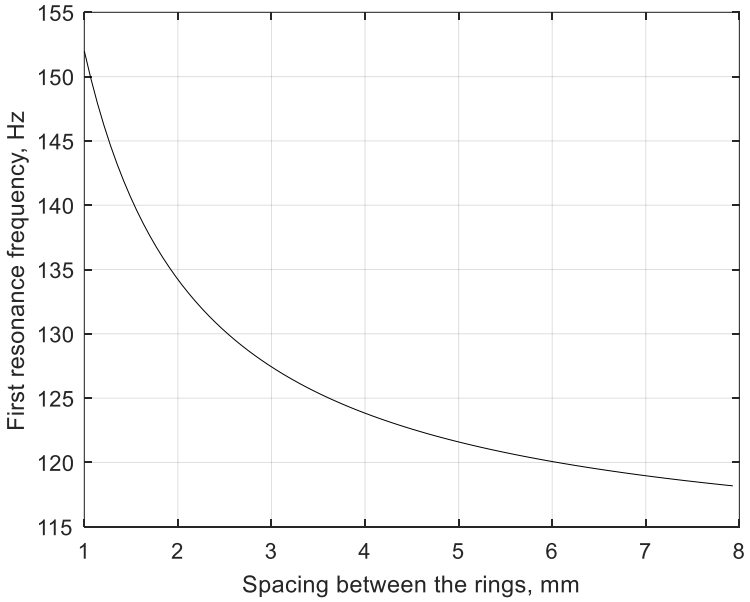

Figure 6.25. First resonance frequency as a function of spacing between rings for pancake absorber with $r_0 = 4$ mm, $L = 60$ mm, $d_p = 1$ mm, $R = 50$ mm, $N_{de} = 15$, and $d_c = 3$ mm. Data shown is that predicted by effective properties model.

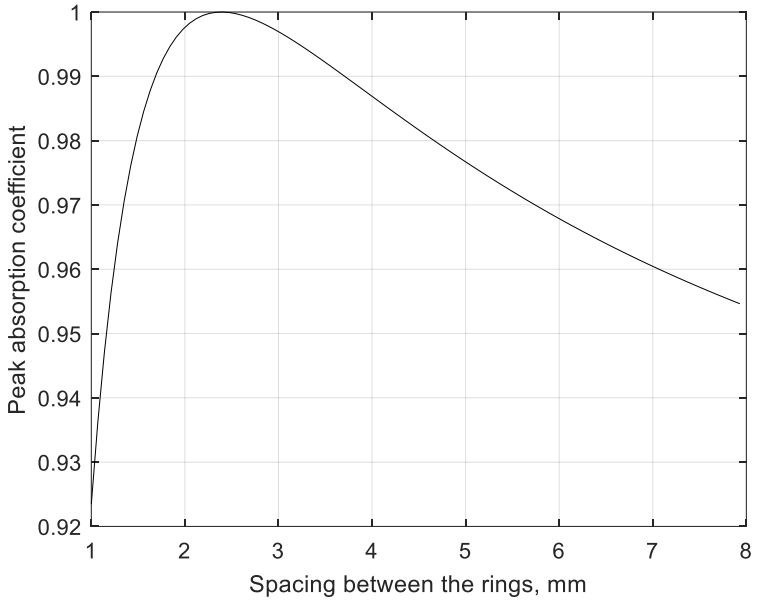

Figure 6.26. Peak absorption coefficient as a function of spacing between rings for pancake absorber with $r_0 = 4$ mm, $L = 60$ mm, $d_p = 1$ mm, $R = 50$ mm, $N_{de} = 15$, and $d_c = 3$ mm. Data shown is that predicted by effective properties model.

Absorption coefficient as a function of frequency for absorbers with lengths $L = 30$ mm → $L = 35$ mm is shown by Figures 6.27 – 6.29. The metamaterial pancakes also differ in their values of d_c. Increasing cavity thickness affects the dependence of α from the geometry and results in variations in the absorber performance. Predictions for Helmholtz resonator absorption coefficient is shown in all figures for comparison with pancake lengths between $L = 30$ mm and $L = 60$ mm. This means that the predictions for the Helmholtz resonator is compared to the different values of cavity depth d_c in the pancake absorber designs. The Helmholtz resonator is modelled as a single plate and the plate thickness is considered of same value to those of the absorbers. This is for a central perforation with radius $r_0 = 4$ mm which is backed by a rigidly-backed air cavity. The Helmholtz resonator is set with equal length L for each of the pancake absorbers considered, for each overall total thickness of the samples. Another consideration used in the model was the application of the end correction for all the samples including the Helmholtz resonator. The end correction is accounted $l_e = \frac{8}{3\pi} r_0$ [141]. The cavity of the Helmholtz resonator is much larger than the value of l_e. For the pancake configurations being rigidly-backed, then only one end-correction is considered. However, this is the contrary for the Helmholtz resonator, where both the internal and external is considered, and resulting in two end corrections being applied. For the pancake absorber comprised $d_c = 1$ mm (shown by Figure 6.27, the first resonance frequency of the measured data (obtained by impedance tube) is $f_r = 262$ Hz and has a peak value $\alpha = 0.87$ (where $L = 31$ mm). Corresponding absorptive peaks are found at frequencies is $f = 572$ Hz, $f = 769$ Hz, and $f = 1015$ Hz. The normalized absorption coefficient values at these frequencies are $\alpha = 0.32$, $\alpha = 0.48$ and $\alpha = 0.26$, respectively. After $f = 1200$ Hz then α reduces to $\alpha = 0.13$ towards the end of the frequency spectrum. The first resonance frequency predicted by the model $f_r = 265$Hz where α had a peak value, $\alpha = 0.97$. Data predicted by the effective properties model for the second and third absorptive peaks was $\alpha = 0.63$ and $\alpha = 0.40$, respectively. Frequency of the second peak is predicted by the model to be $f = 657$ Hz. And third predicted frequency by the model for the third absorptive peak is $f = 854$ Hz.

In Figure 6.28 the data shows the case for when a pancake absorber is built with $d_c = 3$ mm and $L = 30$ mm. The first resonance frequency obtained by the data from the impedance tube is $f_r = 229$ Hz, and is found to be lower than when $d_c = 1$ mm. This results in an absorptive peak value $\alpha = 0.99$. The measured data obtained from impedance tube use is as follows; the second absorptive peak is at $f = 530$ Hz with a peak value $\alpha = 0.71$. Other absorptive peaks are found $f = 765$ Hz and $f = 1027$ Hz in which the absorption coefficient values at these frequencies are $\alpha = 0.77$ and $\alpha = 0.45$, respectively. At $f = 1195$ Hz absorption coefficient is $\alpha = 0.3$ and reduces to $\alpha = 0.1$ towards $f = 1600$ Hz. The effective properties model however, predicts the following data for the pancake with $d_c = 3$ mm. First resonance frequency $f_r = 229$ Hz and the absorption coefficient had peak value $\alpha = 0.96$. Additional peaks predicted by the model are found at $f = 596$ Hz and $f = 813$ Hz with peak values being $\alpha = 0.96$ and $\alpha = 0.78$, respectively.

Data shown by Figure 6.29 is for when $d_c = 6$ mm and when the absorber is built with $L = 35$ mm. The data obtained by the impedance tube for measuring f_r of the pancake is $f_r = 222$ Hz in which f_r for $d_c = 6$ mm is found to be at lower frequency than values of f_r when $d_c = 1$ mm, and $d_c = 3$ mm. The second absorptive peak is around $f = 558$ Hz where $\alpha = 0.85$. The third absorptive peak is at $f = 775$ Hz with $\alpha = 0.83$. Other absorption coefficient values are $\alpha = 0.59$ at $f = 1044$ Hz and $\alpha = 0.4$. at $f = 1200$ Hz. This then reduces to $\alpha = 0.15$ towards $f = 1600$ Hz. It can be determined from the data shown by Figures 6.27 – 6.29 that increasing the cavity thickness d_c reduces the first resonance frequency. Absorption coefficient values are shown to be the same for $d_c = 3$ mm and $d_c = 6$ mm, where $\alpha = 0.99$. This is found to be the case for the first resonance frequency. When $d_c = 3$ mm then $f_r = 229$ Hz and for $d_c = 6$ mm the first resonance frequency is $f_r = 223$ Hz. A difference $f = 6$ Hz exists for same values of α. For the pancake configuration $d_p = 1$ mm and $d_c = 6$ mm shown in Figure 6.29 the effective properties model predictions for the absorption coefficient performance is the following. The model predicts $\alpha = 0.92$ and the first resonance frequency is $f_r = 186$ Hz. The second and third absorptive peak values are predicted $\alpha = 1.0$ and $\alpha = 0.94$ at $f = 512$ Hz and $f = 733$ Hz, respectively.

The pancake is assembled so now $d_c = 1$ mm and the sample is extended by additional plates d_p. Structure dimensions are built $r_0 = 4$ mm, $d_p = 1$ mm length close to $L = 60$ mm. This is so the metamaterial can be investigated with larger values of L, where various pancake configurations are measured in the impedance tube and compared with the effective properties model. The pancake and model are used to determine the optimum parameters for the absorber performance whilst keeping L of the structure relatively short. Figure 6.30 shows absorption coefficient dependence as a function of frequency with f_r measured being $f_r = 144$ Hz. The associated peak absorption value measured $\alpha = 0.88$. The model, however, predicts $\alpha = 0.88$ with $f_r = 139$ Hz. Second and third absorptive peaks for the experimental data was $f = 396$ Hz and $f = 574$ Hz. The model predicted slightly different. For the former (second absorptive peak) it is predicted being $f = 398$ Hz and the third peak around $f = 603$ Hz. Predicted values of the absorption coefficient were $\alpha = 0.66$ (second peak) and $\alpha = 0.47$ (third peak). The measured values of α from the impedance tube was $\alpha = 0.41$ and $\alpha = 0.54$ for the second and third peaks, respectively.

Figure 6.31 data shows the case for when the pancake absorber is built with $d_c = 3$ mm throughout the sample and its length approximately $L = 58$ mm. The absorptive peak value at f_r given by the model

was $\alpha = 1.0$ where $f_r = 125$ Hz. The data differs slightly from the impedance tube data. For instance, the absorption coefficient and the first resonance frequency was $\alpha = 0.99$ at $f_r = 135$ Hz from impedance tube tests. A second peak value predicted by the model is $\alpha = 0.93$ and $f = 367$ Hz. However, data obtained from the measurement results in $\alpha = 0.58$ where $f = 362$ Hz. The third predicted peak value $\alpha = 0.81$ and is found to be at $f = 563$ Hz. Measured data obtained by the impedance tube shows that $\alpha = 0.58$ at $f = 650$ Hz. Absorption coefficient as a function of frequency is shown in Figure 6.32 for the pancake absorber with larger values of d_c where $L = 63$ mm and similar lengths for pancakes built with $d_c = 1$ mm and $d_c = 3$ mm. The cavity depth arranged in the sample was $d_c = 6$ mm. First resonance frequency measured (obtained impedance tube data) $f_r = 134$ Hz and had a maximum absorptive peak value, where $\alpha = 1.0$. In contrast, the model predicts $\alpha = 0.97$ and $f_r = 108$ Hz. The second and third absorptive peak values are measured (from experimental data) $\alpha = 0.64$ and $\alpha = 0.71$ at frequencies $f = 348$ Hz and $f = 524$ Hz, respectively. Data predicted by the effective properties model gives the second and third peak values $\alpha = 0.98$ and $\alpha = 0.92$. The frequency for the second absorptive peak is predicted by the model being $f = 317$ Hz. And the third predicted frequency by the model was $f = 497$ Hz.

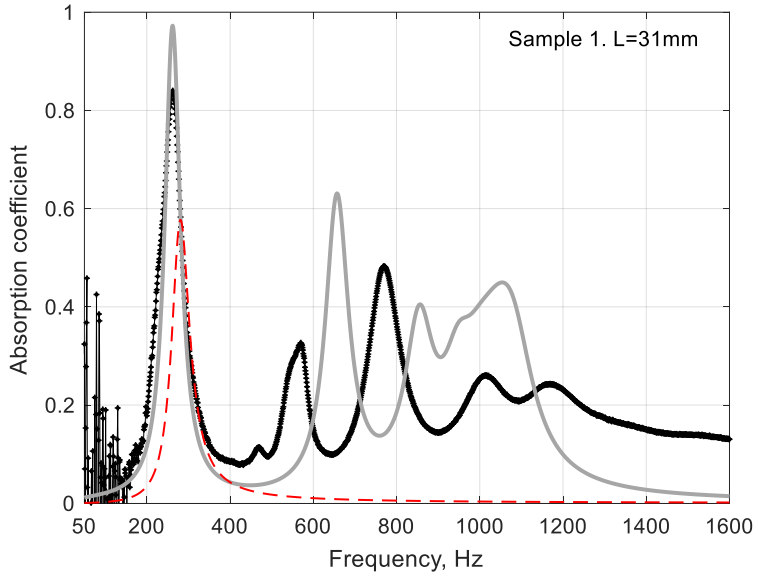

Figure 6.27. Absorption coefficient data (black markers) and full model predictions (grey lines) for hard backed absorbers with $d_p = 1$ mm, $r_0 = 4$ mm, $d_c = 1$ mm, $R = 50$ mm, $N_{de} = 16$, and $L = 31$ mm. Absorption coefficient predictions for Helmholtz resonator same size as the pancake absorber, dashed lines (red).

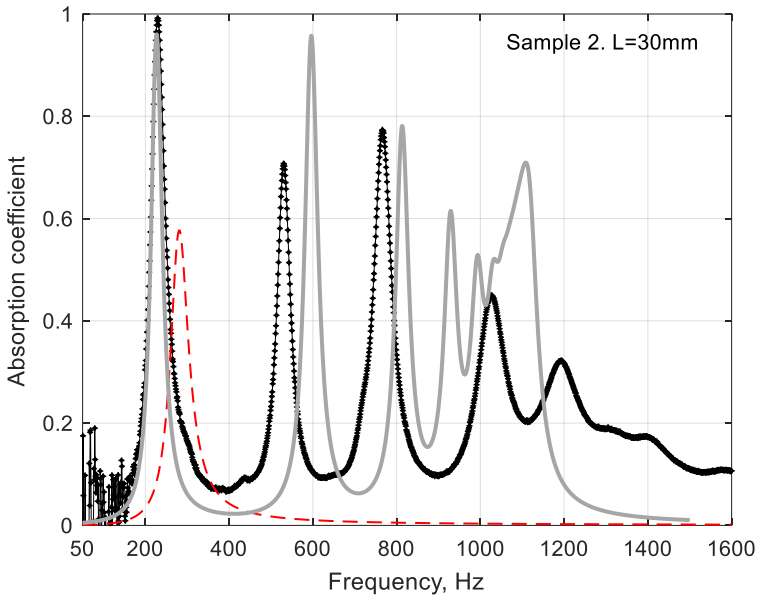

Figure 6.28. Absorption coefficient data (black markers) and full model predictions (grey lines) for hard backed absorbers with $d_p = 1$ mm, $r_0 = 4$ mm, $d_c = 3$ mm, $R = 50$ mm, $N_{de} = 8$, and $L = 30$ mm. Absorption coefficient predictions for Helmholtz resonator same size as the pancake absorber, dashed lines (red).

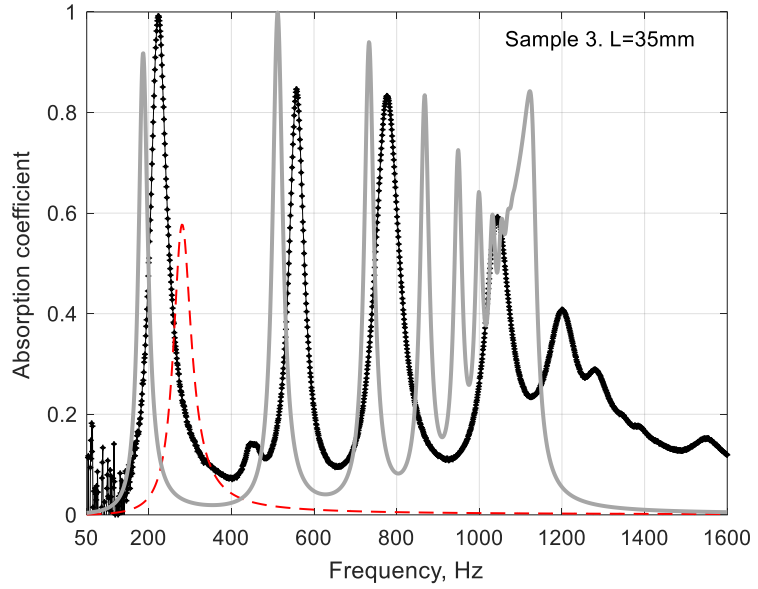

Figure 6.29. Absorption coefficient data (black markers) and full model predictions (grey lines) for hard backed absorbers with $d_p = 1$ mm, $r_0 = 4$ mm, $d_c = 6$ mm, $R = 50$ mm, $N_{de} = 5$, and $L = 35$ mm. Absorption coefficient predictions for Helmholtz resonator same size as the pancake absorber, dashed lines (red).

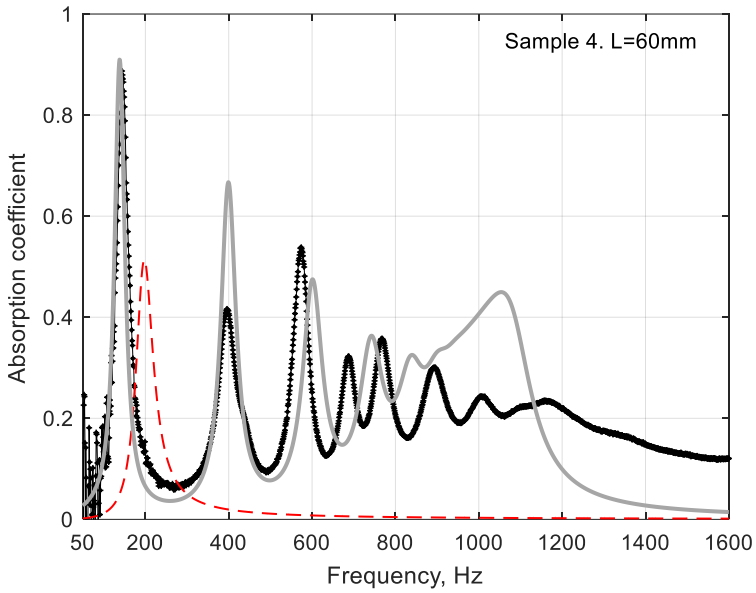

Figure 6.30. Absorption coefficient data (black markers) and full model predictions (grey lines) for hard backed absorbers with $d_p = 1$ mm, $r_0 = 4$ mm, $d_c = 1$ mm, $R = 50$ mm, $N_{de} = 30$, and $L = 60$ mm. Absorption coefficient predictions for Helmholtz resonator same size as the pancake absorber, dashed lines (red).

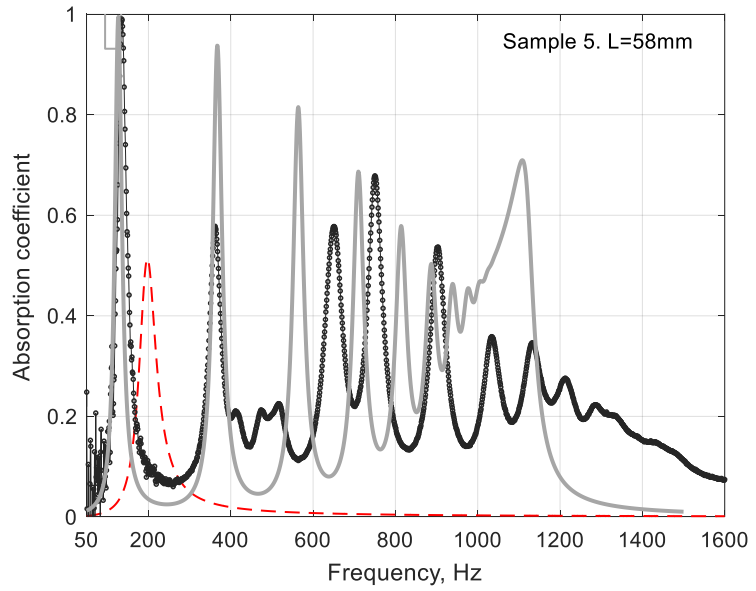

Figure 6.31. Absorption coefficient data (black markers) and full model predictions (grey lines) for hard backed absorbers with $d_p = 1$ mm, $r_0 = 4$ mm, $d_c = 3$ mm, $R = 50$ mm, $N_{de} = 15$, and $L = 58$ mm. Absorption coefficient predictions for Helmholtz resonator same size as the pancake absorber, dashed lines (red).

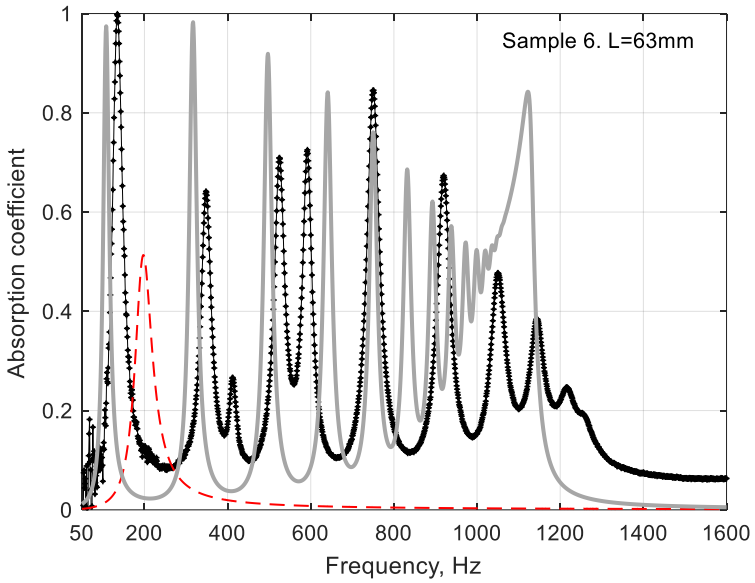

Figure 6.32. Absorption coefficient data (black markers) and full model predictions (grey lines) for hard backed absorbers with $d_p = 1$ mm, $r_0 = 4$ mm, $d_c = 6$ mm, $R = 50$ mm, $N_{de} = 9$, and $L = 63$ mm. Absorption coefficient predictions for Helmholtz resonator same size as the pancake absorber, dashed lines (red).

The computed absorption coefficient values for the Helmholtz resonator and its resonance frequency are given in each of the samples s1 – s7 presented by Figures 6.27 – 6.33. The purpose of this is to show how effective the metamaterials are in comparison to the Helmholtz resonator. In Figure 6.27 for a sample length $L = 31$ mm the resonance frequency of the resonator is $f = 280$ Hz, and $\alpha = 0.58$. Not surprisingly, α is also the same as shown in Figures 6.28 – 6.29, where $\alpha = 0.58$ for lengths $L = 30$ mm and $L = 35$ mm, respectively. The Helmholtz resonator computations given also in the larger pancake structures (around $L = 60$ mm) is shown in Figures 6.30 – 6.32. For a Helmholtz resonator with $L = 60$ mm, see Figure 6.30, $\alpha = 0.51$ and the resonance frequency was $f = 196$ Hz. The value of $\alpha = 0.51$ is also found to be the same for when $L = 58$ mm and $L = 63$ mm, by the Helmholtz resonator data shown by Figures 6.31 – 6.32, respectively. The absorption coefficient α is also given at the same resonance frequency $f = 196$ Hz in Figures 6.33 – 6.34.

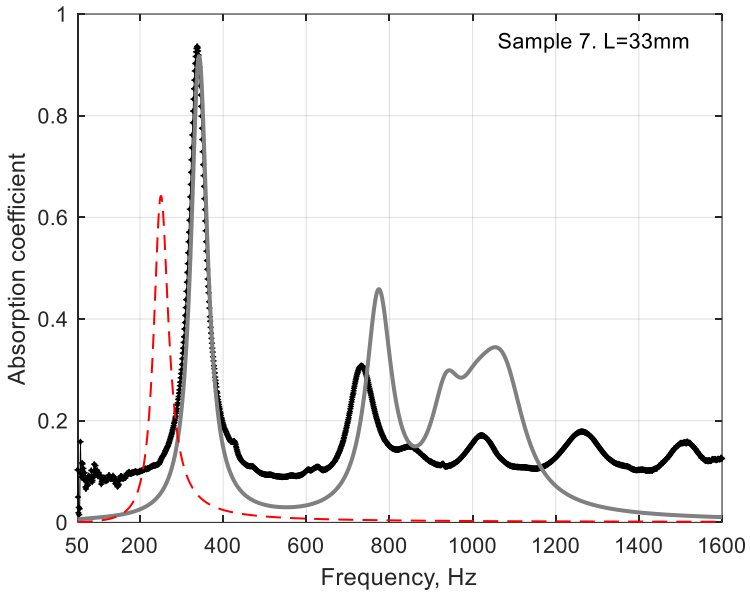

Figure 6.33. Absorption coefficient data (black markers) and full model predictions (grey lines) for hard backed absorbers with $d_p = 3$ mm, $r_0 = 4$ mm, $d_c = 1$ mm, $R = 50$ mm, and $L = 33$ mm. Absorption coefficient predictions for Helmholtz resonator same size as the pancake absorber, dashed lines (red).

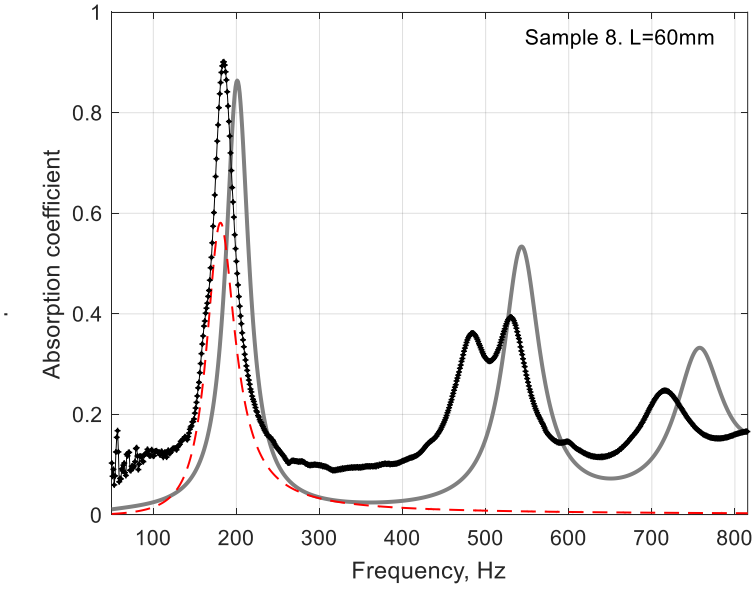

Figure 6.34. Absorption coefficient data (black markers) and full model predictions (grey lines) for hard backed absorbers with $d_p = 3$ mm, $r_0 = 4$ mm, $d_c = 1$ mm, $R = 50$ mm, and $L = 60$ mm. Absorption coefficient predictions for Helmholtz resonator same size as the pancake absorber, dashed lines (red).

Table 6.13 given below, presents the measured values of the absorption coefficient at first resonance α_r and the frequency at first resonance f_r, of the experimental (impedance tube data) and theoretical (predicted by the effective properties model). The values of α_r and f_r are shown for the metamaterial pancake structure consisting of various configurations. Characteristic frequency for the air in the main pore was the same for all configurations, $f_{b\,p} = 2.5$ Hz, the characteristic frequencies $f_{b\,c}$ for air in the cavities were $39.2, 9.8$ and 2.5 Hz for $d_c = 1, 3$ and 6 mm, respectively. Configurations are shown by sample numbers, showing sample length L, cavity thickness d_c, and plate thickness d_p. Constant pore radius $r_0 = 4$ mm for all samples given in Table 6.13.

Sample	L, mm	d_p, mm	d_c, mm	$f_r^{(1)}$, Hz	$f_r^{(2)}$, Hz	$f_r^{(3)}$, Hz ϵ, %	$\alpha_r^{(1)}$	$\alpha_r^{(2)}$	$\alpha_r^{(3)}$
1	31	1	1	262	265	270 3	0.87	0.97	0.98
2	30	1	3	229	229	231 1	0.99	0.96	0.96
3	35	1	6	222	187	189 15	0.99	0.92	0.92
4	60	1	1	146	144	144 2	0.88	0.91	0.92
5	58	1	3	135	125	125 7	0.99	1.0	1.0
6	63	1	6	134	108	108 17	1	0.97	0.97
7	33	3	1	337	343	363 8	0.94	0.92	0.94
8	60	3	1	185	202	206 11	0.90	0.86	0.87

Table 6.13. Measured, $f_r^{(1)}$ and $\alpha_r^{(1)}$, predicted by the full model, $f_r^{(2)}$ and $\alpha_r^{(2)}$, and predicted by approximations (34) and (36), $f_r^{(3)}$ and $\alpha_r^{(3)}$, values of the first resonance frequency f_r and peak absorption coefficient α_r for all samples. Dimensions of the samples – columns 2-4, ϵ is relative error between the measured resonance frequency $f_r^{(1)}$ and approximation $f_r^{(3)}$ given by equation (34), in %.

The data given by Figures 6.27 – 6.34 shows the absorber performance for two different lengths, and when comprised with thicker plates than those presented thus far. This is when the pancake structure is configured with $d_c = 1$ mm, $d_p = 3$ mm, $r_0 = 4$ mm, $R = 50$ mm and sample lengths are $L = 33$ mm and $L = 60$ mm. Absorption coefficient dependence on frequency is shown by Figure 6.33 with the first resonance frequency (measured by impedance tube) $f_r = 337$ Hz. The measured peak value of $\alpha = 0.94$. The model predicted slightly different, where $\alpha = 0.92$ which corresponded to $f_r = 343$ Hz. Second absorptive peak (measured experimental data) is at frequency $f = 732$ Hz with an absorptive peak value $\alpha = 0.31$. The effective properties model predicted the second absorptive peak and resonance frequency slightly higher. For instance, the second peak computed by the model was $f = 777$ Hz with peak value $\alpha = 0.45$. Figure 6.34 shows absorption coefficient as a function of frequency for when the pancake absorber also has cavity thickness $d_c = 1$ mm but with additional d_p and d_c. The sample is built with an additional length of approximately $L = 27$ mm, therefore total length $L = 60$ mm. First resonance frequency measured in the impedance tube is $f_r = 185$ Hz and the absorption coefficient has a peak value $\alpha = 0.90$.

Second and third peak values can be observed in Figure 6.34 from the data obtained by the impedance tube measurement. The second absorptive peak is forked at frequencies $f = 484$ Hz and 531 Hz with peak values $\alpha = 0.36$ and $\alpha = 0.39$, respectively. There is also another peak value found to be at $f = 716$ Hz with absorption coefficient $\alpha = 0.25$. The effective properties model predicts α having slightly different values at different frequencies f. First resonance frequency is seen to be 17 Hz at higher frequency, predicted by the model as $f_r = 202$ Hz. Absorption coefficient has a peak value $\alpha = 0.86$, which is only slightly lower than the data obtained from the direct impedance tube measurement. The second predicted peak had a maximum absorptive value $\alpha = 0.53$ which is slightly larger than α measured in the impedance tube. Lastly, absorption coefficient data for the third peak is predicted by the effective properties model to be $\alpha = 0.33$ with $f = 760$ Hz. Values of α and f for the third peak are predicted as slightly larger for the former, and at 44 Hz higher in frequency. Computed Helmholtz resonator values for the same sample lengths ($L = 33$ mm and $L = 60$ mm) are shown also in Figure

6.33 for the shorter sample, and Figure 6.34 for the larger sample. The Helmholtz resonator data presented in Figure 6.33 for $L = 33$ mm has an absorptive peak value $\alpha = 0.64$ at frequency $f = 250$ Hz.

Helmholtz resonator data shown by Figure 6.34 for $L = 60$ mm has an absorptive peak value $\alpha = 0.58$ at frequency $f = 180$ Hz. It can be observed by the data shown by Figures 6.33 – 6.34 that the Helmholtz resonator has its absorptive peak values found to be at lower frequency than that of the pancake absorbers, for same sample length. For the pancake absorber with $L = 33$ mm, the Helmholtz resonator absorption coefficient data is lower ($f = 80$ Hz) than the first resonance frequency of the pancake. When the pancake structure is built with larger length ($L = 60$ mm) then the difference in the frequency between the Helmholtz resonator and pancake first resonance frequency is much less. For example, when the pancake has $L = 60$ mm the difference of the absorptive peak frequency is only $f = 5$ Hz. This phenomenon of f_r between the Helmholtz resonator and pancake absorbers is seen to be the contrary for the pancake structures that are configured with the smaller plates, where $d_p = 1$ mm. It is seen to be the case irrespective of the sample lengths considered thus far, around $L = 30$ mm and $L = 60$ mm. This is when the pancake structures have a high pore wall porosity and consequently, the first resonance frequency f_r is lower for the pancake than it is for the Helmholtz resonator (for same sample thickness). When the sample consists of a low wall porosity (see sample 7 data presented in Table 6.13) the Helmholtz resonator has lower f_r than the first resonance frequency of the pancake f_r.

As length L increases (for the pancake absorber) a larger number of multiple peaks are observed, see Figures 6.27 – 6.32. This means that pancake structures with length around $L = 30$ mm have fewer resonance peaks than the pancakes structures built $L = 60$ mm. Another realisation of the pancake is that if the metamaterial is developed with a cavity thickness larger than the thickness of the plates, the peak values at resonance are impacted. For instance, larger absorption coefficient values α are consequently greater for each resonance frequency, for samples with $d_c = 6$ mm. This results in the pancake absorbers with $d_c = 3$ mm having slightly lower values of α than those built with $d_c = 6$ mm. Furthermore, the pancakes with $d_c = 1$ mm has lower peak values of α than the pancakes built with $d_c = 3$ mm. The resonance data can be clearly observed in the absorption coefficient plots, see Figures 6.27 – 6.32, including data presented in Table 6.13. Performance of the pancake absorber makes the metamaterial structure advantageous over the Helmholtz resonator when multiple frequencies are required to be attenuated. This is especially the case and most desirable for low frequency sound absorption, where the metamaterial structures with identical sample length outperforms the Helmholtz resonator.

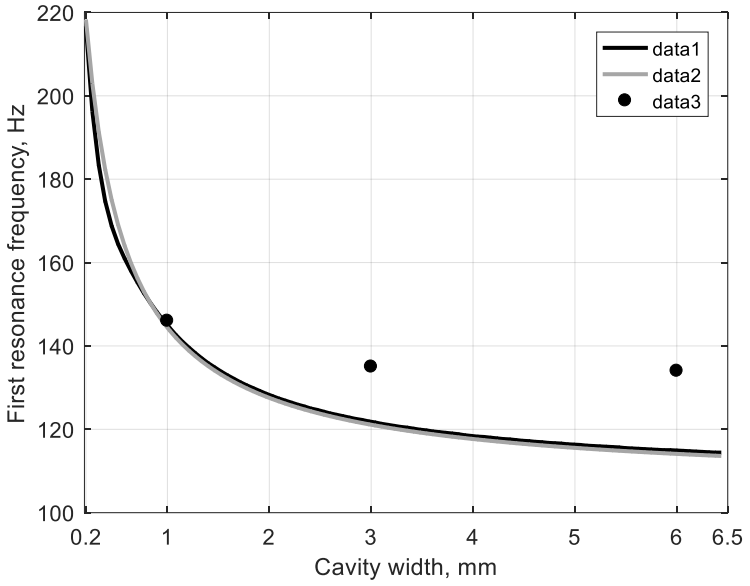

(a)

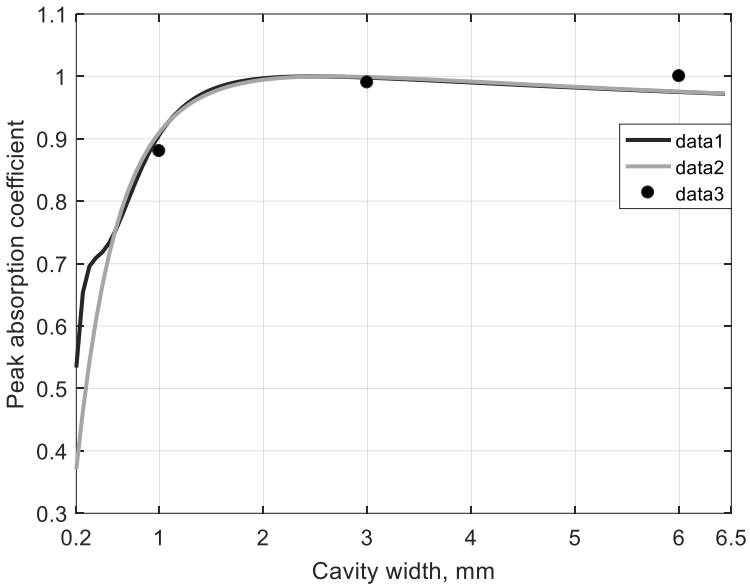

(b)

Figure 6.35. Measurements (markers), model predictions (black lines) and approximations given by equations (34) and (36) (grey lines) for different cavity widths. Sample has $L = 60$ mm, $d_p = 1$ mm, $r_0 = 4$ mm, $R = 50$ mm. (a) Frequency of the first resonance, (b) Absorption coefficient at resonance.

Influence of the cavities present in the pancake structure is shown by Figure 6.35 a, b, for a sample with $d_p = 1\,\mathrm{mm}$, $r_0 = 4\,\mathrm{mm}$, and $R = 50\,\mathrm{mm}$. The first resonance frequency f_r dependence is shown as a function of d_c by the fluid occupied between the separation of the plates in the distributed series of cavities within the structure, see Figure 6.35 a. Similarly, the cavity thickness d_c is used to show the dependence of the peak absorption as a function of d_c, shown in Figure 6.35 b. A comparison is given between the experimental data, given by markers, and the theoretical predictions. Where the solid black line refers to full model used after determination of the effective properties, and solid grey line which refers to equation (34) and equation (36). The effective properties model is seen to be mostly effective in terms of its accuracy for the prediction of f_r. Accuracy of the model becomes slightly less for other

resonance frequencies afterward the first resonance frequency. This phenomenon is the case for all the investigated sample thicknesses of the pancake structures ($L = 30$ mm and $L = 60$ mm) where the assumption $Re(q)h \ll 1$ is only valid at low frequencies. Calculations of the wave speed for the sample with $d_p = 1$ mm and $d_c = 3$ mm give 46 m/s at $f = 50$ Hz decreasing slowly to 29 m/s at $f = 1000$ Hz.

This means that $Re(q)h = 0.5$ at $f = 760$ Hz and at higher frequencies the model is no longer applicable. Model predictions for the first resonance frequency, however, is more accurate for the pancake absorbers with cavity thicknesses $d_c = 1$ mm and $d_c = 3$ mm compared to samples built with $d_c = 6$ mm. For the latter ($d_c = 6$ mm) the disagreement between the model and the experimental data is 15 %. The disagreement is observed because the model based on effective properties is only applicable when $r_0 \gg d_c$. The assumption $r_0 \gg d_c$ implicitly states that the existence of "scale separation" [140] between the main pore r_0 and cavities d_c, and the existence of small parameter $\frac{d_c}{r_0} \ll 1$. This assumption has been reported also in other works, such as [1] where the wave propagating in the structure is described by the surface impedance $Z_{s\,de}$ from the plates with r_0. The compressibility of the pancake structure is modified due to the presence of the distributed cavities. Viscous effects occur mostly in the main pore with radius r_0, and thermal effects occur due to the presence of the dead-ends. The metamaterial pancake with modified compressibility is a structure of high permeability contrast, referred as such in [3], [139]. See also work by [140] equation (103) for double porosity materials. Measured and predicted values of the first resonance frequency f_r and peak absorption α_r differ only around 7 % – 11 % which is dependent on the value for the central pore wall porosity ϕ_w of each sample. Overall, the effective properties model which accounts for the effective density, effective bulk modulus and compressibility is shown to provide a good match for predicting f_r of the pancake structures. Other resonance frequencies and values of the peak absorption α_r are predicted and illustrate good results, which are close to the measured data, obtained from measurements performed in the impedance tube.

6.2.2. Mechanical Disturbance of the Sample Frame due to Plate Resonance

Accelerometer measurements have been performed using an impedance tube and low levels of acoustic excitation to match the measurements performed in linear regime. This was carried out in order to account for mechanical disturbance of the structure from acoustic pressure applied to the front surface and measuring the metallic plate resonance, see Figures 6.36 a, b. Absorption coefficient is plotted as a function of frequency for a pancake absorber with $d_p = 1$ mm and $d_c = 1$ mm, see Figure 6.36 a. Measurements were also performed for a pancake with $d_p = 3$ mm and $d_c = 1$ mm to investigate the effect of plate thickness d_p built within the structure, see Figure 6.36 b. The data obtained after performing the accelerometer measurements clearly indicates that structural resonance is dependent on the thickness d_p of the plate. The mechanical disturbance of the frame results in mechanical resonance, in addition to acoustic resonance. In Figure 6.36 a ($d_p = 1$ mm, $d_c = 1$ mm) the effective properties model is shown accounting for its predicted data for the absorber performance, including mechanical resonance contribution. The accelerometer data is shown by Figure 6.36 a, to follow the trend of the data obtained by acoustic interaction from the impedance tube, at around 300 $f = 300$ Hz –

900 Hz. In Figure 6.36 b, it can be observed that the accelerometer data (for $d_p = 3$ mm and $d_c = 1$ mm) follows the trend of acoustic interaction at frequencies around $f = 300$ Hz $-$ 600 Hz.

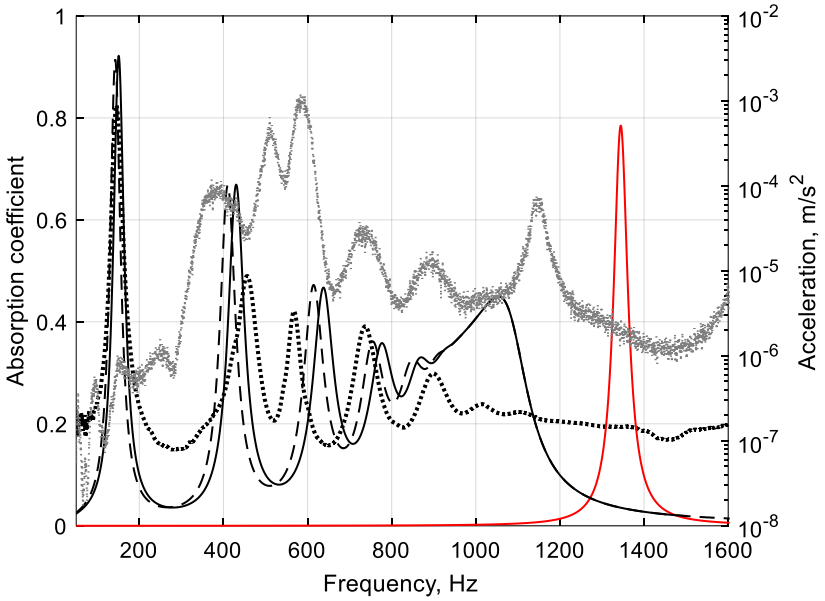

(a)

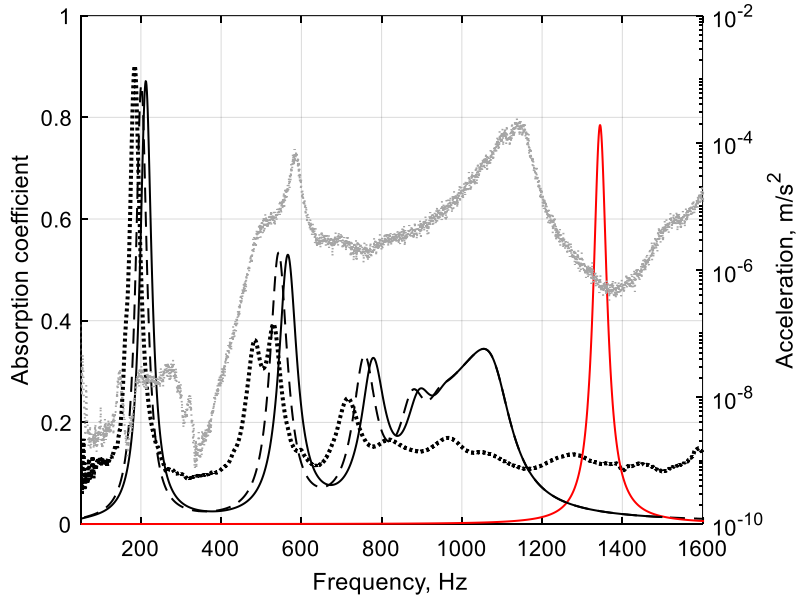

(b)

Figure 6.36. Pancake absorber, (a) $d_p = 1$ mm and $d_c = 1$ mm, (b) $d_p = 3$ mm, $d_c = 1$ mm. Plate radius is $R = 50$ mm. Accelerometer data is plotted showing mechanical disturbance and comparisons with absorption coefficient. Impedance tube data (black dot), accelerometer (grey dot), effective properties model with end correction (dash), effective properties model without end correction (solid black), solid structure with single pore (solid red).

The accelerometer data for pancakes built with $d_p = 1$ mm and $d_p = 3$ mm (Figure 6.36) shows that mechanical resonance is most apparent in the higher frequency range of the spectrum, around $f = 900$ Hz $-$ 1600 Hz. This phenomenon provides a more detailed account of the absorber. And as expected, it validates that the mechanical disturbance of the frame affects the acoustic resonance and peak absorption. The data is also given for when the absorber is predicted by the effective properties model accounting for end-correction effects, and absent any end-correction effects. As the frequency

component becomes higher, after the first resonance frequency f_r, then α results in a reduced value for the pancakes (with increasing frequency). As mentioned in the previous sub chapter, this phenomenon is the manifestation of a bandgap occurring due to quarter wavelength resonance of d_c. Wave speed calculations in the cavities shows that the resonance happens around $f = 950$ Hz. However, $Re(q)h \approx 1$ at $f = 1000$ Hz, therefore the model predictions in this frequency range are not reliable. Mechanical disturbances discussed above shown by Figures 6.36 a, b, of the accelerometer measurements is also a cause for a discrepancy observed at the frequencies in the spectrum higher than the first resonance frequency f_r. For instance, the absorption peak can be explained by the interference of vibrational bandgaps as observed in [3]. According to [142] the first resonance frequency of a thin circular plate with radius R and thickness d_p can be calculated as,

$$f_{plate} = \frac{\lambda^2 d_p}{2\pi R^2}\sqrt{\frac{E}{12\rho(1-\nu)}}, \tag{37}$$

where E, ν and ρ are Young's modulus, Poisson ratio and density of plate material respectively. The value of constant λ^2 depends on the type of boundary conditions. So, $\lambda^2 = 10.2158$ for clamped circular plate and $\lambda^2 = 4.977$ for simply supported plate. Although the boundary conditions for the plate in the absorber are difficult to identify, we could assume that they are between "simply supported" and "clamped". For the aluminum plate with $R = 50$ mm and $d_p = 1$ mm then $f_{plate} = 495.9$ Hz and $f_{plate} = 1011.6$ Hz for a simply supported plate and clamped plate, respectively. This is approximately the frequency range where the signal from the accelerometer is high (see Figure 6.36 a). Moreover the material can also be considered as a periodic array of vibrating plate, then a second stop band effect (a vibrational bandgap effect) can occur around the first structural resonance frequency of the plate. This confirms that the plate resonances might contribute to discrepancies between the model and experiments for frequencies higher than the first absorption peak. And when the pancake is built $d_p = 3$ mm, the resonance frequencies are higher. However, the disagreement between the model and the measurements for the absorbers comprised with $d_p = 3$ mm is still considerable for frequencies above f_r which is due to breaking the low frequency approximation. To conclude, the effective properties model quite accurateley predicts the metamaterial pancake structure for low frequency sound absorption. This is most apparent for the predicted first resonance peak value α_r, at the first resonance frequency f_r of the structure. Moreover, broadband absorption is achieved in some respect, observed across the frequency spectrum where the number of absorptive peaks is dependent on the structure configuration and dimensions of d_p and d_c. The bandgaps are present due to the nature of the metamaterial, which is configured in a periodic arrangement, and due to mechanical disturbance of the material frame.

6.3. Nonlinear Regime – Validation of the Model with the Measured Data

6.3.1. Pancake Absorber – Effective Properties, Nonlinear Model

This section presents the findings of the data obtained by measurments performed in the flow resistivity rig, combined with data from measurements performed in a specially modified impedance tube, for high

sound pressure levels up to 140 dB. The pancake absorber (built with various configurations including sample lengths) has been measured for its performance of absorptive properties at high sound pressure levels, where the results can be seen by the presented data given in Chapter 4. Previous studies show, see [10], [39], [41] (see also Chapter 3, Literature review) that when a porous absorber is targeted with HSPL, a well known nonlinear phenomenon occurs which is result of the interaction of fluid with the absorber (see also, Chapter 5, Flow resistivity measurements). It is reported in Chapter 5 that the nonlinearity associated with rigid porous materials is a Forchheimer's type, characterised by the parameter ξ, which is described by the empirically introduced dependence of flow resistivity of particle velocity v of sound in the pores, $\sigma(v)$, see Chapter 5 for a more detailed account. A developed effective properties model uses the value of the measured Forchheimer's nonlinearity parameter ξ obtained by the flow resistivity measurements, which has been determined to be dependent on sample thickness or length L, and thickness of the cavities d_c contained within the structure. The model uses the measured dependence of the flow resistivity on flow velocity $\sigma(\phi_p|v|)$ which is the same case for each sample, instead of a single linear approximation. After combining with equations (12) and (21), which are expressions for the effective density of air in straight cylindrical pore and cavity respectively, leads to the particle velocity dependent effective density of fluid in the pore ($\alpha_{\infty\, p} = 1$),

$$\rho\,(\omega, v) = \rho_0 \left(1 + \frac{\sigma(\phi_p|v|)}{-i\omega\rho_0} \sqrt{1 + \frac{-4i\omega\rho_0\eta}{\Lambda^2\sigma\left(\phi_p|v|\right)^2}}\right). \tag{38}$$

For the absorber performance in nonlinear regime it is convenient to obtain the dependence of the structure admittance as a function of the incident wave pressure amplitude p_i. In the nonlinear regime where high sound pressure levels are consisdered, the frequency component has quadratic dependence on the flow resistivity and consequently the inertial regime approximation (used previously for linear regime case, $\omega \gg \omega_{b\,p}$) becomes invalid. After assuming a linear dependence of flow resistivity on particle velocity amplitude $\sigma(v) = \sigma_0(1 + \xi\phi_p|v|)$, (see also Chapter 5, Flow resistivity measurements) a new density is defined using the flow resistivity data after increasing the flow velocity in order to obtain the Forchheimer's parameter ξ. Starting point treating the absorber for nonlinear regime is to begin with the conservation equations of momentum and mass for the equivalent fluid saturated material, $-i\omega\rho(\omega, v)v = -(\partial p/\partial x)$ and $-i\omega C(\omega)v = -(\partial v/\partial x)$. The model uses boundary conditions of velocity and pressure continuity, $1 - (p_r/p_i) = \phi_p V(0)$ and $1 + (p_r/p_i) = V(0)\,Z(0)$ for relating the particle velocity and the admittance G at the surface of the sample. To obtain equations for the normalised impedance $Z(X)$ and the normalised particle velocity $V(X)$, a spatial variable X is used to distinguish the boundary conditions applied either at the front, or rear of the sample, containing thickness L, where $X = \frac{x}{L}$. Applying boundary conditions of velocity and pressure continuity, and using spatial variable X, the dependence of the incident pressure amplitude p_i can be determined. Since the effective compressibility is not modified by the nonlinearity then $C(\,\omega) = q/\omega Z$. Normalised impedance $Z(X)$ and the normalised particle velocity $V(X)$ are derived as the following,

$$Z' = +ikL\left(\bar{\rho}\left(\omega, V, \xi\frac{p_i}{\rho_0 c}\right) - \bar{C}(\omega)Z^2\right), \tag{39}$$

$$V' = ikL\,\bar{C}(\omega)VZ. \tag{40}$$

Where $Z(X) = \frac{1}{\rho_0 c}\frac{p(X)}{v(X)}$ and $V(X) = v(X)\frac{\rho_0 c}{p_i}$.

$$\bar{C}(\omega) = \frac{C(\omega)}{C_0} = \frac{\frac{q}{\omega Z}}{C_0}, \tag{41}$$

$$\bar{\rho}\left(\omega, V, \xi\frac{p_i}{\rho_0 c}\right) = \frac{\rho\left(\omega,V,\xi\frac{p_i}{\rho_0 c}\right)}{\rho_0} = 1 + \frac{\sigma\left(\phi_p\frac{p_i}{\rho_0 c}|V|\right)}{-i\omega\rho_0}\sqrt{1 + \frac{-4i\omega\rho_0\eta}{\sigma^2\left(\phi_p\frac{p_i}{\rho_0 c}|V|\right)\Lambda^2}}. \tag{42}$$

Prime represents the derivative with respect to X. Equation (39) represents a Riccati equation for $Z(X)$ is similar to equation (20) from [110], while the scaling function for $\bar{\rho}\left(\omega, V, \xi\frac{p_i}{\rho_0 c}\right)$ resulting from (38) is different from their equation (18). New modified effective density used is due to the nonlinearity and determined using flow resistivity and Forchheimer's parameter ξ. Normalised surface impedance of fluid in the pore $Z(0)$ on the incident pressure amplitude p_i is obtained disregarding the reflected pressure p_r of the applied boundary conditions (velocity and pressure continuity at the sample surface with spatial variable X). Where $X = 0$ refers to sample surface thus, after the boundary condition is applied the dependence of $v(0)$ and $Z(0)$ on the incident pressure amplitude p_i becomes,

$$V(0) = \frac{2}{\phi_p + Z(0)}. \tag{43}$$

Furthermore, the boundary condition is applied at the rear of the sample for the rigid backing case. Spatial variable X is set to $X = 1$ which refers to being the termination point of the pancake structure comprised with solid plate where $r_0 = 0$. Applying the second boundary condition in this case,

$$V(1) = 0. \tag{44}$$

To begin, the nonlinearity parameter is set to zero, $\xi = 0$, and V' and $\bar{C}(\omega)$ given by equations (40) and (41) respectively, are used to obtain values for $V_1(X)$ and $Z_1(X)$. In this case the incident pressure amplitude is set to $p_i = 0$. Since a value for $V_1(X)$ is found then the value for $Z_2(X)$ can be obtained by the next iteration process. Determination of $Z_2(X)$ is achieved by substitution of the previous attained values of $V_1(X)$ with V' using the boundary condition $V(0)$. This numerical process computed by the model is performed to obtain the value of $V_2(X)$, which is consequence of using the value V' with the previous attained value $Z_2(X)$ with boundary condition $V(1)$ denoting backing of the sample. Approximately between 10 – 15 iterations are sufficient enough in order to obtain an accurate account of the absorptive properties for the structure. The performance is given in terms of its absorption coefficient values acquired from usual expression of α. Absorption coefficient data is shown for the pancake structures, samples 1 – 2, see Figures 6.37 a, b (where α for one of the samples is predicted by the model with its dependence on frequency for different values of incident pressure amplitude p_i). Sample 1 configured, $d_p = 1$ mm, $d_c = 1$ mm and $L = 31$ mm. First resonance frequencies used by the measured data and model $f_r^{(1)}$ and $f_r^{(2)}$ are $f = 262$ Hz and $f = 265$ Hz, respectively. Absorption coefficient data for pancake structures (samples 4 – 5) are shown by Figure 6.38 a, b. Detailed information of the different sample configurations is given by Table 6.13. These Figures (of samples 1, 2, 4 and 5) show the comparison from the measured impedance tube data and the theoretical data, as predicted by the nonlinear model and its iteration process solved numerically. Where the dependence of α at the first peak has been measured and predicted by the nonlinear model with a pressure amplitude where $p_i \leq 250$ Pa. The comparisons between the measured data and the model is the frequency at first resonance $f_r^{(1)}$ and $f_r^{(2)}$ values respectively, which is given in Table 6.13.

This means that a slight variation of the measured and predicted $f_r^{(1)}$ and $f_r^{(2)}$ data compared for high sound pressure levels occurs. For instance, see sample 5 of Table 6.13 where there is a difference of approximately $f = 10\ \mathrm{Hz}$, between the measured and predicted data with respect to low sound pressure levels in linear regime. Thus, the nonlinear model uses the measured and predicted data of the values $f_r^{(1)}$ and $f_r^{(2)}$ with peak frequencies obtained first by linear regime only, and hence, $\xi = 0$. Impedance tube measurements were performed in a standard two-microphone set-up with rigid backing applied, based at ISAT, University of Burgundy, France. Rigid backing of the sample is achieved by the end-plate being solid of the structure itself, followed by the use of a transferrable plunger which can be positioned anywhere within the inner tube, prior to being tightly sealed. All measurements are performed using a Mecanum impedance tube according to BS EN ISO 10534-2:2001. The tube had a working range of $50\mathrm{Hz} - 1800\ \mathrm{Hz}$ and the frequency resolution was 1 Hz. The tube was cylindrical, and its wall thickness was sufficient to eliminate any vibrational effects. Separation distances between microphones 1 and 2 was $d = 50\ \mathrm{mm}$. Upstream the tube, microphone position 1 is located $d = 150\ \mathrm{mm}$ from the sample surface, and microphone 2 is fixed at $d = 100\ \mathrm{mm}$ from the sample surface. Measurements are first performed using white noise excitation to gain values of $f_r^{(1)}$ (for the sample configurations given in Table 6.13). After α is obtained for the various samples containing the different configurations, the sound source is then altered to sine wave excitation. Using this approach allows the performance of the structures to be measured at each exact frequency that has been preselected around the absorptive peak values, obtained by white noise measurements. Moreover, the sine wave measurements are performed at each frequency of interest due to the much larger SPL that is achieved. This is the contrary for the white noise sound source. For instance, white noise excitation performed in the impedance tube ranged between 70 dB – 125 dB. However, a larger SPL is achieved for the sine wave noise excitation (70 dB – 145 dB.) This results in the pressures of nearly 250 Pa and 300 Pa being obtained for the HSPL impedance tube measurements. Further details on the impedance tube and measurements performed at both low, and high sound pressure levels can be seen in Chapter 4, Impedance tube measurements of continuous sound. Furthermore, the values obtained of α at each frequency for both white noise and sine wave excitation is given with the peak and RMS pressures, see Chapter 4 section 4.3 (measurements performed for LSPL using white noise excitation) and section 4.4 (measurements performed for HSPL using sine wave excitation). Figure 6.39 shows α for one of the samples as predicted by the model with its dependence on frequency, for different values of incident pressure amplitude p_i. Incident pressure is given for sample 1 where p_i ranges between 1 Pa and 400 Pa. The model predictions illustrate the overall shape of the absorption curve for the various values of α over the entire frequency range, where $f = 50\ \mathrm{Hz} \rightarrow f = 1600\ \mathrm{Hz}$. Peak absorption is severley influenced as amplitude strength grows and reduces accordingly. This is seen to be most apparent for f_r. The nonlinearity, however, does not significantly affect the frequency of the absorptive curves (see Figure 6.39 for an illustration of nonlinearity and its effect on the pancake absorber, sample 1). Parameters must be correctly chosen (d_p, d_c, r_0, L, R) including frame material properties Poisson ratio, Youngs modulus, and skeleton material density (ν, E, ρ_{samp}) in order to achieve the optimal performance of the absorber (for optimal value of α with strength of p_i). Therefore, absorption coefficient may decrease or increase with SPL depending on the parameters selected being below or above their optimal values.

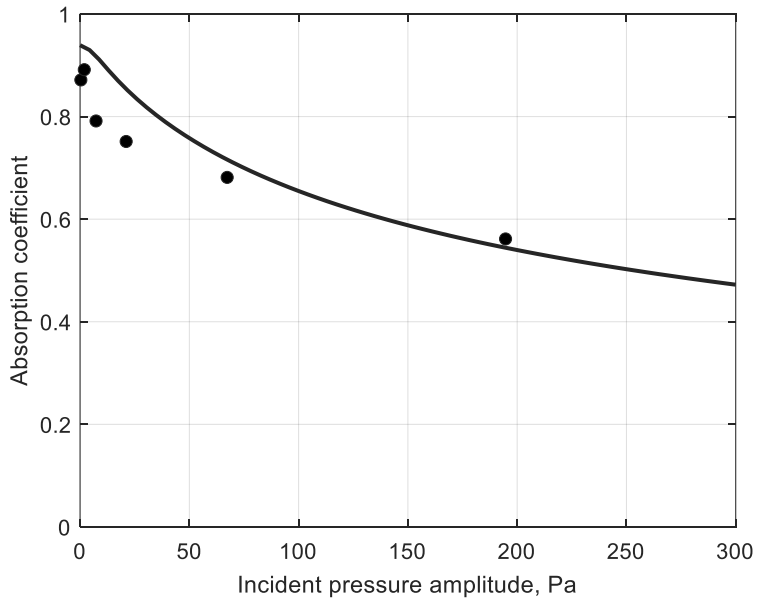

(a)

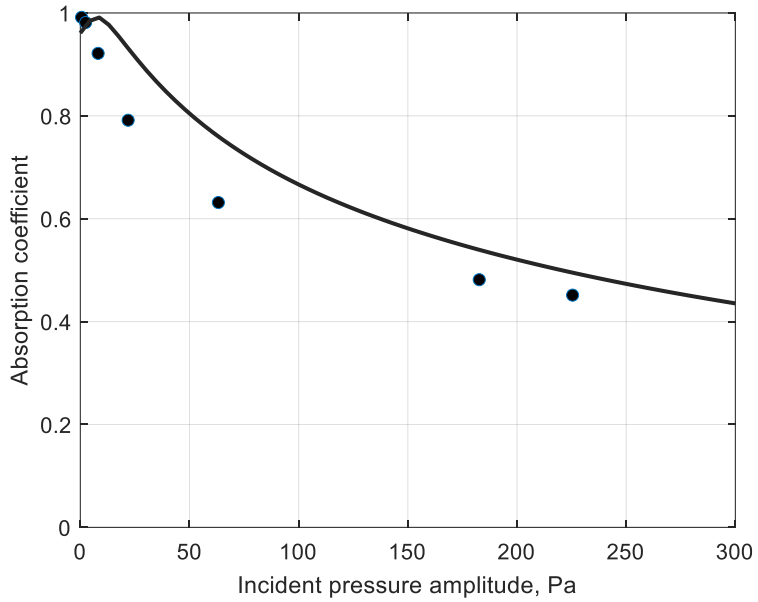

(b)

Figure 6.37. Measurements (markers) and nonlinear model (equations 37-38 and 43-44) predictions (lines) for the first absorption coefficient peak variations with p_i. (a) Sample 1, $L = 31$ mm, $N_{de} = 16$, (b) sample 2, $L = 30$ mm, $N_{de} = 8$. Measurement points are shown for experimental peak frequencies $f_r^{(1)}$, while numerical results are shown for frequencies $f_r^{(2)}$ predicted by the model, given in Table 6.13, also showing individual sample dimensions.

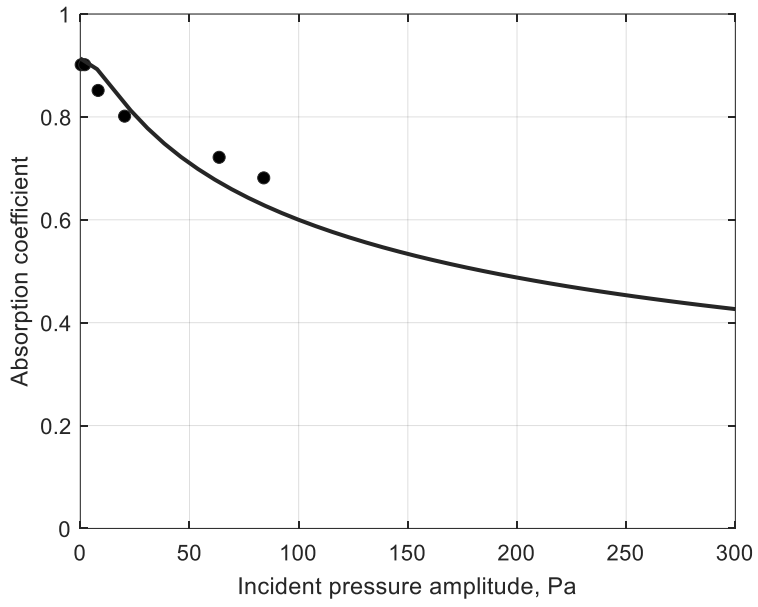

(a)

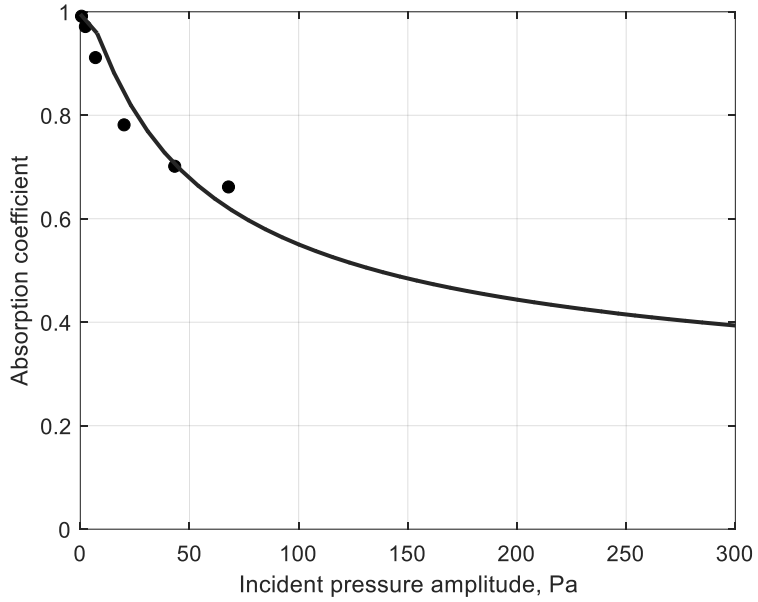

(b)

Figure 6.38. Measurements (markers) and nonlinear model (equations. 37–38 and 43–44) predictions (lines) for the first absorption coefficient peak variations with p_i. (a) Sample 4, $L = 60$ mm, $N_{de} = 30$, (b) sample 5, $L = 58$ mm, $N_{de} = 15$. Measurement points are shown for experimental peak frequencies $f_r^{(1)}$, while numerical results are shown for frequencies $f_r^{(2)}$ predicted by the model , given in Table 6.13, also showing individual sample dimensions.

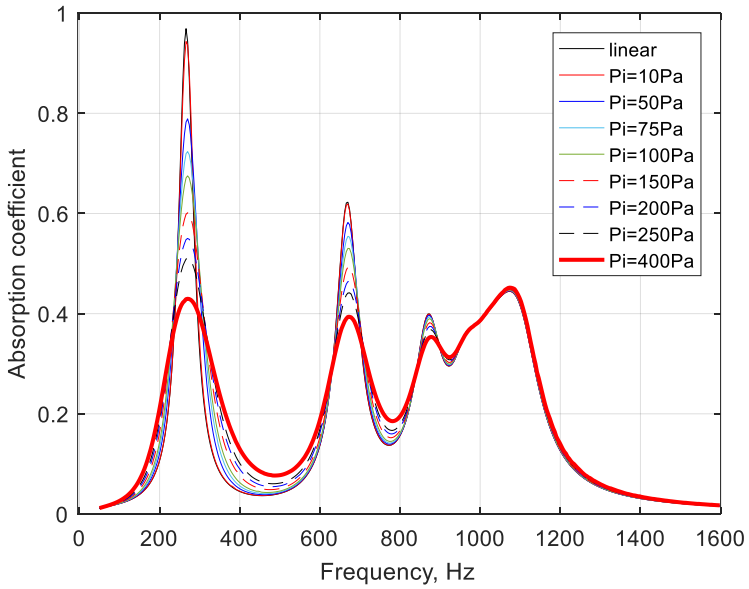

Figure 6.39. Model predictions for the absorption coefficient dependence on frequency at different values of p_i. See Table 6.13 for absorber dimensions, pancake is sample number 1.

6.4. COMSOL – FEM Model Predictions of Absorbers

6.4.1. Pancake Absorber – COMSOL

Computations for pancake and profile structures have been performed using finite element method (FEM) by the software COMSOL Multiphysics. A virtual impedance tube is designed within the system in order to numerically calculate a two-microphone standard impedance tube method for simulating the samples. As a result, the prediction of the absorbers performance in terms of its absorptive properties can be determined. Parabolic tetrahedral elements are used in the computation process which occupy the various acoustic domains of the virtual impedance tube and sample. To investigate the absorbers performance two different approaches of the simulated results have been obtained. The first approach is the determination of the acoustic treatment of the sample by considering a rigid frame assumption only. The second approach is an elastic frame model which accounts for mechanical disturbance of the plates (metallic frame of the structures). In both the former (rigid frame assumption) and latter (elastic frame assumption) JCA model is used for the fluid within the main pore having radius r_0 and cavities with thickness d_c. The rigid frame assumption is therefore modelled with its elements using an effective fluid of complex sound speed and dynamic density, given by $c_{eff} = \omega/k_{eff}$ and $\rho_{eff} = Z_{eff}\, k_{eff}/\omega$. In addition, the vibroacoustic or 'elastic frame assumption' uses the effective fluid approach with addition of the elements of the model accounting for the values of the Poisson ratio ν, Youngs modulus E, and density of the solid frame material $\rho_{samp.}$ This enables the simulation to compute any interaction that exists to the solid material from vibrational effects including fluid effects. In the elastic frame assumption, a loss factor is included within the model to account for damping. Material properties used in the computation of the absorbers are considered for the metallic structure consisting of aluminum. The Poisson ratio used in the elastic frame model is $\nu_{poi} = 0.32$, Youngs modulus $E = 6.9 \times 10^9 \mathrm{Pa}$ and the material density of the frame $\rho_{samp} = 2700\ \mathrm{kg/m^3}$. Plane wave excitation is used to compute the

simulations and at normal incidence which represents the virtual impedance tube with a set pressure of 1 Pa. Hence, the FEM models are computed in linear regime and the frequency spectrum considered ranges between $f = 1\ \text{Hz} - 1600\ \text{Hz}$. Dimensions of the virtual impedance tube radius is $r_0 = 50\ \text{mm}$ and the sample is rigidly backed. The separation distance between the microphone positions 1 and 2 is $m_d = 5\ \text{mm}$. Distance of microphone position 2 to the sample surface is $d = 150\ \text{mm}$. Both rigid and elastic frame assumptions are computed assigning the poro-acoustics module to the absorber designs where properties of air are considered for the common pore, and equivalent fluid approach using JCA model to the main pore and dead-ends. The mesh elements used is calculated using finest and the model is developed using an axisymmetric design. All absorbers are computed with plate radius $R = 50\ \text{mm}$. A loss factor L_f used in the elastic frame assumptions to account for damping is $L_f = 0.12$.

Pancake samples are introduced first and the computed data is given by Figures 6.40 – 6.53 (for the pancake structures with various configurations and sample lengths. Performance of a linear profile structure is also detremined using COMSOL Multiphysics and its data given by Figures 6.54 – 6.57. A pancake geometry and the associated mesh used to compute the sample for the simulation of the calculated sound pressure level is shown by Figure 6.40. And in Figure 6.41 absorption coefficient comparison between the absorber measured impedance tube data and the FEM model (both rigid and elastic frame assumptions) is given. Pancake dimensions are $r_0 = 4$ mm, $d_p = 1$ mm, $d_c = 1$ mm and $L = 31$ mm. Absorption coefficient data for the resonance peaks obtained from impedance tube measurements are included to compare the values predicted by the FEM models, as given by Figure 6.41 and furthermore, the data is presented by Table 6.14 in numeric form. The first resonance frequency of the impedance tube measured pancake absorber is $f_r = 262\ \text{Hz}$ and absorption coefficient is $\alpha = 0.84$ when induced by SPL around 80 dB with white noise excitation. The next three absorptive peaks are at frequencies, $f = 570\ \text{Hz}$, $f = 770\ \text{Hz}$, and $f = 1014\ \text{Hz}$. Absorption coefficient values at these frequencies are $\alpha = 0.33$, $\alpha = 0.68$, and $\alpha = 0.26$, respectively. The FEM model (rigid frame assumption) had a first resonance frequency $f_r = 260\ \text{Hz}$ where $\alpha = 1.00$. The elastic frame assumption predicted the first resonance frequency to be reduced by $f = 11\ \text{Hz}$ compared to the rigid frame assumption, this makes the elastic frame $f_r = 249\ \text{Hz}$. And absorption coefficient is the same so that $\alpha = 1.00$. Second resonance frequency for the rigid frame and elastic frame assumptions are $f = 646\ \text{Hz}$ and $f = 580\ \text{Hz}$ respectively, where $\alpha = 0.60$ and $\alpha = 0.35$, for the former and latter. Third resonance frequency is $f = 836\ \text{Hz}$ and α predicted relatively low where $\alpha = 0.28$, for the rigid frame model. However, in contrast, third absorptive peak for the elastic frame model is predicted to be at higher frequency, $f = 1041\ \text{Hz}$ and has a slightly reduced value of $\alpha\ (\text{where}\ \alpha = 0.20)$. This is due to a bandgap present in the elastic frame model arising from membrane vibration effects. The experimental data shows that α is drastically reduced after f_r and further still, around $f = 800\ \text{Hz}$. It appears that the elastic frame model accounts relatively well for the change in the absorption coefficient values affected by the interacting fluid and the membrane of the structure. Peak absorption data at higher frequencies is given by Table 6.14. Shown also is the frequency region of where the Bandgap appears. Note, the data given by the rigid frame assumption is less compared to the measured and elastic frame assumptions. This is because the elastic frame and measured data shows α at higher frequencies than the rigid framed model.

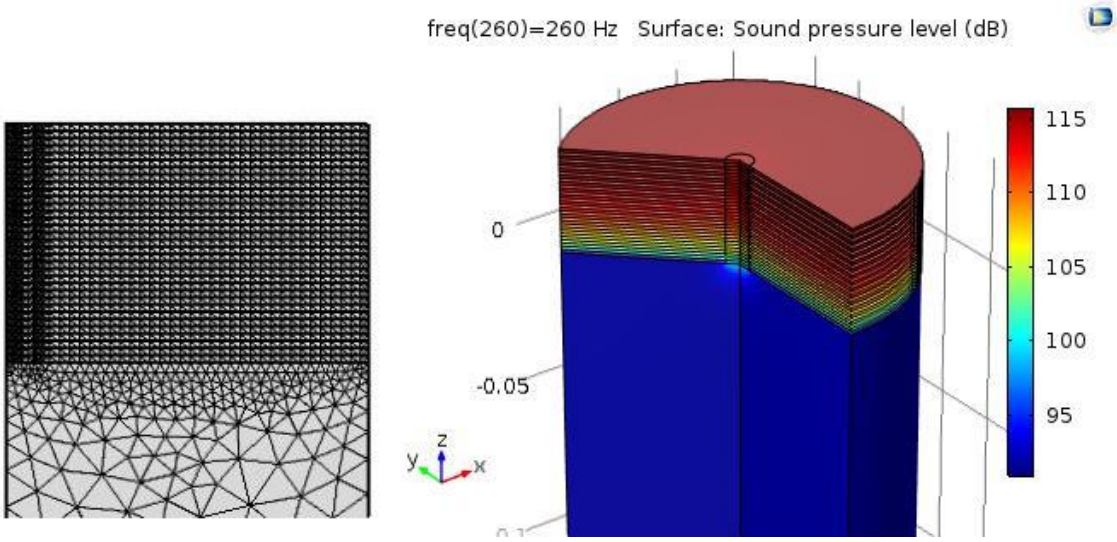

(a) (b)

Figure 6.40. Axisymmetric model and mesh (a) and sound pressure level at f_r (b) computed for pancake absorber with $r_0 = 4$ mm $d_p = 1$ mm, $d_c = 1$ mm, $L = 31$ mm, $N_{de} = 16$, and $R = 50$ mm.

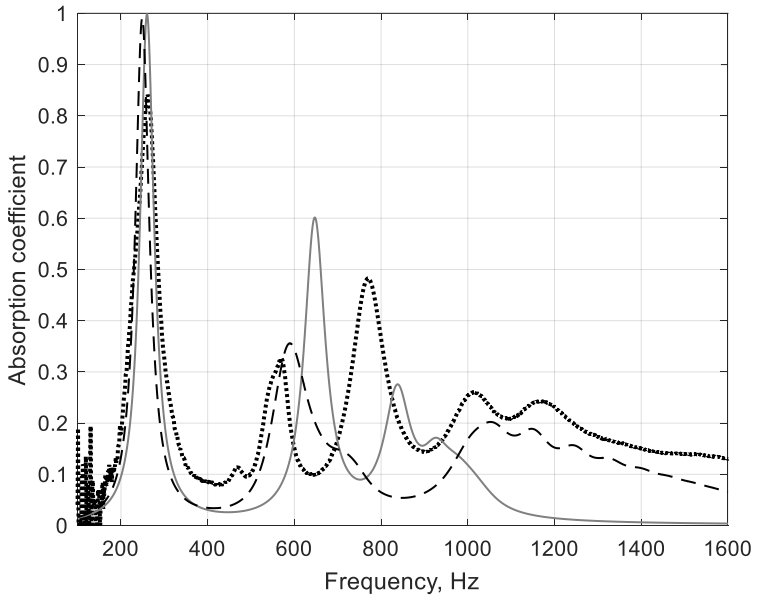

Figure 6.41. Absorption coefficient dependence as a function of frequency showing comparison of FEM data vs experimental results. Pancake absorber with $r_0 = 4$ mm, $d_p = 1$ mm, $d_c = 1$ mm, $L = 31$ mm, $N_{de} = 16$, $L_f = 0.12$, and $R = 50$ mm. Data given by impedance tube measurement, black dot. Computation is Multiphysics software COMSOL with rigid frame, solid, and vibro-acoustic, dash.

Impedance tube data, f (Hz)	**Impedance tube data (α)**	**COMSOL data * f (Hz)**	**COMSOL data * (α)**	**COMSOL data ** f (Hz)**	**COMSOL data ** (α)**
262	0.84	260	1.00	249	1.00
570	0.33	646	0.60	583	0.35
770	0.68	836	0.28	850-1000	Bandgap
1014	0.26	*	*	1041	0.20
1059	0.22	*	*	1059	0.20
1151	0.24	*	*	1151	0.19

Table 6.14. Measured and predicted values of peak absorption coefficient α and frequency f for pancake absorber obtained from impedance tube data and COMSOL Multiphysics software. Pancake absorber $r_0 = 4$ mm $d_p = 1$ mm, $d_c = 1$ mm, $L = 31$ mm, and $R = 50$ mm. Absorption coefficient data shows rigid frame model denoted by * and elastic frame model data is denoted **.

Figure 6.42 shows the mesh from the pancake with $r_0 = 4$ mm, $d_p = 1$ mm, $d_c = 3$ mm, $L = 32$ mm, and $R = 50$ mm, including SPL simulated for the absorber. Absorption coefficient dependence on frequency is given by Figure 6.43 showing the measured impedance tube data along with the data calculated by the rigid and elastic frame models, computed by COMSOL. The dead-end cavities have increased thickness from that of the cavities of the absorber given by Figure 6.41 (where $d_c = 1$ mm) and sample length is $L = 32$ mm. The measured impedance tube data is as follows; first resonance frequency for the measured pancake (Figure 6.43) is $f_r = 229$ Hz and $\alpha = 0.99$. Resonance frequency of the second and third peaks is $f = 530$ Hz and $f = 765$ Hz with absorption coefficient values $\alpha = 0.71$ and $\alpha = 0.77$, respectively. The fourth and fifth absorptive peaks are at $f = 1027$ Hz and $f = 1195$ Hz, where $\alpha = 0.45$ and $\alpha = 0.32$ for the fourth and fifth peak, respectively.

First resonance frequency computed for the rigid frame model is $f_r = 233$ Hz with a peak value $\alpha = 0.81$, and furthermore, the elastic frame model has $f_r = 226$ Hz where absorption coefficient $\alpha = 0.87$. The second and third resonance frequency for the rigid frame model is $f = 604$ Hz and $f = 813$ Hz, where $\alpha = 0.97$ for the former and $\alpha = 0.64$ for the latter. Second and third resonance frequency for the elastic frame model are lower compared to the FEM rigid frame model. For example, $f = 562$ Hz where $\alpha = 0.78$ and $f = 689$ Hz with $\alpha = 0.22$, for the elastic assumption. Absorption coefficient is significantly reduced ($\alpha = 0.32$) for the rigid frame model at the next resonance frequency, $f = 916$ Hz. In contrast, the elastic frame model which accounts for the vibrational effects due to fluid interaction with the frame predicts a bandgap between $f = 740$ Hz and $f = 920$ Hz. The next resonance frequency for the elastic frame model is $f = 1042$ Hz and contains an absorptive peak value $\alpha = 0.28$. This results in a difference of $f = 21$ Hz between the measured resonance frequency and the resonance frequency of the elastic frame assumption. In reality, α is larger for the measured data compared to the elastic frame model since $\alpha = 0.45$ for the impedance tube. Measured and predicted values obtained from the experimental and COMSOL models for the pancake absorber with $r_0 = 8$ mm, $d_c = 3$ mm, and $L = 32$ mm are presented in Table 6.15 showing α at resonance frequency f.

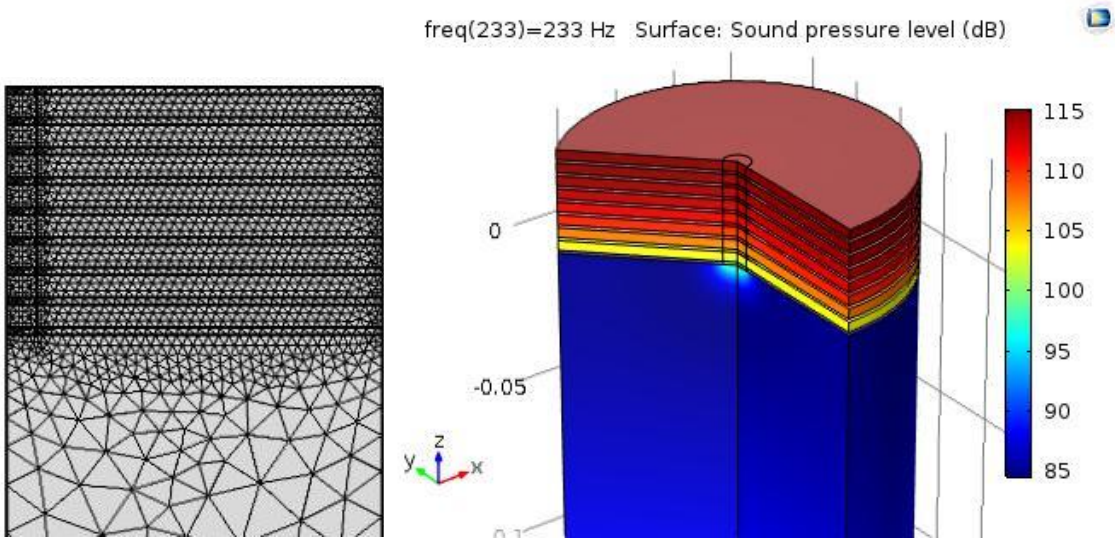

(a) (b)

Figure 6.42. Axisymmetric model and mesh (a) and sound pressure level at f_r (b) computed for pancake absorber with $r_0 = 4$ mm $d_p = 1$ mm, $d_c = 3$ mm, $L = 32$ mm, $N_{de} = 8$, and $R = 50$ mm.

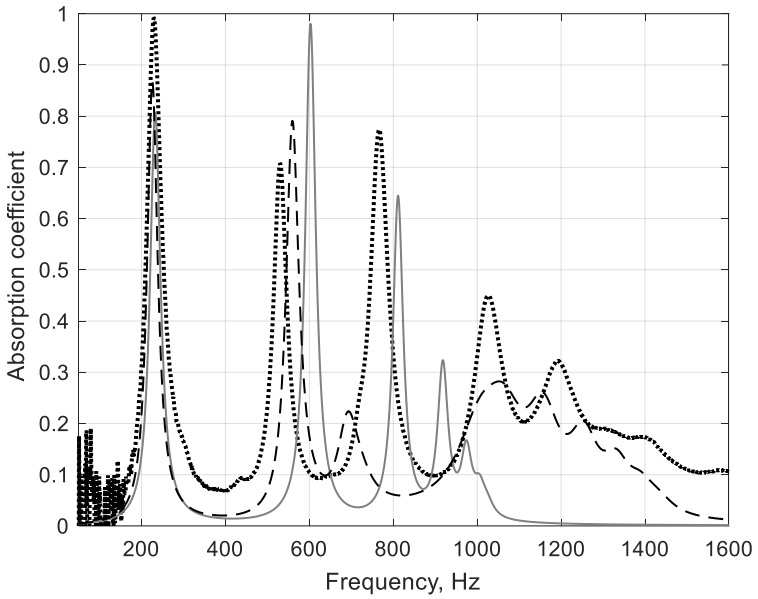

Figure 6.43. Absorption coefficient dependence as a function of frequency showing comparison of FEM data vs experimental. Pancake absorber with $r_0 = 4$ mm, $d_p = 1$ mm, $d_c = 3$ mm, $L = 32$ mm, $N_{de} = 8$, $L_f = 0.12$, and $R = 50$ mm. Data given by impedance tube measurement, black dot. Computation is Multiphysics software COMSOL with rigid frame, solid, and vibro-acoustic, dash.

Impedance tube data, f (Hz)	**Impedance tube data (α)**	**COMSOL data * f (Hz)**	**COMSOL data * (α)**	**COMSOL data ** f (Hz)**	**COMSOL data ** (α)**
229	0.99	233	0.81	226	0.87
530	0.71	604	0.97	562	0.78
765	0.77	831	0.64	689	0.22
1027	0.45	916	0.32	740-920	Bandgap
1195	0.32	974	0.17	1042	0.28
1234	0.24	*	*	1149	0.26
1254	0.21	*	*	1254	0.21

Table 6.15. Measured and predicted values of peak absorption coefficient α and frequency f for pancake absorber obtained from impedance tube data and COMSOL Multiphysics software. Pancake absorber $r_0 = 4$ mm, $d_p = 1$ mm, $d_c = 3$ mm, $L = 32$ mm and $R = 50$ mm. Absorption coefficient data shows rigid frame model denoted by * and elastic frame model data is denoted **.

Figure 6.44 shows a formation of the mesh and the computed sound pressure level simulation for the final pancake absorber measured and modelled with sample length close to $L = 30$ mm, and with largest value of d_c. Figure 6.45 shows absorption coefficient data for when the absorber is built $d_c = 6$ mm. Sample length is slightly larger than previous absorbers of Figures 6.41 and 6.43. Pancake absorber of Figure 6.45 has length $L = 4$ mm larger than the pancake given by Figure 6.41, and additional $L = 3$ mm compared to pancake of Figure 6.43. Absorption coefficient as a function of frequency is shown by Figure 6.45 where $L = 35$ mm. The measured impedance tube data is as follows; first resonance frequency of the pancake absorber is $f_r = 223$ Hz and has an absorption coefficient value $\alpha = 0.99$ when induced by a sound pressure level 80 dB, sound source is white noise excitation. Other absorptive peaks are found at the following frequencies, $f = 558$ Hz, $f = 775$ Hz, 1044 Hz, and $f = 1200$ Hz. The FEM model (rigid frame) consisted of $f_r = 222$ Hz where $\alpha = 0.58$. The elastic frame model predicted $f_r = 216$ Hz and absorption coefficient was $\alpha = 0.67$. The first resonance frequencies of the models agree with the measured data; however, the absorption coefficient is close to $\alpha = 1.00$ for the impedance tube data and consequently over 40 % larger value than that calculated for the FEM data. Second resonance

frequency for the rigid and elastic models was $f = 583$ Hz and $f = 544$ Hz, respectively. These are quite close to the measured data, with a difference of $f = 25$ Hz for the rigid assumption and a difference of only $f = 14$ Hz for the elastic frame. Absorption coefficient by the FEM models is computed with a slightly larger value of α (where $\alpha = 0.96$ and $\alpha = 0.93$ for the rigid and elastic frame models). A bandgap exists between $f = 750$ Hz and $f = 920$ Hz and shown by the data in Figure 6.45. Consequently, this is reflected by the impedance tube data where α is reduced from $\alpha = 0.83$ to $\alpha = 0.59$, from $f = 775$ Hz towards $f = 1044$ Hz. Furthermore, α becomes reduced again at $f = 1200$ Hz prior to another bandgap existing around $f = 1300$ Hz. The measured and predicted α for the pancake absorber at peak resonance frequency f are presented also in Table 6.16. For the pancake built with $d_c = 1$ mm, a better agreement between impedance tube data and the FEM models for the absorptive peak value at first resonance is achieved. This is because α for the FEM models gives a closer result to the measured data at f_r. First resonance frequency for other pancakes ($d_c = 3$ mm and $d_c = 6$ mm) with lengths $L = 30$ mm show that α is much less at f_r (given by the rigid and elastic frame models) when compared to the measured data, see Table 6.16. However, in practice, the measured absorbers with $d_c = 3$ mm and $d_c = 6$ mm show that α is indeed larger in value compared to the pancake with $d_c = 1$ mm.

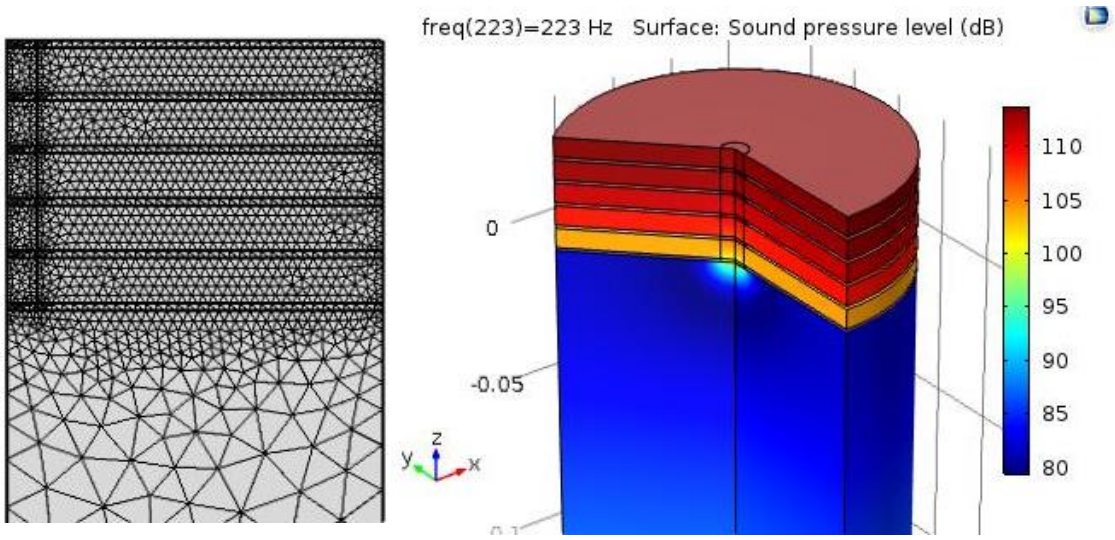

(a) (b)

Figure 6.44. Axisymmetric model and mesh (a) and sound pressure level at f_r (b) computed for pancake absorber with $r_0 = 4$ mm, $d_p = 1$ mm, $d_c = 6$ mm, $L = 35$ mm, $N_{de} = 5$, and $R = 50$ mm.

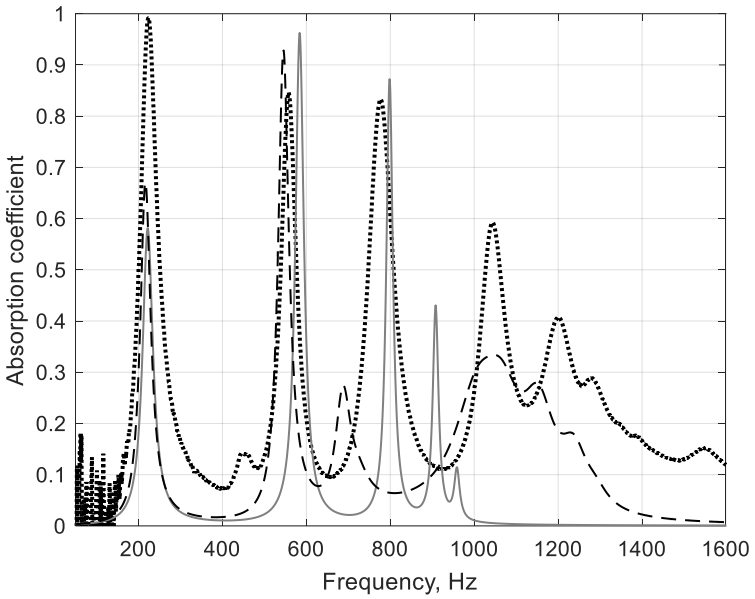

Figure 6.45. Absorption coefficient dependence as a function of frequency showing comparison of FEM data vs experimental. Pancake absorber $r_0 = 4$ mm, $d_p = 1$ mm, $d_c = 6$ mm, $L = 35$ mm, $N_{de} = 5$, $L_f = 0.12$, and $R = 50$ mm. Data given by impedance tube measurement, represented by black dot. Computation is Multiphysics software COMSOL with rigid frame, solid, and vibro-acoustic, dash.

Impedance tube data, f (Hz)	**Impedance tube data (α)**	**COMSOL data * f (Hz)**	**COMSOL data * (α)**	**COMSOL data ** f (Hz)**	**COMSOL data ** (α)**
223	0.99	223	0.58	216	0.67
558	0.85	583	0.96	544	0.93
775	0.83	797	0.86	685	0.27
1044	0.59	908	0.43	750-920	Bandgap
1064	0.48	*	*	1031	0.33
1200	0.41	*	*	1150	0.28
1237	0.30	*	*	1237	0.18

Table 6.16. Measured and predicted values of peak absorption coefficient α and frequency f, for pancake absorber obtained from impedance tube data and COMSOL Multiphysics software. Pancake absorber $r_0 = 4$ mm, $d_p = 1$ mm, $d_c = 6$ mm, $L = 35$ mm and $R = 50$ mm. Absorption coefficient data shows rigid frame model denoted by * and elastic frame model data is denoted **.

Mesh elements of the pancake absorber are shown in Figure 6.46 along with the simulated sound pressure level of the sample. Pancake absorbers with sample length around $L = 60$ mm are now computed for the rigid and elastic framed models, shown by Figures 6.47, 6.49, and 6.51. The sample lengths ranged $L = 60$ mm and $L = 63$ mm. Figure 6.47 shows absorption coefficient as a function of frequency for absorber configuration $r_0 = 4$ mm, $R = 50$ mm, $d_p = 1$ mm, $d_c = 1$ mm and $L = 62$ mm. Measured impedance tube data of the first resonance frequency $f_r = 144$ Hz and the absorption coefficient has the value $\alpha = 0.89$. Resonance frequency for the second and third peaks measured $f = 396$ Hz and $f = 574$ Hz with values $\alpha = 0.42$ and $\alpha = 0.54$, respectively. Fourth and fifth peaks are at $f = 769$ Hz and $f = 895$ Hz, where $\alpha = 0.36$ and $\alpha = 0.30$ for the fourth and fifth absorptive peak values, respectively. The FEM data (rigid frame) calculates the first resonance frequency at $f_r = 147$ Hz with a peak value $\alpha = 0.98$. Second and third absorptive peaks are at $f = 416$ Hz and $f = 755$ Hz with absorption coefficient $\alpha = 0.72$ and $\alpha = 0.28$, respectively. The elastic frame model gives similar results for f_r (between rigid and elastic) being $f_r = 144$ Hz which is lower by only $f = 3$ Hz. And absorption coefficient is the same value at f_r for both the rigid frame and elastic models. The second and third

resonance frequency was $f = 401\ \mathrm{Hz}$ and $f = 579\ \mathrm{Hz}$ where $\alpha = 0.66$ and $\alpha = 0.31$, respectively. Therefore, a difference $f = 15\ \mathrm{Hz}$ exists between the two models for the second resonance frequency. Moreover, the elastic frame model is in fairly good agreement with the resonance frequency by the measured impedance tube data. This is because a difference of only $f = 5\ \mathrm{Hz}$ is found for the peak values of α for the second resonance frequency. Third resonance frequency encounters a difference also of only $f = 5\ \mathrm{Hz}$.

These differences of the resonance frequencies are small, and data for α given by the models are actually in the same region (of the values f) as the impedance tube data. Similarly, like pancakes measured with sample lengths close to $L = 30$ mm, the values of α for the FEM model for second and third resonance frequencies are larger than that of the measured data obtained by the impedance tube. This is the case for when pancake absorbers are built with $d_c = 1$ mm, regardless of the sample lengths investigated thus far. A further resonance peak is at $f = 687\ \mathrm{Hz}$ computed by the model that encompasses the assumption of the elastic frame taking into consideration vibrational effects. Absorption coefficient is low and $\alpha = 0.18$. A bandgap is predicted by the elastic model at around $f = 700\ \mathrm{Hz}$ and $f = 1000\ \mathrm{Hz}$. The measured impedance tube data is shown to be significantly reduced after $f = 574\ \mathrm{Hz}$ and results in the absorption coefficient $\alpha = 0.24$ at $f = 1005\ \mathrm{Hz}$. This shows the effect of bandgaps or stop bands which dramatically present a reduction in α and furthermore, shift the resonance frequency. Therefore, the bandgaps have to be considered for optimisation of the absorbers which is dependent on the dead-end pore volume, or thickness of the cavities d_c after the plate d_p. Pancake absorbers with sample thicknesses close to $L = 60$ mm give a slightly closer match between the experimental and FEM models than it does for pancakes with $L = 30$ mm.

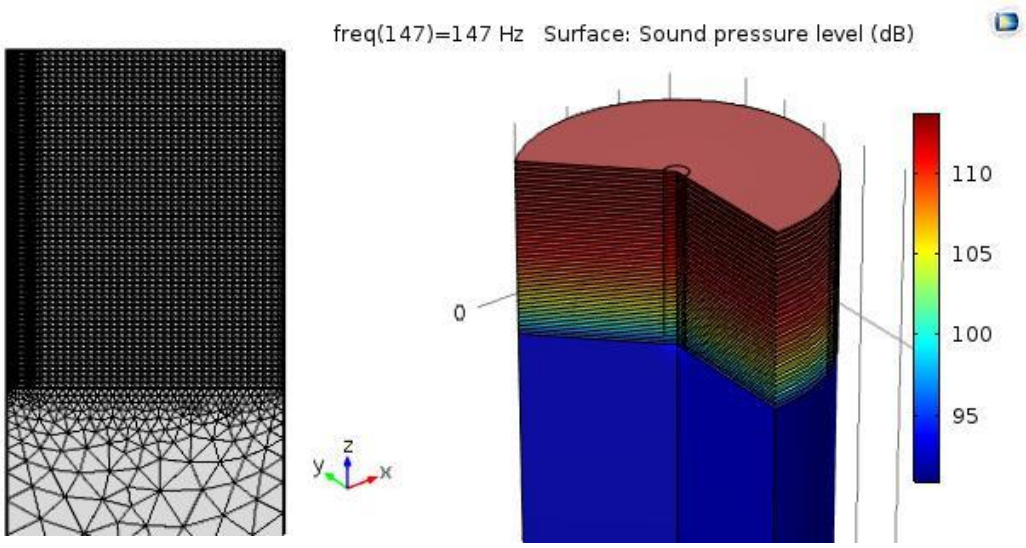

(a) (b)

Figure 6.46. Axisymmetric model and mesh (a) and sound pressure level at f_r (b) computed for pancake absorber with $r_0 = 4$ mm, $d_p = 1$ mm, $d_c = 1$ mm, $L = 62$ mm, $N_{de} = 30$, and $R = 50$ mm.

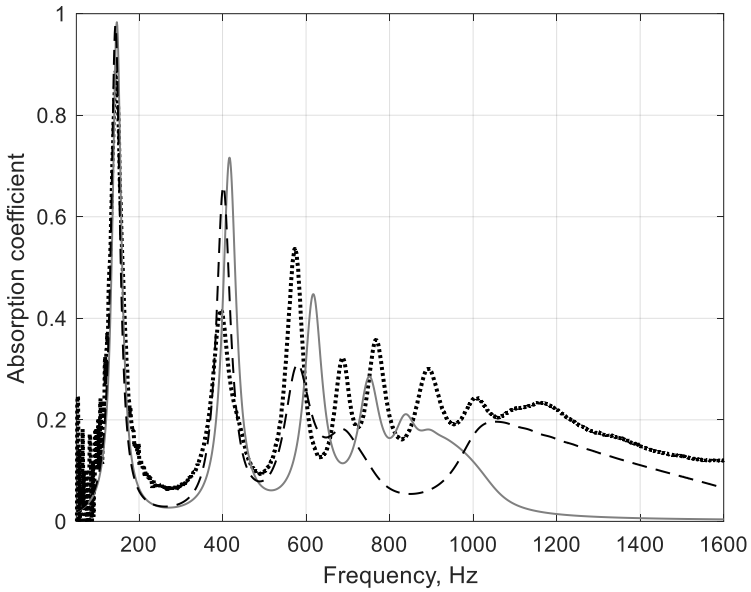

Figure 6.47. Absorption coefficient dependence as a function of frequency showing comparison of FEM data vs experimental. Pancake absorber $r_0 = 4$ mm, $d_p = 1$ mm, $d_c = 1$ mm, $L = 62$ mm, $N_{de} = 30$, $L_f = 0.12$, and $R = 50$ mm. Data given by impedance tube measurement, represented by black dot. Computation is Multiphysics software COMSOL with rigid frame, solid, and vibro-acoustic, dash.

Impedance tube data, f (Hz)	**Impedance tube data (α)**	**COMSOL data * f (Hz)**	**COMSOL data * (α)**	**COMSOL data ** f (Hz)**	**COMSOL data ** (α)**
144	0.89	147	0.98	144	0.98
396	0.42	416	0.72	401	0.66
574	0.54	615	0.44	579	0.31
769	0.36	755	0.28	687	0.18
895	0.30	845	0.21	700-1000	Bandgap
1005	0.24	1005	0.11	1005	0.18
1012	0.23	*	*	1012	0.18

Table 6.17. Measured and predicted values of peak absorption coefficient α and frequency f, for pancake absorber obtained from impedance tube data and COMSOL Multiphysics software. Pancake absorber $r_0 = 4$ mm, $d_p = 1$ mm, $d_c = 1$ mm, $L = 62$ mm and $R = 50$ mm. Absorption coefficient data shows rigid frame model denoted by * and elastic frame model data is denoted **.

Figure 6.49 shows absorption coefficient dependence on frequency for when d_c is extended from the dead-ends of the absorber given by Figure 6.47. The pancake absorber is comprised $d_c = 3$ mm and sample length around $L = 60$ mm. Radius of the external plates and rings is $R = 50$ mm and $d_p = 1$ mm. The measured impedance tube data is given first followed by α values for the FEM models. First resonance frequency for the pancake given by Figure 6.49 is measured $f_r = 135$ Hz and absorption coefficient $\alpha = 0.99$. Resonance frequency of the second and third peaks is measured $f = 364$ Hz and $f = 647$ Hz, where absorption coefficient values are $\alpha = 0.56$ and $\alpha = 0.57$, respectively. Fourth and fifth absorptive peaks are $f = 750$ Hz and $f = 902$ Hz with $\alpha = 0.68$ and $\alpha = 0.54$, for the fourth and fifth peak absorption values, respectively. First resonance frequency of the FEM data for the rigid framed model is $f_r = 132$ Hz which had a peak value $\alpha = 0.88$. The elastic frame model was $f_r = 130$ Hz where $\alpha = 0.90$. The second and third resonance frequency for the rigid frame model was $f = 379$ Hz and $f = 575$ Hz where $\alpha = 1.00$ for the former, and $\alpha = 0.87$ for the latter. Second and third resonance frequencies of the elastic frame model are slightly lower compared to the rigid frame FEM data ($f = 368$ Hz where $\alpha = 0.97$ and $f = 545$ Hz with $\alpha = 0.67$).

It can be observed in Figure 6.49 that a bandgap exists (due to vibrational effects of the material membrane) for the impedance tube data in the frequency region $f = 415$ Hz and $f = 600$ Hz. As a result of the bandgap, the values of α at higher frequencies above $f = 350$ Hz (and after the first resonance frequency) are significantly reduced. The elastic frame model and the measured data obtained from the impedance tube both show peak values at $f = 647$ Hz, (where $\alpha = 0.57$ and $\alpha = 0.32$). After this frequency, the elastic model predicts mechanical resonance and results in a bandgap in the region around $f = 715$ Hz and $f = 950$ Hz. Other resonances and values of α at higher frequencies above $f = 1000$ Hz for the model, and measured impedance tube data, are given in Table 6.18. This shows the peak values of α at resonance frequency f, for the absorber with $r_0 = 8$ mm, $d_c = 3$ mm and $L = 60$ mm.

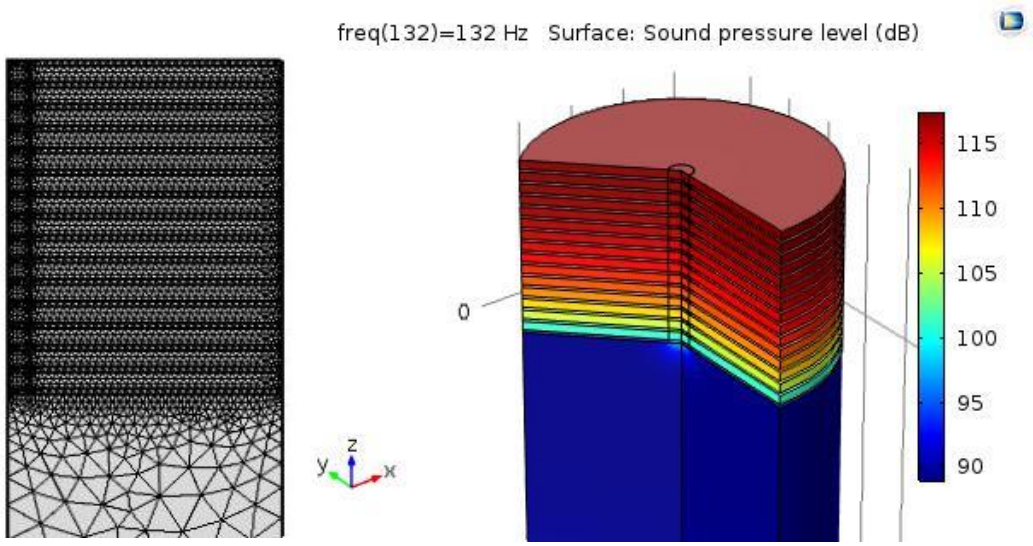

(a) (b)

Figure 6.48. Axisymmetric model and mesh (a) and sound pressure level at f_r (b) computed for pancake absorber with $r_0 = 4$ mm, $d_p = 1$ mm, $d_c = 3$ mm, $L = 60$ mm, $N_{de} = 15$, and $R = 50$ mm.

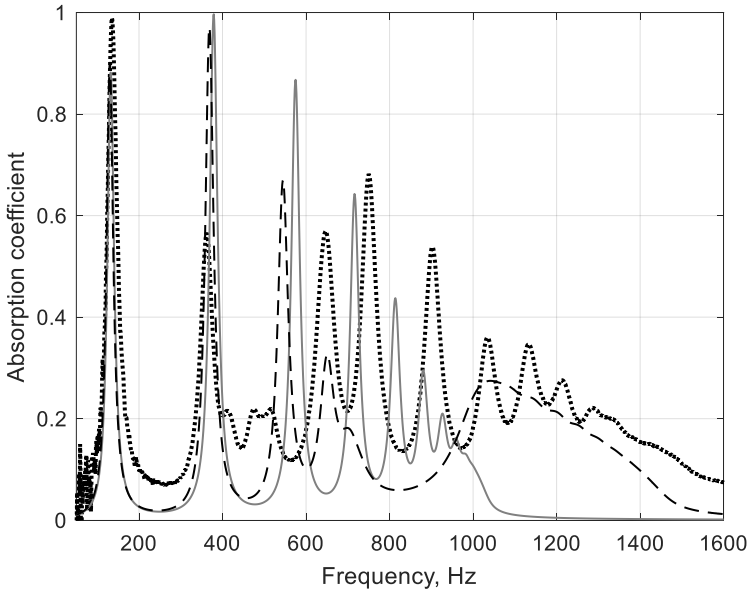

Figure 6.49. Absorption coefficient dependence as a function of frequency showing comparison of FEM data vs experimental. Pancake absorber $r_0 = 4$ mm $d_p = 1$ mm, $d_c = 3$ mm, $L = 60$ mm, $N_{de} = 15, L_f = 0.12$, and $R = 50$ mm. Data given by impedance tube measurement, represented by black dot. Computation is Multiphysics software COMSOL with rigid frame, solid, and vibro-acoustic, dash.

Impedance tube data, f (Hz)	Impedance tube data (α)	COMSOL data * f (Hz)	COMSOL data * (α)	COMSOL data ** f (Hz)	COMSOL data ** (α)
135	0.99	132	0.88	130	0.90
364	0.56	379	1.00	368	0.97
647	0.57	575	0.87	545	0.67
750	0.68	716	0.64	647	0.32
902	0.54	814	0.44	715-950	Bandgap
1034	0.36	880	0.29	1034	0.27
1134	0.35	*	*	1134	0.24

Table 6.18. Measured and predicted values of peak absorption coefficient α and frequency f, for pancake absorber obtained from impedance tube data and COMSOL Multiphysics software. Pancake absorber $r_0 = 4$ mm, $d_p = 1$ mm, $d_c = 3$ mm, $L = 60$ mm, and $R = 50$ mm. Absorption coefficient data shows rigid frame model denoted by * and elastic frame model data is denoted **.

Figure 6.50 shows the mesh and sound pressure level computed for pancake absorber with $r_0 = 4$ mm, $d_p = 1$ mm, $d_c = 6$ mm and sample length $L = 63$ mm. This is when cavity d_c is largest for the pancake absorbers and completes the structures with constant pore radius. In Figure 6.51 impedance tube data shows the first resonance frequency being $f_r = 135$ Hz and has an absorption coefficient value $\alpha = 1.00$ (sound source is white noise excitation). Other absorptive peaks are found at the following frequencies, $f = 348$ Hz, $f = 412$ Hz, $f = 524$ Hz, and $f = 592$ Hz. The absorption coefficient values at these frequencies are $\alpha = 0.64$, $\alpha = 0.27$, $\alpha = 0.71$, and $\alpha = 0.72$ respectively. First resonance frequency computed for the rigid frame model is the same as for the pancake built with $d_c = 3$ mm thus, $f_r = 233$ Hz. Absorption coefficient is predicted lower for the sample with $d_c = 6$ mm. The measured absorptive peak value $\alpha = 0.81$ (absorption coefficient by the rigid frame model with pancake built with $d_c = 3$ mm is $\alpha = 0.88$, see also Figure 6.49).

The elastic frame model predicted the first resonance frequency to be $f_r = 130$ Hz with α slightly larger than the rigid frame model, where $\alpha = 0.71$. Second and third resonance frequency for the rigid frame model was $f = 377$ Hz and $f = 575$ Hz (with $\alpha = 0.93$ and $\alpha = 1.00$, respectively). The elastic frame assumption calculated the second and third resonance frequency slightly lower. For instance, second resonance frequency for the elastic frame model is $f = 367$ Hz (a difference of $f = 10$ Hz between the FEM data for rigid and elastic frames) and difference $f = 32$ Hz for the third resonance frequency, between the models. An absorptive peak for the measured data exists at $f = 524$ Hz which is a difference $f = 51$ Hz, and $f = 19$ Hz, for the rigid and elastic frame models, respectively. The measured impedance tube data shows that α for the pancake is reduced significantly after f_r. At around $f = 350$ Hz and $f = 500$ Hz the bandgap causes low values of α. When d_c is increased the bandgap frequency becomes reduced and first acoustic resonance of the pancake absorber is shifted to lower frequencies. The elastic frame model predicts a bandgap being in the region between $f = 705$ Hz and $f = 960$ Hz, see Figure 6.51. Prior to the predicted bandgap, the rigid frame model has resonance frequencies ranging $f = 719$ Hz and $f = 927$ Hz with α reducing significantly, where $\alpha = 0.86$ at the former frequency and $\alpha = 0.21$ at the latter frequency. Indeed, in contrast to the rigid frame data, the elastic model is accounting for fluid interaction with the membrane from the frame material and therefore shows α being drastically low ($\alpha = 0.05$). A resonance frequency after the bandgap (given by the FEM of the elastic frame) is predicted $f = 1050$ Hz with absorption coefficient $\alpha = 0.33$. The impedance tube data given in Figure 6.51 including Table 6.19 shows $\alpha = 0.48$ at $f = 1050$ Hz, which at the same frequency has

slightly different value of α. Absorption coefficient calculated from the FEM elastic frame assumption then shows to decay towards $f = 1600$ Hz where $\alpha = 0$ due to existence of a stop band.

The measured impedance tube data and FEM data, from rigid and elastic frame models (for the pancake absorber with $r_0 = 8$ mm, $d_c = 6$ mm and $L = 63$ mm) are presented in Table 6.19 showing peak values of α at resonance frequency f. This completes the pancake structures with lengths around $L = 60$ mm. The metamaterial structure with dimensions given above (see Figure 6.51) provides largest values of α. Furthermore, since cavity volume is also largest (compared to lower values d_c used in other structures), which is the case for $d_c = 6$ mm, the lowest acoustic resonance frequency is also attained. Furthermore, a bandgap frequency (when $d_c = 6$ mm) is reduced compared to the structures built with $d_c = 1$ mm (due to the first natural frequency content of the flexural vibration from the frame membrane and its seperating wall). Mechanical resonance of the plates have been investigated also in Chapter 4, see section 4.3.1 (including section 6.1.4 of this Chapter which shows data from the performed accelerometer measurements).

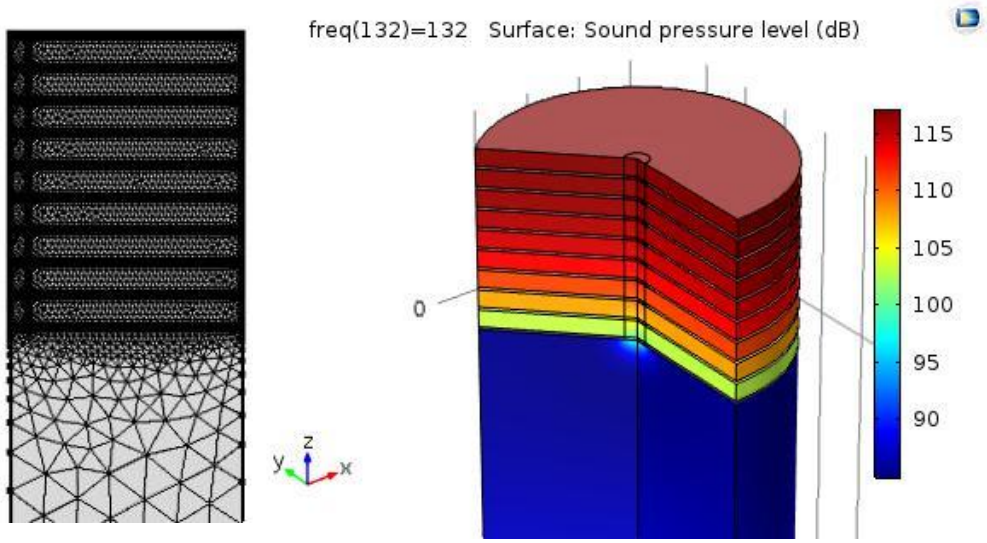

(a) (b)

Figure 6.50. Axisymmetric model and mesh (a) and sound pressure level at f_r (b) computed for pancake absorber with $r_0 = 4$ mm, $d_p = 1$ mm, $d_c = 6$ mm, $L = 63$ mm, $N_{de} = 9$, and $R = 50$ mm.

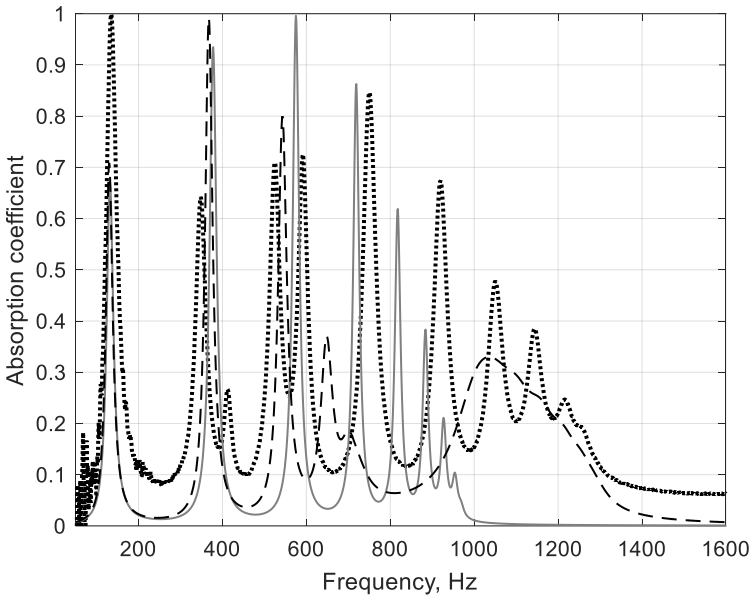

Figure 6.51. Absorption coefficient dependence as a function of frequency showing comparison of FEM data vs experimental. Pancake absorber $r_0 = 4$ mm, $d_p = 1$ mm, $d_c = 6$ mm, $L = 63$ mm, $N_{de} = 9$, $L_f = 0.12$, and $R = 50$ mm. Data given by impedance tube measurement, represented by black dot, and TMM. Computation is Multiphysics software COMSOL, rigid frame, solid, and vibro-acoustic, dash.

Impedance tube data, f (Hz)	**Impedance tube data (α)**	**COMSOL data * f (Hz)**	**COMSOL data * (α)**	**COMSOL data ** f (Hz)**	**COMSOL data ** (α)**
135	1.00	132	0.67	130	0.71
348	0.64	377	0.93	367	0.99
412	0.27	575	1.00	543	0.80
524	0.71	719	0.86	648	0.37
592	0.72	818	0.62	693	0.18
750	0.84	884	0.38	705	Bandgap
919	0.67	927	0.21	960	Bandgap
1050	0.48	*	*	1050	0.33
1143	0.38	*	*	1143	0.25
1215	0.25	*	*	1159	0.19

Table 6.19. Measured and predicted values of peak absorption coefficient α and frequency f, for pancake absorber obtained from impedance tube data and COMSOL Multiphysics software. Pancake absorber $r_0 = 4$ mm, $d_p = 1$ mm, $d_c = 6$ mm, $L = 63$ mm, and $R = 50$ mm. Absorption coefficient data shows rigid frame model denoted by * and elastic frame model data is denoted **.

Figure 6.52 presents absorption coeffcient as a function of frequency and illustrates the difference between the rigid and elastic frame model predictions for f_r. Pancake absorbers built with sample lengths close to $L = 30$ mm are shown in (a) and when sample lengths are close to $L = 60$ mm (b). The elastic frame assumption gives a slightly lower predicted first resonance frequency, for all sample lengths shown in (a) and (b), to that of the rigid frame model. It is also determined that the magnitude of the difference in f_r between the models is largest for when $d_c = 1$ mm and decreases as $d_c = 6$ mm (where differences between the models becomes smallest). Both the rigid and elastic frame models always predict (for all sample lengths) larger values of α of the first resonance frequency for when $d_c = 1$ mm, compared to when $d_c = 3$ mm and $d_c = 6$ mm. Value of α decreases as value of d_c increases from $d_c = 1$ mm → $d_c = 6$ mm. All pancake sample lengths are given in the caption of Figure 6.52. Finally, absorption coefficient is shown by Figure 6.53 to illustrate the effects of a sample containing a simple perforation only (so pore radius is the same as the pancake structures meaning the perforation

consists of $r_0 = 4$ mm). Data for various sample lengths ranging $L = 31$ mm and $L = 63$ mm are shown, where the sample length are the same as the pancake structures discussed previously with different values of d_c. A solid cylinder with only a central perforation therefore has $d_c = 0$. It is shown by Figure 6.53 that the resonance frequency for each sample length is higher in frequency by factor 10, for samples containing a simple perforation. For instance, a sample with central pore only and $L = 31$ mm, the resonance frequency $f = 2529$ Hz and $\alpha = 0.91$. And a sample containing a central perforation with $L = 32$ mm has $f = 2456$ Hz and $\alpha = 0.91$. When the central pore is increased further, so that $L = 35$ mm, then $\alpha = 0.90$. These are the same sample lengths as for when the pancake absorbers are configured with either $d_c = 1$ mm, $d_c = 3$ mm, and $d_c = 6$ mm (for pancakes built with length close to $L = 30$ mm). The resonance frequency is significantly reduced for when the central orifices are extended so that sample lengths now become close to $L = 60$ mm. For instance, a sample containing a central pore where $L = 62$ mm the resonance frequency is $f = 1319$ Hz and the absorption coefficient value $\alpha = 0.80$. For a sample containing a simple pore $L = 60$ mm, the resonance frequency $f = 1362$ Hz and $\alpha = 0.81$. For the largest sample length considered the central perforation is $L = 63$ mm and absorption coefficient is $\alpha = 0.80$. These are same sample lengths for when the pancake absorbers are configured with $d_c = 1$ mm, $d_c = 3$ mm and $d_c = 6$ mm which is for when the pancake absorbers are built with sample lengths close to $L = 60$ mm. This shows that the resonance frequency is nearly halved for solid samples with central perforations close to $L = 60$ mm, when compared to the samples with length around $L = 30$ mm. Moreover, the pancake structures are able to reduce the first resonance frequency by approximately factor 10 compared to the case of the solid samples, with identical length and absent any cavities, but with same pore radius r_0. The computations for the simple pores have been performed using COMSOL Multiphysics.

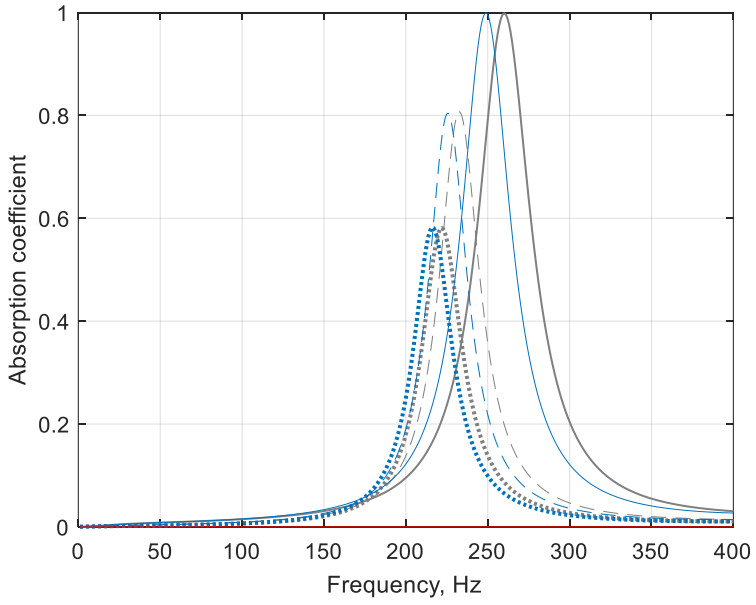

(a)

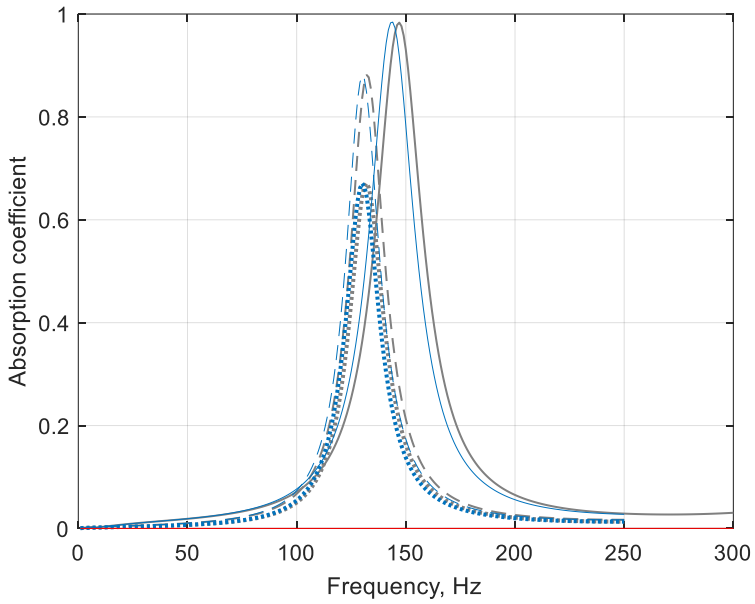

(b)

Figure 6.52. Absorption coefficient as a function of frequency predicted by both the rigid and elastic frame models for pancake samples at first resonance. Data in (a) is pancake with $d_c = 1$ mm and $L = 31$ mm (solid line), $d_c = 3$ mm and $L = 32$ mm (dash), $d_c = 6$ mm and $L = 35$ mm (dot). Rigid model, grey, and elastic model, blue. Data in (b) is pancake with $d_c = 1$ mm and $L = 62$ mm (solid line), $d_c = 3$ mm and $L = 60$ mm (dash), $d_c = 6$ mm and $L = 63$ mm (dot). Rigid model, grey, and elastic model, blue. $R = 50$ mm.

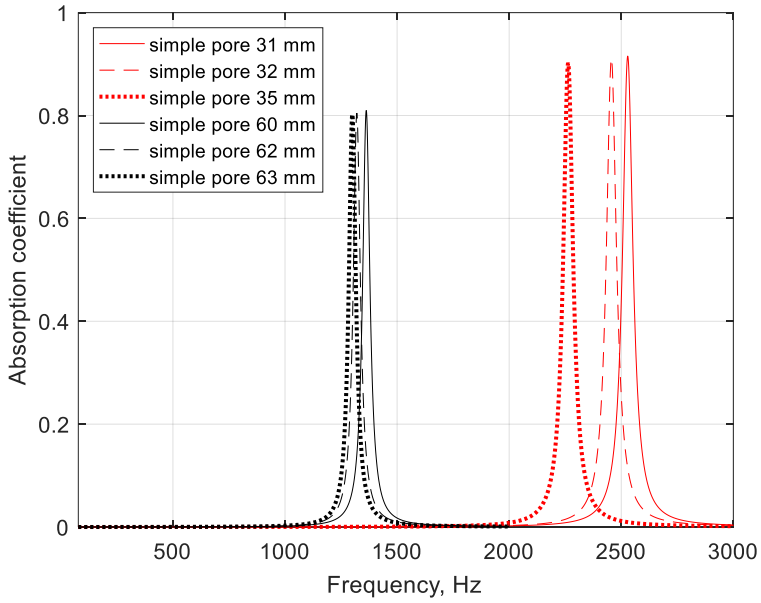

Figure 6.53. Absorption coefficient as a function of frequency for simple pores with lengths close to $L = 30$ mm, $L = 60$ mm, and $R = 50$ mm. Software is COMSOL Multiphysics.

6.4.2. Profile Absorber – COMSOL

Similarly as the pancake absorbers, COMSOL Multiphysics software has been used to determine the performance of the linear profile structure. The mesh and simulation of the computed sound pressure level for the profile is shown by Figure 6.54. Absorption coefficient as a function of frequency is presented in Figure 6.55 for the measured impedance tube data and FEM rigid frame model. COMSOL

multiphysics has been used also accounting for interaction with the fluid and the frame membrane. The structure is built with aluminium plates and rings which have been considered in the elastic frame model. Material properties and values used are Youngs modulus $E = 6.9 \times 10^9 \text{Pa}$, Poisson ratio $\nu = 0.32$, and the material density of the frame $\rho_{samp} = 2700\ \text{kg/m}^3$. Both the rigid and elastic frame models are same as for the metamaterial pancakes (JCA model is used for the interaction of the fluid within the main pore having radius r_0 and dead-ends with thickness d_c and uses equivalent fluid approach. The FEM models are computed in linear regime and the frequency spectrum considered, $f = 1\ \text{Hz} \rightarrow 1600\ \text{Hz}$. Dimension of the virtual impedance tube radius $r_0 = 50\ \text{mm}$ and the sample is rigidly backed. Pressure used in the computation is 1 Pa. Figure 6.55 shows data from a linear profile structure with the surface plate with opening main pore radius $r_0 = 25$ mm, plate thickness $d_p = 1$ mm, the distributed cavities are $d_c = 2$ mm and $L = 80$ mm. First resonance frequency of the measured impedance tube and rigid framed model are $f_r = 313\ \text{Hz}$ and $f_r = 192\ \text{Hz}$ with absorption coefficient values $\alpha = 0.97$ and $\alpha = 0.94$, respectively. The next resonance frequency computed by the model is closer to f_r of the impedance tube data, where $f = 295\ \text{Hz}$ for the rigid frame data. Absorption coefficient is broadband across the entire frequency spectrum for both the measured impedance tube data and COMSOL rigid frame model. Broadband absorption ranged $f = 200\ \text{Hz}$ and $f = 1600\ \text{Hz}$.

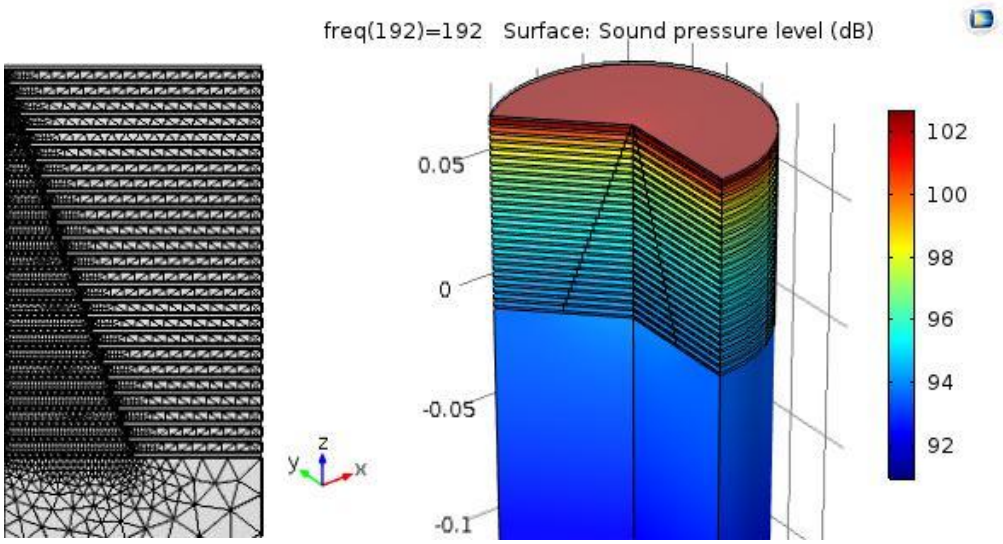

(a) (b)

Figure 6.54. Axisymmetric model and mesh (a) and sound pressure level of first resonance frequency (b) computed for profile absorber with surface plate with opening main pore radius $r_0 = 25$ mm, $d_p = 1$ mm, $d_c = 2$ mm, $L = 80$ mm, $N_{de} = 25$, and $R = 50$ mm.

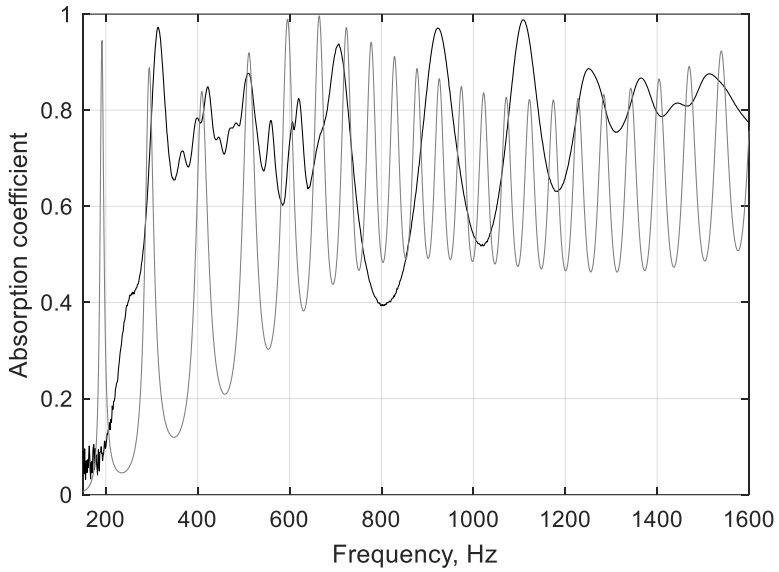

Figure 6.55. Absorption coefficient dependence as a function of frequency showing comparison of FEM data vs experimental. Linear profile with opening main pore radius $r_0 = 25$ mm, $d_p = 1$ mm, $d_c = 2$ mm, $L = 80$ mm, $N_{de} = 25$, and $R = 50$ mm. Data given by impedance tube measurement, black dot. Computation is Multiphysics software COMSOL with rigid frame assumption, grey.

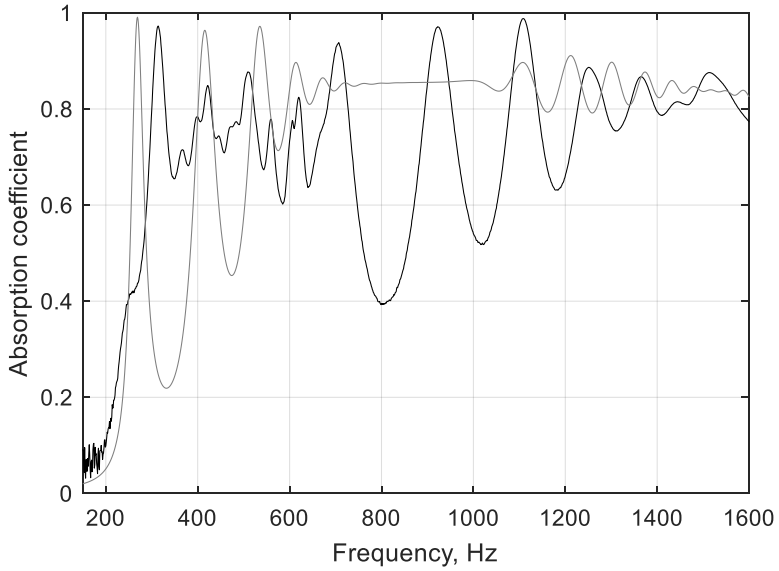

Figure 6.56. Absorption coefficient dependence as a function of frequency showing comparison of FEM data vs experimental. Linear profile with opening main pore radius $r_0 = 25$ mm, $d_p = 1$ mm, $d_c = 2$ mm, $L = 80$ mm, $N_{de} = 25$, $L_f = 0.12$, and $R = 50$ mm. Data given by impedance tube measurement, black. Computation is Multiphysics software COMSOL, elastic frame assumption, grey.

Figure 6.56 shows absorption coefficient as a function of frequency for the same measured linear profile as the one given by Figure 6.55 (but now with an elastic frame assumption and not the rigid). In the elastic frame model, a loss factor ($L_f = 0.12$) is included to account for damping. The first resonance frequency of the elastic frame model given by Figure 6.56 is closer to the measured impedance tube data, as opposed to the rigid frame model given by Figure 6.55. In this case f_r for the elastic frame had $f_r = 269$ Hz and $\alpha = 0.99$, which is a difference $f = 44$ Hz between the elastic model and measured impedance tube data. It can be observed in Figures 6.55 – 6.56 that a discrepancy between the theoretical and experimental data is mostly noticeable especially at low frequencies. This is apparent

for both the rigid frame and elastic frame models in the region around $f = 200$ Hz and $f = 500$ Hz. Where absorption coefficient is much higher for the experimental data than α predicted by the FEM models, for both frames (rigid and elastic). However, both the rigid frame model, Figure 6.55, and elastic frame model of Figure 6.56 are successful at showing that α is most definitely broadband for the profile built with a varying inner pore radius along the sample length. Both the rigid and elastic frame models also show that large values of α are attained for when the sample is regarded to be influenced by a pressure wave. This phenomenon can be seen by the physical measured data obtained from performing the direct measurements using an impedance tube, presented by Figures 6.55 – 6.56. Future work would be to modify the FEM models and investigate other methods of accounting for the acoustic and vibrational effects of the profile structure. Figure 6.57 shows total acoustic pressure fields computed at several frequencies for the linear profile absorber.

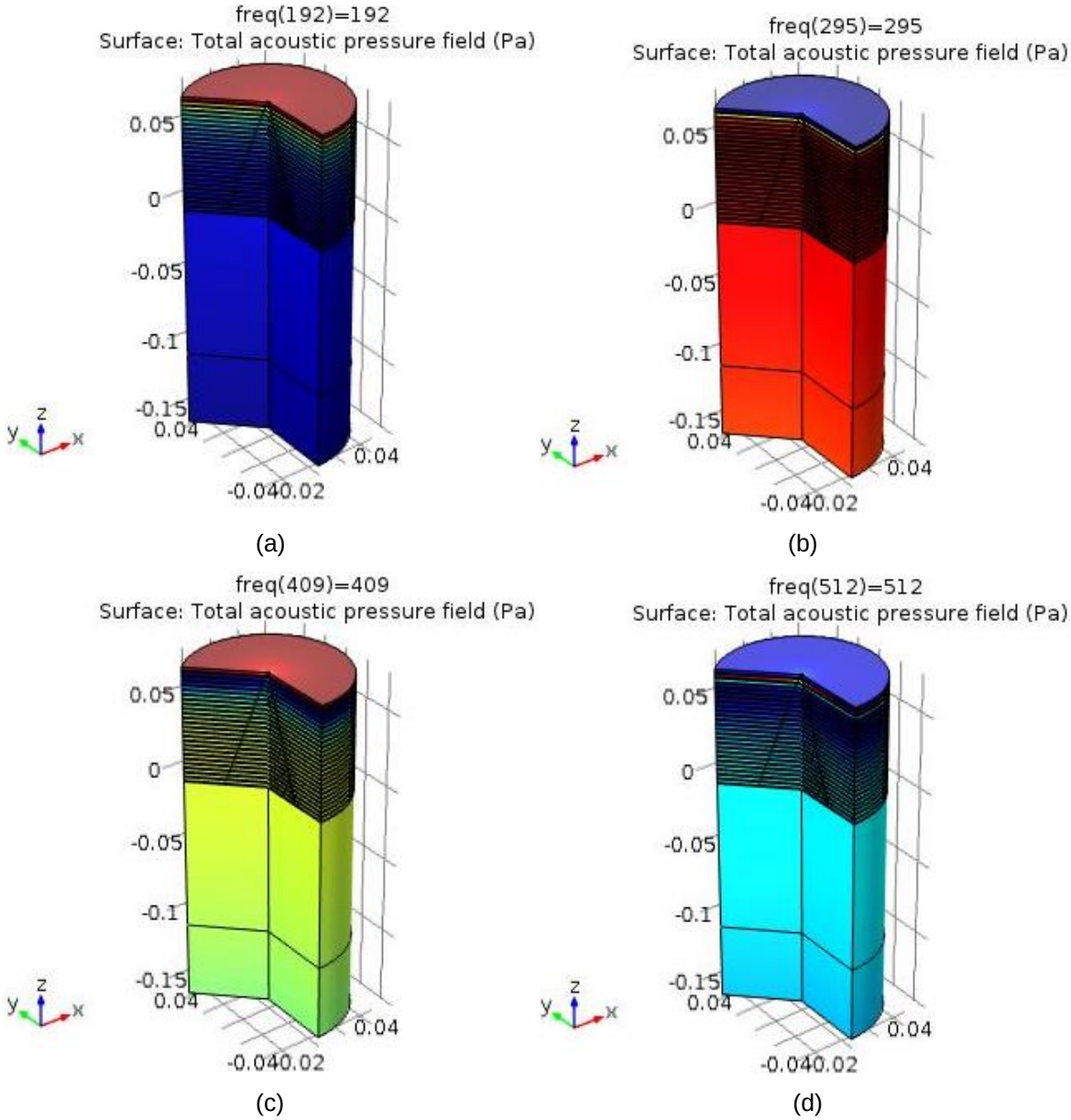

Figure 6.57. Simulation of the computed total acoustic pressure fields for linear profile absorber with a surface plate opening main pore radius $r_0 = 25$ mm, $d_p = 1$ mm, $d_c = 2$ mm, $L = 80$ mm, $N_{de} = 25$, and $R = 50$ mm. Frequencies are (a) 192 Hz, (b) 295 Hz (c) 409 Hz and (d) 512 Hz. Frequencies given (a – d) correspond to the first four low frequency peak values shown in Table 6.20.

6.4.3. Model Comparisons

In order to obtain the effective properties of the absorbers the FEM models use the characteristic viscous and thermal lengths, porosity, density, flow resistivity, and tortuosity factor. This is identical to the previous effective properties model (see section 6.2) which uses the same process of the equivalent fluid approach. The parameters can be seen with their respective values shown by Table 6.12 and are assigned to the main and dead-end pores for each cell, with the exception of the common pore (which uses the properties of air). In addition to these parameters, a loss factor L_f is used in the COMSOL elastic frame model (where $L_f = 0.12$) and is dependent on the material frame structure. To keep all the models consistent with each other, the values of d_p, d_c, r_0, L, R for each structure are equal in all of the model computation processes (TMM, effective properties, and COMSOL). Furthermore, all the measurements performed in the impedance tube (LSPL and HSPL) had each metamaterial absorber configured to the dimensions of those that were used in all of the models. This was so that each measurement and computation process given by each of the models presented thus far had equal material parameter values. It can be seen in the Figures below that the models are closer matched to the measured data for the absorbers with lengths around $L = 60$ mm, as opposed to $L = 30$ mm. It is shown in Chapter 5 that the shorter structures have a higher nonlinearity factor than the larger samples and consequently, provides a slightly larger discrepancy between the measured data. Moreover, bandgaps which exist due to periodicity of the structures affects the peak absorption values which is the result of mechanical resonance and differs with the pore wall porosity. These effects has been discussed previously in [139] including the concept of scale separation. As a result, the models can overestimate the peak value of the absorption coefficient α.

Data obtained by the models from TMM, effective properties and COMSOL Multiphysics are plotted in Figures 6.58 – 6.63 showing absorption coeffcient as a function of frequency, for pancake structures built with various configurations. All samples have pore radius $r_0 = 4$ mm, plate thickness $d_p = 1$ mm, and external plate radius $R = 50$ mm. The linear profile structure is shown by Figure 6.64 with its measured impedance tube data compared with the TMM and FEM models. Data from impedance tube measurements versus each model can be seen by the respective model sections throughout this Chapter, see for a more detailed comparison for each model, where values of absorption coefficient and resonance frequencies are presented. For instance, section 6.1 shows the TMM vs measured impedance tube data, section 6.2 shows the effective properties model and the measured data, section 6.3 shows nonlinear regime model and its validation against measured data and section 6.4 shows the FEM models obtained by using COMSOL Multiphysics. Figure 6.58 provides the data from the pancake with $L = 31$ mm and $d_c = 1$ mm. The FEM data by rigid and elastic frame models show to be at lower frequency for f_r compared to the other models (where effective properties and the TMM data show to be similar and predicted being at slightly higher frequency. Furthermore, all the model data shown have larger α values than the measured impedance tube data. The elastic frame model shows the closest match to the second resonance frequency to the measured data compared to other models given in Figure 6.58. A simple pore for comparison with $r_0 = 4$ mm and same length $L = 31$ mm can be seen in Figure 6.53 where $\alpha = 0.91$ and has a resonance frequency $f = 2529$ Hz. Note, the number of the dead-

ends and loss factor values are given in each of the Figures (where N_{de} and L_f indicates the former and latter, respectively).

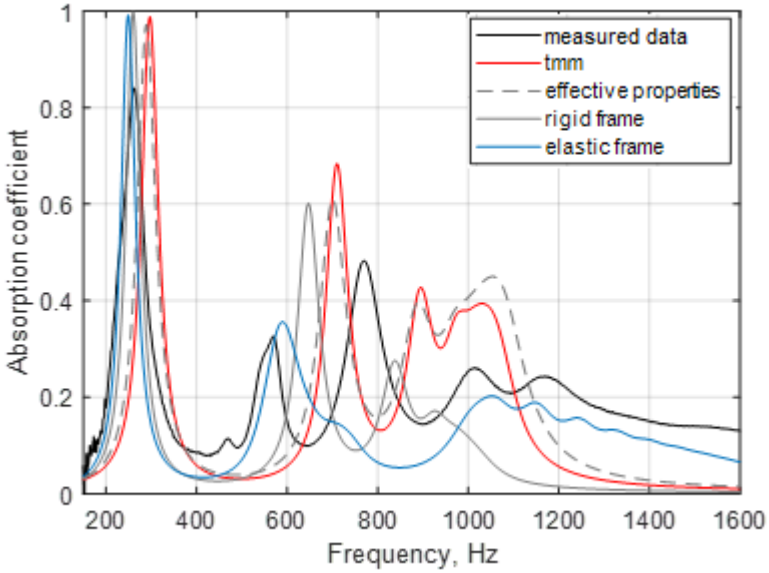

Figure 6.58. Absorption coefficient as a function of frequency showing measured impedance tube data and all model comparisons, linear regime. Pancake, $L = 31$ mm, $d_c = 1$ mm, $r_0 = 4$ mm, $d_p = 1$ mm, $N_{de} = 16$, $L_f = 0.12$, and $R = 50$ mm.

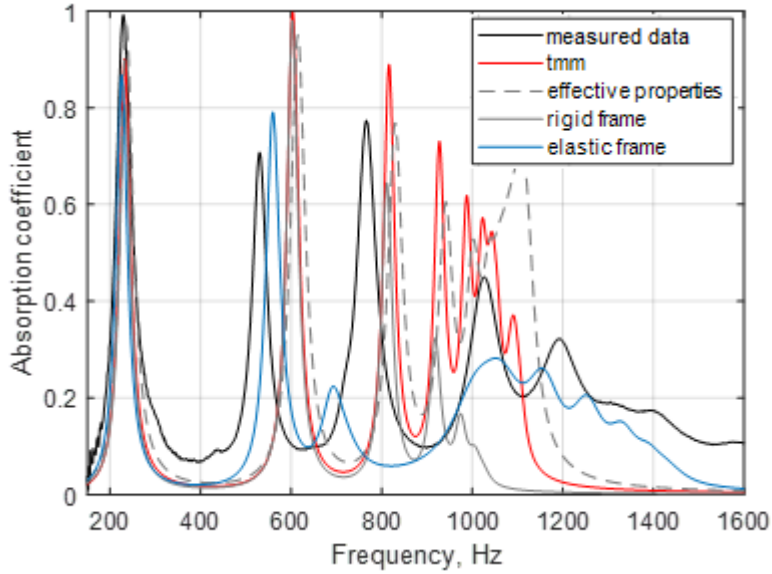

Figure 6.59. Absorption coefficient as a function of frequency showing measured impedance tube data and all model comparisons, linear regime. Pancake, $L = 32$ mm, $d_c = 3$ mm, $r_0 = 4$ mm, $d_p = 1$ mm, $N_{de} = 8$, $L_f = 0.12$, and $R = 50$ mm.

Figure 6.59 shows absorption coefficient as a function of frequency for pancake with $L = 32$ mm and $d_c = 3$ mm. All the models give similar data for the first resonance frequency for the metamaterial pancake absorber and moreover, are in very good agreement with the measured data. The FEM data given by the elastic frame model for the second resonance frequency is closest to that of the measured data. After the second resonance frequency, all models show a slight disagreement with the measured data. However, the effective properties model provides the same value of α but is given at a slightly higher frequency, from the measured data by $f = 66$ Hz. The model that gives the closest match to the position of the third resonance frequency is the FEM rigid frame. The elastic frame assumption gives

around $\alpha = 0.05$ due to the bandgap by the model. Moreover, a sample which contains only a single perforation and therefore absent any cavities has a resonance frequency $f = 2456$ Hz, where absorption coefficient is $\alpha = 0.91$. The pancake structure data therefore shows to effectively reduce f_r to a factor of nearly 11. See also, Figure 6.53 for simple perforations.

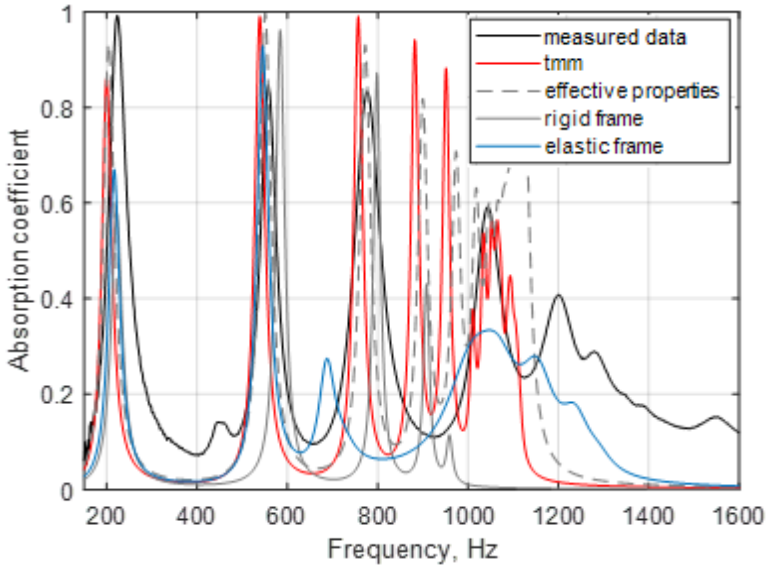

Figure 6.60. Absorption coefficient as a function of frequency showing measured impedance tube data and all model comparisons, linear regime. Pancake $L = 35$ mm, $d_c = 6$ mm, $r_0 = 4$ mm, $d_p = 1$ mm, $N_{de} = 5, L_f = 0.12$, and $R = 50$ mm.

Pancake structure presented by Figure 6.60 shows absorption coefficient as a function of frequency for pancake with sample length $L = 35$ mm and cavity thickness $d_c = 6$ mm. The effective properties model gives the closest values of absorption coefficient to the measured impedance tube data, where $\alpha = 0.94$ for the former, and $\alpha = 0.99$ for the latter. However, the first resonance frequency for the measured impedance tube data is at $f_r = 223$ Hz and the FEM rigid and elastic models give closest agreement for f_r (where $f_r = 223$ Hz and $f_r = 217$ Hz respectively). Data shows that f_r for the TMM and effective properties is $f_r = 200$ Hz and $f_r = 204$ Hz. The effective properties model shows a better agreement to the second and third resonance frequencies when compared to the impedance tube data (which sees only a difference $f = 6$ Hz). Data given by TMM, and FEM models are also close. For example, the TMM model predicts a difference $f = 18$ Hz, and rigid and elastic frame models provide a difference $f = 27$ Hz and $f = 13$ Hz. Absorption coefficient for the measured impedance tube data is $\alpha = 0.85$ whereas α given by the models are predicted with slightly larger values and range from $\alpha = 0.96$ and $\alpha = 0.99$. A simple pore for comparison which consists of a perforation radius $r_0 = 4$ mm and same length $L = 35$ mm has f_r beyond that of the frequency limitation shown by Figure 6.60 where $\alpha = 0.90$ at $f = 2263$ Hz. The metamaterial pancake structure is able to reduce f_r by factor 10 when compared to a simple pore with same sample length, $L = 35$ mm.

Figure 6.61 shows data obtained by the models in comparison to the measured impedance tube data for when sample thickness is double that of Figure 6.58. The pancake absorber is configured $d_c = 1$ mm and $L = 62$ mm. All the models are in extremely good agreement with the measured data at the first resonance frequency in terms of both f_r with closest match of α attained from the effective properties model. Absorption coefficient of the measured impedance tube data is $\alpha = 0.89$ and effective properties

$\alpha = 0.90$. The TMM predicted $\alpha = 0.91$ and rigid and elastic frame models were both $\alpha = 0.98$. Third resonance frequency is $f = 574$ Hz for the impedance tube data. Third resonance frequency that matched best for the models compared to the measured data was given by the elastic frame assumption. The next closest matches were obtained from the FEM rigid frame model and effective properties code, followed by the data given by the TMM. However, this is seen to be the contrary in terms of the best match for α, since TMM and effective properties gives a better agreement of α to the measured impedance tube data. Where $\alpha = 0.54$ for the measured data and $\alpha = 0.53$ predicted by the TMM model. Even though the elastic frame model gives the closest match for the third resonance frequency it provides the lowest value of α (where $\alpha = 0.30$). The rigid frame model in comparison gives $\alpha = 0.44$ at $f = 615$ Hz, see Figure 6.61. A simple pore with the same value of its radius, so $r_0 = 4$ mm and also same length $L = 62$ mm (for the solid sample therefore absent cavities, $d_c = 0$) has an absorption coefficient $\alpha = 0.80$. The associated resonance frequency is at $f = 1319$ Hz. This means that for same sample length, the pancake structure is able to reduce f_r by factor 10. See also, Figure 6.53 for simple perforations.

Figure 6.62 shows absorption coefficient as a function of frequency for pancake with $L = 60$ mm and $d_c = 3$ mm. All the models show that f_r is extremely well matched to the measured impedance tube data and moreover, provide the best agreement of f_r (for pancake $d_c = 3$ mm compared to other structures with $d_c = 1$ mm and $d_c = 6$ mm). The effective properties model provides the closest match of the absorption coefficient for the first resonance frequency f_r where $\alpha = 1.00$, which gives a good agreement to the measured data, where $\alpha = 0.99$. Second resonance frequency of the measured impedance tube data is compared with the models. The TMM data shows to give a slightly better agreement. However, effective properties and the FEM models are also very close to the second resonance frequency of the impedance tube data. All the models give a much larger value of α compared to the value of α obtained by the measured data. For example, $\alpha = 0.57$ for the impedance tube data, whilst α ranges between $\alpha = 0.92$ and $\alpha = 1.00$ for the models (where effective properties predicts the closest value as $\alpha = 0.92$, but still much larger α compared to the measured data).

After the second resonance frequency, all models show a disagreement with the impedance tube data (due to a bandgap occurring between approximately $f = 400$ Hz and $f = 600$ Hz). The FEM data given by the elastic frame assumption is the only model to match the resonance frequency of the measured impedance tube data at $f = 648$ Hz (where $\alpha = 0.32$ for the FEM). However, α for the impedance tube data is larger and has the value $\alpha = 0.57$. The elastic frame accounts for any vibrational effects by the fluid interaction, at higher frequencies, see section 6.4.1 for the FEM model data. A sample containing a simple central perforation and same value $L = 60$ mm gives $\alpha = 0.81$ at $f = 1362$ Hz. The pancake absorber is able to reduce the first resonance frequency by factor 10 and is one of the advantages of the metamaterial structure compared to a sample having same external dimensions. Single pore data can also be seen in Figure 6.53.

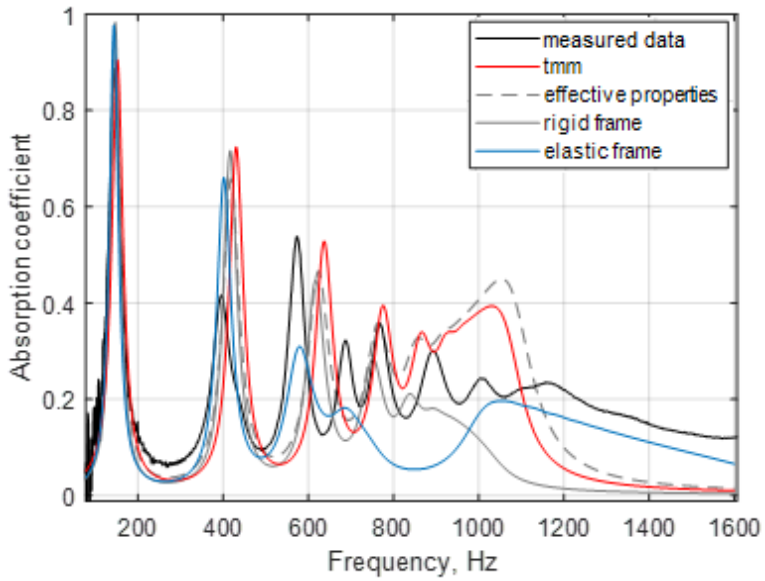

Figure 6.61. Absorption coefficient as a function of frequency showing measured impedance tube data and all model comparisons, linear regime. Pancake, $L = 62$ mm, $d_c = 1$ mm, $r_0 = 4$ mm, $d_p = 1$ mm, $N_{de} = 30$, $L_f = 0.12$, and $R = 50$ mm.

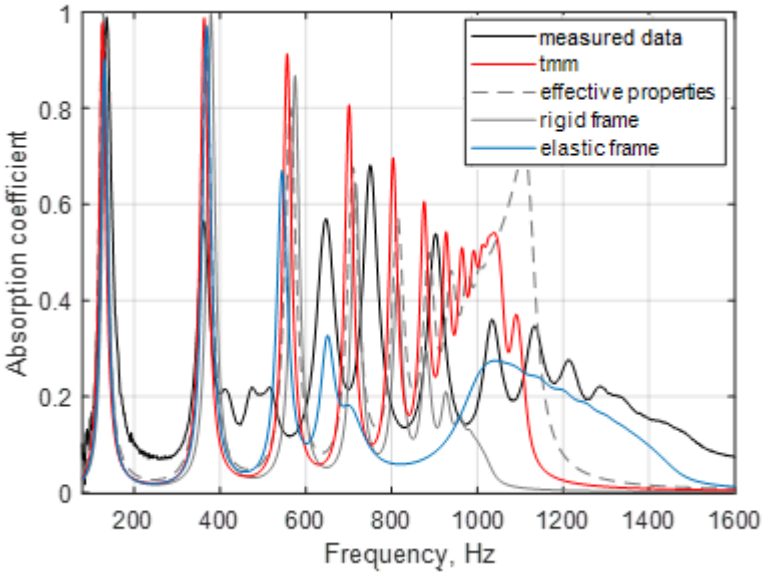

Figure 6.62. Absorption coefficient as a function of frequency showing measured impedance tube data and all model comparisons, linear regime. Pancake, $L = 60$ mm, $d_c = 3$ mm, $r_0 = 4$ mm, $d_p = 1$ mm, $N_{de} = 15$, $L_f = 0.12$, and $R = 50$ mm.

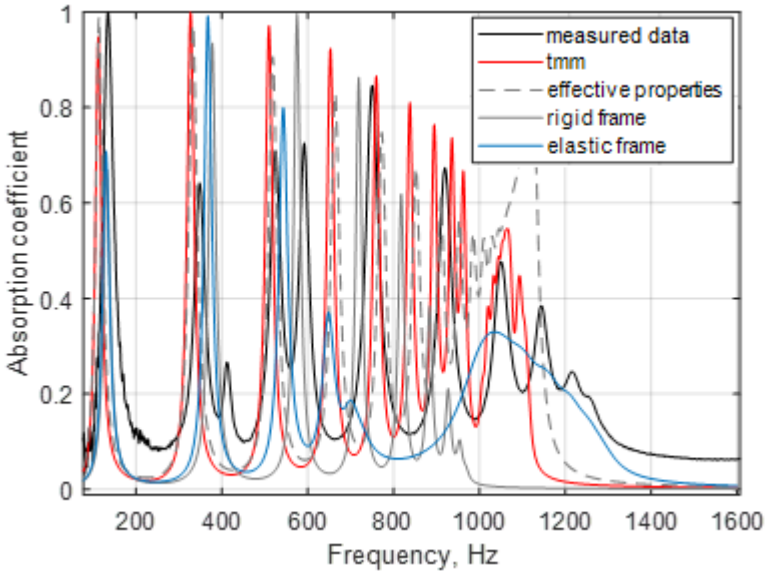

Figure 6.63. Absorption coefficient as a function of frequency showing measured impedance tube data and all model comparisons, linear regime. Pancake, $L = 63$ mm, $d_c = 6$ mm, $r_0 = 4$ mm, $d_p = 1$ mm, $N_{de} = 9$, $L_f = 0.12$, and $R = 50$ mm.

Metamaterial pancake structure shown by Figure 6.63 is when d_c is double from the sample shown in Figure 6.62. Cavity thickness now becomes $d_c = 6$ mm and sample length $L = 63$ mm. This completes the pancake absorbers investigated for the metallic structures with $R = 50$ mm. The effective properties and TMM models give absorption coefficient values at lower resonance frequencies compared to the FEM models (both rigid and elastic frames). This can be seen in Figure 6.63 for all resonance frequencies. Furthermore, the discrepancy between all of the models appears to be largest for when the sample is configured with $d_c = 6$ mm. The elastic frame FEM model gives a slightly better agreement of f_r to the measured impedance tube data for the value of the first resonance frequency. However, the FEM models give the lowest value of α, compared to the other models. For instance, absorption coefficient for the rigid and elastic models was $\alpha = 0.67$ and $\alpha = 0.71$, respectively. The measured impedance tube data is $\alpha = 1.00$. Effective properties model provides the best agreement to the measured data since $\alpha = 0.99$. The data obtained by TMM model also gives a close value of the absorption coefficient, where $\alpha = 0.95$. For the second resonance frequency the TMM and effective properties models both differ around $f = 30$ Hz from the measured data and $f = 29$ Hz from the rigid frame. The elastic frame differs $f = 19$ Hz from the measured data. Absorption coefficient for the TMM and effective properties models have α close to $\alpha = 0.99$ whereas the FEM data shows to be around $\alpha = 0.94$ and $\alpha = 0.99$ for the rigid and elastic models. The measured data is actually less where $\alpha = 0.64$. For the case of a simple pore only (so that $d_c = 0$) absorption coefficient is $\alpha = 0.80$ at resonance frequency $f = 1300$ Hz. This means that for same value L, the pancake structure is able to reduce the first resonance frequency by a factor 10 (α for solid sample containing single pore only can be seen in Figure 6.53).

Data obtained for a linear profile structure is presented in Figure 6.64 showing absorption coefficient dependence as a function of frequency and comparison of the measured data against the TMM model and the FEM rigid frame model, given by (a), and against the FEM elastic frame model shown in (b). The FEM data is obtained by COMSOL Multiphysics. The sample has a surface plate which contains

the main pore radius $r_0 = 25$ mm, plate thickness $d_p = 1$ mm, cavity thickness $d_c = 2$ mm and length $L = 80$ mm. Each orifice decreases until rigid backing is reached at the rear of the sample. The linear profile is investigated in section 6.1.2 which presents the measured data against the TMM model (see for further details and other profile structures containing decreasing central pores). Data for the linear profile with $d_p = 1$ mm and $d_c = 2$ mm is also presented in section 6.4.2 showing the experimental data against two FEM models. The impedance tube data is given here to show the differences between the models which have been used to determine the profile structure performance.

The linear profile absorber had f_r which measured $f_r = 313$ Hz and absorption coefficient had a peak value $\alpha = 0.97$. Sound source used is white noise excitation and sound pressure level is 80 dB. First resonance frequency of the measured data is at slightly higher frequency compared to that predicted by the TMM model and differs $f = 12$ Hz. The TMM data gives the first resonance frequency $f_r = 301$ Hz and $\alpha = 0.99$. A much larger discrepancy is given by the calculated FEM data of the rigid frame model, where $f_r = 192$ Hz and $\alpha = 0.94$. The difference in frequency between the measured impedance tube data and rigid frame model is $f = 121$ Hz, which differs by the TMM model by $f = 109$ Hz. The rigid frame model, however, gives absorption coefficient $\alpha = 0.84$ at frequency $f = 295$ Hz and differs by the measured data by only $f = 18$ Hz, see Figure 6.64 a. Data given by the elastic frame model presented in Figure 6.64 b, shows the first resonance frequency to be $f_r = 269$ Hz and $\alpha = 0.99$, therefore differing from the measured impedance tube data by $f = 44$ Hz. This means that the TMM data predicts a better agreement than that given by either of the rigid or elastic frame models. Second resonance frequency for the sample obtained by the impedance tube data is $f = 421$ Hz and $\alpha = 0.85$. The TMM data for the second resonance frequency was $f = 488$ Hz where $\alpha = 0.93$. The FEM models of the rigid and elastic frames had resonance frequency $f = 409$ Hz and $f = 415$ Hz where $\alpha = 0.84$ and $\alpha = 0.96$ respectively. Next resonance frequency for the measured data is $f = 509$ Hz whereas the TMM predicted the peak value of α being at $f = 679$ Hz. Absorption coefficient for the measured impedance tube data is $\alpha = 0.88$, and $\alpha = 0.94$ predicted by the TMM.

Rigid and elastic frame models have resonance frequencies $f = 512$ Hz and $f = 535$ Hz where $\alpha = 0.92$ and $\alpha = 0.97$, respectively. Many other values of α can be seen in sections 6.1.2 (TMM) and 6.4.2 (FEM). The absorption coefficient is broadband across the entire frequency spectrum for the measured impedance tube data and models given by the TMM and FEM. Broadband absorption ranges from around $f = 200$ Hz → $f = 1600$ Hz. The TMM data gives slightly larger values of α compared to the FEM data by the rigid frame model, at higher frequencies (approximately $f = 800$ Hz – $f = 1600$ Hz). The TMM and elastic frame model, however, have similar values of α at the higher frequencies, see Figure 6.64 b. Rigid framed model shows to have a greater number of absorptive peaks compared to the TMM data, shown in Figures 6.64 a. Across the frequency spectrum there are less resonance frequencies for the measured impedance tube data compared to that given by the TMM and FEM model. This can be seen mostly in Figure 6.64 a, for frequency ranging $f = 800$ Hz towards $f = 1300$ Hz. The impedance tube data, however, has much broader absorptive peaks. Discussion of the profile absorber has been presented also in Chapter 4, see metallic profile absorbers section 4.3.3 (measured values discussed for α at several resonance frequencies). The values of α at various resonance frequencies f, are

presented in Table 6.8 for the measured impedance tube and TMM data for the linear profile with surface pore radius $r_0 = 25$ mm, $d_c = 2$ mm and $L = 80$ mm.

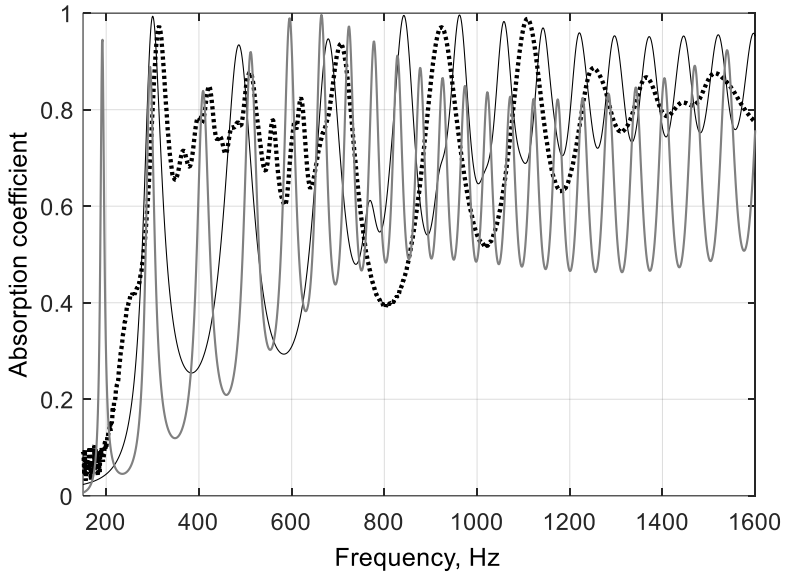

(a)

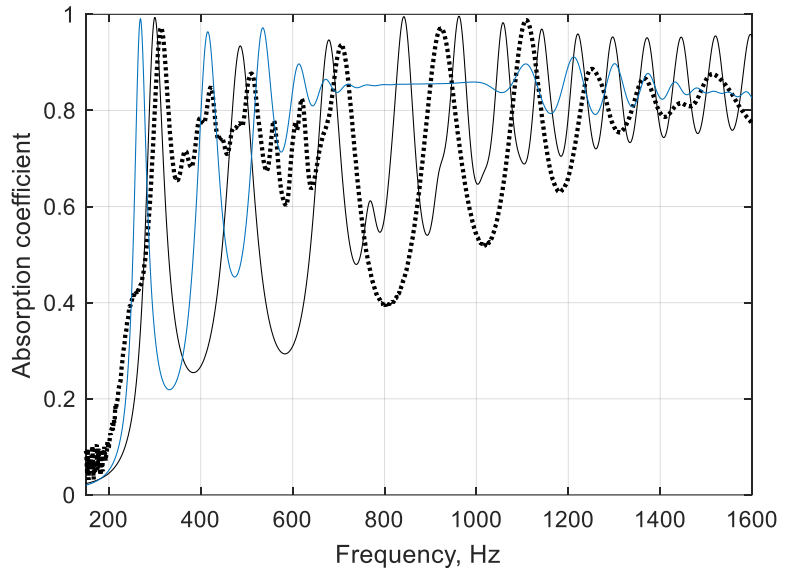

(b)

Figure 6.64. Absorption coefficient dependence as a function of frequency showing comparison of the measured data against TMM model and the FEM rigid frame model, given by (a). Impedance tube data is plotted against the TMM model and FEM elastic frame model presented in (b). FEM data is obtained by COMSOL Multiphysics. Sample is linear profile structure. Surface plate has a main pore radius $r_0 = 25$ mm, $d_p = 1$ mm, $d_c = 2$ mm, $L = 80$ mm, $N_{de} = 25$, $L_f = 0.12$, and $R = 50$ mm. Impedance tube data, black dot, rigid frame assumption, grey line (a), TMM solid black line, elastic frame, solid grey (b).

6.5. Conclusion

It has been demonstrated in Chapter 6 that performance of the pancake and profiled absorbers in terms of their absorptive capablities is in relatively good agreement with model predictions which have been computed using several model techniques. Data from the measured structures has been compared

against the predicted and calculated pancake and profile designs showing the model and experimental comparsions (TMM, Effective properties model, and COMSOL). This is presented in the respective sections (6.1 – 6.4) showing absorption coefficient dependence as a function of frequency. The absorbers are measured and computed for their peak absorptive values and for several configurations consisting of their parameter and material values. It is also demonstrated that absorption coefficient and the first resonance frequency f_r (including higher resonance frequencies after f_r) is dependent upon these parameter values and becomes affected with growth of the incident amplitude. Therefore, the paramerters must be correctly chosen (d_p, d_c, r_0, L, R) including frame material properties, Poisson ratio, Youngs modulus, and frame material density (ν, E, ρ_{samp}). The pancake absorber measured data (obtained from impedance tube use) have been compared in linear regime by the models, including the weakly nonlinear regime (made possible from use of a modified impedance tube for HSPL) and a developed model accounting for the absorbers effective properties which uses the Forchheimer's nonlinearity parameter values (obtained from flow resistivity measurements).

Profiled absorbers have been measured for their absorptive qualities and compared against the TMM and COMSOL models in the linear regime. The profiled structure is capable of achieving broadband absorption within the investigated frequency spectrum and obtaining large values of α. Pancake absorbers are shown to achieve large values of α at low frequency notably for f_r which is where the maximum value of α is obtained. The pancakes behave in a tonal manner whereas broadband absorption is attained by the profile structures. This means that after the first resonance frequency f_r values of the absorption coefficient α reduces at higher frequencies for metamaterial pancakes. Profiled structures, however, are able to achieve large values of α after the first resonance frequency. Accelerometer measurements have also been performed and show that mechanical resonance due to structural vibration must be considered along with the acoustic resonance for the performance of the absorber designs. Moreover, as expected, the mechanical resonance is also shown to be affected by the plate thickness d_p. Therefore, plate and cavity dimensions of the absorber configurations impact the structural resonance frequency. Thus, the selected parameters of the structures need to be carefully considered depending on achieving the optimal performance for the metamaterial structures.

Pancake absorbers have been compared against the Helmholtz resonator to illustrate how effective the metamaterial designs are for low frequency sound absorption. For instance, the pancakes are shown to achieve larger values of α at lower frequency f_r compared to the Helmholtz resonator with same values of the absorber length L, depending on the selected parameters. This is the case for when the samples are configured with low values of d_p and when the absorbers have a high pore wall porosity. However, when the samples have a low pore wall porosity then the Helmholtz resonator is demonstrated to obtain slightly larger values of α and lower f_r, for same sample length. Performance of the pancake absorbers makes the metamaterial structure advantageous over the Helmholtz resonator when the optimum parameter values of the design are selected. This leads to obtaining the improved values of α and f_r for the metamaterial structures, including when α at multiple frequencies are required to be attenuated. The absorbers are therefore shown to be desirable for low frequency sound absorption and can outperform the Helmholtz resonator. The profiled structures which have also been investigated are shown to obtain larger values of α for low, middle and at higher frequencies.

7. Shock Tube Measurements

7.1. Empty Shock Tube

Research focus of the PhD project is aimed at sound absorption at low frequencies for both linear and nonlinear regimes. The largest of the amplitudes created are those obtained by performing measurements in the shock tube, based at University of Salford in the advanced acoustic laboratory. High amplitude shock pulses are investigated with the metamaterial absorbers discussed in previous Chapters. The development of such a structured material is investigated to enable both linear and nonlinear acoustic waves to be absorbed effectively at low frequencies. There are many various designs of acoustic metamaterials (examples are given in Chapter 3). In this work it is rigid metamaterial structures that are developed and use the approach of combining two different geometrical methods for obtaining maximum sound absorption. This allows an effective metamaterial structure developed to be robust and applicable to many circumstances involving high sound levels. Two main approaches for the metamaterial design to be investigated for extreme noise levels continues further (following on from subsequent chapters presented earlier in the thesis). Measurements are performed in the shock tube with main focus being an absorber with 1. Dead-end pore design (DEP) and 2. Profiled absorber employing acoustic black hole effect (ABH). The idea of combining both (ABH) and (DEP) could result in absorbers which are broadband in frequency domain and still relatively thin even when used at very high sound levels close to 200 dB. This is achieved due to utilising structural lateral dimensions. The practical objective is the combination of both approaches to a single design resulting in dead-ends and the main pores having varying sizes which enables the structure to exploit ABH effect whilst keeping perforation surface relatively low for maximum rigidity of the structure.

The aim of this Chapter is to investigate experimentally the interactions of high amplitude pulsed excitation (weak shocks) with pancake absorbers and ABH structures. Firstly, to gain an understanding of high amplitude interactions, shock tube tests have been completed for simple structures such as single orifices followed by micro perforated panel absorbers of cylindrical and cross geometrical pores. These measurements of simple structures are the foundation upon the more complex structures. Shock waves are high amplitude impulsive signals meaning broadband in frequency domain. The absorber for impulsive sound needs to be effective for a wide range of frequencies including very low ones. Shock waves are often characterised by a Mach number, where M<1 and M>1 are the cases of subsonic and supersonic speeds, respectively. For gasses and liquids, the ratio of the characteristic particle velocity and sound speed of the medium is given by,

$$M = \frac{v}{c} \tag{1}$$

where for an ideal gas $c = \sqrt{\gamma \frac{P_0}{\rho_0}}$. When M < 1.0 the shock wave is regarded subsonic. The larger the value of Mach number the larger or greater the speed, thus when $M = 1.0$ it is known as transonic. When $M > 1.0$ classification of the shock wave is supersonic. For a shock wave with a Mach number greater than 5.0 so that $M > 5.0$ it is known to be hypersonic.

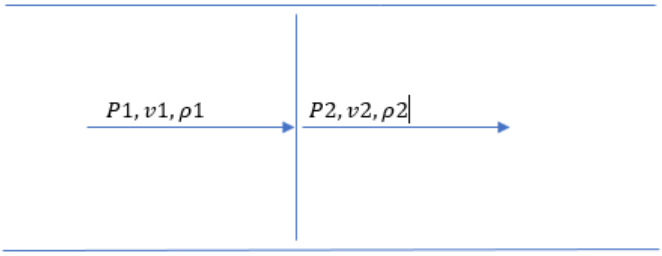

Figure 7.1. Schematic of a normal shock front, upstream pressure, velocity, and density is P1, $v1$, and $\rho 1$ respectively. Downstream pressure, velocity and density is P2,$v2$, and $\rho 2$ respectivley.

Shock waves are produced by nonlinear acoustic propagation arising from compressive sudden changes and energy dissipation [8]. There can be stationary, moving, or oblique shock waves whereas for weak shock waves the upstream and downstream flow remains subsonic. For strong shock waves for example arising from detonations, flow rapidly becomes supersonic for the downstream region [7]. The equations for Mach numbers, temperature, and pressure for one dimensional flow are notated from implying continuity, momentum, and energy.

$$M_1 = \frac{V1}{\sqrt{kRT}} \tag{2}$$

where M_1 is the Mach number of the shock wave upstream. The shock wave downstream becomes the following where Mach number is given by,

$$M_2^2 = \frac{M_1^2 + 5}{7M_1^2 - 1} \tag{3}$$

Temperature of the shock wave is determined using ratio of $T2/T1$ which becomes,

$$\frac{T_2}{T_1} = \frac{(M_1^2 + 5)(7M_1^2 - 1)}{36M_1^2} \tag{4}$$

where pressure of the shock wave using the two pressure different regions is expressed by,

$$\frac{P_2}{P_1} = \frac{7M_1^2 - 1}{6} \tag{5}$$

The Mach number, temperatures and pressures can be calculated to give the information of the disturbed wave. It is however common to use a normal shock flow table accounting for air relations for normal shocks.

M_1	M_2	p_2/p_1	ρ_2/ρ_1	T_2/T_1	p_{02}/p_{01}
1.0100	0.9901	1.0235	1.0167	1.0066	1.0000
1.0200	0.9805	1.0471	1.0334	1.0132	1.0000
1.0300	0.9712	1.0711	1.0502	1.0198	1.0000
1.0400	0.9620	1.0952	1.0671	1.0263	0.9999
1.0500	0.9531	1.1196	1.0840	1.0328	0.9999
1.0600	0.9444	1.1442	1.1009	1.0393	0.9998
1.0700	0.9360	1.1691	1.1179	1.0458	0.9996
1.0800	0.9277	1.1941	1.1349	1.0522	0.9994
1.1000	0.9118	1.2450	1.1691	1.0649	0.9989
1.1100	0.9041	1.2708	1.1862	1.0713	0.9986
1.1200	0.8966	1.2968	1.2034	1.0776	0.9982
1.1300	0.8892	1.3231	1.2206	1.0840	0.9978
1.1400	0.8820	1.3495	1.2378	1.0903	0.9973

Table 7.1. A minority of values for normal shock flow relations. From the normal shock flow table, the values associated for any given Mach number can then be given with relation to the energy, momentum, and pressure quantities. Last column showing p_{02}/p_{01} represents the ratio of the stagnation point pressures in front of and behind a shock wave respectively [9].

A shock tube is one example for the formation of high amplitude pulses and nonlinear acoustics which has been of interest for many decades for creation of exceptional high noise levels [5]. To begin the investigation of high amplitude waves the measurements are performed firstly in an empty shock tube in order to determine the repeatability of each explosion and prepare the set up for material testing. Data is taken at the base and peak of each pulse measured for a range of amplitudes from different membrane ruptures. The software for recording the pressures is Pulse. Each single measurement produces a display of up to three pulses with various amplitude strengths obtained by piezoelectric transducers located at three separate fixed positions. When the samples are mounted there is inevitable superposition of the reflected and incident pulses at the measurement location close to the sample surface and therefore empty tube measurements are performed first in order to record the incident pulse. Each test is performed in the following manner. A membrane is fixed to a compartment at one side of the shock tube known as the rupture chamber. This rupture chamber is then compressed via an electric compressor and doing so creates a high-pressure region on one side of the membrane and a low-pressure region on the other side of the membrane. Moreover, because the membranes used have different thicknesses then there is a change in the tensile strength and consequently the pressure amplitude of the shock pulse, depending on which membrane is ruptured. The membranes are fixed in place inside the rupture chamber to create pulses of different amplitudes for each explosion. Once the rupture chamber is at a strong enough pressure, the membrane is ruptured instantly, and the force created is simply too great thus creating a high amplitude shock pulse. Pressure ranges are between 10 KPa to 100 KPa and recorded by microphones from each explosion. The shock pulse then propagates along the tube and the pressure is measured at fixed positions as the shock travels.

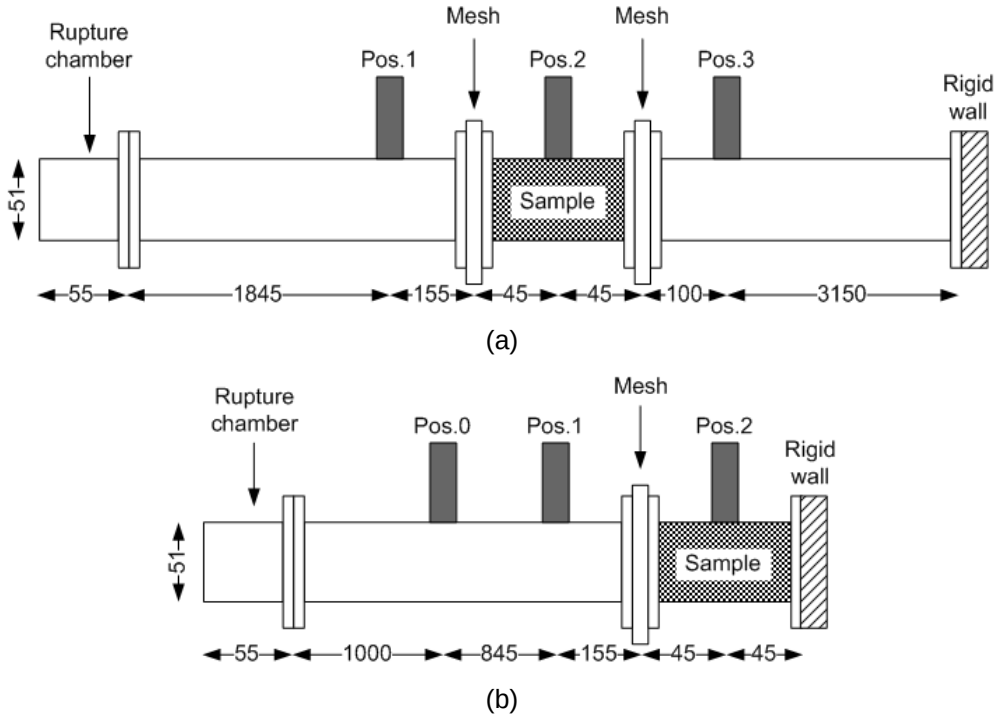

Figure 7.2. Shock tube (a) transmission set up and (b) for rigid backing mode. All dimensions shown in mm [43].

To determine the repeatability and error from each explosion, empty shock tube measurements are performed in transmission mode in time domain giving pressure peak values that are recorded by the three piezoelectric transducers. Shock pulses relating to empty tube and in transmission set up for

various membranes recorded as “signal 2” (seen as position 1 in Figure 7.2 in the shock tube diagram). The maximum peaks are measured for each explosion and the amplitudes are analysed. This procedure is performed for many pulses for each membrane burst and then averaged over a total of at least five pulses. Figure 7.3 shows a signal resulting from a typical explosion by 50 μm Mylar membrane after a measurement is performed using the empty shock tube in time domain. Several measurements of the membranes are tested so that standard deviation and error can be calculated, and repeatability determined. This enabled further data from the tests for various membranes to be obtained with a good degree of accuracy, errors of the measurement amplitudes and their duration. The error in the peak pressure value of pulses generated by the ruptured membranes (with an exclusion of Mylar 40 μm, Signal 1) is less than 5 %. This could be due to the mounting process used for the fixing of membranes to the rupture chamber and remains the same for any given sample that is tested for sound absorption and transmission.

Membrane	Signal 1 (Pa)	Signal 2 (Pa)	Signal 3 (Pa)	Signal 2 duration (s)
Tin foil	16422 ± 495	15498 ± 72	13342 ± 72	$(1.56 \pm 0.06)\ 10^{-3}$
Tin foil x2	19600 ± 680	18584 ± 746	14698 ± 343	$(1.08 \pm 0.04)10^{-3}$
Paper	39384 ± 265	29770 ± 610	24704 ± 311	$(1.23 \pm 0.04)10^{-3}$
Mylar 23 μm	48784 ± 1406	46976 ± 759	36310 ± 227	$(1.60 \pm 0.03)10^{-3}$
Mylar 40 μm	76330 ±8738	65510 ±3888	48214 ±1504	$(1.79 \pm 0.02)10^{-3}$
Mylar 50 μm	80000 ±3551	70578 ±660	54796 ±395	$(1.89 \pm 0.02)10^{-3}$

Table 7.2. Parameters of shock pulses recorded in empty tube for transmission set up. Various membranes recorded at signals 1, 2, and 3 which can be seen as positions 0, 1, and 3 respectively in Figure 7.2 a, b.

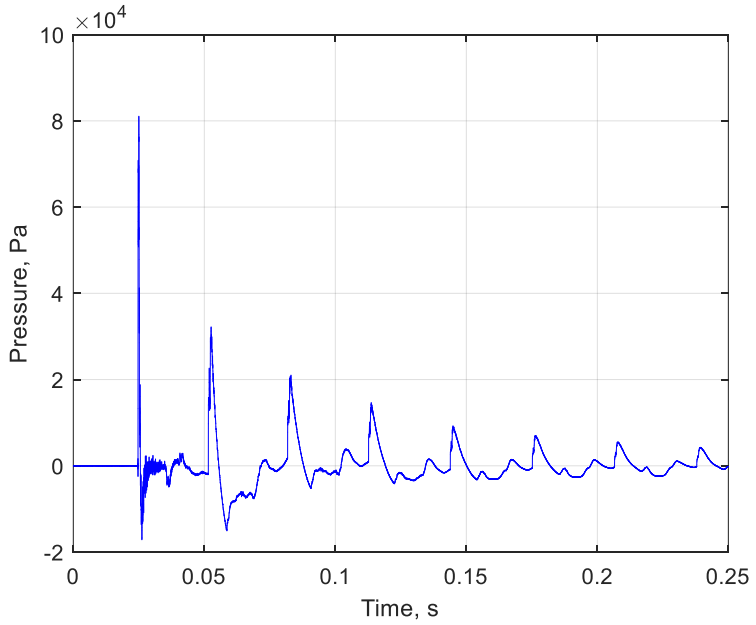

Figure 7.3. Pressure dependence as a function of time for Mylar 50 μm membrane ruptured in empty shock tube.

The pulse duration is calculated by recording times when pressure values are close to zero and identical for each shock pulse. Table 7.2 shows values of peak pressure and pulse duration measured for membranes having various properties and tensile strength. The wavelength of the most frequencies of associated pulses is much larger than the diameter of the tube therefore plane wave propagation hypothesis can be accepted. Extension of the shock tube in transmission set up (approx. 3.25 m) is shown by Figure 7.2a. Because the time of pulse flight is at least twice the duration of the pulses, no

superposition is achieved thus incident and reflected tube-end pulses can be treated as separate occurrences. For each pulse amplitude five sets of data obtained from the maximum peak pressure is also measured and averaged with standard deviation and the error calculated. This procedure is performed for five pulses for each membrane and the average over the total of five pulses calculated. Figure 7.4 shows pressure dependence as a function of time for one of the five pulses from Mylar 50 μm being ruptured in the empty tube. A fixed piezoelectric transducer measures the signal which is located prior to the sample housing position.

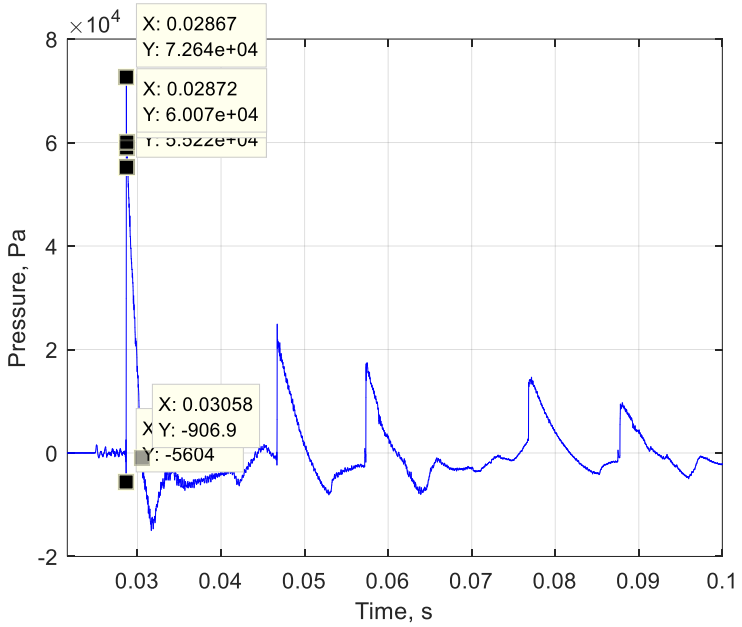

Figure 7.4. Pressure as a function of time for a pulse by a ruptured Mylar 50 μm membrane. Signal represents a measurement conducted in an empty shock tube nearby a sample holder.

During any single shock pulse measurement, the base of each pulse is used to determine the pulse duration. This is obtained from the incident and reflected pulses and calculated by the start of shock front time for the pulse. It is measured thereafter against the time delay of the following corresponding shock front of the next pulse. From determining the distance of travel of pulse d and by change in time between the shock fronts ΔT it is simple to retrieve speed values for any associated pulse,

$$c = \frac{d}{\Delta T} \tag{6}$$

Experimental values of sound speed for different Mylar membranes (23 μm, 40 μm, and 50 μm) are compared, see Figure 7.5 showing theoretical sound speed dependence on pressure [16].

$$c = c_0 + \frac{(\gamma-1)}{2}\frac{c_0}{P_0}p \tag{7}$$

Here c_0 is sound speed for low amplitude signals. Figure 7.5 shows data obtained by the measurements performed in the shock tube are in good agreement with the theoretical values (plotted against pressure up to values with a maximum pressure 10^5 Pa). The sound speed refer to ruptured membrane explosions of various tensile strength, performed in an empty shock tube in transmission set up. Consequently, the pressure values (shown on x axis of Figure 7.5) are recorded by signal 2 and signal 3 from B & K type piezoelectric transducers in the absence of any sample. These results confirm one dimensional pulse propagation in empty tube agrees with predictions of the theory which takes nonlinearity of air equation of state into account. The signal measurement positions relate to positions

1 and 3 respectively shown by Figure 7.2a. Experimental values calculated from the membrane explosions are given by the markers and refer to pulse amplitudes. Depending on the direction of pulse propagation and distance travelled, the pulse amplitude and time difference between each consecutive corresponding pulse is calculated and plotted.

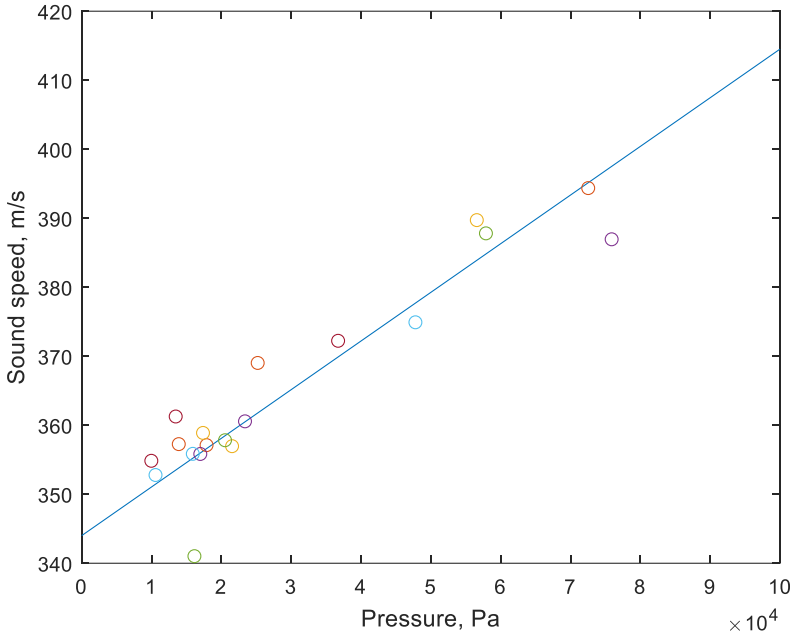

Figure 7.5. Sound speed vs pressure for Mylar membranes ruptured in the shock tube. A comparison of experimental data and the model (Equation 7) is plotted showing calculated sound speed.

7.2. Single Orifice

Firstly, measurements are performed in transmission set-up of the shock tube with metallic plates that contain a single orifice. Later, plates with multiple pores (MPPA's) are tested which is presented by section 7.3. This is to gain an understanding in the simplest case for the interaction of high amplitude waves and small perforations since MPPA's are well known to be effective when constrained with high sound pressure levels. Measurements containing a single orifice in an aluminium plate 1.5 mm thick and pore diameter 1.6 mm was performed in the tube. This was the beginning point from which multiple holes in solid plates having different open-air surface ratios could be later investigated. Figure 7.6 shows pressure as a function of time for a single plate in transmission set-up containing a single orifice. Membrane ruptured is tin foil and pressure is measured immediately after the rupture chamber, signal 1 (see Figure 7.6 a) prior to sample at signal 2 (Figure 7.6 b) and short distance after the sample at signal 3, see Figure 7.6 (c) and obtained from a single measurement. See also Figure 7.2 for microphone positions and shock tube in rigid backing and transmission set-ups. In Figure 7.6 a, it is shown the pulse has no reflection for the first pulse since it is the incident pulse. The pulses appearing later are superpositions of the pulses reflected by the rupture chamber wall and the plate. In Figure 7.6 b, a combination of two pulses is observed. The first peak is that of the incident pulse and the second peak shows the reflected pulse from an aluminum plate containing a single orifice. Figure 7.6 c shows that pressure of the shock pulse is forced to exit the 1.6 mm pore diameter, however, nearly all energy is reflected apart from some slight noise being transmitted, where signal 3 measures after the sample

holder. Peak amplitude of the transmitted pulse is more than 10 times lower than that of the reflected pulse. The transmitted energy of the signal shown in Figure 7.6 c is around 7 % of the incident energy which is due to the interaction of the shock pulse with the solid boundary of the plate. This arises from the disturbance of the plate itself which creates loud noise and is measured immediately after the plate by piezoelectric transducer signal 3.

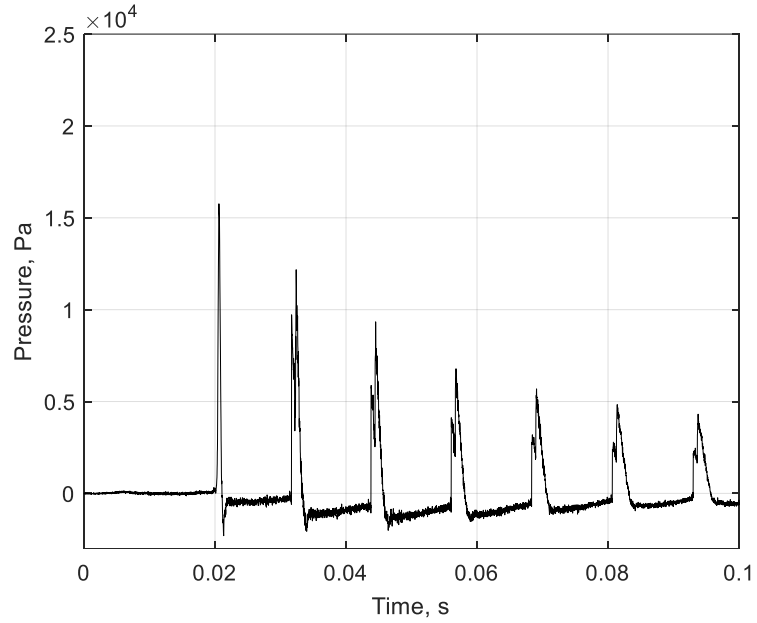

(a)

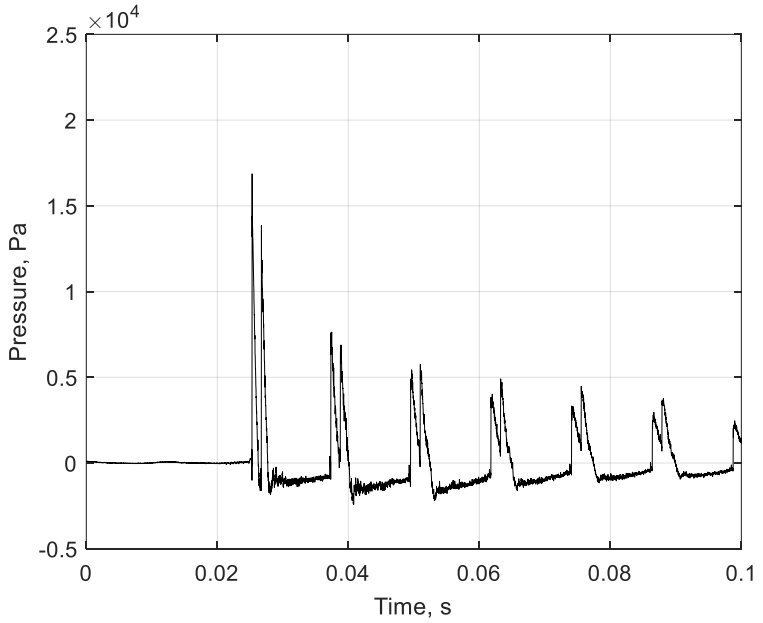

(b)

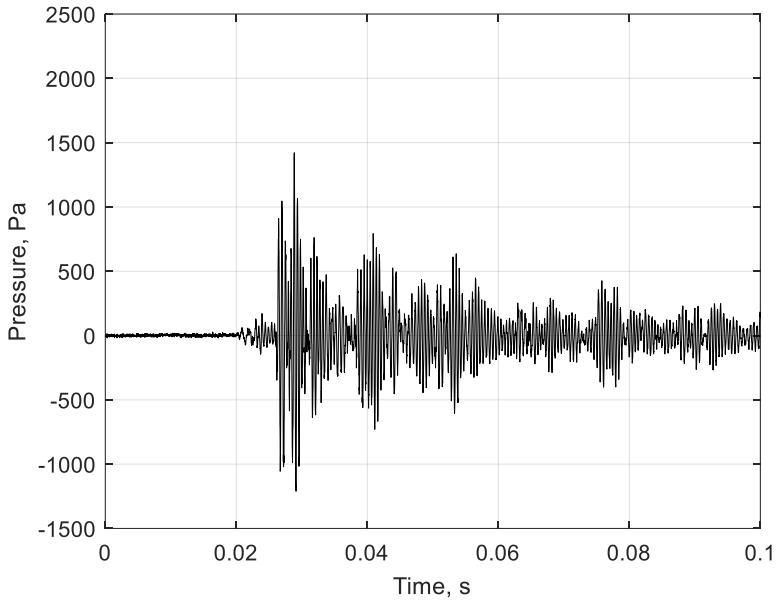

(c)

Figure 7.6. Pressure as a function of time for membrane tin foil showing signals 1 – 3 (a – c) obtained from a single measurement of a thin plate containing a single perforation.

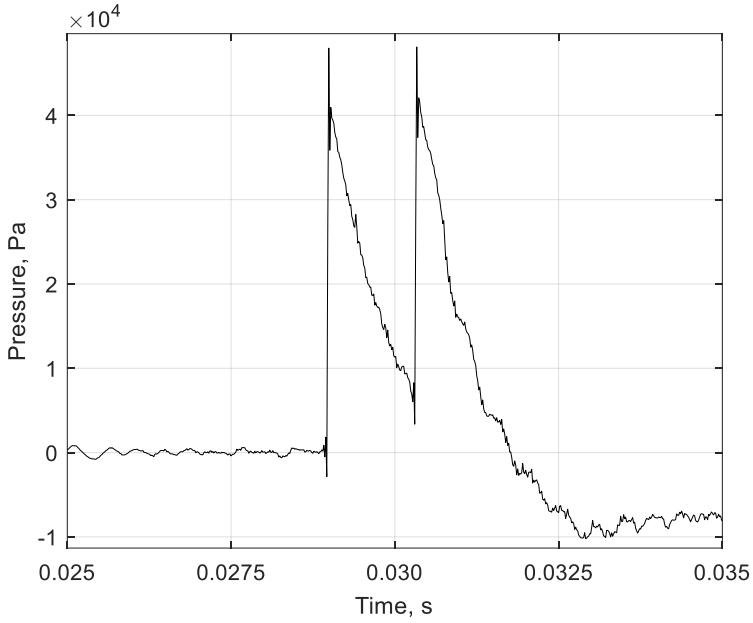

Figure 7.7. Pressure as a function of time for Mylar 23 μm at signal 2. Majority of energy is reflected back similarly like other ruptured membranes for a small single perforation contained in a thin plate.

Figure 7.7 shows the reflected pulse is approximately equal to that of the incident one from the ruptured Mylar 23 μm in the shock tube. Very little energy is therefore transmitted through the plate containing only a single pore. Figure 7.8 shows pressure as a function of time for Mylar membranes ruptured in the shock tube with different tensile strengths. Data given is obtained by signal 2 before the plate for the different explosions. Note how all the pulses begin at different times due to the amplitude variations, and moreover, showing larger amplitudes having greater sound speed. Incident pulses measured at signal 2 prior to the plate containing a single orifice have peak pressures 45000 Pa, 60000 Pa and 72000 Pa. The reflected superimposed peak pressures are 45000 Pa, 62000 Pa and 82000 Pa, respectively. First

pulse analysis of the superimposed pulses for various amplitudes are later performed for perforated plates, pancake absorber and the profiled configurations, given by sections 7.3 – 7.4 and 7.6 – 7.9.

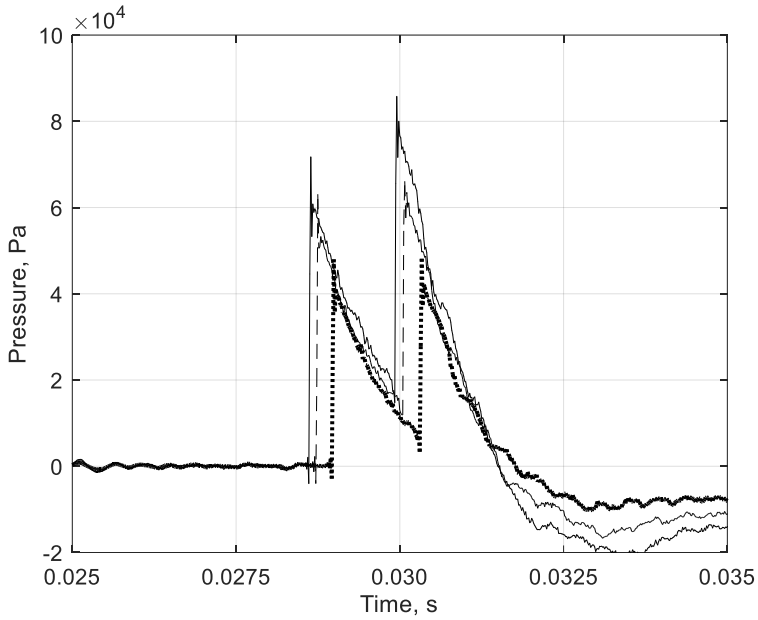

Figure 7.8. Pressure as a function of time for different Mylar membranes at signal 2. Solid line represents data for Mylar 50 μm, dashed line is Mylar 40 μm, and Mylar 23 μm is shown by dotted line.

7.3. Multiple Orifices in Thin Plates (MPPA)

Micro-perforated panel absorbers (MPPAs) are well known to be effective for low frequency sound especially for high amplitude excitation when rigid structures are favoured (see Chapter 3.2 in Literature review, with discussion on MPPA's and rigid porous media). Several porous plates consisting of multiple pores and different specific open area perforation ratios have been studied in other works, as reported in [36]. Following work by Park [36] (who investigated medium and high sound pressure levels for the proposed enhancement of acoustic absorption inside of launch vehicles). An investigation of MPPA's is studied and presented here in Chapter 7 for perforated plates with different geometrical parameters. Firstly, computation of the mass reactance and relative acoustic resistance are performed in both linear and nonlinear regimes for low and high sound pressure levels, respectively. Normalised specific acoustic resistance r_1 and reactance x_1 is re-introduced from Chapter 3.2 for low sound pressure levels are,

$$r_l = \frac{32\eta t}{\rho_0 c_0 d^2}\left(\sqrt{1+\frac{k_p^2}{32}}+\frac{\sqrt{2}}{32}k_p\frac{d}{t}\right) \tag{8}$$

$$x_l = \frac{\omega}{c_0}\frac{t}{\sigma}\left(1+\frac{1}{\sqrt{9+\frac{k_p^2}{2}}}+0.85\frac{d}{t}\right)-\cot\left(\frac{\omega D}{c_0}\right) \tag{9}$$

where ω is angular frequency, ratio between hole diameter and viscous boundary layer is $k_p = 0.5d\sqrt{\frac{\rho_0\omega}{\eta}}$, cavity depth behind the plate is D, perforation ratio is σ, thickness of MPPA is t. At high

sound pressure levels for the micro perforated absorbers nonlinearity phenomena is needed to be accounted thus, nonlinear reactance x_{nl} is given by,

$$x_{nl} = \frac{\omega}{c_0}\frac{t}{\sigma}\left(1 + \frac{1}{\sqrt{9 + \frac{k_p^2}{2}}} + 0.85\frac{d}{t}\left(1 + \frac{u_0\sqrt{2}}{\sigma c_0}\right)^{-1}\right) - \cot\left(\frac{\omega D}{c_0}\right), \tag{10}$$

where the particle velocity is u_0, Nonlinear normalised resistance of the MPPA r_{nl} for high sound pressure levels is,

$$r_{nl} = r_l + 1.59\left(\frac{d}{t}\right)^{0.06}\sigma^{-0.845}\left[\sigma\left(\sqrt{0.25 + \frac{2p_i\sqrt{2}}{\rho_0 c_0^2 \sigma^2}} - 0.5\right) - 0.5\right]. \tag{11}$$

where p_i is incident pressure (see also equations (11) – (12) in [36]). The normalised specific acoustic impedance Z_{nl} is obtained using expressions from both the acoustic reactance and normalised resistance. Here it is re-introduced from Chapter 3.2 equation (22),

$$Z_{nl} = r_{nl} + jx_{nl}. \tag{12}$$

Geometrical parameters used in the model [36] are presented in Table 7.3 showing perforation ratio percentage for three different samples. All samples are backed by a cavity directly after the MPPA which contain several pores. The pore radius $r_0 = 0.5$ mm and $r_0 = 0.1$ mm.

Sample MPPA	Perforation ratio %	Pore radius $(\mathbf{mm})$	Plate thickness $(\mathbf{mm})$	Cavity depth $(\mathbf{mm})$
s1	4.0	0.5	1.0	100.0
s2	2.0	0.5	1.0	100.0
s3	4.0	0.1	1.0	100.0

Table 7.3. Geometrical parameters used in the prediction of MPPA sample performances.

Absorption coefficient is computed using equations (10)-(12) and plotted as a function of frequency for MPPA s1 shown by Figure 7.9. Perforation ratio $\sigma = 4.0$ %, $r_0 = 0.5$ mm, cavity depth $D = 100$ mm and plate thickness $t = 1$ mm. The corresponding sample s1 values of absorption coefficient are given in Table 7.4 for various pressure levels dB. The frequency spectrum ranged $f = 1\,\text{Hz} - 1000\,\text{Hz}$ with increments of $f = 200$ Hz are presented in Table 7.4 along with the associated absorption coefficient values. The data shown by Figure 7.9 and Table 7.4 indicate that maximum absorption coefficient obtained by MPPA s1 ($\alpha = 0.98$ and $\alpha = 1.0$) is when amplitude is around 115 dB – 121 dB. This is seen to be the case at the middle frequency range between $f = 600$ Hz and $f = 800$ Hz. MPPA s1 is predicted least effective when sound pressure level is deemed to be in linear regime below 100 dB. Maximum value of absorption coefficient is only $\alpha = 0.23$ which is found to be at $f = 600$ Hz (for linear regime). However, this is seen to be the contrary for the value of α at the same frequency, at higher sound pressure levels. For instance, value of α is significantly larger for when sound pressure level is much greater (143 dB) where $\alpha = 0.96$. Performance of MPPA s1 shows to be progressive for its absorptive qualities up towards a frequency limit around $f = 700$ Hz. After this frequency, the value of α begin to reduce.

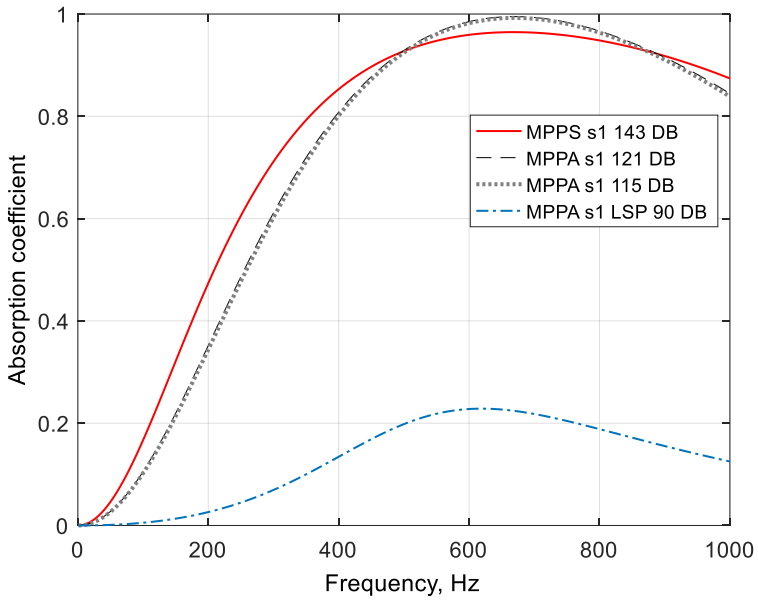

Figure 7.9. Absorption coefficient as a function of frequency for MPPA s1 for pressures ranging 90 dB – 143 dB SPL.

f (Hz)	90 dB	115 dB	121 dB	143 dB
200	0.02	0.34	0.35	0.47
400	0.13	0.80	0.81	0.85
600	0.23	0.98	0.98	0.96
800	0.19	0.96	0.97	0.95
1000	0.12	0.84	0.84	0.87

Table 7.4. MPPA – s1 absorption coefficient values predicted for several SPL.

Figure 7.10 shows absorption coefficient plotted as a function of frequency for MPPA s2. Perforation ratio is 2.0, $r_0 = 0.5$ mm, cavity $d_c = 100$ mm, and $d_p = 1$ mm. Material parameters are similar to MPPA s1 which differ only by the perforation ratio (which is half for MPPA s2 compared to MPPA s1). Values of absorption coefficient for sample s2 are given in Table 7.5 for various sound pressure levels dB. Frequency spectrum is $f = 1$ Hz $- 1000$ Hz and again increments of $f = 200$ Hz are presented, see Table 7.5. Absorption coefficient data given by Figure 7.10 and Table 7.5 indicate that maximum values α obtained by MPPA s2 is between $f = 500$ Hz for low SPL and around $f = 600$ Hz Hz for HSPL. When pressure is 115 dB – 121 dB then α is identical throughout the frequency spectrum, which is given by the data shown in Figure 7.10 and by Table 7.5. At low to middle frequencies ($f = 200$ Hz $- 600$ Hz) the absorption coefficient values for MPPA s2 are higher than values α for MPPA s1 when sound pressure level is 90 dB. And at $f = 600$ Hz value $\alpha = 0.32$ for low amplitude 90 dB and increases significantly when amplitude is considered 25 dB higher (where $\alpha = 0.98$ at $f = 600$ Hz at 115 dB). At a further increase of 6 dB (so now sound pressure level becomes 121 dB) α is seen to only reduce by 0.1. Performance of MPPA s2 is therefore determined most efficient for amplitudes in the region 115 dB – 121 dB. Absorption coefficient predicted by MPPA s2 for low sound pressure levels shows improved predicted values of α compared to MPPA s1, see Figure 7.9 and Figure 7.10. However, this is seen to be the contrary for high sound pressure levels in the frequency region $f = 400$ Hz $- 1000$ Hz where MPPA s1 is seen more desirable than MPPA s2 due to greater values obtained for α. Similarly, to MPPA

s1, value α of MPPA s2 appear to reduce after $f = 600\ \mathrm{Hz}$. This is most apparent for low pressure amplitude when SPL is around 90 dB compared to when SPL is in the region 115 dB – 143 dB.

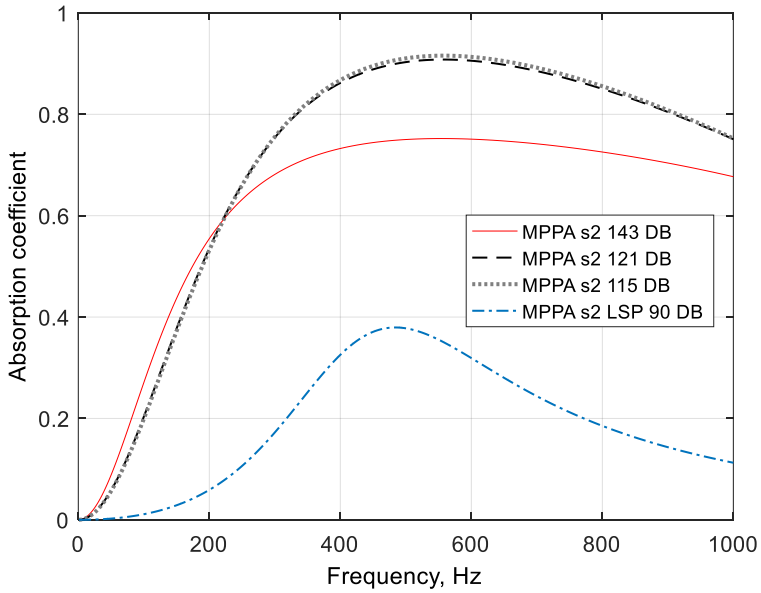

Figure 7.10. Absorption coefficient as a function of frequency for MPPA s2 for sound pressures ranging 90 dB – 143 dB SPL.

f (Hz)	90 dB	115 dB	121 dB	143 dB
200	0.06	0.53	0.54	0.55
400	0.32	0.87	0.87	0.73
600	0.32	0.91	0.90	0.75
800	0.18	0.86	0.85	0.72
1000	0.11	0.75	0.75	0.68

Table 7.5. MPPA – s2 absorption coefficient values predicted for several SPL.

Sample with lowest value of r_0 is MPPA s3 which has material dimensions $r_0 = 0.1\ \mathrm{mm}$, cavity depth $d_c = 100\ \mathrm{mm}$, and $d_p = 1\ \mathrm{mm}$. Perforation ratio is 4.0 which is the same as MPPA s1. Figure 7.11 shows absorption coefficient plotted as a function of frequency for MPPA s3. The corresponding sample s3 values of α for several SPL are given in Table 7.6 similarly as MPPA samples s1 and s2, with increments $f = 200\ \mathrm{Hz}$ ranging to $f = 1000\ \mathrm{Hz}$. Absorption coefficient is shown most effective when SPL is 90 dB for MPPA s3 given by Figure 7.11 in linear regime and SPL deemed low, below 100 dB. Absorption coefficient at $f = 200\ \mathrm{Hz}$ is $\alpha = 0.33$ and increases significantly at $f = 400\ \mathrm{Hz}$ where $\alpha = 0.80$. Maximum value of α is reached at middle frequencies around $f = 600\ \mathrm{Hz} - 800\ \mathrm{Hz}$ where $\alpha = 0.98$ and 0.93.

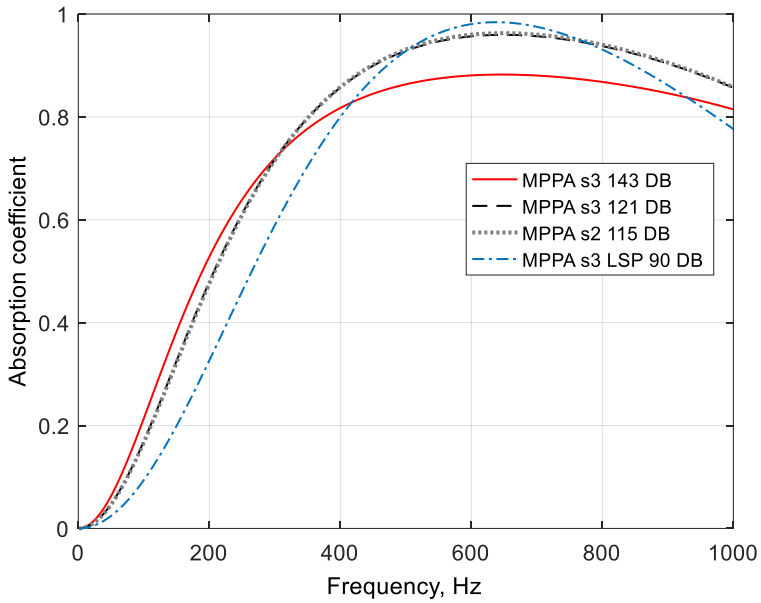

Figure 7.11. Absorption coefficient as a function of frequency for MPPA s3 for pressures ranging 90 dB – 143 dB SPL.

f (Hz)	90 dB	115 dB	121 dB	143 dB
200	0.33	0.48	0.48	0.53
400	0.80	0.86	0.82	0.80
600	0.98	0.96	0.96	0.88
800	0.93	0.94	0.94	0.87
1000	0.78	0.86	0.86	0.81

Table 7.6. MPPA – s3 absorption coefficient values predicted for several SPL.

MPPA s3 is predicted least effective at low frequencies, shown by Table 7.6 with lowest values of absorption coefficient at $f = 200$ Hz. When SPL is lowest so is the value of α (where for 90 dB value for $\alpha = 0.33$) and at greatest SPL (143 dB) $\alpha = 0.53$. The absorption coefficient is shown to reduce irrespective of SPL after around $f = 700$ Hz, see Figure 7.11. Broadband absorption is slightly greater for when SPL is highest at 143 dB. Consequently, lowest values of the α across the frequency spectrum for MPPA s3 is also when SPL is 143 dB. Comparisons of samples MPPA s1, s2 and s3 are presented in Table 7.7 and Figures 7.12 – 7.13 for the various sound pressure levels.

f (Hz)	90 dB	115 dB	121 dB	143 dB
200	s3, s2, s1	s2, s3, s1	s2, s3, s1	s2, s3, s1
400	s3, s2, s1	s2, s3, s1	s2, s3, s1	s1, s3, s2
600	s3, s2, s1	s1, s3, s2	s1, s3, s2	s1, s3, s2
800	s3, s1, s2	s1, s3, s2	s1, s3, s2	s1, s3, s2
1000	s3, s1, s2	s3, s1, s2	s3, s1, s2	s1, s3, s2

Table 7.7. Absorption coefficient comparisons for MPPA samples s1, s2, and s3 at different SPL.

In Table 7.7 the predicted absorption coefficient values are given for various sound pressure levels at frequency intervals of $f = 200$ Hz ranging from $f = 200$ Hz $- 1000$ Hz for MPPA samples s1, s2, and s3. The predictions for different SPL are computed accounting for nonlinear resistivity of the MPPA samples comprised with a rigid termination located 100 mm after the front plate. All samples s1, s2, and s3 are given in the columns, presented by Table 7.7. Each sample number corresponds to the material geometrical parameters from values given in Table 7.3. The order of the sample numbers (shown in Table 7.7) represents the best to least performance of the MPPA sample at each frequency of interest

(from left to right) shown by Table 7.7. This can also be observed by the data presented in Tables 7.4 – 7.6. At low sound pressure level 90 dB and at $f = 200\ \mathrm{Hz} - 600\ \mathrm{Hz}$ sample s3 is predicted being most effective for values of α in linear regime. MPPA s3 is effective also at middle frequencies around $f = 800\ \mathrm{Hz}$, and higher frequencies $f = 1000\ \mathrm{Hz}$. MPPA s1 is seen to be slightly more effective than MPPA s2 at higher frequencies around $f = 1000\ \mathrm{Hz}$. When sound pressure level is regarded to be 25 dB higher (SPL now becomes 115 dB) the best performing MPPA sample at low frequencies $f = 200\ \mathrm{Hz} - 400\ \mathrm{Hz}$ is sample s2 followed by s3, with least effective being s1. MPPA sample s1 is effective at middle frequencies, $f = 600\ \mathrm{Hz} - 800\ \mathrm{Hz}$ with largest value of α and sample s2 being the least effective. Sound pressure level is computed being increased a further 6 dB (SPL now being 121 dB) in which all MPPA samples (s1, s2, and s3) are seen to be identical to the MPPA sample performance for those given at 115 dB. For sound pressure level at 143 dB the sample with the largest value of absorption coefficient at low frequency is MPPA s2, with sample s1 being the least effective. However, this is seen to the contrary for remainder of frequencies investigated ($f = 200\ \mathrm{Hz} - 1000\ \mathrm{Hz}$) at 143 dB. MPPA s1 becomes most effective and sample s2 becomes least effective in terms of values predicted for α. Figures 7.12 – 7.13 shows absorption coefficient for comparisons between MPPA samples s1, s2, and s3 for both the lowest and highest sound pressure levels considered. Figure 7.12 shows the MPPA samples s1, s2, and s3 at sound pressure level 90 dB (linear regime) and clearly presents the greater performance by s3 compared to s1 and s2 (for the entire frequency range $f = 1\ \mathrm{Hz} - 1000\ \mathrm{Hz}$). MPPA s1 overall is least effective from the MPPA plates investigated comprised with cavity depth $d_c = 100\ \mathrm{mm}$. It is therefore determined from data given by Table 7.7 and Figure 7.12 that absorption coefficient is dependent on pore radius of MPPA's, irrespective of the surface open area percentage. Geometrical parameters used in the prediction of the MPPA performances are presented in Table 7.3. Perforation ratio, plate thickness, and cavity depth remain same value for both samples s1 and s3, with only pore radius differing for the MPPA design (where MPPA s3 pore radii is 1/5 to that of MPPA s1).

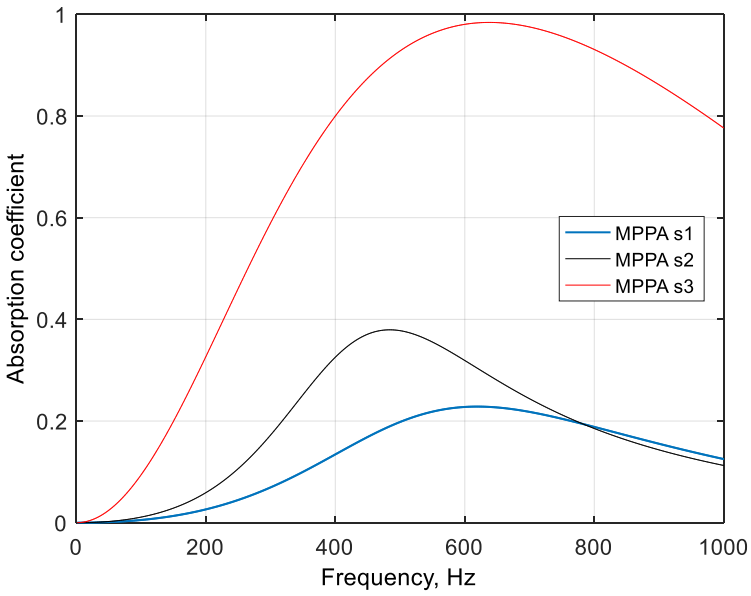

Figure 7.12. Absorption coefficient as a function of frequency for MPPA samples s1, s2 and s3 at LSPL 90 dB.

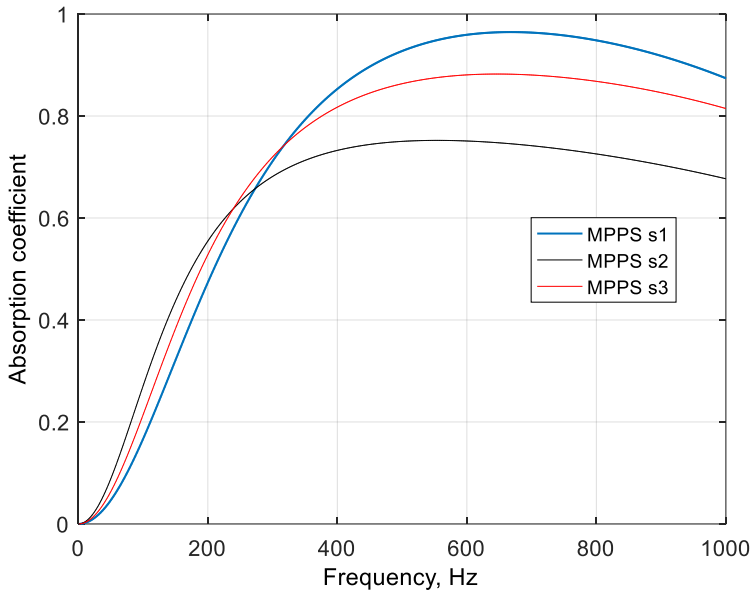

Figure 7.13. Absorption coefficient as a function of frequency for MPPA samples s1, s2 and s3 at HSPL 143 dB.

A comparison is shown in Figure 7.13 for MPPA samples s1, s2, and s3 for case of high sound pressure levels, 143 dB. The best performance is attributed to MPPA s1 for frequencies $f = 300\ \mathrm{Hz} - 1000\ \mathrm{Hz}$ when compared to samples s2 and s3. Pore radii is larger for MPPA s1 and s2 than it is for MPPA s3. Thus, nonlinear phenomena occurs in the form of jet formation exiting the perforations and consequently, results in acoustic dissipation, reported also in works by [21-22] and [36-38]. MPPA samples s1 and s2 are found to be more effective than MPPA s3 when HSPL is considered. Perforated plates with larger values of r_0 and larger open surface area ratios outperform the plates with both small values of r_0 and perforation ratios when sound pressure levels are above 115 dB. However, at LSPL, perforated plates with large values of r_0 are shown to not be as effective for sound absorption. This suggests that structures with larger pore radii are very well suited for high amplitudes and results in a greater performance for the absorbers, as opposed to perforated plates with low values of r_0. The model described above (see also Chapter 3.2 Literature review) has its limitations when sound amplitude is much greater than 143 dB. In a shock tube, pulses with amplitudes around 195+ dB are obtainable. So, the validity of the model described above, looks questionable. A plate containing several perforations is measured for a range of different amplitudes (minimum amplitude that was measured in the shock tube is approximately 175 dB). Material parameters are similar dimensions used as sample 1A in Tayong et al [38] who investigated the interaction effect of pore radii and their separation distance on sound absorption coefficient for micro-perforated panels under medium and high sound levels. A perforated plate was developed and tested in the shock tube. Dimensions was $r_0 = 0.8\ \mathrm{mm}$, cavity depth $d_c = 100\ \mathrm{mm}$ and plate thickness $t = 1.5\ \mathrm{mm}$, $\phi = 1.6\ \%$. A triangular lattice arrangement of the perforations was drilled into a solid plate. The plate surface was filed to ensure no roughness of the front and exit pores. For a triangular lattice, the open area ratio is,

$$\phi = 0.906\ \frac{d^2}{b^2} \tag{13}$$

where d is hole perforation diameter, and b is the pitch (centre-centre hole distance). A schematic of the perforated plate is shown in Figure 7.15. Amplitudes created are much larger than what was used in

[38]. Also tube radius of an impedance tube used by [38] was $r_0 = 50$ mm whereas tube radius of the shock tube has $r_0 = 25$ mm. Furthermore, pulsed signals are created in the shock tube, as opposed to weakly nonlinear wave excitation used by [38]. Experimental method for performing measurements containing the perforated plate is when the shock tube is configured with rigid backing set up (see Figures 7.2 and 7.14).

Figure 7.14. Perforated plate tested using the shock tube. The plate had eight pores and tested in rigid backing set up. A cavity depth 100 mm extends the plate followed by a solid end-plate termination.

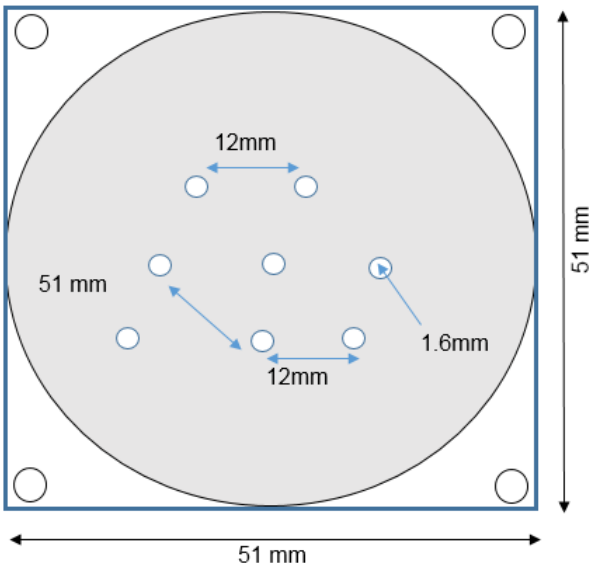

Figure 7.15. Perforated plate with dimensions $d_c = 100$ mm, $r_0 = 0.8$ mm, $t = 1.5$ mm. $\emptyset = 1.6$ %.

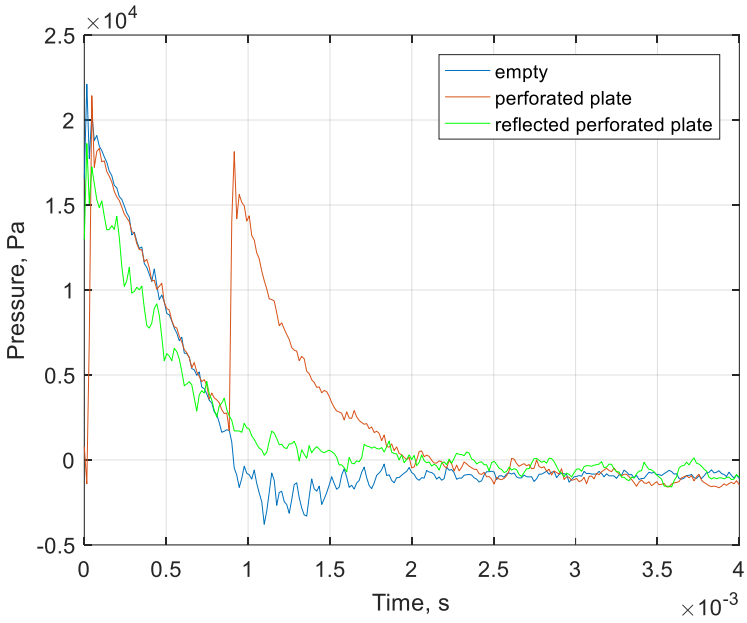

Figure 7.16. Pressure as a function of time for membrane tin foil. First pulse at signal 2, rigid backing. Dimensions are $d_c = 100$ mm, $r_0 = 0.8$ mm, $t = 1.5$ mm, $\emptyset = 1.6$ %.

Three membranes with different tensile strengths are ruptured in the shock tube and the corresponding signals measured in the presence of the plate is shown by Figures 7.16 – 7.18. Data is given for explosions of membranes tin foil, baking paper and Mylar 23 μm, all which include empty tube measurement (this always refers to a rupture of the membrane absent any sample for all descriptions of empty tube measurements). A measurement is included also for the perforated plate alone. A reflected pulse obtained following pulse analysis complements the two measurements for an empty tube and perforated plate measurement. The reflected pulse is obtained by subtracting the empty tube pulse from that of the pulse measured in the presence of the perforated plate. This is necessary since the measurement of the pulse obtained by the perforated plate is the combination of pressures (from superposition of the incident and reflected pulses). Figure 7.16 shows pressure as a function of time for tin foil membrane. Pulses shown represent first pulse at signal 2 with rigid backing and a cavity $d_c = 100$ mm. In the absence of the sample the peak pressure is measured 22100 Pa which corresponds to a sound pressure level of 181 dB. The reflected peak for the perforated plate is measured 18620 Pa where sound pressure level corresponds to 179 dB.

Figure 7.17 shows pressure as a function of time for membrane consisting of baking paper. The measurement shows the first pulse recorded at signal 2 with rigid backing for both empty tube and the perforated plate with $d_c = 100$ mm. Empty tube measurement absent the sample is measured where the pulse had a peak pressure 23870 Pa and SPL being nearly 182 dB. Reflected pulse of the perforated plate is 20930 Pa and sound pressure level is 180 dB. Peak pressure of the superimposed pulse from the perforated plate measured at signal 2 was 23230 Pa and corresponds to a sound pressure level 181 dB. Figure 7.18 shows pressure as a function of time for Mylar 23 μm. The measurement shows the first pulse recorded by signal 2 with rigid backing for both the empty and perforated plate with $d_c = 100$ mm. Empty tube measurement had a sound pressure level 187 dB, and the measured peak pressure was 47200 Pa. Reflected pulse for the perforated plate is 40000 Pa and sound pressure level was 186 dB. Pressure of the reflected pulse before subtraction of the empty pulse absent the perforated plate was

55280 Pa (with sound pressure level 189 dB). Incident and reflected pressures for the Mylar 23 μm explosions have very similar amplitudes and equal durations of 1.6 milliseconds for rigid backing set-up. This is also the case when measurements have been performed in transmission set-up hence, little transmission and attenuation was observed for the rigid backing or transmission set-ups. However, signal 2 measured a lower amplitude (peak pressure of the pulses around 18000 – 20000 Pa), some energy loss is observed resulting in difference in the peak amplitudes between incident and reflected pulses, see Figure 7.18 for rigid backing set-up. Figure 7.19 shows data obtained by a tin foil explosion for a single measurement and plate for the shock tube with transmission set up, see Figure 7.2. Peak pressure of the incident pulse is 24000 Pa (pressure recorded by piezoelectric transducer 1 which is located immediately after the rupture chamber where each membrane explosion occurs). At signal 2 the peak pressure of the pulse was 19960 Pa for the first peak (incident) and 17350 Pa for the second peak (reflected pulse from plate boundary). Any transmitted energy from the incident pulse passing through the perforated plate is measured by the transducer at signal 3. The transmitted pulse was measured 4836 Pa which is the peak pressure of the first pulse from signal 3 data.

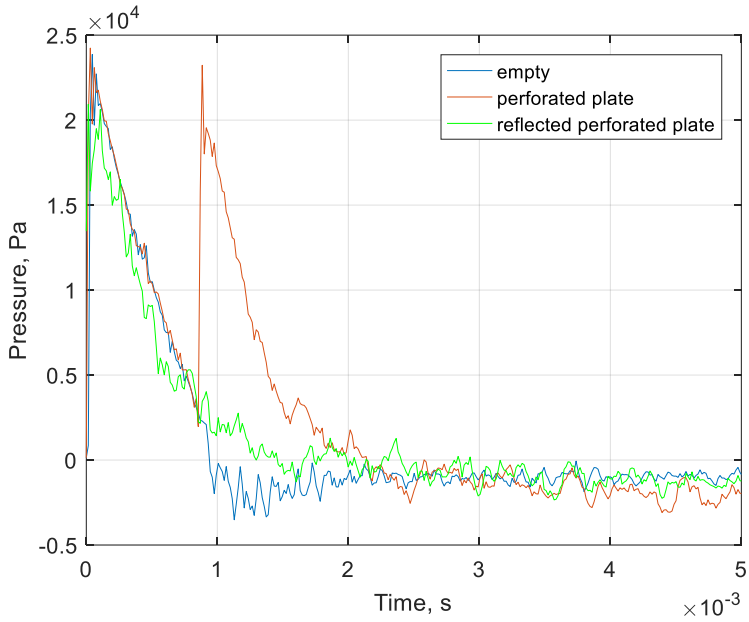

Figure 7.17. Pressure as a function of time for membrane baking paper. Measurement is first pulse at signal 2 with rigid backing. Dimensions are $d_c = 100$ mm, $r_0 = 0.8$ mm, $t = 1.5$ mm, $\emptyset = 1.6$ %.

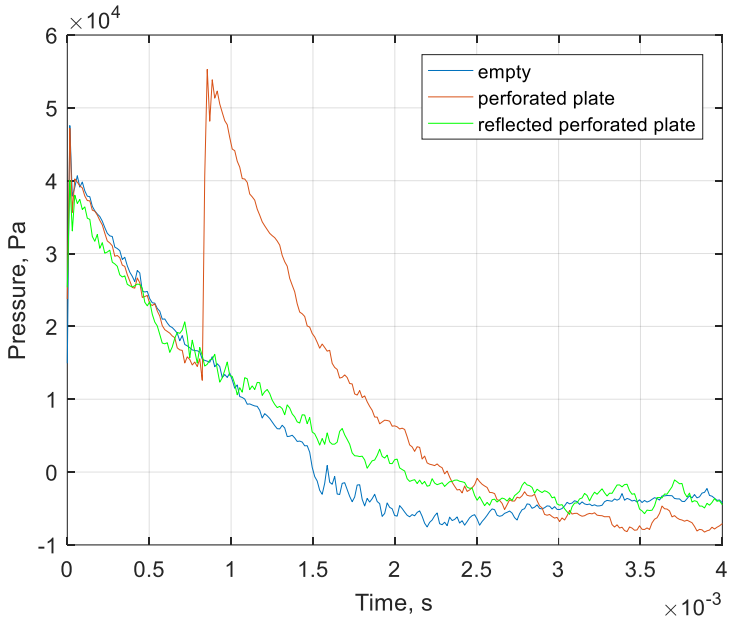

Figure 7.18. Pressure as a function of time for membrane Mylar 23 μm. Measurement is first pulse at signal 2 with rigid backing. Dimensions are $d_c = 100$ mm, $r_0 = 0.8$ mm, $t = 1.5$ mm, $\emptyset = 1.6$ %.

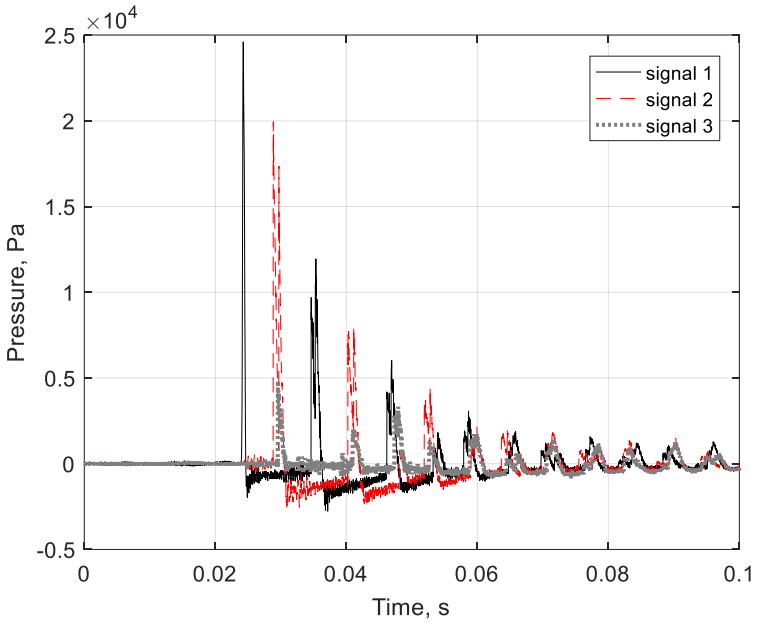

Figure 7.19. Pressure as a function of time for membrane tin foil. The measured pressures are those recorded at signals 1, 2 and 3 when the shock tube is in transmission set-up. Dimensions are $d_c = 100$ mm, $r_0 = 0.8$ mm, $t = 1.5$ mm, $\emptyset = 1.6$ %.

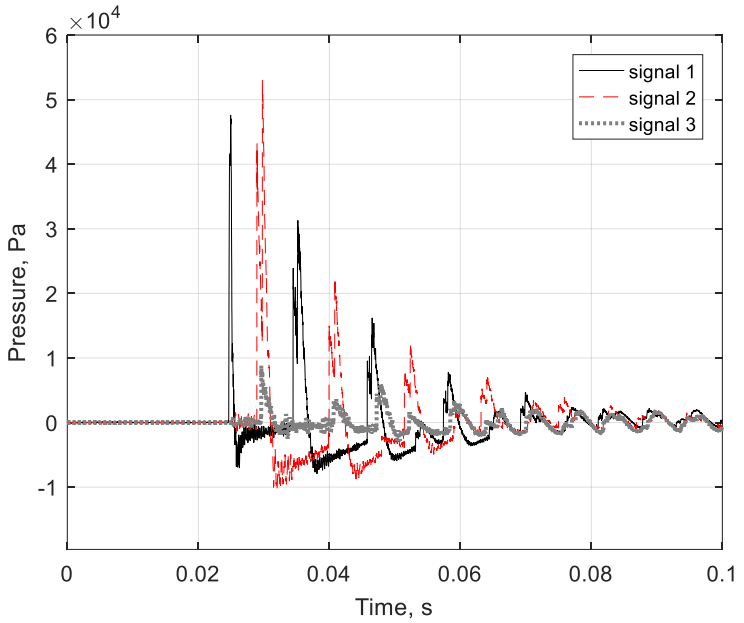

Figure 7.20. Pressure as a function of time for membrane Mylar 23 μm. The measured pressures are those recorded at signals 1, 2 and 3 when the shock tube is in transmission set-up. Dimensions are $d_c = 100$ mm, $r_0 = 0.8$ mm, $t = 1.5$ mm, $\emptyset = 1.6$ %.

Figure 7.20 shows pressure as a function of time for membrane Mylar 23 μm explosion and perforated plate. A single measurement shows the time domain data measured in transmission set-up at signal 1 position (immediately after explosion), signal 2 (prior to sample housing or surface) and signal 3 (shortly after sample housing position). Data shown by Figure 7.20 (for measured pressures at signal 1 and signal 2) is similar to that shown in Figure 7.18, as aforementioned, which consists of a large, reflected shock. Peak pressures are measured 46000 Pa and 42000 Pa, signals 1 and 2, respectively. Figure 7.20 shows additional piezoelectric transducer 3 data from the transmitted energy. Note, transmitted sound measured at signal 3 is much lower than those of incident and reflected pulses and measured 9000 Pa. Micro perforated plates have also been tested in the shock tube increasing the open surface area ratio and installing an additional plate containing a cross geometry. The cross formations which comprise a number of four segments each had length $L = 9$ mm. An illustration of the plate with the cross geometry is shown by Figure 7.21 a. Total number of the cross-formations was equal to nine and the perforation area ratio was close to 15 % (when combined over the surface area for the shock tube). The plate with cross perforated geometry was positioned at a distance $d = 10$ mm after the perforated plate containing cylindrical-perforations.

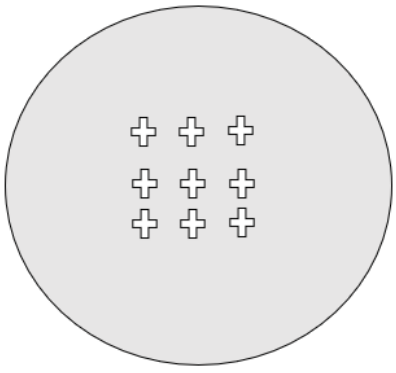

(a)

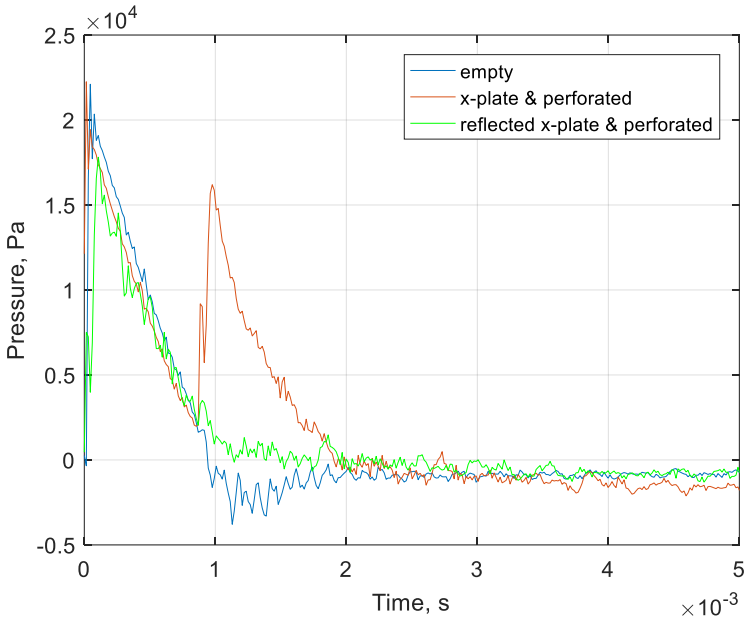

(b)

Figure 7.21. (a) Perforated plate tested in the shock tube which consisted of cross geometrical perforations. Pressure as a function of time for membrane tin foil with plate comprised with cross geometry (b). Measurement is first pulse at signal 2 with rigid backing and cavity with $d_c = 100\ \mathrm{mm}$.

Pressure as a function of time is shown by Figure 7.21 b for a tin foil explosion and aluminum plate with thickness $t = 1.5\ \mathrm{mm}$, including the cross-geometry perforations. Pulses shown represent first pulse at signal 2 with rigid backing including a cavity $d_c = 100\ \mathrm{mm}$. In the absence of the sample the peak pressure of the pulse measured 22100 Pa corresponding to a sound pressure level 181 dB. Reflected pulse for the perforated plate was 16190 Pa with sound pressure level equating to 179 dB. Pressure of the reflected pulse before subtraction of the empty pulse absent the plate was 16960 Pa and SPL being 179 dB. It was determined that the cross-geometrical plate did not provide significant attenuation of the reflected pulse. Figure 7.22 shows pressure as a function of time for Mylar 23 $\mu\mathrm{m}$ including first pulse analysis for the first pulse recorded at signal 2 and rigid backing, for both the empty and perforated plates containing $d_c = 100\ \mathrm{mm}$. Empty tube measurement had a sound pressure level of nearly 188 dB from the measured pulse, for peak pressure 48810 Pa. Reflected pulse of the perforated plate was 37130 Pa and sound pressure level being 185 dB. Pressure of the reflected pulse before subtraction of the empty pulse absent the perforated plate is recorded at signal 2 as 50100 Pa SPL approximately 188 dB. This demonstrates that the arrangement under study is only marginally more effective than the case for the circular perforated plate only, for attenuation of the reflected pulse.

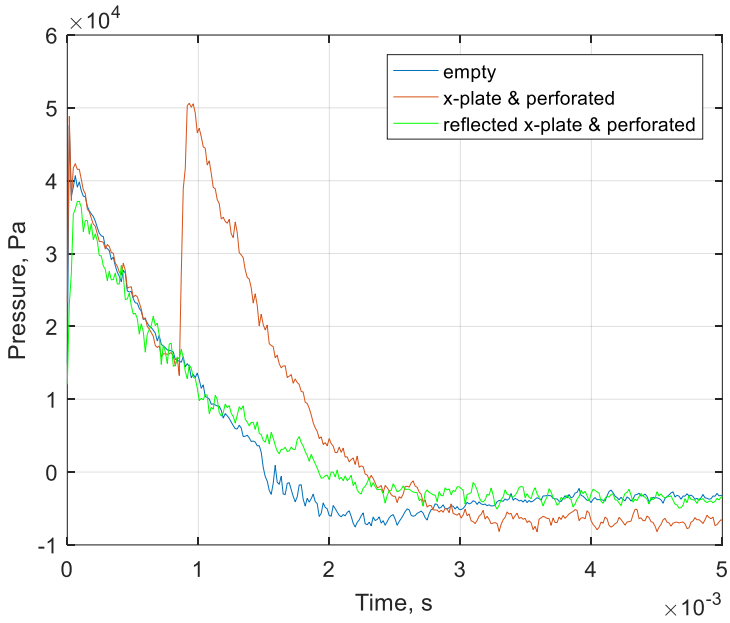

Figure 7.22. Pressure as a function of time for Mylar 23 μm with plate comprising a cross geometry. Measurement is first pulse at signal 2 with rigid backing and cavity with $d_c = 100$ mm.

7.4. Pancake Absorber – 3D Printed

First design for the metamaterial pancake absorber is developed by 3D technology and tested in the shock tube. Amplitudes generated are much larger than those given by Chapter 4, from continuous sound performed in the HSPL impedance tube. Three membranes have been ruptured to test the 3D pancake absorber in the shock tube. Later, data analysis is performed. The experimental data including analysis is shown by Figures 7.23 – 7.24 illustrating the resultant absorber performance. Figures 7.23 – 7.24 show pressure as a function of time for the metamaterial pancake absorber with $d_c = 1$ mm, $d_p = 1$ mm, $L = 50$ mm, $r_0 = 2.5$ mm, and $R = 25$ mm. Pancake absorber dimensions was the smallest of all of the metamaterials tested. The following data representing pressure dependence in time domain for the structure shows it is least effective compared to other metamaterials tested for high amplitude signals. Figures 7.23 – 7.24 shows pancake absorber data from ruptured membranes tin foil and baking paper, respectively. Measurements were also performed for the Mylar membranes at much larger amplitude strengths. Due to the high sound levels reached in the shock tube, the absorber resulted in damage and experiments were stopped. The absorber face became severely indented and cracked when constrained with the larger pressures imposed by the Mylar membranes. The pancake sample was not effective even for the lowest amplitudes created in the shock tube, which is around 10 KPa, see Figure 7.23. Similarly, this was naturally the case for when amplitude were increased to around 25 KPa which is to be expected (since material parameters for the pancake absorber was small including the single perforation), see data given by Figure 7.24. An improved performance for other metamaterials investigated is shown within the remainder subsections (also tested in the shock tube and with large amplitudes, 10 KPa – 100 KPa.

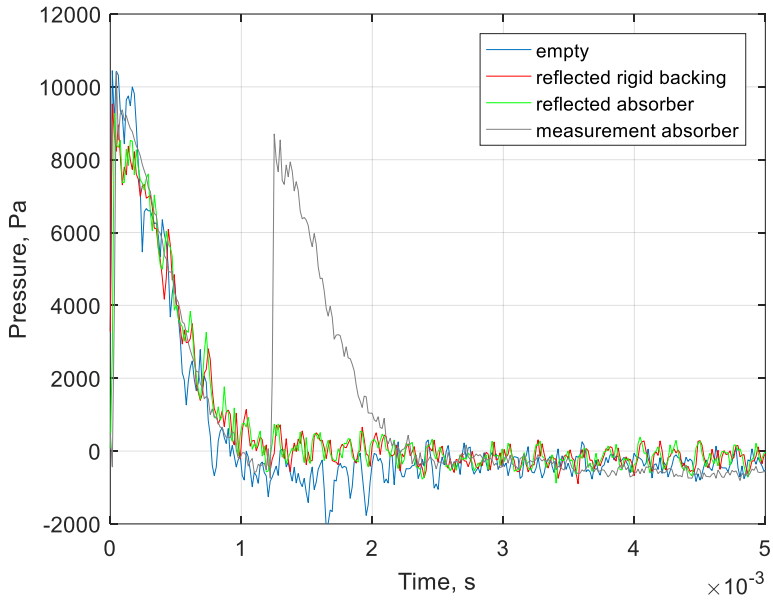

Figure 7.23. Pressure as a function of time for 3D printed metamaterial pancake absorber. Dimensions are $d_c = 1$ mm, $d_p = 1$ mm, $L = 50$ mm, $r_0 = 2.5$ mm, and $R = 25$ mm.

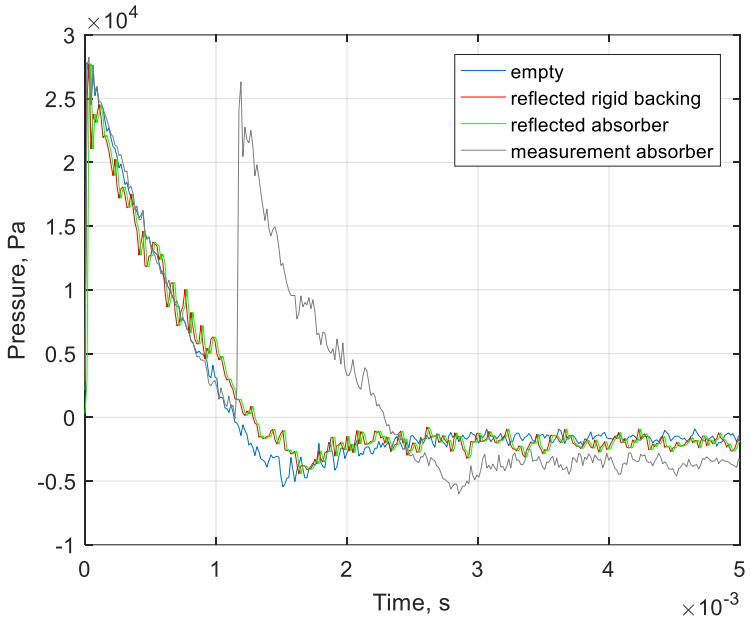

Figure 7.24. Pressure as a function of time for 3D printed metamaterial pancake absorber. Dimensions are $d_c = 1$ mm, $d_p = 1$ mm, $L = 50$ mm, $r_0 = 2.5$ mm, and $R = 25$ mm.

7.5. Cone Structure – Laboratory Built

A cone structure is built in the laboratory (Figure 7.25 showing the outer sample) and tested against five different membranes of various tensile strength. The membranes are ruptured in the shock tube and data analysis is later performed comparing against a linear profile absorber, built also in the laboratory at Salford. Figures 7.26 – 7.27 shows pressure as a function of time for different amplitude strengths (18 KPa – 70 KPa) from the ruptured membranes. A simple cone structure is built with its main opening pore radius $r_0 = 25$ mm. Since cavities are not present within the structure then $d_c = 0$, and plates are not considered so that $d_p = 0$.

Figure 7.25. Laboratory built cone structure tested in the shock tube.

Sample length was reasonably large compared to other samples tested thus far. This also applies throughout the corresponding shock tube measurements which are presented in the remaining subsections of Chapter 7 (excluding the largest of the profile samples tested). The cone structure had sample length L =110 mm. The cone was inserted inside the shock tube and built in the laboratory. Largest part of the cone had external radius $R = 26\,\mathrm{mm}$. The structure decreased linearly towards the termination point which is positioned at the rear of the sample. Walls of the structure are developed with hardened plastic and fixed rigid by inserting into the shock tube. It is then sealed with PTFE tape at the sample surface wall (around the largest point of the opening orifice).

Figures 7.26 – 7.27 shows data obtained by performing a typical measurement for different amplitudes created in the shock tube. Tin foil and baking paper is ruptured (18 KPa and 26 KPa) see Figure 7.26. At these lower generated amplitudes, the cone structure shows to reflect back the pressure of the incident pulse considerably which is clearly observed firstly in Figure 7.26. For instance, reflected pressures of the first pulse from membranes tin foil and baking paper are approximately 16000 Pa and 25000 Pa. This can also be observed by Figure 7.27 showing the measurements for the much larger amplitudes (from ruptured Mylar membranes where amplitudes are 45 KPa and range to 70 KPa). Reflected superimposed pulses are approximately 60000 Pa, 70000 Pa and 110000 Pa for membranes Mylar 23 $\mu\mathrm{m}$, Mylar 40 $\mu\mathrm{m}$, and Mylar 50 $\mu\mathrm{m}$ respectively. Note that each pulse is a time delay of the recorded pressure at signal 2 (fixed piezoelectric transducer located prior to the position of the sample holder which houses the structures). The first peak for the pulse is that given by the incident shock pulse. The second peak of the pulse (see Figures 7.26 – 7.27) represents the reflected part of the shock and in many cases superimposed with that of the incident pulse, especially for the largest amplitudes created in the shock tube. The cone structure causes the shock pulse to be almost completely reflected and furthermore, impedance matching of the acoustic pulse and material to be neglected. This is seen to be the contrary for the profiled absorbers. Influence of the cavities is shown to be effective and impact the performance for the retarding absorbers (compared to the cone structure which encompasses a similarly decreasing inner radius).

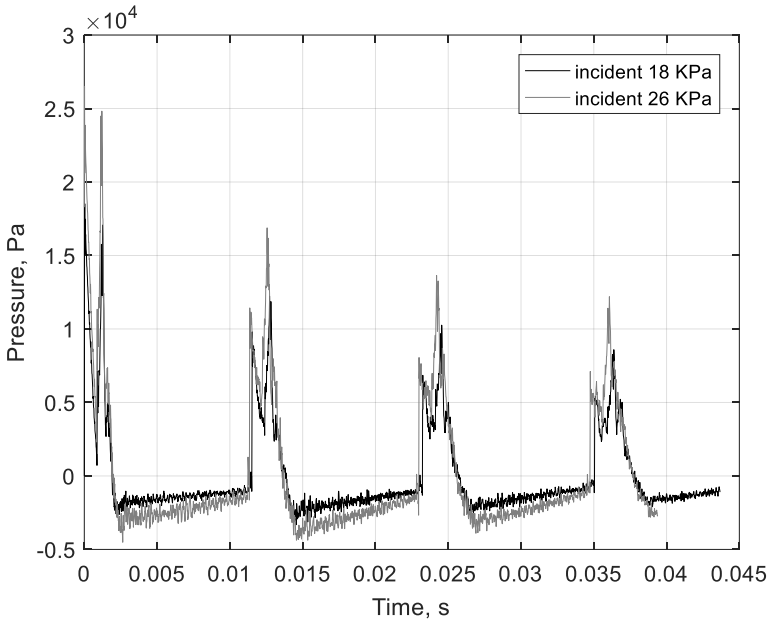

Figure 7.26. Pressure as a function of time for cone structure. Membranes ruptured are tin foil and baking paper. Dimensions are $r_0 = 25$ mm and L =110 mm.

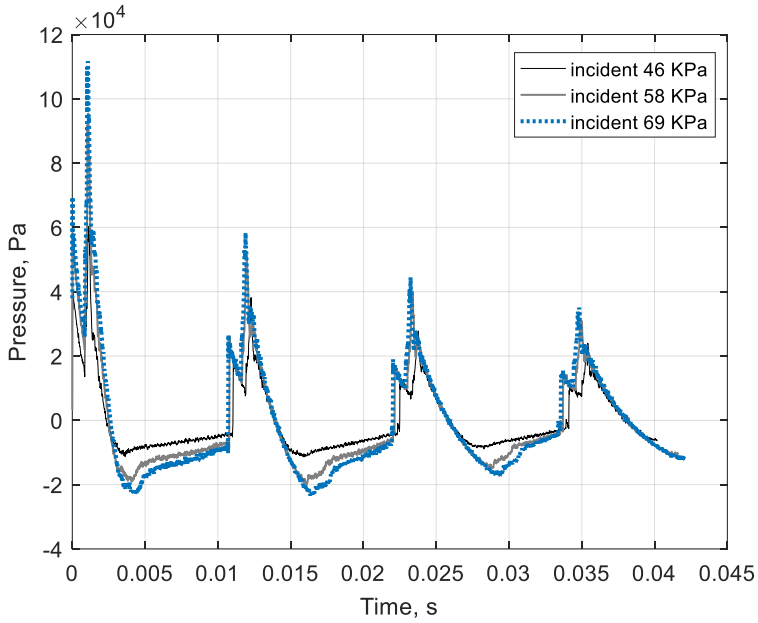

Figure 7.27. Pressure as a function of time for cone structure. Membranes ruptured are Mylar membranes (23 μm, 40 μm and 50 μm). Dimensions are $r_0 = 25$ mm and L =110 mm.

7.6. Profile Absorber – Laboratory Built

A profile structure containing cavities with thickness d_c is investigated in the shock tube against high amplitudes (where sound pressure level >> 150 dB) by performing measurements in time domain. First design of a profile absorber is developed to investigate the influence of dead-end pores. Sample configuration can be seen to be identical to that of work by Mironov [2], also complemented in later work [122], who introduces the concept of “acoustic black hole effect” (see also Chapter 3 – Literature review, section 3.4). The profile samples designed and tested throughout this thesis have dimensions much smaller to those considered by other works such as [2], [96], [98], [103], [122] who investigated acoustic

black hole effect (ABH) of retarding structures. The profile structure built in the laboratory at University of Salford is shown by Figure 7.28 housed in a sample holder for testing samples in the shock tube. Material used is rigid plastic containing plates and rings with radius $r = 25$ mm. The laboratory-built profile differs from the metallic profile structures (introduced later in section 7.9) by material used and its dimensions. The laboratory-built profile is tested in the shock tube using explosions from ruptured membranes tin foil, baking paper, Mylar 23 μm and Mylar 40 μm. Data analysis is performed on the pulses to obtain the reflected pulse from using each membrane explosion by each measurement performed in the empty shock tube. The data analysis is shown by Figures 7.29 – 7.31. Cavity depth was slightly inconsistent for the plastic laboratory profile sample. Cavity thickness for the dead-ends within the structure measured $d_c = 2.5$ mm and $d_c = 3$ mm, and plate thickness was constant at $d_p = 2$ mm. Inconsistency of d_c was due to the accuracy of cutting the rings and fixing of the structure. The desired ring thickness was to be made as minimum possible in order to develop a relatively small structure. However, cutting of the rings and thickness of plates had its limitations due to the material used and building procedure of the sample. Dimensions for the laboratory-built profiled absorber is given by Table 7.3. Absorber dead-ends with cavities d_c are built with approximately with $d_c = 3$ mm for plates with pore radius $r_0 = 23.5$ mm → 18.5 mm and $d_c = 2.5$ mm when plates with central pore radius was $r_0 = 17.5$ mm → 0.5 mm, including termination plate.

Figure 7.29 shows data from first pulse analysis for the linear profiled absorber built in the laboratory. The explosion is from the tin foil membrane. Peak pressure of the incident pulse for the empty tube data was measured 14080 Pa and sound pressure level close to 177 dB. The peak pressure obtained from the measurement with the profile absorber was 11100 Pa and sound pressure level equated to nearly 175 dB. Reflected pulse recorded by a piezoelectric transducer located close to the sample surface measured the peak pressure being 5521 Pa (corresponding to sound pressure level 169 dB). The reflected peak pressure yields a value 7134 Pa and sound pressure level equating to 171 dB (after subtraction of the empty tube pulse following first pulse analysis with addition of the absorber measurement). Figure 7.30 shows the measured data for when pressure is increased further than that of the ruptured tin foil membrane. Baking paper is burst resulting in the formation of a shock pulse. Incident peak pressure for the empty tube measured 23870 Pa for the first pulse at signal 2 (where signal 2 is referred to position 1 given by Figure 7.2). The profile had a peak pressure 25420 Pa when measured at signal 2 before interaction with the absorber. Sound pressure level after interaction with the profile was 179 dB which was obtained from the reflected peak data at signal 2 being 17100 Pa (see superimposed pulse from the absorber measurement, Figure 7.30). After first pulse analysis, reflected pulse is measured 14530 Pa and sound pressure level equates to 177 dB. This results in a reduction of 5 dB of the SPL by the measurement for the linear profile structure for high amplitude pulses.

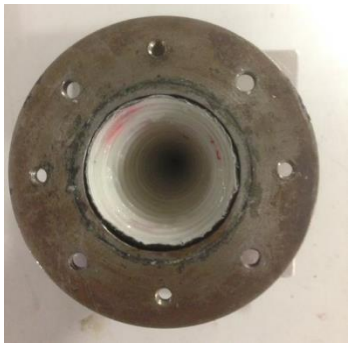

Figure 7.28. Linear profiled structure inserted into the sample holder used for shock tube testing.

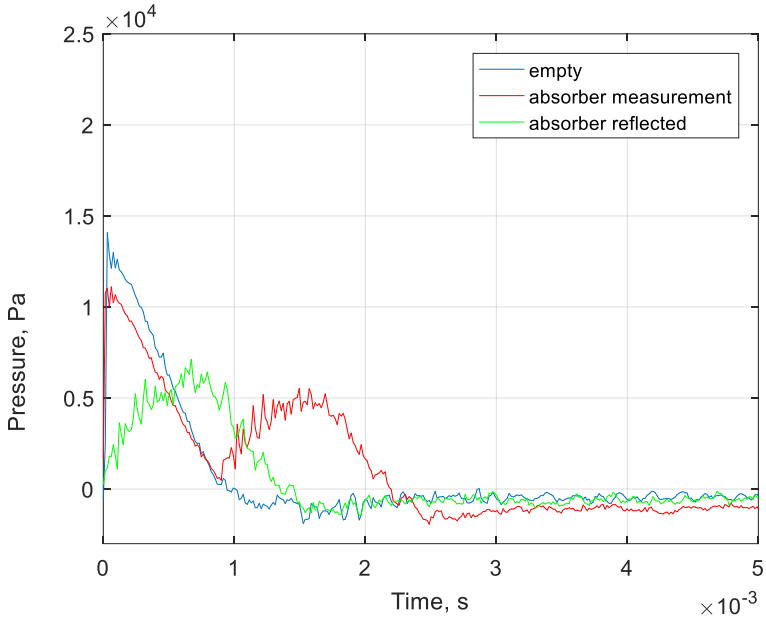

Figure 7.29. Pressure as a function of time for laboratory profile. First pulse analysis and rigid backing. Dimensions are d_c = 3 mm and d_c = 2.5 mm, d_p = 2 mm, L = 100 mm, with $R = 25$ mm.

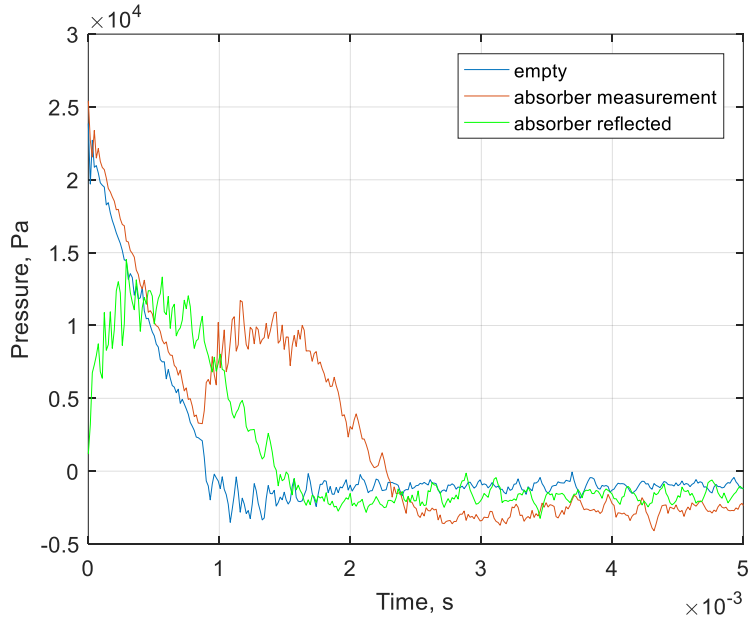

Figure 7.30. Pressure as a function of time for laboratory profile. First pulse analysis and rigid backing. Dimensions are d_c = 3 mm and d_c = 2.5 mm, d_p = 2 mm, L = 100 mm, with $R = 25$ mm.

The profile absorber is shown to be effective for some of the largest amplitudes created in the shock tube. Figure 7.31 a shows pressure as a function of time for ruptured membrane Mylar 40 μm. Peak pressure of the incident shock pulse for an empty tube measurement is 62160 Pa and sound pressure level was 190 dB. The shock pulse from the profile absorber measurement had a peak pressure 60820 Pa and SPL 189.6 dB. Reflected pulse for the profile absorber recorded by piezoelectric transducer signal 2 was measured 61480 Pa. The reflected peak pressure for the profile was 50490 Pa which was obtained after subtraction of the empty pulse following first pulse analysis. Sound pressure levels for the reflected pulses at signal 2 prior to first pulse analysis, and after first pulse analysis was around 189 dB and 188 dB, respectively. Total reduction of SPL is around 2 dB for when amplitude of the incident pulse is over 60000 Pa. Pressure values given are those of shock pulses calculated at signal 2 only and not the pressures of the incident pulses created at the formation of the shock. Pressure values and sound speeds of the shock pulses created at the time each membrane is ruptured (measured at signal 1) is given by Table 7.2. Location of the rupture chamber can be seen in Figure 7.2.

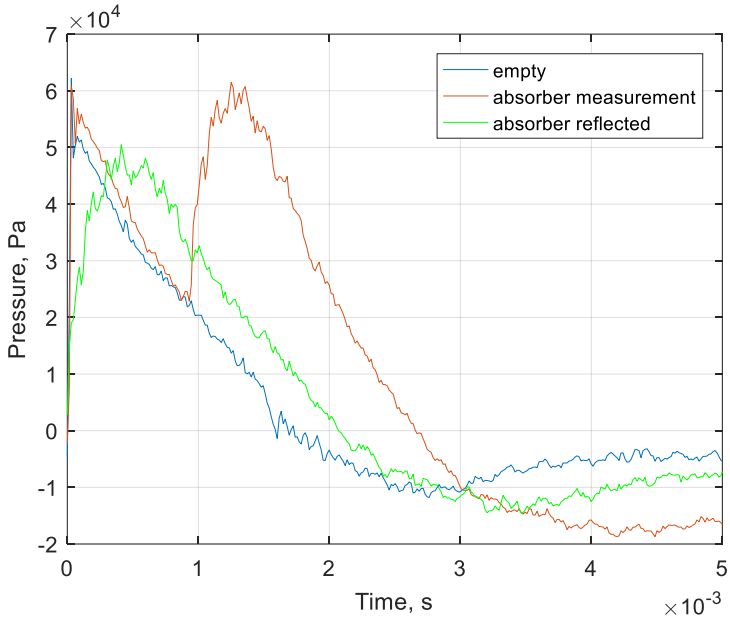

(a)

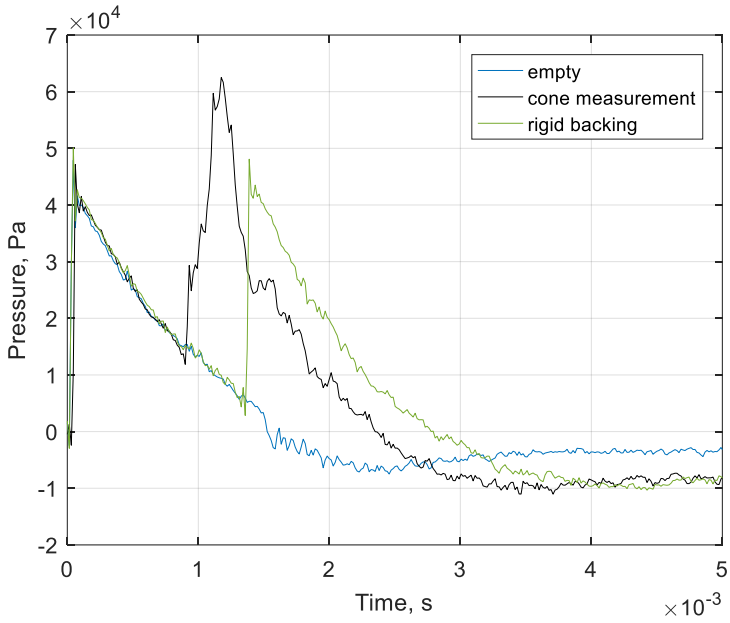

(b)

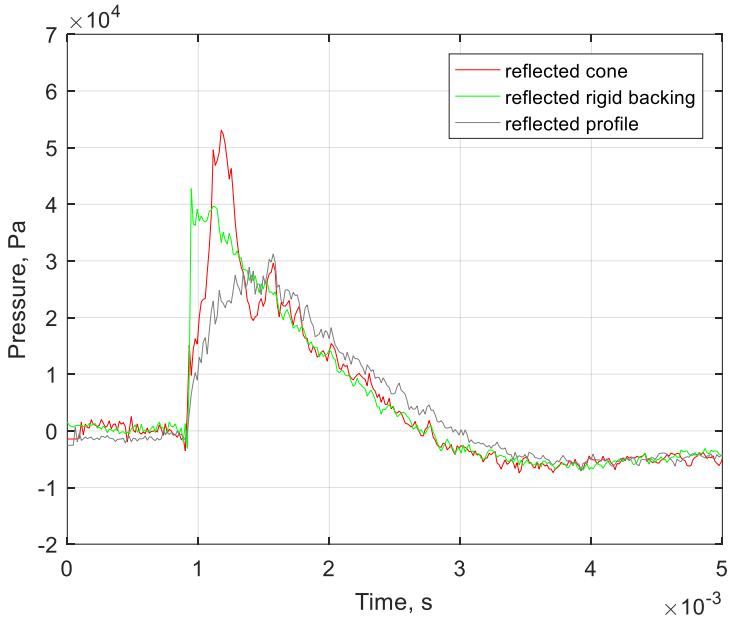

(c)

Figure 7.31. (a) Pressure as a function of time for membrane Mylar 40 μm. Measurement is first pulse at signal 2 with rigid backing. Analysis is shown in (b) for comparison of Mylar 23 μm explosions for the linear profile, for empty, rigid backing, and cone measurements. Figure 7.31 (c) shows the reflected peak pressures after first pulse analysis is performed from the data shown by Figure 7.31 (b). The cone sample and its design are first introduced in section 7.5. Measurements are performed in rigid backing and a schematic of the shock tube set-ups are given by Figure 7.2 a, b.

Figure 7.31 b shows pressure dependence on time for comparison of Mylar 23 μm explosions for the linear profile and cone sample (for cone design see section 7.5). This is shown to demonstrate how a series of cavities d_c distributed throughout the sample length L changes the performance of the sample dramatically, when measured for its acoustical reflective, or absorptive properties. Peak pressure of the incident shock pulse from empty tube measured at signal 2 was 47570 Pa and had a sound pressure level 187 dB. Incident pulse at signal 2 for rigid backing was 48340 Pa. Moreover, the profile measured at signal 2 had an incident peak pressure 47200 Pa for the incident pulse and sound pressure level 188

dB. The reflected pulse measured by signal 2 had a superimposed pulse with peak pressure (absent the profile) 49400 Pa corresponding to sound pressure level 187 dB. Reflected superimposed pulse from the measured signal of the profile measurement before first pulse analysis is 34040 Pa and sound pressure level 185 dB. For the cone structure, where $d_p = 0$ (absent plates) and $d_c = 0$ (absent cavities) the incident pulse had a peak pressure 47150 Pa, again measured at signal 2. After interaction with the cone structure the reflected superimposed pulse was 62500 Pa. Sound pressure levels for incident and superimposed pulses were 187 dB and 190 dB, respectively.

In Figure 7.31 c, pressure as a function of time is shown for the reflected pulses from a Mylar 23 μm explosion and complements the data given by Figure 7.31 b. The reflected rigid backing, and profile absorber measurements have peak pressures 42740 Pa and 31000 Pa respectively, after first pulse analysis. Their associated SPL are 187 dB for rigid backing and 184 dB for the profile structure. After subtraction of the cone and empty tube measurements, the reflected pulse at signal 2 is measured 52370 Pa equating to sound pressure level 188 dB. A laboratory developed profile absorber has been measured in the shock tube to determine its performance when constrained with large amplitudes. The linear profile clearly indicates the influence of the distributed cavities built within the structure compared to a simple cone like structure (measured data for the previous cone sample is given in section 7.5). Reflected peak pressures obtained from the profile measurements can be seen by Figures 7.29 – 7.31 a, b, and c, where the first pulse is reduced and shown after performing first pulse analysis. For instance, the peak pressure of the reflected pulse is reduced by around 10000 Pa from that of the incident pulse, measured at signal 2, see Figure 7.31 a. The pulse from the profile measurement for the reflected pressure is reduced around 16000 Pa, see Figures 7.31 b, c. The profile structure is later developed improving the accuracy of the build which is achieved by 3D printed technology. This allows dimensions for d_c and d_p values being more consistent.

Plate no.	$2R$ (mm)	r_0 (mm)	d_p (mm)	d_c (mm)
1	50	47	2	2.5 - 3
2	50	45	2	2.5 - 3
3	50	42	2	2.5 - 3
4	50	40	2	2.5 - 3
5	50	37	2	2.5 - 3
6	50	35	2	2.5
7	50	32	2	2.5
8	50	30	2	2.5
9	50	27	2	2.5
10	50	25	2	2.5
11	50	22	2	2.5
12	50	20	2	2.5
13	50	17	2	2.5
14	50	15	2	2.5
15	50	12	2	2.5
16	50	10	2	2.5
17	50	7	2	2.5
18	50	5	2	2.5
19	50	3	2	2.5
20	50	1	2	2.5
21	50	0	2	2.5

Table 7.8. Dimensions for laboratory-built profile with d_c, d_p and R. Sample with $L = 100$ mm.

7.7. Profiles – 3D Printed Absorber with ABH Effect

Profiled absorbers have been 3D printed and developed so that $d_c = 2$ mm and $d_p = 2$ mm. The structures are tested in the shock tube with much larger amplitude than those presented by Chapter 4 (continuous sound measurements with SPL being around 140 dB). The 3D printed absorbers are first designed using COMSOL Multiphysics and later printed using 3D printer technology based in the laboratory at University of Salford. Both linear and exponential profiles constitute the designs where for the former, inner radius r, decreases linearly along sample length L, where $r\,(L) = 0$ at the far end of the sample according to equation $r(x) = R\left(1 - \frac{x}{L}\right)$. For case of the latter, the design is developed with $r(x) = R\left(2 - e^{x \ln 2/L}\right)$, where x is the distance from the absorber and R is plate radius. Pore radius of the samples for both the linear and exponential profiles varies along sample length L, first introduced in Chapter 4 (see Figure 4.8) which is reintroduced here for visualisation of the profile configurations, given by Figure 7.32.

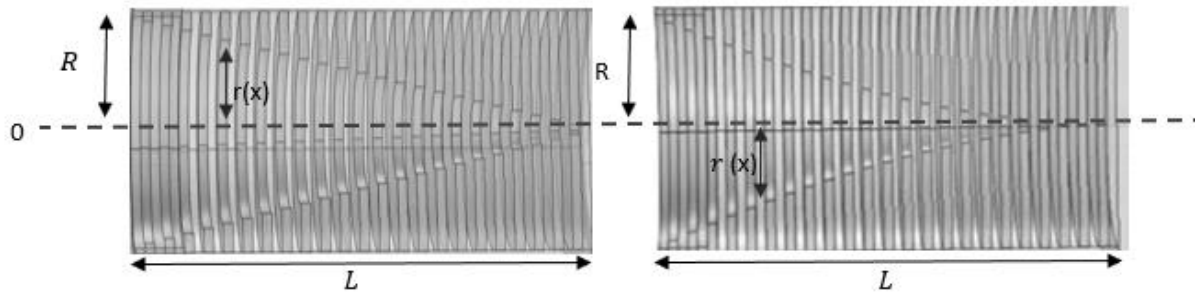

Figure 167. Linear profile (left) and exponential profile (right) with structure length L, and decreasing pore radii $r(x)$ from plate radius R to zero.

The 3D printed absorbers are built (see Figure 7.33) with dimensions close to those used for the laboratory profile sample (built with rigid plastic). 3D printed structures differed from the laboratory-built profile sample by the following: 1. The cavities were fixed at similar locations but d_c for the 3D printed samples are built rigid and contained within a solid casing surrounding the absorbers externally. 2. The dead-ends, or d_c of the laboratory-built profile absorber is sealed by using PTFE and isolation tape whereas the 3D printed sample is built as a complete structure. 3. Mounting procedure for the 3D printed including laboratory profiled structures also differed. This is because the laboratory-built absorber is tested in the shock tube by the insertion of the sample itself, see Figure 7.28. However, in the case of the 3D printed samples the profile absorbers are mounted externally to the shock tube. Cavity thickness throughout the sample is built constant after each plate containing pores with radius r_0. The time signals for the measured 3D profile which consists of a linear configuration (of decreasing pore radius r_0) can be seen by Figures 7.34 – 7.36. The data shows different membranes ruptured absent the absorber for case of an empty shock tube measurement, and additionally when the profile sample is tested. Shock pressures given are those measured by transducer signal 2. Figure 7.34 shows linear profile data obtained by performing first pulse analysis from a tin foil explosion. Peak pressure of the incident pulse by an empty tube measurement was 18930 Pa with SPL close to 179 dB. Peak pressure of the pulse for the profile measured 20630 Pa and sound pressure level equated to 180 dB. Reflected super positioned pulse for the profile had a peak pressure measuring 8004 Pa and corresponding to a SPL

172 dB. After first pulse analysis the peak pressure at signal 2 was 7599 Pa – 10270 Pa where the latter value is peak pressure for only small amount of time from the recorded pulse duration.

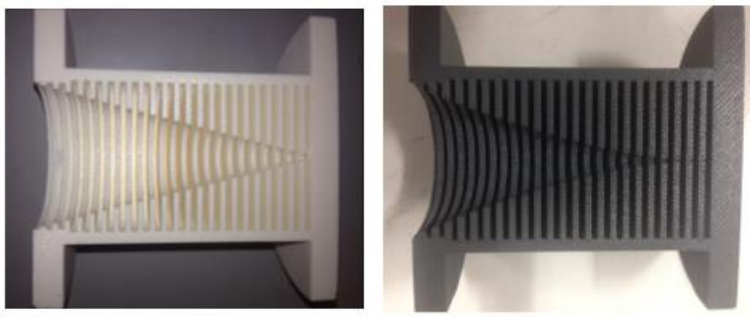

Figure 7.33. 3D printed linear profile (left), exponential profile (right). The front and end terminations included the external shell of the structure.

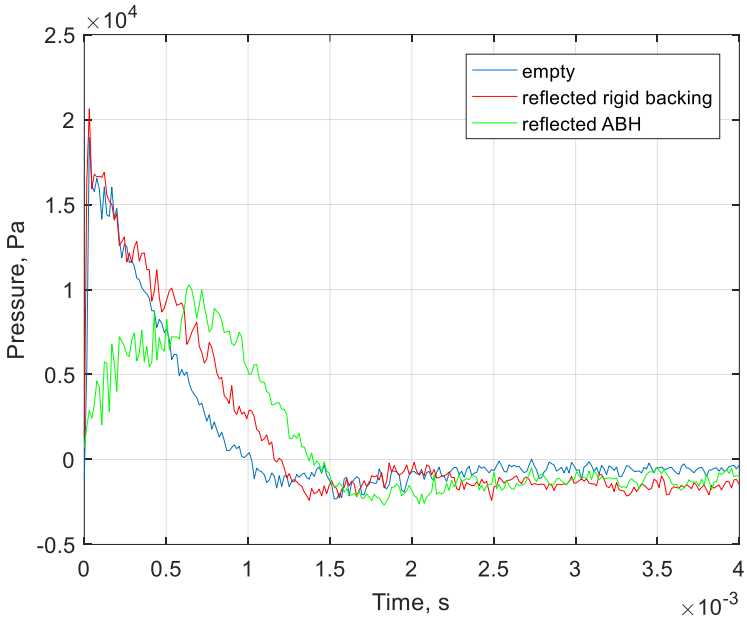

Figure 7.34. Pressure as a function of time for linear profile and ruptured membrane tin foil. Dimensions are $d_c = 2$ mm, $d_p = 2$ mm, $L = 100$ mm, and $R = 25$ mm.

Figures 7.35 – 7.36 shows larger amplitudes created by membrane explosions Mylar 23 μm and Mylar 50 μm respectively. In Figure 7.35 peak pressure for the empty pulse at signal 2 (absent the profile sample) was 47570 Pa. The linear profile absorber at signal 2 had a pulse with amplitude 45200 Pa. Superposition of the reflected pulse after interaction with the profile was 33880 Pa. After first pulse analysis, obtained by subtracting peak pressure of empty and reflected pulses, the peak pressure for the reflected pressure at signal 2 measured 29140 Pa (for SPL 183 dB). For rigid backing the reflected pulse was 49400 Pa at signal 2 which equated to a sound pressure level nearly 188 dB. Figure 7.36 shows pressure as a function of time from ruptured Mylar 50 μm. The empty tube measurement at signal 2 had an incident pulse 68840 Pa (sound pressure level 191 dB). Peak pressure for 3D printed profile at signal 2 measured 67060 Pa with SPL approximately 191 dB. Reflected pressure of the super-positioned pulse in rigid backing was 83370 Pa (without the 3D printed profile and 4315 Pa with 3D printed profile). After first pulse analysis the reflected pulses have peak pressures 66370 Pa (for case of rigid backing mode absent the profile) and 50950 Pa (with the profile). Single-sided spectrum for the reflected signals of the 3D printed linear profile is shown by Figures 7.37 – 7.38 for a range of amplitudes

between 10 KPa – 50 KPa. Absorption coefficient as a function of frequency is given by Figures 7.39 – 7.40 for the same amplitudes. The reflected pulse from ruptured tin foil (shown by Figure 7.34) for the profile had a peak reduction 10000 Pa. For the Mylar 23 μm rupture (Figure 7.35) the 3D printed profile produces a reduction of the peak pressure of nearly 20000 Pa. Similarly, value for the peak reduction had a similar value from the ruptured Mylar 50 μm membrane, where up to 20000 Pa of the peak pressure is reduced, see Figure 7.36.

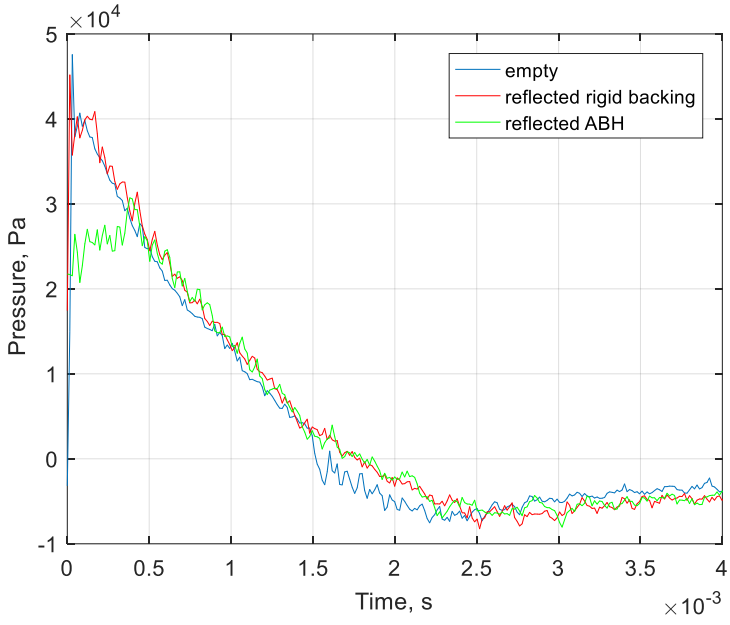

Figure 7.35. Pressure as a function of time for linear profile and ruptured membrane Mylar 23 μm. Dimensions are $d_c = 2$ mm, $d_p = 2$ mm, $L = 100$ mm, and $R = 25$ mm.

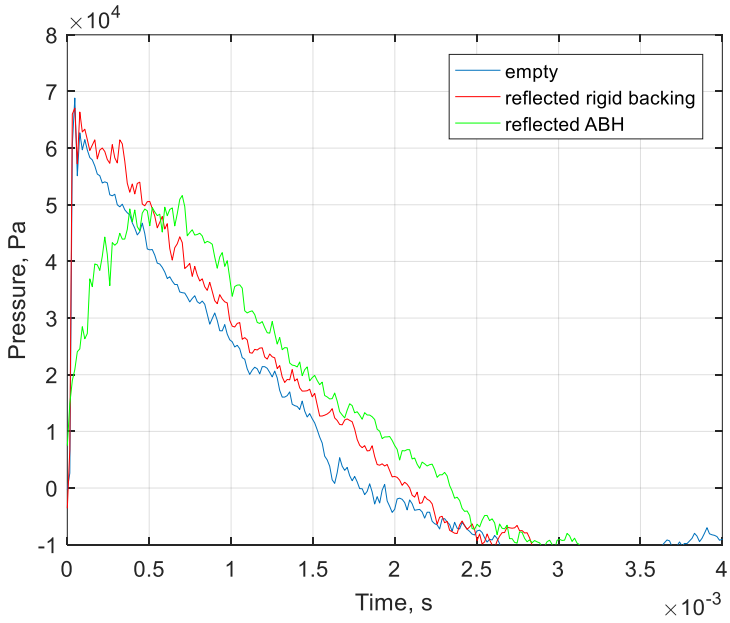

Figure 7.36. Pressure as a function of time for linear profile and ruptured membrane Mylar 50 μm. Dimensions are $d_c = 2$ mm, $d_p = 2$ mm, $L = 100$ mm, and $R = 25$ mm.

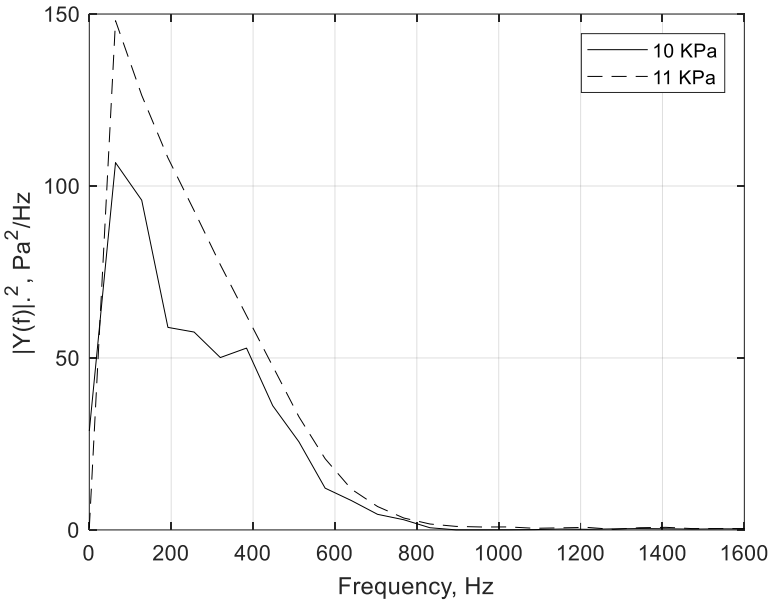

Figure 7.37. Single-sided amplitude spectrum of reflected signals for 3D printed linear profiled absorber. Membranes ruptured are tin foil (solid line) and baking paper (dash). Dimensions are $d_c = 2$ mm, $d_p = 2$ mm, $L = 100$ mm, and $R = 25$ mm.

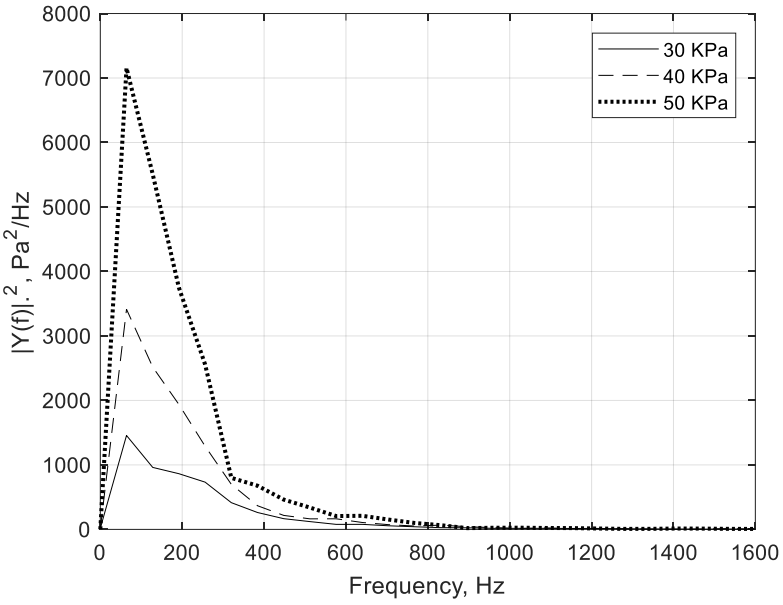

Figure 7.38. Single-sided amplitude spectrum of reflected signals for 3D printed linear profiled absorber. Membranes ruptured are Mylar 23 μm (solid line), Mylar 40 μm (dash) and Mylar 50 μm (dot). Dimensions are $d_c = 2$ mm, $d_p = 2$ mm, $L = 100$ mm, and $R = 25$ mm.

Fast Fourier Transform (FFT) is computed using mathematical software MATLAB by data obtained from measurements performed in rigid backing. The reflected original signals for both the reflected rigid backing and profile absorber is used in the calculation process. Amplitude spectrum of the rigid backing signals is not included here in Chapter 7, due to already a large number of graphs. Single-sided spectra and absorption coefficient for the profile only, is given. However, energy values calculated from reflected signals in rigid backing are given in Table 7.9. Single-sided amplitude spectrum for reflected signals by the linear profile is shown by Figure 7.39 for membranes tin foil and baking paper (for amplitudes 10 KPa and 11 KPa). Energy of the reflected pulses is associated mostly in the frequency region up to $f = 800$ Hz. Figure 7.40 shows single-sided amplitude spectrum of reflected signals for amplitudes 30 KPa

(Mylar 23 μm), 40 KPa (Mylar 40 μm) and 50 KPa (Mylar 50 μm). Largest portion of energy is found to be within $f = 400$ Hz. FFT is computed using sampling frequency and sample length of both the rigid backing and profile data, where the pulse signals have been modified during the first pulse analysis at signal 2, therefore eliminating reflected part of the pulse. This results in performing FFT on the incident pulses where original reflected pulses are used. After FFT of the original pulse is performed then single-sided spectra of the signals is calculated using the FFT data of the considered pulse and using Nonuniform Fast Fourier Transform (NFFT). Length of the segment is therefore used in the computation as opposed to length of the signal. Fast Fourier Transform FFT is computed using function NFFT. Spectral density of the reflected pulses is calculated by squaring the absolute value of the single-sided spectra of the pulses (obtained by FFT of the original signals). The above process is performed for all data where necessary throughout Chapter 7 for showing single-sided spectra of the reflected signals (for all pancake and profile absorber measurements, linear and exponential).

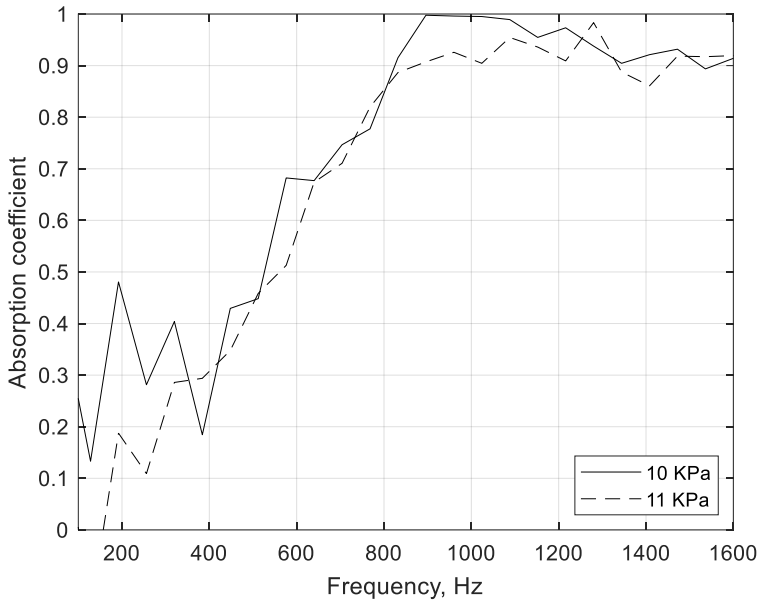

Figure 7.39. Absorption coefficient as a function of frequency for 3D printed linear profile. Membranes ruptured are tin foil (solid line), baking paper (dash). Dimensions are $d_c = 2$ mm, $d_p = 2$ mm, $L = 100$ mm, and $R = 25$ mm.

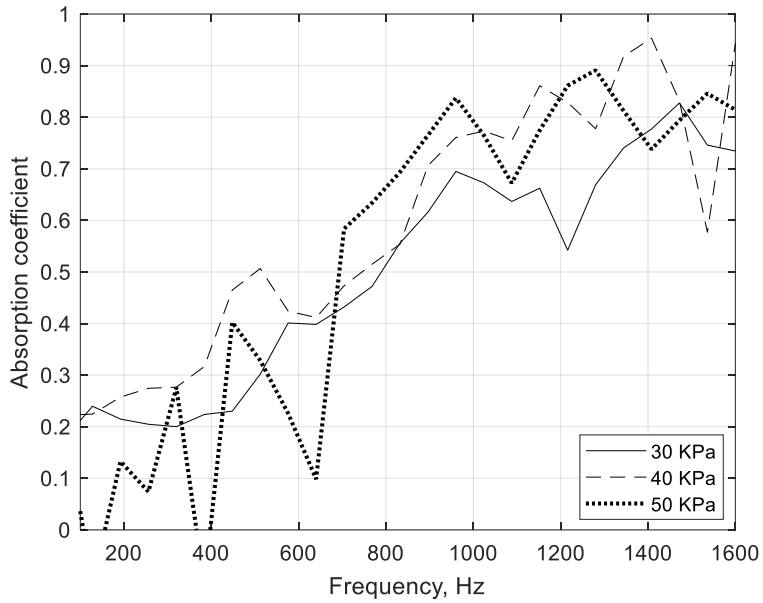

Figure 7.40. Absorption coefficient as a function of frequency for 3D printed linear profile. Membranes ruptured are Mylar 23 μm (solid line), Mylar 40 μm (dash) and Mylar 50 μm (dot). Dimensions are $d_c = 2$ mm, $d_p = 2$ mm, $L =$ 100 mm, and $R = 25$ mm.

Membrane ruptured	Energy original pulse	Energy reflected pulse	Energy absorption coefficient α_{energy}
Tin foil	999.6132	562.0413	0.4377
Baking paper	1.2098e+03	779.3428	0.3558
Mylar 23 μm	7.6209e+03	5.5678e+03	0.2694
Mylar 40 μm	1.6783e+04	1.1488e+04	0.3155
Mylar 50 μm	2.7944e+04	2.2366e+04	0.1996

Table 7.9. Energy absorption coefficient data for 3D printed linear profiled absorbers. Shock tube, first pulse analyses calculations, signal 2 in rigid backing set up.

Table 7.9 shows values of energy calculated using the FFT of the original reflected pulses for both rigid backing and reflected profile signals. Values are presented also for other membranes ruptured where energy is calculated by integrating the spectral density of the signals over frequency, see Figures 7.37 – 7.38. Energy absorption coefficient is calculated as $1 - E_{ab}/E_{rb}$ where E_{ab} is energy of original reflected signal (absorber) and E_{rb} is energy in original rigid backing signal. Energy is calculated in arbitrary units by integrating the spectral density as shown by Figures 7.37 – 7.38. It is clear by the data presented by Figures 7.34 – 7.36 including values given in Table 7.9 that the 3D printed absorber is effective when compared to the case of rigid backing. Energy calculated from the reflected pulse is significantly reduced to that of the rigid backing pulse especially for when amplitudes are lowest (tin foil and baking paper explosions). Consequently, this is reflected in the values obtained for the calculated energy absorption coefficient. It is shown in Table 7.9 that energy absorption coefficient is greater for pulses with lower energy (and amplitude): largest value being $\alpha = 0.4377$ is obtained for tin foil membrane. The lowest value was $\alpha = 0.1996$ by the Mylar 50 μm explosion. In the latter case, energy of the incident pulse is more than 28 times higher than the former. Furthermore, as amplitude strength of the reflected signals grow, α is reduced for frequencies above $f = 600$ Hz, see Figures 7.39 – 7.40. Absorption coefficient, however, increases with frequency irrespective of amplitude strength for the measured profile absorber. The next set of measurements have been performed on 3D printed exponential profiled absorbers. Dimensions are identical to the linear profile with exception to the

decreasing pore radius r_0. Profile parameters are given by Table 4.1 of Chapter 4. Figure 7.41 shows pressure as a function of time for a ruptured tin foil membrane. The empty tube measurement at signal 2 had a peak pressure 18930 Pa and sound pressure level 179 dB. 3D printed profile at signal 2 had a pulse measuring 20010 Pa with SPL approximately 180 dB. Reflected pressure of the super-positioned pulse in rigid backing was 19040 Pa (without the 3D printed profile) and 9958 Pa with the profile. After first pulse analysis the reflected pulses have peak pressures 20010 Pa (for case of rigid backing mode absent the profile) and 11060 Pa (with the profile). Figure 7.42 shows data from first pulse analysis for the exponential profile by Mylar 23 μm explosion. Peak pressure of the incident shock pulse from empty tube data was measured 47570 Pa and SPL 187 dB. Pulse for the profile had a peak pressure 46800 Pa and sound pressure level equating 187 dB. The reflected pulse recorded by the transducer at signal 2 (absent the profile) was 49400 Pa and corresponding to SPL nearly 188 dB. Reflected pulse from the measured signal for the profile, before first pulse analysis is 38990 Pa and SPL close to 186 dB. Sound pressure level of the reflected pulse, following first pulse analysis for rigid backing only is 187 dB (pulse with peak pressure 45200 Pa). Reflected peak pressure for the profile after first pulse analysis measured 30590 Pa and sound pressure level around 184 dB.

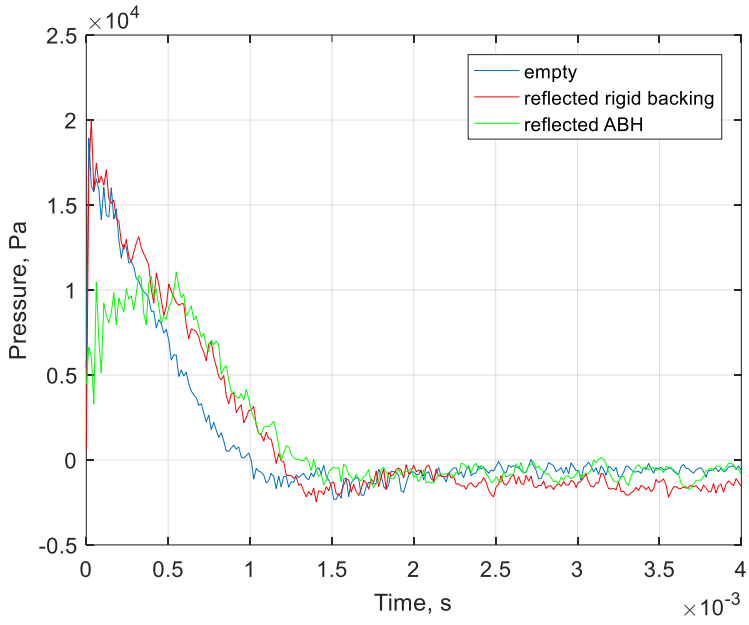

Figure 7.41. Pressure as a function of time for exponential profile and ruptured membrane tin foil. Dimensions are $d_c = 2$ mm, $d_p = 2$ mm, $L = 100$ mm, and $R = 25$ mm.

Data given by Figure 7.43 shows when pressure is increased (membrane Mylar 50 μm) so amplitudes are much larger than the values given prior to that of tin foil and Mylar 23 μm. Incident peak pressure of the first pulse at signal for the Mylar 50 μm is measured 68840 Pa (for explosion in empty tube). Peak pressure for the profile measurement at signal 2 before interaction with the sample was 69890 Pa. Sound pressure levels were 191 dB. After first pulse analysis the reflected pulses for rigid backing and the profile was measured 66400 Pa and 49830 Pa, respectively. This equated to SPL 190 dB (for reflected rigid backing) and 188 dB (profile). Furthermore, the profile absorber was able to produce a 3 dB reduction in SPL. The reflected peak pressure of the profile measurement for the ruptured tin foil membrane (shown by Figure 7.41) has a peak reduction of around 10000 Pa. For the Mylar 23 μm (see Figure 7.42) the profile absorber produces a peak reduction of nearly 20000 Pa. This peak reduction

was of similar value also from the ruptured Mylar 50 μm explosion, (see Figure 7.43) where a peak reduction around 20000 Pa is measured, after first pulse analysis has been performed.

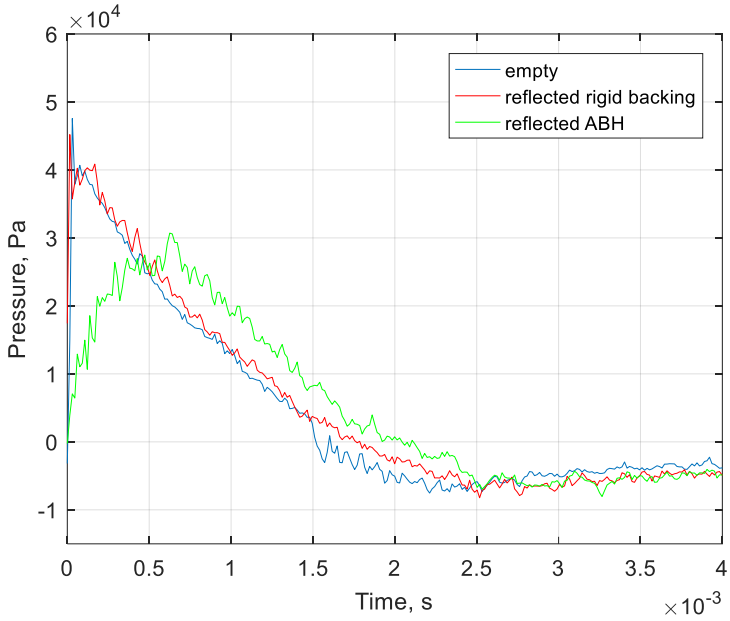

Figure 7.42. Pressure as a function of time for exponential profile and ruptured membrane Mylar 23 μm. Dimensions are $d_c = 2$ mm, $d_p = 2$ mm, $L = 100$ mm, and $R = 25$ mm.

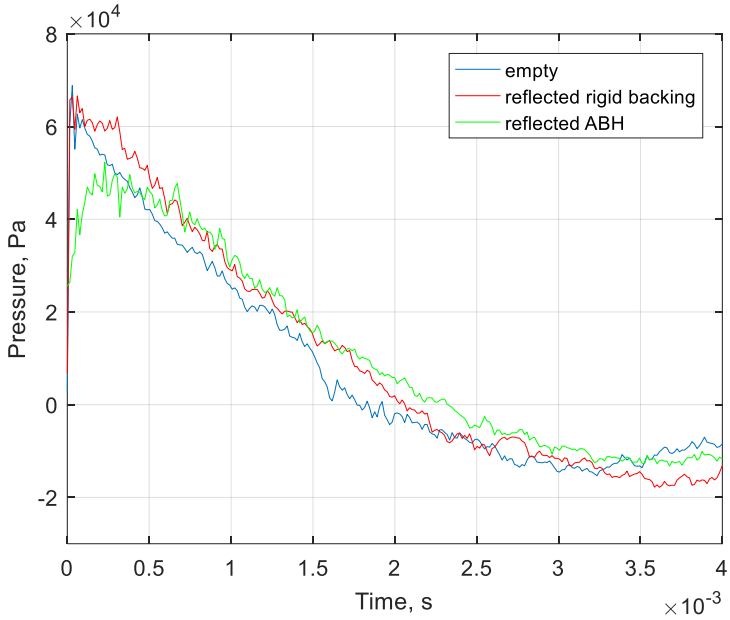

Figure 7.43. Pressure as a function of time for exponential profile and ruptured membrane Mylar 50 μm. Dimensions are $d_c = 2$ mm, $d_p = 2$ mm, $L = 100$ mm, and $R = 25$ mm.

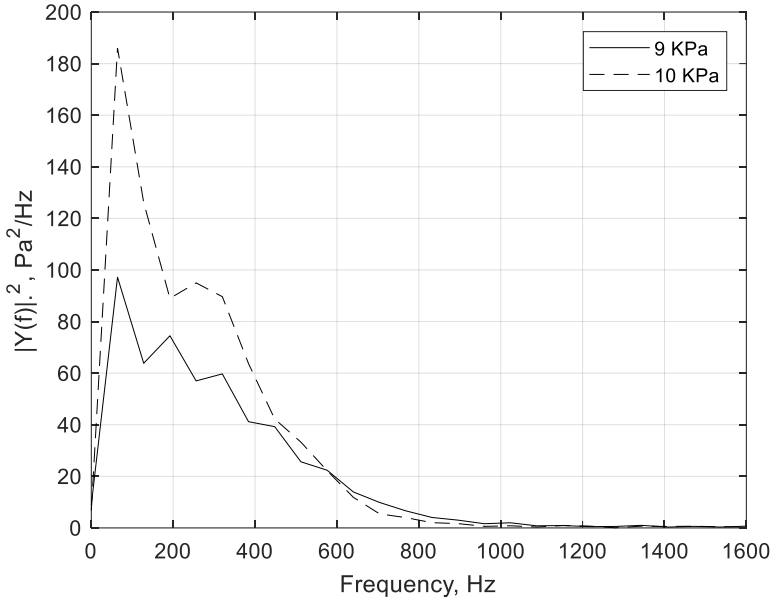

Figure 7.44. Single-sided amplitude spectrum of reflected signals for 3D printed exponential profiled absorber. Membranes ruptured are tin foil (solid line) and baking paper (dash). Dimensions are $d_c = 2$ mm, $d_p = 2$ mm, $L =$ 100 mm, and $R = 25$ mm.

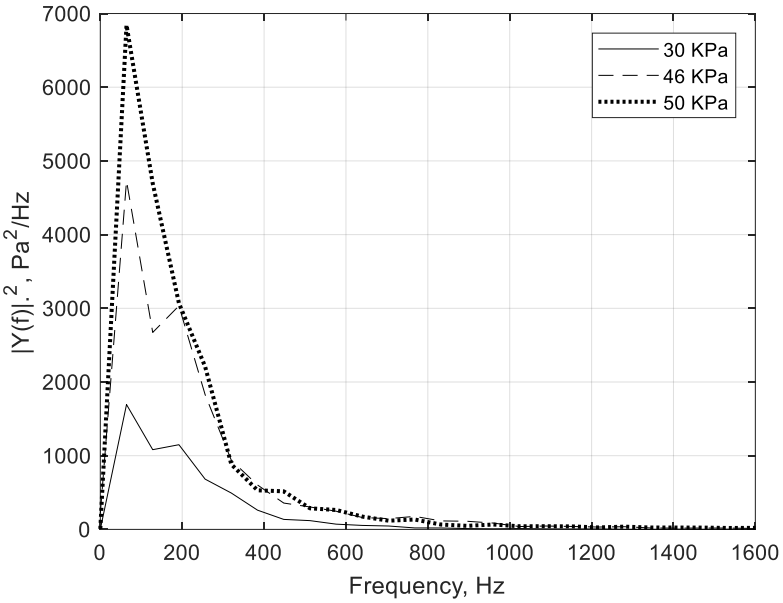

Figure 7.45. Single-sided amplitude spectrum of reflected signals for 3D printed exponential profiled absorber. Membranes ruptured are Mylar 23 μm (solid line), Mylar 40 μm (dash) and Mylar 50 μm (dot). Dimensions are $d_c =$ 2 mm, $d_p = 2$ mm, $L = 100$ mm, and $R = 25$ mm.

Single-sided amplitude spectrum for the reflected signals of membranes tin foil and baking paper is given by Figures 7.44. The amplitude for these membranes differ slightly compared to the linear profile by 1 KPa. Amplitudes are 9 KPa and 10 KPa for the ruptured tin foil and baking paper, respectively. For the weaker amplitudes, the energy of the reflected pulses is contained mostly in the frequency region up to $f = 800$ Hz. The single-sided amplitude spectrum for Mylar 23 μm, Mylar 40 μm, and Mylar 50 μm is shown by Figure 7.45. The largest portion of energy found is found to be in the region up to $f =$ 400 Hz. Absorption coefficient values are given in Figures 7.46 a-b for the different membrane ruptures. Values for the calculated energy absorption coefficient using FFT of the original reflected pulses for both rigid backing case and the profile signals is given by Table 7.10. The energy is calculated summing

spectral density components of the signals over all frequencies. Energy absorption coefficient is calculated ($1 - E_{ab}/E_{rb}$). Where E_{ab} is the energy in original reflected signal (absorber) and E_{rb} is energy in original rigid backing signal. This way, any energy losses due to propagation in the shock tube are compensated. The exponential profile shows a similar performance to that of the linear profile and is much more effective than a simple rigid backing case. Energy calculated (reflected pulse of the exponential profile) is significantly reduced compared to that of the rigid backing pulse especially for when amplitudes are lowest.

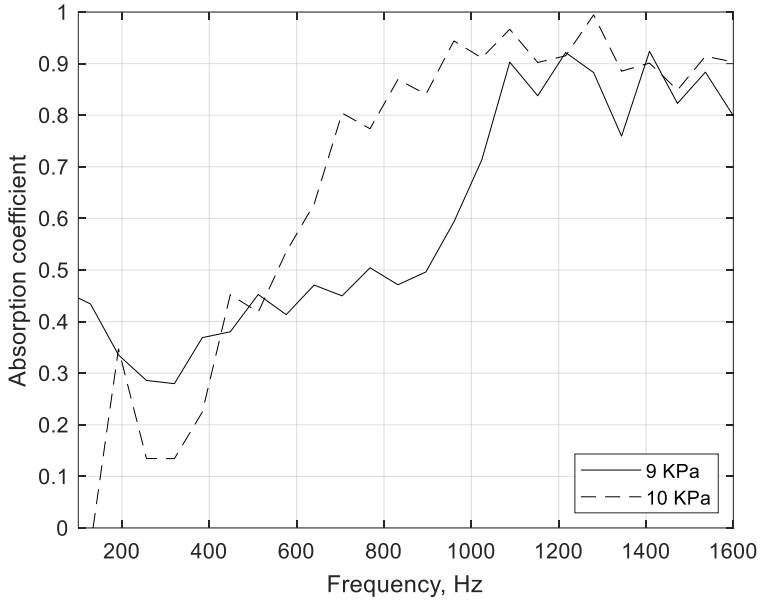

(a)

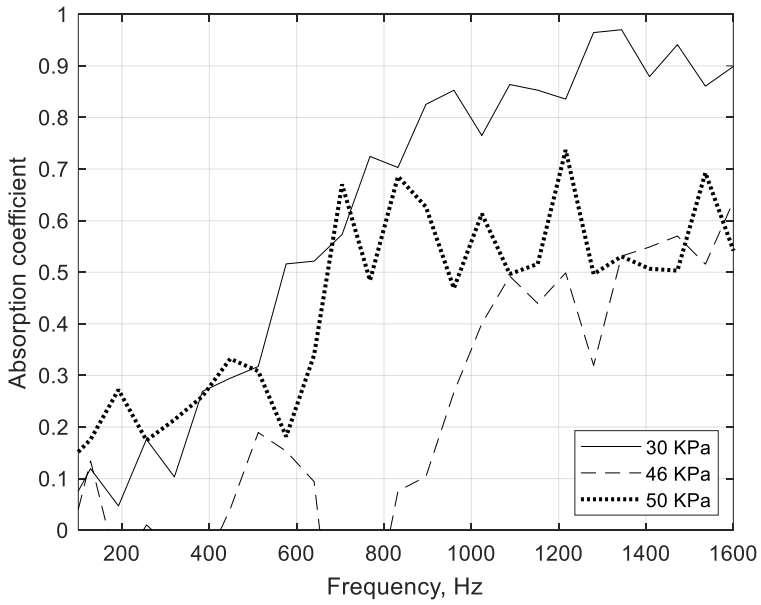

(b)

Figure 7.46. (a) Absorption coefficient as a function of frequency for 3D printed exponential profile. Membranes ruptured are tin foil (solid line), baking paper (dash). In (b) membranes ruptured are Mylar 23 μm (solid line), Mylar 40 μm (dash) and Mylar 50 μm (dot). Dimensions are $d_c = 2$ mm, $d_p = 2$ mm, $L = 100$ mm, and $R = 25$ mm.

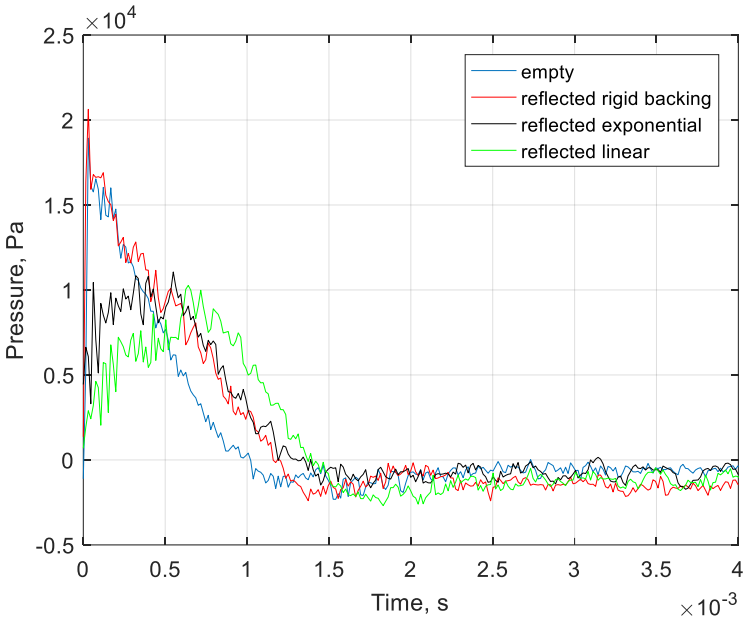
×10^4
2.5
2
1.5
1
0.5
0
-0.5
Pressure, Pa
0
0.5
1
1.5
2
2.5
3
3.5
4
Time, s
×10^-3
empty
reflected rigid backing
reflected exponential
reflected linear

(a)

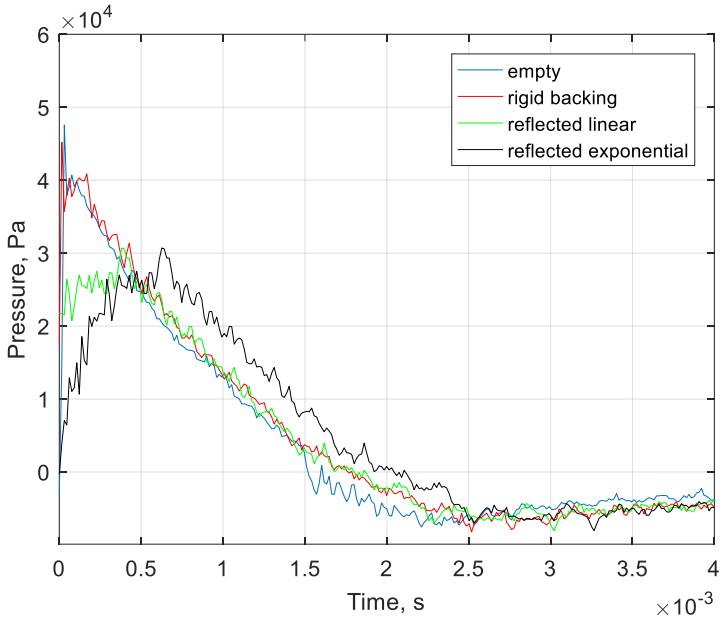
×10^4
6
5
4
3
2
1
0
Pressure, Pa
0
0.5
1
1.5
2
2.5
3
3.5
4
Time, s
×10^-3
empty
rigid backing
reflected linear
reflected exponential

(b)

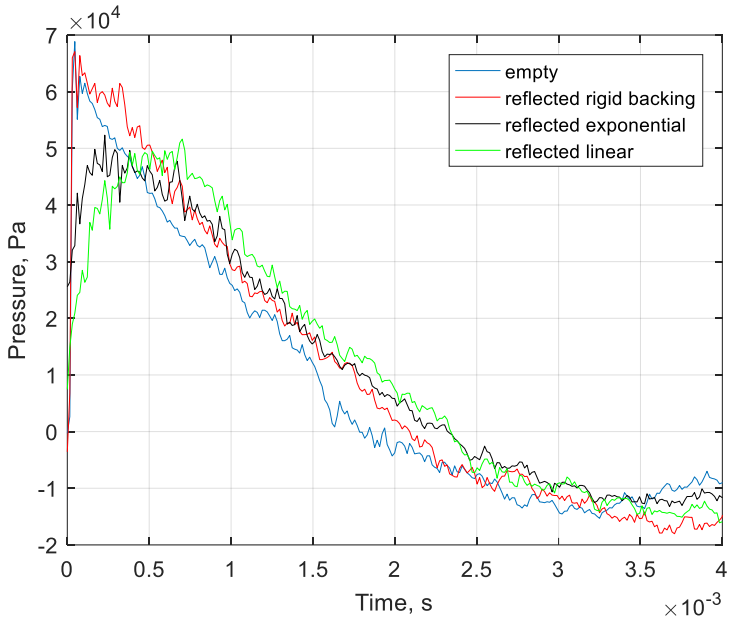

(c)

Figure 7.47. Pressure as a function of time showing comparison of reflected shock pressures for the linear and exponential profile absorbers. (a) Membrane ruptured is tin foil. In (b) membrane ruptured is Mylar 23 μm. The ruptured Mylar 50 μm membrane is shown by (c).

Comparison between the 3D printed profiles (linear and exponential) shows their performance is quite similar for the same ruptured membranes and amplitudes created thus far (see values of energy absorption coefficients in Tables 7.9 and 7.10). The amplitude ratios of the reflected pressures for the linear profile absorber are calculated from the data shown by Figures 7.34 – 7.36 for membrane ruptures of tin foil, Mylar 23 μm and Mylar 50 μm. The reflected and incident pulses of the peak pressure ratios are 49.8 %, 64.5 % and 75.9% respectively. This demonstrates that the performance of the absorber deteriorates as the amplitude increases. The exponential profile reflected peak pressure ratios are given by using data from Figures 7.41 – 7.43 and are 55.3 %, 65.4 % and 71.3 % respectively. Incident and reflected peak pressures for the tin foil membrane for the linear and exponential profiles are 20630 Pa, 20010 Pa (incident) and 10270 Pa and 11060 Pa (reflected), as shown by Figures 7.34 and 7.41, respectively. Reflected peak reductions are 50.2 % for the linear profile and 44.7 % for the exponential profile. The measured pressure at signal 2 for the incident Mylar 23 μm membrane is 45200 Pa and 46800 Pa for the linear and exponential profiles respectively, see Figures 7.35 and 7.42. This results in a peak reduction of the reflected pressure 35.5 % for the linear profile and 34.6 % for the exponential profile, where reflected peak pressures are measured 29140 Pa and 30590 Pa for the linear and exponential profile absorbers, respectively. Reduction of the reflected peak pressure for the Mylar 50 μm membrane is 24.1 % and 28.7 % for the linear (Figure 7.36) and exponential (Figure 7.43) profiles, respectively. Incident and reflected peak pressures for the linear profile are 67060 Pa and 50950 Pa. The incident and reflected peak pressures for the exponential absorber was 69890 Pa and 49830 Pa. Comparisons of the reflected peak pressures for the linear and exponential structures are given by Figure 7.47 a, for tin foil, Figure 7.47 b for Mylar 23 μm, and Figure 7.47 c for Mylar 50 μm ruptures.

Membrane ruptured	Energy original pulse	Energy reflected pulse	Energy absorption coefficient α_{energy}
Tin foil	1.0008e+03	573.7361	0.4267
Baking paper	1.2026e+03	815.5194	0.3219
Mylar 23 μm	7.5913e+03	5.9521e+03	0.2159
Mylar 40 μm	1.6717e+04	1.6435e+04	0.1168
Mylar 50 μm	2.6854e+04	2.0586e+04	0.2334

Table 7.10. Energy absorption coefficient data for 3D printed exponential profiled absorbers. Shock tube, first pulse analyses calculations, signal 2 in rigid backing set up.

7.8. Pancake Absorber – Metallic Transmission Set-Up

The pancake absorber has been investigated further (previous sample was 3D printed) for high amplitudes. A metallic structure is developed and later tested in the shock tube. The latest sample comprised of aluminium plates. External radius of the plates was twice that of the 3D printed sample. The metamaterial pancake was built with the following dimensions, where $d_c = 3$ mm, $d_p = 1$ mm, $L = 30$ mm, $r_0 = 4$ mm, and $R = 50$ mm. The shock tube is a natural progression for testing the pancake with increased pressures to those previously, by data given by Chapter 4 (Continuous sound in a HSPL impedance tube). Note, all membranes were ruptured (tin foil, baking paper, and Mylar membranes) when performing the measurements for the pancake absorber, however, only the results for weaker membranes are presented here due to absorber performance. Figure 7.48 shows a metamaterial pancake absorber assembled and comprised a series of distributed cavities along the sample length. It is sealed by PTFE tape to reduce any leakages prior to the fixing and clamping process used for the shock tube.

Figures 7.49 – 7.50 show absorption coefficient and reflection coefficient respectively, from a pancake absorber measurement performed with a Mylar 23 μm explosion. Figure 7.49 shows absorption coefficient dependence on frequency where values of α can be seen both negative, and positive at different frequencies. Negative values of α is given when reflection coefficient of the same measurement is greater than the value 1.0. The reflection coefficient data is given by Figure 7.50 showing reflection coefficient dependence on frequency. See also Figures 7.57 – 7.58 showing single-sided amplitude spectrum for the reflected shock pressures, including data given by Table 7.11. Note, the negative values of α present in the pancake absorber measurements (at some frequencies due to large reflections of similar energies of incident and reflected shocks) is not seen in the metallic profile measurements (see sections 7.9 – 7.10). The negative values of α for particular frequencies are the result of energy redistribution between different frequency components, due to nonlinear interactions. This has also been observed in the measurements reported in previous parts, but not to the same extent. The energy absorption coefficient, calculated in time domain, is a more suitable way to characterise the performance of the absorbers for high amplitude pulse excitation. However, in the following, the absorption coefficient obtained in frequency domain, will still be shown for completeness. Three of the membranes ruptured in the shock tube and tested against the pancake are given by Figures 7.51 – 7.56 showing absorber performance in time domain.

Figure 7.48. Metamaterial pancake absorber front view sealed at the circumference. Dimensions are $d_c = 3$ mm, $d_p = 1$ mm, $L = 30$ mm, $r_0 = 4$ mm, and $R = 50$ mm.

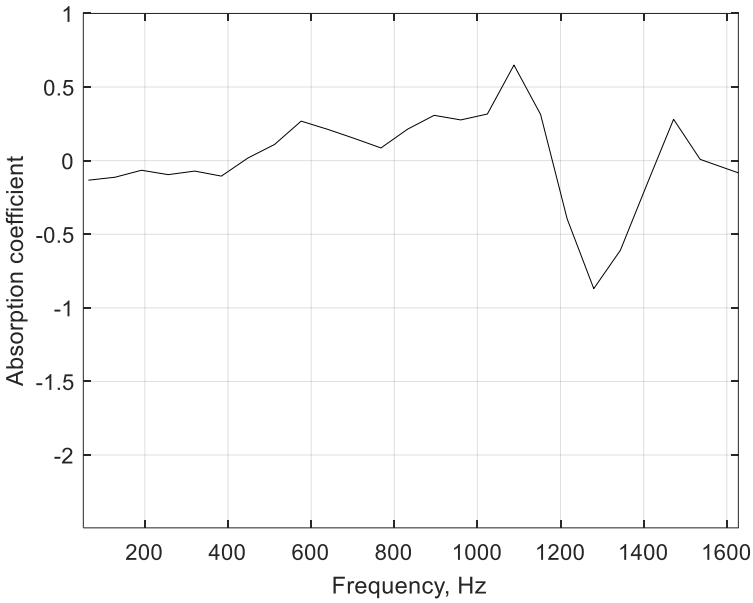

Figure 7.49. Absorption coefficient as a function of frequency for pancake absorber showing negative values of α. Membrane ruptured is Mylar 23 μm.

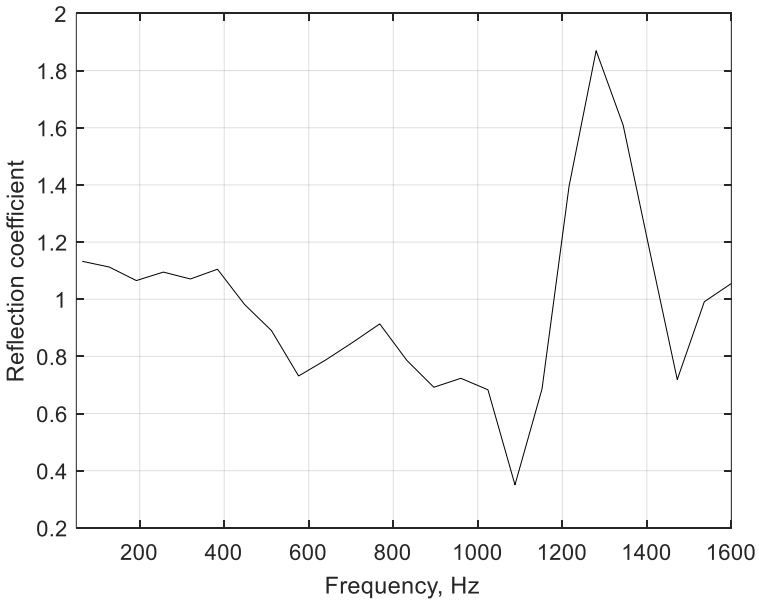

Figure 7.50. Reflection coefficient as a function of frequency for pancake absorber. Membrane is Mylar 23 μm.

The lowest pressure tested against the pancake was nearly 25000 Pa, see Figures 7.51 – 7.52. This is when the measured data is obtained immediately after the ruptured tin foil membrane by signal 1. The measured pressure at signals 2 and 3 are also included, where signal 2 measures the pulse prior to, and after interaction of the pancake. And signal 3 shows the pressure obtained after interaction with the sample. Measurements for the pancake absorber have been performed in transmission set-up, hence why three-signal data is shown. The peak pressures for the first pulse shown by Figure 7.51 are the following: Signal 1 is 24630 Pa, signal 2 incident 22360 Pa, signal 2 reflected 19100 Pa, and signal 3 (transmitted) 1900 Pa.

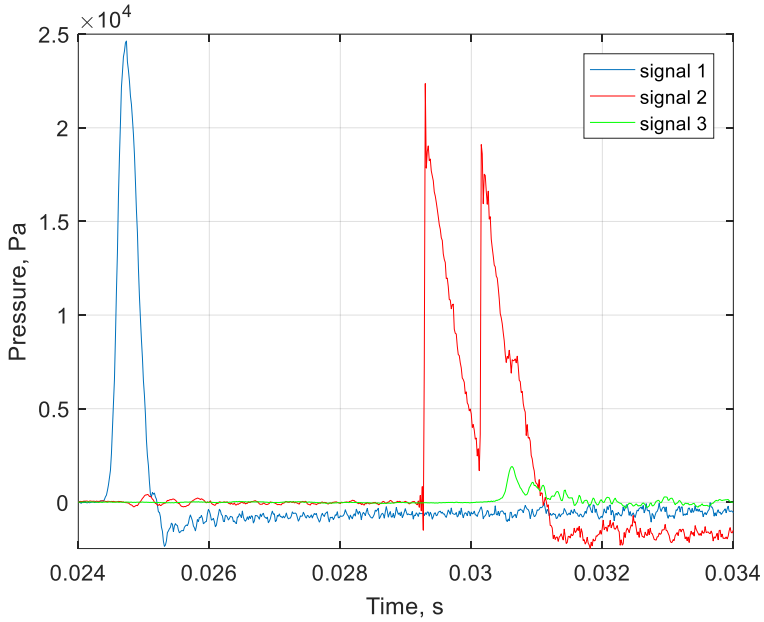

Figure 7.51. Pressure as a function of time for pancake absorber tested in shock tube with membrane tin foil. Dimensions are $d_c = 3$ mm, $d_p = 1$ mm, $L = 30$ mm, $r_0 = 4$ mm, $N_{de} = 8$, and $R = 50$ mm.

Data analysis is performed on the pulses (for ruptured tin foil) and given in Figure 7.52. The empty tube measurement used to obtain the signal reflected from rigid backing is measured with a peak pressure 18930 Pa, at signal 2. Peak pressure of the reflected from the rigid backing pulse was 20100 Pa. Reflected peak pressure measured after interaction with the metamaterial pancake is 18580 Pa. The position of rigid backing in these experiments was the same as the position of the front surface of the pancake absorber. This creates the potential nonlinear pulse distortion due to propagation in the tube. The slightly larger recorded pressure of the pulse reflected from rigid backing is due to a short spike at the peak, it is observed that this pulse is nearly identical to that reflected from the pancake absorber. Hence, nearly all energy is reflected backwards, with exception of very little transmission able to pass beyond the furthest plate with exit pore radius $r = 4$ mm. The amplitude of the transmitted pulse is more than 10 times lower than the incident one, while the duration is similar. Less than 7 % of the incident energy is transmitted. The amplitude generated from ruptured baking paper is used to create an incident peak pressure 35570 Pa, see Figure 7.53. Peak pressures given by signal 2 are measured 25390 Pa and 26330 Pa. Transmitted pressure measured at signal 3 was 2311 Pa, which is again more than 10 times lower than the amplitude of the incident pulse. Figure 7.54 shows all signal 2 data for the empty, reflected rigid backing, and reflected pancake interaction. The pulse measured in empty tube was 23870 Pa and the peak pressures of the reflected pulses after first pulse analysis are 21770 Pa for rigid

backing, and 20880 Pa for the reflected pulse by the pancake sample. The rigid backing measurement before analysis had peak pressures 24330 Pa (signal 2 incident) and 20460 Pa (reflected signal 2). Pulses from the pancake absorber measurement (before analysis) had peak pressures 23640 Pa and 23070 Pa, for incident and reflected pulses respectively, obtained from piezoelectric transducer signal 2.

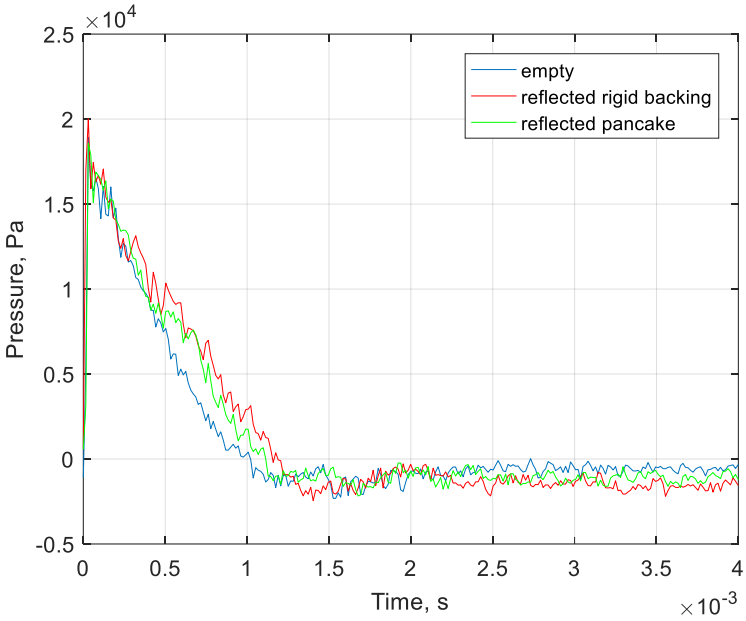

Figure 7.52. Pressure as a function of time for pancake absorber and membrane tin foil. First pulse analysis. Dimensions are $d_c = 3$ mm, $d_p = 1$ mm, $L = 30$ mm, $r_0 = 4$ mm, $N_{de} = 8$, and $R = 50$ mm.

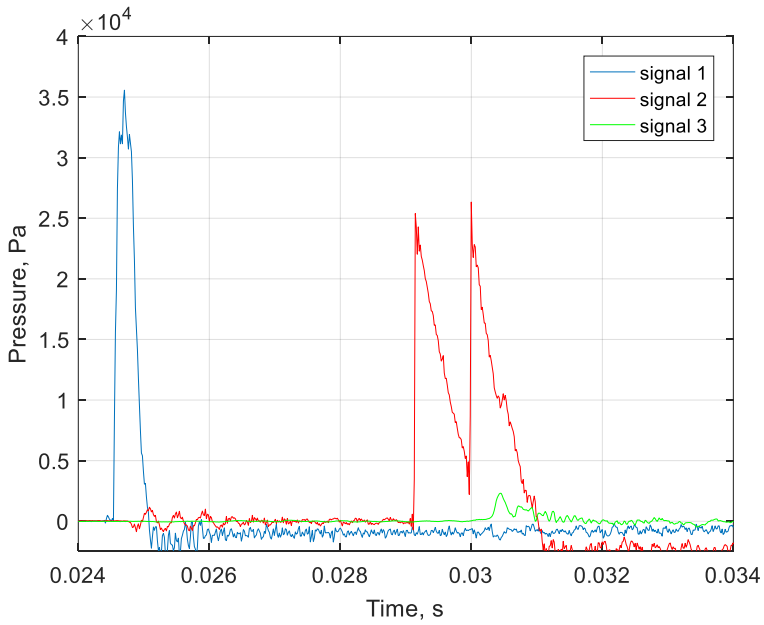

Figure 7.53. Pressure as a function of time for pancake absorber tested in shock tube with membrane baking paper. Dimensions are $d_c = 3$ mm, $d_p = 1$ mm, $L = 30$ mm, $r_0 = 4$ mm, $N_{de} = 8$, and $R = 50$ mm.

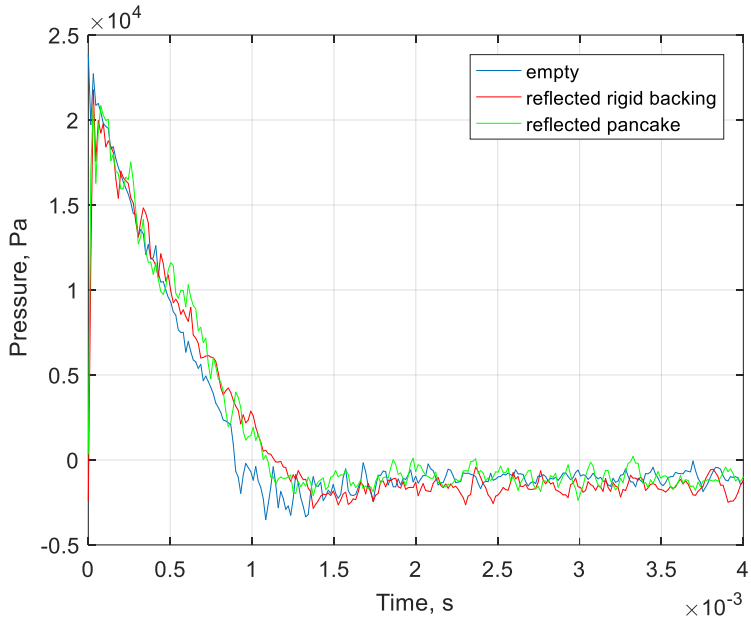

Figure 7.54. Pressure as a function of time for pancake absorber and membrane baking paper. First pulse analysis. Dimensions are $d_c = 3$ mm, $d_p = 1$ mm, $L = 30$ mm, $r_0 = 4$ mm, $N_{de} = 8$, and $R = 50$ mm.

The data presented by Figure 7.55 shows when Mylar 23 μm is ruptured and its amplitude at various signal locations for a typical measurement performed in the shock tube. Peak pressure at signal 1 is measured 48000 Pa and at signal 2 incident pulse before interaction with the sample is 47870 Pa. Peak pressure at signal 2 after interaction with the sample is 59510 Pa. And pressure measured at signal 3 was 4255 Pa. The corresponding sound pressure levels associated are 187 dB (signal 1) 187 dB, 189 dB (signal 2) and 166 dB (signal 3). First pulse analysis is later performed for the shock pulses measured at the fixed signal locations, see Figure 7.56 a. Reflected peak pressures for the rigid backing and pancake absorber are 47570 Pa and 42590 Pa, respectively. Sound pressure level was 187 dB for both the reflected rigid backing and pancake. Little transmission is measured by transducer signal 3.

Figure 7.56 b shows pressure as a function of time for the super positioned shock pulses of the pancake absorber measurement, and rigid backing. Large reflection of the pressure by the pancake is measured at signal 2 slightly after 29 milliseconds, and close to 30 milliseconds for the rigid backing measurement. The shock has propagated an additional distance 200 mm for case of rigid backing, due to the change of its position compared with earlier measurements. This results in a slightly lower value of the super positioned shock for rigid backing compared to the super positioned pulse from the pancake measurement. Energy absorption coefficient is shown at low or negative value (Mylar 23 μm explosion) due to the calculated energy of the reflected pressure of the pancake absorber being slightly larger than it is for case of the measurement performed absent the sample, in rigid backing. Peak pressures of the super positioned shocks for the rigid backing and pancake measurements is approximately 49000 Pa and 59000 Pa, respectively. The incident peak pressures are nearly 48000 Pa for both the rigid backing and pancake measurements, obtained at signal 2, prior to any reflection from the rigid backing plate, or pancake sample surface.

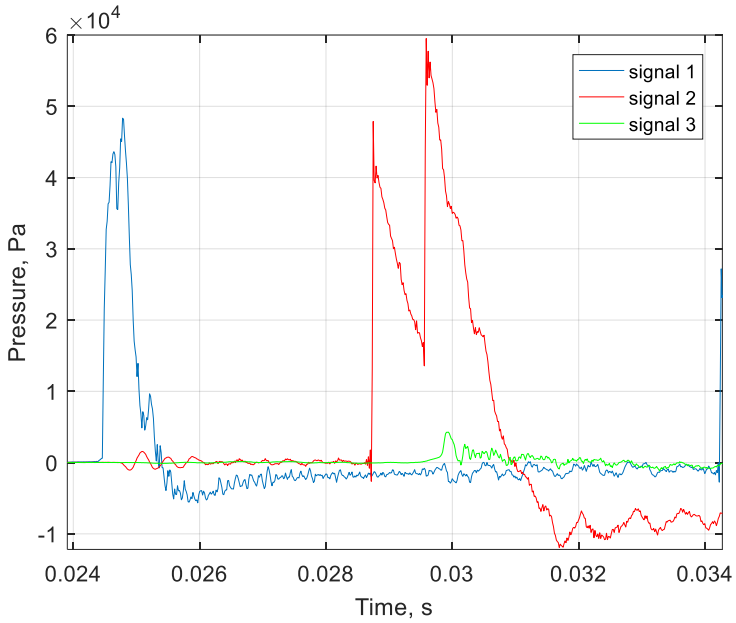

Figure 7.55. Pressure as a function of time for pancake absorber tested in shock tube with membrane Mylar 23 μm. Dimensions are $d_c = 3$ mm, $d_p = 1$ mm, $L = 30$ mm, $r_0 = 4$ mm, $N_{de} = 8$, and $R = 50$ mm.

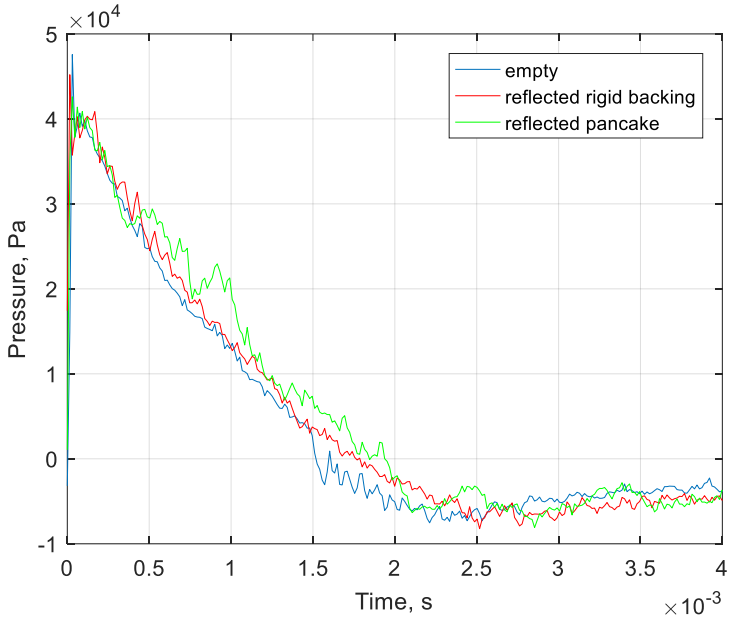

(a)

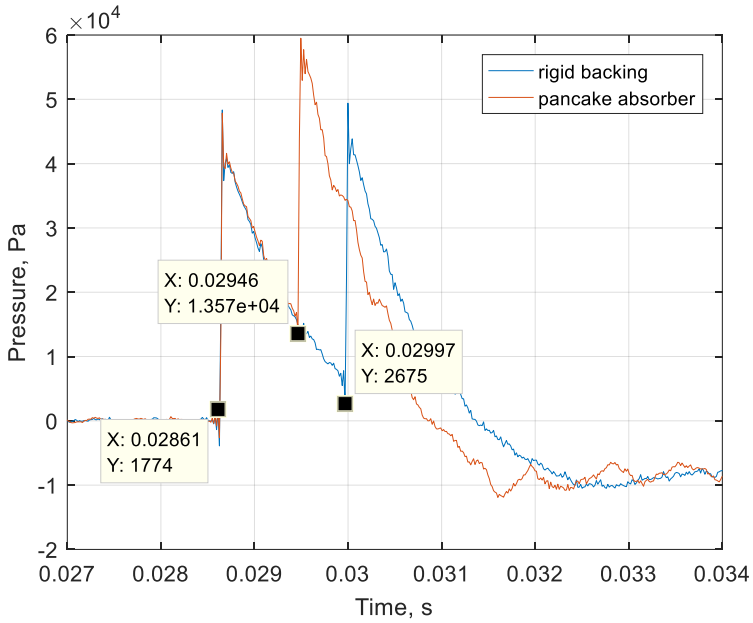

(b)

Figure 7.56. (a) Pressure as a function of time for pancake absorber and membrane Mylar 23 μm. And (b) Pressure as a function of time for ruptured Mylar 23 μm with pulse signal 2 times. The duration is shown for the point of reflection of the shock pulses from the solid boundary. Super positioned pressures are shown for the pancake including the measurement performed in rigid backing, absent a sample. Dimensions are $d_c = 3$ mm, $d_p = 1$ mm, $L = 30$ mm, $r_0 = 4$ mm, $N_{de} = 8$, and $R = 50$ mm.

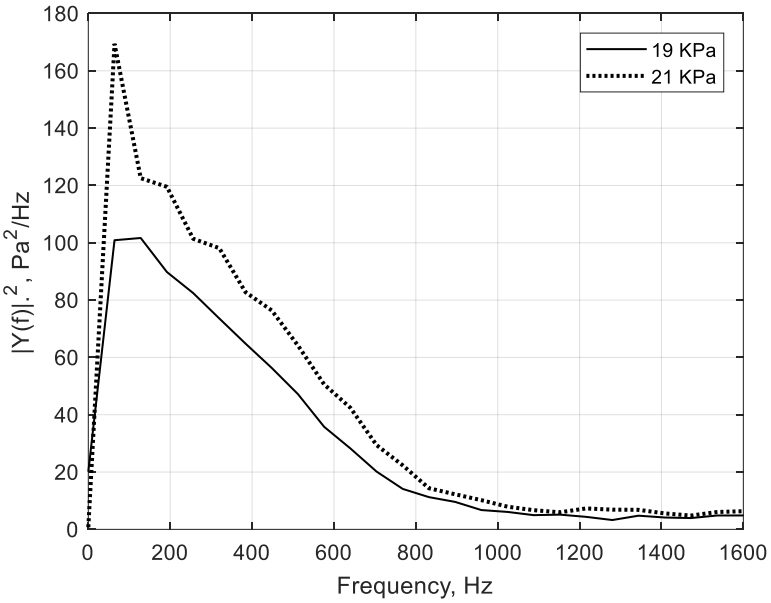

Figure 7.57. Single-sided amplitude spectrum of reflected signals for membrane tin foil (solid line) and membrane baking paper (dash). Absorber reflected signals for pancake absorber. Dimensions are $d_c = 3$ mm, $d_p = 1$ mm, $L = 30$ mm, $r_0 = 4$ mm, and $R = 50$ mm.

Single-sided amplitude spectrum of reflected signals for membranes tin foil and baking paper is shown by Figure 7.57. The former corresponds to an amplitude 19000 Pa and 21000 Pa for the latter. Energy of the reflected pulses is mostly in the region up to $f = 800$ Hz. Figure 7.58 shows single-sided amplitude spectrum of a reflected signal from ruptured Mylar 23 μm where peak pressure equates to 43000 Pa. For tin foil and baking paper membranes the largest portion of energy is found to be within $f = 1000$ Hz. Reflected pulse by the Mylar 23 μm rupture having a larger amplitude has majority of energy mostly in

the region up to $f = 600$ Hz. Table 7.11 presents the data computed for reflected energies of the membranes discussed above, for tin foil, baking paper and Mylar 23 μm. Energy absorption coefficient is shown being much less compared to the previous tested profile absorbers, given by Table 7.10 (shown in section 7.7 for 3D printed profile absorbers).

Figure 7.59 shows absorption coefficient as a function of frequency for tin foil, baking paper and Mylar 23 μm membranes. It can be noticed that positive and negative values at different frequencies nearly compensate each other due to energy redistribution over the frequency components. This confirms that the frequency domain analysis is not suitable for these cases where large super positioned pulses result from the pancake absorber being ineffective against the large amplitudes of the incident pulse. A negative value is shown in Table 7.11 from data by the ruptured baking paper and Mylar 23 μm membranes for the calculated energy absorption coefficient. Energy absorption coefficient is calculated as $1 - (E_{ab} + E_{tr})/E_{rb}$ where E_{ab} is energy in original reflected signal (absorber) and E_{rb} is energy in original rigid backing signal. Energy from the transmitted pulse is E_{tr}. The ruptured tin foil membrane has values of α being close to zero. This is result of the energy absorption coefficient using the energy of both the reflected rigid backing and the pancake sample. In the reflected energy of the former, it corresponds to the pulse data obtained at the signal 2 transducer (measured prior to the absorber face) after the pulse has propagated a distance of approximately 350 mm. However, for the pancake the surface of the absorber is fixed into position at a distance measuring 150 mm from signal 2. Consequently, the shock pulse associated to the pancake absorber will have larger amplitude and contain slightly more energy, for the reflected measured pulse at signal 2. This is plausible since the reflected pulse measured from the rigid backing measurement has propagated slightly further and has additional time of decay rate, see Figure 7.56 b (which shows a lower value of the peak pressure for the super positioned shock compared to the pancake absorber measurement).

The measurements performed in the shock tube for the samples also have an error of the shock pulse amplitudes, which can be up to 5 % in some cases and must be considered. These measurements are also independent from one another. However, many are performed for each sample to try and reduce any errors for each individual measurement, and moreover, to perform analysis on identical peak pressures of the recorded data. It has been demonstrated that when the pancake absorber is tested with reasonably large amplitudes (20000 Pa +) performance of the absorber is much worse when compared to the results of pancake absorbers tested in linear regime, see Chapter 4, Continuous sound measurements. It is also demonstrated that the performance of the metamaterial pancake absorber is significantly worse than profile absorbers (both linear and exponential) for high amplitude pulses ranging with peak pressures 18000 Pa – 80000 Pa (see data presented in sections 7.6 (laboratory-built profile) and section 7.7 (3D printed profiles). It is therefore deemed more desirable to use the impedance matching approach, which is exploited within the profile design (realisation of taking advantage of the so-called “acoustic black hole effect”). The combination of applying both the dead-end pore and ABH approach is demonstrated in section 7.9 with the development of metallic profile absorbers.

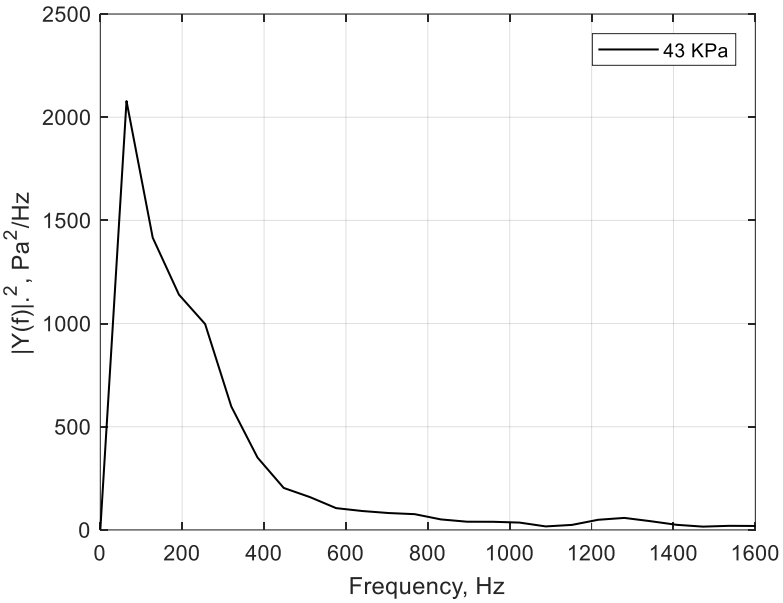

Figure 7.58. Single-sided amplitude spectrum of reflected signal for membrane Mylar 23 μm. Absorber reflected signals for pancake absorber. Dimensions are $d_c = 3$ mm, $d_p = 1$ mm, $L = 30$ mm, $r_0 = 4$ mm.

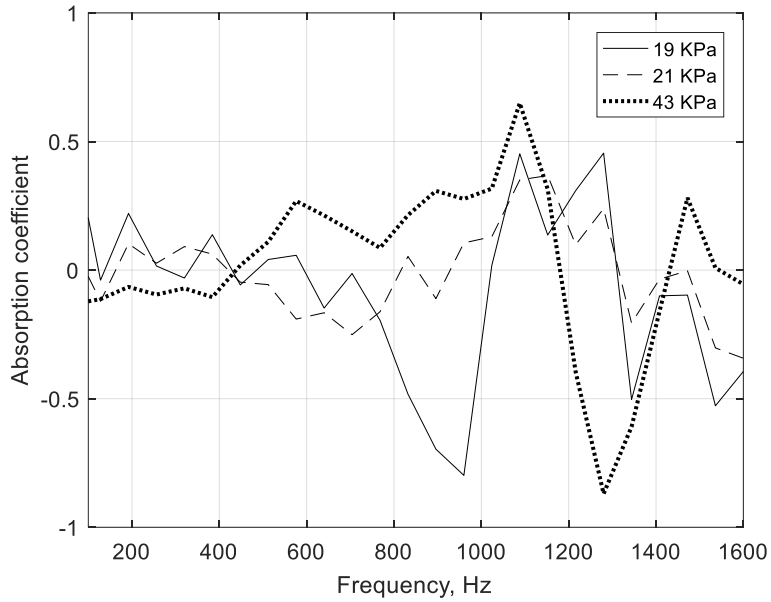

Figure 7.59. Absorption coefficient as a function of frequency for pancake absorber showing negative values. Membranes ruptured are tin foil (solid line), baking paper (dash) and Mylar 23 μm (dot). Dimensions are $d_c = 3$ mm, $d_p = 1$ mm, $L = 30$ mm, $r_0 = 4$ mm.

Membrane ruptured	**Energy original pulse**	**Energy reflected pulse**	**Energy transmitted pulse**	**Energy absorption coefficient α_{energy}**
Tin foil	1.0081e+03	895.0747	7.0597	0.1051
Baking paper	1.2098e+03	1.2033e+03	10.9479	-0.0037
Mylar 23 μm	7.6816e+03	8.1991e+03	44.4468	-0.0711

Table 7.11. Energy absorption coefficient calculations for pancake absorber. Shock tube, first pulse analyses. Dimensions are $d_c = 3$ mm, $d_p = 1$ mm, $L = 30$ mm, $r_0 = 4$ mm, and $R = 50$ mm.

7.9. Profile Absorber – Metallic. Rigid Backing Set-Up

Profile absorbers (both linear and exponential configurations) have been developed further from that of the previous laboratory-built (section 7.6) and 3D printed profiles (section 7.7). All linear and exponential profile structures presented here in section 7.9 consist of metallic plates. Each sample has plate thickness 0.5 compared to other profiles (therefore $d_p = 1$ mm) shown by sections 7.6 – 7.7. External plates of the structures have radius double to that of the aforementioned profiles given by sections 7.6 – 7.7. Thus, plate radius $R = 50$ mm (metallic) $= 2R$ (of plastic and 3D printed profiles). The metallic profiles are also built with a constant cavity thicknesses for each sample, where $d_c = 2$ mm and $d_c = 3$ mm. Full description of dimensions used for linear and exponential profiles is presented elsewhere, see Chapter 4 data, Table 4.1. Performance of the metallic absorbers in both linear and weakly nonlinear regimes can be seen also in Chapters 4 – 6 (Impedance tube data for low and relatively high sound levels, flow resistivity, and model comparisons). The profiles developed for testing in the shock tube are built with different sample lengths. Emphasis is on the absorber performance when excited with a greater amplitude of sound from those already presented by previous Chapters (where SPL ranges 70 dB – 140 dB). Figures 7.62 – 7.82 shows the data from measurements performed in rigid backing set-up with the metallic linear profile. This is followed by Figures 4.83 – 4.96 which present the metallic exponential profile. Data for the former (Figures 7.62 – 7.82) is presented firstly and begins with a linear profile which has a main pore opening $2r_0 = 30$ mm, plate thickness $d_p = 1$ mm, cavity thickness $d_c = 3$ mm and sample length $L = 60$ mm. Main pore with radius r_0 is then made larger by reassembling the sample (see data given by Figures 4.69 – 4.75) where main pore opening becomes $2r_0 = 50$ mm, $d_p = 1$ mm, $d_c = 2$ mm and sample length increases to $L = 80$ mm. The linear configuration is then extended further and the absorber performance tested (structure with additional d_c). This is when $d_c = 3$ mm instead of $d_c = 2$ mm, however, main pore opening remains the same, where $r_0 = 25$ mm, $d_p = 1$ mm, and sample length becomes $L = 100$ mm. Data is given by Figures 7.76 – 7.82.

Figure 7.60. Profile structure sections comprised of plates with varying pore radius r_0.

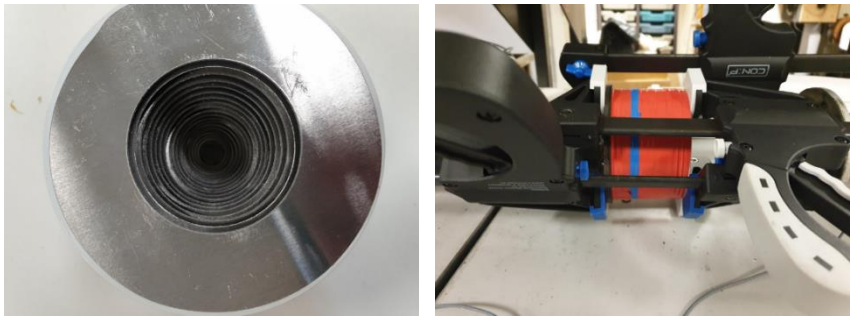

Figure 7.61. Profile structure complete (left) and absorber fixed and clamped ready for shock tube measurements to be performed (right).

Figure 7.60 shows sectional components of a profile build. The sample is constructed together using various sections of plates and rings which are stacked, before combining together. And Figure 7.61 shows the profile structure complete including when the profile is in its mounted position and fixed to the shock tube, for performing the high amplitude shock measurements. Exponential profiled absorbers are built later and tested in the shock tube with sample lengths same as the linear profile configurations, for when front pore radius is $r_0 = 25$ mm. Data for the exponential configurations is presented by Figures 7.83 – 7.89 and shown first when $d_p = 1$ mm, $d_c = 2$ mm and sample length is $L = 80$ mm. The absorber is then re-built with thicker cavity depths so that $d_c = 3$ mm. Plate thickness remains the same therefore $d_p = 1$ mm, and sample length increases from $L = 80$ mm to $L = 100$ mm. The main pore opening remains the same similarly like the linear configuration so that the radius is $r_0 = 25$ mm. This means that the exponential profile has identical sample length L for when $d_c = 2$ mm and $d_c = 3$ mm, see data given by Figures 7.90 – 7.96. Data for the profile with the shortest sample length is given first. Figures 7.62 – 7.64 show pressure measured as a function of time for linear profile with pore radius $r_0 = 15$ mm, $d_p = 1$ mm and $d_c = 3$ mm. Measurements are performed using ruptured tin foil, Mylar 23 μm and Mylar 50 μm. Sample length $L = 60$ mm. Figure 7.62 shows first pulse analysis for a tin foil rupture for the linear profile absorber. Peak pressure of the incident shock pulse in empty tube is measured 18930 Pa and has SPL close to 179 dB. Incident and reflected pulses from the rigid backing measurement are 15900 Pa and 12350 Pa, respectively. Analysis of the reflected pulses measured from signal 2 transducer is performed and reflected pulses are obtained for the rigid backing and profile absorber. Peak pressure for reflected rigid backing was 13440 Pa which corresponds to a sound pressure level of 176 dB. Profile reflected pulse had a measured peak value 9000 Pa and SPL was 173 dB.

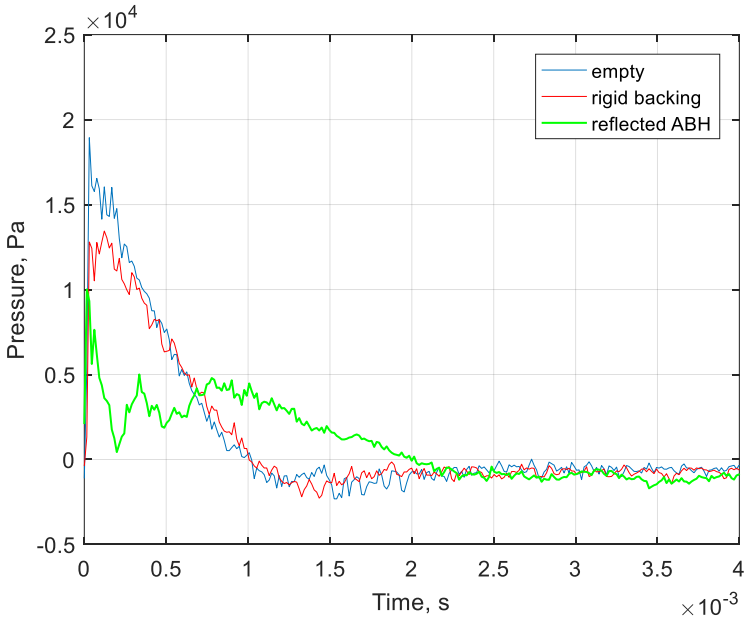

Figure 7.62. Pressure as a function of time for linear profile absorber. Dimensions are $r_0 = 15$ mm, $d_p = 1$ mm, $d_c = 3$ mm, $R = 50$ mm, and $L = 60$ mm. Shock tube, first pulse analysis, signal 2 in rigid backing set up. Membrane ruptured is tin foil.

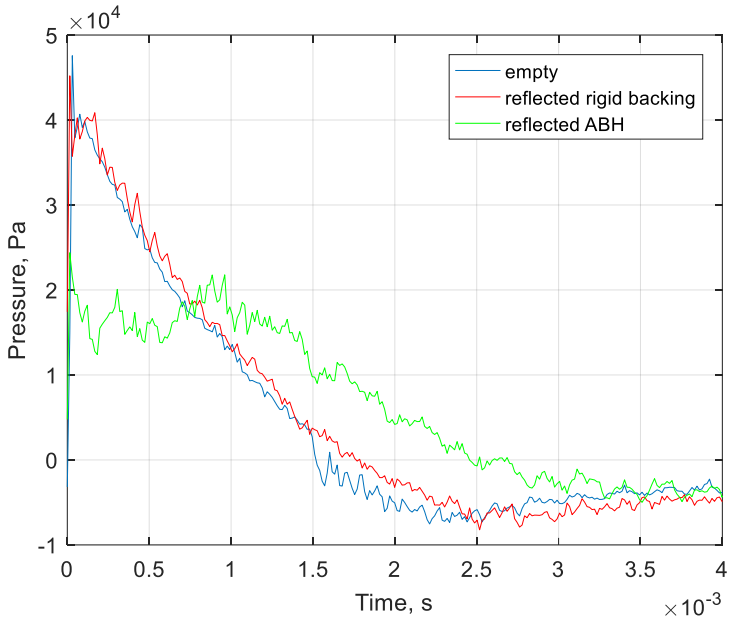

Figure 7.63. Pressure as a function of time for linear profile absorber. Dimensions are $r_0 = 15$ mm, $d_p = 1$ mm, $d_c = 3$ mm, $R = 50$ mm, and $L = 60$ mm. Shock tube, first pulse analysis, signal 2 in rigid backing set up. Membrane ruptured is Mylar 23 μm.

Figure 7.63 shows first pulse analysis for a linear profile absorber by Mylar 23 μm explosion. Peak pressure for the incident pulse from empty tube was 47570 Pa and had sound pressure level close to 187 dB. Incident and reflected pulses from the rigid backing measurement were 48340 Pa and 49400 Pa, respectively. Analysis is then performed for rigid backing and profile reflected pulses measured at signal 2. Peak pressure for reflected rigid backing is measured 45200 Pa which equates to a SPL being 187 dB. Reflected pulse measured for the profile has a peak pressure 24380 Pa which is significantly less to that of the simple rigid backing case. The associated SPL is nearly 182 dB. Data presented by Figure 7.64 shows when pressure is increased from a Mylar 50 μm explosion. Pulse amplitude is significantly larger than other membranes ruptured. Incident peak pressure of the first pulse at signal 2 for ruptured Mylar 50 μm and empty tube data measured 68840 Pa. The pulse from the profile measurement at signal 2 before and after interaction with the sample was 70880 Pa and 75120 Pa, respectively. Sound pressure levels for the former and latter is close to 191 dB and 192 dB. After first pulse analysis the reflected peak pressures for rigid backing and profile are 67060 Pa and 45200 Pa, respectively. The sound pressure levels were 190 dB (for reflected rigid backing) and 187 dB (profile). This results in the profile absorber producing a SPL reduction of nearly 4 dB for high amplitudes and peak pressures around 70000 Pa.

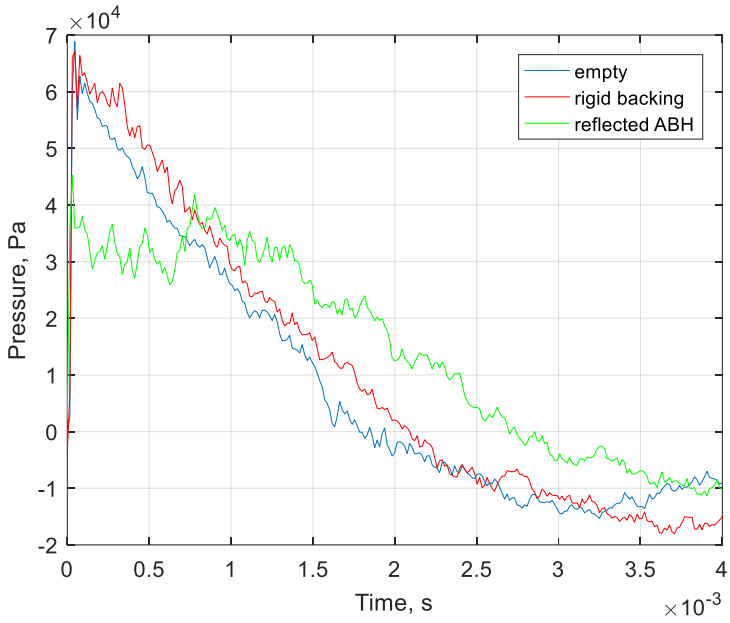

Figure 7.64. Pressure as a function of time for linear profile absorber. Dimensions are $r_0 = 15$ mm, $d_p = 1$ mm, $d_c = 3$ mm, $R = 50$ mm, and $L = 60$ mm. Shock tube, first pulse analysis, signal 2 in rigid backing set up. Membrane ruptured is Mylar 50 μm.

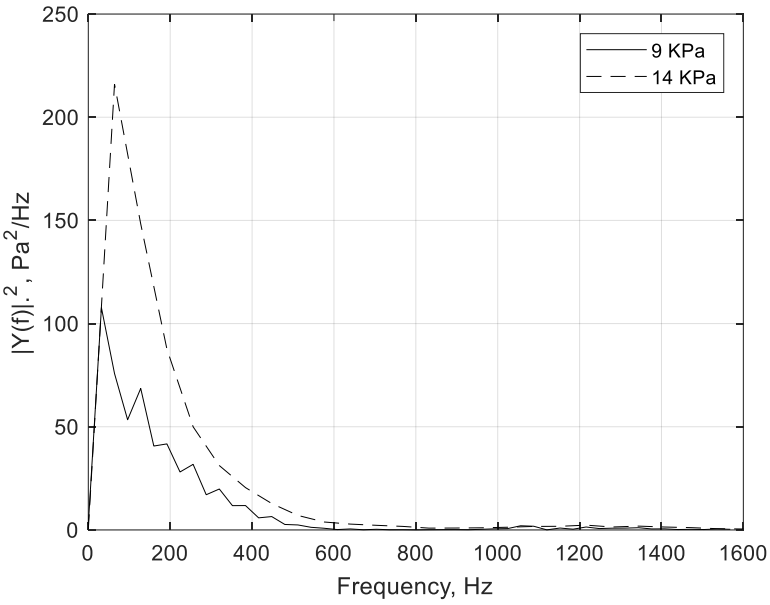

Figure 7.65. Single-sided amplitude spectrum of reflected signals for the linear profile. Membranes ruptured are tin foil (solid line) and baking paper (dash).

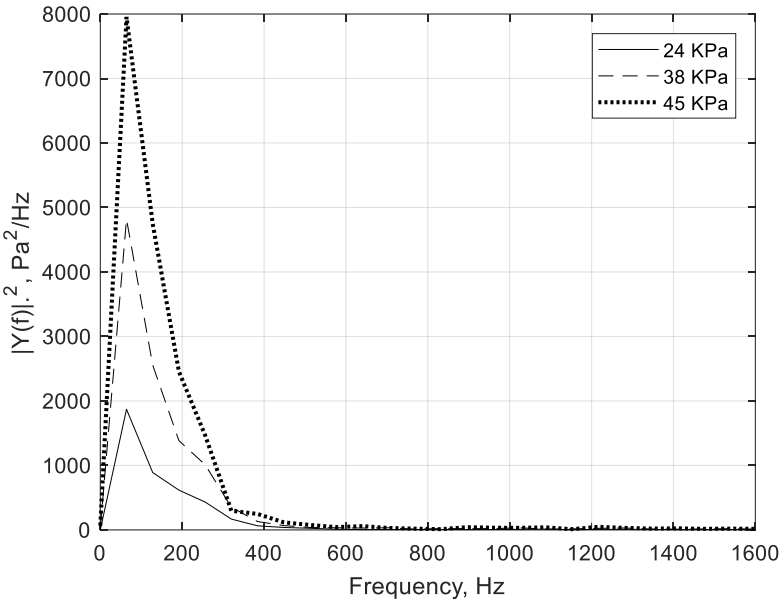

Figure 7.66. Single-sided amplitude spectrum of reflected signals for the linear profile. Membranes ruptured are Mylar 23 μm (solid line), Mylar 40 μm (dash) and Mylar 50 μm (dot).

The amplitude ratios of the reflected pressures for the linear profile absorber is calculated from the data shown by Figures 7.62 – 7.64 (membrane ruptures tin foil, Mylar 23 um and Mylar 50 μm). Reflected pressure ratios from the ruptured membranes are 45.0 %, 50.8 % and 63.8 % respectively. Incident and reflected peak pressures from the tin foil explosion (with linear profile configuration $r_0 = 15$ mm, $d_p = 1$ mm, $d_c = 3$ mm and $L = 60$ mm) are 20000 Pa and 9000 Pa, respectively. The peak amplitudes ratios from ruptured Mylar 23 μm are calculated using pressures 48000 Pa and 24380 Pa. Measured values used from the Mylar 50 μm rupture are incident and reflected pulses with peak pressures 70880 Pa and 45200 Pa. This results in a peak reduction for the incident peak pressure 55.0 % (from the tin foil measurement). Profile data of the ruptured Mylar membranes show that incident amplitude of the shock pulse at signal 2 obtained peak reductions 49.2 % and 36.2 % for Mylar 23 μm and Mylar 50 μm, respectively. Single-sided amplitude spectra of reflected signals from explosions tin foil and baking paper is shown by Figure 7.65. The former membrane corresponds to an amplitude 9000 Pa and 14000 Pa for the latter. Energy of the reflected pulses is associated mostly up to $f = 600$ Hz. Figure 7.66 shows single-sided amplitude spectra for reflected signals of ruptured Mylar 23 μm, Mylar 40 μm and Mylar 50 μm membranes. Their corresponding peak pressures equates to 24000 Pa, 38000 Pa and 45000 Pa, respectively.

Majority of energy associated with the reflected pulses for the ruptured Mylar membranes is toward $f = 400$ Hz. The data from the Mylar 50 μm explosion shows a reflected pulse with significantly larger amplitude compared to other reflected pulses by membranes of less tensile strength. Table 7.12 shows data computed for reflected energies of the membranes discussed above (tin foil, baking paper, Mylar 23 μm, Mylar 40 μm and Mylar 50 μm). Energy absorption coefficient (see Table 7.12) calculated for the metallic profile shows how effective the absorber is, similarly, like data from other profile measurements (see Tables 7.9 – 7.10 in section 7.7 for 3D printed profile absorbers). In Figures 7.67 – 7.68 absorption coefficient is plotted as a function of frequency, obtained from performing FFT on the reflected pulses (see section 7.7 for a more comprehensive description). Reflected pulses with lowest measured

pressures from tin foil and baking paper is shown by Figure 7.67 where α is sufficiently broadband. Maximum absorption occurs at frequencies around $f = 500\ \mathrm{Hz} - 1000\ \mathrm{Hz}$ where α is close to 1.0. Obviously, large values of α are due to low amplitudes of spectral components at higher frequencies.

Figure 7.68 shows absorption coefficient as a function of frequency for reflected pressures 24000 Pa, 38000 Pa and 45000 Pa, from ruptured Mylar membranes. Absorption coefficient is close to $\alpha = 0.9$ between $f = 500\ \mathrm{Hz} - 1000\ \mathrm{Hz}$. Peak absorption values are slightly lower for the Mylar membranes across the frequency spectrum compared to membranes consisting of lesser tensile strength, shown in Figure 7.67. However, in the case of the Mylar membranes, even though α is reduced slightly across the spectrum, onset of absorption coefficient is shifted to lower frequencies. It is determined from the data presented thus far that the profile absorber performance far exceeds far the performance of the pancake absorber. The pancake absorber was measured against much lower amplitudes compared to the profile, yet the metallic linear profile is far superior when constrained with high amplitude shock formations.

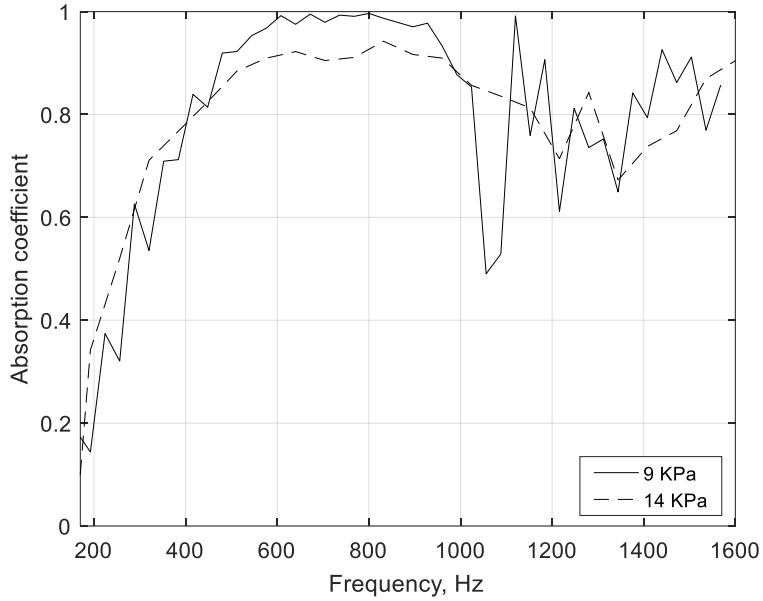

Figure 7.67. Absorption coefficient as a function of frequency for linear profile. Membranes ruptured are tin foil (solid line), baking paper (dash).

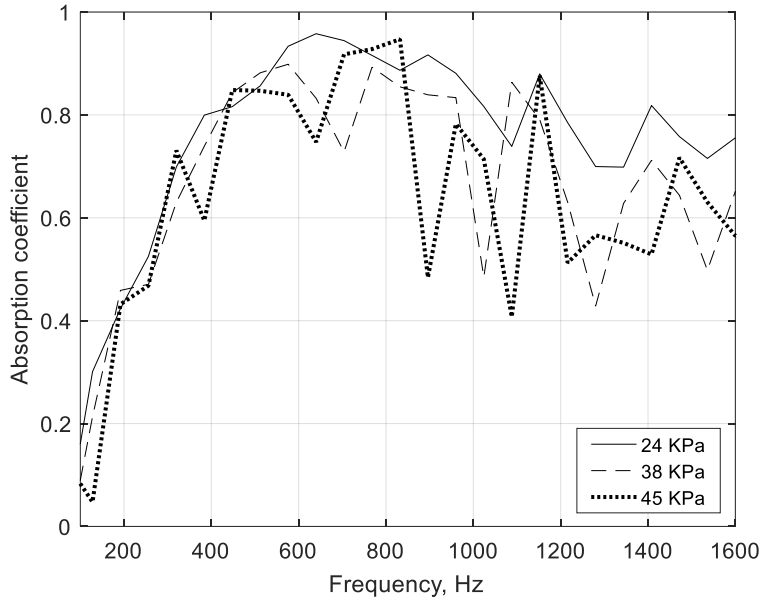

Figure 7.68. Absorption coefficient as a function of frequency for linear profile. Membranes ruptured are Mylar 23 µm (solid line), Mylar 40 µm (dash) and Mylar 50 µm (dot).

Membrane ruptured	Energy original pulse	Energy reflected pulse	Energy absorption coefficient α_{energy}
Tin foil	1.0310e+03	596.2956	0.4216
Baking paper	1.2098e+03	653.3640	0.4599
Mylar 23 µm	7.6816e+03	4.3639e+03	0.4319
Mylar 40 µm	1.6900e+04	1.1074e+04	0.3448
Mylar 50 µm	2.7944e+04	1.8435e+04	0.3403

Table 7.12. Energy absorption coefficient for the linear profile absorber. Dimensions are $r_0 = 15$ mm, $d_p = 1$ mm, $d_c = 3$ mm and $L = 60$ mm. Shock tube, first pulse analysis, signal 2 with rigid backing.

Figures 7.69 – 7.71 shows the linear profile data from measurements performed with additional d_p and d_c distributed along the sample length in rigid backing set-up. The linear profile with main pore $r_0 = 15$ mm is reassembled so that the main pore now begins with $r_0 = 25$ mm. Dimensions of d_c is changed to $d_c = 2$ mm and sample length is extended due to the increased number of cavities d_c and plates d_p. The sample length therefore becomes 20 mm larger and becomes $L = 80$ mm. Plate thickness remains unchanged therefore $d_p = 1$ mm. This is to ensure that total sample length is kept to a reasonable thickness and not too large. Figure 7.69 shows pressure as a function of time for ruptured tin foil. Empty tube measurement of the pulse reflected from rigid backing at signal 2 had a peak pressure 19000 Pa and SPL 179 dB. The pulse reflected from the absorber at signal 2 is measured 20560 Pa and sound pressure level around 180 dB. Incident pulse of the rigid backing measurement at signal 2 had a peak pressure 23200 Pa. The reflected pressure of the super-positioned pulse in rigid backing was 19040 Pa (absent the profile) and 6510 Pa with the profile. After first pulse analysis the reflected pulses have peak pressures 18930 Pa (for case of rigid backing mode absent the profile) and 7520 Pa (with the profile).

Figure 7.70 shows data from first pulse analysis from a Mylar 23µm explosion. Peak pressure of the incident pulse obtained from empty tube measured 47570 Pa at signal 2 and sound pressure level was 187 dB. Incident pulse at signal 2 for the rigid backing measured 48340 Pa. Incident pulse of the profile absorber at signal 2 had a peak pressure measuring 48990 Pa and SPL equating 188 dB. Reflected pulse measured by transducer signal 2 for the superimposed pulse had a peak pressure (absent the

profile) 49400 Pa corresponding to SPL 187 dB. Reflected pulse measured 30590 Pa for the profile signal before first pulse analysis was performed and SPL was close to 186 dB. After first pulse analysis the peak pressure for the pulse is obtained and measures 21560 Pa with sound pressure level 184 dB. Data given by Figure 7.71 is for ruptured membrane Mylar 50 μm. The incident peak pressure of the first pulse at signal 2 measured 68840 Pa (empty shock tube explosion). The profile measurement at signal 2 before interaction with the sample was 69470 Pa. Sound pressure levels for the former and latter is approximately 191 dB. Incident pulse measured at signal 2 for rigid backing is 69850 Pa. The reflected super positioned shock pulses for rigid backing and linear profiled absorber had peak pressures 83370 Pa and 43150 Pa, respectively. Following first pulse analysis the reflected peak pressure for the rigid backing is measured 66370 Pa and sound pressure level equates to 190 dB. The linear profile was able to dramatically reduce the incident pulse, where the reflected shock pulse had a peak pressure 39000 Pa.

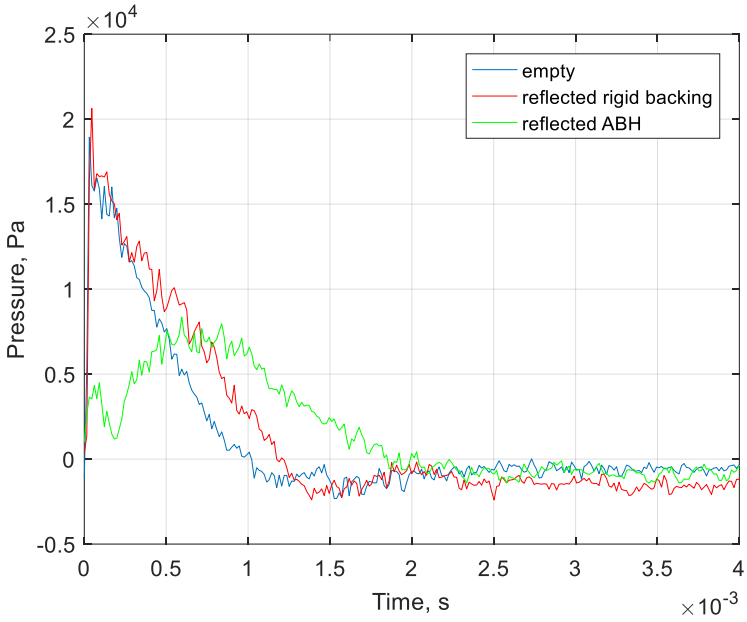

Figure 7.69. Pressure as a function of time for linear profile absorber. Dimensions are $r_0 = 25$ mm, $d_p = 1$ mm, $d_c = 2$ mm, $R = 50$ mm, and $L = 80$ mm. Shock tube, first pulse analysis, signal 2 in rigid backing set up. Membrane is tin foil.

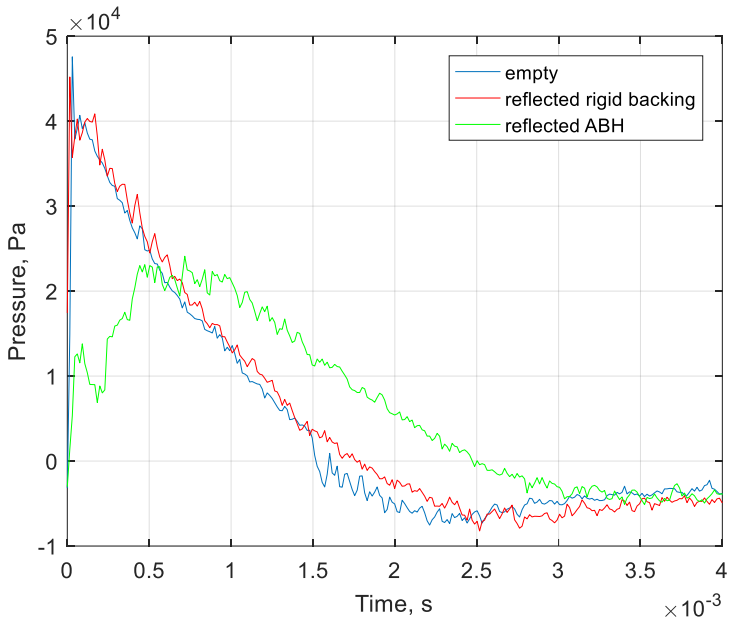

Figure 7.70. Pressure as a function of time for linear profile absorber. Dimensions are $r_0 = 25$ mm, $d_p = 1$ mm, $d_c = 2$ mm, $R = 50$ mm, and $L = 80$ mm. Shock tube, first pulse analysis, signal 2 in rigid backing. Membrane is Mylar 23 µm.

Amplitude ratios of the reflected pressures for the linear profile are calculated from the data shown by Figures 7.69 – 7.71. The reflected peak pressure ratios from that of the incident pulses for the membrane explosions are 36.6 %, 44.0 % and 56.1 % respectively. Incident and reflected peak pressures for the tin foil were 20560 Pa and 7520 Pa, respectively. For Mylar 23 µm, the peak amplitudes ratios are calculated using values 48990 Pa and 21560 Pa. The ruptured Mylar 50 µm membrane provided incident and reflected pulses with peak pressures 69470 Pa and 39000 Pa, respectively. This results in a peak reduction of the incident pulse 63.4 % for the ruptured tin foil measured at signal 2. Incident amplitude of the shock pulse for the profile from the ruptured Mylar membranes show that the measured data at signal 2 result in peak reductions 56.0 % and 43.9 % for Mylar 23 µm, 50 µm, respectively.

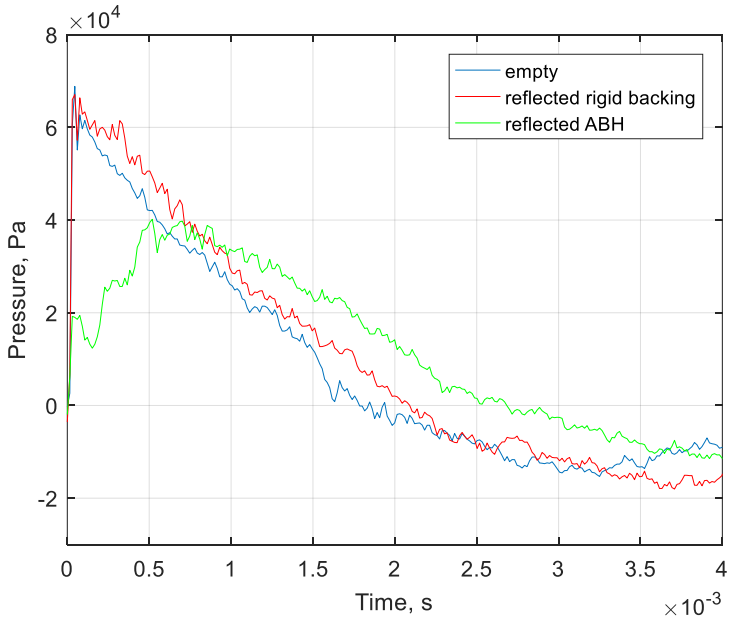

Figure 7.71. Pressure as a function of time, linear profile. Dimensions, $r_0 = 25$ mm, $d_p = 1$ mm, $d_c = 2$ mm, $R = 50$ mm, and $L = 80$ mm. Shock tube, first pulse analysis, signal 2 rigid backing. Membrane ruptured Mylar 50 µm.

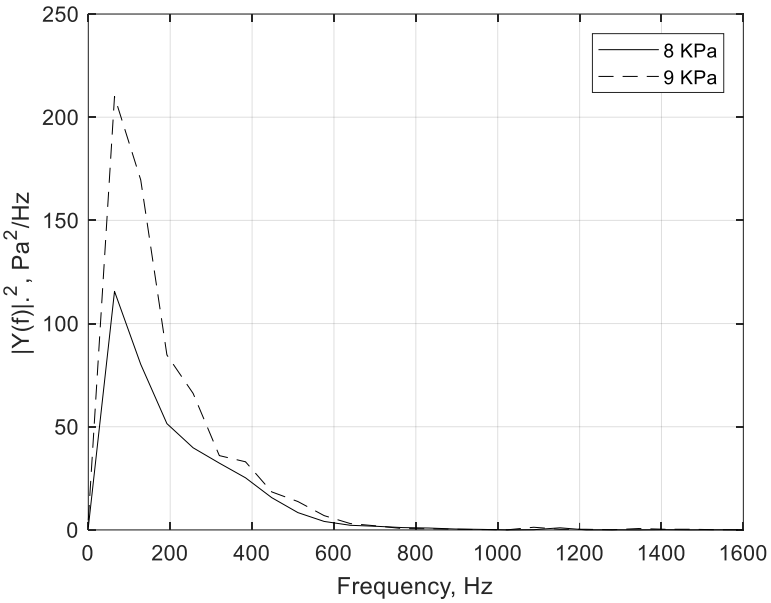

Figure 7.72. Single-sided amplitude spectrum of reflected signals for linear profiled absorber. Membranes ruptured are tin foil (solid line) and baking paper (dash).

Single-sided amplitude spectra of reflected signals for the metamaterial linear profile absorber is given by Figure 7.72 (for membranes tin foil and baking paper). The former corresponds to an amplitude 8000 Pa and 9000 Pa for the latter. Energy of the reflected pulses is associated mostly in the frequency region toward $f = 600\ \mathrm{Hz}$. Figure 7.73 shows single-sided amplitude spectrum of reflected signals from ruptured Mylar membranes (23 μm, 40 μm, 50 μm). Their peak pressures are 22000 Pa, 33000 Pa and 38000 Pa, respectively. Energy of their reflected pulses are mostly contained up to $f = 400\ \mathrm{Hz} - 500\ \mathrm{Hz}$. Table 7.13 presents the calculated data for the reflected energies obtained from different explosions by membranes of different tensile strength. The values are more desirable than previous data given by other structures tested (from pancake and previous profile absorbers presented in earlier sections of Chapter 7, for high amplitude shocks). Energy absorption coefficient is computed as the ratio of total energy from reflected pulses of rigid backing and profiled absorber and is obtained after first pulse analysis of the measured shock pulses (using reflected pulses from signal 2).

The linear profile structure produces a significant peak reduction including when amplitude strength is large. Energy absorption α_{energy} coefficient is calculated as $1 - E_{ab}/E_{rb,}$ where E_{ab} is energy in original reflected signal (absorber) and E_{rb} is energy in original rigid backing signal. A description of how the pulses are used and FFT performed to obtain the spectral density is given in section 7.7. It is clear from data shown by Figures 7.69 – 7.71 and values presented in Table 7.13 that the profile absorber is much more effective compared to simple rigid backing (especially when amplitude strength is least i.e. for the tin foil and baking paper explosions). Consequently, this is reflected in the values obtained for the calculated energy absorption coefficient. As amplitude strength of the reflected signals grows, absorption coefficient is seen to reduce across the frequency spectrum, however, large values of α exist (where $\alpha = 0.9$ at $f = 600\ \mathrm{Hz} - 1600\ \mathrm{Hz}$ for peak pressures nearly 1000 Pa, and $\alpha = 0.9$ at around $f = 800\ \mathrm{Hz} - 1600\ \mathrm{Hz}$ for the pulses with peak pressure toward 40000 Pa). Absorption coefficient becomes close to $\alpha = 1.0$ for tin foil and baking paper explosions at around $f = 1000\ \mathrm{Hz} - 1600\ \mathrm{Hz}$ and similarly for Mylar membrane explosions but at slightly higher frequencies. However, at lower frequencies $f =$

$200\ \mathrm{Hz} - 400\ \mathrm{Hz}$ then $\alpha = 0.7$ for tin foil and baking paper. For the Mylar membranes, α varies with amplitude strength and ranges $\alpha = 0.4 - 0.7$ at lower frequencies, see Figures 7.74 – 7.75.

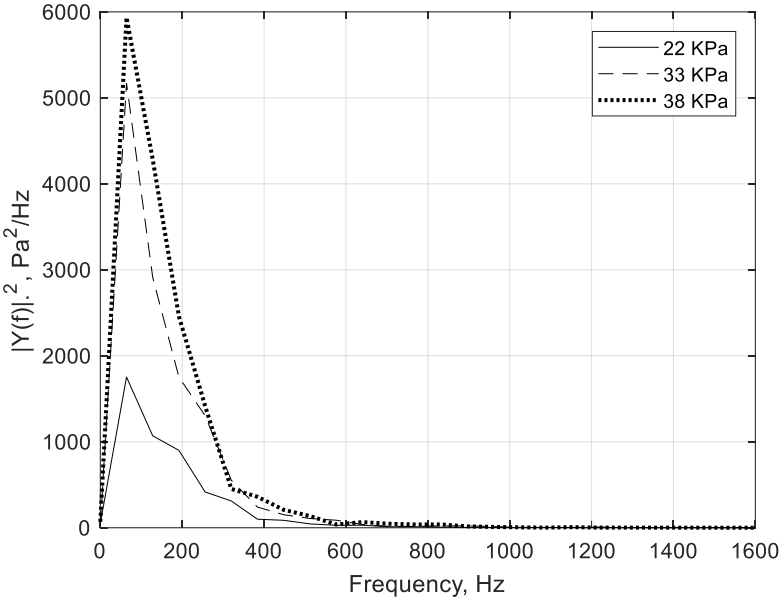

Figure 7.73. Single-sided amplitude spectrum of reflected signals for linear profiled absorber. Membranes ruptured are Mylar 23 μm (solid line), Mylar 40 μm (dash) and Mylar 50 μm (dot).

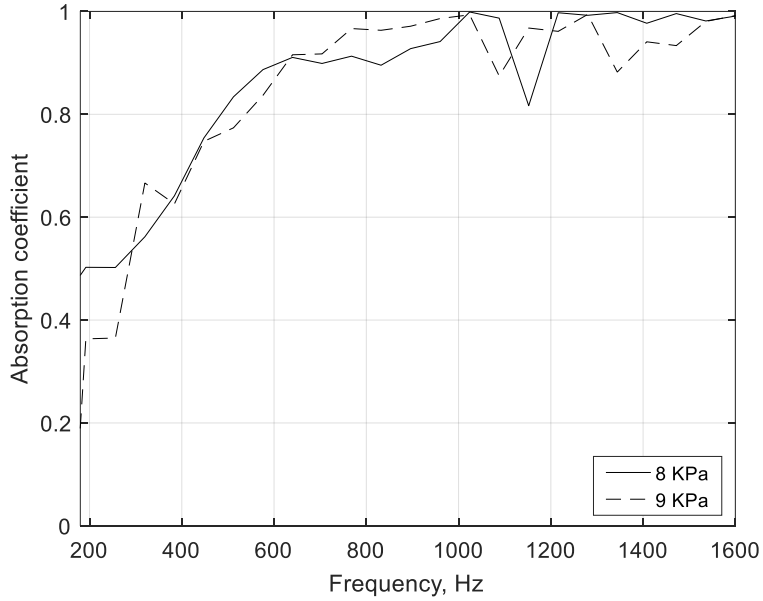

Figure 7.74. Absorption coefficient as a function of frequency for linear profile. Membranes ruptured are tin foil (solid line), baking paper (dash).

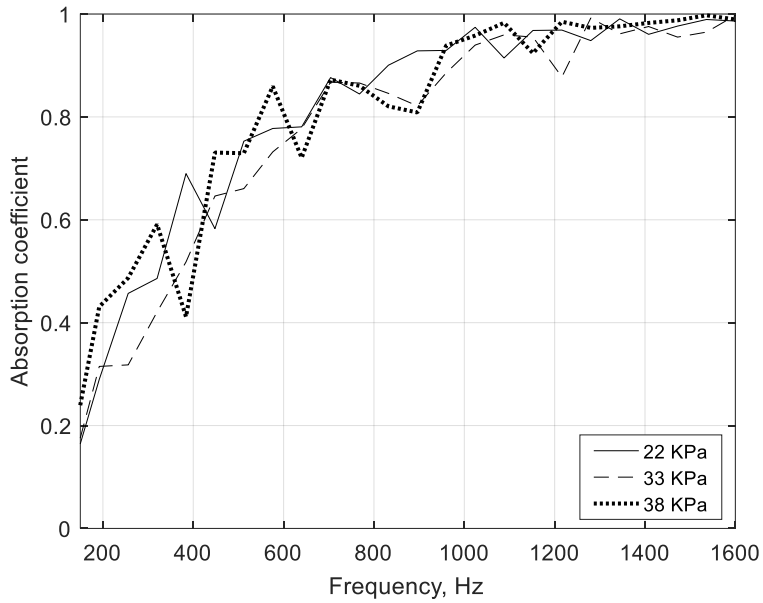

Figure 7.75. Absorption coefficient as a function of frequency for linear profile. Membranes ruptured are Mylar 23 μm (solid line), Mylar 40 μm (dash) and Mylar 50 μm (dot).

Membrane ruptured	Energy original pulse	Energy reflected pulse	Energy absorption coefficient α_{energy}
Tin foil	1.0335e+03	394.4887	0.6183
Baking paper	1.2098e+03	678.9416	0.4388
Mylar 23 μm	7.6221e+03	4.9053e+03	0.3564
Mylar 40 μm	1.6900e+04	1.2582e+04	0.2555
Mylar 50 μm	2.7944e+04	1.5741e+04	0.4367

Table 7.13. Energy absorption coefficient for the linear profile absorber. Dimensions are $r_0 = 25$ mm, $d_p = 1$ mm, $d_c = 2$ mm and $L = 80$ mm. Shock tube, first pulse analysis, signal 2 with rigid backing.

The profile is again rebuilt larger by reassembling the sample with different values of d_c so that $d_c = 3$ mm instead of the previous case (when $d_c = 2$ mm). The main pore however, remains the same value where $r_0 = 25$ mm. Plate thickness $d_p = 1$ mm, and sample length is altered by applying the new values d_c and therefore results in new sample length $L = 100$ mm. Configuration of the profile absorber is linear and has an external plate radius $R = 50$ mm. The linear profile data is shown by Figures 7.76 – 7.82.

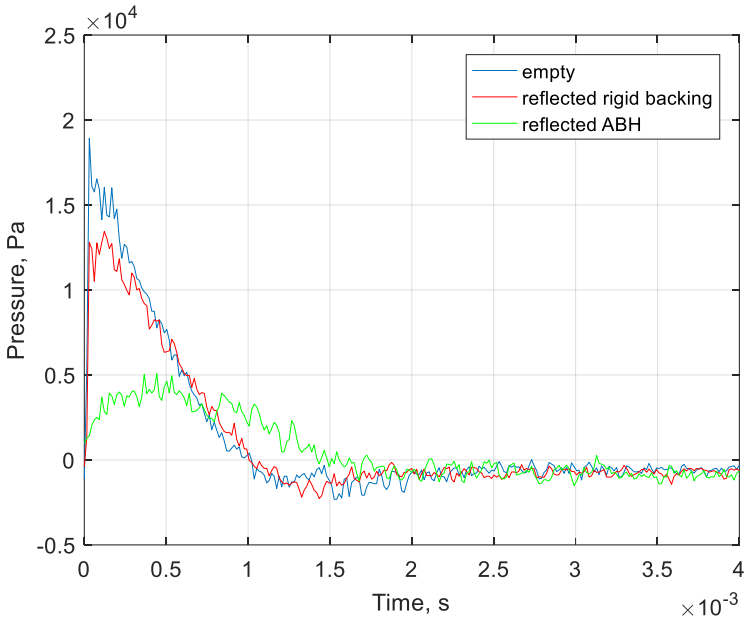

Figure 7.76. Pressure as a function of time for linear profile. Dimensions, $r_0 = 25$ mm, $d_p = 1$ mm, $d_c = 3$ mm, $R = 50$ mm, and $L = 100$ mm. Shock tube, first pulse analysis, signal 2 in rigid backing set up. Membrane is tin foil.

Figure 7.76 shows pressure as a function of time from ruptured membrane tin foil. Empty tube measurement at signal 2 for rigid backing had peak pressure 19000 Pa and sound pressure level 179 dB. Incident pulse of the rigid backing measurement at signal 2 had peak pressure 23200 Pa. The profile measurement at signal 2 (incident) had a measured peak pressure 19260 Pa and SPL 180 dB. Reflected pressure of the super-positioned pulse in rigid backing mode is 19040 Pa absent the profile and 4753 Pa with profile absorber present. After first pulse analysis the reflected pulses have peak pressures 14000 Pa for the rigid backing absent the profile, and 4500 Pa with the profile.

This corresponds to sound pressure levels 177 dB for the former, and 166 dB for the latter. Figure 7.77 shows data obtained from first pulse analysis for linear profile absorber with Mylar 23μm explosion. Peak pressure of the incident shock pulse from empty tube measured at signal 2 was 47570 Pa and had a sound pressure level 187 dB. Incident pulse measured at signal 2 for the rigid backing measured 48340 Pa. The incident pulse for the profile absorber measurement at signal 2 had peak pressure 48300 Pa and SPL 188 dB. Reflected pulse measured at signal 2 had superimposed pulse with peak pressure (absent the profile) being 49400 Pa corresponding to sound pressure level 187 dB. Reflected superimposed pulse from the measured signal of the profile measurement before first pulse analysis was 16740 Pa and SPL 178 dB. Reflected rigid backing and profile absorber measurements after first pulse analysis have peak pressures 45200 Pa and 15000 Pa, respectively. Their associated sound pressure levels are 187 dB for rigid backing and 177 dB for the profile structure.

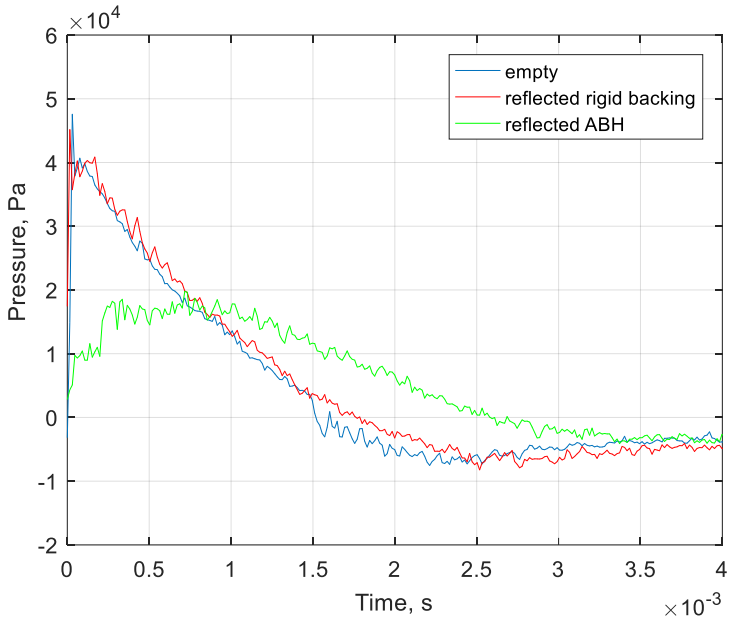

Figure 7.77. Pressure as a function of time for linear profile. Dimensions, $r_0 = 25$ mm, $d_p = 1$ mm, $d_c = 3$ mm, $R = 50$ mm, and $L = 100$ mm. Shock tube, first pulse analysis, signal 2 in rigid backing. Membrane ruptured is Mylar 23 μm.

Mylar 50 μm membrane is ruptured and its data for reflected pressures are presented in Figure 7.78. Explosion in empty tube had an incident peak pressure (first pulse at signal 2) 69000 Pa. Peak pressure for the profile measurement at signal 2 for the incident pulse before interaction with the sample is 71080 Pa. Incident pulse measured at signal 2 for rigid backing was 69850 Pa. Sound pressure levels for the measurements performed in empty tube, rigid backing only, and with the profile are all identical at nearly 191 dB. Reflected super positioned shock pulses for rigid backing and the linear profiled absorber had peak pressures 83370 Pa and 36160 Pa, respectively. Following first pulse analysis the reflected peak pressure for the rigid backing measurement is 67000 Pa. Its associated sound pressure level is nearly 191 dB. The linear profile absorber was able to dramatically reduce the incident shock pulse after interaction with the sample at extremely high pressures. After first pulse analysis peak pressure of the reflected shock for the profile sample is measured 33000 Pa. The amplitude ratios of the reflected peak pressures for the linear profile are calculated from data shown in Figures 7.76 – 7.78 from membrane ruptures of tin foil, Mylar 23 μm and Mylar 50 μm.

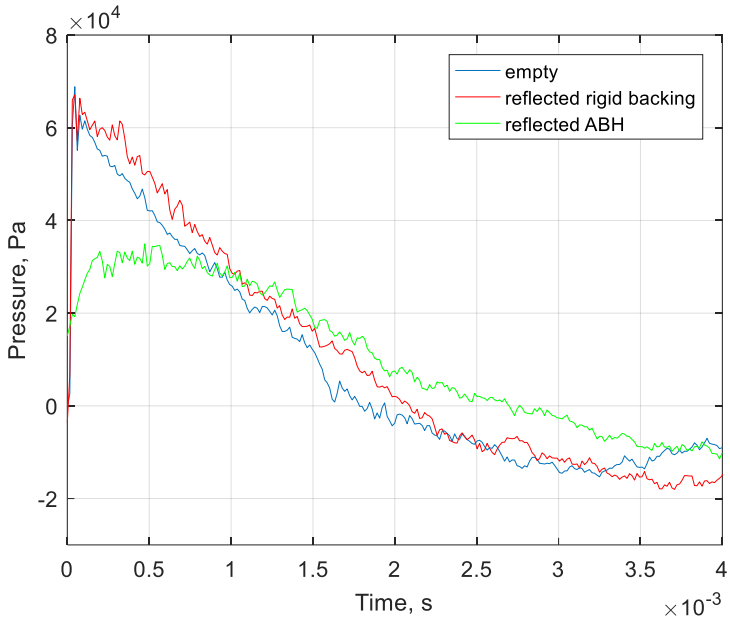

Figure 7.78. Pressure as a function of time for linear profile. Dimensions, $r_0 = 25$ mm, $d_p = 1$ mm, $d_c = 3$ mm, $R = 50$ mm, and $L = 100$ mm. Shock tube, first pulse analysis, signal 2 in rigid backing set up. Membrane ruptured is Mylar 50 μm.

Reflected peak pressure ratios from that of the incident pulses from the above membrane ruptures are 23.3 %, 31.0 % and 46.4 % respectively. Profile configuration is when $r_0 = 25$ mm, $d_p = 1$ mm and cavity thickness altered from $d_c = 2$ mm to $d_c = 3$ mm, sample length $L = 100$ mm. Incident and reflected peak pressures for the ruptured tin foil membrane were 19260 Pa and 4500 Pa, respectively, see Figure 7.76. For Mylar 23 μm the peak amplitudes ratios are calculated using values 48300 Pa and 15000 Pa. Measured values of the Mylar 50 μm ruptured membrane are for incident and reflected peak pressures 71080 Pa and 33000 Pa, respectively. This results in a peak reduction of the incident peak pressure 76.7 % for tin foil measured at signal 2. The Mylar membranes show that incident amplitude of the shock pulse measured at signal 2 have peak reductions 69.0 % for Mylar 23 μm and 53.6 % for Mylar 50 μm, see Figures 7.77 – 7.78, respectively. Single-sided amplitude spectra plots (see Figures 7.79 – 7.80) show majority of energy of the reflected pulses is contained mostly in the region toward $f = 600$ Hz. Absorption coefficient given by Figures 7.81 – 7.82 shows that the linear profile is capable of broadband absorption across the entire frequency range $f = 50$ Hz $- 1600$ Hz. Measurements performed for all samples thus far show that as amplitude strength of the reflected signals grow, peak absorption coefficient reduces slightly across the frequency spectrum. Absorption coefficient values from the reflected profile signals from tin foil and baking paper explosions see $\alpha = 0.6$ around $f = 200$ Hz and ranges close to $\alpha = 1.0$ across remainder of the frequency spectrum. For the Mylar membrane explosions $\alpha = 0.6$ from $f = 200$ Hz and has values close to $\alpha = 0.9$ toward $f = 1600$ Hz.

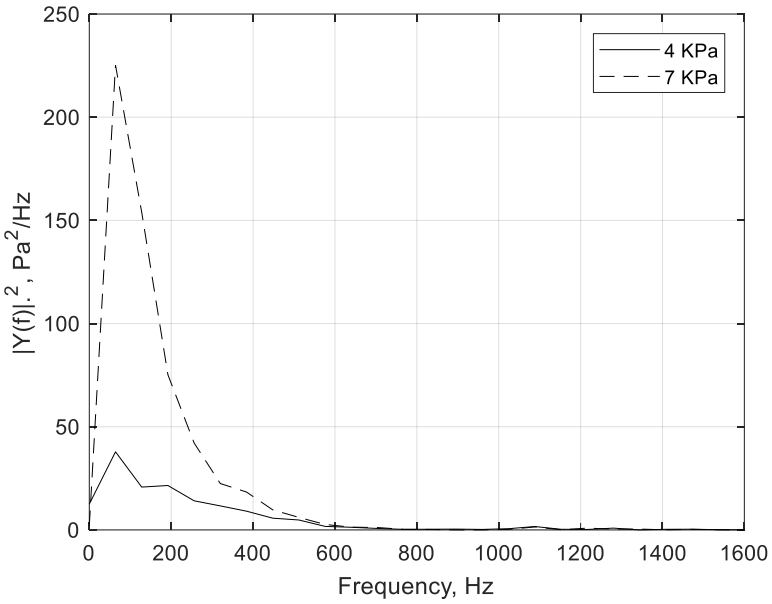

Figure 7.79. Single-sided amplitude spectra of reflected signals for linear profile. Membranes ruptured are tin foil (solid line) and baking paper (dash).

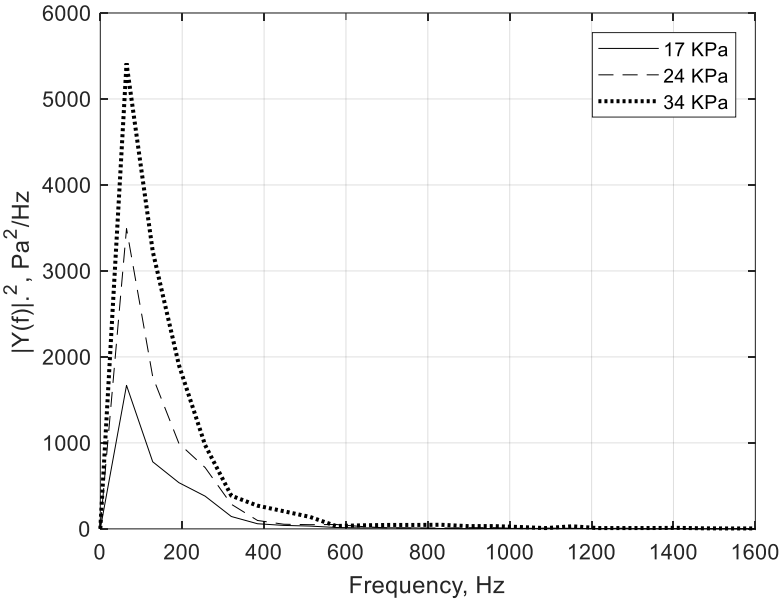

Figure 7.80. Single-sided amplitude spectra of reflected signals for linear profile. Membranes ruptured are Mylar 23 μm (solid line), Mylar 40 μm (dash) and Mylar 50 μm (dot).

Values of the calculated energy absorption coefficient (obtained from performing FFT on the original reflected pulses for both rigid backing and reflected profile signals) is shown by Table 7.14. Values are presented also for other membranes ruptured where energy is calculated using sum of the spectral density of the signals. Energy absorption coefficient α_{energy} is calculated as $1 - E_{ab}/E_{rb}$ where E_{ab} is energy in original reflected signal (absorber) and E_{rb} is energy in original rigid backing signal. Data given by Figures 7.76 – 7.78 and values presented in Table 7.14 show clearly that the metallic linear profile absorber with increased cavity depths is effective against exceptionally large amplitudes which are created in the shock tube. Energy calculated using the reflected pulses show that the linear profile with slightly larger cavity thickness and sample length is more effective (where $d_c = 3$ mm instead of $d_c =$

2 mm and where $L = 100$ mm instead of $L = 80$ mm). This completes the measurements performed in the shock tube for the linear profiled configurations and rigid backing set-up.

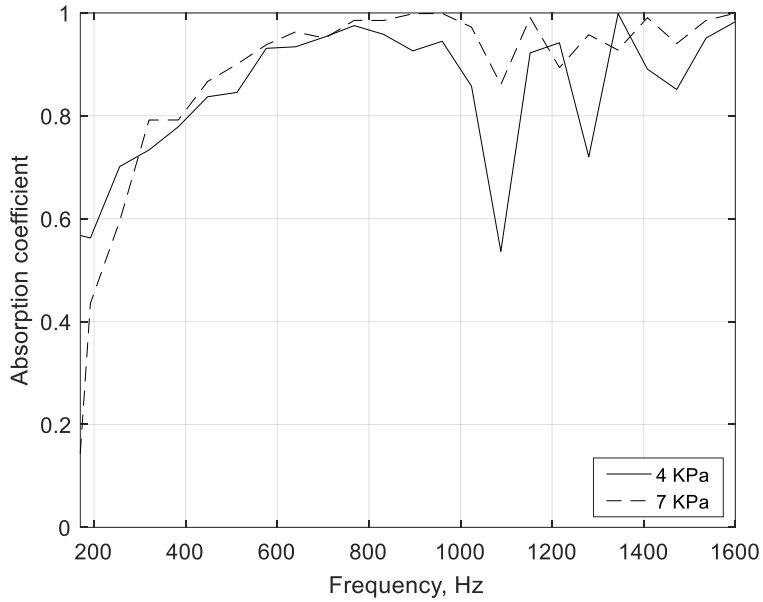

Figure 7.81. Absorption coefficient as a function of frequency for linear profile. Membranes ruptured are tin foil (solid line) and baking paper (dash).

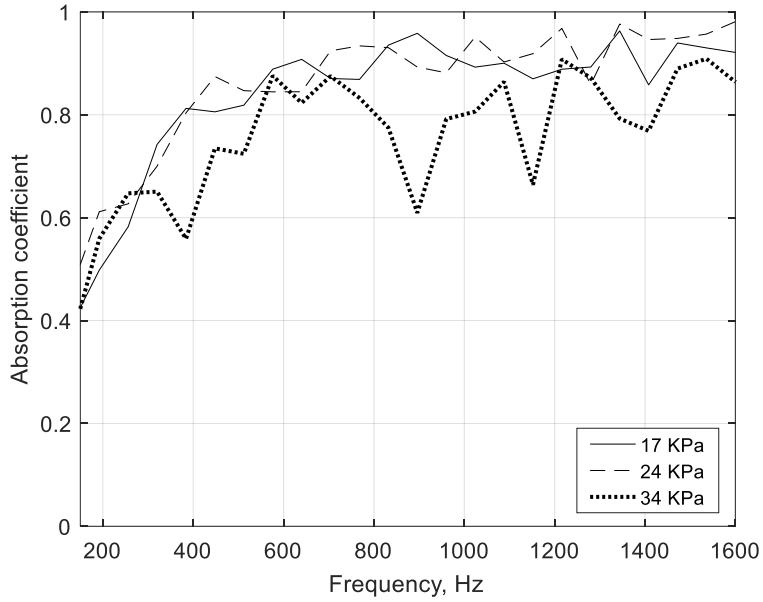

Figure 7.82. Absorption coefficient as a function of frequency for linear profile. Membranes ruptured are Mylar 23 μm (solid line), Mylar 40 μm (dash) and Mylar 50 μm (dot).

Membrane ruptured	Energy original pulse	Energy reflected pulse	Energy absorption coefficient α_{energy}
Tin foil	516.2272	155.6852	0.6984
Baking paper	1.2098e+03	584.0947	0.5172
Mylar 23 μm	7.6816e+03	3.7776e+03	0.5082
Mylar 40 μm	1.6900e+04	7.7142e+03	0.5435
Mylar 50 μm	2.7944e+04	1.3081e+04	0.5319

Table 7.14. Energy absorption coefficient for the linear profile absorber. Dimensions are $r_0 = 25$ mm, $d_p = 1$ mm, $d_c = 3$ mm and $L = 100$ mm. Shock tube, first pulse analysis, signal 2, rigid backing.

The linear profile is disassembled and configured with a new development for the inner pore trajectory. Figures 7.83 – 7.85 show pressure as a function of time for the exponential profile structure. Single-sided amplitude spectrum is given by Figures 7.86 – 7.87 and absorption coefficient by Figures 7.88 – 7.89. Dimensions are as follows; $d_p = 1$ mm, $d_c = 2$ mm, $L = 80$ mm and $R = 50$ mm. Cavity thickness d_c and sample length L is kept consistent with one of the linear profile samples and allows for investigation for a change of decreasing pore radius r_0 with identical d_p, d_c, L, R, and $r_0 = 25$ mm. Figure 7.83 shows pressure as a function of time for ruptured membrane tin foil. Empty tube measurement at signal 2 in the rigid backing set-up has a peak pressure 18930 Pa and sound pressure level 179 dB. The exponential profile measurement at signal 2 has an incident peak pressure 22280 Pa and SPL 181 dB. Reflected pressure from the sample surface superimposed measured at signal 2 is 7500 Pa. Reflected pressures of incident and super-positioned pulses in rigid backing mode is 23200 Pa and 19040 Pa, respectively. Sound pressure levels were 181 dB and 180 dB. After first pulse analysis the reflected pulses have peak pressures 18930 Pa (for case of rigid backing mode absent the profile) and 8627 Pa (with the profile). The former and latter have sound pressure levels close to 180 dB and 172 dB, respectively. Figure 7.84 shows data from first pulse analysis for the exponential profile from Mylar 23 μm explosion. Peak pressure of the incident shock pulse in empty tube is measured 47570 Pa and sound pressure level 187 dB. The profile absorber incident pulse had peak pressure 47190 Pa and sound pressure level also 187 dB. Reflected pulse recorded by the piezoelectric transducer signal 2 measured the incident and reflected pressures (absent the profile absorber) to be 48340 Pa and 49400 Pa respectively corresponding to a SPL 188 dB. Reflected pulse for the measured signal 2 profile, before first pulse analysis is 26100 Pa and SPL close to 182 dB. Sound pressure level of the reflected pulse, following first pulse analysis for the rigid backing was 187 dB (where the peak pressure was 45200 Pa). And the profile measured reflected peak pressure (after first pulse analysis) is 24610 Pa with sound pressure level being nearly 182 dB.

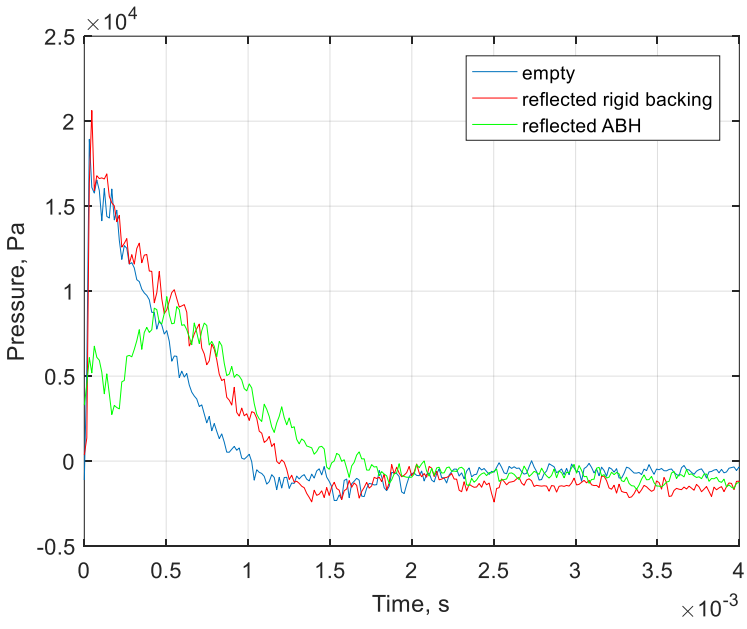

Figure 7.83. Pressure as a function of time for exponential profile absorber. Dimensions are $r_0 = 25$ mm, $d_p = 1$ mm, $d_c = 2$ mm, $R = 50$ mm, and $L = 80$ mm. Shock tube, first pulse analysis, signal 2 in rigid backing set up. Membrane ruptured is tin foil.

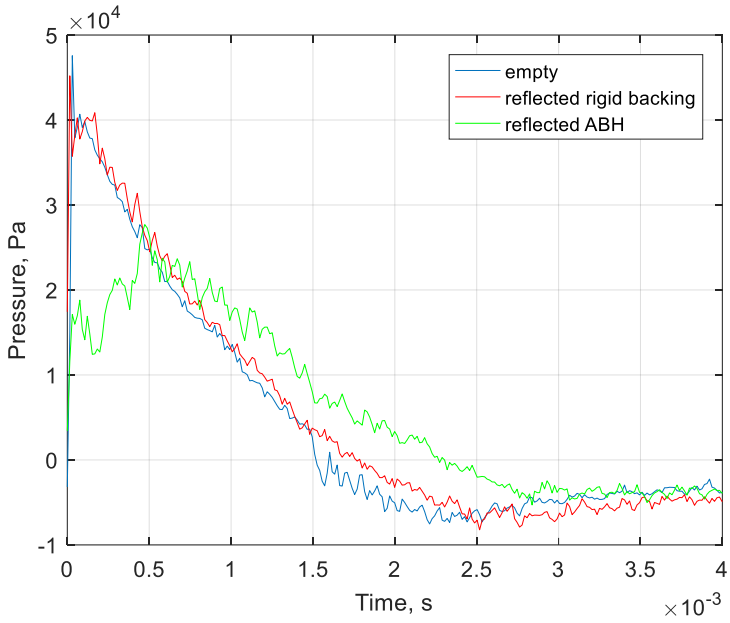

Figure 7.84. Pressure as a function of time for exponential profile absorber. Dimensions are $r_0 = 25$ mm, $d_p = 1$ mm, $d_c = 2$ mm, $R = 50$ mm, and $L = 80$ mm. Shock tube, first pulse analysis, signal 2 in rigid backing set up. Membrane ruptured is Mylar 23 μm.

Data presented by Figure 7.85 shows a Mylar 50 um rupture and its reflected peak pressures as a function of time. Incident peak pressure for the first pulse at signal 2 is 68840 Pa (measurement performed in empty tube). Peak pressure for the pulse obtained from the profile measurement at signal 2 before interaction with the sample surface was 68540 Pa. Sound pressure levels for the former and latter were approximately 191 dB. Incident peak pressure at signal 2 for rigid backing only was 69850 Pa. Before first pulse analysis the reflected superimposed pulses for rigid backing and profile measured 83370 Pa and 49090 Pa, respectively. After first pulse analysis the reflected peak pressures for the rigid backing and profile absorber were 67060 Pa and 42620 Pa, respectively. The resultant sound pressure levels are 190 dB (for reflected rigid backing) and 186 dB (reflected profile). Furthermore, this shows that the exponential profile absorber produces a reduction of sound pressure level of 5 dB from the large amplitudes from peak pressures around 70000 Pa.

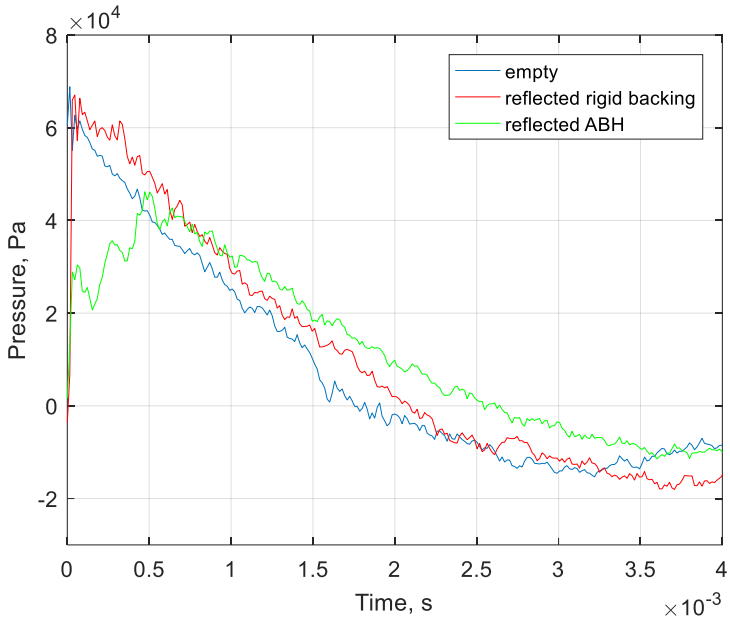

Figure 7.85. Pressure as a function of time for exponential profile absorber. Dimensions are $r_0 = 25$ mm, $d_p = 1$ mm, $d_c = 2$ mm, $R = 50$ mm, and $L = 80$ mm. Shock tube, first pulse analysis, signal 2 in rigid backing set up. Membrane ruptured is Mylar 50 μm.

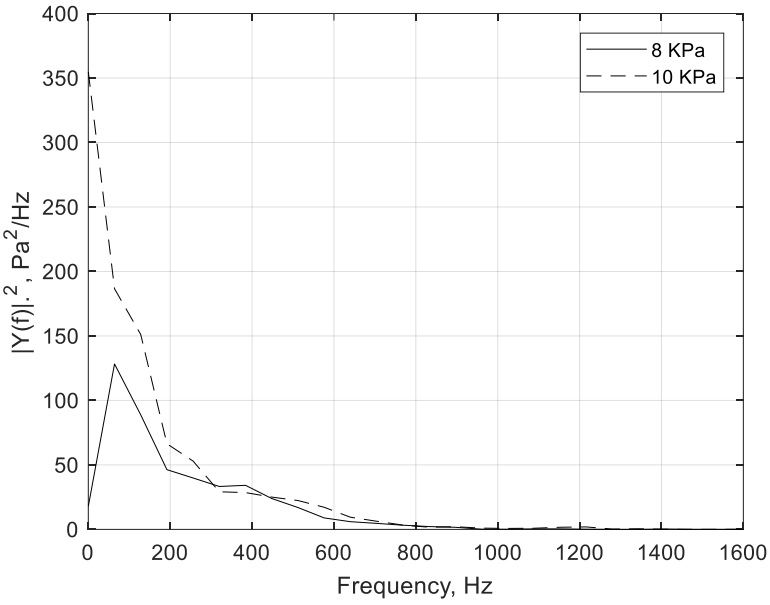

Figure 7.86. Single-sided amplitude spectra of reflected signals for exponential profile. Membranes ruptured are tin foil (solid line) and baking paper (dash).

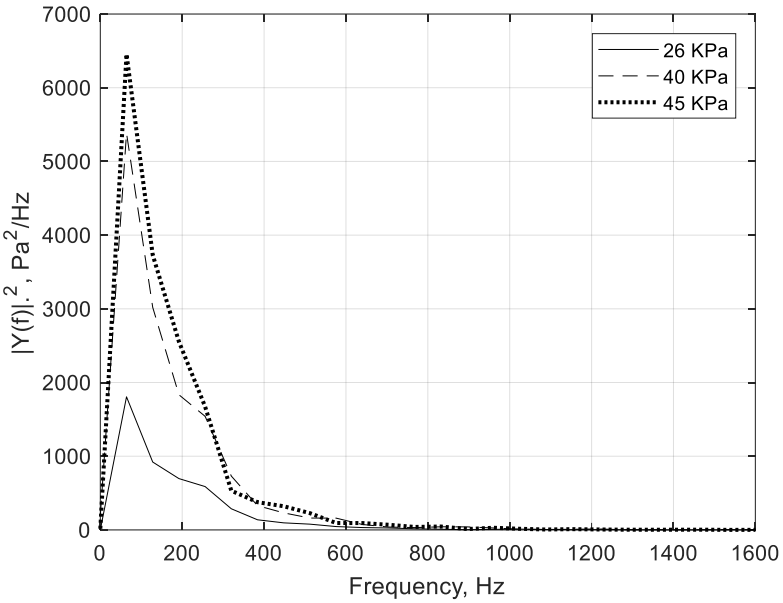

Figure 7.87. Single-sided amplitude spectra of reflected signals for exponential profile. Membranes ruptured are Mylar 23 μm (solid line), Mylar 40 μm (dash) and Mylar 50 μm (dot).

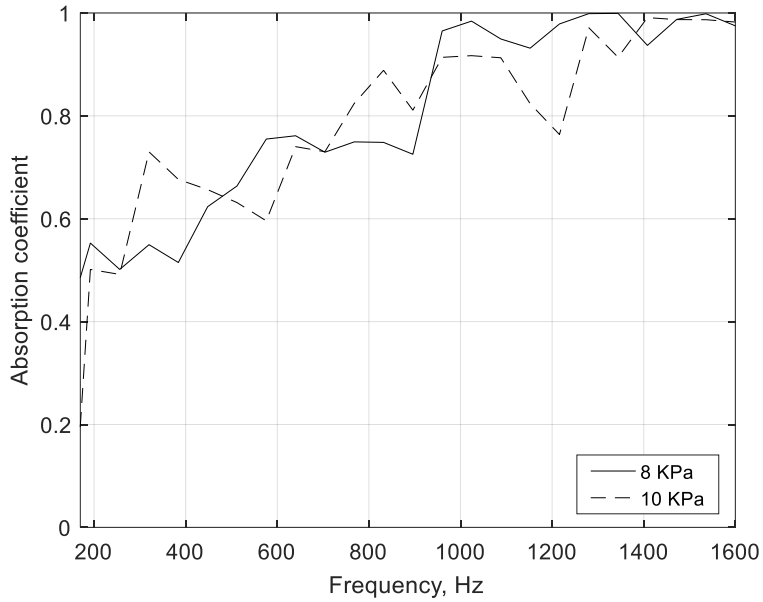

Figure 7.88. Absorption coefficient as a function of frequency for exponential profile. Membranes ruptured are tin foil (solid line) and baking paper (dash).

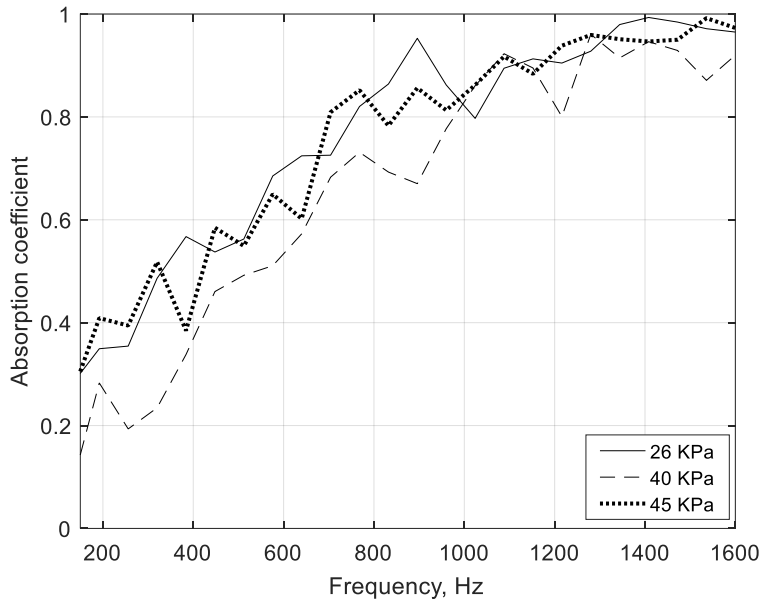

Figure 7.89. Absorption coefficient as a function of frequency for exponential profile. Membranes ruptured are Mylar 23 μm (solid line), Mylar 40 μm (dash) and Mylar 50 μm (dot).

Amplitude ratios for the exponential profile are calculated from data given by Figures 7.83 – 7.85 for ruptured tin foil, Mylar 23 μm and Mylar 50 μm. Reflected peak pressure ratios to that of the incident peak pressures are 23.3 %, 31.0 % and 46.4 %. The exponential profile consisted of $r_0 = 25$ mm, $d_p = 1$ mm, $d_c = 2$ mm, $L = 80$ mm and $R = 50$ mm. Incident and reflected peak pressures for the tin foil membrane were 22280 Pa and 8627 Pa respectively, see Figure 7.83. For Mylar 23 μm the peak amplitude ratios are calculated using values 47190 Pa and 24610 Pa. For Mylar 50 μm, the incident and reflected peak pressures have values 68540 Pa and 42620 Pa, respectively, see Figures 7.84 – 7.85. This results in a peak reduction of the incident peak pressure 61.3 % for the tin foil measurement from signal 2. Profile data obtained by the ruptured Mylar membranes show that incident amplitude of the shock pulse measured at signal 2 have peak reductions 47.9 % (Mylar 23 μm) and 37.8 % (Mylar 50 μm).

Table 7.15 presents the calculated energy values using the FFT of the original reflected pulses for both rigid backing case and the reflected profile signals. Values are presented also for other membranes ruptured where energy is calculated using sum of the frequency components of spectral density of the signals. Energy absorption coefficient is calculated as $1 - E_{ab}/E_{rb}$ where E_{ab} is energy in original reflected signal (absorber) and E_{rb} is energy in original rigid backing signal. The data shown by Figures 7.83 – 7.85 and values presented in Table 7.15 clearly show that the absorber is effective against the large amplitudes. Energy calculated from the reflected pulse is significantly reduced compared to that of the rigid backing reflected pulse, seen for all amplitude variations especially for when amplitudes are lowest. Consequently, this is reflected in the values obtained for the calculated energy absorption coefficient. Broadband absorption is possible due to the performance of the absorber. Absorption coefficient values from the reflected profiled signals and membrane explosions tin foil and baking paper show $\alpha = 0.5$ → 0.9 from $f =$ 200 Hz – 900 Hz including α to be nearly 1.0 for the remainder of the frequency spectrum, see Figure 7.88. Absorption coefficient for the Mylar membranes (see Figure 7.89)

$\alpha = 0.3$ and $\alpha = 0.4$ from $f =$ 200 Hz increasing to $\alpha = 0.9$ in the region of $f =$ 1000 Hz. Absorption coefficient values are larger still increasing for the rest of the frequency spectrum where $\alpha = 1.0$.

Membrane ruptured	Energy original pulse	Energy reflected pulse	Energy absorption coefficient α_{energy}
Tin foil	1.0335e+03	475.5079	0.5399
Baking paper	1.2098e+03	994.1463	0.4783
Mylar 23 µm	7.6816e+03	4.8695e+03	0.3661
Mylar 40 µm	1.6900e+04	1.4124e+04	0.4643
Mylar 50 µm	2.7944e+04	1.6586e+04	0.4065

Table 7.15. Energy absorption coefficient for exponential profile. Dimensions are $r_0 = 25$ mm, $d_p = 1$ mm, $d_c = 2$ mm and $L = 80$ mm. Shock tube, first pulse analysis, signal 2 with rigid backing.

The exponential profile is built larger by reassembling the sample with a change of cavity depth so that $d_c = 3$ mm instead of $d_c = 2$ mm. The front main pore however, remains the same value where $r_0 = 25$ mm. Plate thickness $d_p = 1$ mm, and sample length with new cavity dimensions is $L = 100$ mm. Dimensions of the profiled absorbers both linear and exponential are given in Chapter 4, see Table 4.1. Data from the performed measurements and analysis for the exponential profile is given by Figures 7.90 – 7.92 for pressure as a function of time. Single-sided amplitude spectra is shown by Figures 7.93 – 7.94 and α for the profile with $d_c = 3$ mm is given by Figures 7.95 – 7.96.

Figure 7.90 shows pressure as a function of time from ruptured membrane tin foil. Empty tube measurement at signal 2 for rigid backing has a peak pressure 18930 Pa and sound pressure level 179 dB. The exponential profile measured at signal 2 had an incident peak pressure 21900 Pa and SPL 181 dB. Reflected pressure from the profile surface superimposed is measured by transducer signal 2 as 6634 Pa. Reflected pressure of incident and superimposed pulse in rigid backing set-up is 23200 Pa and 19000 Pa with SPL 181 dB and 180 dB, respectively. After first pulse analysis the reflected pulses have peak pressures 18930 Pa for case of rigid backing absent the profile and 7285 Pa after interaction with the profile. The former and latter have sound pressure levels close to 180 dB and 171 dB, respectively. Figure 7.91 shows data from first pulse analysis for the exponential profile and Mylar 23 µm explosion. Peak pressure of the incident shock pulse from empty tube measured 47570 Pa equating to SPL 187 dB. The pulse from the profile measured 49010 Pa and sound pressure level around 188 dB. Reflected pulse recorded by the piezoelectric transducer signal 2 measured the incident and reflected pressure (absent the profile in rigid backing) to be 48340 Pa and 49000 Pa, respectively which corresponds to SPL 188 dB. Reflected pulse for the profile measured at signal 2 before first pulse analysis was 22090 Pa and SPL nearly 181 dB. Sound pressure level of the reflected pulse following first pulse analysis for rigid backing is 187 dB from a peak pressure 45200. Reflected peak pressure of the profile measurement after first pulse analysis was 22000 Pa and sound pressure level close to 181 dB.

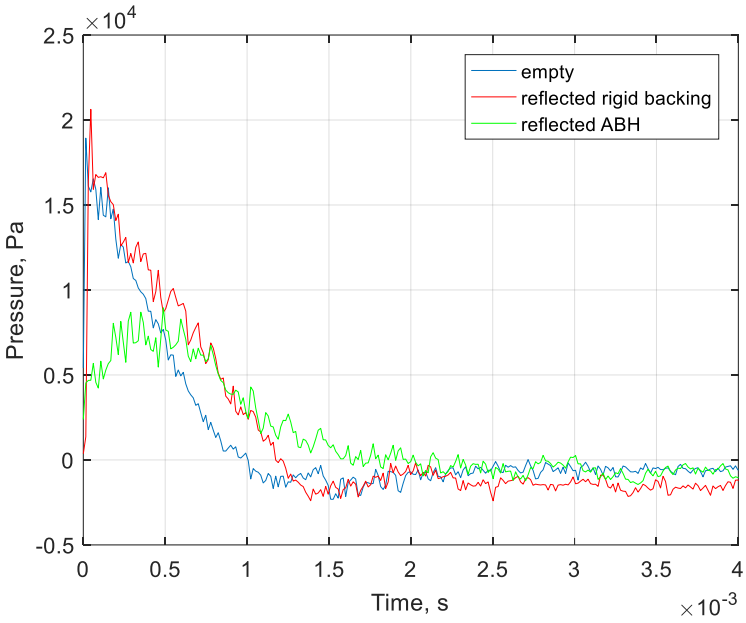

Figure 7.90. Pressure as a function of time for exponential profile absorber. Dimensions are $r_0 = 25$ mm, $d_p = 1$ mm, $d_c = 3$ mm, $R = 50$ mm, and $L = 100$ mm. Shock tube, first pulse analysis, signal 2 in rigid backing set up. Membrane ruptured is tin foil.

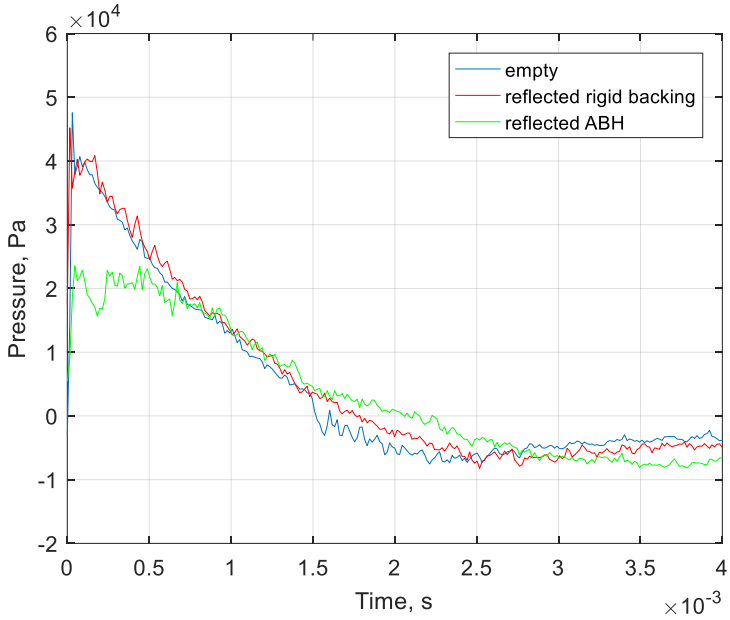

Figure 7.91. Pressure as a function of time for exponential profile absorber. Dimensions are $r_0 = 25$ mm, $d_p = 1$ mm, $d_c = 3$ mm, $R = 50$ mm, and $L = 100$ mm. Shock tube, first pulse analysis, signal 2 in rigid backing set up. Membrane ruptured is Mylar 23 μm.

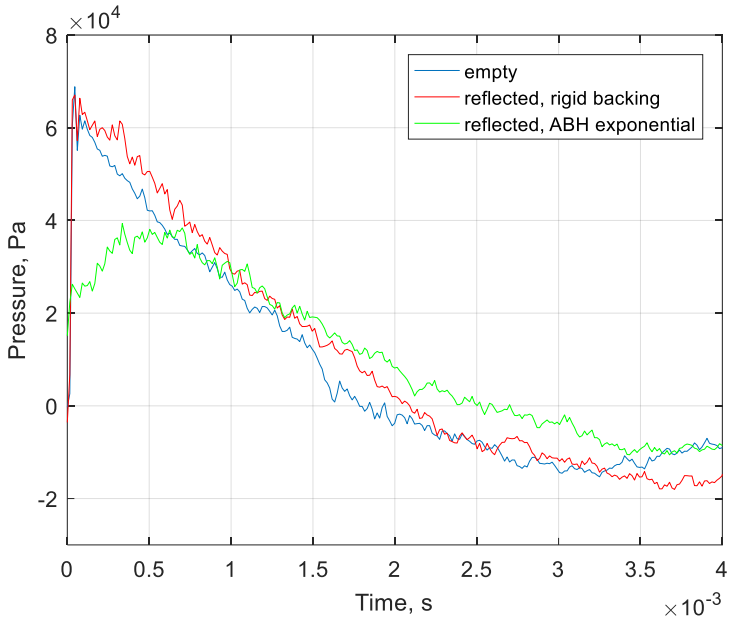

Figure 7.92. Pressure as a function of time for exponential profile absorber. Dimensions are $r_0 = 25$ mm, $d_p = 1$ mm, $d_c = 3$ mm, $R = 50$ mm, and $L = 100$ mm. Shock tube, first pulse analysis, signal 2 in rigid backing set up. Membrane ruptured is Mylar 50 μm.

Data for the ruptured Mylar 50 μm membrane and its reflected peak pressures after first pulse analysis is given by Figure 7.92 showing pressure as a function of time. Incident peak pressure of the first pulse at signal 2 for the Mylar 50 μm explosion is measured 68840 Pa (in empty shock tube). Peak pressure of the incident pulse for the profile measurement at signal 2 before interaction with the absorber was 69610 Pa. Sound pressure levels for the former and latter are approximately 191 dB. The incident peak pressure at signal 2 for rigid backing only absent the sample was 69850 Pa. Prior to first pulse analysis the reflected pulse for rigid backing was 83370 Pa. The reflected superimposed pulse of the profile measurement had a peak measuring 4330 Pa. After first pulse analysis the reflected peak pressures for the rigid backing and profile absorber were 67000 Pa and 36240 Pa, respectively. Sound pressure levels are 190 dB (for reflected rigid backing) and 185 dB (reflected profile). Moreover, the performance of the exponential profile absorber is shown to produce a reduction in SPL around 5 dB and 6 dB. Single-sided amplitude spectra given by Figures 7.93 – 7.94 show majority of energy from the reflected pulses is contained mostly toward $f = 600$ Hz. Absorption coefficient presented by Figures 7.95 – 7.96 shows that the exponential profile is capable of broadband absorption at frequencies ranging $f = 50$ Hz $-$ 1600 Hz . As amplitude strength of the reflected signals become larger the peak absorption coefficient values reduce slightly across the frequency spectrum. Absorption coefficient values (for reflected profile signals of ruptured membranes tin foil and baking paper) see $\alpha = 0.6$ and $\alpha = 0.7$ beginning at $f = 200$ Hz and ranges to $\alpha = 0.8$ toward $f = 600$ Hz. Absorption coefficient increases to $\alpha = 0.9$ nearer the end of the frequency spectrum, $f = 1600$ Hz. The Mylar membrane explosions show α ranges from $\alpha = 0.4$ and $\alpha = 0.7$ at $f = 200$ Hz. And at around $f = 800$ Hz $- 1600$ Hz then $\alpha = 0.8$ and becomes close to $\alpha = 0.9$.

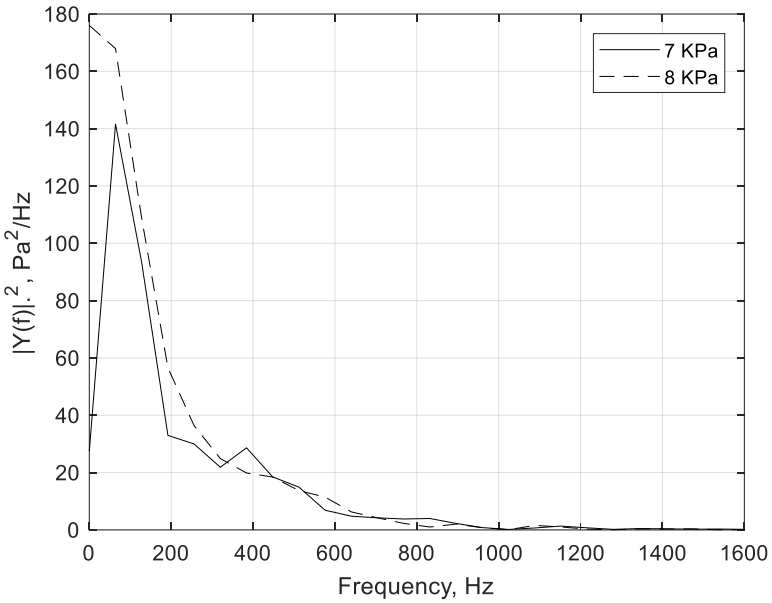

Figure 7.93. Single-sided amplitude spectra of reflected signals for exponential profile. Membranes ruptured are tin foil (solid line) and baking paper (dash).

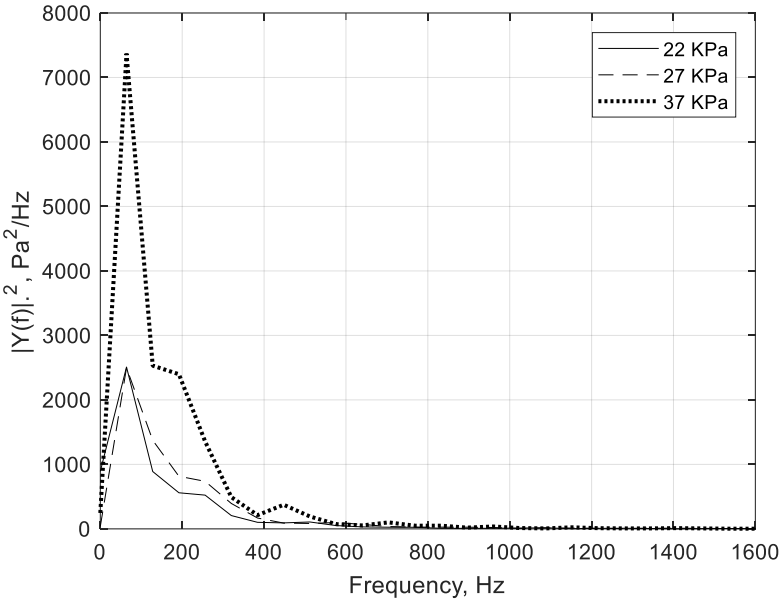

Figure 7.94. Single-sided amplitude spectra of reflected signals for exponential profile. Membranes ruptured are Mylar 23 μm (solid line), Mylar 40 μm (dash) and Mylar 50 μm (dot).

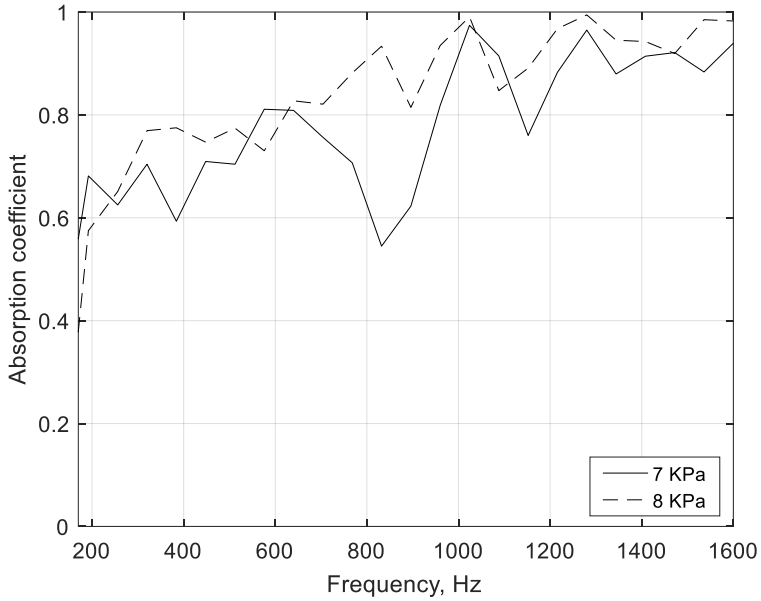

Figure 7.95. Absorption coefficient as a function of frequency for exponential profile. Membranes ruptured are tin foil (solid line) and baking paper (dash).

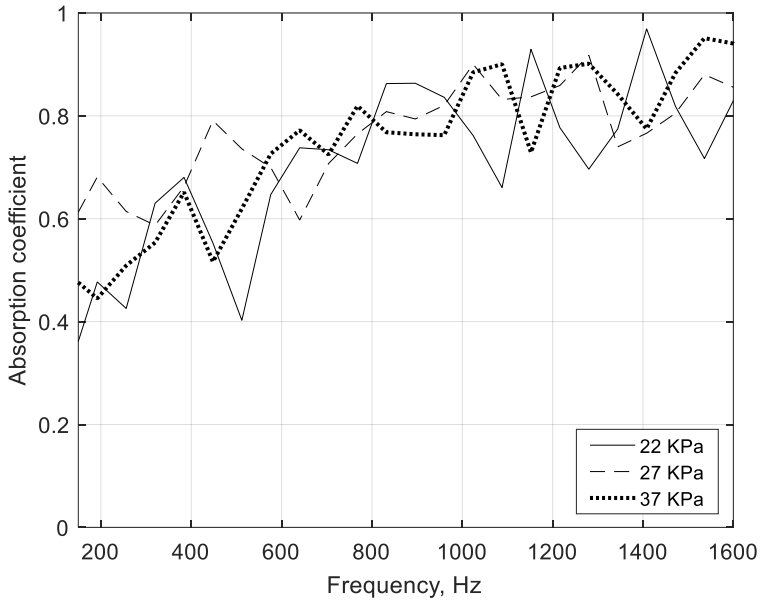

Figure 7.96. Absorption coefficient as a function of frequency for exponential profile. Membranes ruptured are Mylar 23 μm (solid line), Mylar 40 μm (dash) and Mylar 50 μm (dot).

Amplitude ratios for the exponential profile ($r_0 = 25$ mm, $d_p = 1$ mm, $d_c = 3$ mm, $L = 100$ mm and $R = 50$ mm) of the reflected pressures are calculated using the data given by Figures 7.90 – 7.92 (ruptured membranes tin foil, Mylar 23 μm and Mylar 50 μm). The reflected peak pressure ratios are 38.7 %, 52.1 % and 62.2 % respectively. Incident and reflected peak pressures measured from the tin foil explosion are 21900 Pa and 7285 Pa, see Figure 7.90. For Mylar 23 μm the peak amplitudes ratios are calculated using the obtained values 49010 Pa and 22000 Pa. Measured shock values used for the ruptured Mylar 50 μm were incident and reflected peak pressures 69610 Pa and 36240 Pa, respectively (see Figures 7.91 – 7.92). This results in a peak reduction of the incident pressure 66.7 % (ruptured tin foil measured at signal 2). Profile measurement from the ruptured Mylar 23 μm (see Figure 7.91) shows that the incident peak amplitude is reduced 55.1 %. Figure 7.92 shows pressure as a function of time from a

Mylar 50 μm explosion for the profile. Peak reduction of the incident amplitude is 47. 9 %. Values of the amplitude ratios and incident peak reductions are calculated using the measured data (obtained from piezoelectric transducer signal 2) and using reflected peak pressures of the shocks, by performing first pulse analysis. Energy calculated for the pulses is presented in Table 7.16 which has been obtained by performing FFT of the original reflected pulses for both rigid backing case and reflected profile signals. Values are presented also for other membranes ruptured where energy is calculated using sum of the spectral density of the signals. Energy absorption coefficient α_{energy} is calculated for the exponential absorber using the same procedure as for the linear structures. The data shown by Figures 7.90 – 7.92 (including values presented in Table 7.16) clearly indicate that the exponential profiled absorber is effective for shock wave reduction, similarly as linear profiled structures. Energy calculated from the reflected pulses is significantly reduced compared to that of the rigid backing pulses, especially for lower shock amplitudes.

Membrane ruptured	Energy original pulse	Energy reflected pulse	Energy absorption coefficient α_{energy}
Tin foil	1.0335e+03	455.1020	0.5597
Baking paper	1.2098e+03	668.3327	0.4476
Mylar 23 μm	7.6816e+03	6.2214e+03	0.4901
Mylar 40 μm	1.6900e+04	6.7713e+03	0.5993
Mylar 50 μm	2.7944e+04	1.5846e+04	0.4329

Table 7.16. Energy absorption coefficient for exponential profile. Dimensions are $r_0 = 25$ mm, $d_p = 1$ mm, $d_c = 3$ mm and $L = 100$ mm. Shock tube, first pulse analysis, signal 2 with rigid backing.

Comparison of the linear and exponential profile performance.

A comparison of the pressure amplitudes for the linear and exponential profiled absorbers is given by Figures 7.97 a, b, and c for absorbers with same thicknesses (where $L = 80$ mm). Plate and cavity thicknesses are the same for both profiles so $d_p = 1$ mm and $d_c = 2$ mm. Main opening pore had radius $r_0 = 25$ mm. This means that only the inner trajectory of the pore radii differs. Comparison between the linear and exponential profile configurations show that their performance is quite similar by the ruptured membranes and obtained pressure amplitudes thus far. The pressure amplitude ratios are calculated using the data shown by Figures 7.69 – 7.71 and Figures 7.83 – 7.85, for the absorbers. The linear profile is slightly more effective in reducing the incident peak amplitude of the shock pulse measured by the piezoelectric transducer located at signal 2 (transducer positions are shown by shock tube set-ups, see Figure 7.2 a, b). Values of the pressure amplitude ratios and incident peak reductions for both the linear and exponential profile absorbers are presented in Table 7.17. Pressure amplitude ratios for the ruptured tin foil membrane is 36.6 % and 38.7 % for the linear and exponential structures, respectively. Incident shock pulse is reduced 63.4 % for the linear profile and 61.3 % for the exponential profile. For the Mylar membranes the pressure amplitude ratios are the following: 44.0 % for the linear profile and 52.1 % for the exponential profile (for ruptured membrane Mylar 23 μm). Incident shock pulses are reduced 56 % and 47.9 % for the linear and exponential profiles, respectively. Membrane with highest tensile strength is Mylar 50 μm and pressure amplitude ratios for both the linear and exponential absorbers are 56.1 % and 62.2 % respectively. Incident peak reductions are 43.9 % and 37.8 %. This results in the linear profile reducing the incident pulse amplitude 2.1 % lower than the exponential profile, from tin foil explosions (where incident peak pressure is around 20000 Pa). For the ruptured Mylar 23 μm membrane the incident peak pressure ranged between 48000 Pa – 49000 Pa. The linear profile

reduced the incident peak pressure approximately 8.1 % compared to the exponential absorber. Moreover, the linear profile reduced the incident peak pressure 6.1 % lower than the exponential profile, for the ruptured Mylar 50 µm. The incident amplitude ranged between 68500 Pa and 71000 Pa (for Mylar 50 µm). All measured peak pressures of incident shock pulses are the values obtained before interaction with the samples and measured by piezoelectric transducer 2. For values of the incident amplitudes of the shock pulses created immediately after shock formation, see Table 7.2. Furthermore, see Figure 7.2 for signal 1 location as referred to position 0. See also signal 2 data presented in Table 7.2 and Figure 7.2 for signal 2 location, position 1.

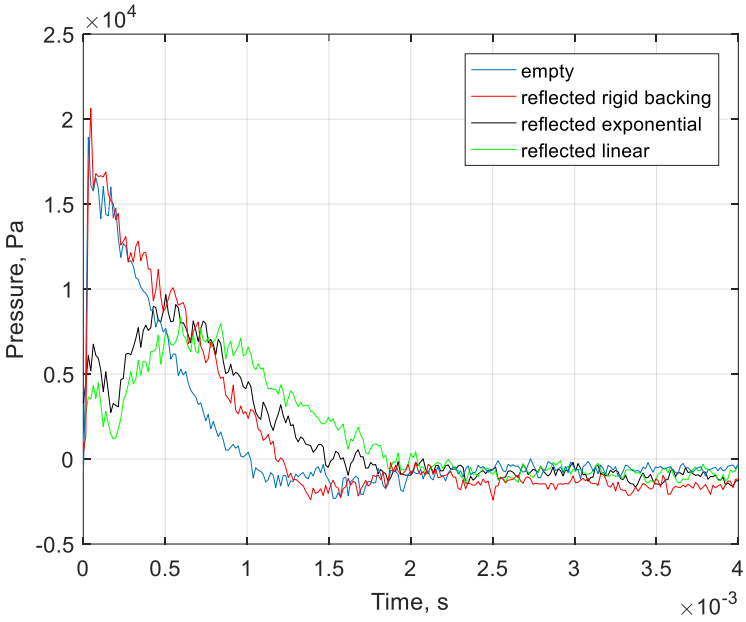

(a)

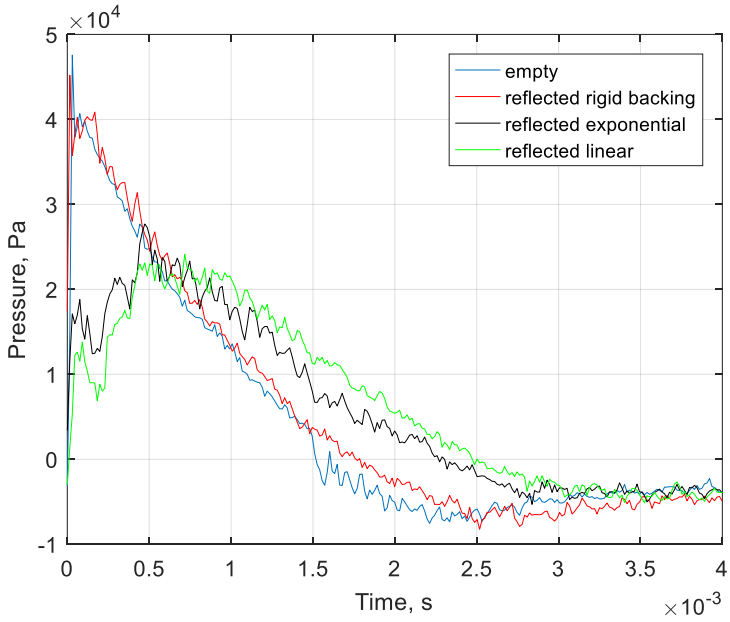

(b)

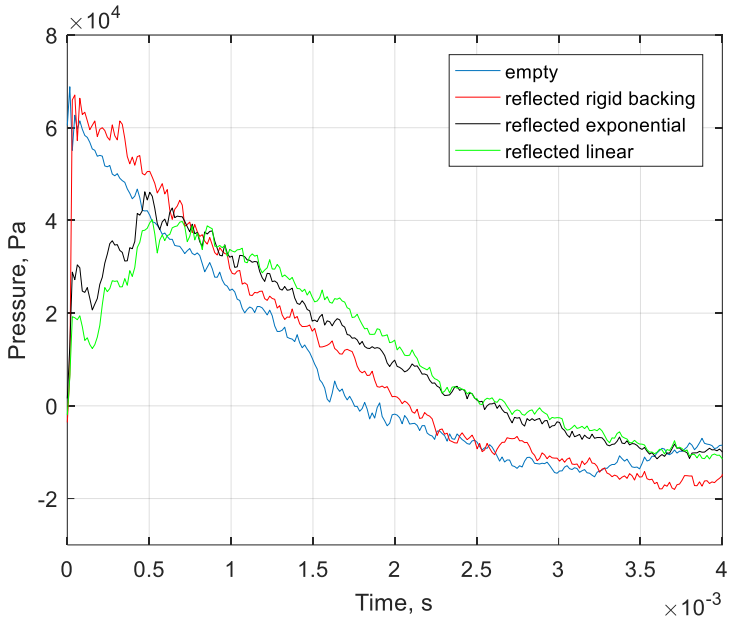

(c)

Figure 7.97. Pressure as a function of time showing comparison of reflected shock pressures for linear and exponential profiles. (a) Membrane ruptured is tin foil. (b) Membrane ruptured is Mylar 23 μm and (c) membrane is Mylar 50 μm. Dimensions $r_0 = 25$ mm, $d_p = 1$ mm, $d_c = 2$ mm, $R = 50$ mm, and $L = 80$ mm.

Membrane ruptured	Pressure amplitude ratio % Linear profile	Incident pulse reduction % signal 2 Linear profile	Pressure amplitude ratio % Exponential profile	Incident pulse reduction % signal 2 Exponential profile
Tin foil	36.6	63.4	38.7	61.3
Baking paper	44.0	56.0	52.1	47.9
Mylar 23 μm	56.1	43.9	62.2	37.8

Table 7.17. Pressure amplitude ratios and incident peak reductions for linear and exponential profile absorbers with $d_p = 1$ mm, $d_c = 2$ mm, $r_0 = 25$ mm and $L = 80$ mm.

The profiles are compared again after being built with larger sample length. For instance, the linear and exponential profiles with a main pore beginning $r_0 = 25$ mm, $d_p = 1$ mm, $d_c = 3$ mm, $L = 100$ mm and $R = 50$ mm are compared for their reflected peak pressures and shown by Figures 7.98 a, b, and c. Pressure amplitude ratios for the absorbers are calculated using data given in Figures 7.76 – 7.78 (for the linear profile) and Figures 7.90 – 7.92 (exponential profile). Performance between the different profile configurations is given in terms of the amplitude ratios similarly like the comparison for the profiles with $d_c = 2$ mm and $L = 80$ mm. Values for reduction of the incident shock pulse is presented in Table 7.17 including values of the amplitude ratios. The pressure amplitude ratios for the ruptured tin foil membrane are 23.3 % and 33.3 % for linear and exponential profiles, respectively. For the Mylar 23 μm membrane explosion the pressure amplitude ratios are 31.0 % (linear profile) and 44.9 % (exponential profile). The Linear and exponential absorbers have pressure amplitude ratios 46.4 % and 52.1 % respectively obtained by the Mylar 50 μm measurements. Incident shock pulse reductions measured at signal 2 are calculated as the following: 76.7 % and 66.7 % for linear and exponential profiles, respectively. Tin foil explosion is measured with incident peak pressure ranging between 19000 Pa – 21000 Pa. Incident peak pressure is reduced 69.0 % for the linear profile and 55.1 % by the exponential profile for the ruptured Mylar 23 μm (where incident peak pressures ranged between 48000 Pa – 49000 Pa). Incident pulse reductions calculated from the Mylar 50 μm membrane explosions are 53.6 % and 47.9 % for the linear and exponential profiles, respectively. This means the linear profile reduced the incident pulse

amplitude 10 % lower than the exponential profile for the tin foil explosions. The linear profile also reduced the incident peak pressure 13.9 % than the exponential absorber for the ruptured Mylar 23 μm membrane. Furthermore, the linear profile absorber reduces the incident peak pressure 5.7 % than the exponential profile for Mylar 50 μm. Comparison of the pressure amplitude ratios and incident peak reductions for the profile structures are given in Table 7.18.

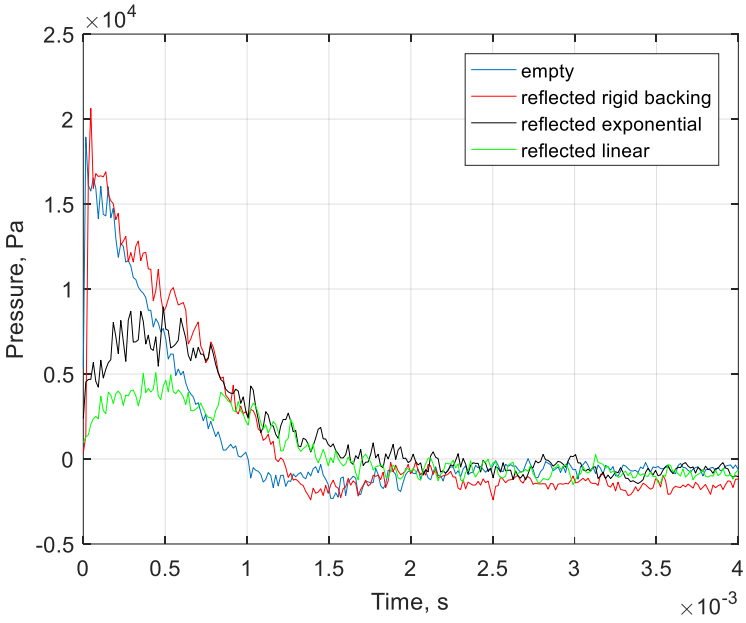

(a)

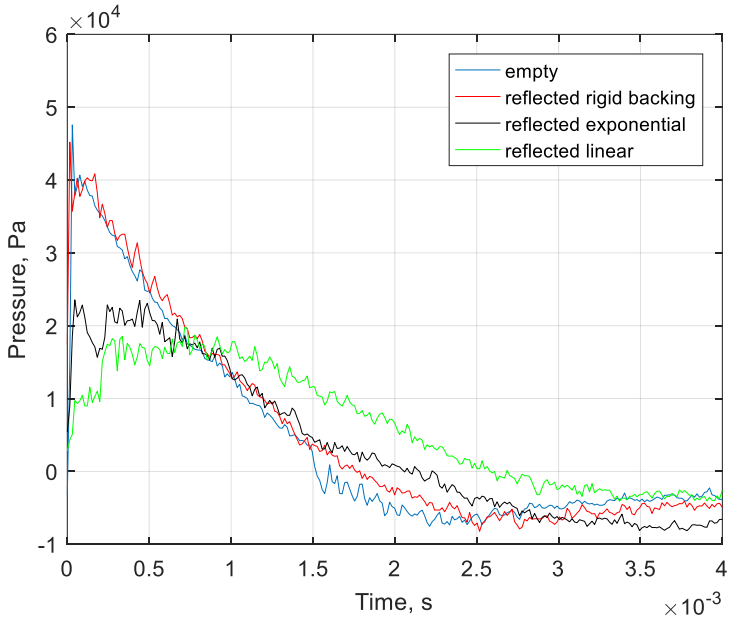

(b)

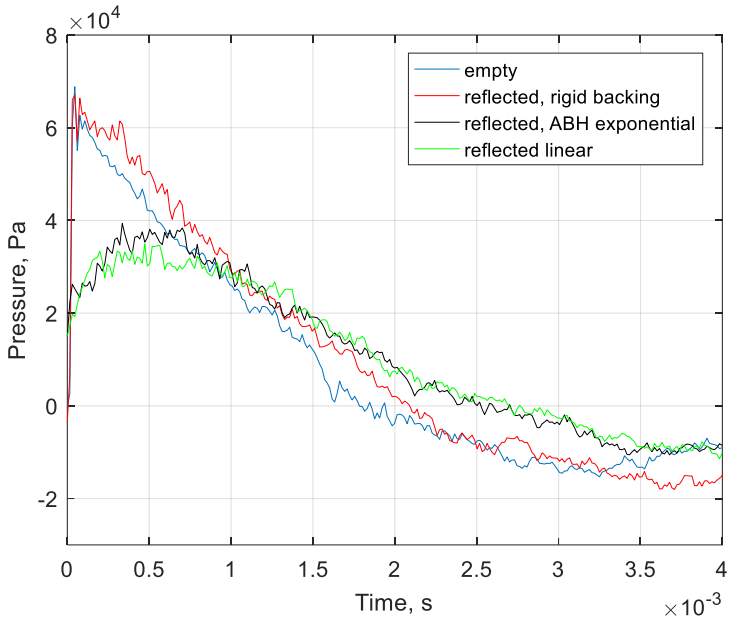

(c)

Figure 7.98. Pressure as a function of time showing comparison of reflected shock pressures for the linear and exponential profile absorbers. (a) Membrane ruptured is tin foil. (b) Membrane ruptured is Mylar 23 μm and in (c) the ruptured membrane is Mylar 50 μm. Dimensions are $r_0 = 25$ mm, $d_p = 1$ mm, $d_c = 3$ mm, $R = 50$ mm, and $L = 100$ mm.

Membrane ruptured	Pressure amplitude ratio % Linear profile	Incident pulse reduction % signal 2 Linear profile	Pressure amplitude ratio % Exponential profile	Incident pulse reduction % signal 2 Exponential profile
Tin foil	23.3	76.7	33.3	66.7
Baking paper	31.0	69.0	44.9	55.1
Mylar 23 μm	46.4	53.6	52.1	47.9

Table 7.18. Pressure amplitude ratios and incident peak reductions for linear and exponential profile absorbers with $d_p = 1$ mm, $d_c = 3$ mm, $r_0 = 25$ mm and $L = 100$ mm.

7.10. Conclusion

Chapter 7 presents a portion of the data obtained from conducting measurements in a shock tube for both pancake and profiled absorbers. High amplitude shock waves have been targeted at the metamaterial structures for determination of the absorber performance by investigating the incident and reflected peaks for several amplitude strengths. Single and multiple orifices including a cone structure have also been tested in the shock tube in addition to the metamaterial absorbers. This was carried out to compare conventional structured materials to the metamaterial structures at large amplitudes. The pancake absorber shows to have a small impact on reducing incident pulse signals at large amplitudes within the shock tube due to the high nonlinearity of the pancake and low pore wall porosity. However, this is seen to be the contrary for the case of the profiled structures which show to be successful in reducing the incident pulse after interacting with the sample when constrained against the generated large amplitudes. This is due to the influence of combining dead-end pores and utilising impedance matching from taking advantage of using the so-called “acoustic black hole effect” which significantly improves the profiled absorber capabilities. The response of the structures have been analysed by performing first pulse analysis on the signals measured prior to and after interaction with the sample

surface in rigid backing set-up of the shock tube. Additionally, in transmission set-up of the shock tube the transmitted pulse is accounted for when performing analysis on the shock signals. Energy absorption coefficient has been calculated for the metamaterial structures by using the calculated spectral density and performing Fast Fourier Transform on the signal data of the pulses. Single-sided amplitude spectrum accompanies the absorption coefficient data and pressure dependence plots for the measurements showing pressure as a function of time by the measured piezoelectric transducers for the various membrane explosions. The best performing structure in terms of reducing the incident peak pressure and its absorptive properties is attributed to the linear profiled configuration. Absorber dimensions were $d_p = 1$ mm, $d_c = 3$ mm, $R = 50$ mm and $L = 100$ mm. This is followed by the exponential profile configuration with same material parameters (excluding pore radius). Shorter profiled absorbers which had $d_p = 1$ mm, $d_c = 2$ mm, $R = 50$ mm and $L = 80$ mm also showed to be effective for high amplitude sound absorption. Note, that linear configuration of the profile absorber is slightly more effective than exponential configuration for same sample length. This is thought to be due to the linear configuration having larger pore radii contained within the plates along the sound propagation axis. Sound pressure level reductions for the extremely high amplitudes ranged between 10 dB and 20 dB, for the metamaterial profiles structures.

8. Conclusion and Future Work

An absorbing structure comprising of periodically arranged plates separated by air cavities and with a central perforation traversing the periodic structure, was built, and tested in both linear and nonlinear regimes. In the first type of structure (pancake absorber), the central pore radius has been kept constant throughout the thickness of the sample. In the second type (profile absorber), the central pore decreases away from the absorber surface following the linear or the exponential law. The characteristic feature of this work is that the absorber performance has been tested and modelled for a range of sound excitations. This includes continuous and pulsed sound with amplitudes up to 100 kPa. Both types of the absorbers belong to the class acoustic metamaterials. They possess a relatively simple geometry, which means that with the help of the models developed, it can be tuned to achieve the desired absorption in the frequency and amplitude range of interest. The results of this work will be useful when designing absorbers for applications in the environments where high sound pressure levels are achieved.

The following results have been achieved for the pancake absorbers:

1. New models for the linear and the nonlinear acoustic behaviours of this structure were proposed, together with absorption coefficient measurements in the linear regime, flow resistivity and Forchheimer's nonlinearity parameter measurements at high flow rates and finally absorption coefficient measurements in the nonlinear regime. The results of measurements were compared with the models – the analytical linear model and a numerical model accounting for Forchheimer's type nonlinearity. A good agreement was demonstrated between the model and the absorption coefficient data in the linear regime, i.e. for low levels of the incident sound, and at low frequencies. Simple expressions have been derived that adequately describe the frequency of the first peak and the peak absorption coefficient value. With careful choice of parameters for this absorbing structure, an absorption peak at much lower frequency and higher peak value than that provided by a Helmholtz resonator of same thickness and diameter could be achieved. Furthermore, this absorber can provide higher frequency absorption peaks and a broader absorption range.
2. Accelerometer measurements and FEM calculations confirm that the vibrations of the plates contribute to the performance of the absorber, particularly near the frequencies of structural resonances of the plates. This phenomenon should be considered in the absorber design.
3. Flow resistivity measurements for a range of flow velocities were carried out for the absorbers. Typical value of the Forchheimer's nonlinearity parameter were obtained, which is high relative to porous and granular materials so that strong nonlinear effects are expected for the absorber. A dependence of flow resistivity on the sample thickness for high flow rates was observed with higher values achieved for shorter samples. A qualitative explanation was given for this behaviour. In the nonlinear model, a measured value of Forchheimer's parameter was used for each absorber sample.
4. It was shown that the absorption peak frequencies weakly depend on the incident pressure amplitude, while the peak values are strongly attenuated as incident pressure grows. This means, that the linear model will overestimate the absorption capacity of the structure, if the

latter is used for high sound pressure levels. The new numerical model accounting for Forchheimer's nonlinearity adequately describes the effects observed.

5. Measurements in the shock tube with pulsed excitation with amplitude up to 100kPa have shown very limited applicability of the structure for attenuation of high amplitude pulsed signals. The deterioration in the performance is associated with a strong Forchheimer's nonlinearity confirmed by flow resistivity measurements at high flow rates.

For the profile absorbers the following results have been achieved:

1. 3D printed and metallic structures have been investigated. The inner porosity of the matrix and inaccuracies in the geometry due to printing influence the performance of 3D absorbers, making metallic plates preferable for the profile absorber design.
2. The profile absorbers, contrary to pancake structures, offer broadband performance in the linear regime. TMM model has been developed to predict the absorber performance, accounting for the presence of cavities and variations in the central pore radius. The model predictions are in a satisfactory agreement with the measurements and reflect the main trends in the absorption coefficient dependence on frequency.
3. The profile absorbers have been tested using high amplitude continuous sound and the deterioration in their performance at high SPL is not as pronounced as for pancake structures.
4. Experiments in the shock tube have shown, that profile absorbers are effective for attenuation of high amplitude pulsed signals. Combined with a structural strength, this makes them candidates for blast sound attenuation.

Future work will concentrate on the optimum design of the pancake structure allowing perfect absorption at the desired frequency or frequencies. Reducing the number of interstitial walls inside the pancake absorber will eventually lead to Helmholtz resonator while doing the opposite will lead to a quarter wavelength circular cavity. The resonance frequencies associated with these structures are well known. The first resonance frequency of the pancake absorber is lower than that of the Helmholtz resonator (not between that of the Helmholtz and that of the quarter wavelength cavity as expected). This means that the resonance frequency experiences a minimum depending on the number of interstitial walls. This observation shows the importance of optimizing the number of cavities and their sizes in the pancake structure.

For the profile structures future work will include developing a numerical model which accounts for the grading in Forchheimer's nonlinearity parameter. This is a challenging task which should be combined with establishing a correlation between this parameter and the central perforation radius. This time domain model will be used to further improve the design to achieve the optimal performance in attenuation of high amplitude pulsed sounds.

References

[1] P.Leclaire, O.Umnova, T.Dupont, R.Panneton, Acoustical properties of air-saturated porous material with periodically distributed dead-end pores, Journal of the Acoustical Society of America 137 (4) pp 1772-1782, (2015).

[2] M.A Mironov, V.V. Pislyakov, One-dimensional acoustic waves in retarding structures with propagation velocity tending to zero, Acoustical Physics. Vol 48, pp347-352, (2002).

[3] T.Dupont, P.Leclaire, R.Panneton, O.Umnova, A microstructure material design for low frequency sound absorption, Applied Acoustics 136, pp 86-93, (2018).

[4] O.Umnova, K.Attenborough, K.M.Li. A cell model for the acoustical properties of packings and spheres, acta Acustica- ACUSTICA vol 87, pp 226-235, (2001).

[5] O.Umnova, K.Attenborough, H.Shin, A.Cummings, Response of multiple rigid porous layers to high levels of continuous acoustic excitation, Journal of the Acoustical Society of America 116 (2) pp 703–712, (2004).

[6] D.Turo, O.Umnova, Influence of Forchheimer's nonlinearity and transient effects on pulse propagation in air saturated rigid granular materials Journal of the Acoustical Society of America 134 (6) pp 4763–4774, (2013).

[7] V.Veselago, The electrodynamics of substances with simultaneously negative values of permittivity and permeability. Soviet Physics USPECKHI, Vol 10 (4), (1968).

[8] R. Hull, C.Jagadish R. Osgood, J.Parisi, Z.Wang. Acoustic Metamaterials: Negative Refraction, Imaging, Lensing and Cloaking. Springer series (2013).

[9] V.V.Krylov, Acoustic black holes: Recent developments in the theory and applications. IEEE Transactions on ultrasonics.Vol 61, Issue 8, pp 1296-1306, (2014).

[10] A.S. Elliott, R. Venegas, J.P. Groby, and O. Umnova Omnidirectional acoustic absorber with a porous core and a matching layer Journal of Applied Physics 115, 204902 (2014).

[11] R.D.Ford, Introduction to Acoustics, Elsevier Publishing Company, (1970).

[12] M.F.Hamilton, D.T.Blackstock, Nonlinear Acoustics, Academic Press, (1998).

[13] https://www.grc.nasa.gov/www/k-12/airplane/mach.html (2017).

[14] A.Ferri, Fundamental Data obtained from shock tube experiments, Agardograph N0.41, Pergamon Press (1961).

[15] G.J.Sharpe, Fluid Dynamics, Longman Scientific & Technical (1994).

[16] K.Naugolnykh, L.Ostrovsky, Nonlinear Wave Processes in Acoustics , Cambridge Texts In Applied Mathematics (1998).

[17] L.J.Sivian, Acoustic Impedance of small orifices, Acoustical Society of America 7,94 (1935).

[18] Westervelt, The Interaction of a finite amplitude acoustic wave with small obstacles and orifices, PhD thesis (1951).

[19] U.Ingard, S.Labate, Acoustic circulation effects and the nonlinear impedance of orifices, Journal of the Acoustical Society of America 22 (2) pp 211-218, (1950).

[20] W.K.R.Lippert. Measurement of sound transmission through an orifice in a duct with an application to a resonator, ACUSTICA. Vol 8, (1958)

[21] U.Ingard, H,Ising, Acoustic nonlinearity of an orifice, Research Laboratory of Electronics and Department of Physics, Massachusetts Institute of Technology, Cambridge, Massachusetts 02139, Volume 42, Number 1, (1967)

[22] W.Zorumski, T.Parrott, Nonlinear acoustic theory for thin-porous sheets. Progress of NASA Research Relating to Noise Alleviation of Large Subsonic Jet Aircraft, NASA SP-189, pp. 17-27, (1971).

[23] U.Ingard, Nonlinear distortion of sound transmitted through an orifice, Journal of the Acoustical Society of America Volume 48 N01 (Part1) pp 32-33, (1970)

[24] T.H.Melling, The acoustic impedance of perforations at medium and high sound pressure levels, Journal of Sound and Vibration, 29(1), pp 1-65, (1973)

[25] A.Hersh, B.Walker, Fluid mechanical model of the Helmholtz resonator, NASA CR-2904, (1977).

[26] A.Sharkawy, Nonlinear attenuation of sound in circular lined ducts. Applied Acoustics Vol 11, Issue 4, pp 259-268, (1978).

[27] D. W. Bechert, American institute of aeronautics and astronautics, 5th Aeroacoustics Conference Paper No. 79-0575*.* Sound absorption caused by vorticity shedding demonstrated with a jet flow, (1979).

[28] A.Cummings, W.Eversman, High amplitude acoustic transmission through duct terminations. Theory, Journal of Sound and Vibration, 91(4), 503-518, (1983).

[29] W.Zorumski, T.L.Parrott, NASA, Langley, Research Centre, Hampton. Va.23365, (1971).

[30] M.S.Howe, Journal of Fluid Mechanics 91, 202-229*.* Attenuation of sound in a low Mach number nozzle flow, (1979).

[31] M.S.Howe American Institute of Aeronautics and Astronautics 6th Aeroacoustics, Conference Paper No. 80-0972*.* The dissipation of sound at sharp edges, (1980).

[32] Cummings, Acoustic nonlinearities and power losses at orifices, AIAA Journal, Vol 22, N0 6, pp796-792, (1984).

[33] Cummings, Transient and multiple frequency sound transmission through perforated plates at high amplitude, Acoustical Society of America, Vol 79, N0 4, pp 940-951, (1986).

[34] Cummings, Chang, The transmission of intense transient and multiple frequency sound waves through orifice plates with mean fluid flow, Revue de Physique Appliquee, 21 (2), pp.151-161, (1986).

[35] Chang, Cummings, A time domain solution for the attenuation at high amplitudes of perforated tube silencers and comparison with experiment, Journal of Sound and Vibration 122 (2), pp 243-259, (1988).

[36] S.Park, A design method of micro-perforated panel absorber at high sound pressure environment in launcher fairings, Journal of Sound and Vibration 332, pp 521-535, (2012).

[37] D.Maa, Potential of micro perforated panel absorber, Journal of the Acoustical Society of America 104 (5) 2861-2866, (1998).

[38] R.Tayong, T.Dupont, P.Leclaire , Experimental investigation of holes interaction effect on the sound absorption coefficient of micro-perforated panels under high and medium sound levels, Applied Acoustics 72, 777-784, (2011).

[39] O.Umnova, K.Attenborough, E.Standley, A.Cummings, Behavior of rigid-porous layers at high levels of continuous acoustic excitation: Theory and experiment. Journal of the Acoustical Society of America 114 (3) pp 1346-1356, (2003).

[40] O.Umnova, K.Attenborough, H.Shin, A.Cummings. Response of multiple rigid porous layers to high levels of continuous acoustic excitation. Journal of the Acoustical Society of America (2) pp 703-712, (2004).

[41] D.Turo, O.Umnova, Influence of Forchheimer's nonlinearity and transient effects on pulse propagation in air saturated rigid granular materials Journal of the Acoustical Society of America 134 (6) pp 4763–4774, (2013).

[42] D.L.Johnson, J.Koplik, R.Dashen, Theory of dynamic permeability and tortuosity in fluid-saturated porous media, Journal of Fluid Mechanics vol. 176, pp 379-402, (1987).

[43] D.Turo, A relaxation approach for time domain modelling of sound propagation in porous media, PhD Thesis, University of Salford, (2011).

[44] P.Leclaire, A.Lardeau, T.Dupont, A.Geslain, D.Brooke, O.Umnova, Recent developments in the acoustical properties of perforated and porous materials containing dead-end pores – applications to low frequency sound absorption. ICSV24, pp 1-8, (2017).

[45] P.Leclaire, O.Umnova, T.Dupont, R.Panneton, Low frequency sound absorption in a porous material with periodically distributed dead-end pores, Euronoise, pp 983-988, (2015).

[46] A.R.Patterson, A first course in fluid dynamics, Cambridge University Press, (1983).

[47] Merle C.Potter, Fluid mechanics demystified McGraw-Hill Companies, (2009).

[48] http://ae.metu.edu.tr/~ae342/17/normal_shock.pdf (2017).

[49] L.F.Henderson, General laws for propagation of shock waves through matter, Handbook of shockwaves, Volume 1, Academic Press, (2001).

[50] D.R.Raichel, The science and applications of acoustics, AIP Press, (2000).

[51] M.Salikuddin and W.H.Brown. Nonlinear effects in finite amplitude wave propagation through orifice plate and perforated plate terminations, Journal of Sound and Vibration 139 (3), pp 383-405, (1990).

[52] W.Bechert, Sound absorption caused by vorticity shedding demonstrated with a jet flow, Journal of Sound and Vibration 70, 389-405, (1980).

[53] M. S. Howe, The dissipation of sound at an edge, Journal of Sound and Vibration 70, 407-411, (1980).

[54] M.Salikuddin, Acoustic behaviour of orifice plates and perforated plates with reference to low-frequency sound absorption, Journal of Sound and Vibration 139 (3), pp 361-381, (1990).

[55] U.Ingard, On the theory and design of acoustic resonators, Journal of the Acoustical Society of America 25, pp 1037-1061, (1953).

[56] J.D.McIntosh, R.F.Lambert, Nonlinear wave propagation through rigid porous materials. I: Nonlinear parametrization and numerical solutions, Journal of the Acoustical Society of America 88, pp 1939-1949 (1990).

[57] A. Cummings and W. Eversman, An investigation of acoustic energy loss in radiation from ducts to the far field at low frequencies, low Mach numbers, and high sound pressure levels, Lockheed-Georgia Engineering Report LG80ER0164, (1980).

[58] Sung-Hwan Ko, Sound attenuation in lined rectangular ducts with flow and Its application to the reduction of aircraft engine noise, The Journal of the Acoustical Society of America 50, 1418, (1971).

[59] J.F.Wilby, Aircraft interior noise, Journal of Sound and Vibration, pp 545-564, (1996).

[60] W.Tempest, M.E. Bryan, Low frequency sound measurement in vehicles, Volume 5, Issue 2, pp 133-139, (1972).

[61] A.H.Nayfeh, M.S.Tsai, Nonlinear acoustic propagation in two-dimensional ducts, The Journal of the Acoustical Society of America, (1974).

[62] Ali H.NayfehM.-S.Tsai, Nonlinear wave propagation in acoustically lined circular ducts, Volume 36, Issue 1, Journal of Sound and Vibration, pp 77-89, (1974).

[63] D.Maa, Theory and design of microperforated panel sound absorbing construction, (1975).

[64] Lord Rayleigh, Theory of sound II, MacMillan, New York, (1929).

[65] I.B.Crandall, Theory of vibration system and sound, Van Nostrand, New York, (1926).

[66] P.M.Morse, U.Ingard, Theoretical Acoustics, McGraw-Hill, New York, (1968).

[67] U.Ingard, On the theory and design of acoustic resonators, The Journal of the Acoustical Society of America 25, 1044, (1953).

[68] X.Jing, X.Sun, Sound-excited flow and acoustic nonlinearity at an orifice, Vol 14 No. 1, American Institute of Physics, (2002).

[69] P.G.Saffman, On the formation of vortex rings, App Math, 54, 261, (1975).

[70] H.Rouse, A.Abul-Fetouh, Characteristics of irrotational flow through axially symmetric orifices, Journal of Applied Mechanics, 17, 421, (1950).

[71] X.Jing, X.Sun, Discrete vortex simulation on the acoustic nonlinearity of an orifice, AIAA J. 38, 1565 (2000).

[72] W.T.Chu, Transfer function technique for impedance and absorption measurements in an impedance tube using a single microphone, The Journal of the Acoustical Society of America 80, 555, (1986).

[73] M.A.Nemitallah, R.Ben-Mansour, M.A.Habib, W.H.AhmedI.H.Toor, Z.M.Gasem, H.M.Badr, Solid particle erosion downstream of an orifice, Journal of Fluids Engineering, vol 137, no2, (2014).

[74] A.A.Araoye, H.M.Badr, W.H.Ahmed, Dynamic behaviour of flow through multi-stage restricting orifices, 3rd International conference on fluid flow, Heat and mass transfer no.161 (2016).

[75] N.Atalla, F.Sgard, Modelling of perforated plates and screens using rigid frame porous models, Journal of sound and Vibration, 303, pp195-208, (2007).

[76] J.F.Allard, Propagation of sound in porous media, Elsevier, London, (1993).

[77] R.Tayong, T.Dupont, P.Leclare, Sound absorption of a microperforated plate backed by a porous material under high sound excitation: measurement and prediction, International Journal of Engineering and Technology 2 (4) pp 281-292 (2013).

[78] R.Tayong, T.Dupont, P.Leclare, On the variation of acoustic absorption peak with particle velocity in micro-perforated panels at high level of excitation, The Journal of the Acoustical Society of America 127 (5), pp 2875-2882, (2010).

[79] M.J.Brenan, W.M.To, Acoustic properties of rigid-frame porous materials — an engineering perspective, Applied Acoustics Vol 62, 7, pp 793-811, (2001).

[80] D.L.Johnson, J.Koplik, R.Dashen, Theory of dynamic permeability and tortuosity in fluid-saturated porous media, Journal of Fluid Mechanics vol. 176, pp 379-402, (1987).

[81] D.L.Johnson, T.J Plona, Acoustic slow waves and the consolidation transition, The Journal of the Acoustical Society of America 72, pp 550-565, (1982).

[82] D.L.Johnson, Recent developments in the acoustic properties of porous media, Frontiers in Physical Acoustics, Proc. Enrico Fermi, Course XCIII, pp 255-290 (1986).

[83] Y.Champoux, J.F.Allard, Dynamic tortuosity and bulk modulus in air saturated porous media, Journal of Applied Physics Vol 70, No 4, pp 1975-1979, (1991).

[84] M.C.M.Wright, Lecture notes on the mathematics of acoustics, Imperial College Press, (2005).

[85] D.A.Nield, A.Bejan, Convection in porous media, Springer Books fifth edition, (2017).

[86] S.Whitaker, The Forchheimer equation: A theoretical development, Transport in porous media, 25: pp 27-61, (1996).

[87] H.L.Kuntz, D.T.Blackstock, Attenuation of intense sinusoidal waves in air saturated, bulk porous materials, The Journal of the Acoustical Society of America 81, pp 1723-1731, (1987).

[88] J.P.Groby, W.Huang, A.Lardeau, Y.Auregan, The use of slow waves to design simple sound absorbing materials, J. Appl. Phys. 117, 124903 (2014).

[89] P.Sheng, Introduction to wave scattering, localization and mesoscopic phenomena, Berlin: Springer, (2006).

[90] N.S Dickey, A Selamet, Helmholtz resonators: one-dimensional limit for small cavity length to diameter ratios, Journal of Sound and Vibration 195 (3), pp 512-517, (1996).

[91] M.A.Mironov, Propagation of a flexural wave in a plate whose thickness decreases smoothly to zero in a finite interval, Soviet Physics: Acoustics 34 (3) pp 318-319 (1988).

[92] V.V.Krylov, Acoustic black holes for flexural waves and their potential applications, Proceedings of the Institute of Acoustics Spring Conference, Salford, UK (2002).

[93] V.V.Krylov, F.J.B.S. Tilman, Acoustic black holes for flexural waves as effective vibration dampers, Journal of Sound and Vibration 274 pp 605-619, (2004).

[94] V.V.Krylov, New type of vibration dampers utilising the effect of acoustic black holes, Acta Acustica united with Acustica 90 (5) pp 830-837 (2004).

[95] V.V.Krylov, R.E.T.B. Winward, Experimental investigation of the acoustic black hole effect for flexural waves in tapered plates, Journal of Sound and Vibration 300 (1) pp 43-49, (2007).

[96] D.J.O'Boy, V.V.Krylov, Damping of flexural vibrations in circular plates with tapered central holes, Journal of Sound and Vibration 330 (1) pp 2220-2236, (2011).

[97] L.Zhaou, S.C.Conlon, F.Semperlotti, Broadband energy harvesting using acoustic black hole structural tailoring, Smart Materials and Structures 23, pp 1-9, (2014).

[98] V.Denis, F.Gautier, A.Pelat, J.Poittevin, Measurement and modelling of the reflection coefficient of an acoustic black hole termination, Journal of Sound and Vibration 349 pp 67-79, (2015).

[99] E.E.Narimanov, A.V.Kildishev, Optical black hole: Broadband omnidirectional light absorber, Applied Physics Letters 95, 041106, (2009).

[100] A.El-Ouahabi, V.Krylov, D.O.Boy, Experimental Investigation of the acoustic black hole for sound absorption in air, Proceedings of the 22nd International Congress on Sound and Vibration, Florence, Italy, (2015).

[101] D.R.Raichel, The Science and Applications of Acoustics, Modern acoustics and signal processing, Springer-Verlag New York, Inc (2000).

[102] A.Climente, D.Torrent, J.Sanchez-Dehesa, Omnidirectional broadband acoustic absorber based on metamaterials, Applied Physics Letters, 100, 144103 (2012).

[103] A.El-Ouahabi, V.Krylov, D.O.Boy, Investigation of the acoustic black hole termination for sound waves propagating in cylindrical waveguide, INTER-NOISE and NOISE-CON Congress and Conference Proceedings, Institute of Noise Control Engineering, San Francisco, USA, (2015).

[104] O.Guasch, M.Arnela, P.Sanchez-Martin, Transfer matrices to characterise linear and quadratic acoustic black holes in duct terminations, Journal of Sound and Vibration 395 pp 65-79, (2017).

[105] A.R.Studart, R.M. Erb, R.Libanori, Chapter 8, Hierarchically porous materials in nature, Pp 299-300, Springer International Publishing Switzerland, (2015).

[106] D.Lafarge, P.Lemarinier, J.F.Allard, V. Tarnow, Dynamic compressibility of air in porous structures at audible frequencies, The Journal of the Acoustical Society of America 102, (4) pp 1995 – 2006, (1997).

[107] G.Ma, P.Sheng, Acoustic metamaterials: From local resonances to broad horizons, http://advances.sciencemag.org pp 1-16, (2016).

[108] D.A.Nelson, Propagation of finite-amplitude sound in air-filled porous materials, M.S thesis, The University of Texas at Austin (1984). Also issued, with addition, as 'Interaction of finite-amplitude sound with air-filled porous materials, Tech. Rep. ARL-TR-85-15 Applied Research Laboratories, The University of Texas at Austin (ADA 155 986) (1985).

[109] S.Kuwabara, The forces experienced by randomly distributed parallel circular cylinders or spheres in a viscous flow at small Reynold numbers, Journal Physics Society, Japan 14, pp 527-532 (1959).

[110] D.K.Wilson, J. D. McIntosh, and R. F. Lambert, ''Forchheimer-type

nonlinearity for high intensity propagation of pure tones in air-saturated

porous media,'' J. Acoust. Soc. Am. 84, 350–359 (1988).

[111] P.C.Carmen, Flow of gases through porous media (Academic, New York) (1956).

[112] J.Happel, Viscosity of suspension of uniform spheres, Journal of Applied Physics 28, pp 1288-1292, (1957).

[113] T.A.Strout, Attenuation of sound in high-concentration suspensions: development and application of an oscillatory cell model, Ph.D Thesis, University of Maine, (1991).

[114] O.Umnova, K.Attenborough, K.M.Li. Cell model calculations of viscous drag parameters in packings of spheres, The Journal of the Acoustical Society of America 107, pp 3113-3119, (2000).

[115] Y.Lucas, M.Panfilov, M.Bues, High velocity flow through fractured and porous media: the role of flow non-periodicity, European Journal of Mechanics B/Fluids 26, pp 295-303, (2007).

[116] Y.Auregan, M.Pachebat, Measurement of the nonlinear behaviour of acoustical rigid porous materials, Physics of Fluids 11, pp 1342-1345, (1999).

[117] S.Ergun, A.A.Orning, Fluid flow through randomly packed columns and fluidized beds, Industrial and Engineering Chemistry, vol 41, No 6, pp1179-1184, (1949).

[118] D.T.Blackstock, On plane, spherical, and cylindrical sound waves of finite amplitude in lossless fluids, The Journal of the Acoustical Society of America 36, pp 217-219, (1964).

[119] A.N.Kolmogorov, The local structure of turbulence in incompressible viscous fluid for very large Reynolds numbers, Proceedings Mathematical and Physical Sciences, vol 434, No 1890, pp 9-13, (1991).

[120] D.A.Nield, The limitations of the Brinkman-Forchheimer equation in modelling flow in a saturated porous medium and at an interface, International Journal of Heat and Fluid Flow, vol 12, No 3, pp 269-272, (1991).

[121] V.Achilleos, O.Richoux, G.Theocharis, Coherent perfect absorption induced by the nonlinearity of a Helmholtz resonator, The Journal of the Acoustical Society of America 140 (1), pp 94-100, (2016).

[122] Z.Laly, N.Atalla, S.A.Meslioui, Acoustic modelling of micro-perforated panel at high sound pressure levels using equivalent fluid approach, Journal of Sound and Vibration, pp 1-125, (2018).

[123] S.T.Kawell, L.H.Humphreys, D.C.Stubbs, D.E.Scarborough, A theoretical investigation of the nonlinear acoustic response of abrupt area contractions, The Journal of the Acoustical Society of America 147 (1), pp 500-507, (2020).

[124] J.F.Allard, N.Atalla, Propagation of sound in porous media: Modelling sound absorbing materials, second edition, Wiley, UK, (2009).

[125] D.Y.Maa, Microperforated panel at high sound intensity, Proceedings of Inter Noise 94, Yokohama, Japan, pp 1511-1514, (1994).

[126] B.S.Beck, N.H.Schiller, M.G.Jones, Impedance assessment of a dual-resonance acoustic liner, Applied Acoustics 93, 15-22, (2015).

[127] M.A Mironov, V.V. Pislyakov, One-dimensional sonic black holes: Exact analytical solution and experiments, Journal of Sound and Vibration, 473 (2020).

[128] C.D.Smith, T.L.Parrott, Comparison of three methods for measuring acoustic properties of bulk materials, The Journal of the Acoustical Society of America 74 (5), pp 1577-1582, (1983).

[129] Allard et al, Wave Motion 17 (4), 329 (1993).

[130] Y. Salissou, R.Panneton, O.Doutres, Three-microphone two cavity method for measuring sound transmission loss in a modified impedance tube, 17 - Vol. 39 No. 3, Canadian Acoustics / Acoustique Canadienne, (2011).

[131] Y. Salissou, R.Panneton, O.Doutres, Complement to standard method for measuring

normal incidence sound transmission loss with three microphones, The Journal of the Acoustical Society of America 131, EL216 (2012).

[132] A.Emmanuel, B.Dubus, N.Cote, C.Granger, G.Pot, C.Vasseur, T.Shimizu, C.Croenne, Experimental characterization of foliage and substrate samples by the three- microphone two-load method, INTER-NOISE (2016).

[133] BS EN 29053:1993, ISO 9053:199, Acoustics. Materials for acoustical applications. Determination of airflow resistance.

[134] G.Astavita, G.Greco, “Excess pressure drop in laminar flow through sudden contraction. Newtonian liquids”, Ind. Eng. Chem. 7, 27 – 31 (1968).

[135] P.J. Oliveira, F.T. Pinho, “Pressure drop coefficient of laminar Newtonian flow in axisymmetric sudden expansions”, Int. J. Heat and Fluid Flow 18, 518 – 529 (1997).

[136] J.F.Bartram, Fundamentals of acoustical oceanography, Academic Press, San Diego, California, (1998).

[137] A.Boardman, Pioneers in metamaterials: John Pendry and Victor Veselago, Journal of Optics, Volume 13, Number 2 (2010).

[138] V.G.Veselago, The electrodynamics of substances with simultaneously negative values of ϵ and μ, SOV PHYS USPEKHI, 10 (4), 509–514 (1968).

[139] D.Brooke, O.Umnova, P.Leclaire, T.Dupont, Acoustic Metamaterial for Low Frequency Sound Absorption in Linear and Nonlinear regimes, Journal of Sound and Vibration, 485 -115585 (2020).

[140] X. Olny, C. Boutin, Acoustic wave propagation in double porosity media, The Journal of the Acoustical Society of America 114, 73 - 89 (2003).

[141] L.E. Kinsler and A. R. Frey, A. B. Coppens, J. V. Sanders, Fundamentals of acoustics Wiley, p.274. New York, (2000).

[142] A.W. Leissa, Vibrations of plates, Scientific and Information Division (NASA, Washington, 1969), pp.8-9.

Appendix A. Training and Conferences

DSTL/DGA – Annual Symposium, Paris, France, January 2016.

DSTL/DGA – Annual Symposium, Portsmouth, UK, June 2017.

DENORMS Training School, Le Mans France, December 2017.

SAPEM Conference, Le Mans, France, December 2017.

KTNM – Metamaterials Conference. The Knowledge Transfer Network Metamaterials event. Organised in partnership with Innovate UK. London, January 2018.

DSTL/DGA – Annual Symposium, Paris, France, July 2018.

IOA – Institute of Acoustics Spring Conference, Cardiff, UK, April 2018.

DSTL/DGA – Symposium, Portsmouth, UK, June 2019.

ICSV 26 – International Congress on Sound and Vibration. Montreal, Canada, July 2019.

DENORMS Training School, Budapest, Hungary, December 2019.

UKAN – Physical Acoustics Webinar, UK, April 2020.

COMSOL – Webinar, UK, June 2020.

Appendix B. Publication Paper

Accepted for publication by the Journal of Sound and Vibration July 2020

Journal of Sound and Vibration 485 (2020) 115585

Contents lists available at ScienceDirect

Journal of Sound and Vibration

journal homepage: www.elsevier.com/locate/jsv

Acoustic metamaterial for low frequency sound absorption in linear and nonlinear regimes

Daniel C. Brooke[a,*], Olga Umnova[a], Philippe Leclaire[b], Thomas Dupont[c]

[a] University of Salford, Manchester, England, UK
[b] DRIVE – ISAT Universitie de Bourgogne, Nevers, France
[c] Ecole de Technologie Superieure (ETS) – Universitie du Quebec, Montreal, Canada

ARTICLE INFO

Article history:
Received 20 March 2020
Revised 12 July 2020
Accepted 14 July 2020
Available online 16 July 2020

Keywords:
Acoustic metamaterials
Dead-end pores
Low frequency
Sound absorption
Nonlinear regime
Forchheimer's nonlinearity

ABSTRACT

Acoustic metamaterial absorbers have been built and tested with focus on low frequency airborne sound absorption in linear and nonlinear regimes. The absorbers are made up of a series of piled up flat cavities, separated by thin walls and traversed by a perforation at their centre. A model for absorber effective properties is developed and compared with experimental data. The model is used to derive simple formulae for the frequency and the peak value of the absorption coefficient at the lowest frequency resonance, depending on the geometrical parameters of the structure. Different absorbers have been built with several cavity thicknesses to allow comprehensive comparisons with the model. Nonlinear properties of the absorbers are investigated experimentally using sine wave excitation around the resonance frequency with the amplitude of the incident wave up to 250 Pa. Flow resistivity measurements at low flow rates show that the periodic set of cavities does not modify resistivity significantly when compared to a simple perforated cylinder with same thickness. As flow rate increases, the flow resistivity grows linearly according to Forchheimer's law and has a significant dependence on the absorber thickness. A numerical model is developed accounting for the linear growth of flow resistivity with particle velocity amplitude in the central perforation and compared with the measurements at high amplitudes of the incident wave.

List of symbols

ω	angular sound frequency
p	pressure of sound wave
v	particle velocity of sound wave
c	sound speed in air
ρ_0	density of air
η	viscosity of air
$C_0 = \frac{1}{\rho_0 c^2}$	compressibility of air
$k = \frac{\omega}{c}$	wavenumber of air

* Corresponding author.
E-mail addresses: D.C.Brooke@edu.salford.ac.uk (D.C. Brooke), O.Umnova@edu.salford.ac.uk (O. Umnova), Philippe.Leclaire@u-bourgogne.fr (P. Leclaire), Thomas.Dupont@etsmtl.ca (T. Dupont).

https://doi.org/10.1016/j.jsv.2020.115585

N_{pr}	Prandtl number
γ	adiabatic constant
Re	Reynolds number
R	outer radius of the absorber
r_0	radius of central perforation
d_p	plate thickness
d_c	width of lateral cavity (distance between the plates)
L	absorber thickness
$\rho(\omega), C(\omega)$	effective density and effective compressibility of air inside the perforation with the lateral cavities
$\rho_p(\omega), C_p(\omega)$	effective density and effective compressibility of air inside the main perforation without lateral cavities
$\rho_c(\omega), C_c(\omega)$	effective density and effective compressibility of air inside the lateral cavities
$k_c = \omega\sqrt{C_c(\omega)\rho_c(\omega)}$	wavenumber of air in the lateral cavity
$q = \omega\sqrt{\rho(\omega)C(\omega)}$	wavenumber of air inside the absorber
$\phi_p = (\frac{r_0}{R})^2$	surface porosity of the absorber
$\phi_w = \frac{d_c}{d_c+d_p}$	porosity of the main perforation wall
ξ	Forchheimer's nonlinearity parameter
V_f	flow velocity in the flow resistivity rig tube
$U = \frac{V_f}{\phi_p}$	flow velocity in the main perforation
$\sigma_{p,\,c}, \sigma$	static flow resistivity of the main perforation, cavity and the whole sample, respectively
$\Lambda_{\mathrm{p,\,c}}$	characteristic viscous length for the main perforation and cavity, respectively
$\alpha_{\infty p,\,c}$	high frequency tortuosity for the main perforation and cavity, respectively
$\kappa'_{p,c}$	thermal permeability for the main perforation and cavity, respectively
$\Lambda'_{p,c}$	thermal characteristic length for the main perforation and cavity, respectively
f_r	frequency of the first absorber resonance
α_r	peak value of the absorption coefficent at resonance
p_i	incident pressure amplitude

1. Introduction

In recent work by Dupont et al., [1], a 3D printed microstructure was considered that contains a periodic arrangement of thin plates with central perforation separated by cavities (Fig. 1), the so-called "pancake absorber". This absorber is one of the realizations of the microstructure design suggested earlier in work by Leclaire et al [2] where the additional laterally arranged pores are coupled with the main perforation. Low value of sound speed through the perforation achieved in these structures [3] leads to the existence of the absorption peaks at low frequencies. In [1], a transfer matrix model (TMM) is used to predict the frequency dependence of the absorption coefficient, which gives a good agreement with the measurements. The pancake absorbers are proven to be effective for low frequency sound absorption at only a few centimetres in thickness.

Metamaterial structures, studied in this work, are similar to pancake absorbers (and for this reason we use the same name) but made of periodically arranged metallic plates with the central perforation. They are mechanically robust and do not contain any fibrous materials or foams. This makes them good candidates, alongside with microperforated absorbers, for the use in hostile environments for attenuation of high amplitude noise [4]. It is known that the dominating nonlinearity in

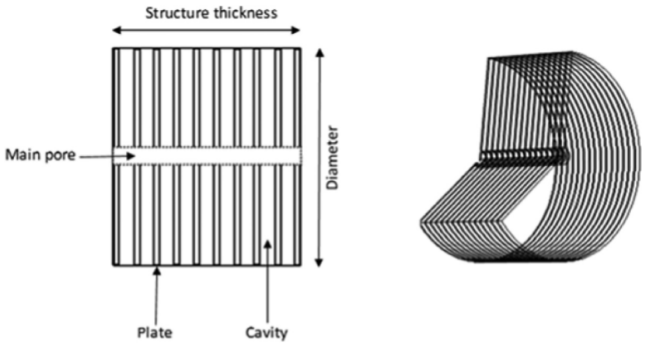

Fig. 1. Geometry of the sample.

rigid porous materials is of Forchheimer's type, associated with the growth of static flow resistivity with the Reynold's number (and consequently pressure amplitude). It was noted by Kuntz and Blackstock, [5] that although the usual manifestation of acoustic nonlinearity in fluids is harmonics generation, this does not happen in porous materials where the losses are high. Instead, the losses themselves become amplitude dependent. In the last three decades, the Forchheimer's nonlinearity in rigid porous materials has been studied in numerous papers, see for instance [6–13]. Numerical and analytical models have been developed, based on modifications of the effective material density to include particle velocity dependence of flow resistivity, and sucessfully compared with the data.

Nonlinear behaviour of absorbers with low surface porosity, single orifices and micro perforated plates (MPP), has been studied extensively starting from a pioneering work by Sivian [14]. Ingard and Ising [15] measured acoustic resistance and reactance of an orifice as a function of velocity amplitude in it, demonstrating strong nonlinearity of acoustic resistance and lower effect of velocity on acoustic reactance. The high values of particle velocity reached at the perforation lead to the formation of vortices, which, in turn, affect the acoustic resistance. The acoustic nonlinearity of orifices have then been studied both theoretically and experimentally by Cummings and co authors. In [16] the model was developed for the sound transmission through the duct termination at high amplitudes in the presence and in the absence of steady flow. It was compared with the data obtained using broadband signals, and a good agreement has been demonstrated. The model was then validated for tone bursts by measuring transmission coefficent through the orifice at different sound pressure levels [17]. The vortices, generated at both sides of the orifice, have been visualised and their translational velocity measured for different peak velocities inside the orifices. A good agreement of the frequency domain model with both high amplitude broadband signals and tone bursts can be considered as a confirmation that in the case of strong nonlinear losses, the interactions between different frequency components is weak and Fourier transform could still provide useful results. The simple model accounting for the nonlinear resistance of the orifice, has been recently used in work of Achilleos et al [18] to study the nonlinearity of Helmholtz resonators, side loaded to the waveguide. It has been shown that, due to the increase of resistance with incident pressure amplitude, the initially low peak absorption of Helmholtz resonator increases and reaches the unity at 160 dB. Nonlinearities in microperforated panel (MPP) absorbers have first been studied by Maa in [19] The resistance of the orifice has been expressed as a linear function of the Mach number inside it and of the open area (equivalent to front surface porosity). The weak nonlinearity of the acoustic reactance of the orifice has also been accounted for. A more precise, empirical model for the nonlinear resistance has been proposed in [4] based on the data obtained for SPL around 140 dB, characteristic for launcher fairings applications. Tayong et al in [20] studied the dependence of the peak absorption of the MPP backed by air cavity, both theoretically and numerically. It has been demonstrated that the peak absorption coefficient can grow up to a maximum value of 1 as Mach number increases to a critical value, similar results were obtained for Helmholtz resonators in [18]. When the Mach number is higher than the critical value, the absorption decreases with it. In subsequent work [21] by Tayong et al the interaction between the multiple holes in MPP in the nonlinear regime has been studied experimentally. The model which treats the nonlinearity of the MPP absorber using equivalent fluid approach [22] was developed by Laly et al in [23]. They have shown that the nonlinear correction to the acoustic resistance of MPP expressed as a linear function of velocity can be interpreted in terms of velocity dependent flow resistivity of the plate, i.e. Forchheimer's nonlinearity. Unlike rigid porous material models, they also considered velocity dependence of the tortuosity due to nonlinear decrease of the end correction.

The pancake absorbers are different from conventional porous materials in two respects. First, the surface porosity, defined as the ratio of the main perforation surface area to the front surface area of the absorber, is much lower than that of a conventional porous absorber. This means the early onset of nonlinearity, due to large values of Reynolds number inside the main perforation, similar to MPP absorbers. However, contrary to MPPs, these absorber thickness is much larger than the size of the perforation. The latter means that the models should account for sound propagation within the structure. A simple approximation of the surface impedance assuming that the wavelength is much larger than the thickness of the sample, used for instance in [24], might not be valid.

Second difference with the conventional rigid porous materials is the particular microstructure of the absorber. The presence of the lateral cavities makes it effectively a double porosity structure as described by Olny and Boutin in [25] with the first porosity scale associated with the main perforation and the second with the lateral cavities. The interaction of high amplitude sound with double porosity materials is a new topic to be studied.

The paper is organised as follows. In Section 2, we start with developing a linear model for the effective properties, density and bulk modulus, of the absorber and use it to predict the dependence of the position of the lowest resonance frequency and the peak value of the absorption coefficient on the structure geometry. For these, we derive simple analytical approximations. This model is validated against the experimental results obtained in standard impedance tube using white noise excitation. The measurements have been done on several samples, with different thicknesses and cavity widths, to investigate the limitations of the model. In Section 3, the measurements of flow resistivity of the samples are described. These measurements are necessary to obtain the Forchheimer'sparameters, to be used in the nonlinear model. To investigate the effect of lateral cavities on the static flow resistivity values and on Forchheimer's nonlinearity parameter, the measurements performed on several absorbers and also on the corresponding solid cylinders with same thickness and central perforation size (thus eliminating the effect of cavities completely). The samples of different thicknesses have been tested in flow resistivity rig too. In Section 4, the nonlinear model is described and validated using pure tone signals of different amplitudes. The model does not have any adjustable parameters and uses independently measured Forchheimer's nonlinearity parameters, as described in Section 3. The absorption coefficient measurements are performed in specially designed high

sound pressure level (HSPL) impedance tube. The highest-pressure level of the incident wave achieved in the tube is around 160 dB. The Conclusions summarise the main results of the work.

2. Absorber in the linear regime – model and its experimental validation

2.1. Model

2.1.1. Effective properties

We consider an absorber composed of equally spaced identical rigid plates with radius R and thickness d_p, where subscript "p" stands for "plate". Each plate has a central perforation with radius r_0. The spacing between the plates is d_c, where subscript "c" stands for "cavity". The cavities are rigidly backed at the outer boundary, R. The geometry is shown in Fig. 1.

To obtain effective properties of the structure, the results derived in a previous publication [2] will represent a starting point for establishing the model adapted to the new geometry. In the current design, periodically spaced cylindrical dead end (subscript "de") pores, as they are referred in [2], are replaced by the annular cavities with the outer radius R, inner radius r_0 and thickness d_c. Low frequency approximation is considered, meaning that wavelength of sound travelling through the main perforation is much larger than the period of the structure, $Re(k_{mp}h) \ll 1$. Here subscript mp stands for "main perforation", k_{mp} is wavenumber of air in the main perforation without cavities present and $h = d_p + d_c$ is the period of the structure. Expressions for the characteristic impedance Z and wavenumber q of air in the pore with the dead ends present are given by Eqs. (28) and (32) in [2]:

$$Z = \frac{Z_{mp}}{\sqrt{1 + \frac{2X}{ik_{mp}h}}} \tag{1}$$

$$q = k_{mp}\sqrt{1 + \frac{2X}{ik_{mp}h}} \tag{2}$$

where time convention is $e^{-i\omega t}$.

Parameter X is defined by Eq. (2) in [2]

$$X = -\frac{NA_{de}}{2\ A_{mp}}\frac{1}{Z_{s\ de}} \tag{3}$$

here N is the number of dead end pores per period, A_{mp} is the cross sectional area of the main pore and A_{de} is the cross section area of the dead end pore opening into the main pore. $Z_{s\,de}$ is the surface (hence subscript "s") impedance of the single dead end pore normalised to the characteristic impedance of air in the main pore, Z_{mp}. For the current design, NA_{de}, which is the total surface area of the cavity opening into the main perforation per period, is equal to $2\pi r_0 d_c$ (therefore $NA_{de} \to 2\pi r_0 d_c$). The surface area of the main cylindrical perforation is πr_0^2 (therefore $A_{mp} \to \pi r_0^2$). Introducing surface admittance of the cavity normalised by the characteristic admittance of air $\frac{1}{\rho_0 c}$, $G(\omega) = \frac{\rho_0 c}{Z_{s\ de}\ Z_{mp}}$, Eq. (3) can be rewritten as

$$X = -\frac{1}{\rho_0 c}\frac{d_c}{r_0}\ G(\omega)\ Z_{mp}. \tag{4}$$

Now expressions for the effective density $\rho(\omega)$ and effective compressibility $C(\omega)$ of air within the perforation with the side cavities can be derived from (1), (2) and (4). Note that to reflect the change in geometry, the subscript p is now used for the quantities related to "perforation" ($mp \to p$) and subscript c is used for the quantities related to "cavity" ($de \to c$):

$$\rho(\ \omega) = \frac{qZ}{\omega} = \rho_p, \tag{5}$$

$$C(\ \omega) = \frac{q}{\omega Z} = C_p + iC_0\frac{2}{kr_0}\ G_w(\omega), \tag{6}$$

where $k = \frac{\omega}{c}$ is wavenumber of air, $C_0 = \frac{1}{\rho_0 c^2}$ is compressibility of air, the admittance of the main perforation wall is $G_w(\omega) = G(\omega)$, $\phi_w = \frac{\rho_0 c}{Z_{s\ c}\ Z_p}\phi_w$ and $\phi_w = \frac{d_c}{h}$ can be treated as porosity of the main perforation wall. It follows from Eq. (5) that the presence of the lateral cavities does not affect the effective density of air in the main perforation and it remains equal to that of the perforation without the cavities $\rho_p = \frac{Z_p k_p}{\omega}$. The effective compressibility of air inside the structure is not equal to that of the perforation, $C_p = \frac{k_p}{\omega Z_p}$, and is dependent of the geometry of the cavities.

Surface impedance of the perforation wall $G_w(\omega)$ is calculated assuming no angular dependence of pressure inside the cavities so that it varies only with the polar coordinate r, which is defined as the distance from the centre of the main pore. Helmholz equation for pressure inside the cavity in this case is

$$p'' + \frac{1}{r}p' + k_c^2 p = 0, \tag{7}$$

Table 1
Parameters of JCAL model for the perforation and the cavities [27].

Parameter	Perforation (subscript p)	Cavity (subscript c)
$\sigma_{p,\,c}$	$8\eta/r_0^2$	$12\eta/d_c^2$
$\alpha_{\infty p,\,c}$	1	1
$\Lambda_{p,\,c}$	r_0	d_c
$\Lambda'_{p,c}$	r_0	d_c
$\kappa'_{p,c}$	$r_0^2/8$	$d_c^2/12$
$\omega_{b\ p,c} = \omega'_{b\ p,c}$	$16\eta/\rho_0\ r_0^2$	$36\eta/\rho_0\ d_c^2$

where $k_c(\omega)$ is effective wavenumber of air in the cavity of thickness d_c between two rigid plates. The derivatives are with respect to r.

Relationship between the radial component of particle velocity $v(r)$ and pressure $p(r)$ in the fluid with effective density $\rho_c(\omega)$ is followed from the Euler's equation

$$v = \frac{-ip'}{\omega\rho_c(\omega)}. \tag{8}$$

General solution of Eq. (7) can be written as $p = A\,J_0(k_c r) + BH_0(k_c r)$, where J_0 and H_0 are Bessel function and Hankel function of the first kind respectively, A and B are arbitrary constants. The cavity is rigidly backed at $r = R$, so boundary condition $p'(R) = 0$ is applied. This results in the following expression for pressure and particle velocity in the cavity

$$p = A\left(J_0(k_c r) - \frac{J_1(k_c R)}{H_1(k_c R)}H_0(k_c r)\right) \tag{9}$$

$$v = \frac{iAk_c}{\omega\rho_c}\left(J_1(k_c r) - \frac{J_1(k_c R)}{H_1(k_c R)}H_1(k_c r)\right) \tag{10}$$

Normalised surface admittance of the wall of the main perforation is calculated as $G_w = \rho_0 c\phi_w \frac{v(r_0)}{p(r_0)}$ giving

$$G_w = \frac{i\ \phi_w\rho_0 c}{Z_c}\frac{\left(J_1(k_c r_0) - \frac{J_1(k_c R)}{H_1(k_c R)}H_1(k_c r_0)\right)}{\left(J_0(k_c r_0) - \frac{J_1(k_c R)}{H_1(k_c R)}H_0(k_c r_0)\right)} \tag{11}$$

where $Z_c(\omega) = \sqrt{\frac{\rho_c(\omega)}{C_c(\omega)}}$ is characteristic impedance of air in the cavity.

The model for the effective properties of air inside the structure, $\rho(\omega)$ and $C(\omega)$, defined by Eqs. (5), (6) and (11) can be used to calculate the surface impedance Z_s of the absorber and its absorption coefficient α using the usual expressions. In case of rigidly backed absorber of thickness L they are

$$Z_s = i\frac{Z}{\phi_p}\ \mathrm{cotan}(qL), \tag{12}$$

$$\alpha = 1 - \left|\frac{Z_s - \rho_0 c}{Z_s + \rho_0 c}\right|^2, \tag{13}$$

with $\phi_p = (\frac{r_0}{R})^2$ being the front surface porosity, $Z = \sqrt{\frac{\rho(\omega)}{C(\omega)}}$, $q(\omega) = \omega\sqrt{\rho(\omega)C(\omega)}$.

For further calculations, expressions for effective density and compressibility of air in straight cylindrical pore and in the cavity, i.e. slit with thickness d_c, $\rho_{p,c}(\omega)$ and $C_{p,c}(\omega)$, are required. These are obtained using Johnson-Champoux -Allard -Lafarge (JCAL) equivalent fluid model [22,26,27]:

$$\rho_{p,\ c}(\omega) = \rho_0\ \alpha_{\infty\ p,c}\left(1 + \frac{\sigma_{p,c}}{-i\omega\alpha_{\infty\ p,c}\rho_0}\sqrt{1 + \frac{-i\omega}{\omega_{b\ p,c}}}\right) \tag{14}$$

$$C_{p,\ c}(\omega) = C_0\left(\gamma - \frac{\gamma - 1}{1 + \frac{\eta}{-i\omega'\rho_0\kappa'_{p,c}}\sqrt{1 + \frac{-i\omega'}{\omega'_{b\ p,c}}}}\right) \tag{15}$$

where $\omega' = \omega N_{pr}$, N_{pr} is Prandtl number, $\omega_{b\ p,c} = \frac{\sigma_{p,c}^2\Lambda_{p,c}^2}{4\,\alpha_{\infty\ p,c}^2\,\rho_0\eta}$ and $\omega'_{b\ p,c} = \frac{\Lambda'^2_{p,c}\eta}{4\,\kappa'^2_{pc}\rho_0}$ are characteristic viscous and thermal frequencies of the main pore (p) and lateral cavities (c). The parameters of the model, static air flow resistivity σ, characteristic viscous length Λ, high frequency tortuosity α_∞, thermal permeability κ' and thermal characteristic length Λ' can be calculated using simple expressions (given in Table 1) for the central perforation (straight cylindrical pore of radius r_0) and for the cavity (slit of thickness d_c).

The model described in this section will be further referred to as "full model". It is applicable when the wavelength of sound propagating through the structure is much larger than the period of the microstructure, i.e. $Re(q)h \ll 1$.

2.1.2. Estimation of resonance frequency f_r *and absorption coefficient* α_r *at first resonance*

To estimate the frequency of the first resonance f_r of the hard-backed layer with thickness L the following assumptions are used. First, it is assumed that

$$|k_c(2\pi f_r)|R \ll 1 \tag{16}$$

which allows to use Bessel functions' expansions for small arguments. This assumption means that at resonance the wavelength of sound within the lateral cavities is much larger than their radius R. Second, resonance frequency is assumed to be much higher than characteristic viscous and thermal frequencies for both main perforation and lateral cavities, $f_r \gg f_{b\ p,c} = \frac{\omega_{b\ p,c}}{2\pi}$ and $f_r \gg f'_{b\ p,c} = \frac{\omega'_{b\ p,c}}{2\pi}$. Using expressions for JCAL model parameters given in Table 1, these conditions can be rewritten as

$$f_r \gg \frac{1}{2\pi}\frac{36\eta}{d_c^2\rho_0} \text{and} f_r \gg \frac{1}{2\pi}\frac{16\eta}{\rho_0 r_0^2}. \tag{17}$$

These assumptions mean that that sound propagates in inertial regime through both main perforation and lateral cavities. Third, it is required that porosity of the central perforation wall is much higher than the surface porosity of the sample, $\phi_w \gg \phi_p$. The validity of these approximations for the measured samples will be checked further in the paper.

Now, the following derivation steps are performed. Bessel functions and their combinations are expanded in Taylor series for small arguments $k_cR = O(\varepsilon)$ and $k_cr_0 = O(\varepsilon)$, accounting for terms linear in ε [28]:

$$\begin{aligned} &J_0(k_cr_0) \approx 1 \\ &J_1(k_cr_0) \approx \tfrac{k_cr_0}{2} = O(\varepsilon) \\ &\tfrac{J_1(k_cR)}{H_1(k_cR)}H_0(k_cr_0) \approx -(k_cR)^2\log k_cr_0 = o(\varepsilon) \\ &\tfrac{J_1(k_cr_0)}{H_1(k_cR)}H_1(k_cR) \approx \tfrac{k_cR}{2}\tfrac{R}{r_0} = O(\varepsilon) \end{aligned} \tag{18}$$

These expansions are used to obtain approximation for the second term in the Eq. (6) for the effective compressibility:

$$iC_0\frac{2}{kr_0}\ G_w(\omega) \approx \phi_w C_0\frac{\rho_0 c}{k}\frac{k_c}{Z_c}\left(\left(\frac{R}{r_0}\right)^2 - 1\right) = \frac{(1-\phi_p)\phi_w}{\phi_p}C_c. \tag{19}$$

This results in a simple expression for the effective compressibility $C(\omega)$ of the fluid in the structure

$$C(\ \omega) \approx C_p + \frac{(1-\phi_p)\phi_w}{\phi_p}C_c, \tag{20}$$

where it is presented as a weighted sum of fluid compressibilities in the main perforation and in the lateral cavities, $C_{p,\,c}$.

Second, using expressions for JCAL model parameters given in Table 1 and assumption of the inertial regime achieved in the pore and in the cavities at resonance (17) effective compressibilities of air in the perforation and in the lateral cavities, $C_{p,\,c}$ are approximated as

$$C_{p,c}(\ \omega) \approx C_0\left(1 + (\gamma-1)\frac{2}{x_{p,c}}\sqrt{\frac{\eta}{-i\omega N_{pr}\rho_0}}\right), \tag{21}$$

where $x_p = r_0$ and $x_c = d_c$. Together with Eq. (20) and approximation of a low porosity ϕ_p, $\phi_w \gg \phi_p$, this leads to the final approximation of $C(\omega)$:

$$C(\ \omega) \approx C_0\left(\ 1 + \frac{\phi_w}{\phi_p} + \frac{(\gamma-1)}{\sqrt{N_{pr}}}\frac{2}{r_0}\sqrt{\frac{\eta}{-i\omega\rho_0}}\left(1 + \frac{r_0}{d_c}\frac{\phi_w}{\phi_p}\right)\right), \tag{22a}$$

Although $\frac{\phi_w}{\phi_p} \gg 1$ for the designs considered in this work, the first terms in the brackets, are left here to demonstrate that in the absence of the cavities ($\phi_w = 0$), the compressibility of air in the straight cylindrical pore given by Eq. (21) is recovered from Eq. (22a). In the following, however, this term will be neglected transforming (22a) into

$$C(\ \omega) \approx C_0\frac{\phi_w}{\phi_p}\left(\ 1 + \frac{(\gamma-1)}{\sqrt{N_{pr}}}\frac{2}{r_0}\sqrt{\frac{\eta}{-i\omega\rho_0}}\frac{r_0}{d_c}\right), \tag{22b}$$

In the inertial regime defined by Eq. (17), effective density (5) is approximated as

$$\rho(\ \omega) \approx \rho_0\left(1 + \frac{2}{r_0}\sqrt{\frac{\eta}{-i\omega\rho_0}}\right). \tag{23}$$

Finally, combining Eqs. (22b) and (23) an approximation for the wavenumber $q(\omega) = \omega\sqrt{\rho(\omega)C(\omega)}$ and characteristic impedance $Z = \sqrt{\rho(\omega)/C(\omega)}$ of air in the pancake absorber are obtained

$$q(\omega) \approx k\sqrt{\frac{\phi_w}{\phi_p}}\left(1 + \frac{1}{r_0}\sqrt{\frac{\eta}{-i\omega\rho_0}}\left(1 + \frac{\gamma - 1}{\sqrt{N_{pr}}}\frac{r_0}{d_c}\right)\right). \tag{24a}$$

$$Z(\omega) \approx \rho_0 c\sqrt{\frac{\phi_p}{\phi_w}}\left(1 + \frac{1}{r_0}\sqrt{\frac{\eta}{-i\omega\rho_0}}\left(1 - \frac{\gamma - 1}{\sqrt{N_{pr}}}\frac{r_0}{d_c}\right)\right). \tag{24b}$$

Condition of a quarter wavelength resonance for the hard backed structure, $Re(q)L = \frac{\pi}{2}$, leads to a quadratic equation for the square root of the resonance frequency $\sqrt{f_r}$. Its positive solution is

$$\sqrt{f_r} = \frac{\sqrt{f_0}}{2}\left(-\mu + \sqrt{\mu^2 + 4\sqrt{\frac{\phi_p}{\phi_w}}}\right), \tag{25}$$

where

$$\mu = \frac{1}{r_0}\sqrt{\frac{\eta}{-i\omega\rho_0 f_0}}\left(1 + \frac{\gamma - 1}{\sqrt{N_{pr}}}\frac{r_0}{d_c}\right) \tag{26}$$

and $f_0 = \frac{c}{4L}$ is the quarter wavelength resonance frequency of air slab of thickness L. Further approximation is made assuming $|\mu^2| \gg 4\sqrt{\frac{\phi_p}{\phi_w}}$, or, roughly,

$$\sqrt{\frac{\phi_p}{\phi_w}} \gg 0.01\ \frac{f_{b\,p}}{f_0} \tag{27}$$

where $f_{b\,p} = \frac{\omega_{b\,p}}{2\pi} = \frac{8\eta}{\pi\rho_0 r_0^2}$ and the characteristic viscous frequency ω_{bp} for the main perforation is given in Table 1.

The validity of this approximation for the experimental designs will be confirmed later. Final estimate for the resonance frequency is

$$f_r \approx f_0\sqrt{\frac{\phi_p}{\phi_w}}\left(1 - \frac{1}{4}\sqrt{\frac{f_{b\,p}}{2f_0}}\sqrt{\frac{\phi_w}{\phi_p}}\left(1 + \frac{\gamma - 1}{\sqrt{N_{pr}}}\frac{r_0}{d_c}\right)\right). \tag{28}$$

Under the same assumptions, absorption coefficient at resonance is now estimated. First, we note that at the resonance frequency $qL = \frac{\pi}{2}(i + 1 - \frac{f_r}{f_0}\sqrt{\frac{\phi_w}{\phi_p}})$ and, using Eq. (24b), obtain the following estimation of the normalised surface impedance (12):

$$Z_s \approx \frac{\rho_0 c}{\sqrt{\phi_w\phi_p}}\left(1 + \frac{1}{r_0}\sqrt{\frac{\eta}{-i\omega\rho_0}}\left(1 - \frac{\gamma - 1}{\sqrt{N_{pr}}}\frac{r_0}{d_c}\right)\right)\frac{1 - e^{-n}}{1 + e^{-n}}, \tag{29}$$

where $n \approx \pi(1 - \frac{f_r}{f_0}\sqrt{\frac{\phi_w}{\phi_p}})$. Then, this is substituted into the expression (13) for the absorption coefficient. Since $\sqrt{\phi_w\phi_p} \ll 1$ and $|\frac{1}{r_0}\sqrt{\frac{\eta}{-i\omega\rho_0}}| \ll 1$, their products are neglected. Finally, the following estimation of the absorption coefficient at resonance α_r is obtained

$$\alpha_r \approx \frac{4\sqrt{\phi_w\phi_p}\left(1 - e^{-2n}\right)}{\left(\left(\sqrt{\phi_w\phi_p} + 1\right) - e^{-n}\left(1 - \sqrt{\phi_w\phi_p}\right)\right)^2}. \tag{30}$$

Estimations given by Eqs. (28) and (30) are convenient to investigate the dependence of the resonance frequency and the peak value of the absorption coefficient on the geometry of the structure.

2.2. Experiments and linear model validation

The experiments have been performed on the samples composed of plates with thickness $d_p = 1$ mm and spacings between them $d_c = 1$ mm, 3 mm, 6 mm and plates with thickness $d_p = 3$ mm with spacings $d_c = 1$ mm. The radius of the central perforation was kept $r_0 = 4$ mm and the outer radius of all samples was $R = 50$ mm. This means that for all samples the surface porosity was $\phi_p = 6.4 \times 10^{-3}$.

Table 2
Measured, $f_r^{(1)}$ and $\alpha_r^{(1)}$, predicted by the full model, $f_r^{(2)}$ and $\alpha_r^{(2)}$, and predicted by approximations (28) and (30), $f_r^{(3)}$ and $\alpha_r^{(3)}$,values of the first resonance frequency f_r and peak absorption coefficient α_r for all samples. Dimensions of the samples – columns 2-4, ϵ is relative error between the measured resonance frequency $f_r^{(1)}$ and approximation $f_r^{(3)}$ given by Eq. (28), in %.

Sample	L, mm	d_p, mm	d_c, mm	$f_r^{(1)}$, Hz	$f_r^{(2)}$, Hz	$f_r^{(3)}$, Hzϵ, %	$\alpha_r^{(1)}$	$\alpha_r^{(2)}$	$\alpha_r^{(3)}$
1	31	1	1	262	265	270 3	0.87	0.97	0.98
2	30	1	3	229	229	231 1	0.99	0.96	0.96
3	35	1	6	222	187	189 15	0.99	0.92	0.92
4	60	1	1	146	144	144 2	0.88	0.91	0.92
5	58	1	3	135	125	125 7	0.99	1.0	1.0
6	63	1	6	134	108	108 17	1	0.97	0.97
7	33	3	1	337	343	363 8	0.94	0.92	0.94
8	60	3	1	185	202	206 11	0.90	0.86	0.87

The structures are constructed of aluminium alloy for both plates and spacers (thin rings with outer radius equal to R). The thickness of the spacers was 1 mm and the cavities' thickness could be varied depending on the number of spacers used.

Absorption coefficients of the rigidly terminated structures were measured in a standard B&K impedance tube with inner radius 100 mm, using two microphone method. The working range of the apparatus was 50Hz – 1600 Hz. The frequency resolution was 1 Hz. The purpose of these measurements was to provide a variety of data for the comparisons with the model. Fig. 2(a–c) shows comparisons of the impedance tube data for the absorption coefficient with the model based on Eqs. (5), (6), (11), (14), (15) (referred to as "full model" in the following) for samples with thickness close to 30 mm. Corresponding results for samples with thickness close to 60 mm are shown in Fig. 3(a–c). The range of the thicknesses was due to the discrete nature of the material structure and imperfections of the plates and the spacers.

Porosity of the main pore walls due to the presence of the cavities were $\phi_w = 0.5$ for $d_c = 1$ mm, $\phi_w = 0.75$ for $d_c = 3$ mm and $\phi_w = 0.87$ for $d_c = 6$ mm.

In addition to the samples constructed of 1 mm plates, we performed impedance tube measurements on the samples constructed of 3 mm plates with spacings between them equal to 1 mm. The aim of these measurements was to test the model in the case of a relatively low ($\phi_w = 0.25$) porosity of the wall. The results are shown in Fig. 4.

The predictions for Helmholtz resonator absorption coefficient are shown in all figures for comparison. The Helmholtz resonator was modelled as a single plate (plate thickness was kept the same as those of the absorbers) with 8 mm diameter perforation backed by a rigidly backed air cavity. The overall thickness of the resonator was in each case equal to that of the absorber. In calculations for both absorber and Helmholtz resonator the end correction $l_e = \frac{8}{3\pi} r_0$ [29] was accounted for. In case of Helmholtz resonator two end corrections (external and internal) have been added to the thickness of the plate. This is justified by the fact that Helmholtz resonator cavity size was much larger than l_e. For the absorbers only external end correction has been considered.

Table 2 summarizes the results of the measurements for the first absorption peak frequency. Full model predictions and those given by the simplified Eqs. (28) and (30) for the frequency of the first resonance and the peak value of the absorption coefficient. The characteristic frequency for the air in the main pore was the same in all configurations, $f_{b\,p} = 2.5$ Hz, the characteristic frequencies f_{bc} for air in the cavities were $39.2, 9.8\,and\,2.5$ Hz for $d_c = 1,\ 3$ and 6 mm respectively.

To make sure that the approximations given by Eqs. (28) and (30) can be used, the conditions of their applicability given by Eqs. (16), (17) and (27) were checked and proven valid. The only marginal case is the second of conditions (17) for Sample 4 which results in inequality $39.2 << 146$. However, a good agreement is still observed between the measurements and the predictions for the first resonance peak for this sample. The disagreements between the measurement and the predictions for f_r are the strongest ($\geq$ 15%) for samples 3 and 6 with wider cavities, $d_c = 6$ mm. However, the full and the approximate models give nearly identical predictions for these samples, so the disagreement is observed because the model based on effective properties is only applicable when $r_0 > d_c$. This has been assumed in our previous work [2] when the dead-end pore was described by the surface's impedance $Z_{s\,de}$ for the wave travelling through the main pore and is essential for Eqs. (1)–(3) to be valid. The assumption $r_0 > d_c$ implicitly states the existence of "scale separation" [25] between the main pore and the cavities, and the existence of small parameter $\frac{d_c}{r_0} < 1$. Indeed, by inspecting Eq. (6) it becomes clear, that the modification of the compressibility due to the presence of the side cavities (6) is identical to that predicted for a double porosity material with high permeability contrast, given by Eq. (103) from [25]. The structures we studied could indeed be described as double porosity material with one porosity scale formed by the main pore and another by the side cavities.

Apart from this case, the difference between the predicted and measured values of the first resonance frequency f_r and peak absorption α_r are no more than 11% (Sample 8).

The resonance frequency f_r depends strongly on the porosity of the central pore wall ϕ_w decreasing from 337 Hz for Sample 7 with $\phi_w = 0.25$ to 222 Hz for Sample 3 with $\phi_w = 0.75$ (the samples have close thicknesses of 33 mm and 35 mm respectively). This is the decrease of more than 30%. The measured peak value of the absorption coefficient, however, grows only slightly, from 0.94 for Sample 7 to 0.99 for Sample 3. A similar decrease (29%) in the frequency of the first resonance

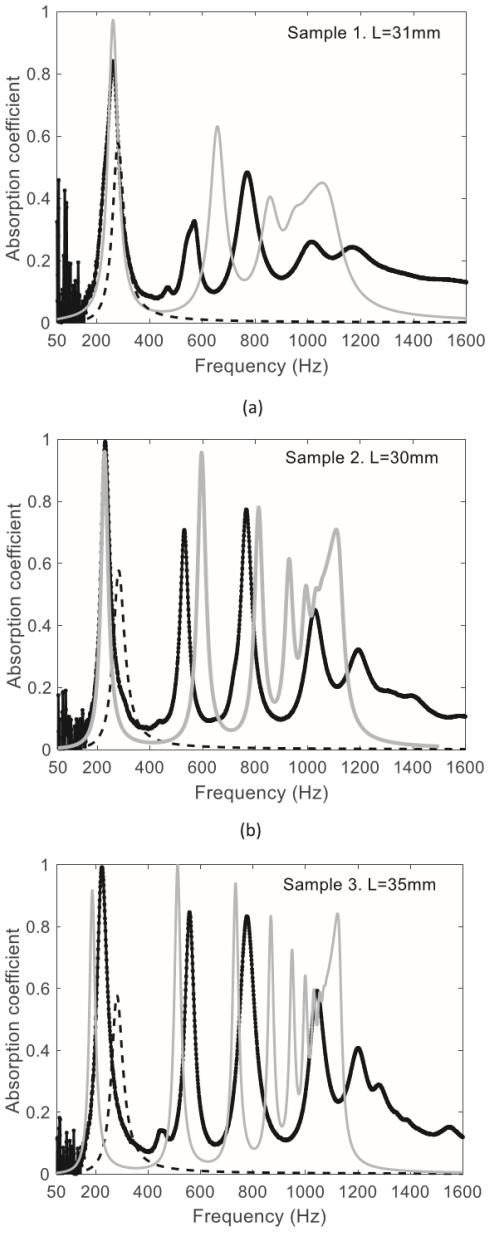

Fig. 2. Absorption coefficient data (markers) and full model predictions (grey lines) for hard backed absorbers composed of 1 mm thick plates, absorber thickness is around $L = 30$ mm. Spacings between the plates are $d_c = 1$ mm (a), $d_c = 3$ mm (b) and $d_c = 6$ mm (c). Absorption coefficient predictions for Helmholtz resonator of same size as the absorber is shown by dashed lines. Exact thicknesses are given in each figure.

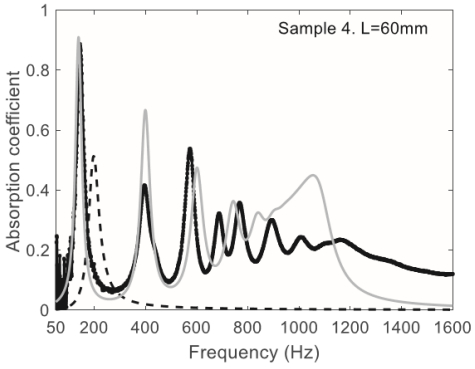

(a)

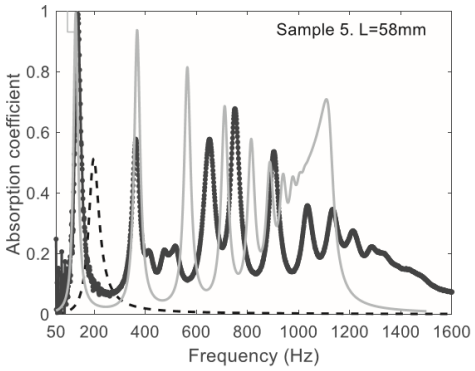

(b)

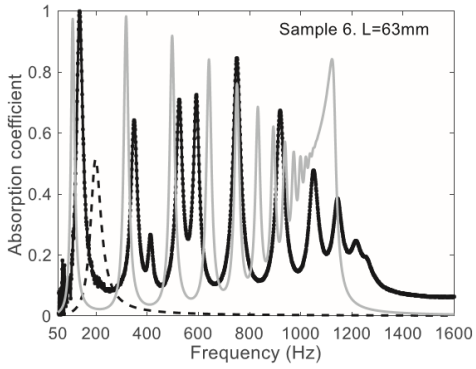

(c)

Fig. 3. Absorption coefficient data (markers) and full model predictions (grey lines) for hard backed absorbers composed of 1 mm thick plates, absorber thickness is around $L = 60$ mm. Spacings between the plates are $d_c = 1$ mm (a), $d_c = 3$ mm (b) and $d_c = 6$ mm (c). Absorption coefficient predictions for Helmholtz resonator of same size as the absorber is shown by dashed lines. Exact thickness value is given in each figure.

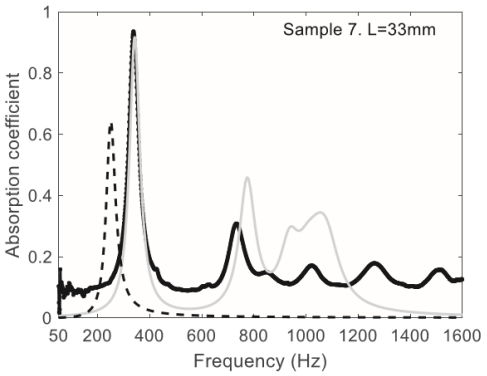

(a)

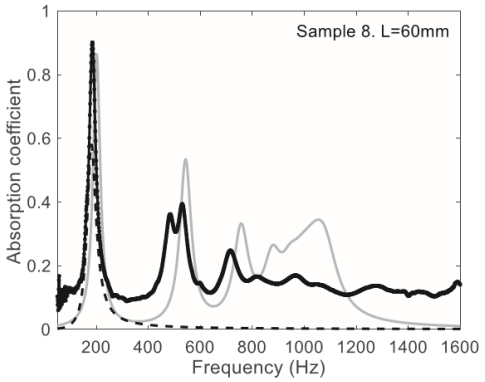

(b)

Fig. 4. Absorption coefficient data (markers) and full model predictions (grey lines) for hard backed absorber composed of 3 mm plates with spacings between the plates $d_c = 1$ mm, (a) - absorber thickness $L = 33$ mm, (b) – absorber thickness $L = 60$ mm (b). Absorption coefficient predictions for Helmholtz resonator of same size as the absorber is shown by dashed lines.

is observed for thicker samples, where measured f_r decreases from 185 Hz (Sample 8, thickness 60 mm, $\phi_w = 0.25$) to 131 Hz (Sample 5, thickness 58 mm, $\phi_w = 0.75$). The increase in the measured peak value of the absorption coefficient is more substantial in this case, from 0.9 to 0.99. To illustrate this dependence, the frequency of the first peak and the peak value of the absorption coefficient are plotted against cavity width d_c in Fig. 5a and b respectively for the absorbers with thickness made from the plates with thickness 1mm. The predictions of the full model are close to the approximate expressions (28) and (30) when the cavity width is not too small. In the latter case the characteristic frequency of air in the cavities f_{bc} is no longer small compared to the frequency of the first resonance, so the inertial regime assumed in the derivation of the approximate expressions is no longer valid. The theoretical values are in good agreement with the data for the peak value of the absorption coefficient. For the frequency of the first resonance, the disagreement is more substantial for Sample 5 and 6. The cause for disagreement for Sample 6 is discussed above. Part of the reason for disagreement between the data and the predictions for Sample 5 is the sample thickness which was 58 mm, not 60 mm as assumed in the model. If the comparisons are made for the same sample thicness, the disagreement in the frequency of the first resonance is 7% (see Table 2).

As demonstrated in Figs. 2–4, the first resonance peak of the pancake absorbers is always much higher than that of the Helmholtz resonator when the structures are compared with the same thickness. The resonance frequency f_r is lower for the pancake absorbers than that of the Helmholtz resonator for high pore wall porosity, see data for sample 1–6. However, for sample 7 with low wall porosity, the resonance of the metamaterial structure is observed at higher frequency than that of the Helmholtz resonator. Due to the presence of multiple cavities and coupling between them, multiple absorption peaks are achieved in the low frequency range for the metamaterial absorber when the cavity width exceeds the plate thickness

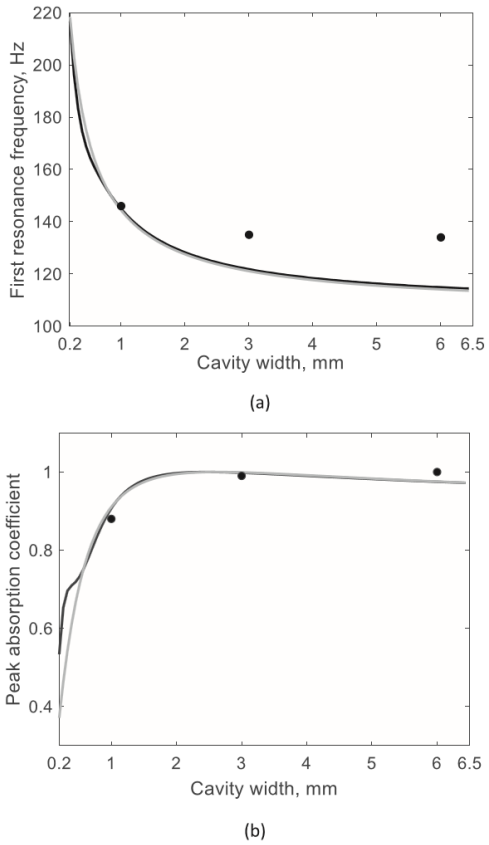

Fig. 5. Measurements (markers), full model predictions (black lines) and approximations given by Eqs. (28) and (30) (gray lines) for different cavity widths. Sample thickness in calculations is 60 mm, plate thickness 1 mm, radius of central perforation is 4 mm. (a) Frequency of the first resonance, (b) Absorption coefficient at resonance.

($d_c > d_p$), as can be seen in Figs. 2c and 3c. This makes metamaterial absorber advantageous over the Helmholtz resonator when multiple frequencies are required to be attenuated.

As follows from Fig. 2–4, the accuracy of the model worsens at higher frequencies, so the predictions of the frequency of the second resonance peak is inaccurate. This is because the assumption $Re(q)h \ll 1$ is only valid at low frequencies. Calculations of the wave speed for the sample with $d_p = 1$mm and $d_c = 3$mm give 46 m/s at 50 Hz decreasing slowly to 29 m/s at 1000 Hz. This means that at $Re(q)h = 0.5$ at 760 Hz and at higher frequencies the model is no longer applicable.

At high frequencies absorption coefficient is low for all samples. This is manifestation of a bandgap occurring due to quarter wavelength resonance of the cavities. Calculations of the wave speed in cavities show that, for the example considered above, this resonance happens around 950 Hz. However, $Re(q)h \approx 1$ at 1000 Hz, so the model predictions in this frequency range are not reliable.

Yet another contribution to discrepancies observed at frequencies higher than the first absorption peak can be explained by the interference of vibrational bandgaps as observed in [1]. According to [30] the first resonance frequency of thin circular plate with radius R and thickness d_p can be calculated as

$$f_{plate} = \frac{\lambda^2 d_p}{2\pi R^2}\sqrt{\frac{E}{12\rho(1-\nu)}}, \tag{31}$$

where E, ν and ρ are Young's modulus, Poisson ratio and density of plate material respectively. The value of constant λ^2 depends on the type of boundary conditions. So, $\lambda^2 = 10.2158$ for clamped circular plate and $\lambda^2 = 4.977$ for simply supported plate. Although the boundary conditions for the plate in the absorber are difficult to identify, we could assume that they

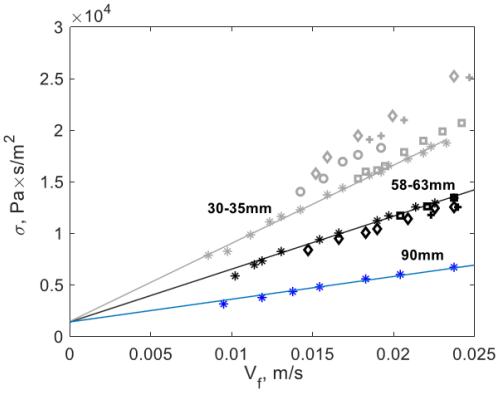

Fig. 6. Flow resistivity of the absorbers and the solid cylinders with central perforation for low flow rates, thicknesses 30–35 mm, 58–63 mm and 90 mm at low flow rates V_f. Stars – solid cylinders with central perforation, squares – 1mm cavities, crosses – 3 mm cavities, circles – 5 mm cavities, diamonds – 6 mm cavities, lines – linear fit for solid cylinders with central perforation.

are between "simply supported" and "clamped". For the aluminum plate with $R = 50$ mm and $d_p = 1$ mm $f_{plate} = 495.9$ Hz for the simply supported plate and $f_{plate} = 1011.6$ Hz for clamped plate. Moreover the material can also be considered as a periodic array of vibrating plate, then a second stop band effect (a vibrational bandgap effect) can occur around the first structural resonance frequency of the plate. This confirms that the plate resonances might contribute to discrepancies between the model and experiments for frequencies higher than the first absorption peak, as observed in Figs. 2 and 3. For thicker plates, the resonance frequencies are higher. However, the disagreement between the model and the measurements for the absorbers comprised of plates with $d_p = 3$ mm is still considerable for frequencies above the first resonance, as shown in Fig. 4. This is apparently due to breaking the low frequency approximation, as explained above.

It could be concluded, that the model developed accurately predicts the absorber behavior at low frequencies. In general, the first absorption peak frequency for the tested absorbers is much higher than that for the corresponding Helmholtz resonator. In addition, the tested structures have several absorption peaks in the frequency range below the bandgap and hence much broader absorption band than the Helmholtz resonators.

3. Flow resistivity measurements and determination of Forchheimer's nonlineariy parameter

Flow resistivity was measured for samples 1-6 (Table 2) to investigate its dependence on the sizes of the lateral cavities. In addition, a 30 mm thick sample with 5 mm cavities, i.e. $d_c = 5$ mm, was constructed and measured. We also measured flow resistivity of three solid cylindrical samples with thicknesses $L = 30$, 60 and 90 mm, an outer radius $R = 50$ mm, all having central perforation of radius $r_0 = 4$ mm.

The flow resistivity measurements have been performed at low flow rates in the laminar regime (inside the rig tube) using University of Salford measurement rig described by Turo in [31]. The rig was fitted with a tube having radius 50 mm in order to fit the samples. According to BS EN29053 [32] a flow rate of 0.5 mm/s is recommended, however the lowest we could achieve was 10 mm/s. The static flow resistivity σ_0 has been determined measuring pressure drop along the sample ΔP at several flow rates V_f and using straight line interpolation at zero flow velocity, in accordance with Forchheimer's law [33]

$$\sigma(V_f) = \frac{\Delta P}{V_f L} = \sigma_0(1 + \xi V_f) \tag{32}$$

where ξ is Forcheimer's nonlinearity parameter. Static flow resistivity values for low flow rates were measured for all samples in the flow range $V_f \leq 3$ cm/s are shown in Fig. 6. Different markers are used for samples with different cavity widths and solid cylinders with the central perforation, as explained in Fig. 6 caption. Straight lines are the least squares approximations, according to Eq. (32), for solid cylinder samples. The experimental error was estimated around 2.5% and mostly due to inaccuracies of flow rate measurements. This resulted in regression error of intercept (static flow resistivity) and slope (Forchheimer's pameter) of about 10% for most samples.

The values of static flow resistivity σ_0 and Forchheimer's parameter ξ for all measured samples are given in Table 3. The theoretical value for the straight cylindrical pore with $r_0 = 4$mm calculated using expression given in Table 1 is 1405 $\frac{\text{Pa}\cdot\text{s}}{\text{m}^2}$. The values of static flow resistivity σ_0 for all measured samples were close (within 10% error margin) to that theoretical value, indicating weak influence of the cavities in $V_f \to 0$ limit. The thickness of the sample has little influence on σ_0.

Table 3
Measured static flow resistivity σ_0 and Forchheimer's parameter ξ for all samples.

L, mm	d_p, mm	d_c, mm	σ_0, $\frac{\text{Pa s}}{\text{m}^2}$	ξ, $\frac{\text{s}}{\text{m}}$
31	1	1	1482.5	529.8
30	1	3	1471.2	642.6
30	1	5	1505.9	592.1
35	1	6	1414.5	710.6
30	Circular	orifice	1481.0	511.1
60	1	1	1422.5	360.2
58	1	3	1541.6	297.8
63	1	6	1456.2	327.1
60	Circular	orifice	1449.4	346.9
90	Circular	orifice	1425.8	154.4

The weak dependence of the static flow resistivity on the presence of the cavities confirms the high permeability contrast between the two porosity scales mentioned in Section 2.3 and the use of Eq. (5) for the effective density.

Forchheimer's parameter values for our samples are much higher than those measured before for conventional porous materials. For instance, the Forchheimer's parameter value for lead shot and gravel reported in [13] were 3.70 s/m and 4.06 s/m and did not depend on the thickness of the sample. Some values we measured are two orders of magnitude higher than that. This difference is due to a very low surface porosity $\phi_p = 6.4 \times 10^{-3}$ of our samples and hence high flow velocity inside the perforation $U = \frac{V_f}{\phi_p}$ and the large pore scale Reynolds number $Re = \frac{2r_0 U \rho_0}{\eta} = \frac{2r_0 V_f \rho_0}{\phi_p \eta}$ achieved even at moderate flow rates V_f inside the rig. In fact, for $V_f = 0.01 \frac{\text{m}}{\text{s}}$, pore scale Reynold's number is $Re = 829$. For the samples with close thickness, measured values of Forchheimer's parameters are also close to each other. However, a clear trend was observed, that Forchheimer's parameter values are higher for thinner samples. For samples with the thickness in the range $30 - 35$ mm, the range of Forchheimer's parameter values is $511.1 - 710.6 \frac{\text{s}}{\text{m}}$. For those with thickness $58 - 63$ mm, Forchheimer's parameter range is $297.8 - 360.2 \frac{\text{s}}{\text{m}}$. And, finally, for the sample with thickness $L = 90$ mm, measured Forchheimer's parameter is $154.4 \frac{\text{s}}{\text{m}}$.

The dependence of the Forchheimer's parameter on the thickness of the sample could be explained empirically, if we consider the extra losses at the entrance and the exit of the sample as suggested by Astarita and Greco [34] and Oliveira and Pinho [35]. Following [34], the pressure drop through the sample $\Delta P = p_{ent} - P_0$, where p_{ent} and P_0 are pressure values some distance upstream and downstream of the sample, where the end effects are negligible, could be decomposed in the following way $\Delta P = (p_{ent} - p_a) + (p_a - p_b) + (p_b - P_0)$. Here p_a and p_b are pressure at the positions a and b inside the pore, where the flow is fully developed. The excess pressure drops $\Delta p_1 = p_{ent} - p_a$ and $\Delta p_2 = p_b - P_0$ are due to sudden changes in the tube aperture at the entrance and the exit of the sample. They consist of the reversible pressure decrease and increase attributable to Bernoulli effects due to change in velocity. As $\phi_p \ll 1$, it can be assumed that the net effect of these pressure drops is zero. There are also irreversible pressure drops which happen when the fluid accelerates and decelerates creating recirculation zone [35]. For large Reynolds numbers the main contribution to these pressure drops is proportional to V_f^2, (see Fig. 9a in [35] and Fig. 4 in [34], so that the combined effect can be described as $(p_{ent} - p_a) + (p_b - P_0) = AV_f^2$, where A is some coefficient.

This means that the contributions of the end effects to the measured flow resistivity value could be approximated as:

$$\sigma(V_f) = \frac{\Delta P}{V_f L} \approx \frac{AV_f}{L} + \sigma_{tube}(V_f) \tag{32'}$$

where $\sigma_{tube}(V_f) = \frac{(p_a - p_b)}{V_f L}$ is the flow resistivity value in case of infinite tube and no end effects and $\frac{AV_f}{L}$ is the contribution of the extra losses occurring in the regions of sudden contraction and sudden expansion. Comparisons between (32) and (32') allow us to conclude that the excess pressure drops in the flow through sudden contraction and expansion contributes to the gradient of $\sigma(V_f)$, i.e. Forchheimer's parameter. Moreover, the appearance of the sample thickness L in denominator of the first term in (32') explains the stronger influence of the end effects on the Forchheimer's parameter value of shorter samples.

A similar trend, showing higher flow resistivity values and higher $\sigma(V_f)$ gradients for shorter samples, is observed for higher flow rates. Fig. 7, a shows flow resistivity dependence on the flow rate for $0.05 \frac{\text{m}}{\text{s}} \le V_f \le 0.25 \frac{\text{m}}{\text{s}}$ (pore scale Reynolds number range $4000 \le Re \le 20718$) for samples 1, 2 and 4, 5 from Table 2. According to Landau and Lifshitz [36], p.177 this corresponds to turbulent flow regime of air in the pore. Flow resistivity of samples 1 and 4 with thicknesses close to 30 mm are much higher than those of 2 and 5 with thicknesses close to 60 mm in the whole range of flow rates. Alongside with the measured results, predictions of flow resistivity $\sigma_{tube}(V_f)$ in the turbulent regime is plotted. It is given in the implicit

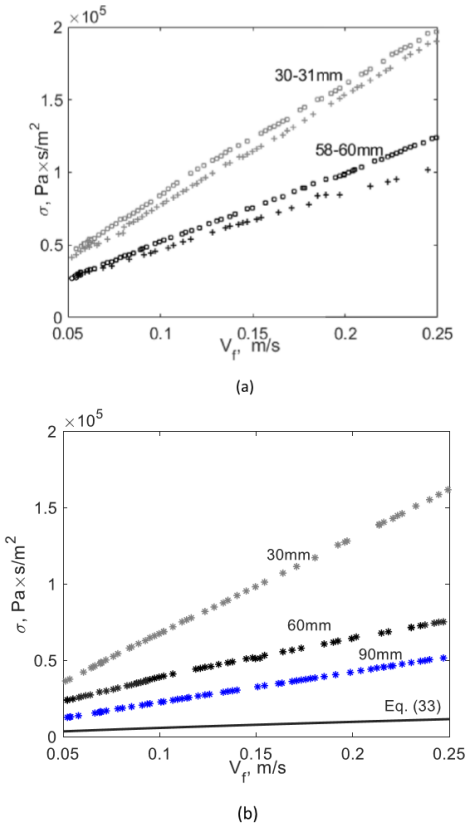

Fig. 7. Flow resistivity of the absorbers (a) and solid cylinders with the central perforation (b) for high flow rates. Crosses – 3 mm cavities, squares - 1 mm cavities, stars – solid cylinders with central perforation, line – flow resistivity of the tube as predicted by Eq. (33).

form by Eqs. (43.4) and (43.5) from [36]. These equations were combined to give dependence $\sigma_{tube}(V_f)$ as

$$\sigma_{tube}(V_f) = \frac{\rho_0 V_f}{4 r_0 \phi_p^2}\left(0.44 \ln\left(\frac{16 r_0^3 \rho_0 V_f}{\eta^2}\sigma_{tube}(V_f)\right) - 0.85\right)^{-2}. \tag{33}$$

This equation does not account for any end effects and considers losses within the pore only. In Fig. 7b these results are compared with the data for flow resistivity of three cylinders with the central perforation, with thickness 30 mm, 60 mm and 90 mm. For thicker samples the flow resistivity is lower, staying however much higher than predictions of Eq. (33), presumably due to the end effects. It is also noted by comparing Fig. 7a and b, that for the high flow rates, the flow resistivity of the absorbers is significantly higher than that of the cylinders with central perforation. This means, that although the presence of cavities has little effect on the flow resistivity measured at conventional i.e. low flow rates (Fig. 6), this is not the case for high flow rates. However, there is relatively little difference between the data for samples with 1mm and 3 mm cavities (squares and crosses in Fig. 7a) and this difference is more noticeable for longer samples. This is to be expected as the contribution of end effects to flow resistivity values is stronger for shorter samples (see Eq. (32')) and hence the difference in flow conditions within the central pore is masked.

4. Absorber in the nonlinear regime – model and its experimental validation

4.1. Model

Here we follow an approach adopted in previous studies of porous absorbers' interactions with high amplitude sound, see for example [6,10,13]. This means, that the only source of nonlinearity is the empirically introduced dependence of flow

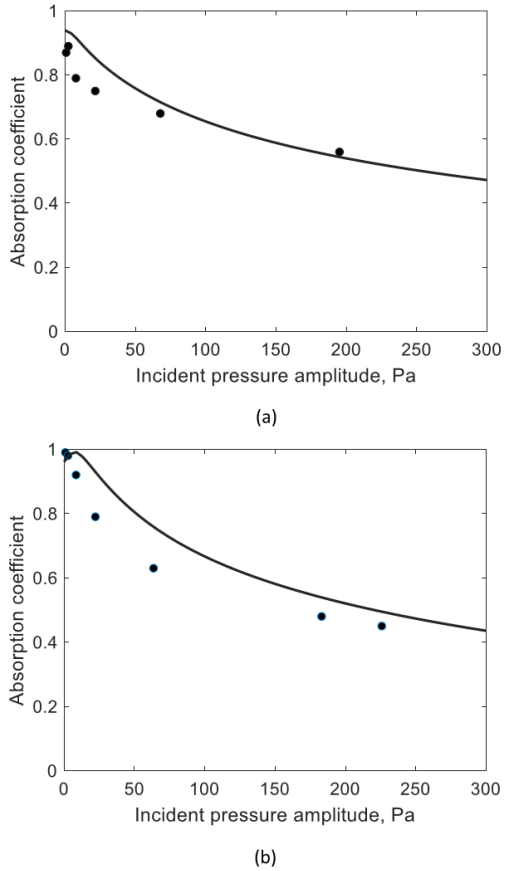

Fig. 8. Measurements (markers) and nonlinear model (Eqs. (37), (38) and (43), (44)) predictions (lines) for the first absorption coefficient peak variations with incident pressure amplitude. (a) Sample 1, thickness 31 mm (b) Sample 2, thickness 30 mm. Measurement points are shown for experimental peak frequencies $f_r^{(1)}$, while numerical results are shown for frequencies $f_r^{(2)}$ predicted by the model, given in Table 2. Sample dimensions are given in Table 2.

resistivity of particle velocity v of sound in the pores, $\sigma(v)$. In previous studies, this dependence is approximated by the linear relationship $\sigma(v) = \sigma_0(1 + \xi\phi_p|v|)$, which is similar to (32) with $V_f = \phi_p v$. It was also postulated that the parameter of nonlinearity, ξ, can be measured in static flow resistivity tests. However, the characteristic feature of our samples is that the Forchheimer's parameter depends on the thickness of the sample and on the size of the cavities. For this reason, in the model a measured dependence of the flow resistivity on flow velocity $\sigma(\phi_p|v|)$ was used, for each sample, instead of a single linear approximation. This was combined with Eqs. (5) and (14) to result in the following particle velocity dependent effective density of fluid in the pore ($\alpha_{\infty\ p} = 1$)

$$\rho(\omega,\ v) = \rho_0 \left(1 + \frac{\sigma(\phi_p|v|)}{-i\omega\rho_0} \sqrt{1 + \frac{-4i\omega\rho_0\eta}{\Lambda^2\sigma(\phi_p|v|)^2}}\right). \tag{34}$$

It was shown in the previous section, that for low intensity sound, the inertial regime approximation $\omega \gg \omega_{bp}$ is valid around the frequency of the first resonance. In the nonlinear regime this assumption is no longer valid as the frequency ω_{bp} has a quadratic dependence on flow resistivity, $\omega_{b\ p} = \frac{\sigma(\phi_p|v|)^2\Lambda^2}{4\rho_0\eta}$, and consequently could attain very high values at high amplitudes. Assuming harmonic excitation, we start with the usual momentum and mass conservation equations for the equivalent fluid saturated the material

$$-i\omega\rho(\omega, v)v = -\frac{\partial p}{\partial x}, \tag{35}$$

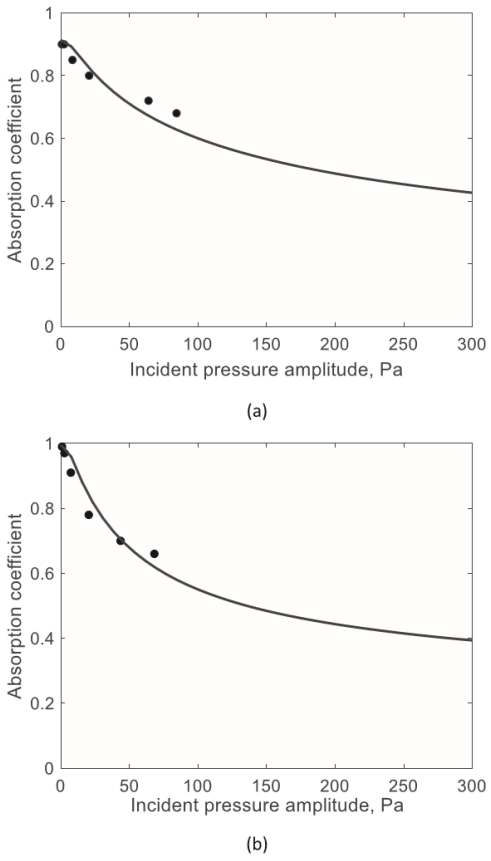

Fig. 9. Measurements (markers) and nonlinear model (Eqs. (37), (38) and (43), (44)) predictions (lines) for the first absorption coefficient peak variations with incident pressure amplitude. (a) Sample 4 thickness 60 mm (b) Sample 5, thickness 58 mm. Measurement points are shown for experimental peak frequencies $f_r^{(1)}$, while numerical results are shown for frequencies $f_r^{(2)}$ predicted by the model, given in Table 2. Sample dimensions are given in Table 2.

$$-i\omega C(\omega)v = -\frac{\partial v}{\partial x}. \tag{36}$$

Effective compressibility $C(\omega)$ remains unaffected by the nonlinearity and is defined by Eq. (6). The aim now is to derive equations which eventually enable us to get the dependence of the surface admittance of the sample as a function of the incident wave pressure amplitude p_i. This approach is similar to that used in [6] and [10]. First, we introduce a dimensionless spatial variable $X = \frac{x}{L}$, where L is the thickness of the sample. This way, the surface of the sample corresponds to $X = 0$ and its backing to $X = 1$. Then the equations for the normalised impedance $Z(X) = \frac{1}{\rho_0 c}\frac{p(X)}{v(X)}$ and the normalised particle velocity $V(X) = v(X)\frac{\rho_0 c}{p_i}$, are derived

$$Z' = +ikL\left(\tilde{\rho}\left(\omega, V, \xi\frac{p_i}{\rho_0 c}\right) - \tilde{C}(\omega)Z^2\right), \tag{37}$$

$$V' = ikL\,\tilde{C}(\omega)VZ. \tag{38}$$

Here

$$\tilde{C}(\omega) = \frac{C(\omega)}{C_0}, \tag{39}$$

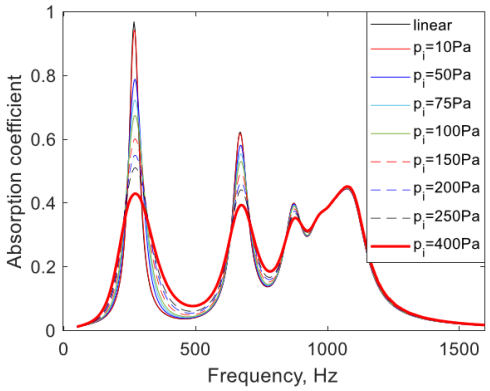

Fig. 10. Model predictions for the absorption coefficent dependence on frequency at different values of incident presure amplitude p_i. Sample 1.

$$\tilde{\rho}\left(\omega, V, \xi \frac{p_i}{\rho_0 c}\right) = \frac{\rho\left(\omega, V, \xi \frac{p_i}{\rho_0 c}\right)}{\rho_0} = 1 + \frac{\sigma\left(\phi_p \frac{p_i}{\rho_0 c}|V|\right)}{-i\omega\rho_0} \sqrt{1 + \frac{-4i\omega\rho_0\eta}{\sigma^2\left(\phi_p \frac{p_i}{\rho_0 c}|V|\right)\Lambda^2}}. \tag{40}$$

Prime stands for the derivative with respect to X. The Riccati Eq. (37) for $Z(X)$ is similar to Eq. (20) from [6], while the scaling function for $\tilde{\rho}(\omega, V, \xi \frac{p_i}{\rho_0 c})$ resulting from (34) is different from their Eq. (18).

The boundary conditions relating particle velocity v and the admittance G at the surface of the sample $X = 0$ is derived from the conditions of velocity and pressure continuity i.e

$$1 - \frac{p_r}{p_i} = \phi_p V(0), \tag{41}$$

$$1 + \frac{p_r}{p_i} = V(0)Z(0). \tag{42}$$

Eliminating reflected pressure amplitude p_r, the dependence of particle velocity $v(0)$ and the normalised surface impedance of fluid in the pore $Z(0)$ on the incident pressure amplitude p_i is obtained

$$V(0) = \frac{2}{\phi_p + Z(0)}. \tag{43}$$

The second boundary condition is applied at the hard backing of the sample

$$V(1) = 0. \tag{44}$$

Hence, the surface impedance $\frac{Z(0)}{\phi_p}$ of the sample and consequently its absorption coefficient could be found from the solution of Eqs. (37) and (38) with boundary conditions (43) and (44). These values depend on the amplitude of the incident pressure p_i, as it determines the strength of nonlinearity present in Eq. (37). If $p_i = 0$, the solution of the linear model obtained in the previous sections can be recovered.

The equations are solved numerically using the following method. First, the analytical solutions of Eqs. (37) and (38) with boundary conditions (43) and (44), $V_1(X)$ and $Z_1(X)$ are found, assuming $p_i = 0$ and hence no nonlinearity. Then, $V_1(X)$ is substituted in Eq. (37) and the next iteration of the impedance, $Z_2(X)$ is obtained by numerically solving this equation with boundary condition (43) in the form $Z_2(0) = \frac{2}{V_1(0)} - \phi_p$. $Z_2(X)$, in turn, is substituted in Eq. (38), which is solved numerically to obtain $V_2(X)$, with boundary condition (44) $V_2(1) = 0$. The procedure is repeated and stopped only when the difference between two successive iterations of the absorption coefficient is less than 5% in the whole range of p_i values. In the measured frequency range and for $p_i \leq 250250$ Pa, 15 or less iterations is enough to achieve the required accuracy.

4.2. Experiments and model validation

The measurements for high amplitude sound have been performed using a specially designed impedance tube at the ISAT, University of Burgundy, France. Sine wave excitation has been used for a better control over the amplitude of the incident wave. For the usual white noise excitation, there is no guarantee that each frequency component has the same amplitude. The measurements have been performed at the frequency of the absorption coefficient peaks for samples 1, 2, 4 and 5 (Table 1). To obtain the dependence of the peak absorption coefficent on the amplitude of incident wave, the following

procedure has been followed. The surface impedance measurements have been performed for each voltage applied. Two microphone method has been used with the microphones positioned at the distances 100 mm and 150 mm in front of the sample. Additionally, the amplitude of pressure $|p| = P_i(e^{-ikd_0} + Re^{ikd_0})$ has been measured at the distance $d_0 = 50$ mm in front of the sample. The value of the reflection coefficient R has been calculated from the measured surface impedance and then incident pressure amplitude has been calculated as $p_i = \frac{|p|}{e^{-ikd_0}+Re^{ikd_0}}$ for each measurements. For Samples 1 and 2 the measurements have been performed for p_i values in the range of up to 300 Pa. However, for longer samples the range of measured p_i was lower due to limitations of the equipment.

The comparisons between the measured and predicted by nonlinear model dependence of the absorption coefficient at the first peak are shown in Fig. 8a, b for Samples 1 and 2 and in Fig. 9a, b for Samples 4 and 5. It should be noted, that the comparisons have been performed at peak frequencies according to measurements and predictions for low amplitude data, shown in Table 2. For instance for Sample 5, the data points shown in Fig. 8b correspond to frequency $f_r^{(1)} = 135$ Hz, while model predictions have been calculated for predicted peak frequency $f_r^{(2)} = 125$ Hz

To illustrate how the increase of the incident wave amplitude affects the overall shape of the absorption curve, equations have been solved for different frequencies assuming that each frequency component has the same amplitude for $p_i = 0.01$ Pa (linear case) and several increasing values up to $p_i = 400$ Pa. The results are shown in Fig. 10 for Sample 1. The effect of nonlinearity does not significantly change the frequency of the first resonance, while the peak absorption coefficient values are strongly decreased.

5. Conclusions

An absorbing structure comprising of periodically arranged metallic plates separated by air cavities and with a central perforation traversing the periodic structure, was built and tested in both linear and nonlinear regimes.

New models for the linear and the nonlinear acoustic behaviours of this structure were proposed, together with absorption coefficient measurements in the linear regime, flow resistivity and Forcheimer nonlinearity parameter measurements at high flow rates and finally absorption coefficient measurements in the nonlinear regime.

The results of measurements were compared with the models – the analytical linear model and a numerical model accounting for Forchheimer's type nonlinearity.

A good agreement was demonstrated between the model and the absorption coefficient data in the linear regime, i.e. for low levels of the incident sound, and at low frequencies. Simple expressions have been derived that adequately describe the frequency of the first peak and the peak absorption coefficient value.

With carefull choice of parameters for this absorbing structure, an absorption peak at much lower frequency and higher peak value than that provided by a Helmholtz resonator of same thickness and diameter could be achieved. Furthermore, this absorber can provide higher frequency absorption peaks and a broader absorption range.

Flow resistivity measurements for a range of flow velocities were carried out for the absorbers. Typical value of the Forcheimer non linearity parameter were obtained, which is high relative to porous and granular materials so that strong nonlinear effects could be expected for the absorber.

A dependence of flow resistivity on the sample thickness for high flow rates was observed with higher values achieved for shorter samples. A qualitative explanation was given for this behaviour. In the nonlinear model, a measured value of Forcheimer parameter was used for each absorber sample.

It was shown that the absorption peak frequencies weakly depend on the incident pressure amplitude, while the peak values are strongly attenuated as incident pressure grows. This means, that the linear model will overestimate the absorption capacity of the structure, if the latter is used for high sound pressure levels. The new numerical model accounting for Forchheimer's nonlinearity adequately describes the effects observed.

The results of this work will be useful when designing absorbers of tonal sounds for applications in the environments where high sound pressure levels are achieved. Future work will concentrate on the optimum design of the pancake structure allowing perfect absorption at the desired frequency or frequencies. Reducing the number of interstitial walls inside the pancake absorber will eventually lead to Helmholtz resonator while doing the opposite will lead to a quarter wavelength circular cavity. The resonance frequencies associated with these structures are well known. The first resonance frequency of the pancake absorber is lower than that of the Helmholtz resonator (not between that of the Helmholtz and that of the quarter wavelength cavity as expected). This means that the resonance frequency experiences a minimum depending on the number of interstitial walls. This observation shows the importance of optimizing the number of cavities and their sizes in the pancake structure.

Declaration of Competing Interest

The authors declare that they have no known competing financial interests or personal relationships that could have appeared to influence the work reported in this paper.

CRediT authorship contribution statement

Daniel C. Brooke: Conceptualization, Investigation, Methodology, Writing - original draft. **Olga Umnova:** Conceptualization, Methodology, Formal analysis, Supervision, Writing - original draft. **Philippe Leclaire:** Conceptualization, Supervision, Writing - original draft. **Thomas Dupont:** Methodology, Formal analysis, Writing - original draft.

Acknowledgement

The work was supported by DSTL UK through Anglo – French PhD Scheme.

References

[1] T. Dupont, P. Leclaire, R. Panneton, O. Umnova, A microstructure material design for low frequency sound absorption, Appl Acoust 136 (2018) 86–93.
[2] P. Leclaire, O. Umnova, T. Dupont, R. Panneton, Acoustical properties of air-saturated porous material with periodically distributed dead-end pores, J Acoust Soc Am 137 (2015) 1772–1782.
[3] J.P. Groby, W. Huang, A. Lardeau, Y. Auregan, The use of slow waves to design simple sound absorbing materials, J Appl Phys 117 (2014) 124903.
[4] S. Park, A Design method of micro-perforated panel absorber at high sound pressure environment in launcher fairings, J Sound Vib 332 (2012) 521–535.
[5] H.L. Kuntz, D.T. Blackstock, 'Attenuation of intense sinusoidal waves in air-saturated, bulk porous materials, J Acoust Soc Am 81 (1987) 1723–1731.
[6] D.K. Wilson, J.D. McIntosh, R.F. Lambert, Forchheimer-type nonlinearity for high intensity propagation of pure tones in air—saturated porous media, J Acoust Soc Am 84 (1988) 350–359.
[7] J.D. McIntosh, R.F. Lambert, Nonlinear wave propagation through rigid porous materials. I. Nonlinear parametrization and numerical solutions,, J Acoust Soc Am 88 (1990) 1939–1949.
[8] R.F. Lambert, J.D. McIntosh, Nonlinear wave propagation through rigid porous materials. II. Approximate analytical solutions, J Acoust Soc Am 88 (1990) 1950–1959.
[9] Y. Auregan, M. Pachebat, 'Measurement of the nonlinear behaviour of acoustical rigid porous materials, Phys Fluids 11 (1999) 1342–1345.
[10] O. Umnova, K. Attenborough, E. Stanley, A. Cummings, Behaviour of rigid-porous layers at high levels of continuous acoustic excitation: theory and experiment, J Acoust Soc Am 114 (2003) 1346–1356.
[11] O. Umnova, K. Attenborough, H.- Ch. Shin, A. Cummings, Response of multiple rigid porous layers to high levels of continuous acoustic excitation, J Acoust Soc Am 116 (2004) 703–712.
[12] B. Zhang, T. Chen, Y. Zhao, W. Zhang, J. Zhu, Numerical and analytical solutions for sound propagation and absorption in porous media at high sound pressure levels, J Acoust Soc Am 132 (2012) 1436–1449.
[13] O.Umnova D.Turo, Influence of Forchheimer's nonlinearity and transient effects on pulse propagation in air saturated rigid granular materials, J Acoust Soc Am 134 (2013) 4763–4774.
[14] L.J. Sivian, Acoustic impedance of small orifices, J Acoust Soc Am 7 (1935) 94–101.
[15] U. Ingard, H. Ising, Acoustic nonlinearity of an orifice, J Acoust Soc Am 42 (1967) 6–17.
[16] A. Cummings, W. Eversham, High amplitude acoustic transmission through duct terminations: theory, J Sound Vib 91 (1983) 503–518.
[17] A. Cummings, Acoustic nonlinearities and power losses at orifices, AIAA J 22 (1984) 786–792.
[18] V. Achilleos, O. Richoux, G. Theocaris, Coherent perfect absorption induced by nonlinearity of a Helmholtz resonator, J Acoust Soc Am 140 (2016) EL94.
[19] D.Y. Maa, Microperforated panel at high sound intensity, Internoise, Yokohama, Japan, 1994.
[20] R. Tayong, T. Dupont, P. Leclaire, On the variations of acoustic absorption peak with particle velocity in micro – perforated panels at high levels of excitaion, J Acoust Soc Am 127 (2010) 2875–2882.
[21] R. Tayong, T. Dupont, P. Leclaire, Experimental investigation of holes interaction effect on the sound absorption coefficient of micro - perforated panels under high and medium levels, J Appl Acoust 72 (2011) 777–784.
[22] D.L. Johnson, J. Koplik, R. Dashen, Theory of dynamic permeability and tortuosity in fluid – saturated porous media, J Fluid Mech 176 (1987) 379–402.
[23] Z. Laly, N. Atalla, S.- A. Meslioui, Acoustical modelling of micro – perforated panel at high sound pressure levels using equivalent fluid approach, J Sound Vib 427 (2018) 134–158.
[24] N. Atalla, F. Sgard, Modelling of perforated plates and screens using rigid frame porous models, J Sound Vib 303 (2007) 195–208.
[25] X. Olny, C. Boutin, Acoustic wave propagation in double porosity media, J Acoust Soc Am 114 (2003) 73–89.
[26] Y. Champoux, J.F. Allard, Dynamic tortuosity and bulk modulus in air saturated porous media, J Appl Phys 70 (1991) 1975–1979.
[27] D. Lafarge, P. Lemariner, J.F. Allard, V. Tarnow, Dynamic compressibility of air saturated porous structures at audible frequencies, J Acoust Soc Am 102 (1997) 1995–2006.
[28] M. Abramowitz, I.A. Stegun, in: Handbook of mathematical functions, National Bureau of Standards, Washington D. C., 1970, p. 360. eqs. 9.1.10-9.1.11.
[29] L.E. Kinsler, A.R. Frey, A.B. Coppens, J.V. Sanders, in: Fundamentals of Acoustics, Wiley, New York, 2000, p. 274.
[30] A.W. Leissa, in: Vibrations of plates", scientific and information division, NASA, Washington, 1969, pp. 8–9.
[31] D. Turo, A relaxation approach for time domain modelling of sound propagation in porous media PhD thesis, University of Salford, UK, 2011.
[32] BS EN 29053:1993, ISO 9053:1991 "Acoustics. Materials for acoustical applications. Determination of airflow resistance".
[33] P.H. Forchheimer, Wasserbewegung durch Boden, Z Ver Dtsch Ing 45 (1901) 1782–1788.
[34] G. Astavita, G. Greco, Excess pressure drop in laminar flow through sudden contraction. Newtonian liquids, Ind Eng Chem 7 (1968) 27–31.
[35] P.J. Oliveira, F.T. Pinho, Pressure drop coefficient of laminar Newtonian flow in axisymmetric sudden expansions, Int J Heat Fluid Flow 18 (1997) 518–529.
[36] L.D. Landau, E.M. Lifshitz, in: Fluid mechanics, Oxford, Pergamon, 1987, pp. 176–178. §43.